

AD-A073 468

DEFENSE ATOMIC SUPPORT AGENCY WASHINGTON DC

F/G 15/6

OPERATION UPSHOT-KNOTHOLE, NEVADA PROVING GROUNDS, MARCH - JUNE--ETC(U)

JUL 55 E V GALLAGHER, T H SCHIFFMAN

UNCLASSIFIED

DASA-WT-721

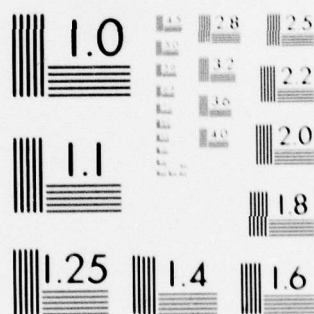
NL

1 OF 4

AD  
A073468







MICROCOPY RESOLUTION TEST CHART  
NATIONAL BUREAU OF STANDARDS-1963-A

UNCLASSIFIED

415987  
TECHNICAL LIBRARY

of the

ARMED FORCES  
SPECIAL WEAPONS PROJECT  
5 MAR 1956

WT-721

Copy No. 189 A

# Operation UPSHOT-KNOTHOLE

NEVADA PROVING GROUNDS

March - June 1953

Classification (Cancelled) changed to **UNCLASSIFIED**  
By Authority of DASASC-3 memo 17 Jan 62  
By Ref 101 Date 18 Jan 62

Project 3.1

TESTS ON THE LOADING  
OF BUILDING AND EQUIPMENT SHAPES

**DECLASSIFIED**  
**UNCLASSIFIED**  
This document contains information which is exempt from automatic declassification under E.O. 13526, 13527, and 13528. It is to be controlled, stored, handled, and disposed of in accordance with the provisions of E.O. 13526, 13527, and 13528. No person is to be denied access to this information on the basis of its classification.

HEADQUARTERS FIELD COMMAND, ARMED FORCES SPECIAL WEAPONS PROJECT  
SANDIA BASE, ALBUQUERQUE, NEW MEXICO

Statement A  
Approved for public release  
Distribution unlimited

**UNCLASSIFIED**

Pl...  
Approved for public release  
Distribution unlimited

DASA 47252

79 08 21 041

ADA073468

D12019,07

Incl A +

Information relative to this project may be found in  
the Annual Report of the National Science Foundation  
Washington, D. C.





**UNCLASSIFIED**

**CANCELED**  
**SECRET**

WT-721

This document consists of 370 pages  
No. 189 of 275 copies, Series A

## TESTS ON THE LOADING OF BUILDING AND EQUIPMENT SHAPES

by

E. V. Gallagher

and

T. H. Schiffman

July 1955

**CANCELED DATA**  
This document contains restricted data as  
defined by Executive Order 12958 of 1954.  
The disclosure of its  
contents in any manner to an unauthorized  
person is prohibited.

Statement A

Approved for public release;

Distribution unlimited.

Air Materiel Command  
Wright-Patterson Air Force Base  
Dayton, Ohio

**UNCLASSIFIED**

**SECRET**  
**CANCELED**

**CONFIDENTIAL**

## ABSTRACT

This report deals with pretest and post-test work on the Air Force Structures Test, Project 3.1, *Tests on the Loading of Building and Equipment Shapes*.

The test was designed to check and improve upon previously developed methods of predicting blast loadings on simple structures representative of targets of military interest. The specific test objectives dealt with the influence of certain geometric and blast parameters on the loading of solid structures (e.g., the effects of shock strength on building height, width, shielding, orientation, etc.). The test items consisted of a series of 17 cubical structures of reinforced concrete construction which were designed to rigidly withstand the effects of the blast. The structures were rather extensively instrumented with pressure gages and were included in both Shots 9 and 10. Most of the structures were located in the Mach reflection region on both shots; two structures were located in the regular reflection region of Shot 9 and in the precursor region of Shot 10.

Primary emphasis was placed on the study of diffraction phenomena since the pressure gage data were not expected to be sufficiently accurate to resolve the relatively small drag forces. A comparison between measured and predicted diffraction loads served to confirm certain aspects of the pretest load prediction methods and led to revisions of others. In the remaining instances the form of the data was inadequate to either confirm or revise the methods. This latter category includes those cases in which the test data clearly disagreed with predictions but was too sparse to warrant revision of the prediction scheme.

Experimental drag coefficients were computed on the basis of three different forms of the dynamic pressure-time variation: (1) the pretest predictions based on an approximate one-dimensional theory, (2) adjusted measurements obtained from Sandia q-gages, and (3) a post-test theoretical drag curve developed in Appendix B. The net drag coefficients (based on net impulse ratios) determined by the latter method are lower than those obtained from either of the other two methods but are still higher than the predicted constants.

A method is presented for predicting loadings on rectangular parallelepipeds in the precursor region. This empirically determined loading is based on data from a single structure of Shot 10, and the predicted loading may well vary considerably for other precursor shot conditions and for other building shapes. This report includes separate appendices which deal with precursor loadings, wave forms for dynamic pressure, and regular shock refraction theory.

## FOREWORD

This report is one of the reports presenting the results of the 78 projects participating in the Military Effects Tests Program of Operation UPSHOT-KNOTHOLE, which included 11 test detonations. For readers interested in other pertinent test information, reference is made to Report WT-782, Summary Report of the Technical Director, Military Effects Program. This summary report includes the following information of possible general interest:

1. An over-all description of each detonation, including yield, height of burst, ground zero location, time of detonation, ambient atmospheric conditions at detonation, etc., for the 11 shots.
2. Compilation and correlation of all project results on the basic measurements of blast and shock, thermal radiation, and nuclear radiation.
3. Compilation and correlation of the various project results on weapons effects.
4. A summary of each project, including objectives and results.
5. A complete listing of all reports covering the Military Effects Tests Program.



AD A 073468

DDC ACCESSION NUMBER

II
LEVEL

DATA SHEET

PHOTOGRAPH

THIS SHEET

1
INVENTORY

WT-721  
DOCUMENT IDENTIFICATION

<table border="1"><tr><td>DISTRIBUTION STATEMENT A</td></tr><tr><td>Approved for public release; Distribution Unlimited</td></tr></table>	DISTRIBUTION STATEMENT A	Approved for public release; Distribution Unlimited
DISTRIBUTION STATEMENT A		
Approved for public release; Distribution Unlimited		
DISTRIBUTION STATEMENT		

Accession For	
NTIS GRA&I	<input checked="" type="checkbox"/>
DDC TAB	<input type="checkbox"/>
Unannounced	<input type="checkbox"/>
Justification	
By	per Doc.
Distribution/	
Availability Codes	
Dist	Avail and/or special
A	

DISTRIBUTION STAMP

DDC RECEIVED SEP 5 1979 E
------------------------------------

DATE ACCESSIONED

79 08 21 041
--------------

DATE RECEIVED IN DDC

PHOTOGRAPH THIS COPY

## PREFACE

In a letter dated 12 March 1952, the Air Materiel Command (AMC) was requested by Air Research and Development Command to submit, for testing in Operation UPSHOT-KNOTHOLE, existing requirements for a structures program which would be based on the needs of the Air Force for target analysis and Indirect Bomb Damage Assessment information. Within the AMC the responsibility for designing and executing such a program was delegated to the Special Studies Office, Engineering Branch of the Installations Division. The requirements that were submitted and approved became part of Program 3 of the operation and were designated as Projects 3.1, 3.3, 3.4, 3.5, 3.6, and 3.26.1. B. J. O'Brien of the Special Studies Office was appointed Project Officer and, as such, coordinated and successfully directed the planning and operational phases of five of the six projects. Owing to the similarity in test objectives involving railroad equipment, the projects proposed by the Transportation Corps, U. S. Army, and the U. S. Air Force were combined into Project 3.6 with Lt Col Donald G. Dow, TC, USA, as Project Officer and B. J. O'Brien as Assistant Project Officer.

Armour Research Foundation of the Illinois Institute of Technology was awarded a contract to assist the Special Studies Office in planning and designing the experiments and analyzing and reporting of test results. During the period of planning, close liaison was maintained with other interested Air Force agencies, particularly the Physical Vulnerability Division, Directorate of Intelligence, Headquarters, USAF. Many valuable suggestions were contributed by Col John Weltman, USAF, Lt Col John Ault, USAF, R. G. Grassy, S. White, F. Genevise and others of that division and by Louis A. Nees, Chief, Engineering Branch, Installations Division, AMC.

Personnel of the Special Studies Section, who were intimately connected with the program, were Eric H. Wang, Chief, Special Studies Office, who was the technical and scientific monitor for the Air Force Program; Arthur Stansel; and Mrs. Maisie G. Ridgeway, secretary to Mr. Wang. Other members of the office who were associated with the program were R. R. Birukoff, P. A. Cooley, J. C. Noble, and Lt T. M. Murray and Lt G. A. Rockwell, USAF.

Most of the introduction section of this report was taken from the preface of the Preliminary Report, Operation UPSHOT-KNOTHOLE, Project 3.1 authored by Eric H. Wang and Bernard J. O'Brien.

The responsibility within the Air Force for execution of the six projects was transferred from the Special Studies Office, Installations Division, AMC to Blast Effects Research, Mechanics Branch, Aeronautical Research Laboratory, Wright Air Development Center, on 15 November 1954.

## ACKNOWLEDGMENTS

This report covers the activities of the Armour Research Foundation in connection with the Air Force Structures Program, Project 3.1 of Operation UPSHOT-KNOTHOLE. The work reported herein was sponsored by the Air Research and Development Command and performed for the Air Materiel Command (AMC), Wright-Patterson Air Force Base, Dayton, Ohio, under the terms of Air Force Contract No. AF33(038)30029. This program was technically monitored by the Special Studies Office of the Installations Division, AMC, now the Blast Effects Research Group, Wright Air Development Command.

Foundation personnel who have contributed to this report include D. Anderson, S. Ball, B. Briggs, R. L. Calvin, V. J. Cushing, D. Eastwood, S. J. Fraenkel, E. V. Gallagher, R. Heyman, E. Iwanski, F. B. Porzel, T. H. Schiffman, L. A. Schmidt, E. Sevin, A. Sherman, A. J. Smith, M. R. Smith, H. Ward, A. Wiederman, and M. Wolf. The body of the report was written by E. V. Gallagher and T. H. Schiffman; Appendix A was written by L. A. Schmidt; Appendix B was written by F. B. Porzel; Appendix C was written by T. H. Schiffman and A. Sherman. Mrs. M. R. Smith prepared the figures.

UNCLASSIFIED

UNCLASSIFIED



## CONTENTS

	Page
ABSTRACT . . . . .	3
FOREWORD . . . . .	5
PREFACE . . . . .	7
ACKNOWLEDGMENTS . . . . .	8
ILLUSTRATIONS . . . . .	12
TABLES . . . . .	21
CHAPTER 1 INTRODUCTION . . . . .	23
1.1 Purpose of Air Force Test Programs . . . . .	23
1.2 Specific Objectives . . . . .	24
1.3 Responsibilities . . . . .	25
1.4 Presentation . . . . .	26
CHAPTER 2 GENERAL DESCRIPTION OF TEST . . . . .	27
2.1 Test Items . . . . .	27
2.1.1 Test Site Layout . . . . .	27
2.2 Instrumentation . . . . .	30
2.2.1 General . . . . .	30
2.2.2 Air-pressure Measurements . . . . .	30
2.2.3 Instrument Records . . . . .	30
CHAPTER 3 PRETEST CONSIDERATIONS . . . . .	73
3.1 Introduction . . . . .	73
3.2 Terminology . . . . .	73
3.2.1 Terms Not Associated with Structures . . . . .	74
3.2.2 Terms Associated with Structures . . . . .	74
3.3 Description of Loading Phenomena . . . . .	75
3.3.1 Sources of Basic Information on Loading . . . . .	76
3.4 Discussion of Detailed Loading Predictions . . . . .	77
3.4.1 Shock Relations . . . . .	78
3.4.2 General Considerations for Loading Predictions . . . . .	79
3.4.3 Loadings on Structures 3.1a to c, e, f, i, s, and t . . . . .	79
3.4.4 Loadings on Elevated Structures 3.1o and p . . . . .	81
3.4.5 Loadings on Thin Wall Structures . . . . .	84

## CONTENTS (Continued)

	Page
3.4.6 Loadings on Oriented Structures 3.1g and h . . . . .	86
3.4.7 Loadings on Irregularly Shaped Rectangular Structure 3.1q . . . . .	89
3.4.8 Loading in Region of Regular Reflection, Structures 3.1s and t (Shot 9) . . . . .	91
 CHAPTER 4 POST-TEST ANALYSIS . . . . .	 116
4.1 Introduction . . . . .	116
4.1.1 Basic Pressure Curves . . . . .	116
4.1.2 Free Stream Pressure . . . . .	116
4.1.3 Side-on Pressure Curves . . . . .	117
4.1.4 Drag Pressure . . . . .	118
4.2 Discussion of Data and Forms for Presenting Results . . . . .	119
4.2.1 Records . . . . .	119
4.2.2 Individual Pressure-Time Records . . . . .	119
4.2.3 Comparison of SRI and BRL Check Gages . . . . .	120
4.2.4 Wave Duration . . . . .	121
4.2.5 Average Pressures on Surface . . . . .	121
4.2.6 Net Pressure Curves . . . . .	123
4.2.7 Average Pressures on Strips of Surfaces . . . . .	124
4.2.8 Graphical Comparisons Between Pretest Predictions and Experimental Average Pressures . . . . .	124
4.3 Criteria for Use in the Post-test Analysis . . . . .	124
4.4 Diffraction and Drag Phenomena . . . . .	125
4.4.1 Relief of Reflected Pressures on Upstream Surfaces . . . . .	125
4.4.2 Build-up of Pressure on Rear Surfaces . . . . .	125
4.4.3 Dimensionless Relief and Build-up Time As a Function of the Various Geometric Parameters . . . . .	126
4.4.4 Effect of Vortex Activity . . . . .	127
4.4.5 Drag Phase Loads and Net Loading . . . . .	129
4.5 Effects of Width . . . . .	130
4.5.1 Rear Surfaces . . . . .	131
4.5.2 Top Surfaces . . . . .	131
4.5.3 Princeton Shock Tube Comparisons . . . . .	132
4.5.4 Conclusions on Width Effects . . . . .	132
4.6 Effects of Length . . . . .	132
4.6.1 Rear Surfaces . . . . .	133
4.6.2 Loading on Top Surfaces . . . . .	133
4.6.3 Comparisons of Structure 3.1i (UPSHOT-KNOTHOLE) to Structure 3.3.8a (GREENHOUSE) . . . . .	134
4.6.4 Conclusions on Length Effects . . . . .	135
4.7 Size Effects . . . . .	135
4.7.1 Pressures on Scaled Structures . . . . .	135
4.7.2 Peaked Shock Effect . . . . .	135
4.7.3 Conclusions on Size Effects . . . . .	136
4.8 Effects of Orientation . . . . .	136
4.8.1 Variation of Peak Pressure on Obliquely Loaded Surfaces . . . . .	136
4.8.2 Impulses on Obliquely Loaded Surfaces . . . . .	136
4.8.3 Conclusions on Orientation Effects . . . . .	137
4.9 Effects of Shielding . . . . .	137
4.9.1 Comparison to Isolated Thin Walls—Assumptions Required To Obtain Net Loads . . . . .	138
4.9.2 Conclusions on Shielding Effects . . . . .	139

~~CONFIDENTIAL~~  
**UNCLASSIFIED**

## CONTENTS (Continued)

	Page
4.10 Effect of Elevation Above Ground (Ground Proximity)	139
4.10.1 Conclusions on Effects of Elevation Above Ground	139
4.11 Irregularly Shaped Rectangular Structure 3.1q	140
4.11.1 Relation Between Pretest and Post-test Analysis	140
4.11.2 Presentation of Data	141
4.11.3 Comparison of Individual Gages on the Same Surface	141
4.11.4 Comparison of Pretest Predictions to Pressure Records	141
4.11.5 Comparison with Shock Tube Results	142
4.11.6 Conclusions on Effects of Irregularly Shaped Rectangular Structure	143
4.12 Regular Reflection Effects, Structures 3.1s and t (Shot 9)	143
4.12.1 Conclusions on Regular Reflection Effects	143
4.13 Precursor Effects, Structures 3.1s and t (Shot 10)	143
4.13.1 Conclusions on Precursor Effects	145
4.14 Effects of Orientation Due to Differences Between Actual and Designated Ground Zeros	145
 CHAPTER 5 DEVELOPMENT OF INCREASED DRAG TRENDS	 250
5.1 Introduction	250
5.2 Net Loadings	251
5.3 Side-on Pressures	252
5.4 Drag Pressures	253
5.5 Drag Coefficients	255
5.6 Drag Impulse Coefficients and Total Impulse Ratio	256
5.7 Discussion of Results and Conclusions	258
 CHAPTER 6 SUMMARY AND CONCLUSIONS	 273
6.1 Test Items and Instrumentation	273
6.2 Pretest Predictions	274
6.3 Post-test Analysis	274
6.3.1 Width Effects	274
6.3.2 Length Effects	274
6.3.3 Size Effects	275
6.3.4 Orientation Effects	275
6.3.5 Shielding Effects	275
6.3.6 Effect of Elevation	275
6.3.7 Irregularities of Shapes, Cavities, Setbacks, Etc.	276
6.3.8 Regular Reflection Effects	276
6.3.9 Precursor Effects	276
6.3.10 Effects of Shock Strength	276
6.4 Increased Drag Trends	277
6.5 Precursor Theory	277
6.6 Wave Shape Theory	277
6.7 Regular Refraction Theory	278
6.8 General Conclusions	278
 APPENDIX A LOADING IN PRECURSOR REGION	 280
A.1 Introduction	280
A.2 Test Arrangement	280
A.3 Description of Test Results	281
A.3.1 Introduction	281

~~SECRET - RESTRICTED DATA~~  
**UNCLASSIFIED**



## CONTENTS (Continued)

	Page
A.3.2 Incident Blast Wave Pressures . . . . .	281
A.3.3 Pressure Records on Structure 3.1t . . . . .	282
A.3.4 Pressure Records on Structure 3.1s . . . . .	285
A.3.5 Possible Explanation of Phenomena . . . . .	286
A.4 Values of Drag Pressures Determined from Test Results . . . . .	290
A.4.1 Magnitudes of Drag Loadings . . . . .	290
A.4.2 Schematic Loading Method . . . . .	291
 APPENDIX B COMPARISON OF WAVE FORMS FOR STATIC AND DYNAMIC PRESSURES . . . . .	 319
B.1 Statement of the Problem . . . . .	319
B.1.1 Purpose . . . . .	319
B.1.2 Customary Procedure . . . . .	319
B.1.3 Plan of Attack . . . . .	320
B.2 Argument from Spherical Divergence . . . . .	321
B.3 Free Air Wave Forms from Machine Calculations . . . . .	322
B.3.1 Description . . . . .	322
B.3.2 Positive Duration . . . . .	322
B.3.3 Wave Forms . . . . .	322
B.3.4 Dynamic Pressure Impulse . . . . .	326
B.4 Applicability of Divergence Arguments . . . . .	327
B.4.1 Positive Duration . . . . .	327
B.4.2 Surface Conditions . . . . .	328
B.5 Conclusions . . . . .	328
 APPENDIX C REGULAR SHOCK REFRACTION THEORY . . . . .	 338
C.1 Introduction . . . . .	338
C.2 Boundary Conditions for the Basic Problem . . . . .	339
C.3 Basic Equations . . . . .	339
C.3.1 Shock Regimes . . . . .	339
C.3.2 Shock-Rarefaction Regimes . . . . .	340
C.3.3 Transition Between the Two Regimes . . . . .	340
C.3.4 Limiting Solutions for Head-on Reflection . . . . .	343
C.4 Engineering Approximations . . . . .	344
C.4.1 Three-shock Regimes . . . . .	344
C.4.2 Two-shock Rarefaction Regime . . . . .	348
C.5 Numerical Example: Oxygen-Nitrogen and Nitrogen-Oxygen Regular Refraction . . . . .	350
C.6 Application to UPSHOT-KNOTHOLE (Shot 9) . . . . .	352
 APPENDIX D SYMBOLS . . . . .	 361

## ILLUSTRATIONS

### CHAPTER 2 GENERAL DESCRIPTION OF TEST

2.1 Location of Structures at Test Site . . . . .	33
2.2 Location of Structures at Test Site . . . . .	34
2.3 Structures for Testing Shock Strength Effects (Shot 10 Only) . . . . .	35
2.4 Structures for Testing Width Effects . . . . .	35

~~SECRET~~  
**UNCLASSIFIED**

## ILLUSTRATIONS (Continued)

	Page
2.5 Structures for Testing Size Effects . . . . .	36
2.6 Structures for Testing Orientation Effects . . . . .	36
2.7 Structures for Testing Length Effects . . . . .	37
2.8 Structures for Testing Effects of Elevation . . . . .	37
2.9 Structures for Testing Shielding Effects . . . . .	38
2.10 Structures for Testing Re-entrant Corner Effects . . . . .	38
2.11 Photographs of Structures 3.1f (Above) and o (Below) . . . . .	39
2.12 Photographs of Structures 3.1m (Above) and q (Below) . . . . .	40
2.13 Structure 3.1a, Plan View and Rear Elevation . . . . .	41
2.14 Structure 3.1a, Front, Left, and Right Elevations . . . . .	42
2.15 Structure 3.1b, Plan View and Rear Elevation . . . . .	43
2.16 Structure 3.1c, Plan View and Front and Rear Elevations . . . . .	44
2.17 Structure 3.1d, Plan View and Side Elevation . . . . .	45
2.18 Structure 3.1d, Front and Rear Elevations . . . . .	46
2.19 Structure 3.1e, Plan View and Rear Elevation . . . . .	47
2.20 Structure 3.1e, Front Elevation . . . . .	48
2.21 Structure 3.1f, Plan View and Rear Elevation . . . . .	49
2.22 Structure 3.1f, Front Elevation . . . . .	50
2.23 Structure 3.1g, Plan View and Rear Elevation . . . . .	51
2.24 Structure 3.1g, Front, Left, and Right Elevations . . . . .	52
2.25 Structure 3.1h, Plan View and Rear Elevation . . . . .	53
2.26 Structure 3.1h, Front, Left, and Right Elevations . . . . .	54
2.27 Structure 3.1i, Plan View and Rear Elevation . . . . .	55
2.28 Structure 3.1i, Plan View and Side Elevation . . . . .	56
2.29 Structure 3.1i, Sections A-A and B-B . . . . .	57
2.30 Structure 3.1m, Plan View and Side Elevation . . . . .	58
2.31 Structure 3.1m, Sections A-A, B-B, and C-C . . . . .	59
2.32 Structure 3.1n, Plan View and Side Elevation . . . . .	60
2.33 Structure 3.1n, Sections A-A and B-B . . . . .	61
2.34 Structure 3.1o, Plan View and Side Elevation . . . . .	62
2.35 Structure 3.1o, Front and Rear Elevations and Section A-A . . . . .	63
2.36 Structure 3.1p, Plan View and Side Elevation . . . . .	64
2.37 Structure 3.1p, Front and Rear Elevations and Section A-A . . . . .	65
2.38 Structure 3.1q, Plan View and Front Elevation . . . . .	66
2.39 Structure 3.1q, Sections A-A, B-B, and C-C . . . . .	67
2.40 Structure 3.1q, Left and Rear Elevations . . . . .	68
2.41 Structure 3.1s, Plan View and Front Elevation . . . . .	69
2.42 Structure 3.1s, Right and Rear Elevations . . . . .	70
2.43 Structure 3.1t, Plan View and Front Elevation . . . . .	71
2.44 Structure 3.1t, Right and Rear Elevations . . . . .	72

### CHAPTER 3 PRETEST CONSIDERATIONS

3.1 Average Pressure on Front and Rear of Structures 3.1a to c, e, f, i, s, and t . . . . .	93
3.2 Average Pressure on Top of Structures 3.1a to c, e, f, i, s, and t . . . . .	93
3.3 Three-dimensional Effect of Pressure Build-up on Rear Surface . . . . .	94
3.4 Average Pressure on Front and Rear of Structure 3.1d and First Wall of Structure 3.1n . . . . .	94
3.5 Average Pressure on Front and Rear of Structures 3.1o and p . . . . .	95
3.6 Average Pressure on Top and Bottom of Structures 3.1o and p . . . . .	95
3.7 Analogy Between Flow Through Channel Contraction and Flow Under Elevated Structures . . . . .	96

UNCLASSIFIED

## ILLUSTRATIONS (Continued)

	Page
3.8 Average Pressure on Front and Rear of First Wall of Structure 3.11 . . . . .	97
3.9 Average Pressure on Front and Rear of Second Wall of Structure 3.11 . . . . .	97
3.10 Average Pressure on Front and Rear of First Wall of Structure 3.1m . . . . .	98
3.11 Average Pressure on Front and Rear of Second Wall of Structure 3.1m . . . . .	98
3.12 Average Pressure on Front and Rear of Second Wall of Structure 3.1n . . . . .	99
3.13 Geometry of Problem for Shock Loading Predictions on Block at Various Orientations . . . . .	99
3.14 Peak Pressure in Reduced Channel . . . . .	100
3.15 Drag Coefficient for Each Face Vs the Flow Direction Angle for Solid Rectangular Blocks Which Are Approximately Square in Plan . . . . .	101
3.16 Drag Coefficient for Each Face Vs the Flow Direction Angle for Solid Rectangular Blocks Which Are Not Square in Plan . . . . .	102
3.17 Diffraction Loading Predictions for Vertical Walls of Structures 3.1g and h . . . . .	103
3.18 Average Pressure on Top of Structures 3.1g and h . . . . .	103
3.19 Shock Entering True Re-entrant Corner . . . . .	104
3.20 Nomenclature for Structure 3.1q . . . . .	104
3.21 Average Pressure on Front Wall and Corner No. 1 of Structure 3.1q . . . . .	105
3.22 Average Pressure in Corner No. 2 of Structure 3.1q . . . . .	105
3.23 Average Pressure in Corner No. 3 of Structure 3.1q . . . . .	106
3.24 Average Vertical Pressure on Eaves of Structure 3.1q . . . . .	106
3.25 Initial Shock Wave Configuration . . . . .	107
3.26 Reflected Pressure As a Function of Shock Strength . . . . .	108
3.27 $\alpha_{ex}$ As a Function of Shock Strength . . . . .	109
3.28 Net Loading on Closed Buildings in Regular Reflection Region and Mach Reflection Region . . . . .	110
3.29 Velocity of Shock Front Vs Overpressure ( $P_0 = 14.7$ Psi) . . . . .	111
3.30 Pressures $p_r$ , $p_1$ , and $p_2$ Vs Overpressure for Closed Buildings ( $P_0 = 14.7$ Psi) . . . . .	112
3.31 $p_4$ Vs Overpressure Closed Buildings ( $P_0 = 14.7$ Psi) . . . . .	113
3.32 Drag Pressure As a Function of Shock Strength . . . . .	114
3.33 The Quantity, $t_b/h$ , Vs Overpressure ( $P_0 = 14.7$ Psi) . . . . .	115

### CHAPTER 4 POST-TEST ANALYSIS

4.1 Free Stream Gages at Ground Level, Shot 9 . . . . .	147
4.2 Free Stream Gages at Various Elevations, Shot 9 . . . . .	148
4.3 Free Stream Gages at Ground, Shot 10 . . . . .	149
4.4 Average of Free Stream Gages, Shot 9 . . . . .	150
4.5 Peak Pressure Vs Distance from Ground Zero, Shot 9 . . . . .	151
4.6 Peak Pressure Vs Distance from Ground Zero, Shot 10 . . . . .	151
4.7 Peak Side-on Pressure Vs Arc Distance from Blast Line for Various Gages . . . . .	152
4.8 Free Stream Dynamic Pressure, Shot 9 . . . . .	153
4.9 Free Stream Dynamic Pressure, Shot 10 . . . . .	153
4.10 Individual Gage Records, Structure 3.1a, Front Surface, Shot 9 . . . . .	154
4.11 Individual Gage Records, Structure 3.1a, Front Surface, Shot 9 . . . . .	154
4.12 Individual Gage Records, Structure 3.1a, Front Surface, Shot 10 . . . . .	155
4.13 Individual Gage Records, Structure 3.1a, Top Surface, Shot 9 . . . . .	155
4.14 Individual Gage Records, Structure 3.1a, Rear Surface, Shot 9 . . . . .	156
4.15 Individual Gage Records, Structure 3.1c, Front Surface, Shot 9 . . . . .	156
4.16 Individual Gage Records, Structure 3.1c, Top Surface, Shot 9 . . . . .	157

**UNCLASSIFIED**



## ILLUSTRATIONS (Continued)

	Page
4.17 Individual Gage Records, Structure 3.1c, Rear Surface, Shot 9 . . . . .	157
4.18 Comparison of SRI and BRL Check Gages, Structure 3.1a, Gages 1 and 1a, Shot 9 . . . . .	158
4.19 Comparison of SRI and BRL Check Gages, Structure 3.1a, Gages 8 and 8a, Shot 9 . . . . .	158
4.20 Comparison of SRI and BRL Check Gages, Structure 3.1a, Gages 8 and 8a, Shot 10 . . . . .	158
4.21 Comparison of SRI and BRL Check Gages, Structure 3.1a, Gages 17 and 17a, Shot 9 . . . . .	159
4.22 Comparison of SRI and BRL Check Gages, Structure 3.1e, Gages 5 and 5a, Shot 9 . . . . .	159
4.23 Comparison of SRI and BRL Check Gages, Structure 3.1e, Gages 5 and 5a, Shot 10 . . . . .	159
4.24 Comparison of SRI and BRL Check Gages, Structure 3.1g, Gages 11 and 11a, Shot 10 . . . . .	160
4.25 Average Pressure on Front Surfaces, Structures 3.1a, c, d, and g, Shot 9 . . . . .	160
4.26 Average Pressure on Top Surfaces, Structures 3.1a to c and e to i, Shot 9 . . . . .	161
4.27 Average Pressure on Rear Surfaces, Structures 3.1a to e, i, and o, Shot 9 . . . . .	161
4.28 Average Pressure on Front Surfaces, Structures 3.1a, c, d, and f to h, Shot 10 . . . . .	161
4.29 Average Front, Rear, and Net Pressures, Structure 3.1a, Shot 9 . . . . .	162
4.30 Average Front, Rear, and Net Pressures, Structure 3.1a, Shot 10 . . . . .	162
4.31 Average Front, Rear, and Net Pressures, Structure 3.1c, Shot 9 . . . . .	163
4.32 Average Front, Rear, and Net Pressures, Structure 3.1c, Shot 10 . . . . .	163
4.33 Average Front, Rear, and Net Pressures, Structure 3.1d, Shot 9 . . . . .	164
4.34 Average Front, Rear, and Net Pressures, Structure 3.1d, Shot 10 . . . . .	164
4.35 Average Front, Rear, and Net Pressures, Structure 3.1e, Shot 9 . . . . .	165
4.36 Average Front, Rear, and Net Pressures, Structure 3.1e, Shot 10 . . . . .	165
4.37 Average Front, Rear, and Net Pressures, Structure 3.1f, Shot 9 . . . . .	166
4.38 Average Front, Rear, and Net Pressures, Structure 3.1f, Shot 10 . . . . .	166
4.39 Average Front, Rear, and Net Pressures, Structure 3.1g, Shot 9 . . . . .	167
4.40 Average Front, Rear, and Net Pressures, Structure 3.1g, Shot 10 . . . . .	167
4.41 Average Front, Rear, and Net Pressures, Structure 3.1h, Shot 10 . . . . .	168
4.42 Average Front, Rear, and Net Pressures, Structure 3.1o, Shot 10 . . . . .	168
4.43 Average Front, Rear, and Net Pressures, Structure 3.1p, Shot 9 . . . . .	169
4.44 Average Front, Rear, and Net Pressures, Structure 3.1p, Shot 10 . . . . .	169
4.45 Average Front, Rear, and Net Pressures, Structure 3.1s, Shot 9 . . . . .	170
4.46 Average Front, Rear, and Net Pressures, Structure 3.1s, Shot 9 . . . . .	170
4.47 Average Front, Rear, and Net Pressures, Structure 3.1t, Shot 9 . . . . .	171
4.48 Average Front, Rear, and Net Pressures, Structure 3.1t, Shot 9 . . . . .	171
4.49 Net Average Pressure, Structure 3.1i, Shielding Wall, Shot 9 . . . . .	172
4.50 Net Average Pressure, Structure 3.1n, Shielding Wall, Shot 9 . . . . .	172
4.51 Net Average Pressure, Structure 3.1i, Shielded Wall, Shot 9 . . . . .	173
4.52 Net Average Pressure, Structure 3.1m, Shielded Wall, Shot 9 . . . . .	173
4.53 Net Average Pressure, Structure 3.1d, Shot 9 . . . . .	174
4.54 Net Average Pressure, Structure 3.1i, Shielding Wall, Shot 9 . . . . .	174
4.55 Net Average Pressure, Structure 3.1m, Shielding Wall, Shot 9 . . . . .	175
4.56 Net Average Pressure, Structure 3.1i, Shielded Wall, Shot 9 . . . . .	176
4.57 Net Average Pressure, Structure 3.1m, Shielded Wall, Shot 9 . . . . .	176

**UNCLASSIFIED**

## ILLUSTRATIONS (Continued)

	Page
4.58 Average Pressures on Strips of Rear Surface, Structure 3.1a . . . . .	177
4.59 Average Pressures on Strips of Rear Surface, Structure 3.1b . . . . .	178
4.60 Average Pressures on Rear Surfaces of Structures 3.1c and d . . . . .	179
4.61 Average Pressures on Rear Surfaces of Structures 3.1g and h . . . . .	180
4.62 Average Pressures on Strips of Rear Surface, Structure 3.1i . . . . .	181
4.63 Average Pressure on Strips of Front Surface, Structure 3.1a . . . . .	182
4.64 Average Pressure on Strips of Top Surface, Structure 3.1a . . . . .	183
4.65 Average Pressure on Strips of Top Surface, Structure 3.1b . . . . .	184
4.66 Average Pressure on Strips of Top Surface, Structure 3.1c, and Front Surface, Structure 3.1h . . . . .	185
4.67 Average Pressure on Front Surface, Structure 3.1a, Shot 9 . . . . .	186
4.68 Average Pressure on Front Surface, Structure 3.1a, Shot 10 . . . . .	186
4.69 Average Pressure on Front Surface, Structure 3.1c, Shot 9 . . . . .	187
4.70 Average Pressure on Front Surface, Structure 3.1c, Shot 10 . . . . .	187
4.71 Average Pressure on Front Surface, Structure 3.1d, Shot 9 . . . . .	188
4.72 Average Pressure on Front Surface, Structure 3.1d, Shot 10 . . . . .	188
4.73 Average Pressure on Front Surface, Structure 3.1e, Shot 9 . . . . .	189
4.74 Average Pressure on Front Surface, Structure 3.1e, Shot 10 . . . . .	189
4.75 Average Pressure on Front Surface, Structure 3.1f, Shot 9 . . . . .	190
4.76 Average Pressure on Front Surface, Structure 3.1f, Shot 10 . . . . .	190
4.77 Average Pressure on Top Surface, Structure 3.1a, Shot 9 . . . . .	191
4.78 Average Pressure on Top Surface, Structure 3.1a, Shot 10 . . . . .	191
4.79 Average Pressure on Top Surface, Structure 3.1b, Shot 9 . . . . .	191
4.80 Average Pressure on Top Surface, Structure 3.1b, Shot 10 . . . . .	192
4.81 Average Pressure on Top Surface, Structure 3.1c, Shot 9 . . . . .	192
4.82 Average Pressure on Top Surface, Structure 3.1c, Shot 10 . . . . .	192
4.83 Average Pressure on Top Surface, Structure 3.1e, Shot 9 . . . . .	193
4.84 Average Pressure on Top Surface, Structure 3.1e, Shot 10 . . . . .	193
4.85 Average Pressure on Top Surface, Structure 3.1f, Shot 9 . . . . .	193
4.86 Average Pressure on Top Surface, Structure 3.1f, Shot 10 . . . . .	194
4.87 Average Pressure on Rear Surface, Structure 3.1a, Shot 9 . . . . .	194
4.88 Average Pressure on Rear Surface, Structure 3.1a, Shot 10 . . . . .	194
4.89 Average Pressure on Rear Surface, Structure 3.1b, Shot 9 . . . . .	195
4.90 Average Pressure on Rear Surface, Structure 3.1b, Shot 10 . . . . .	195
4.91 Average Pressure on Rear Surface, Structure 3.1c, Shot 9 . . . . .	195
4.92 Average Pressure on Rear Surface, Structure 3.1c, Shot 10 . . . . .	196
4.93 Average Pressure on Rear Surface, Structure 3.1d, Shot 9 . . . . .	196
4.94 Average Pressure on Rear Surface, Structure 3.1d, Shot 10 . . . . .	196
4.95 Average Pressure on Rear Surface, Structure 3.1e, Shot 9 . . . . .	197
4.96 Average Pressure on Rear Surface, Structure 3.1e, Shot 10 . . . . .	197
4.97 Average Pressure on Rear Surface, Structure 3.1f, Shot 9 . . . . .	197
4.98 Average Pressure on Rear Surface, Structure 3.1f, Shot 10 . . . . .	198
4.99 Average Pressure on Rear Surface, Structure 3.1i, Shot 9 . . . . .	198
4.100 Average Pressure on Rear Surface, Structure 3.1i, Shot 10 . . . . .	198
4.101 Effect of Width (L and H Constant) . . . . .	199
4.102 Effect of Length (W and H Constant) . . . . .	199
4.103 Effect of Size (Ratio W:H:L = Constant) . . . . .	200
4.104 Effect of Ground Proximity (L, W, and H Constant) . . . . .	200
4.105 Effect of Orientation (L, H, and W Constant) . . . . .	201
4.106 Effect of Shielding on Relief Time (W:H:L = Constant) . . . . .	202
4.107 Effect of Shielding on Build-up Time (W:H:L = Constant) . . . . .	202
4.108 Clearing Time Vs Clearing Distance for Typical Gages, Shot 9 . . . . .	203

~~RESTRICTED DATA~~  
**UNCLASSIFIED**



## ILLUSTRATIONS (Continued)

	Page
4.109 Clearing Time Vs Clearing Distance for Typical Gages, Shot 10 . . . . .	203
4.110 Effect of Vortex on Top Surface, Structures 3.1b and c, Shot 9 . . . . .	204
4.111 Effect of Vortex on Top Surface, Structures 3.1a to c, Shot 10 . . . . .	204
4.112 Effect of Vortex on Top Surfaces, Structures 3.1a to c, Shot 9 . . . . .	205
4.113 Effect of Vortex on Top Surfaces, Structures 3.1a to c, Shot 10 . . . . .	205
4.114 Time-dependent Drag Coefficients, Top Surfaces, Structures 3.1a to c, e, f, and i, Shot 9 . . . . .	206
4.115 Time-dependent Coefficients, Top Surfaces, Structures 3.1a and b, Shot 10 . . . . .	207
4.116 Time-dependent Drag Coefficients, Top Surfaces, Structures 3.1c, e, f, and i, Shot 10 . . . . .	208
4.117 Simplified Average Pressure, Structures 3.1a to c, Shot 9 . . . . .	209
4.118 Simplified Average Pressure, Structures 3.1a to c, Shot 9 . . . . .	210
4.119 Effect of Width on Build-up Time on Rear Surface, Shot 9 . . . . .	211
4.120 Effect of Width on Build-up Time on Rear Surface, Shot 10 . . . . .	211
4.121 Simplified Average Pressure, Structures 3.1a, d, and i, Shot 9 . . . . .	212
4.122 Simplified Average Pressure, Structures 3.1a, d, and i, Shot 10 . . . . .	213
4.123 Effect of Length on Build-up Time on Rear Surface, Shot 9 . . . . .	214
4.124 Effect of Length on Build-up Time on Rear Surface, Shot 10 . . . . .	214
4.125 Rear Build-up Coefficient $n$ . . . . .	215
4.126 Individual Gage Records, Structures 3.1a and i, Top Surface, Shot 9 . . . . .	216
4.127 Individual Gage Records, Structures 3.1a and i, Top Surface, Shot 10 . . . . .	216
4.128 Comparison of UPSHOT-KNOTHOLE to GREENHOUSE, Top Surface Pressures . . . . .	217
4.129 Comparison of UPSHOT-KNOTHOLE to GREENHOUSE, Rear Surface Pressures . . . . .	217
4.130 Comparison of UPSHOT-KNOTHOLE to GREENHOUSE, Top Surface Normalized Pressures . . . . .	218
4.131 Comparison of UPSHOT-KNOTHOLE to GREENHOUSE, Rear Surface Normalized Pressures . . . . .	218
4.132 GREENHOUSE Free Stream Pressure . . . . .	219
4.133 Gage Locations on Structures 3.1a, e, f, and i . . . . .	219
4.134 Individual Gage Records Showing Time Scaling on Rear Surfaces, Gages a10 and e5, Shot 9 . . . . .	220
4.135 Individual Gage Records Showing Time Scaling on Rear Surfaces, Gages a10 and e5, Shot 10 . . . . .	220
4.136 Individual Gage Records Showing Time Scaling on Rear Surfaces, Gages a8 and e6, Shot 9 . . . . .	221
4.137 Individual Gage Records Showing Time Scaling on Rear Surfaces, Gages a8 and e6, Shot 10 . . . . .	221
4.138 Individual Gage Records Showing Time Scaling on Top Surface, Gages a26 and e2, Shot 9 . . . . .	222
4.139 Individual Gage Records Showing Time Scaling on Top Surface, Gages a26 and e2, Shot 10 . . . . .	222
4.140 Individual Gage Records Showing Time Scaling on Rear Surface, Gages a10 and f4, Shot 9 . . . . .	222
4.141 Individual Gage Records Showing Time Scaling on Rear Surface, Gages a10 and f4, Shot 10 . . . . .	222
4.142 Individual Gage Records Showing Time Scaling on Top Surface, Gages a26 and f5, Shot 9 . . . . .	223
4.143 Individual Gage Records Showing Time Scaling on Top Surface, Gages a26 and f5, Shot 10 . . . . .	223



## ILLUSTRATIONS (Continued)

	Page
4.144 Peak Pressure As a Function of Surface Orientation . . . . .	224
4.145 Comparison of Experimental to Predicted Diffraction Impulse on Obliquely Loaded Semi-front Surfaces . . . . .	224
4.146 Comparison of Predicted to Experimental Pressure on Front Surface, Structure 3.1g, Shot 9 . . . . .	225
4.147 Comparison of Predicted to Experimental Pressures on Front Surface, Structure 3.1g, Shot 10 . . . . .	225
4.148 Comparison of Predicted to Experimental Pressures on Front Surface, Structure 3.1h, Shot 10 . . . . .	226
4.149 Comparison of Predicted to Experimental Pressure on Right Side Surface, Structure 3.1h, Shot 10 . . . . .	226
4.150 Comparison of Predicted to Experimental Pressure on Right Side Surface, Structure 3.1h, Shot 9 . . . . .	227
4.151 Comparison of Predicted to Experimental Pressure on Right Side Surface, Structure 3.1g, Shot 10 . . . . .	228
4.152 Comparison of Predicted to Experimental Pressure on Right Side Surface, Structure 3.1g, Shot 9 . . . . .	228
4.153 Shielding Effects . . . . .	229
4.154 Simplified Average Pressure, Structures 3.1d, l, m, and n, Shot 9 . . . . .	230
4.155 Ratio of Net Impulse on Shielding Walls (Structures 3.1l and m) to That on Isolated Wall (Structure 3.1d), Shot 9 . . . . .	231
4.156 Ratio of Net Impulse on Shielding Walls (Structures 3.1l and m) to That on Isolated Wall (Structure 3.1d), Shot 10 . . . . .	231
4.157 Simplified Average Pressure, Structures 3.1a, o, and p, Shot 9 . . . . .	232
4.158 Simplified Average Pressure, Structures 3.1a, o, and p, Shot 10 . . . . .	233
4.159 Comparison of Pretest Prediction to Experimental Pressure on Underside of Structure 3.1o, Shot 9 . . . . .	234
4.160 Comparison of Pretest Prediction to Experimental Pressure on Underside of Structure 3.1p, Shot 9 . . . . .	234
4.161 Comparison of Pretest Prediction to Experimental Pressure on Underside of Structure 3.1o, Shot 10 . . . . .	235
4.162 Comparison of Pretest Prediction to Experimental Pressure on Underside of Structure 3.1p, Shot 10 . . . . .	235
4.163 Diffraction Loading on Underside of Elevated Cubicles, Structures 3.1o and p . . . . .	236
4.164 Comparison of Pretest Prediction to Experimental Pressure on Rear Surface, Structure 3.1o, Shot 9 . . . . .	237
4.165 Comparison of Pretest Prediction to Experimental Pressure on Rear Surface, Structure 3.1o, Shot 10 . . . . .	237
4.166 Comparison of Pretest Prediction to Experimental Pressure, Structure 3.1q, Section A-A, Shot 9 . . . . .	238
4.167 Comparison of Pretest Prediction to Experimental Pressure, Structure 3.1q, Section A-A, Shot 10 . . . . .	238
4.168 Comparison of Pretest Prediction to Experimental Pressure, Structure 3.1q, Section B-B, Shot 9 . . . . .	239
4.169 Comparison of Pretest Prediction to Experimental Pressure, Structure 3.1q, Section B-B, Shot 10 . . . . .	239
4.170 Pressure Records on Structure 3.1q, Section C-C, Shot 9 . . . . .	240
4.171 Pressure Records on Structure 3.1q, Section C-C, Shot 10 . . . . .	240
4.172 Comparison of Pretest Prediction to Experimental Pressure, Structure 3.1q, Corner 1, Shot 9 . . . . .	241

~~SECRET RESTRICTED DATA~~  
**UNCLASSIFIED**

## ILLUSTRATIONS (Continued)

	Page
4.173 Comparison of Pretest Prediction to Experimental Pressure, Structure 3.1q, Corner 1, Shot 10 . . . . .	241
4.174 Comparison of Geometry of Princeton Double Block and Notch, Structure 3.1q . . . . .	242
4.175 Comparison of Princeton Double Block Pressures to Gage 3, Structure 3.1q . . . . .	242
4.176 Comparison of Princeton Double Block Pressures to Gages 8 and 10, Structure 3.1q . . . . .	243
4.177 Comparison of Princeton Double Block Pressures to Gages 1 to 3, Structure 3.1q . . . . .	243
4.178 Comparison of Princeton Double Block Pressures to Gage 4, Structure 3.1q . . . . .	244
4.179 Comparison of Princeton Double Block Pressures to Gage 1, Structure 3.1m . . . . .	244
4.180 Comparison of Predicted to Experimental Average Pressures; Front, Rear, and Net; Structure 3.1s, Shot 9 . . . . .	245
4.181 Comparison of Predicted to Experimental Average Pressures; Front, Rear, and Net; Structure 3.1s, Shot 9 . . . . .	246
4.182 Comparison of Predicted to Experimental Average Pressures; Front, Rear, and Net; Structure 3.1t, Shot 9 . . . . .	247
4.183 Comparison of Predicted to Experimental Average Pressures; Front, Rear, and Net; Structure 3.1t, Shot 9 . . . . .	248
4.184 Comparison of Experimental Average Net Pressure on Structure 3.1t (Shot 10) to That of Simplified Prediction Method for Precursor Loading . . . . .	249
<b>CHAPTER 5 DEVELOPMENT OF INCREASED DRAG TRENDS</b>	
5.1 Definition of Diffraction and Drag Impulses . . . . .	261
5.2 Three-dimensional Effect of Pressure Build-up on a Rear Surface . . . . .	262
5.3 Coefficient, $\beta$ and $\gamma$ , for Computing Diffraction Impulse $I_{df}$ . . . . .	263
5.4 Reduced Drag Impulses As a Function of Side-on Pressure for Various Values of Shape Factors . . . . .	264
5.5 Exponential Coefficient $c$ Used in Blast Wave Equations (Scaled to 1 Kt) . . . . .	265
5.6 Side-on Pressure Time Relations . . . . .	266
5.7 Dynamic Pressure Time Relations . . . . .	267
5.8a Net Forces on Structures 3.1a, c, d, and p, Shot 9 . . . . .	268
5.8b Net Pressures on Structures 3.1a, c, f, and h, Shot 10 . . . . .	269
5.9a Drag Coefficients on Structures 3.1a, c, d, and p, Shot 9 . . . . .	270
5.9b Drag Coefficients on Structures 3.1a, c, f, and h, Shot 10 . . . . .	271
5.10 Comparisons Between Wind Tunnel Drag Coefficients and Those Found in the Shock Tube and in Field Tests . . . . .	272
<b>APPENDIX A LOADING IN PRECURSOR REGION</b>	
A.1 Location of Structures 3.1s and t and Blast Line Gages . . . . .	293
A.2a Structure 3.1t, Plan View and Rear Elevations . . . . .	294
A.2b Structure 3.1t, Right and Rear Elevations . . . . .	295
A.2c Structure 3.1s, Plan View and Front Elevations . . . . .	296
A.2d Structure 3.1s, Right and Rear Elevations . . . . .	297
A.3 Location of Pressure Gages for Program 3.1u . . . . .	298
A.4 Postshot Photograph of Structure 3.1s . . . . .	299

~~SECRET RESTRICTED DATA~~  
**UNCLASSIFIED**

## ILLUSTRATIONS (Continued)

	Page
A.5 Ground Level Peak Pressure As a Function of Distance from Ground Zero, Shot 10 . . . . .	300
A.6 Estimated Ground Level Pressure Incident on Structure 3.1s, Shot 10 . . . . .	301
A.7 Estimated Ground Level Pressure Incident on Structure 3.1t, Shot 10 . . . . .	301
A.8 Average Pressure on the Front Face of Structure 3.1t, Shot 10 . . . . .	302
A.9 Average Pressures on the Rear Face of Structure 3.1t, Shot 10 . . . . .	302
A.10 Average Pressures on the Top Face of Structure 3.1t, Shot 10 . . . . .	302
A.11 Average Pressure on the Side Face of Structure 3.1t, Shot 10 . . . . .	303
A.12 Average Pressures on All Faces of Structure 3.1t, Shot 10 . . . . .	303
A.13 Difference Between Free Stream Pressure and the Average Pressure on the Faces of Structure 3.1t . . . . .	304
A.14 Average Pressure on Front Surface of Structure 3.1s, Shot 10 . . . . .	304
A.15 Average Pressure on Rear Surface of Structure 3.1s, Shot 10 . . . . .	305
A.16 Average Pressure on Top Surface of Structure 3.1s, Shot 10 . . . . .	305
A.17 Average Pressure on Side Surface of Structure 3.1s, Shot 10 . . . . .	305
A.18 Time of Arrival of Heavy Dust Loads on Sandia Q-gages at Various Elevations Above Ground . . . . .	306
A.19 Constant Pressure Contours from Blast Line As a Function of Gage Height and Absolute Time at 924 Ft from Ground Zero . . . . .	307
A.20 Constant Pressure Contours from Blast Line As a Function of Gage Height and Absolute Time at 1417 Ft from Ground Zero . . . . .	307
A.21 Constant Pressure Contours from Blast Line As a Function of Gage Height and Absolute Time at 1916 Ft from Ground Zero . . . . .	308
A.22 Constant Pressure Contours from Blast Line As a Function of Gage Height and Absolute Time at 2416 Ft from Ground Zero . . . . .	308
A.23 Constant Pressure Contours from Blast Line As a Function of Gage Height and Absolute Time at 2916 Ft from Ground Zero . . . . .	309
A.24 Schematic Drawing of Blast and Dust Fronts in Precursor Region . . . . .	309
A.25 Net Pressure on Structure 3.1t . . . . .	310
A.26 Net Impulse As a Function of Time on Structure 3.1t, Shot 10 . . . . .	311
A.27 Predicted Hydrodynamic Variables over an Ideal Surface for Structure 3.1t . . . . .	312
A.28 Ideal Surface Loadings for Structure 3.1t . . . . .	313
A.29 Schematic Loading Scheme in a Precursor . . . . .	314
A.30 Individual Gage Records, Front Surface, Structure 3.1t, Shot 10 . . . . .	315
A.31 Individual Gage Records, Rear Surface, Structure 3.1t, Shot 10 . . . . .	316
A.32 Individual Gage Records, Top Surface, Structure 3.1t, Shot 10 . . . . .	317
A.33 Individual Gage Records, Right Side, Structure 3.1t, Shot 10 . . . . .	318

### APPENDIX B COMPARISON OF WAVE FORMS FOR STATIC AND DYNAMIC PRESSURES

B.1 Interrelations Between Radius Time, Pressure Time, and Material Velocity Time in a Shock Wave . . . . .	330
B.2 Positive Durations Vs Peak Overpressure Levels, Spherical Wave, 1 Kt, Free Air . . . . .	331
B.3 Normalized Wave Forms for a Spherical Wave in Free Air, 1-Kt Yield, 950 Ft Slant Distance . . . . .	332
B.4 Normalized Wave Forms for a Spherical Wave in Free Air, 1-Kt Yield, 1400 Ft Slant Distance . . . . .	332
B.5 Pressure-Time Fit for a Spherical Wave in Free Air, Using Conventional Form at 7.65 Psi . . . . .	333
B.6 Pressure-Time Fit for a Spherical Wave in Free Air, Using Conventional Form at 4.2 Psi . . . . .	333



## ILLUSTRATIONS (Continued)

	Page
B.7 Comparisons Between Various Empirical Fits to a Pressure-Time Curve . . . . .	334
B.8 Normalized Wave Forms of Pressure, Material Velocity, and Dynamic Pressure for a Spherical Wave in Free Air, 1-Kt Yield, 960-ft Slant Distance . . . . .	335
B.9 Normalized Wave Forms of Pressure, Material Velocity, and Dynamic Pressure for a Spherical Wave in Free Air, 1-Kt Yield, 1400-ft Slant Distance . . . . .	335
B.10 Normalized Impulses for Static Pressure, Material Velocity, and Dynamic Pressure of Fig. B.8. . . . .	336
B.11 Normalized Impulses for Static Pressure, Material Velocity, and Dynamic Pressure of Fig. B.9. . . . .	336
B.12 Qualitative Comparison of a Free Air Wave with Its Reflected Wave. . . . .	337

### APPENDIX C REGULAR SHOCK REFRACTION THEORY

C.1 Cascade of Regular Refraction Problems . . . . .	355
C.2 Three-shock and Two-shock Rarefaction Regimes . . . . .	355
C.3 The Oxygen-Nitrogen Regular Refraction Problem [ $\xi'$ Vs $\alpha$ for $(c_0/c_0^*)^2 = 0.875$ ] . . . . .	356
C.4 The Oxygen-Nitrogen Regular Refraction Problem [ $\xi'$ Vs $\alpha$ for $(c_0/c_0^*)^2 = 1.143$ ] . . . . .	356
C.5 The Oxygen-Nitrogen Regular Refraction Problem [ $\alpha''$ Vs $\alpha$ for $(c_0/c_0^*)^2 = 0.875$ ] . . . . .	357
C.6 The Oxygen-Nitrogen Regular Refraction Problem [ $\alpha''$ Vs $\alpha$ for $(c_0/c_0^*)^2 = 1.143$ ] . . . . .	357
C.7 Delay Time As a Function of Elevation at 837-ft Station . . . . .	358
C.8 Regular Refraction Regime Neglecting Thermal Layer at 837-ft Station . . . . .	359
C.9 Regular Refraction Regime with Assumed Constant Thermal Layer at 837-ft Station . . . . .	359
C.10 Comparison of Measured and Calculated Wave Shapes at 814-ft Station, Ground Level . . . . .	360
C.11 Comparison of Measured and Calculated Wave Shapes at 837-ft Station, 10-ft Elevation . . . . .	360

## TABLES

### CHAPTER 2 GENERAL DESCRIPTION OF TEST

2.1 Cubical Shapes, Pressure Instrumentation, and Purposes . . . . .	31
2.2 Grouping of 3.1 Structures for Intended Testing of Various Effects . . . . .	31
2.3 Distribution of Gages with Respect to Surfaces . . . . .	32

### CHAPTER 3 PRETEST CONSIDERATIONS

3.1 Pressure Computation Formulas . . . . .	88
---	----

### CHAPTER 4 POST-TEST ANALYSIS

4.1 Peak Pressures in Vicinity of 3.1 Structures at Various Elevations . . . . .	117
4.2 Field Conditions . . . . .	120
4.3 Comparison of SRI and BRL Check Gages . . . . .	121
4.4 Duration of Positive Phase for Individual Gages on Structures (Shot 9 Only) . . . . .	122

~~SECRET RESTRICTED DATA~~  
**UNCLASSIFIED**

## TABLES (Continued)

	Page
4.5 Data for Figs. 4.101 to 4.107 . . . . .	127
4.6 Gages Which Were Not Used To Evaluate Vortex Activity . . . . .	128
4.7 Values of $n$ for Build-up Units . . . . .	130
4.8 Actual Angles of Incidence, $\theta$ , for Obliquely Loaded Structures 3.1g and h. . . . .	137
4.9 Ratio of Net Impulses on Structures 3.1l to n to Impulse on Structure 3.1b (Shot 9) . . . . .	138
4.10 Ratio of Peak Pressures to Side-on Pressure at Bottom of Elevated Structures . . . . .	140

### CHAPTER 5 DEVELOPMENT OF INCREASED DRAG TRENDS

5.1 Reduced Side-on Impulse for Various Values of the Decay Coefficient $c$ . . . . .	253
5.2 Reduced Drag Impulse for Various Values of the Decay Coefficient $c$ . . . . .	254
5.3 Ratio of Reduced Side-on Impulse to Reduced Drag Impulse for Various Values of the Decay Coefficient $c$ . . . . .	255
5.4 Predicted and Measured Net Impulses . . . . .	257
5.5 Summary of Treatment Given Various 3.1 Structures in Net Drag Analysis . . . . .	259

### APPENDIX C REGULAR SHOCK REFRACTION THEORY

C.1 Basic Parameters of Chosen Refraction Problems . . . . .	351
C.2 Critical Angles . . . . .	351
C.3 Reflected Shock $\xi'$ , at Head-on Reflection, $\alpha = 0$ . . . . .	351
C.4 Reflected Shock, $\xi'$ , Before Transition, $\alpha \leq \alpha_t$ . . . . .	351
C.5 Reflected Shock, $\xi'$ , After Transition, $\alpha \geq \alpha_t$ . . . . .	352

~~SECRET~~  
UNCLASSIFIED

## CHAPTER 1

### INTRODUCTION

#### 1.1 PURPOSE OF AIR FORCE TEST PROGRAMS

The series of tests conducted by the Air Force in Operation UPSHOT-KNOTHOLE is part of a continuing Air Force program designated as "Determination of Blast Effects on Buildings and Structures." The United States Air Force (USAF) is mainly interested in the offensive aspects of such research.

The UPSHOT-KNOTHOLE projects sponsored by the Air Force and their specific objectives cannot be fully understood without some knowledge of the general objectives of the over-all program. The research results emanating from these studies and experiments conducted by the Air Force are used by a number of government agencies to improve their own systems of determining blast effects, or to further their own research.

One of these agencies is the Directorate of Intelligence, Headquarters, USAF, which feeds results as they are obtained into its own system of vulnerability classes, thereby making it possible to analyze prospective enemy targets with greater accuracy and to recommend the desired Ground Zero. Another principal user of the research results is the Strategic Air Command (SAC), which applies them toward improvement of an existing Indirect Bomb Damage Assessment (IBDA) system. The purpose of this system is to make it possible to dispense with the usual reconnaissance after a strike, using, instead, information on the actual Ground Zero, height of burst, and yield of the weapon which is brought back to the operational base by the strike aircraft to determine the damage inflicted.

The task of determining the effect of blast on various types of building structures and tactical equipment is a rather formidable one. However, its difficulty is somewhat relieved by the fact that, for the offensive purposes, in which the Air Force is interested, it is not necessary to determine the effect of transient loads on these items with the same accuracy as would normally be employed for static design purposes. In fact, even if it were possible to solve the dynamic problems satisfactorily, intelligence information would be far too sketchy to furnish the information necessary to justify the use of an accurate analysis for items located in prospective enemy countries. From the experience that is so far available, it is expected that it will be possible within the foreseeable future to determine blast damage within broad limits with sufficient accuracy for planning as well as for operational purposes.

In view of the complex phenomena attending shock waves emanating from various types of atomic blasts and the uncertainties inherent in determining significant parameters, an investigator's first idea would be to obtain solutions through a long series of very elaborate and properly designed full-scale tests. However, neither funds nor time will allow such an approach. It has therefore been the objective of the agencies involved to obtain sufficiently accurate results by judicious use of theoretical analyses, laboratory tests, high explosive field tests, and a small number of full-scale atomic tests.

~~SECRET~~  
~~RESTRICTED DATA~~  
UNCLASSIFIED



Three of these research projects have involved full-scale atomic testing. The first was GREENHOUSE, the second was JANGLE (the first, and so far only, underground burst of an atomic weapon to which an Air Force structures program was subjected), and the third is the present UPSHOT-KNOTHOLE program.

From previous analysis, laboratory tests, and full-scale tests (the latter especially as conducted in GREENHOUSE), methods of damage prediction have been developed by Armour Research Foundation (ARF) and others. These prediction methods have attempted to describe the character of the blast loads acting on a variety of items. Response computations based on the predicted loadings permit, in turn, an estimate of physical damage. However, the relation between the deflection or movement of a body and significant military damage has never been clearly established except for extreme cases, e.g., total destruction or no destruction. Another aim of these tests is, therefore, to establish the relation between deflection and functional damage. A full-scale test also affords an excellent opportunity to determine scaling check points for laboratory tests.

In addition to the scientific aspects of the tests, most of the results of the Air Force projects can be used by other government agencies, such as the Directorate of Intelligence, to furnish "rough and ready" experimental answers to the behavior of various kinds of structures under blast. In many cases there is a statistically significant number of items involved which, added to previous experimental data such as those gathered at Hiroshima and Nagasaki, will help round out the present vulnerability picture. In other cases mathematical analysis may have to rely on *ad hoc* information to furnish parameters which cannot be obtained in any other way.

The foregoing remarks are designed to furnish the background necessary for a full understanding of the objectives of this and other of the Air Force projects. The full significance and value of the results of each test will be realized only when they are correlated with results of past, current, and future analyses; laboratory tests; high explosive field tests; and full-scale atomic investigations.

## 1.2 SPECIFIC OBJECTIVES

One of the most important, and at the same time uncertain, variables which enters into the determination of damage to structures exposed to atomic blast is the transient force which acts upon obstacles. It has been found that the same time-pressure relation in air near the ground will produce vastly different forces acting on structures, depending on their size, shape, orientation, height, length, and other characteristics. In addition the time-pressure curve in front of the structure will, as such, be influenced by factors that will affect its history, such as shielding, topography, and the usual atomic parameters. This will show itself in blast characteristics, such as peak shock strength and wave form. The main objective of this test was to increase our knowledge of the manner in which some of these parameters affect the transient forces acting on the structure.

Another objective of this test was to determine how loading on a rigid rectangular parallelepiped is influenced by changes in certain blast and structural parameters; specifically the effects of the following structural and blast parameters were desired:

1. The effect of shock strength on loading.
2. The effect of width on loading of essentially two-dimensional structures as compared with three-dimensional structures.
3. The effect on loading of the size of obstacles whose height, width, and length are related to each other by a single given ratio.
4. The effect on loading of orientation characterized by the angle between the plane of the shock front and the front face of the structure.
5. The effect on loading of varying absolute length in the direction of flow of an obstacle whose absolute height and width dimensions are kept constant.
6. The effect of multiple ground reflection as it varies with the distance of the ground to the bottom of the elevated structure.
7. The effects of shielding with varying distances between obstacles.

8. Effect of multiple reflection and clearance caused by various types of re-entrant corners and cavities in the structure.

9. A comparison between loading in the Mach region and that in the regular reflection region.

### 1.3 RESPONSIBILITIES

ARF was retained by the Air Materiel Command (AMC) of the USAF to carry out the following specific objectives of the program:

1. Consultation on the selection of the test items.
2. Design of the test items.
3. Specification of instrumentation requirements.
4. Location of the structures at the test site.
5. Supervision of construction of the test items.
6. Theoretical and experimental analyses concerning pretest predictions of blast loading and response of the test items where required.
7. Analysis of the test results.
8. Submission of reports accounting for the Foundation's activities pursuant to the objective of the program.

Preparation of the construction drawings for most of the test items was subcontracted by the Foundation to the firm of Holabird and Root and Burgee. That organization also supervised the actual construction under the general direction of ARF. As-built drawings of all the items were prepared by the Silas Mason Company, which also was in charge of the actual construction work.

The design and installation of the instrumentation and subsequent recording and reduction of the data were handled by the Ballistic Research Laboratories (BRL), Naval Ordnance Laboratory (NOL), and Stanford Research Institute (SRI). A portion of the reduction and the final plotting of the individual pressure records was prepared by Telecomputing Corporation.

### 1.4 PRESENTATION

This chapter deals with a statement of objectives and responsibilities. Chapter 2 presents the general discussion of test items and instrumentation. Chapter 3 gives the pretest analysis, i.e., specific predictions for the objectives outlined in this chapter. Chapter 4 treats the post-test analysis in two phases. Before dealing with the specific objectives, topics which apply to all the structures are treated. These general topics include (1) development of basic free stream, side-on, and drag pressure curves; (2) a discussion of the data; and (3) a detailed treatment of loading phenomena, such as build-up time, vortex activity, and drag loading. After this general treatment, the individual objectives of Program 3.1, i.e., the effects on loading of the variation in specific geometric parameters, are each treated separately. Measured pressures are exhibited and compared to the pretest predictions of Chap. 3. Where good agreement exists between the measured pressures and the computed values of the pretest predictions, it is concluded that the method of prediction is valid. In those cases where test results disagree with the prediction, either the predictions are revised or further study is recommended. If the experimental evidence can be classed as good, with reference to both quantity and quality, the pretest predictions are revised; if the evidence is weak, further study is recommended. In addition, comparisons are made between the GREENHOUSE report (*Blast Loading and Response of Structures*, WT-87) on large-scale models and shock tube results (*The Diffraction of Shock Waves*, W. Bleakney; *Shock Loading of Rectangular Structures*, W. Bleakney et al; and *The Shock Tube as an Instrument*, F. W. Geiger and C. W. Mautz).\*

\* Complete reference to the publications mentioned in parentheses may be found in the Bibliography at the end of the report.

Chapter 5 presents a detailed analysis of drag loadings with the emphasis on net loadings. Although this was not one of the original objectives of Program 3.1, it is treated in this report as an additional observation regarding an aspect of blast loading which has evolved to a position of greater importance in recent time. Chapter 6 summarizes the conclusions of the post-test analyses. Appendixes A, B, and C present contributions to precursor, wave shape, and regular refraction theory, respectively. Appendix D is a list of symbols used in the body of this report.

~~SECRET RESTRICTED DATA~~  
**UNCLASSIFIED**



## CHAPTER 2

### GENERAL DESCRIPTION OF TEST

#### 2.1 TEST ITEMS

##### 2.1.1 Test Site Layout

Of 17 models in the 3.1 test group (see Table 2.1), 15 were located along a circular arc at a distance of 4900 ft from intended Ground Zero. The remaining two models were at distances of 1150 and 2200 ft, respectively, from intended Ground Zero. Of the 17 test structures, 14 were cubicles and 3 consisted of pairs of thin walls separated by a varying shielding distance. The buildings were spaced at distances varying from 80 to 200 ft along an arc length of 2000 ft.

Fifteen of the structures were located on the ground and were 6 ft high, 12 ft wide, and 6 ft long with the exceptions discussed below. All were constructed of reinforced concrete, were mounted on firm foundations and, except for the thin walls, were filled with soil. The structures were considered to be perfectly rigid and were designed not to move during the blast loading. One of the cubicles was used as a control structure; it was 6 ft high and 6 ft long in the direction of the shock propagation, and 12 ft wide in the direction parallel to the plane of the shock front, and located on the ground. The remaining cubicles were grouped in pairs, with one of the structural parameters of the control structure varying within each pair. This arrangement provided for models in groups of three (the control structure belonged to each group) with all parameters, except one, being held constant within a group. One of the structures minimized the length to slightly more than 1 ft, forming an isolated thin wall for comparison with the three pairs of shielded walls, while the maximum length used was 18 ft; the largest structure was 18 ft high. Most of them were 12 ft wide, but two had the maximum width of 36 ft. Normal incidence of the shock wave was intended for all the structures except two, which were designed to measure orientation effects with a maximum orientation of 45 deg. Thus, length, height, width, elevation above grade, angle of shock incidence, distance from Ground Zero, over-all shape of structure, and distance between shielding walls were varied systematically throughout the Project 3.1 group of models to determine the corresponding variations in loading. Pressure gages were mounted on the surfaces of the structures for this purpose. (Table 2.3.)

Some of the surfaces had as many as 8 to 10 gages. However, many of the surfaces had only one gage mounted on them and still others had none at all. The control structure was very heavily gaged since the loadings on all other structures were to be referred to it. In addition to the pressure gages mounted on these surfaces of the models, gages were installed at five locations along the arc between the structures for the purpose of measuring free stream pressure.

The free stream gages measured the wave shape in the neighborhood of these structures, that is, the variation of pressure with time as the wave passes the point where the flow is not disturbed by the presence of obstacles such as one of these test models. Since this wave shape varies, depending upon the height of burst, the distance from Ground Zero, and perhaps on other

factors that are not yet thoroughly understood, it had to be measured experimentally. The importance of this measurement stems from the fact that the type of loading on the surface of a structure depends upon the wave shape as well as on the various structural parameters of the building. (Therefore the wave shape must be known in order to isolate its effect upon loading from those due to the variation of specific structural parameters.)

The plot plan for Program 3.1 is shown in Figs. 2.1 and 2.2. Figures 2.13 to 2.44 give the dimensions and gage locations of the individual buildings as built.

When a shock wave strikes the rigid model, it causes a rapid variation of pressure on all exterior surfaces. Based on previous test results obtained in the laboratory and in the field, as well as theoretical considerations and assumptions, the approximate loads on these models were predicted beforehand. In this test the specific objectives were to be met with the following detailed structures (see Table 2.2).

#### 2.1.1.1 Effect of Shock Strength

In the past it has been assumed that the type of loading obtained at one particular shock strength could be applied directly to other shock strengths if expressed in terms of percentage of side-on pressure and certain other parameters. However, recent experiments at Princeton University on a two-dimensional block (1:1 height-to-length ratio) with shock strengths ranging from very weak shocks, ( $\xi = 1.126$ ) to very strong shocks ( $\xi = 5.0$ ) show basic differences for the loading on the roof. Although these effects, which are due to differences in vortex development, will probably be less important in three-dimensional structures, a basic investigation is in order to confirm this likelihood.

In the UPSHOT-KNOTHOLE test three identical structures were to be placed in different overpressure regions—Structures 3.1a, s, and t (s and t for Shot 10 only).

#### 2.1.1.2 Two-dimensional Vs Three-dimensional Effects

The results of the GREENHOUSE (*Blast Loading and Response of Structures*, WT-87) field tests seem to confirm the supposition that different types of loading phenomena occur in two- and in three-dimensional structures. Some changes, notably the build-up time on the back surface, have already been incorporated into the present prediction schemes; other changes from two- to three-dimensional loadings have been made arbitrarily in the past. It is hoped that from these tests on structures with length-to-width ratios ranging from 1:1 to 1:6, (Structures 3.1a to c), a more reliable procedure may be developed to supersede previous estimates.

#### 2.1.1.3 Effect of Size of Structure

The effect of size is important if results on field test models are to be applied to larger structures. Although it is beyond the scope of this program to cover a wide variation of Reynolds' numbers which, if covered, might well show sharp changes in drag coefficient values, changes in loading caused by scale changes may be detected in restricted Reynolds' number regions. An arrangement of full- and quarter-scale models was already a part of the GREENHOUSE program, but the industrial type structures treated were insufficiently instrumented and too complex to yield basic information.

In this test structures having identical height-to-width-to-length ratios, but varying in height by a factor of three, were placed in the same overpressure region (Structures 3.1a, e, and f).

#### 2.1.1.4 Effect of Orientation

In the past the buildings treated in field test programs were struck by shocks under normal incidence, i.e., the flow direction coincided with the normal to the front wall; oblique incidence was considered only briefly. Even in those cases where it was considered, it was restricted to special components, such as saw-tooth type roofs. Normal incidence was favored because the theory is much simpler and the largest structural damage was expected for some type of incidence normal to one of the walls. Since in an actual situation the incidence angle may vary,

it is important to provide basic loading information from which the damage can be predicted more accurately for intermediate angles.

In this test identical building shapes were oriented at intervals of approximately  $22\frac{1}{2}$  deg. and subjected to the same shock strength (Structures 3.1a, g, and h).

#### 2.1.1.5 Effect of Length of Structure in Direction of Flow

Shock tube experiments have established that the loading on the back of a thin wall is different from the loading on blocks of greater length. The problems of obtaining more basic information on various lengths and of applying these conclusions to large-scale models can be investigated by including structures of identical height and width, but having different lengths. These lengths (measured in the direction of flow) ranged from the thickness of a thin wall to three times the height of the structure (Structures 3.1a, d, and i).

#### 2.1.1.6 Effect of Ground Reflection on Elevated Structures

The effect of ground reflection is important in the study of pressures on the undersides of various structures and equipment. Although some analysis has been attempted, there exist practically no experimental data in support of such analysis. Therefore this phase of the overall program fills an important gap in the basic information on loadings on elevated equipment.

In this test identical structures were arranged at various elevations above ground level (one-half and one-third their height) and exposed to the same shock (Structures 3.1a, o, and p).

#### 2.1.1.7 Effect of Shielding

The effect of shielding is of particular importance if loading predictions are attempted for adjacent structures, as in a city, or for closely spaced equipment. Practically the only data on shielding available in the literature are those from the Princeton shock tube, where a pair of two-dimensional models of 1:1 height-to-length ratio are separated by a distance of  $1\frac{1}{2}$  times their height (*The Diffraction of Shock Waves*, W. Bleakney; and *Shock Loading of Rectangular Structures*, W. Bleakney et al).

In this test sets consisting of two thin walls having various distances between them (one-half or one-third times their height) were placed in the same overpressure region (Structures 3.1d, l, m, and n).

#### 2.1.1.8 Effects of Cavities, Setbacks, and Re-entrant Corners on Loading

Pressure increase due to multiple reflections and action of rarefaction waves is important for structures in the regular reflection region and for all shock loaded structures which possess eaves, protuberances, wings, etc. Structure 3.1q, chosen to represent a few aspects of these problems, illustrates various phenomena expected to occur in actual structures, such as the delay of pressure relief on walls protected by eaves, multiple reflection in a channel with the shock spilling over the top and one open side, and clearing of pressure from a front surface to a parallel but setback surface.

#### 2.1.1.9 The Effect on Loading from Placement of Structures in the Regular Reflection Region

Whereas structures located in the Mach region of the atomic blast are struck by a single shock—the Mach stem under normal incidence—structures located in the regular reflection region are struck by both the free air shock and the ground reflected shock. Two structures were chosen with the intention of having regular reflected region shock strengths of 2.0 and 2.6 and vertical incident angles of 43 and 20 deg., respectively, on Shot 9 (Structures 3.1a, s, and t). The initial diffraction loading should illustrate the pressure multiplication in the re-entrant corners formed by the front wall and the ground.



## 2.2 INSTRUMENTATION

### 2.2.1 General

The measurements of direct concern in Program 3.1 were those related to the point pressure on the structures and the free stream measurements in the vicinity of these structures. As indicated in the plot plan, responsibility for these measurements was divided among three agencies, BRL, SRI, and NOL. A detailed description of the instrumentation of each of these three agencies is given in Reports WT-738, WT-739, and WT-740.

These free stream measurements were augmented by values deduced from head-on reflected pressures observed on front wall gages. It is desirable to get as accurate a measurement of free stream pressures as possible.

The selection of the location for gages on the cubicles was dictated by the test objectives. Since an impracticably large number of channels of instrumentation would have been required to completely cover all the buildings, only a minimum number were provided in order to provide check points on the various issues in question on the list of test objectives.

### 2.2.2 Air-pressure Measurements

All air-pressure-vs-time measurements were obtained by the use of Wiancko type gages, which consist of a differential inductance bridge actuated by a pressure sensitive Bourdon tube. The output of gages provided by BRL and NOL was fed into magnetic tape recorders, the Webster-Chicago and Ampex systems, respectively, being used by the two agencies. BRL used a phase-modulated system, whereas NOL used a frequency-modulated system. The output of the SRI gages was fed directly into oscillograph type recorders.

The pressure gages were calibrated statically in conjunction with the recording system prior to the test. Complete details of the pressure gage installations are contained in the final reports of Projects 3.28.1, 3.28.2, 3.28.3 (*Structures Instrumentation*).

### 2.2.3 Instrument Records

NOL and SRI were each responsible for approximately one-quarter of the pressure gages used. BRL handled all the other gages. ARF was supplied by NOL with the original playbacks of the pressure records and pertinent calibration information. SRI supplied their records in linearly calibrated tabulated form. BRL was prepared to put their records in final plotted form, but they were requested to submit calibrated data in the form of tabulated values and punched IBM cards. This was done in order that all the records would be presented in a uniform fashion.

ARF contracted with Telecomputing Corp., Burbank, Calif., to present all the pressure records in final plotted form according to specifications set down by ARF. This work consisted of reading, calibrating, and plotting the NOL records in a linear fashion and plotting the SRI and BRL records from supplied data. These referred to only the individual pressure-time curves from the various gages and did not include any averaging of the pressures on cubicle faces.

With the exception of the pressure gages handled by SRI, all the instrument records were recorded on magnetic tape. The signals were played back from the tape onto oscillograph paper by the agencies in charge of the original installations. The records in this form exhibit certain nonlinear characteristics (e.g., the ordinate scale is markedly nonlinear) which made them rather undesirable for purposes of interpretation and comparison. For that reason all the records were reduced and presented in linear calibrated form.

TABLE 2.1—Cubicle Shapes, Pressure Instrumentation, and Purposes

Structure	Instrument channels	Height (ft)	H : W : L ratios	Remarks or purposes	Instrumenting agency
3.1a	27	6	1 : 2 : 1	The basic 3.1 control structure (4900 ft from nominal GZ)	BRL
3.1b	16	6	1 : 6 : 1	Nearly two-dimensional at center section	BRL
3.1c	10	6	1 : 1 : 1	Cube	SRI
3.1d	8	6	1 : 2 : 1/6	Thin wall	SRI
3.1e	6	18	1 : 2 : 1	Triple size of 3.1a	BRL
3.1f	5	12	1 : 2 : 1	Double size of 3.1a	SRI
3.1g	25	6	1 : 2 : 1	To be oriented 22½ deg. from normal shock incidence	BRL
3.1h	25	6	1 : 2 : 1	To be oriented 45 deg. from normal shock incidence	BRL
3.1i	6	6	1 : 2 : 3	Triple length (in flow direction of 3.1a)	SRI
3.1l	5	6	1 : 2 : 1/6	Shielding: two thin walls, close spacing (3 ft)	BRL
3.1m	6	6	1 : 2 : 1/6	Shielding: two thin walls, intermediate spacing (6 ft)	SRI
3.1n	2	6	1 : 2 : 1/6	Shielding: two thin walls, wide spacing (18 ft)	SRI
3.1o	7	6	1 : 2 : 1	Elevated version of 3.1a: 21 in. above grade	BRL
3.1p	7	6	1 : 2 : 1	Elevated version of 3.1a: 34 in. above grade	BRL
3.1q	11	4½	1 : 2 : 2	Tests three deviations from cubicle form	SRI
3.1s	24	6	1 : 2 : 1	Close-in version of 3.1a: intended GZ 1150 ft	NOL
3.1t	24	6	1 : 2 : 1	Close-in version of 3.1a: intended GZ 2200 ft	NOL

TABLE 2.2—Grouping of 3.1 Structures for Intended Testing of Various Effects

Effect of change in:	Group of structures
Peak pressure	3.1a, s, and t (Shot 10 only)
Width	3.1a, b, and c
Size	3.1a, e, and f
Length	3.1a, d, and i
Elevation above grade	3.1a, o, and p
Orientation	3.1a, g, and h
Shielding distance	3.1d, l, m, and n
Incident wave shape (Mach vs regular reflection)	3.1a, s, and t (Shot 9 only)
Shape (non-cubical forms)	3.1q

**UNCLASSIFIED**

TABLE 2.3—Distribution of Gages with Respect to Surfaces

Structure	H : W : L	Height (ft)	Number of Gages on Surface					Sec. A-A	Sec. B-B	Sec. C-C	Grade
			Front	Top	Left	Right	Rear				
3.1a	1 : 2 : 1	6	8	9	1	1	13				0
3.1b	1 : 6 : 1	6	0	8	0	0	8				0
3.1c	1 : 1 : 1	6	2	4	0	0	4				0
3.1d	1 : 2 : 1/4	6	3	0	0	0	5				0
3.1e	1 : 2 : 1	18	1	3	0	0	3				0
3.1f	1 : 2 : 1	12	1	3	0	0	1				0
3.1g	1 : 2 : 1	6	9 <sup>a</sup>	3	6	10 <sup>b</sup>	8				0
3.1h	1 : 2 : 1	6	8 <sup>c</sup>	3	5 <sup>d</sup>	9 <sup>e</sup>	7 <sup>f</sup>				0
3.1i	1 : 2 : 3	6	0	1	0	0	5				0
3.1l	1 : 2 : 1/4	6	0	0	0	0		5 <sup>g</sup>	5 <sup>h</sup>		1
3.1m	1 : 2 : 1/4	6	0	0	0	0		1	5 <sup>i</sup>	5 <sup>j</sup>	1
3.1n	1 : 2 : 1/4	0	0	0	0	0		1	1		0
3.1o	1 : 2 : 1	6	1	0	0	0	2	(bottom)			0
								4			
3.1p	1 : 2 : 1	6	1	0	0	0	2	(bottom)			0
								4			
3.1q	1 : 2 : 2	4 1/2	1	0	3	0	0	2	1	3	0
3.1s	1 : 2 : 1	6	8	7	0	3	6				0
3.1t	1 : 2 : 1	6	8	7	0	3	6				0

<sup>a</sup>3.1g F 4 Gages Averaged, 3 Gages Averaged<sup>b</sup>3.1g R 3 Gages Averaged, 3 Gages Averaged<sup>c</sup>3.1h F 3 Gages Averaged, 3 Gages Averaged<sup>d</sup>3.1h F 3 Gages Averaged, 3 Gages Averaged<sup>e</sup>3.1h R 3 Gages Averaged, 3 Gages Averaged<sup>f</sup>3.1h B 2 Gages Averaged, 2 Gages Averaged<sup>g</sup>3.1l A-A 4 Gages Averaged, front of Wall No. 2<sup>h</sup>3.1l B-B 4 Gages Averaged, back of Wall No. 1<sup>i</sup>3.1m B-B 4 Gages Averaged, front of Wall No. 2<sup>j</sup>3.1m C-C 4 Gages Averaged, back of Wall No. 1



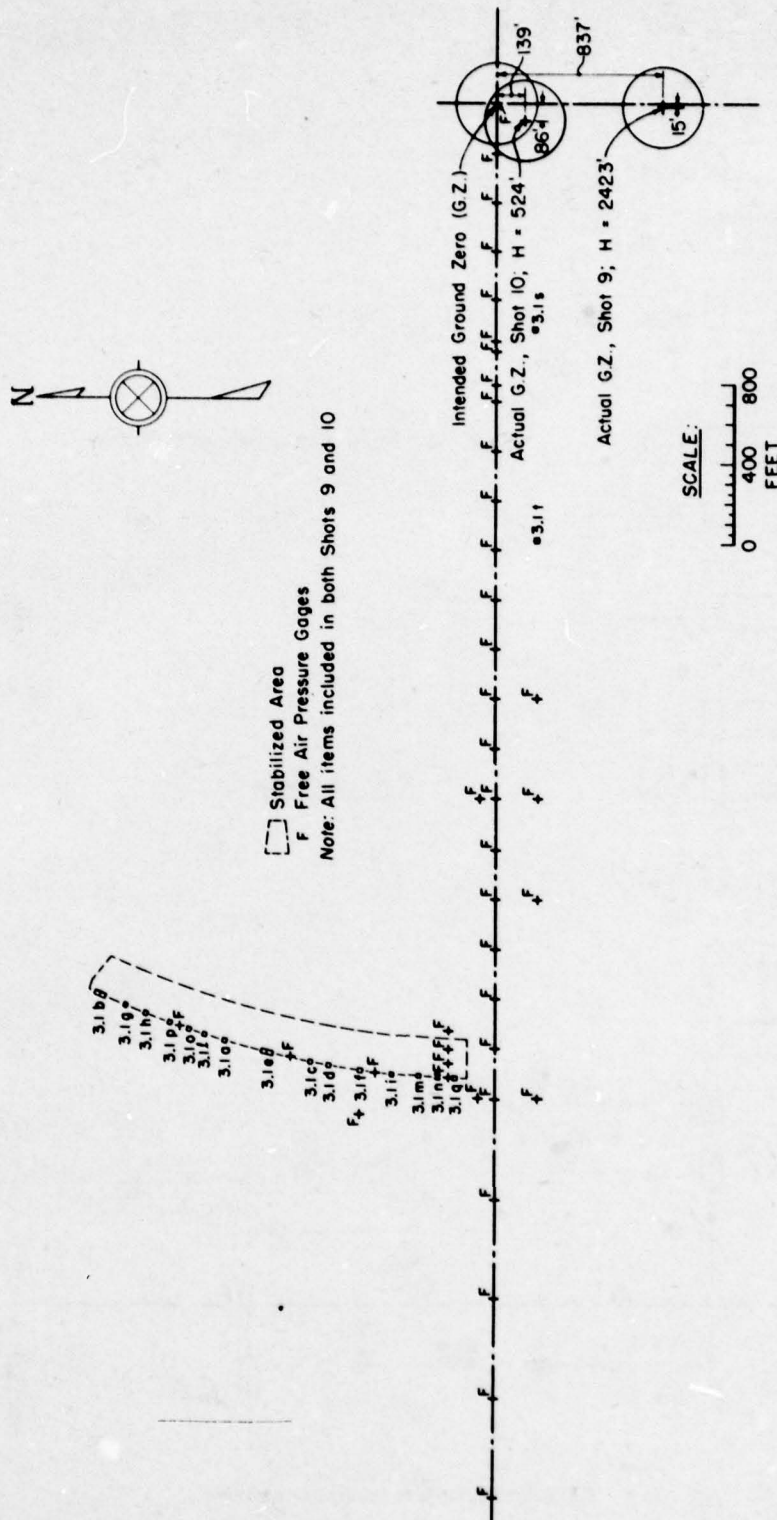
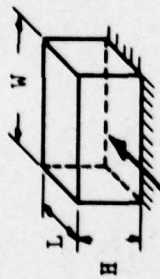
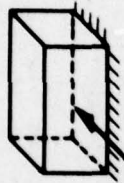


Fig. 2.1—Location of structures at test site.



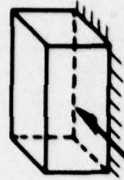


Structure 3.1a



Structure 3.1b

$H:W:L = 1:2:1$   
 $H = L = 6 \text{ ft}$



Structure 3.1c

Fig. 2.3—Structures for testing shock strength effects (Shot 10 only).



Structure 3.1a

$H:W:L = 1:2:1$



Structure 3.1b

$H:W:L = 1:6:1$



Structure 3.1c

$H:W:L = 1:1:1$

Fig. 2.4—Structures for testing width effects.



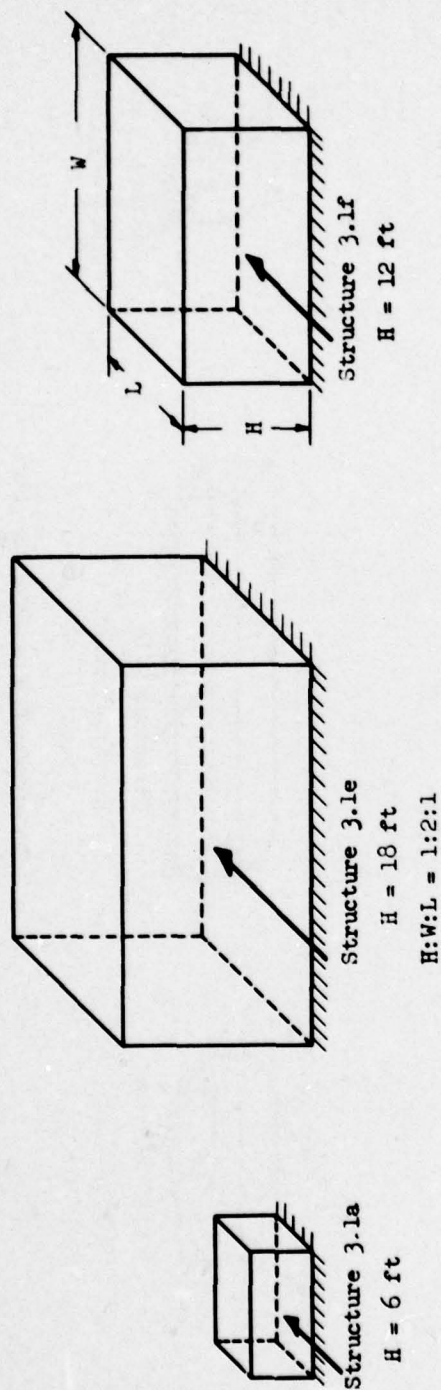


Fig. 2.5 — Structures for testing size effects.

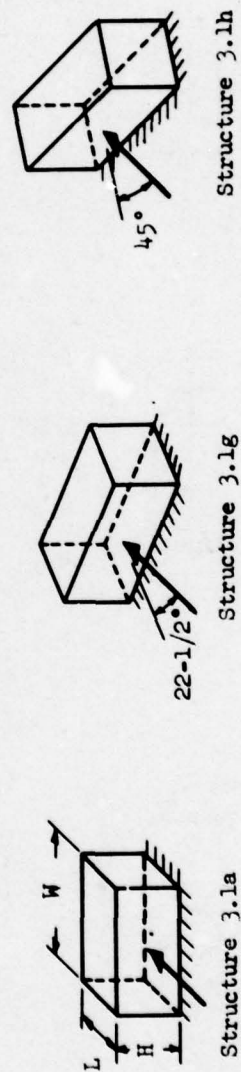
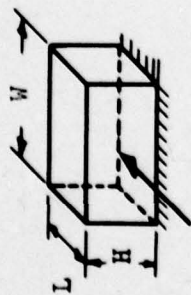
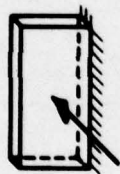


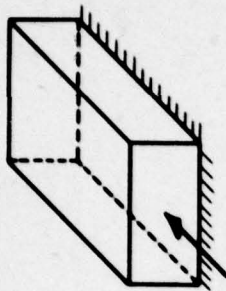
Fig. 2.6 — Structures for testing orientation effects.



Structure 3.1a  
 $H:W:L = 1:2:1$   
 $H = 6 \text{ ft}$

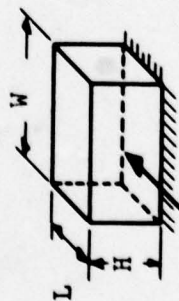


Structure 3.1d  
 $H:W:L = 1:2:1/6$   
 $H = 6 \text{ ft}$

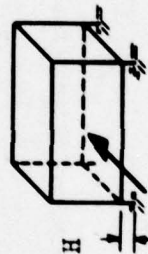


Structure 3.1i  
 $H:W:L = 1:2:3$   
 $H = 6 \text{ ft}$

Fig. 2.7—Structures for testing length effects.



Structure 3.1a  
 $H = 0$

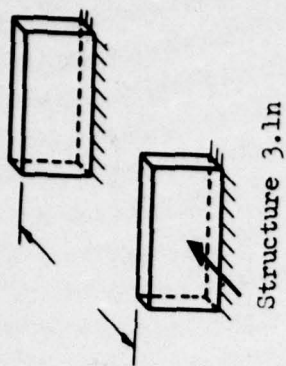


Structure 3.1o  
 $H = H/6$   
 $H:W:L = 1:2:1, H = L = 6 \text{ ft}$

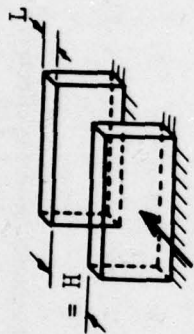


Structure 3.1p  
 $H = H/3$

Fig. 2.8—Structures for testing effects of elevation.



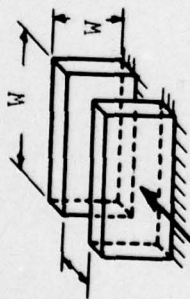
Structure 3.1n



Structure 3.1m

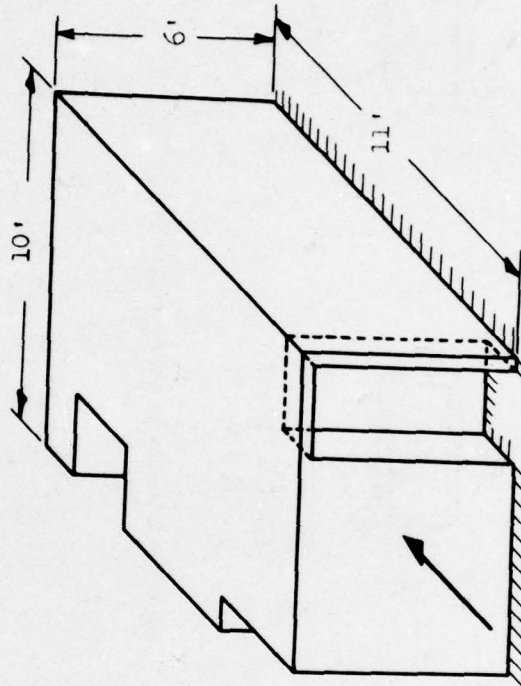
$H:W = 1:2$ ,  $L = 1 \text{ ft}$ ,  $H = 6 \text{ ft}$

Fig. 2.9—Structures for testing shielding effects.



Structure 3.1

$= H/2$



Structure 3.1q

Fig. 2.10—Structures for testing re-entrant corner effects.



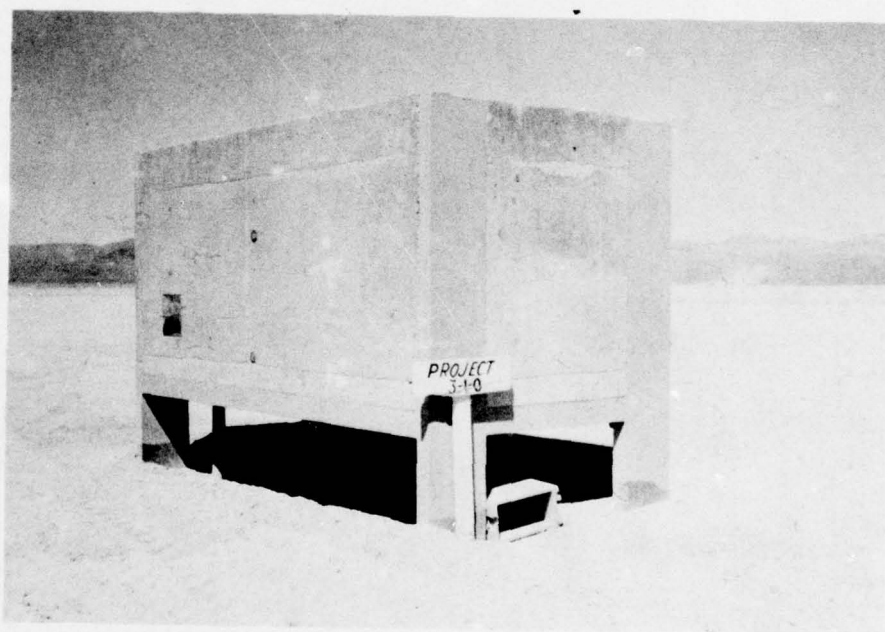
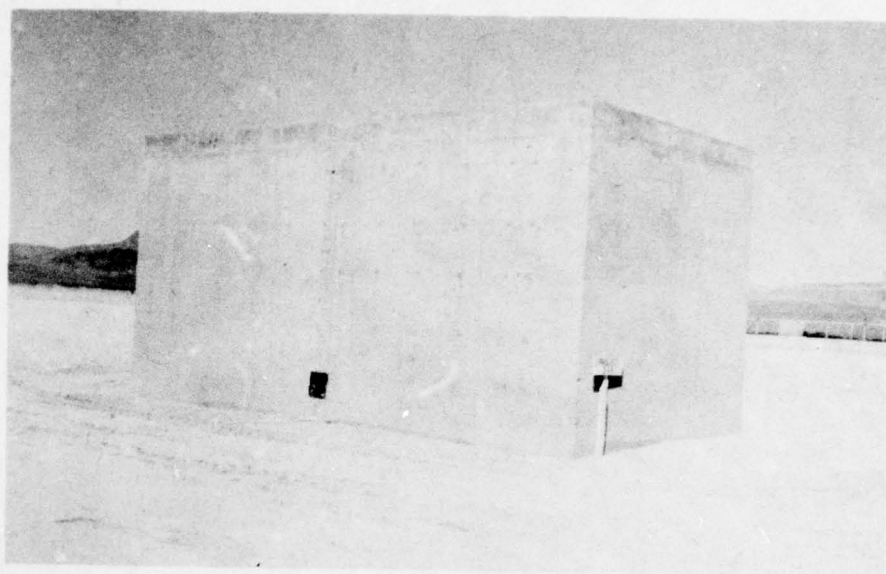


Fig. 2.11 — Photographs of Structures 3.1f (above) and o (below).

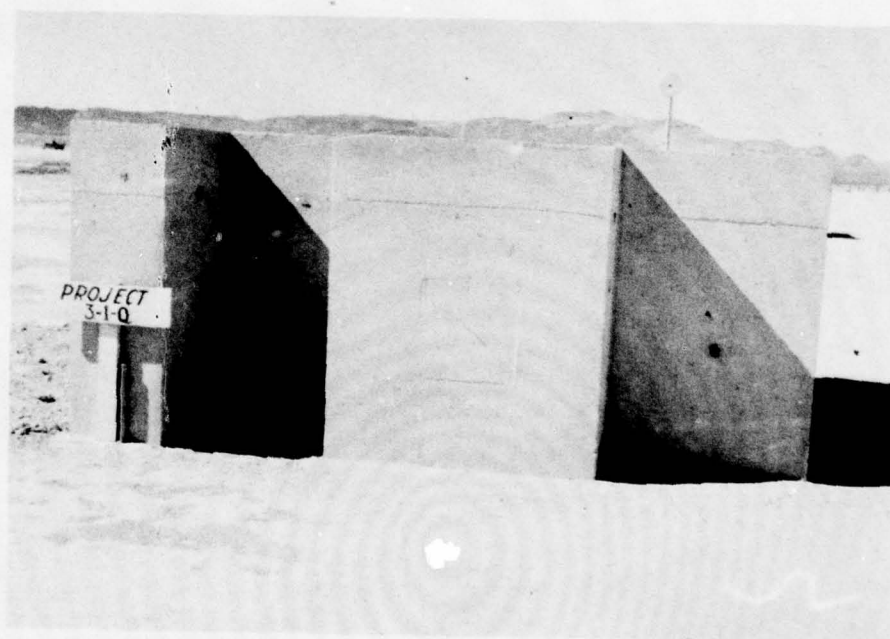
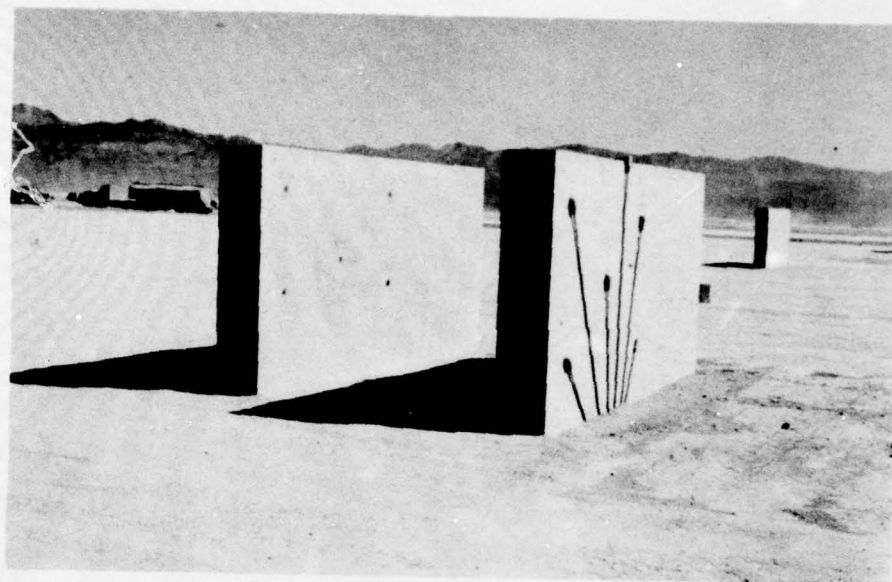
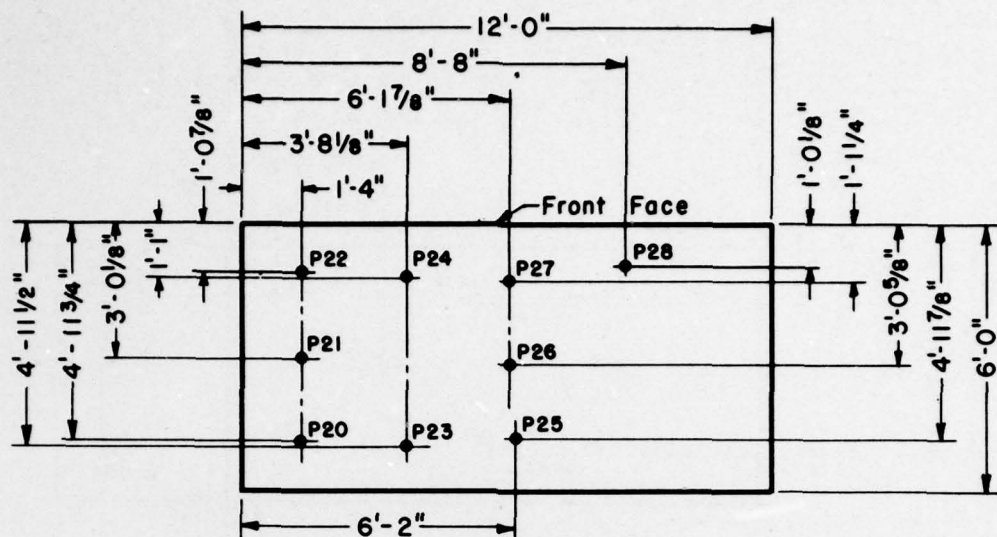
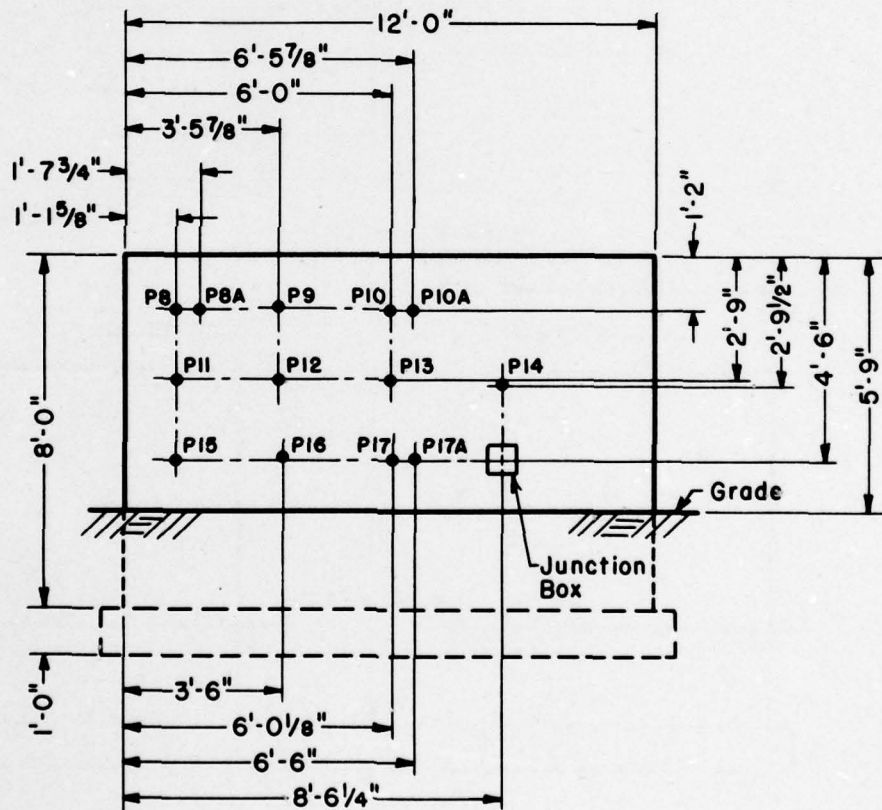


Fig. 2.12—Photographs of Structures 3.1m (above) and q (below).



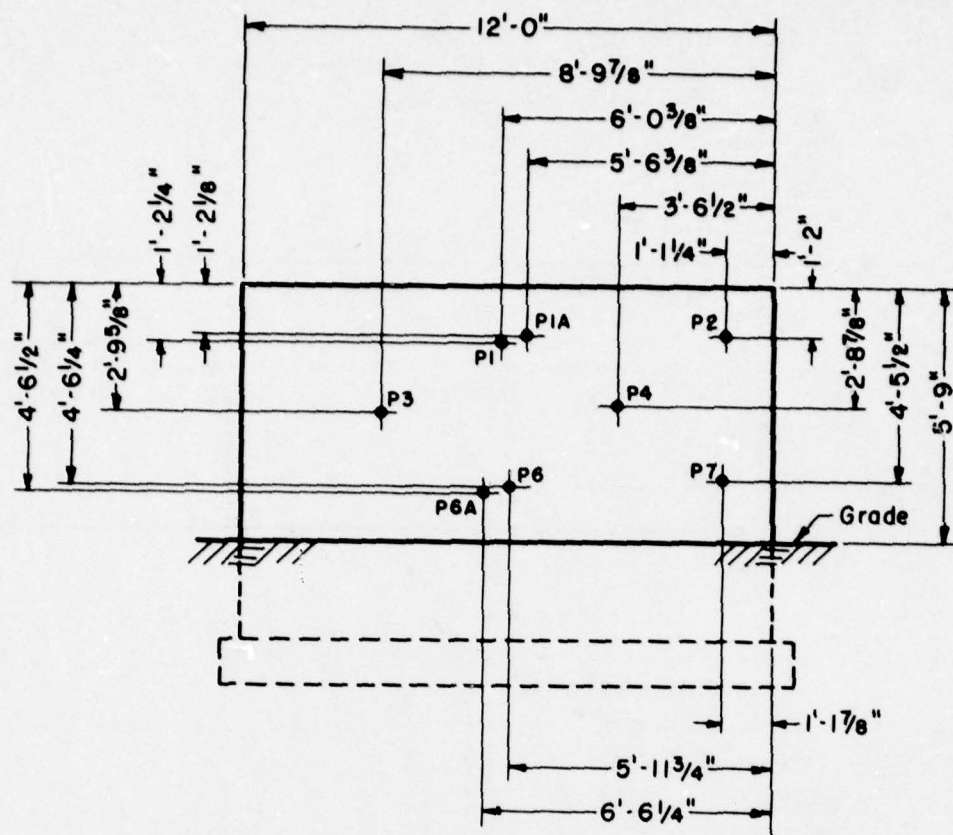
Plan View



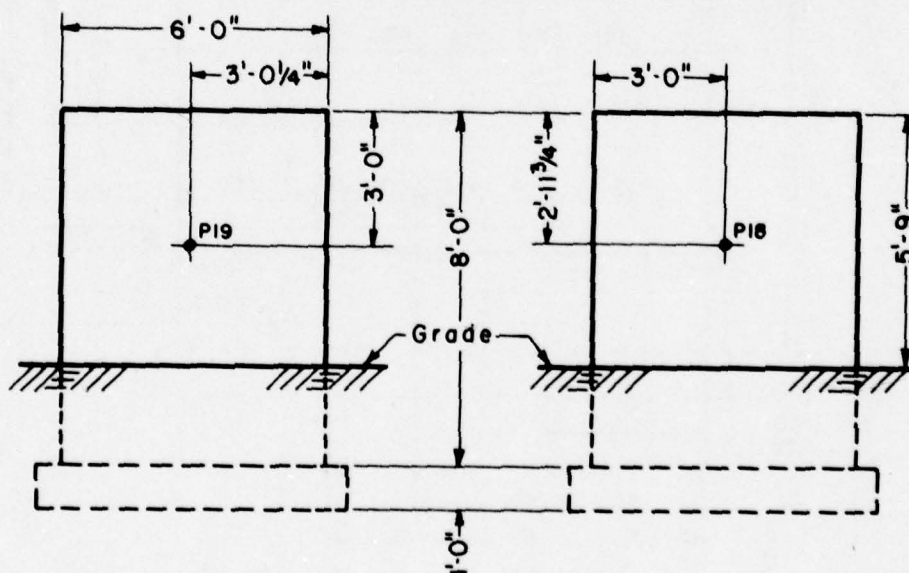
Rear Elevation

Fig. 2.13—Structure 3.1a, plan view and rear elevation.





Front Elevation



Left Elevation

Right Elevation

Fig. 2.14—Structure 3.1a, front, left, and right elevations.

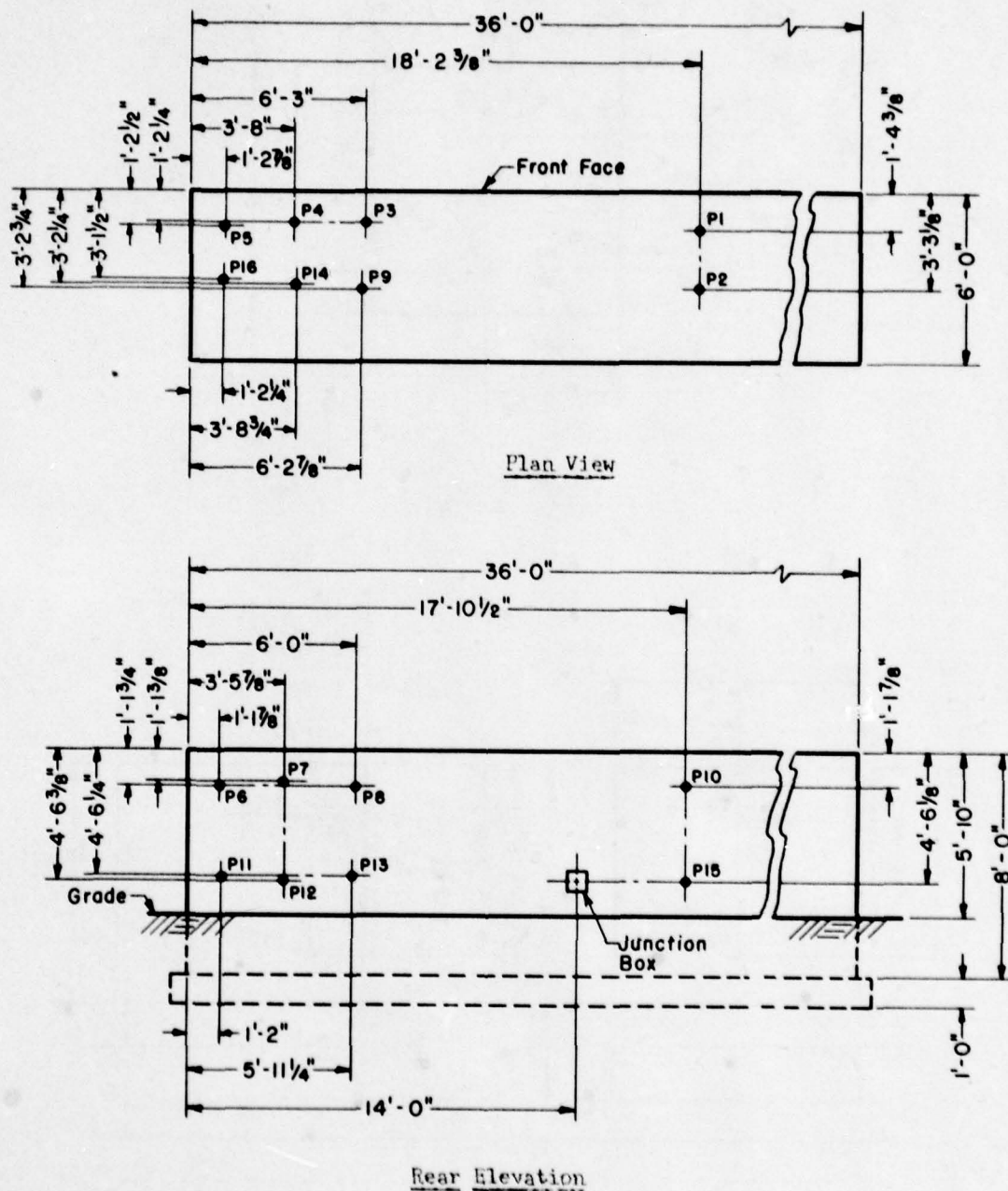
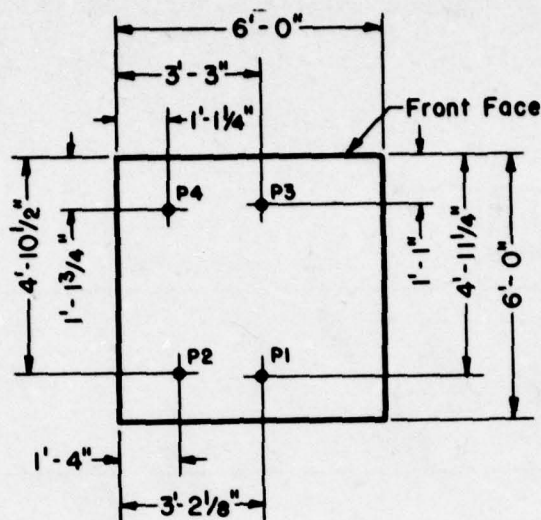
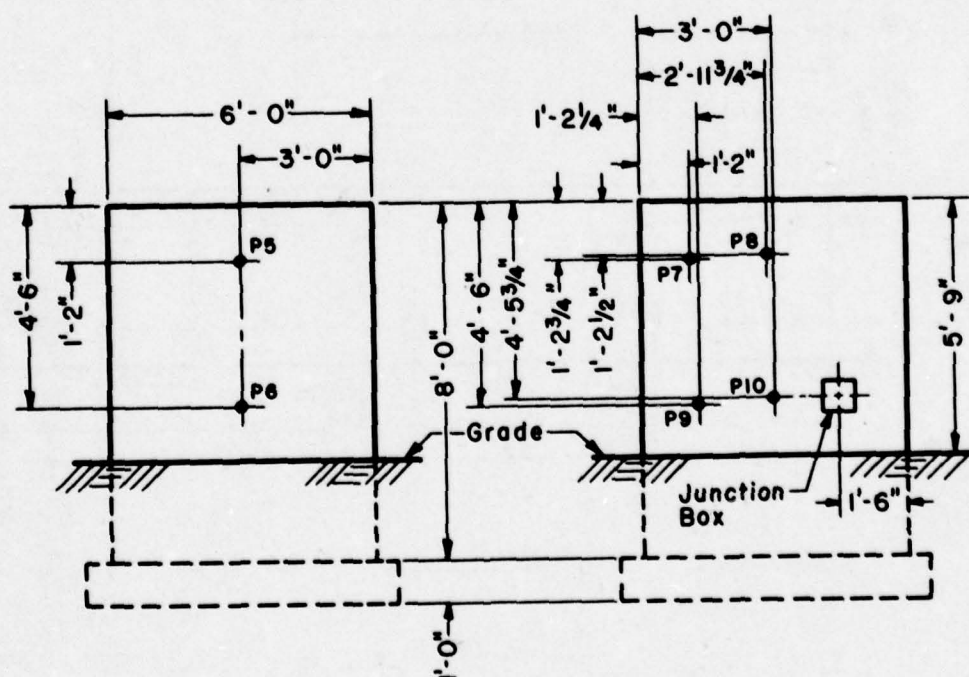


Fig. 2.15—Structure 3.1b, plan view and rear elevation.



Plan View

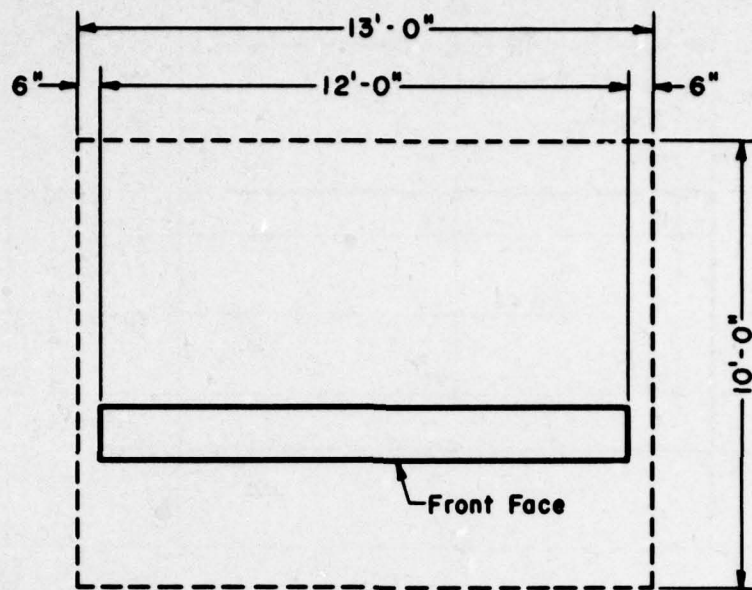


Front Elevation

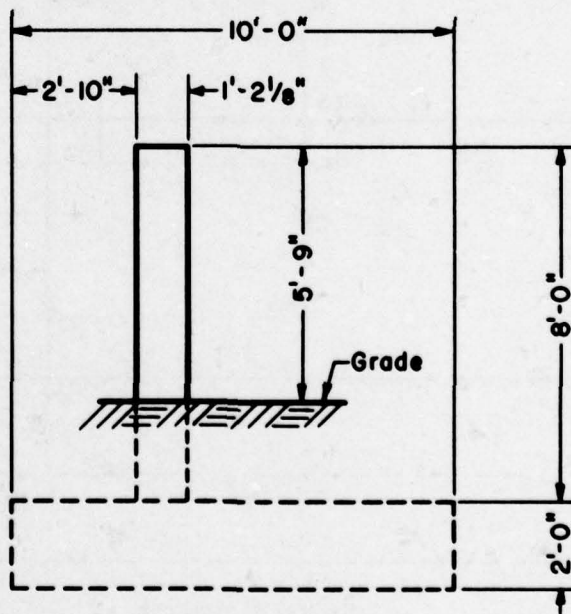
Rear Elevation

Fig. 2.16—Structure 3.1c, plan view and front and rear elevations.





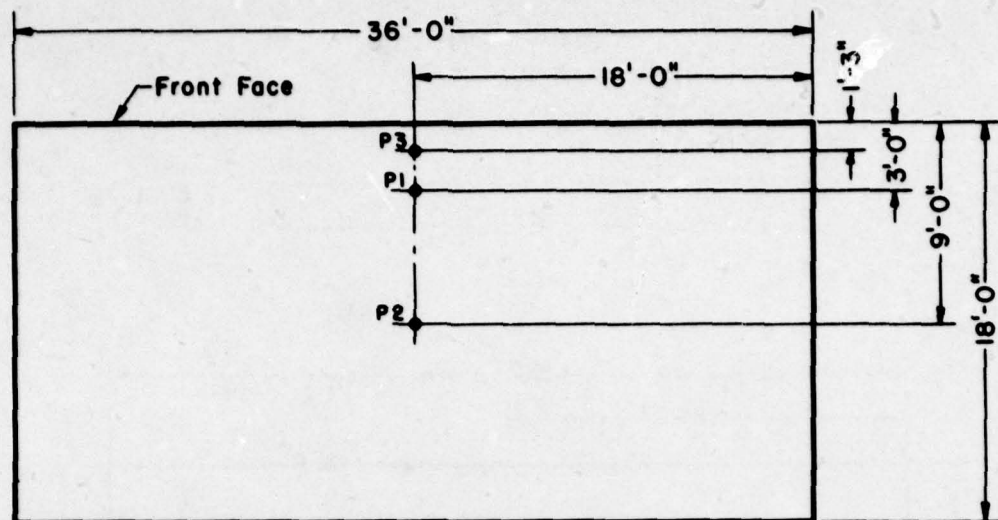
Plan View



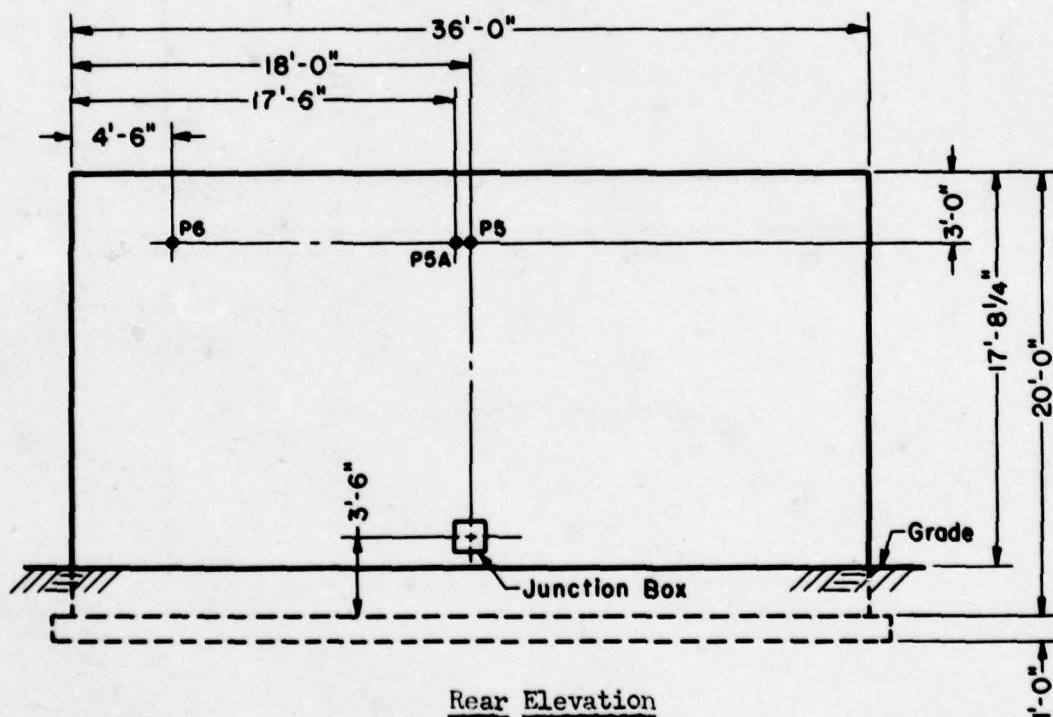
Side Elevation

Fig. 2.17—Structure 3.1d, plan view and side elevation.





Plan View



Rear Elevation

Fig. 2.19—Structure 3.1e, plan view and rear elevation.



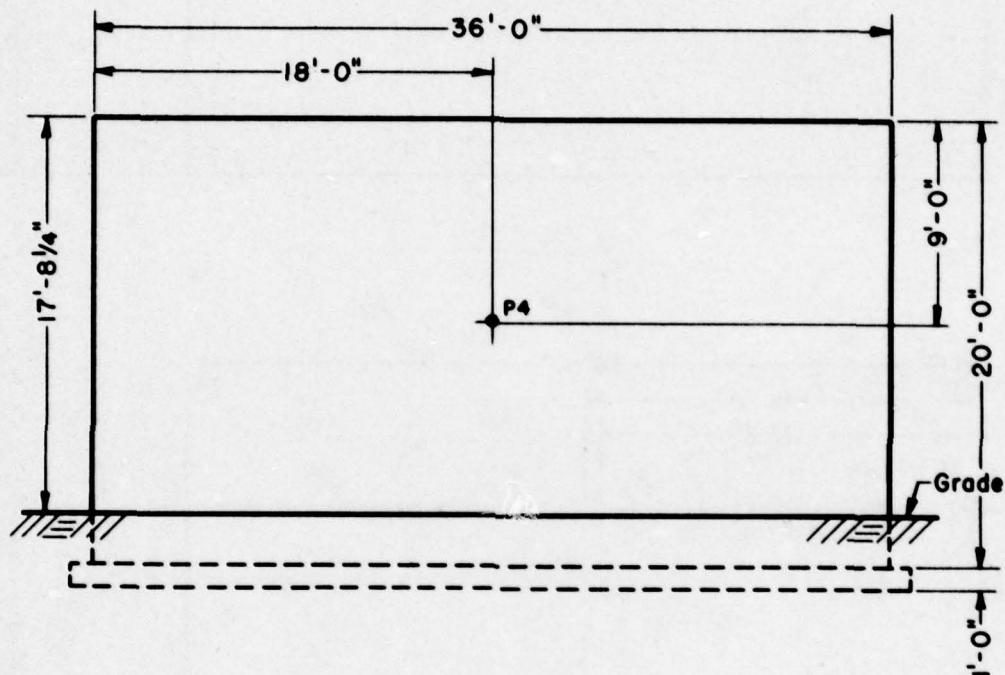
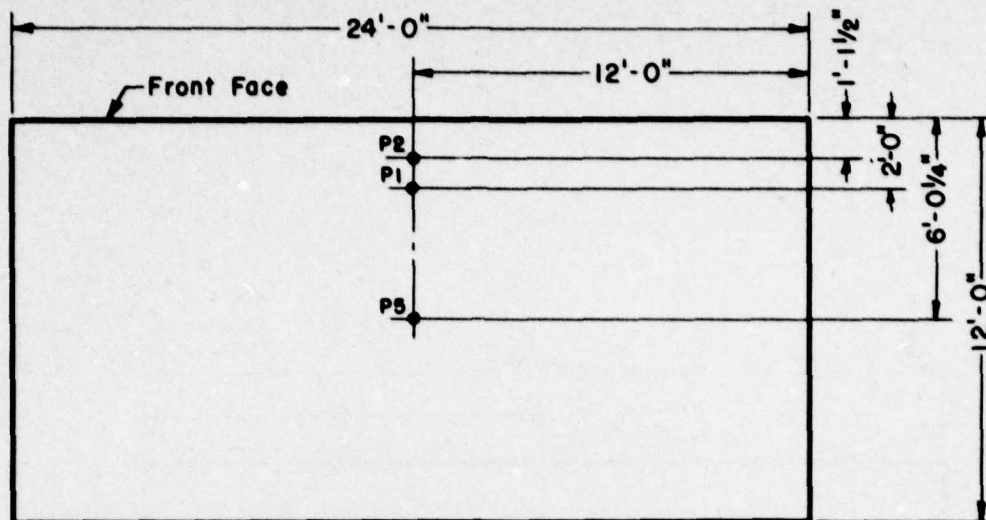
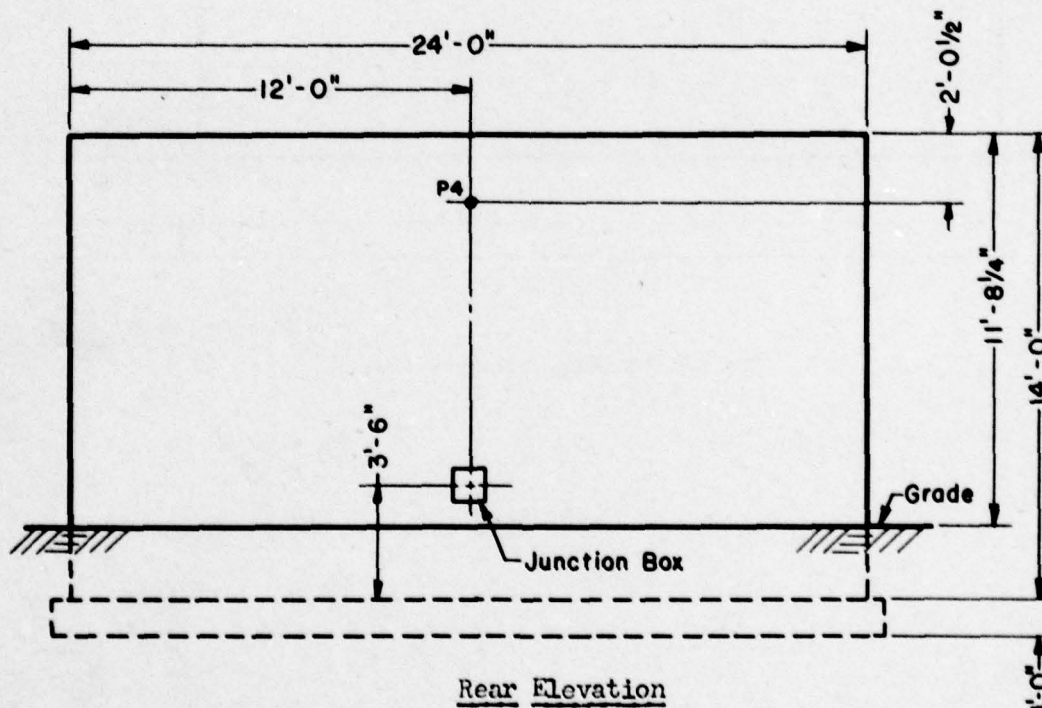


Fig. 2.20—Structure 3.1e, front elevation.



Plan View



Rear Elevation

Fig. 2.21 — Structure 3.1f, plan view and rear elevation.

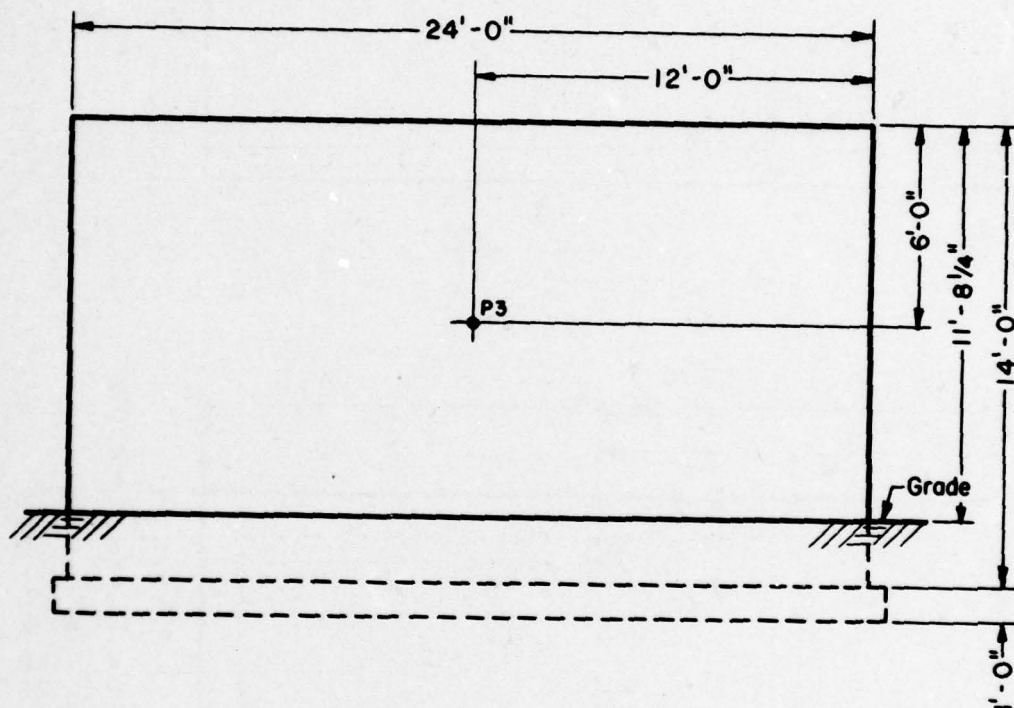
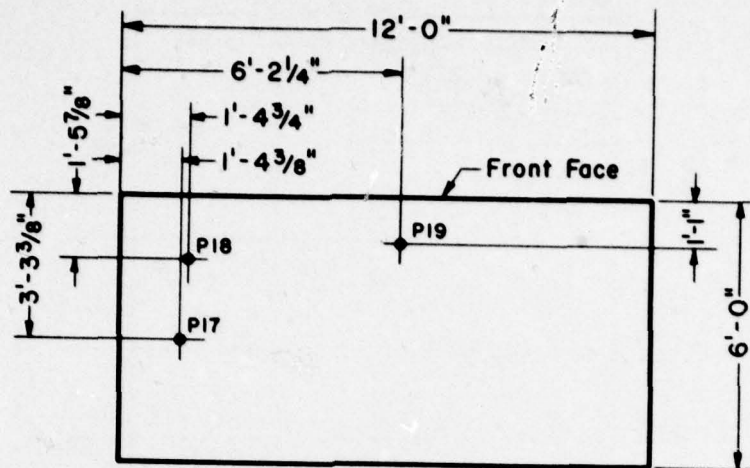
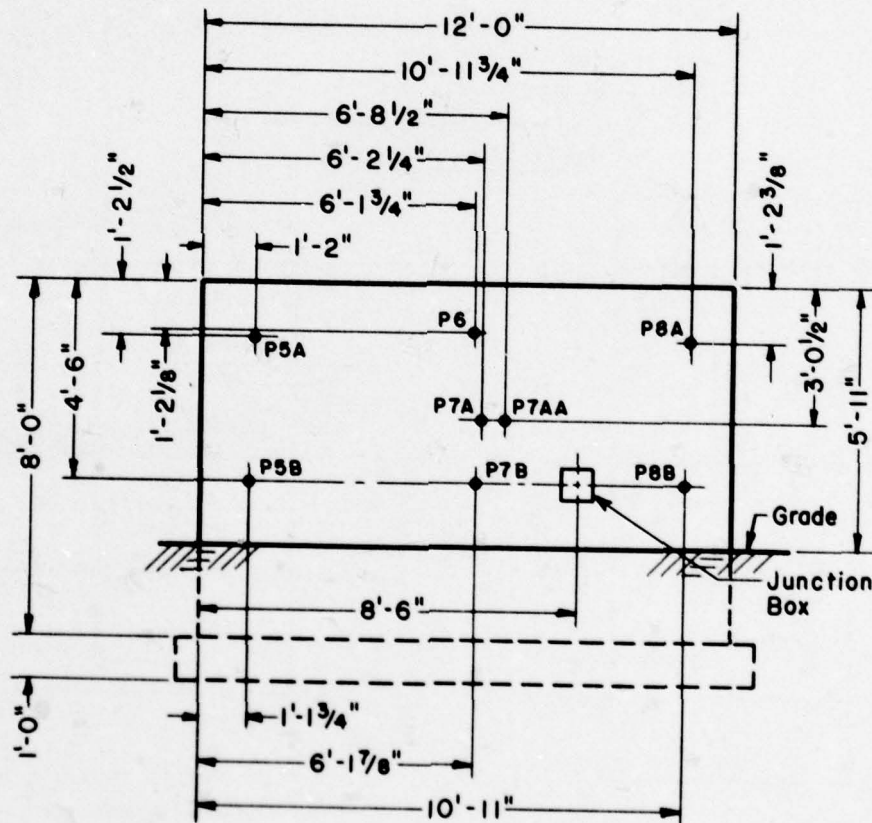


Fig. 2.22—Structure 3.1f, front elevation.





Plan View



Rear Elevation

Fig. 2.23—Structure 3.1g, plan view and rear elevation.

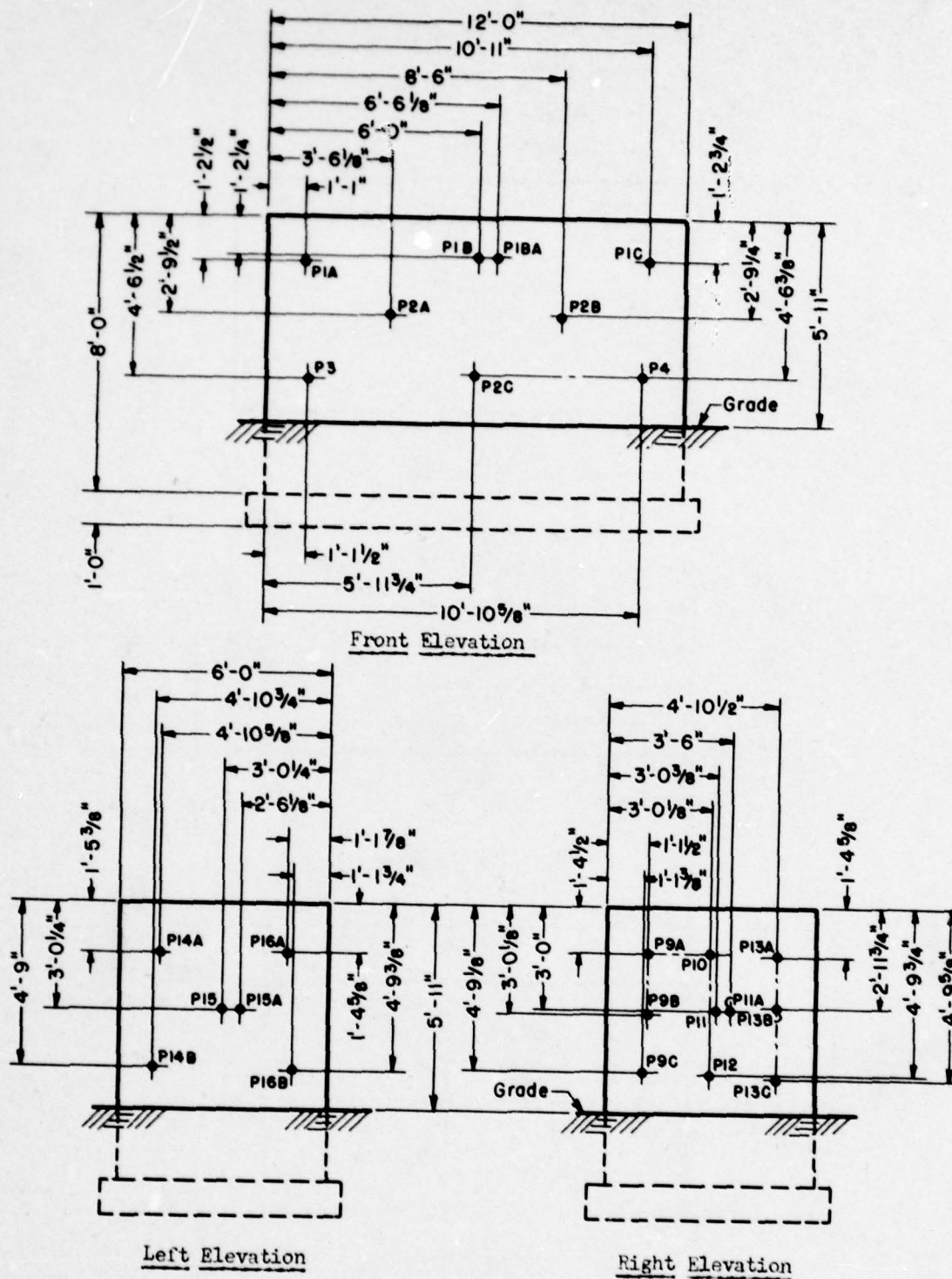
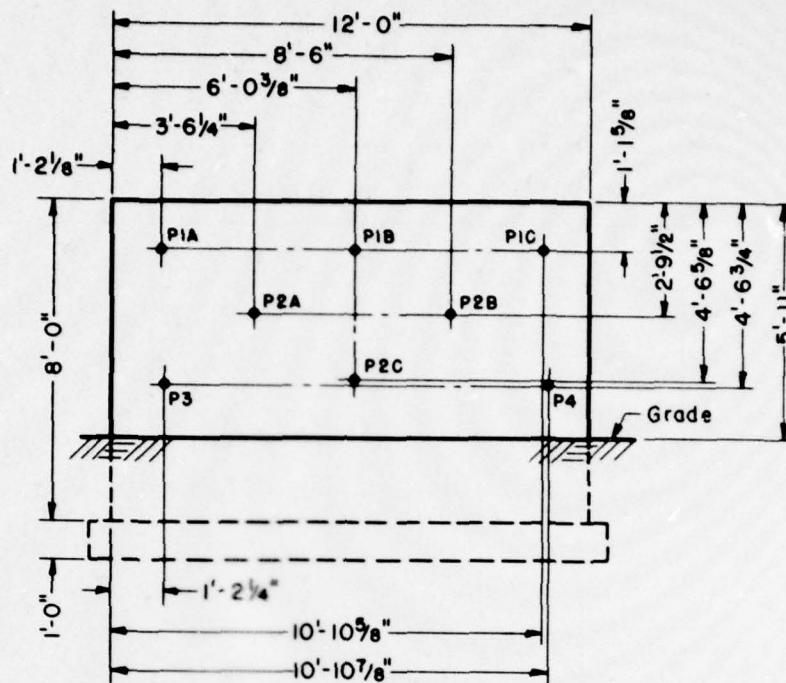


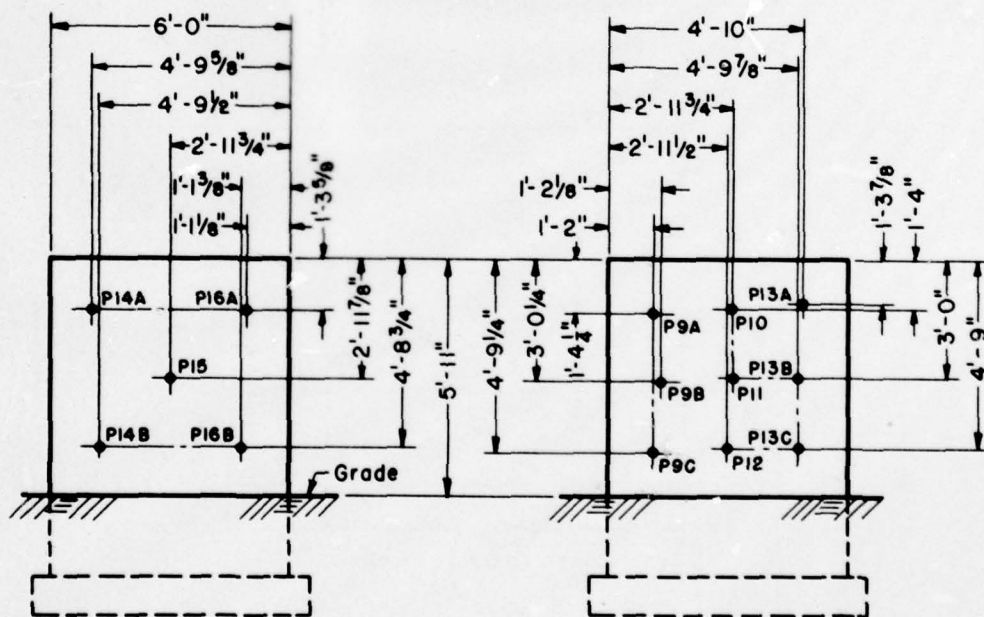
Fig. 2.24—Structure 3.1g, front, left, and right elevations.







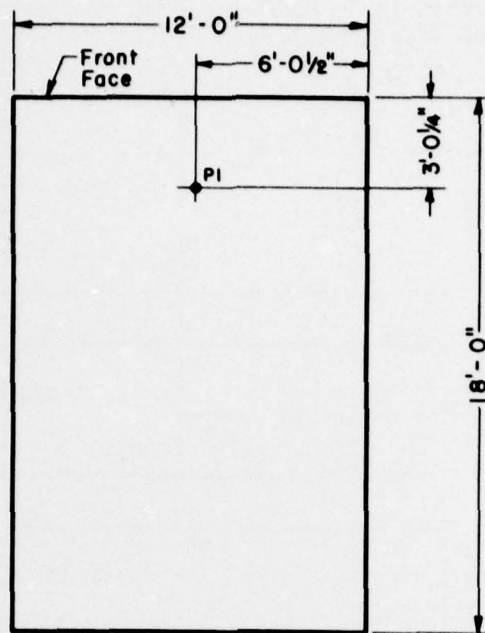
Front Elevation



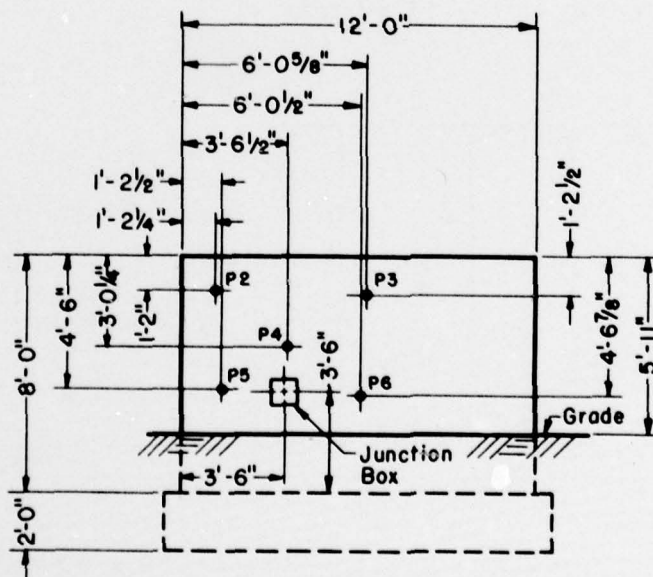
Left Elevation

Right Elevation

Fig. 2.26—Structure 3.1h, front, left, and right elevations.

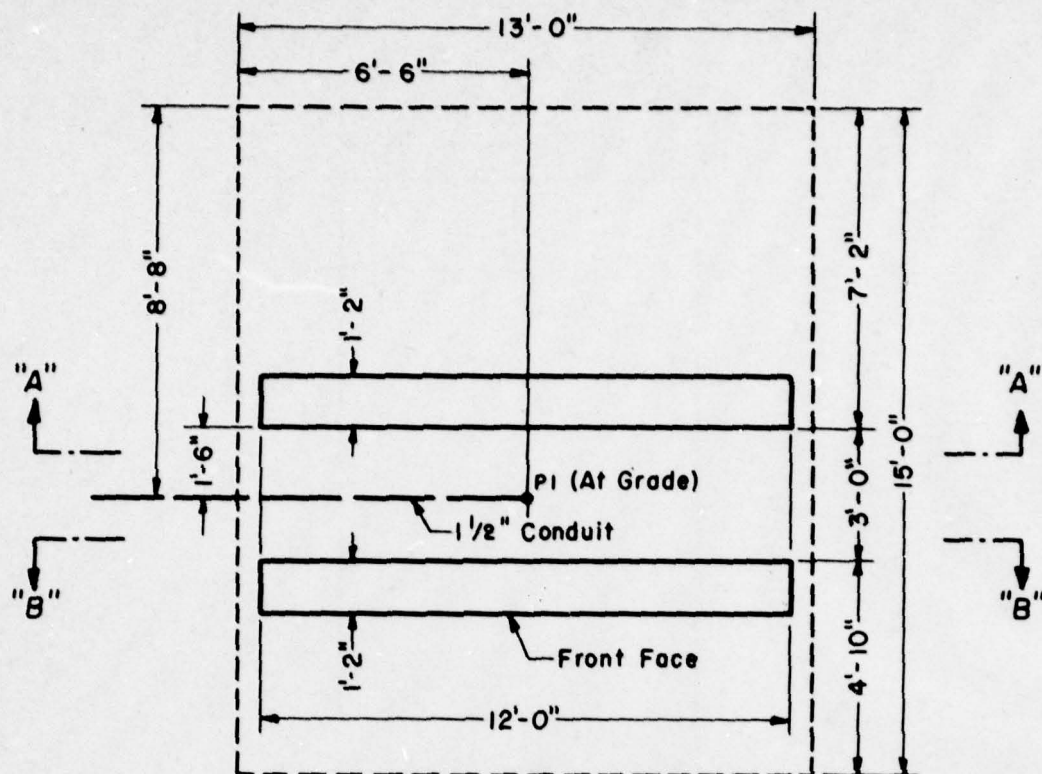


Plan View

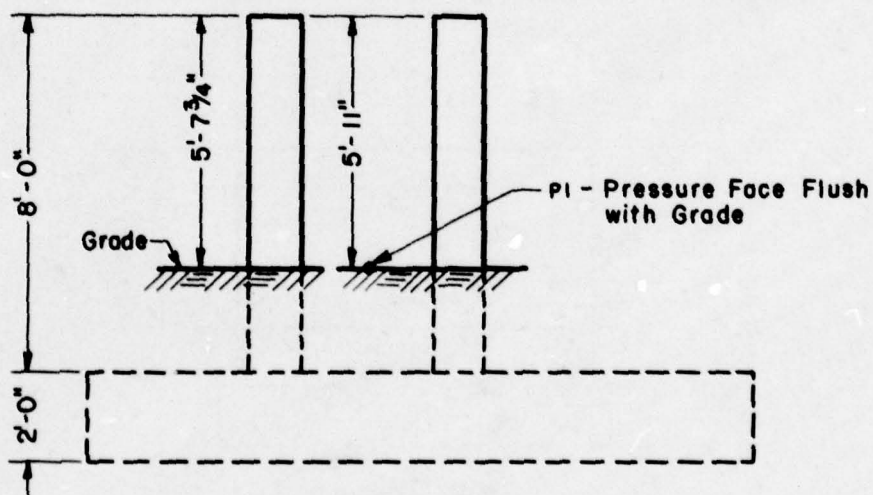


Rear Elevation

Fig. 2.27—Structure 3.11, plan view and rear elevation.



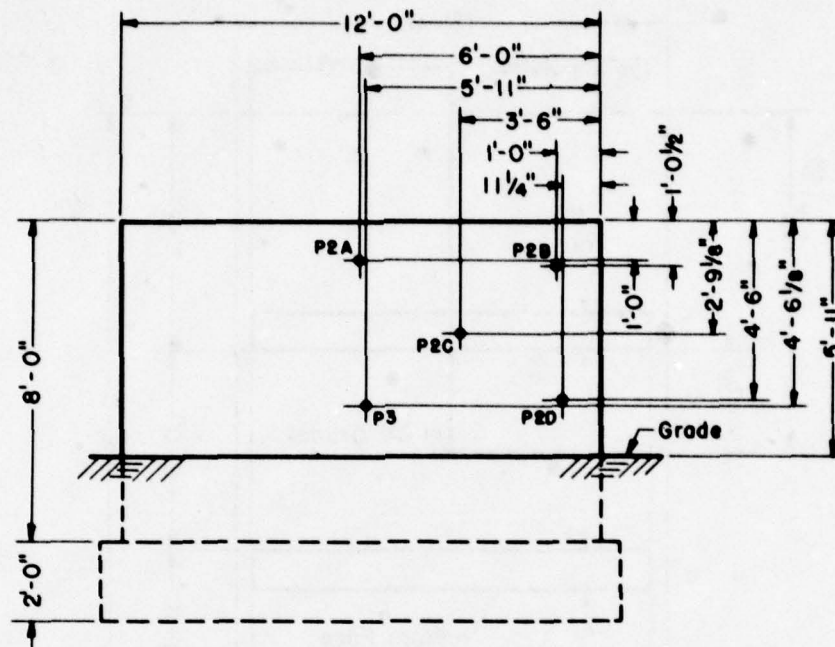
Plan View



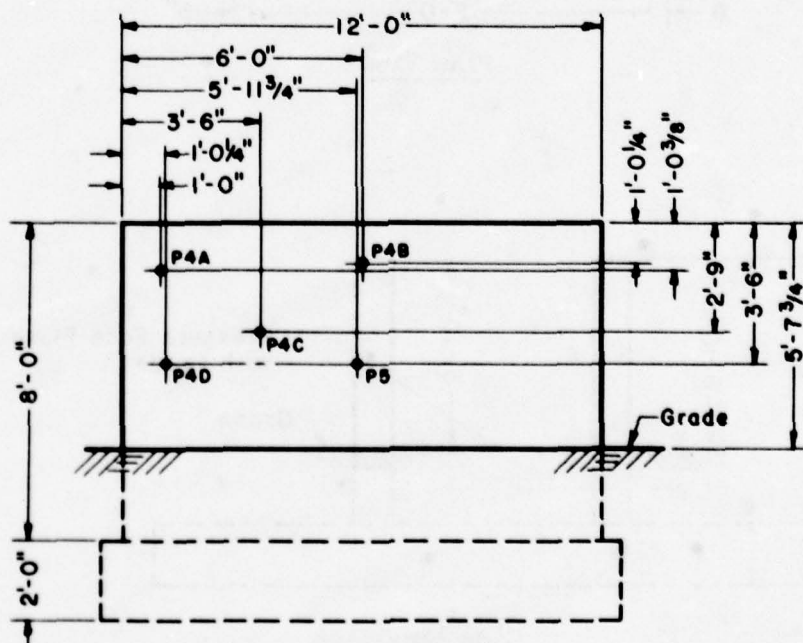
Side Elevation

Fig. 2.28—Structure 3.11, plan view and side elevation.





Section A-A



Section B-B

Fig. 2.29—Structure 3.11, Sections A-A and B-B.

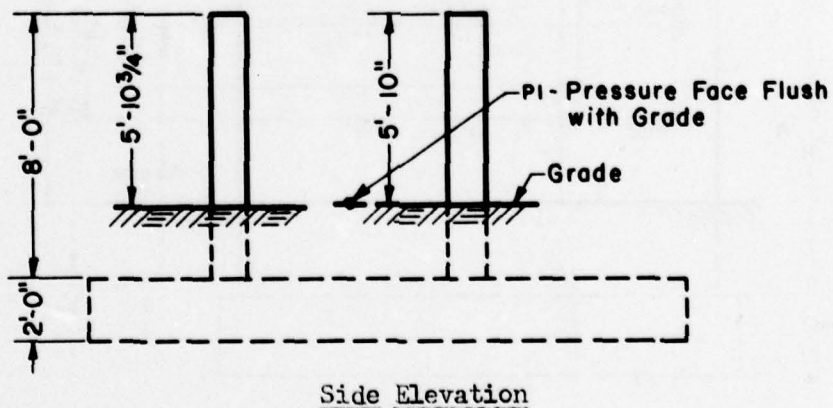
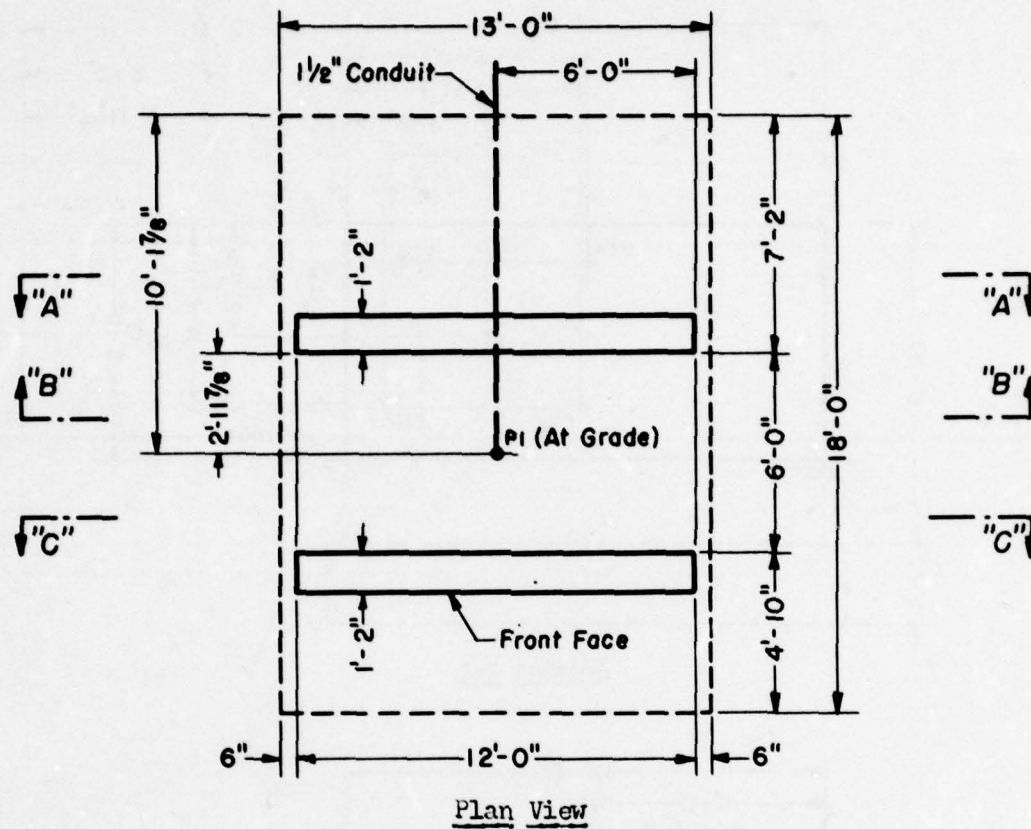


Fig. 2.30—Structure 3.1m, plan view and side elevation.

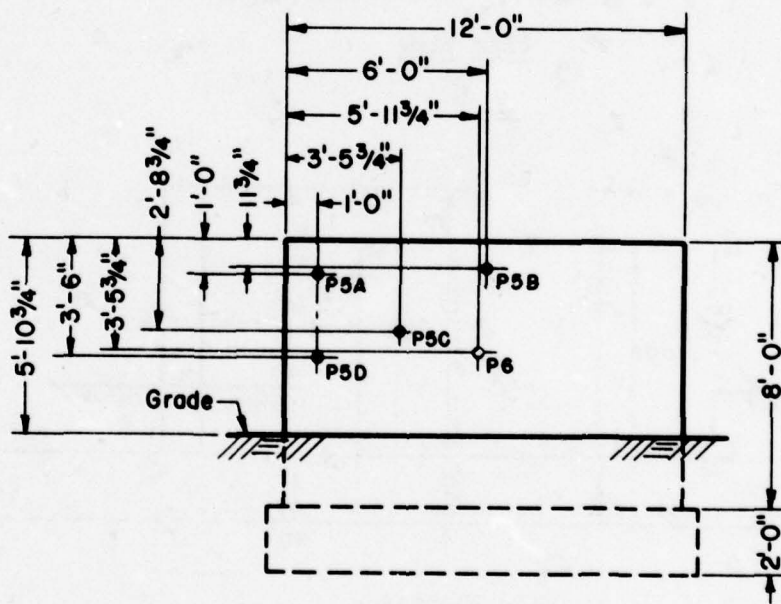
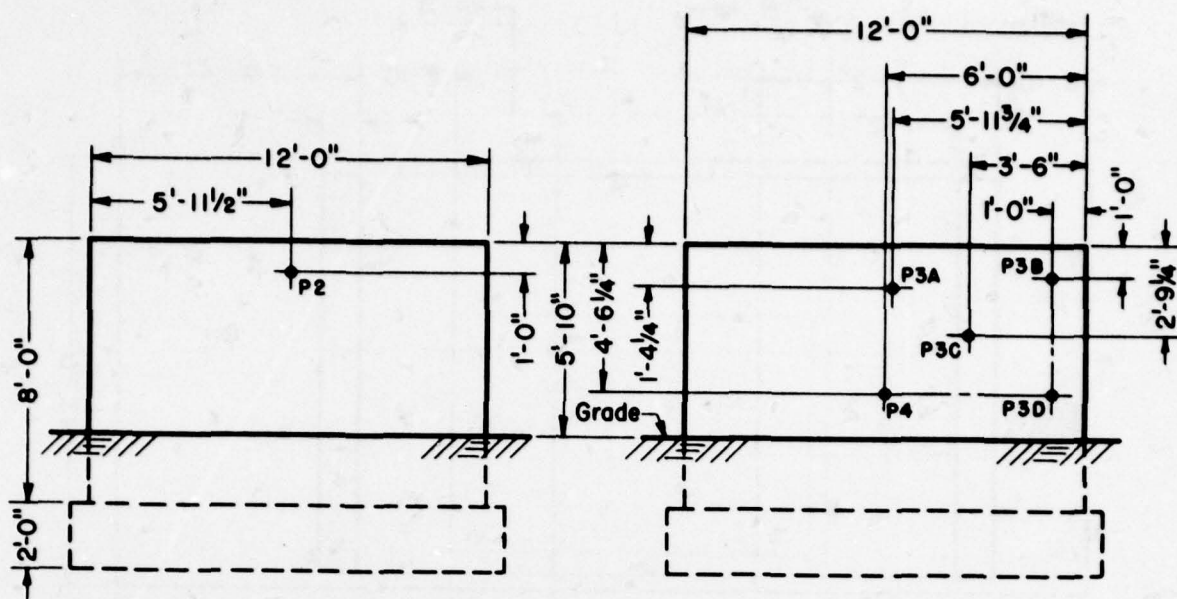


Fig. 2.31 — Structure 3.1m, Sections A-A, B-B, and C-C.



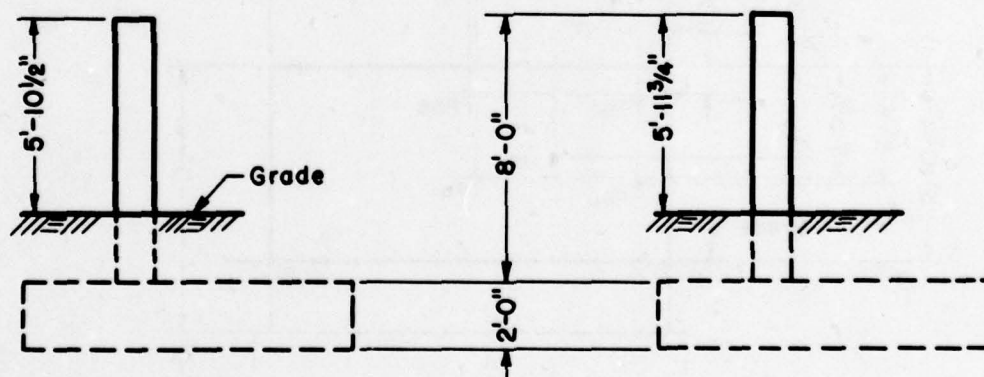
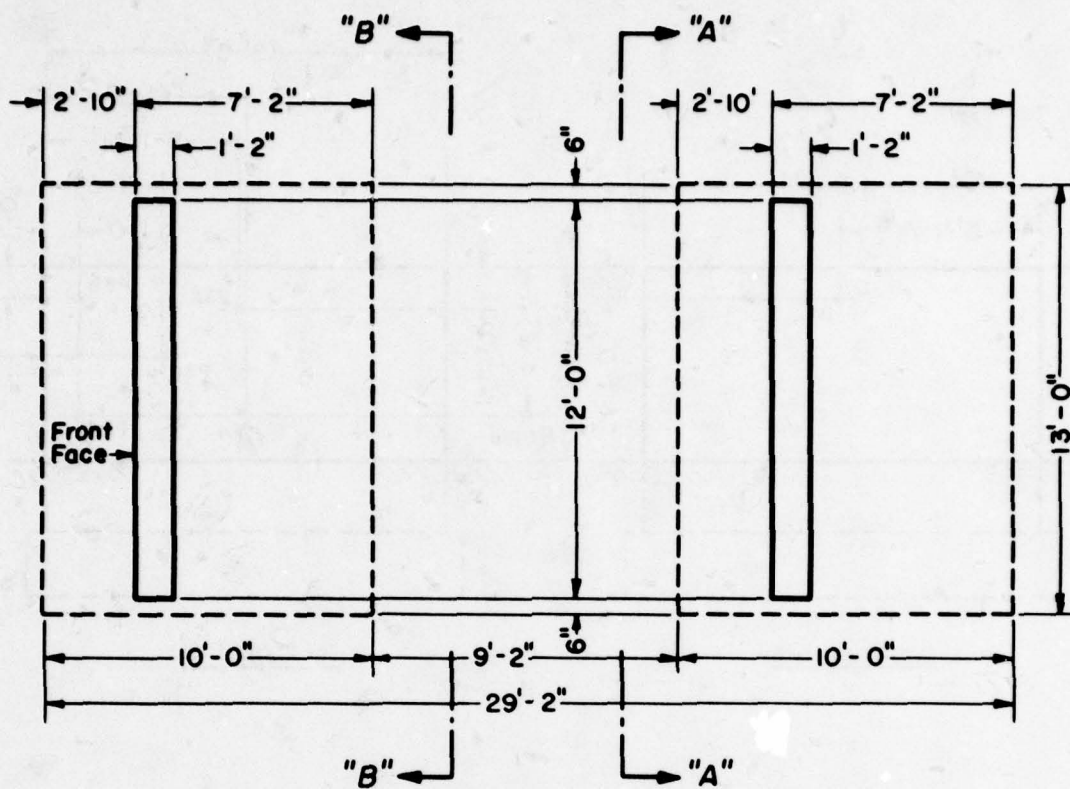
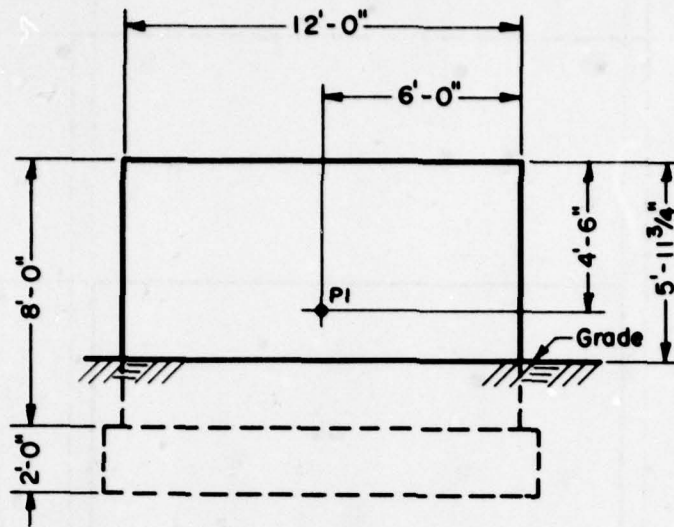
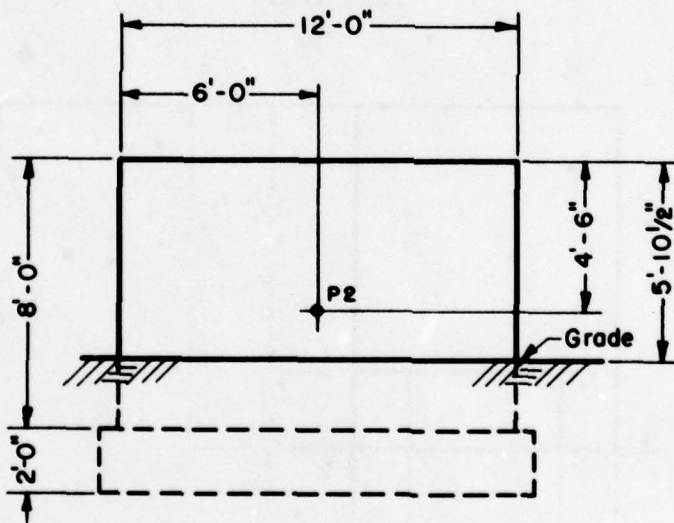


Fig. 2.32—Structure 3.1n, plan view and side elevation.

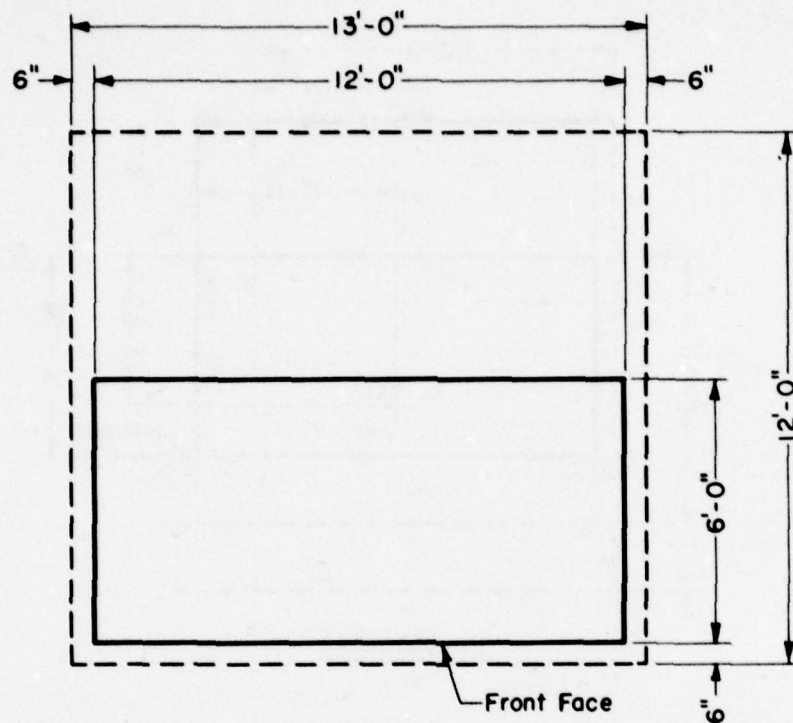


Section A-A

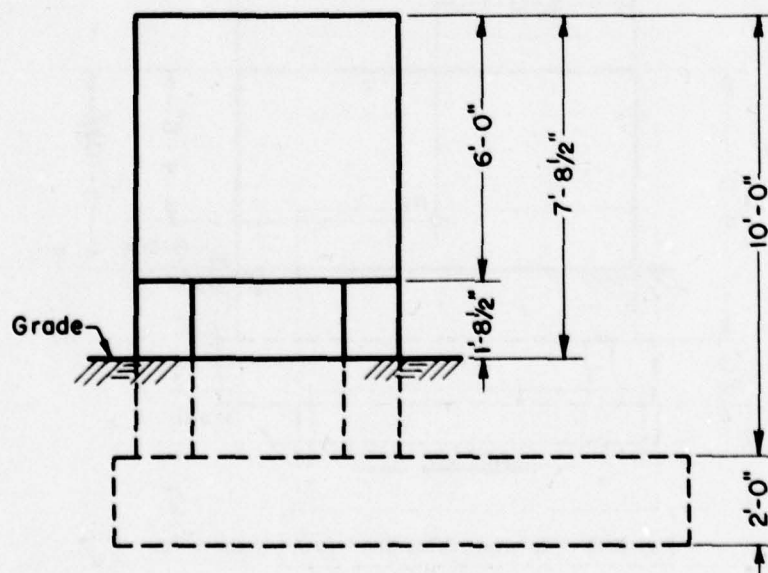


Section B-B

Fig. 2.33—Structure 3.1n, Sections A-A and B-B.



Plan View



Side Elevation

Fig. 2.34—Structure 3.10, plan view and side elevation.



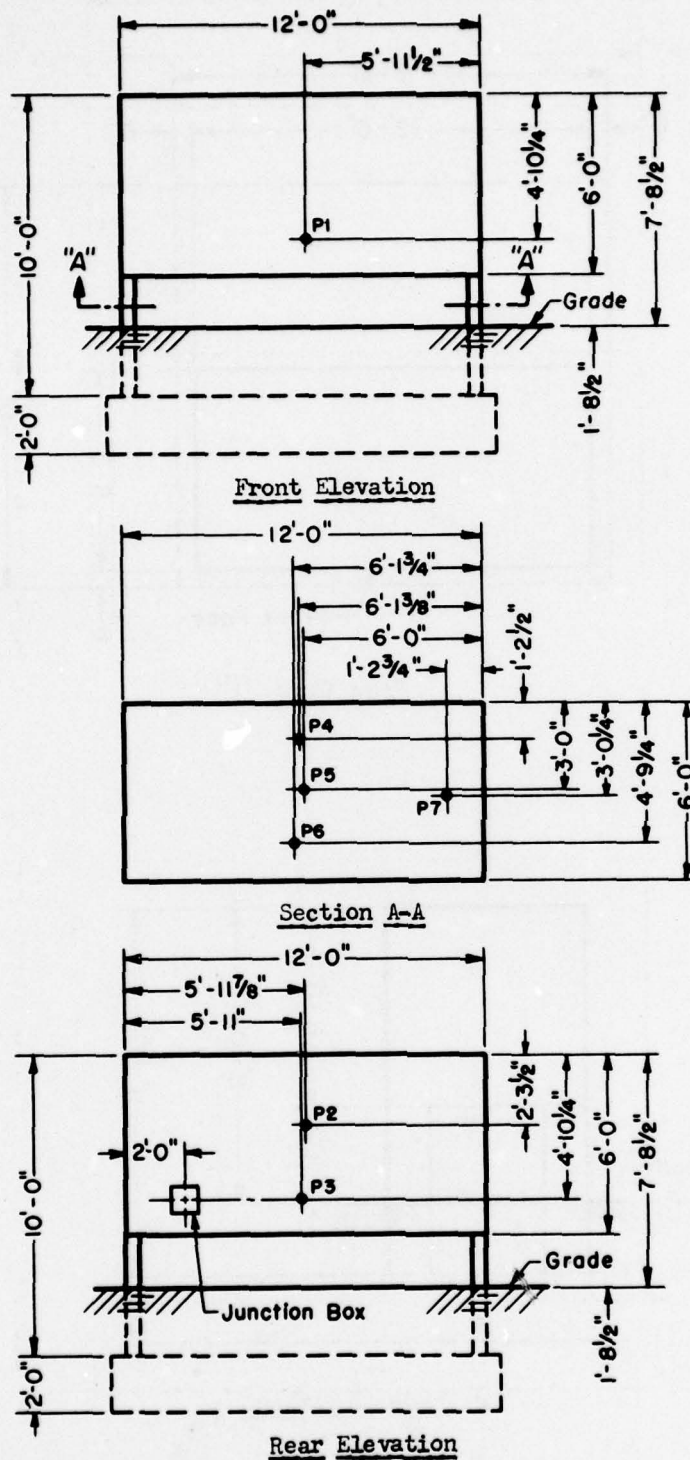
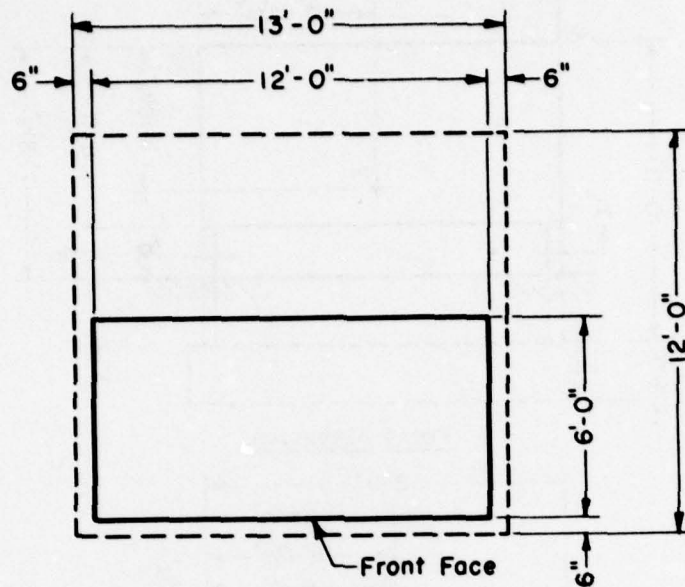
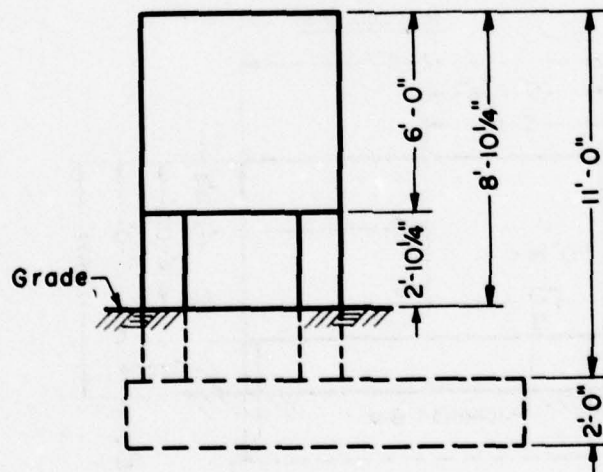


Fig. 2.35—Structure 3.10, front and rear elevations and Section A-A.



Plan View



Side Elevation

Fig. 2.36—Structure 3.1p, plan view and side elevation.

UNCLASSIFIED

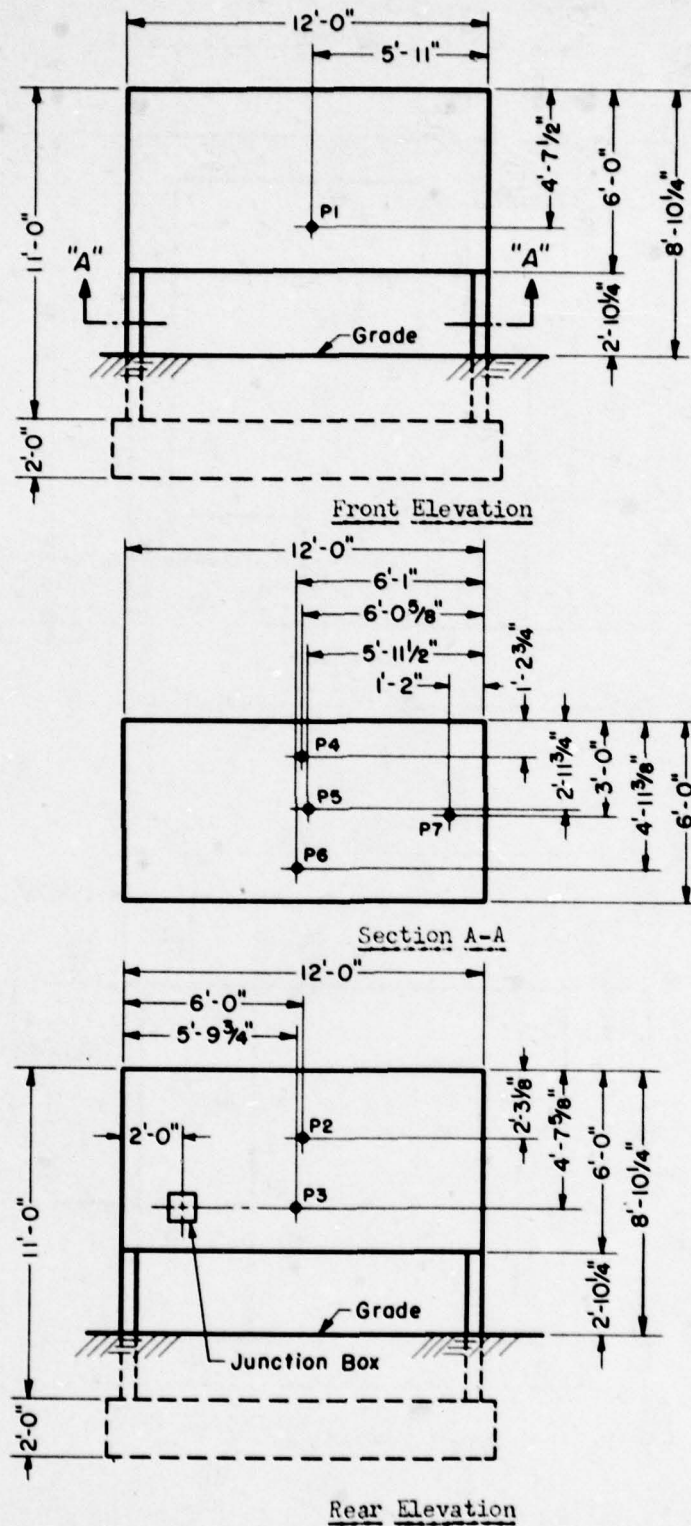
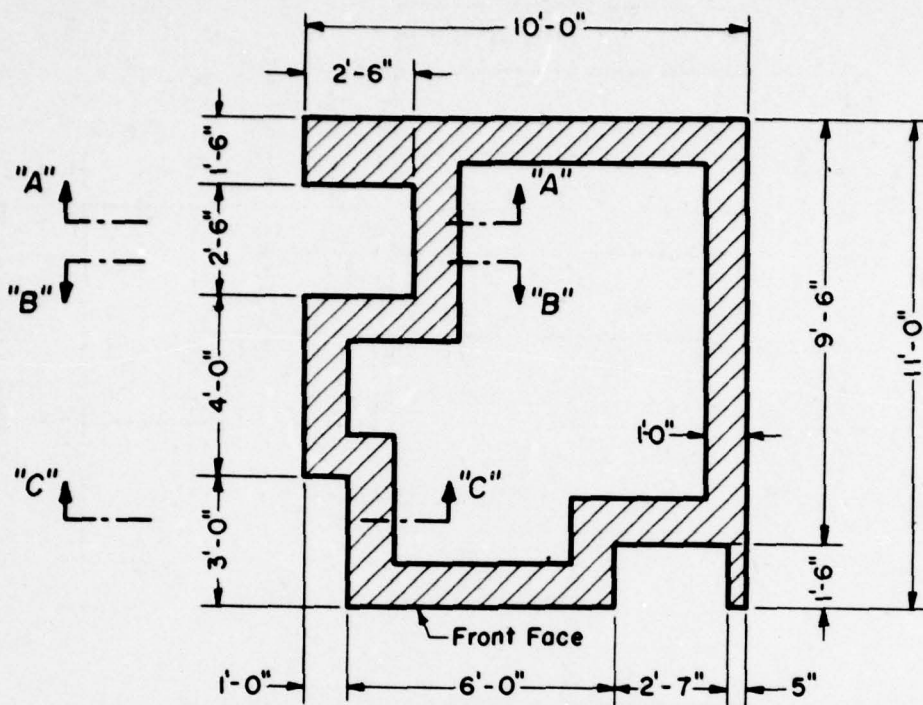
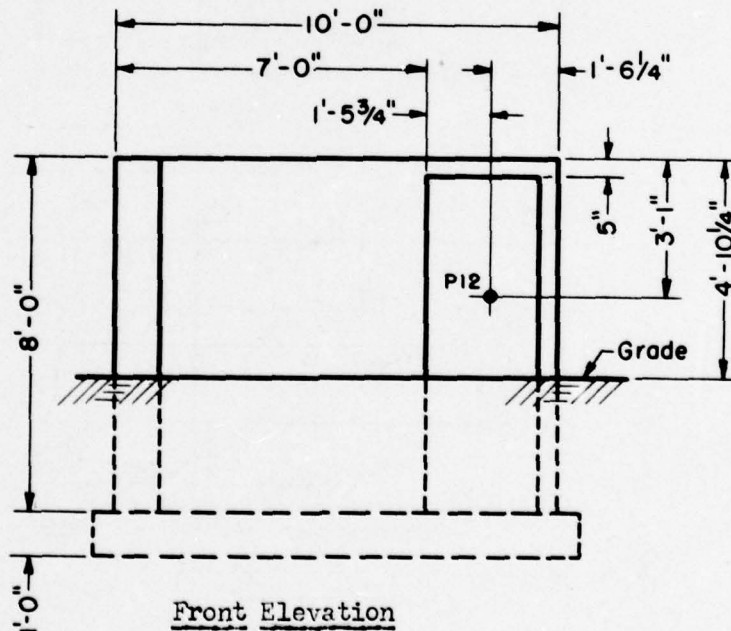


Fig. 2.37—Structure 3.1p, front and rear elevations and Section A-A.





Plan View



Front Elevation

Fig. 2.38—Structure 3.1q, plan view and front elevation.

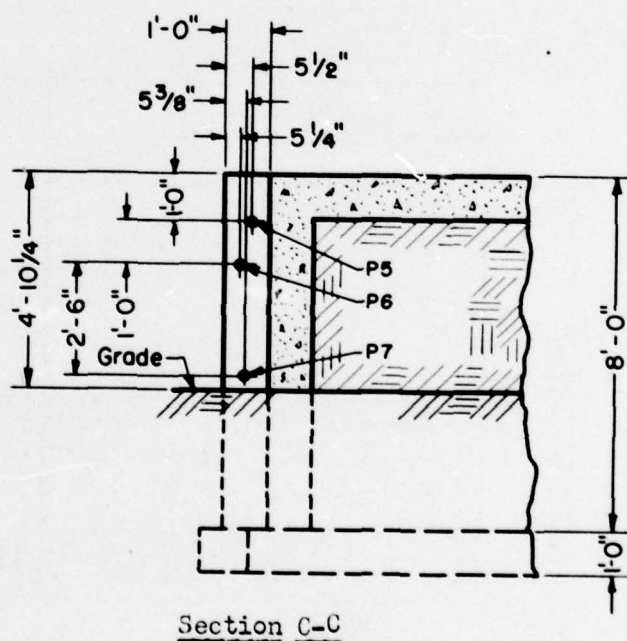
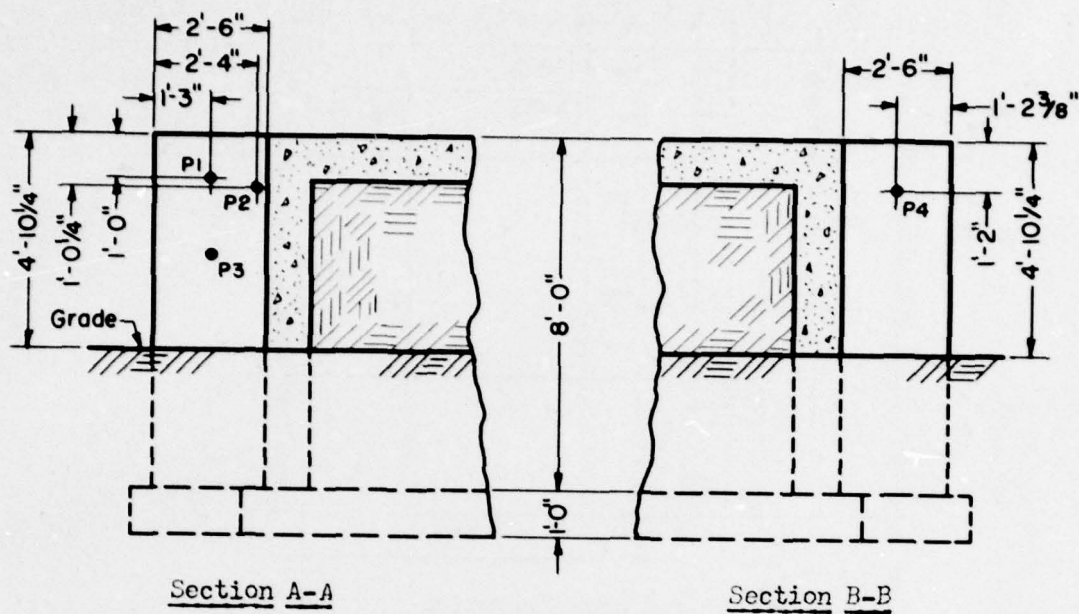


Fig. 2.39—Structure 3.1q, Sections A-A, B-B, and C-C.

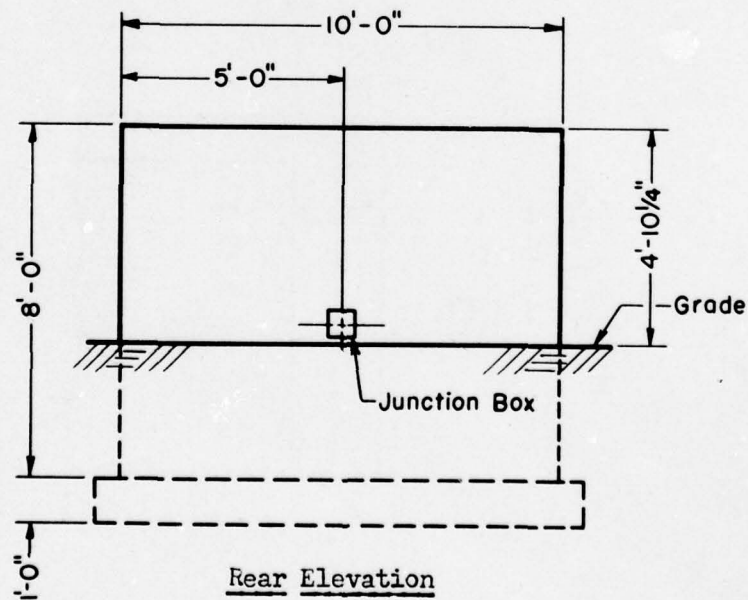
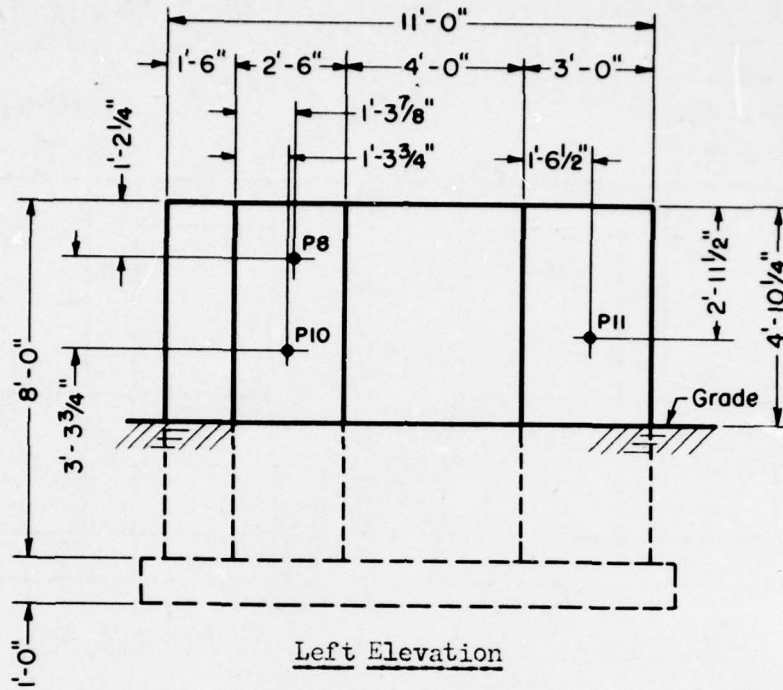


Fig. 2.40—Structure 3.1q, left and rear elevations.

UNCLASSIFIED



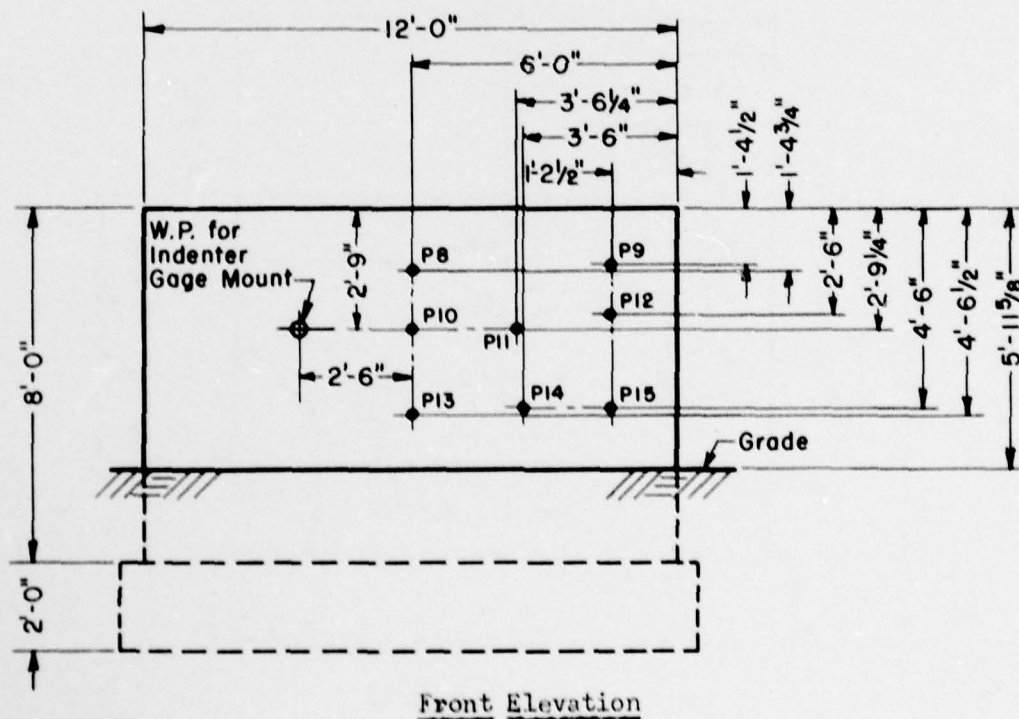
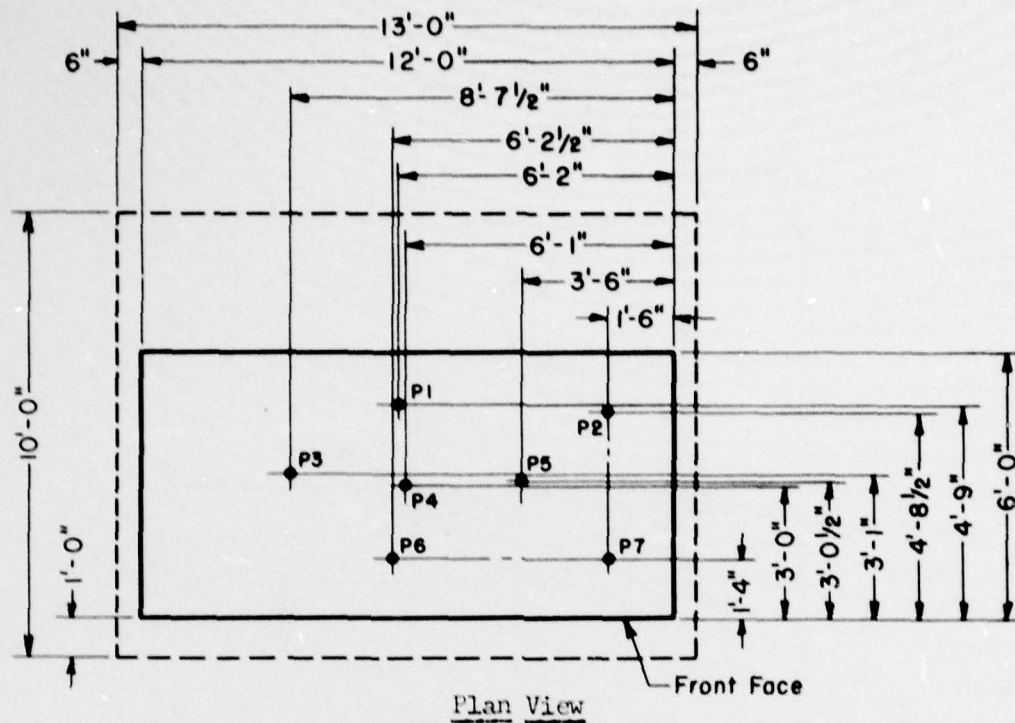
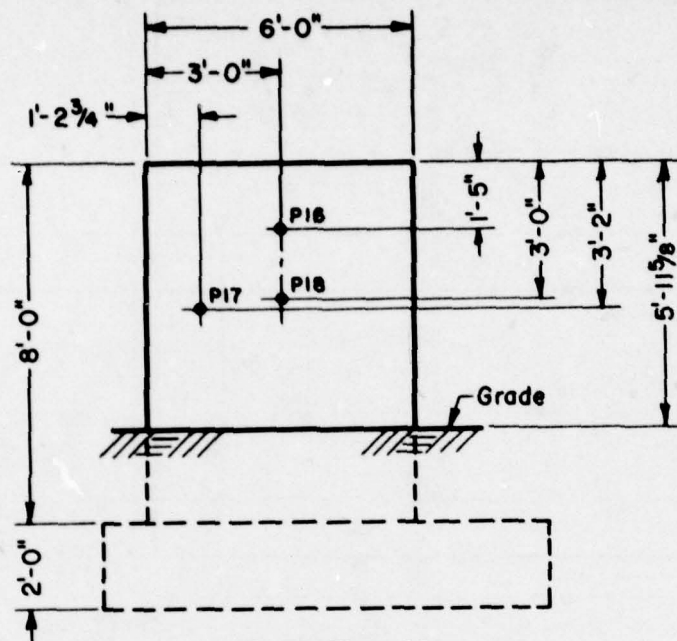
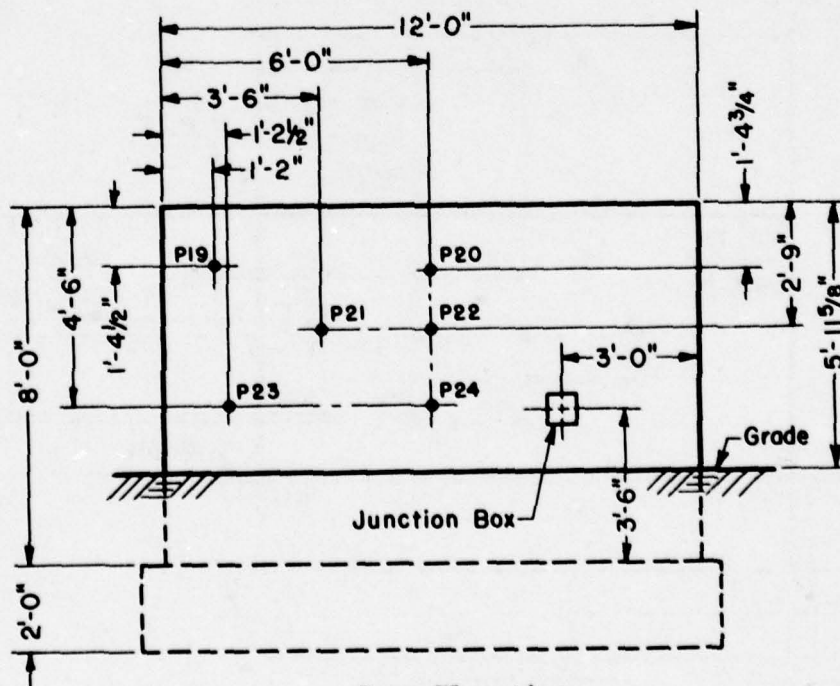


Fig. 2.41 — Structure 3.1s, plan view and front elevation.



Right Elevation



Rear Elevation

Fig. 2.42—Structure 3.1s, right and rear elevations.

UNCLASSIFIED

~~SECRET - RESTRICTED DATA~~

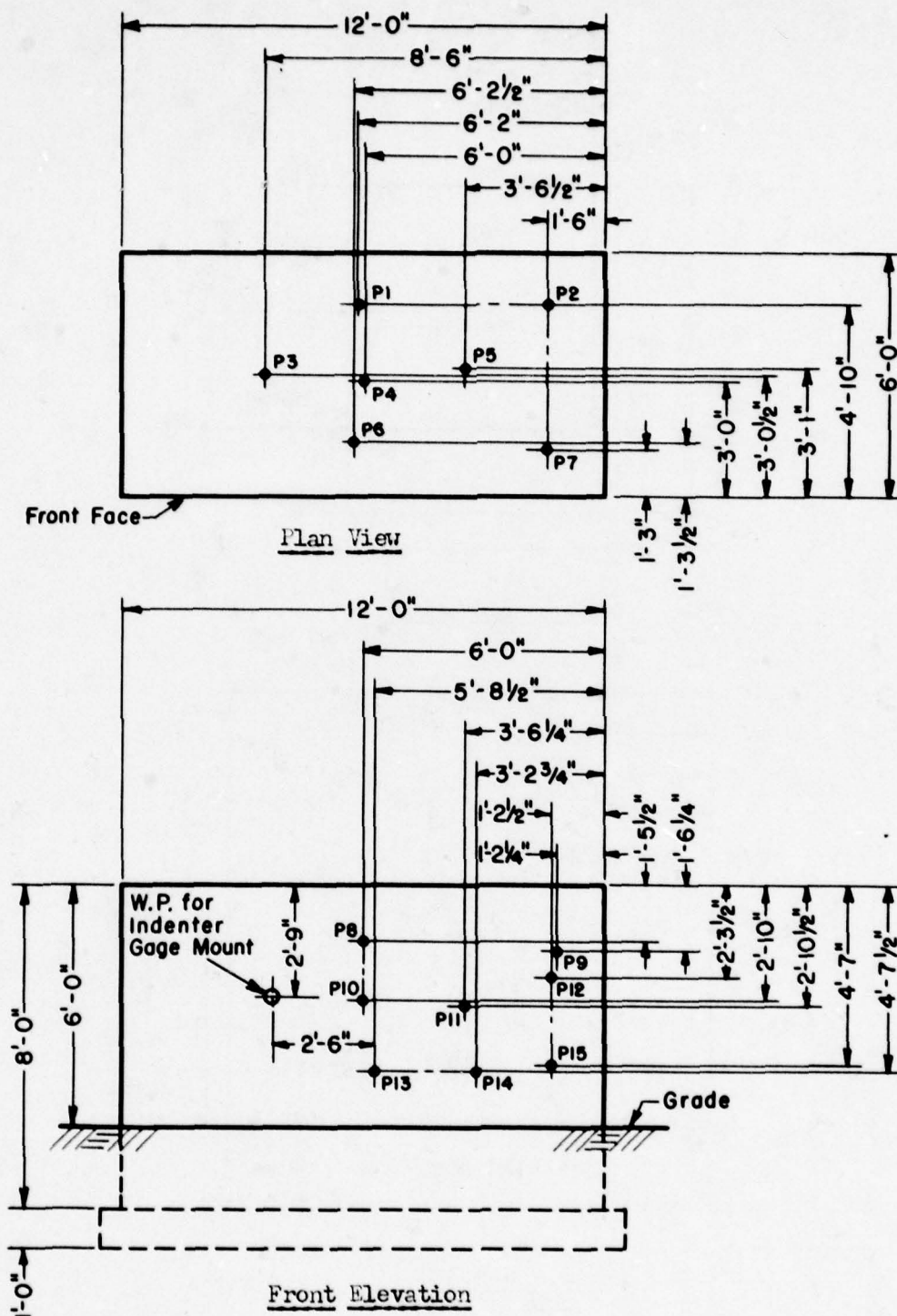


Fig. 2.43—Structure 3.1t, plan view and front elevation.



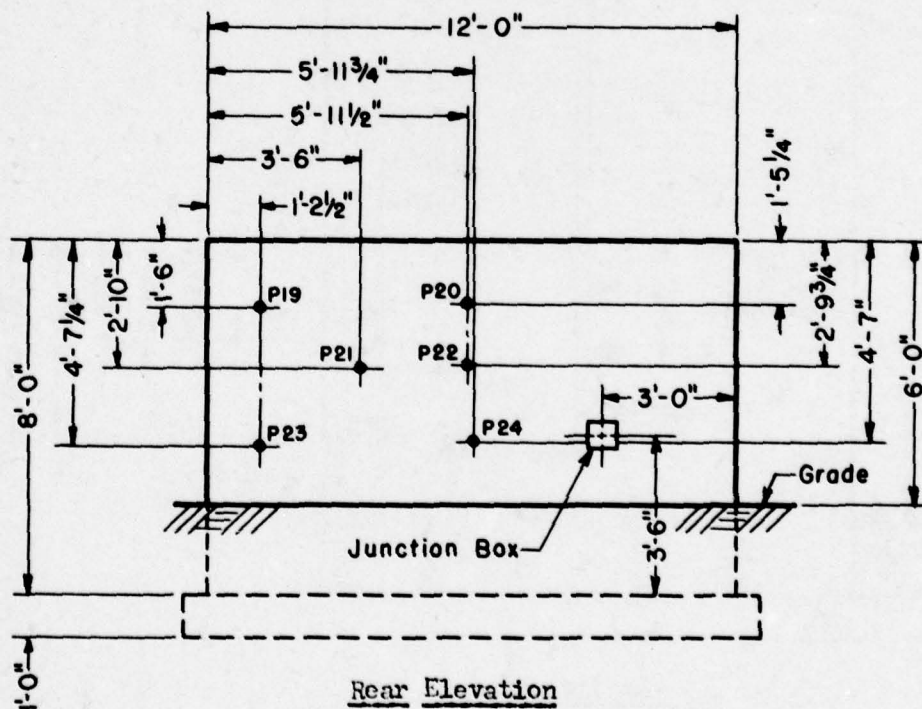
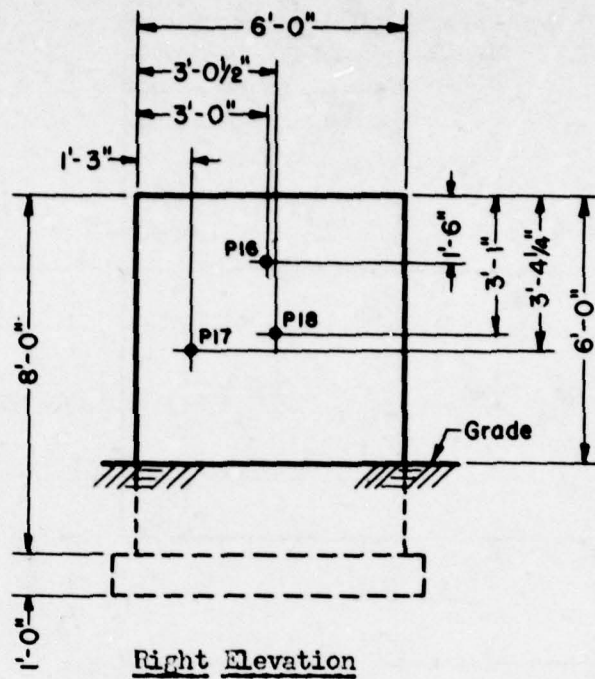


Fig. 2.44—Structure 3.1t, right and rear elevations.

## CHAPTER 3

# PRETEST CONSIDERATIONS

### 3.1 INTRODUCTION

The blast loading of a structure is a highly transient process generally consisting in the following sequence of flow phenomena.

First, the shock front reflects from the surfaces that face upstream. Then the shock front moves around the structure, diffracting so that the flow is carried to the surfaces which do not face upstream. The initial pressures created by the reflected and diffracted shock are quite temporary; a period of development of flow follows in which flow becomes established, approaching to some degree the steady flow which would occur if the structure were exposed to a steady wind. Then, as the blast disturbance dies out, pressures drop off to zero on all parts of the structure.

If the blast wave is of rather long duration, these steps may be fairly distinct on each surface of the structure; with shorter durations, the decrease of pressure behind the shock front may follow the reflection and diffraction process so closely that development of flow patterns and decrease of flow strength may occur simultaneously. Furthermore, in such a case the decrease of flow may be so rapid that new phenomena due simply to the flow deceleration may become quite pronounced.

If, instead of a shock front, the blast wave has a gradually rising front (compression wave), the reflection and diffraction will occur but will differ somewhat.

The foregoing is intended as a basis for the interpretation and prediction of blast loads. In the following sections, a qualitative description of this sequence of phenomena is given for solid, rectangular blocks.

The period referred to above in which the flow is well developed and corresponds to the flow established by steady winds is called the "pseudo-steady-state" period. That is, the pseudo-steady-state period is the phase of loading during which drag forces act. As noted earlier, this period might be eliminated if the wave duration is very short.

A section on terminology precedes the discussion on loading.

### 3.2 TERMINOLOGY

An attempt has been made to utilize terms and symbols throughout in the sense in which they are most generally used in the relevant literature. Occasional departures or additions have been made where sufficient reason seemed to warrant.

Some of the most frequently used words and phrases are defined below in the senses in which they have been employed. These terms are divided into two classes. The first group refers to shock characteristics, which may be defined without discussing whether obstacles are present in the flow, and the second group refers to the interaction between shocks and structures.

### 3.2.1 Terms Not Associated with Structures

**Shock Front:** A very thin surface which moves through a fluid, accelerating and compressing the fluid masses which it crosses. Pressure, density, temperature, entropy, and velocity of the fluid rise instantaneously as the fluid is passed over by the shock front. This is true of all shocks moving into still air; a blast wave is an example of such a shock. However, some secondary shocks, which arise when shock fronts strike obstacles, travel into moving air with the result that the fluid may be then decelerated when crossed by these shock fronts.

**Shock Wave (or Shock):** The shock front plus the disturbed region following it. In the case of a blast wave, pressure, fluid and velocity throughout the disturbed region drop off after the front passes and ultimately but not necessarily at the same time, almost reach their original at-rest values. A period of reversal of flow and of pressure below atmospheric then disturbs the air again but once more leaves the fluid in approximately its previous at-rest state.

**Compression Wave:** A disturbance which may be exactly like a shock wave except that the initial increase in pressure and changes in air velocity occur gradually rather than instantaneously. Explosions will, under certain conditions, create compression waves rather than shock waves near the ground surface. The time for the pressure to rise to a peak is called the "rise time" of the compression wave. After the peak pressure is reached a compression type blast wave may be the same as a shock type blast wave.

**Peaked Shock:** A shock in which pressure and fluid velocity immediately begin to drop off after passage of the front. A typical case is the blast wave as discussed above under "shock wave."

**Flat-topped Shock:** The variety of shock characterized by constant conditions of pressure, fluid velocity, etc., for some time after passage of the shock front. The shock wave ordinarily utilized in shock tube experiments is of this type and is called a "flat-topped" shock in reference to the flat pressure-vs-time curve characterizing this wave. A flat-topped shock cannot be maintained indefinitely unless energy in the form of high-pressure and high-velocity fluid is continually supplied to maintain the region behind the shock front.

**Side-on Pressure:** Free stream, static, gage pressure at any point behind the shock front, measured from datum pressure in undisturbed air ahead of the shock. (The term "side-on" originated in early gage studies of blast in which gage faces parallel to flow were said to record "side-on" pressure, and gage faces perpendicular to flow were said to record "face-on" pressure.)

**Overpressure:** Side-on pressure.

**Rarefaction:** A disturbance which moves through a fluid lowering the pressure, changing the velocity, and inducing change in other flow variables. A rarefaction wave is the inverse of a compression wave.

**Shock Strength:** The ratio of absolute pressure immediately behind (after passage of) a shock (front) to the absolute pressure in front of the shock.

**One-dimensional Shock Front:** A shock front which is a plane surface; the pressure behind the shock front is the same at all points that are equidistant from the shock front.

### 3.2.2 Terms Associated with Structures

**Pressure:** Used to refer to overpressure (i.e., gage pressure) unless the context clearly indicates otherwise. Frequently, when the term is referred in reference to a surface of a structure, it means the average pressure across the surface. The predictions of loading give only the average pressures or total forces on surfaces, never the pressure at a single point. Hence, it is convenient to adopt the above abbreviated terminology.

**Normal Reflection:** Reflection of a one-dimensional shock from a plane surface which is parallel to the plane of the incident shock front.



*Clearing, Relief:* After a shock front has created high pressures on a surface upon which it reflects, these pressures must drop to lower values (e.g., to the wind pressure due to steady flow impinging on the surface). This process of decreasing the reflected pressure is termed "clearing or relief."

*Front Wall:* That wall which faces upstream, that is, toward the blast source.

*Pseudo-steady State:* The period when the flow on a given surface is well developed and corresponds to the flow which would be established by steady winds. Pseudo-steady state does not occur until after reflection of all shock fronts have been completed on that surface. Pseudo-steady-state flow may commence at different times for different surfaces of a structure, e.g., for opposite sides of a wall. If the wave duration is sufficiently short, flow may be completed so rapidly that pseudo-steady-state flow is never established.

*Peaked-shock Effect:* A variation in side-on pressure along the length of a structure as a result of the fact that the building length (in the flow direction) is a substantial percentage of the shock wave length. When a structure is immersed in a peaked shock, at any given instant after the pressure has built up on the rear, the rear surface is exposed to a higher side-on pressure than the front surface. This effect occurs particularly during the pseudo-steady-state period when each surface of the building is exposed to drag pressure as a result of its local free stream conditions.

Another type of peaked-shock effect is less obvious, but has been shown to exist experimentally. Departures from pseudo-steady-state pressures have been observed on front and rear walls after reflection, and diffraction effects have disappeared. These departures are in addition to the effect described above and are probably caused somehow by the deceleration of the flow in the neighborhood of the surface. When these decelerative peaked-shock effects occur, pressures on surfaces facing upstream are lower than the ordinary pseudo-steady-state values, and pressures on downstream facing surfaces are higher. This would tend to decrease the drag.

*Two-dimensional Flow:* Flow which is confined geometrically so that particles can move only in planes; all planes in which particles can move are parallel to each other. Two-dimensional flow occurs around an obstacle which is infinitely wide crosswise to the flow. It will also be two dimensional in a rectangular duct (wind tunnel or shock tube) if an obstacle of unvarying cross section crosses the duct completely in a direction perpendicular to flow. Approximately two-dimensional flow will occur on the center section of a very wide obstacle.

*Scaling:* If flow tests of a model can be used to predict flow around a prototype structure, scaling of the flow is said to be possible.

*Drag or Dynamic Pressure:* Drag pressure or dynamic pressure is used to denote either the pressure head associated with the kinetic energy of the blast wave, i.e.,  $\frac{1}{2}\rho u^2$ , or the portion of this pressure head which acts on a surface causing the pressure to deviate from side-on pressure by an amount that depends upon the drag coefficient.

*Loading:* The average pressures or forces which are imposed on a structure by a shock wave. Whenever it is essential that a distinction be made, the context in which the term is used indicates whether pressures or forces are referred to.

### 3.3 DESCRIPTION OF LOADING PHENOMENA

The loading phenomena described here for Project 3.1 are accurately known and are rather general. The shock wave first strikes the front wall of a building (surface facing upstream), and reflection of the impinging portion of the shock front occurs, immediately raising the front wall pressure to a value more than double the initial side-on pressure. Since side-on pressure now exists at all points above and to the sides of the front wall, rarefaction waves immediately begin to move across the front surface from each exposed edge. These waves initiate the clearing process, which ultimately lowers the front wall average pressure from

the reflected pressure to the pseudo-steady-state pressure, i.e., the instantaneous value of side-on pressure plus the drag pressure on the front wall. The period taken for one sweep of the surface by rarefaction waves is approximately one-third the period required to accomplish this clearing process. Subsequent to relief, the front wall pressure drops to zero as side-on pressure and drag decrease to zero.

Surfaces parallel to flow (roof and sides) are raised approximately to side-on pressures as the shock front sweeps the length of the building. However, a vortex that is immediately formed at all front face edges moves toward the rear, degenerates into turbulence, and carries low pressures (below side-on) across at least part of the surface.

In three-dimensional flow these low-pressure regions on the top and sides of the block would be exposed to zones of higher pressure: the zones lying between imaginary extensions of the side walls and the roof. Higher pressure air in these zones can be expected to move into the low-pressure regions on the roof and side walls created by turbulence, raising the pressure nearer to side-on pressure.

The vortex and the turbulence on the roof may be considered as the wake created by the sharp front corner. Thus, this wake may be expected to be less severe if the corner is rounded or if an opening is present in the front wall, permitting some flow to go inside rather than being deflected around the corner.

When the shock front crosses the rear edge of such a rectangular structure the shock travels down the back wall. This diffracted section of the shock is greatly weakened and spreads pressures considerably less than side-on across this surface. A period of time much longer than that required for sweeping by this diffracted shock must pass before the back wall average pressure reaches its pseudo-steady-state value.

The structural types considered in the foregoing are those which have been studied most extensively up to the present; however, the features of flow which have been described will be encountered, to some degree, on all structures.

### 3.3.1 Sources of Basic Information on Loading

The precise form of a blast wave depends upon many factors, some of which are not well understood at the present. The present state of blast knowledge leaves loading predictions for complex shapes somewhat inaccurate. Therefore it is convenient to adopt a single standard shape of blast wave for use in loading calculations.

$$p_{\sigma}(t) = p_{\sigma}(0)e^{-xc} (1 - x)$$

where  $x = t/t_0$  and  $c$  is a number which depends upon the height of burst and horizontal distance from Ground Zero (see Chap. 5) and is introduced to allow the wave shape to vary somewhat. This equation describes the shape of the positive phase of the wave in terms of peak over-pressure and the duration of the positive pressure phase. If free stream measurements are available, they can be used to determine the incident wave shape.

A number of other features of the blast wave, in addition to its pressure variation with time, are needed for the determination of the loads which this wave will create on a structure. Among these, are the velocity of the wave front, the air velocity (not to be confused with the velocity of the disturbance which moves faster than the air), the density throughout the wave, and the change in shape of the wave as it travels along the length of the structure. Some of these quantities are computed from the pressure-time variation described above, by equations in Sec. 3.4.1.

As far as the shock loading process itself is concerned, only some facts are certain. The instantaneous value of reflected pressure on a surface facing upstream is well known for almost all angles of reflection. The diffraction process (the phase following reflection) has been solved analytically for a few types of "infinite corners." Solutions for diffraction and for development of pseudo-steady-state flow around a two-dimensional rectangular block would be of far greater complexity than these diffraction solutions which have been obtained at present. Thus, the analytical solutions referred to above are not of great significance as working trends



for analyzing real structures. Continuing work on the analytical approach may some day provide some knowledge of trends in shock-loading predictions (e.g., the type of changes in loading which result when the shock overpressure is changed). However, for the present, beyond the initial values of reflected pressures, shock-loading determination must be based wholly on experimental data obtained from simple shapes. To apply these data to complicated structures, the results must be interpreted by relatively few principles as to the behavior of compressible flows and by intuitive speculation.

The major body of experimental data relevant to the loading problem has come from shock tube tests, wind tunnel tests, and from instrumented structures exposed to actual blast waves. Pressure gages mounted on the structural models record the passage of the shock wave over the structure for both shock tube and full-scale blast tests. In addition, optical methods, such as schlieren photography, shadowgraphs, and interferograms, are used with great success in shock tube studies to record the various and often extremely complicated shock configurations occurring in the diffraction phase of loading.

Presentation of pressure data in the form of individual pressure-vs-time records at a particular point on a surface is of value principally for comparing sets of data from different tests when one set of data consists of a few pressure gage readings (too few to obtain average pressures over an entire surface with the accuracy desired for the comparison). These comparisons are used to study the scaling of pressures from very small to very large bodies.

Average pressure-vs-time readings on each surface of a test structure are the most useful bases for developing predictions. This format can be used with data obtained by use of the interferometer and with data obtained by various types of pressure gages if each surface is gaged sufficiently to deduce average pressures.

The optical methods mentioned above are helpful as a supplement in the development of predictions. Some of the phenomena which give rise to the pressures recorded by pressure gages are seen quite clearly in shadowgraphs or schlieren photographs of the flow. When it is necessary to speculate about the pressures which might occur on shapes which have never been tested, it is sometimes easiest to imagine the phenomena which would be present (from inspection of shadowgraphs of other shapes) and to then assume the pressures which would be produced by these assumed phenomena. This latter step, from phenomena to pressures, can be based in part on a comparison of shadowgraphs, showing phenomena with recorded pressure profiles.

#### 3.4 DISCUSSION OF DETAILED LOADING PREDICTIONS

The following discussion of the pressure predictions for normally oriented building is taken from the *Planning Program for Air Force Structures Tests*, Final Report, Part IV). The discussion of the loading for the obliquely oriented models is taken from *Study of the Effect of Orientation on Dynamic Loading and Response of Structures*, Final Report, AMC. The discussion of the loading for the structures in the regular reflection region is taken from the *Ad Hoc Analytical Services for Physical Vulnerability Division*, USAF, Phase Report III.

The general scheme is to deal with the development of each prediction on the basis of the structure and shock parameters. These predictions will be used to point out the areas of agreement and disagreement by plotting the computed loadings and displaying them on the field-measured loading.

As can be seen from Tables 2.1 and 2.3, some buildings were heavily instrumented and others were not; therefore, the average pressures obtained by field measurements will in some cases not be realistic. However, these loadings referred to in the above reports represent the best estimates now available. It is instructive to graph the predicted and measured values of the loading.



### 3.4.1 Shock Relations

The following equations are necessary in order to perform numerical computations from the symbolic loadings developed in Sec. 3.4.2. No attempt is made here to describe them since they were developed in the GREENHOUSE report *Blast Loading and Response of Structures*, Report WT-87 and in the pretest report *Planning Program for Air Force Structures Tests*. Final Report, Part I.

The side-on pressure-time variations are approximated by

$$p_{\sigma}(t) = p_{\sigma}(0) e^{-ct/t_0} \left(1 - \frac{t}{t_0}\right) \quad (3.1)$$

where  $c$  is given in Fig. 5.5.

The nominal drag pressure is defined as†

$$p_d(t) = \frac{\rho(t)}{2} [u(t)]^2 \quad (3.2)$$

The initial value of drag pressure  $p_d(0)$  can be expressed in terms of the side-on pressure by means of the basic flow equation:

$$p_d(0) = \frac{1/2 p_{\sigma}^2(0)}{7P_0 + p_{\sigma}(0)}$$

It is assumed that the variation of drag pressure with time,  $p_d(t)$  is given by the same equation if  $p_{\sigma}(0)$  is replaced by  $p_{\sigma}(t)$ , i.e.

$$p_d(t) = \frac{1/2 p_{\sigma}^2(t)}{7P_0 + p_{\sigma}(t)} \quad (3.3)$$

If  $p_{\sigma}(t)$  is small compared to  $7P_0 \approx 103$  psi, i.e., STP conditions, an approximate relation for  $p_d(t)$  is given by

$$p_d(t) = p_d(0) e^{-2c(t/t_0)} (1 - t/t_0)^2 \quad (3.4)$$

where  $p_d(0)$  is evaluated from Eq. 3.3 at  $t = 0$ .

The shock velocity  $U$  is given by

$$\begin{aligned} U &= 422\sqrt{1 + 6\xi} \\ &= 422\sqrt{7 + 0.41 p_{\sigma}(0)} \end{aligned} \quad (3.5)$$

for standard atmospheric conditions.

The reflected pressure is derived from the Rankine-Hugoniot relations as

$$p_r = p_{\sigma}(0) \frac{6 + 8\xi}{6 + \xi} \quad (3.6)$$

or in terms of  $p_{\sigma}(0)$  alone

$$p_r = \frac{206 + 8p_{\sigma}(0)}{103 + p_{\sigma}(0)} \quad (3.7)$$

where  $P_0 = 14.7$  psi.

† See also Chap. 5.

### 3.4.2 General Considerations for Loading Predictions

The development of the loading follows the methods presented in the GREENHOUSE report *Blast Loading and Response of Structures*, Project 3.3, Appendix I wherever possible. In addition, results from the latest available literature and from large-scale field tests have been included wherever it was felt that significant improvements could be made. For example, typical changes include:

1. Higher drag coefficients on front and back walls (and hence, larger total horizontal drag forces).
2. Shorter build-up times on the backwalls of three-dimensional structures.
3. Selection of the condition of "minimum turbulence," see GREENHOUSE report *Blast Loading and Response of Structures*, Report WT-87, as the most probable for three-dimensional objects.

In addition, new problems are raised, such as those of elevation, shielding, orientation, and re-entrant corners. Some effects, for example, those resulting from orientation, have already been touched upon briefly in the GREENHOUSE report *Blast Loading and Response of Structures*, Report WT-87 (the shaped roof of the industrial type structure) and are treated here in more detail with the help of wind tunnel studies on differently oriented blocks.

Other problems (e.g., shielding effect) are treated in this report on the basis of available information concerning the loading on related objects. The shielding problem is essentially solved by considering a Princeton shielded block test and drag studies on shielded plates undertaken by Eiffel and later by Nøkkentved.

The loading schemes are subdivided as follows:

1. Cubicles resting on the ground and struck by the blast under normal incidence (Structures 3.1a to c, e, f, i, s, and t).
2. Thin walls on the ground struck by the blast under normal incidence (Structure 3.1d and the first wall of 3.1n). The walls of Structure 3.1n are separated by a distance equal to three heights and the first wall is assumed to be unaffected by the second wall.
3. Structures elevated at various heights above the ground and struck by the blast under normal incidence (Structures 3.1o and p).
4. Shielded thin walls resting on the ground and struck by the blast under normal incidence (Structures 3.1l and m and the second wall of Structure 3.1n).
5. Oblique structures resting on the ground and struck by a blast at an incident angle of  $22\frac{1}{2}$  or 45 deg. between the plane of the shock front and the front face (Structures 3.1g and h). Here the front face is considered the same face as for normal incidence, i.e., the 6 by 12-ft face.
6. A special structure with re-entrant corners (Structure 3.1q).
7. Cubicles in the regular reflection region (Structures 3.1s and t, Shot 9).

The loading schemes are presented symbolically in the form of graphs in Figs. 3.1 to 3.33.

### 3.4.3 Loadings on Structures 3.1a to c, e, f, i, s, and t†

These structures rest on the ground and are hit by shocks under normal incidence. The loading scheme follows essentially that developed in the ARF GREENHOUSE report, with the improvements gained from interpreting the GREENHOUSE test results and latest literature on diffraction and drag loadings. These improvements represent more recent values for the drag coefficients and shorter build-up time on the back due to three-dimensional effects.

† Structures 3.1s and t were in a heavy precursor zone, Shot 10. The revised method of prediction is given in Appendix A and Sec. 3.4.9. For Shot 9, Structures 3.1s and t were in the regular reflection region and are treated in Sec. 3.4.8.

The recommended drag coefficient for the front wall is

$$C_{df} = \frac{3}{4} \quad (3.8)$$

for the back wall it is,

$$C_{db} = -\frac{1}{2} \quad (3.9)$$

and on the roof,

$$C_{dr} = -0.55 \quad (3.10)$$

Figure 3.1 gives the loading scheme for the front and back surfaces, and Fig. 3.2 gives the loading for the roof. The net horizontal loading is the difference between the front and the back loadings.

The following equations are used in conjunction with Figs. 3.1 and 3.2.

$$\begin{aligned} f_{os} &= f_{os}(t) = p_{\sigma}(t) + \frac{3}{4} p_d(t) \\ b_{os} &= b_{os}(t) = p_{\sigma}(t) - \frac{1}{2} p_d(t) \\ r_{os} &= r_{os}(t) = p_{\sigma} [tP - 0.55 p_d(t)] \end{aligned} \quad (3.11)$$

In these figures  $f_0(t)$ ,  $b_0(t)$ , and  $r_0(t)$  are average pressures on front, back, and roof at any time,  $t$ , during the loading. The expressions  $f_{os}(t)$ ,  $b_{os}(t)$ , and  $r_{os}(t)$  are average pressures on front, back, and roof during the pseudo-steady-state phase.  $L$  is the length of the structure in the direction of flow;  $S$  is the height or half-width, whichever is smaller;  $U$  is the shock velocity. The upper curve pertains to the thin wall ( $L/S < \frac{1}{3}$ ), and the lower curve pertains to all other structures for which  $L/S > \frac{1}{2}$ . These curves serve as bounds for values of  $L/S$  greater than  $\frac{1}{3}$  but less than  $\frac{1}{2}$ .

To illustrate the use of Fig. 3.3, let it be required to find the build-up time on the back surface for Structure 3.1s in which the ratio  $H:W:L$  is  $1:1:1$  and  $H$  is equal to 6 ft. Hence,

$$S = \frac{W}{2} = 3 \text{ ft}$$

and the abscissa in Fig. 3.3 is

$$\frac{2H}{W} = \frac{12}{6} = >1$$

Now,

$$\frac{L}{S} = \frac{6}{3} = 2 > \frac{1}{2}$$

Hence, the lower curve must be used to obtain

$$n = 3.5$$

for

$$\frac{2H}{W} = 2$$



Thus, the build-up time on the back wall is

$$n \frac{S}{U} = (3.5) \frac{S}{U}$$

For  $p_a(0) = 13.5$  psi,

$$U = 422 \sqrt{7 + 6 \frac{p_a(0)}{14.7}} = 1500 \text{ ft/sec (from Eq. 3.5)}$$

and the build-up time on the back is

$$n \frac{S}{U} = \frac{10.5}{1500} = 0.007 \text{ sec} \quad (3.12)$$

#### 3.4.4 Loadings on Elevated Structures 3.1o and p

Structures 3.1o and p are elevated by distances  $\Delta H = H/6$  and  $\Delta H = H/2$ , respectively (Figs. 2.8 and 2.11). The loadings on the front, back, and top are essentially the same as those on the Structures discussed in Sec. 3.4.3 (Figs. 3.1 and 3.3). However,  $S$  (Fig. 3.3) is replaced by  $S^*$ , which is defined as the arithmetic mean of  $H/2$  and the total distance from the ground to the top of the block, i.e.,

$$S^* = \frac{1}{2} \left( \Delta H + H + \frac{H}{2} \right) \quad (3.13)$$

where the form of the Eq. 3.13 is assumed to apply only for Structures 3.1o and p. For Structure 3.1o, where  $\Delta H = H/6$ ,  $S^*$  becomes  $5H/6$ , and for Structure 3.1p, where  $\Delta H = H/2$ ,  $S^*$  becomes  $H$ . The loadings on the front, back, top, and under side of these structures are given in symbolic form in Figs. 3.5 and 3.6. Equations 3.11 are again applicable and in addition,  $l_0 = l_0(t)$ , is the average pressure on the underside. The underside pseudo-steady-state average pressure is  $l_{os}$ , as given in Eq. 3.14.

$$l_{os} = l_{os}(t) = p_{\sigma}(t) - 1p_d(t) \quad (3.14)$$

The average pressure-time variation on the underside of the elevated structures is, in general, assumed to be similar to the loading on the top surface. That is, the average pressure builds up from zero to a peak value, decays to the pseudo-steady-state value, and then maintains this value for the remainder of the positive phase. The characteristic build-up and clearing times are taken to be identical with those associated with the top surface. The peak loading on the under surface is deduced in the following paragraphs and stems from an analogy with flow in a restricted channel.

Figure 3.7 shows a channel with a reduced cross section. The dashed lines illustrate how this profile is assumed to represent the geometry of the elevated structure. From considerations of symmetry, the center line of the narrow section is taken to be ground level since there can be no flow across this surface.

When the free stream shock of strength  $\xi$ , reaches the dividing cross section o-o in Fig. 3.7, a shock of strength  $\xi_r$  is reflected back in the upstream direction, and a shock of strength  $\xi_1$  is transmitted through the narrow channel in the downstream direction. The higher pressure,  $P_r$ , behind the reflected shock causes flow into the narrow channel. This relieves the reflected pressure and gives rise to a rarefaction wave emanating from the throat of the channel. Thus, the flow conditions shown in Fig. 3.7 are assumed to take place at some time after the free stream shock reaches the reduced cross section.

If the assumption is made that the ratio of the cross-sectional area of the narrow section to that of the wide section is sufficiently small, then the reflected shock is essentially the

same as that reflected from a plane wall. From the Rankine-Hugoniot relations, one can express the particle velocity  $u_1$  behind the transmitted shock in terms of the transmitted shock strength  $\xi_1$ . The particle velocity  $u_2$  associated with the rarefaction wave is known from the theory of adiabatic waves. Thus, pressure, density, and particle velocity are related for the wide and narrow channel sections.

The particle velocity behind the transmitted shock is given by Eq. 3.15 (*The Shock Tube as an Instrument for Investigation of Transonic and Supersonic Flow Patterns*, F. W. Geiger and C. W. Mautz).

$$u_1 = c_0 \frac{(\lambda - 1) \left(1 - \frac{P_0}{P_1}\right)}{\left[\frac{P_0}{P_1} (\lambda + 1) \left(\lambda + \frac{P_0}{P_1}\right)\right]^{1/2}} \quad (3.15)$$

where the pressures are defined in Fig. 3.7 and are given in absolute values and

$c_0$  = sound velocity in undisturbed region

= 1130 ft/sec

$$\lambda = \frac{c_p + c_v}{c_p - c_v} = 6$$

where  $c_p$  and  $c_v$  are the specific heats of air at constant pressure and volume, respectively.

The particle velocity behind the rarefaction wave is given by

$$u_2 = c_1 (\lambda - 1) \left[1 - \left(\frac{P_2}{P_r}\right)^{1/(\lambda+1)}\right] \quad (3.16)$$

where the pressures are again in absolute values and  $c_1$  is the sound velocity behind the reflected shock.

The following additional assumptions are now made concerning the flow shown in Fig. 3.7:

1. The values of the pressure and density behind the transmitted shock and the rarefaction wave in the throat are equal, i.e.,  $P_2$  is equal to  $P_1$  and  $\rho_2$  is equal to  $\rho_1$ .

2. The lines of constant pressure and velocity in the rarefaction wave are concentric semicircles emanating from the throat.

3. The particle velocity behind the rarefaction wave is proportional to the particle velocity behind the transmitted shock,  $u_1$ . Thus,

$$u_2 = K u_1 \quad (3.17)$$

where  $K$  is a factor of proportionality.

In order to justify these assumptions, it is again necessary that the cross-sectional area of the narrow section be much smaller than that of the wide section. That is, in Fig. 3.7,

$$\eta = \frac{A_2}{A_1} \ll 1$$

If Eqs. 3.15 and 3.16 are substituted into Eq. 3.17 and the following definition is made

$$\frac{P_1}{P_0} = \xi_m$$

then

$$\frac{P_0}{P_r} = \frac{1}{\xi_m} \left(1 - K \frac{c_0}{c_1} \frac{\xi_m - 1}{\sqrt{4\xi_m + 7}}\right)^7 \quad (3.18)$$

The expression for the peak pressure  $p_1$ , in the channel ( $p_1 = P_1 - P_0$ ), is independent of the cross-sectional area ratio  $\eta$ . This is not surprising, considering the development presented above. The assumption was first made that  $\eta$  was sufficiently small in order to assign a known value independent of  $\eta$  to the reflected shock. Thus, parameters of the transmitted shock, which are related to those of the reflected shock, must also be independent of  $\eta$ .

However, from physical considerations, one feels that this should not be the case and that some dependency on  $\eta$  should occur. Certainly, as the channel assumes a constant cross section (i.e., as  $\eta \rightarrow 1$ ), the pressure  $p_1$  becomes the side-on pressure  $p_\sigma$ . On the other hand, for values of  $\eta$  sufficiently small, the pressure  $p_1$  given by the above analysis is assumed to apply.

As a first-order approximation, it is suggested that a linear dependency on  $\eta$  be incorporated into the expression for  $p_1$ . That is, the actual peak pressure  $p_m$  in the narrow channel is to be given by

$$p_m = p_1(1 - \eta) + p_\sigma \eta \quad (3.19)$$

Equation 3.19 has the property that, as  $\eta$  becomes very small (but remains finite),  $p_m$  approaches  $p_1$ . On the other hand, as  $\eta$  approaches unity,  $p_m$  approaches  $p_\sigma$ .

Due to multiple reflections, the value of the constant  $K$  in Eq. 3.18 must be such that the overpressure  $p_1$  in the channel turns out to be larger than the incident side-on pressure,  $p_\sigma$ . With today's state of knowledge, however,  $K$  cannot be deduced from theoretical considerations alone and thus must be obtained either from shock tube or large-scale field tests. From the results on Shots 9 and 10 on Structures 3.1o and p, one finds approximately,  $K \approx 0.65$ . If this value is substituted into Eq. 3.18, one obtains Fig. 3.8 as the solution of Eq. 3.18 for the ratio of the peak pressure in the channel to the outside overpressure,  $p_1/p_\sigma$ .

Inspection of Fig. 3.8 shows that, for the range of overpressures considered in this report, an average value for  $p_1$  may be taken as

$$p_1 = 1.25 p_\sigma$$

Then Eq. 3.19 may be further simplified as

$$p_m = \frac{p_\sigma}{4}(5 - \eta) \quad (3.20)$$

The value of  $p_m$  given by Eq. 3.20 is then taken to be the peak pressure acting on the under side of the elevated structures. For Structure 3.1o

$$\eta = \frac{\Delta H}{\Delta H + H} = \frac{H/6}{(H/6) + H} = \frac{1}{7}$$

and for Structure 3.1p

$$\eta = \frac{H/3}{(H/3) + H} = \frac{1}{4}$$

Thus, from Eq. 3.20, the peak pressure for Structure 3.1o is

$$p_m = 1.21 p_\sigma$$

and that for Structure 3.1p is

$$p_m = 1.19 p_\sigma$$

The loading on the bottom of the elevated structure is shown symbolically in Fig. 3.6.



The drag coefficient for the bottom part is deduced from wind tunnel studies on flow through a similar opening. It seems, in general, that the drag coefficients  $C_{dr}$  are closer to -1 than to -0.55, the value used on the roof surface, and the former value is given in the symbolic loading of Fig. 3.6.

### 3.4.5 Loadings on Thin Wall Structures

#### 3.4.5.1 Structure 3.1d and Upstream Wall of Structure 3.1n

The study of fringe-shift diagrams behind a thin wall (*The Diffraction of Shock Waves Around Obstacles and the Resulting Transient Loading on Structures*, W. Bleakney) shows that at a time equivalent to that necessary for a shock to cover twice the wall separation of  $\Delta = 3H$ , the wave reflected from a second wall probably will not reach the first wall because a large vortex breaks up the flow. (This is true at least for the two-dimensional cases.) Hence, for  $\Delta = 3H$  the influence of shielding is considered only in so far as the downstream (second) wall is affected by the upstream (first) wall. The inverse influence is neglected, and the front wall of 3.1n is considered free.

The drag coefficients to be used are those listed in Sec. 3.4.3, and the build-up time on the back is accelerated by the three-dimensional effects discussed there and shown in Fig. 3.3.

The schematic loading is shown in Fig. 3.4 for the front and back loadings. The value of  $n$  for the back loading is obtained from the upper curve of Fig. 3.3 and is found to be  $n = 4$  for the structures under consideration. The net horizontal loading is obtained by subtracting the loading on the back wall from that on the front wall. Eq. 3.11 defines these loads,  $f_{os}(t)$  and  $b_{os}(t)$ .

#### 3.4.5.2 Structures 3.1l and m and the Second (Shielded) Wall of Structure 3.1n

These sets of two thin walls at various distances apart are included in the tests for the purpose of investigating the effect of shielding. (See Fig. 2.9.)

(a) Structure 3.1l. For Structure 3.1l,  $\Delta$  is equal to  $H/3$ . The loading is deduced from the Princeton thin wall (*The Diffraction of Shock Waves Around Obstacles and the Resulting Transient Loading on Structures*, W. Bleakney).

The loading on the front of the first wall is the same as that on a free wall. The strength of the shock traveling down the back of the first wall is apparently about one-quarter that of side-on pressure, and this shock is reflected from the bottom. From the time of this reflection, the additional time required to reach the pseudo-steady-state time is deduced from the Princeton double block as  $t = 6H/U$ . It is assumed that the loadings on the back of the first wall and the front of the second wall are the same.

The loading on the back of the second wall is considered as the average of that of a block of  $H:L = 1:1/3$  and that of a free thin wall. From Fig. 3.3, the build-up time is

$$\begin{aligned} t &= \frac{1}{2} \left( \frac{2S}{U} + \frac{4S}{U} \right) \\ &= \frac{3S}{U} = \frac{3H}{U} \end{aligned} \quad (3.21)$$

The drag coefficients as deduced from Nøkkentved (*Wind Pressure on Buildings, Experimental Researches*, J. O. V. Irminger and C. Nøkkentved) and others are for the first wall

$$C_{df} = +\frac{3}{4} \quad (3.22)$$

$$C_{db} = -\frac{3}{4} \quad (3.23)$$

and for the second wall they are

$$C_{df} = -\frac{3}{4} \quad (3.24)$$

$$C_{db} = -\frac{1}{2} \quad (3.25)$$

The loadings are given in symbolic form in Fig. 3.8 for the front and back of the first wall and in Fig. 3.9 for the front and back of the second wall. Both the  $f_{os}$  terms have the form of the expression,  $p_r(t) + C_d p_d(t)$  using  $C_d$  from Eq. 3.22 and 3.25.

(b) Structure 3.1m. The diffraction loading is deduced from the Princeton double block for Structure 3.1m, where the distance  $\Delta$  is equal to  $H$ . It is possible that, for times later than those shown in the Princeton double block, the vortex behind the upstream wall affects the front of the downstream wall, but this effect is neglected since it is believed that for the three-dimensional problems the "minimum turbulence" case prevails.

The pressure on the front of the first wall is assumed to be the same as if the wall were free. On the back of the wall the pressure rises linearly to roughly the same value as that on the front at the time,  $t = 4H/u$ , i.e.,  $b_0(4H/U) \cong f_{os}(4H/U)$ , and then drops in an additional  $2H/U$  units to the pseudo-steady-state value for the back.

The pressure on the front of the second wall was greater than the side-on pressure but was not so large as the fully reflected pressure because the shock front was weakened as it was diffracted around the first wall. Results from the Princeton double block (*The Diffraction of Shock Waves Around Obstacles and the Resulting Transient Loading on Structures*, W. Bleakney) suggest that the pressure be taken as the mean value of side-on and reflected pressure and that it drops to pseudo-steady state in  $6H/U$  time units. The pressure on the back of the second wall is assumed to be the same as that on a free wall.

The drag loading is again deduced from studies such as that by J. O. V. Irminger and C. Nøkkentved in *Wind Pressure on Buildings*, who show that, even at  $\Delta = 11.5H$ , the drag coefficient on the front of the downstream wall is still negative, which could lead to a net force in the upstream direction on the downstream wall. Only for very large separations can the second wall be considered free. The values of the drag coefficients for the first wall are

$$C_{df} = +\frac{3}{4} \quad (3.26)$$

$$C_{db} = -\frac{1}{2} \quad (3.27)$$

For the second wall they are

$$C_{df} = -\frac{3}{4} \quad (3.28)$$

$$C_{db} = -\frac{1}{2} \quad (3.29)$$

The loadings are given in symbolic form in Fig. 3.11 for the front and back of the first wall and in Fig. 3.12 for the front and back of the second wall. Again  $f_{os}$  and  $b_{os}$  are of the form,  $p_r(t) + C_d p_d(t)$ , using Eqs. 3.26 and 3.29 for  $C_d$ .

(c) Structure 3.1n. For Structure 3.1n,  $\Delta$  is equal to  $3H$ . The first wall is considered free as it is in Structure 3.1d (see Fig. 3.4). For the diffraction phase, the second wall is considered unshielded, and the only effect of shielding on the structure appears in the drag phase on the second wall. A heavy vortex behind the first (upstream) wall probably prevents the shock reflected from the second wall from reaching the first wall. Again, the effect of this

vortex on the front of the second wall is neglected, since it is believed that in three-dimensional problems "minimum turbulence" effects are predominant.

The drag coefficients for the second wall, as deduced from Nøkkentved and Irminger in *Wind Pressure on Buildings*, are

$$C_{df} = -\frac{1}{4} \quad (3.30)$$

$$C_{db} = -\frac{1}{2} \quad (3.31)$$

The loading on the second wall is given in symbolic form for the front and back surfaces in Fig. 3.12. By using Eqs. 3.30 and 3.31,  $f_{os}$  and  $b_{os}$  are of the form given above.

#### 3.4.6 Loadings on Oriented Structures 3.1g and h

These structures are included to determine the effects of orientation. Structure 3.1g has an intended angle of incidence  $\theta = 22\frac{1}{2}$  deg. between the planes of the shock front and the front face. For Structure 3.1h, the intended angle of incidence  $\theta$  is 45 deg. These angles provide check points for the general loading method of oriented structures.

The general loading notation has already been given in Sec. 3.4.1. Figure 3.13 illustrates the geometry of the shock-loading problem for a building at various orientations. The angle,  $\theta$ , of orientation is defined as the angle between the normal to the small face and the normal to the approaching shock front. The width of the small face is  $a$  and the length of the structure (the width of the large face) is  $b$ .

Values of  $C_d$  the drag coefficients for the various faces of the structures which are used to compute the pseudo-steady-state drag pressures are found in Figs. 3.15 and 3.16. They are given as a function of the orientation angle.

##### 3.4.6.1 Limitations

The loadings given in this section apply only when the following conditions are satisfied:

- (a) Shock Wave. 1. Peak pressure:  $\xi < 2.5$ ; for standard atmosphere  $p_\sigma(0) \leq 22$  psi.
2. Duration relative to building height: The equation for which is

$$\tau_0 = \frac{U t_0}{H} > 50 \quad (3.32)$$

3. Shock front: The front must be a plane vertical surface and must not be a compression wave.

4. Flow behind shock wave: The pressure must vary smoothly throughout the entire duration of flow. No secondary shocks or secondary compression waves are included.

(b) The Structure. 1. Shape: The structure must be a solid rectangular block (without openings), the walls must be relatively smooth, and the three dimensions (see Fig. 3.13) must satisfy the inequalities.

$$H/5 \leq a \leq 6H \quad (3.33)$$

$$H/5 \leq b \leq 6H \quad (3.34)$$

2. Size relative to wave duration.

(c) Scope. The effects of vortices on the side walls and roof have not been included in this loading method. Experimental evidence indicates that this is not an important omission. In the computation of net forces the effects of vortices tend to cancel out.



### 3.4.6.2 Drag Loading

The regular equations expressing the pseudo-steady-state drag pressure for the various 3.1 structures are also used for oriented structures. The effects of orientation are taken into account by making the drag coefficient vary with orientation angle.

The curves plotted in Figs. 3.15 and 3.16 give approximate values of the drag coefficient  $C_d$  for rectangular solids at various orientations relative to the flow. The curves are based on data given by Chien et al. in *Wind Tunnel Studies of Pressure Distribution on Elementary Building Forms* and by Irminger and Nøkkentved in *Wind Pressure on Buildings, Experimental Researches*. The first of these references gives data for nine different shapes at 0, 45, and 90 deg; the second gives data for a single shape at 15-deg intervals. The Irminger data were used to determine the general shape of the curves, and the Chien data provided the numerical values at 0, 45, and 90 deg.

Before construction of the curves described above, the data were simplified by averaging values, so that, instead of separate curves for each of nine discrete shapes, two sets of curves were drawn (Figs. 3.15 and 3.16) which apply approximately over a range of rectangular shapes. The block shapes used in establishing Figs. 3.15 and 3.16 had dimensions in the ranges  $2H/3 \leq a \leq 2H$  and  $2H/3 \leq b \leq 8H$ . Hopefully, the figures have been applied over the somewhat different range of shapes treated here.

$$H/5 \leq a \leq 6H \quad (3.35)$$

and

$$H/5 \leq b \leq 6H \quad (3.36)$$

The average values given in the figures at 0, 45, and 90 deg are equal (within 0.1 unit on the  $C_d$  scale) to the values obtained for any particular shape from Chien's report. However, disagreements between the Chien and the Irminger data for the 2:1:1 high block amount to over 0.2 unit in several instances; therefore, the values in Figs. 3.15 and 3.16 are probably moderate approximations, at best.

### 3.4.6.3 Diffraction Loading

Calculation of the diffraction forces consists again in simply computing the coordinates of the points shown in Fig. 3.17. The curves with the peak designated by "Q" applies to the two front faces 1 and 4. The coordinates of this curve must be found for each front face. Similarly, the other curve applying to the two rear faces 2 and 3 must also be computed for each of these faces.

As the shock front diffracts over the edge of the structure formed by faces 1 and 4, the pressure builds up on these faces until the entire face has been swept. The time consumed is then for face 1,  $(a \sin \theta)/U$  and for face 4,  $(b \cos \theta)/U$ . At the end of these times the pressure on the faces is  $Q$ , which is computed using the formulas in Table 3.1.

The clearing process is completed in an additional time  $3S/U$  where for Structures 3.1g and h,  $S = a/2$  for face 1, and  $S = b/2$  for face 4. At the end of a total time  $[a \sin \theta + 3(a/2)]/U$  for face 1 and  $[b \cos \theta + 3(b/2)]/U$  for face 4, the pressure reached the steady-state drag value of  $f_{os}$ .

The rear faces 2 and 3 start their pressure build-up precisely at the time the peak pressure,  $Q$ , is reached on faces 1 and 4. As the shock front proceeds toward the corner formed by faces 2 and 3, the average pressure on the rear faces increases to the pseudo-steady-state pressure  $b_{os}(t)$ .

The loading curves are then obtained by connecting the computed coordinates with straight lines and drawing in the  $f_{os}(t)$  and  $b_{os}(t)$  curves.

The pressure variation on the roofs of Structures 3.1g and h is similar to that on the roof, a structure at normal orientation except that the build-up of the force is no longer linear, since equal areas are not covered in equal intervals of time. However, this variation will not

TABLE 3.1—Pressure Computation Formulas

Time t	Average wall pressure
<b>Front face 1</b>	
0	0
$\frac{a \sin \theta}{U}$	$Q = f_s(t) + \left(1 - \frac{2\theta}{\pi}\right) [P_r - f_{os}(t)]$
$\frac{a \sin \theta + 3(a/2)}{U}$	$f_{os}(t)$
<b>Front face 4</b>	
0	0
$\frac{b \cos \theta}{U}$	$Q = f_{os}(t) + \frac{2\theta}{\pi} [P_r - f_{os}(t)]$
$\frac{b \cos \theta + 3(b/2)}{U}$	$f_{os}(t)$
<b>Rear face 2</b>	
0	0
$\frac{a \sin \theta}{U}$	0
$\frac{[a \sin \theta + b \cos \theta + n \left(\frac{2\theta}{\pi}\right) \frac{b}{2} \sin \theta]}{U}$	$b_{os}(t)$
<b>Rear face 3</b>	
0	0
$\frac{b \cos \theta}{U}$	0
$\frac{[a \sin \theta + b \cos \theta + n \left(1 - \frac{2\theta}{\pi}\right) \frac{a}{2} \cos \theta]}{U}$	$b_{os}(t)$
<b>Roof</b>	
0	0
$\frac{a \sin \theta + b \cos \theta}{U}$	$r_{os}(t)$

affect the total vertical impulse significantly. Thus the build-up is taken as an approximately straight line from zero to the steady-state value in the time the shock wave has swept across the roof,  $(a \sin \theta + b \cos \theta)/U$ . From then on it follows the pseudo-steady-state curve  $r_{os}(t)$ . The drag coefficient  $C_{dr}$  was found by Chien et al. to have a value of  $C_{dr} = -1$ . The loading picture is given in Fig. 3.18.

#### 3.4.7 Loadings on Irregularly Shaped Rectangular Structure 3.1q

This structure is especially designed to measure the pressure multiplication in re-entrant corners (Figs. 2.10 and 3.20).

In corners 1 and 2 of Fig. 3.20, the shock enters under normal incidence. The only difference between the loading in such a corner and that on a free surface is the longer relief time for the corner. This is a consequence of the longer distances which the rarefaction waves originating at free edges must travel to bring instantaneous reflected pressures down to side-on pressure.

In corner 3, however, the shock enters in a manner similar to that observed in the region between the Princeton double block (see Fig. 3.19). The shock front, reduced in strength because of the diffraction around the first block, enters the corner under oblique incidence. It is shown in Appendix D of *Planning Program for Air Force Structures Tests*, Part I, Final Report [Contract No. AF33(038)-30029], that the reflection coefficient rises above that of normal reflection and is approximately

$$\frac{p_{rc}}{p_{\sigma}^*} = 1 + \xi^* + (\xi^*)^2 + (\xi^*)^3 \quad (3.37)$$

where  $p_{rc}$  is the reflected pressure,  $p_{\sigma}^*$  is the local incident side-on pressure, and  $\xi^*$  is the local incident shock strength. The pressure  $p_{\sigma}^*$  is roughly 25 per cent of the incident side-on pressure.

The loading on this structure will be similar to that on the Structure 3.1a (Figs. 3.1 and 3.2), except for the re-entrant corners 1, 2, and 3 (Fig. 3.20). For this reason, the loadings on the back and top of Structure 3.1q are assumed to be those shown in Figs. 3.1 and 3.2, respectively.

The loadings on the front wall and the re-entrant corners are given graphically in Figs. 3.21 to 3.23. The loadings on the eaves above corner 1 are given in Fig. 3.24. In these figures,  $t = 0$  refers to the time when the shock strikes the front wall. The loadings are deduced below.

##### 3.4.7.1 Front Wall

The pressure drops from instantaneous reflected pressure,  $p_r$ , to pseudo-steady-state pressure,

$$f_{os}(t) = p_{\sigma}(t) + \frac{3}{4} p_d(t)$$

in the time

$$t = \frac{3H}{U} \quad (3.38)$$

Note that

$$H = \frac{1}{2} (W' + L_1 + W_1 + L_1) \quad (3.39)$$



so that relief takes place in the same amount of time from side to side as from top to bottom. The pressure is assumed to follow the pseudo-steady-state values as shown in Fig. 3.21.

#### 3.4.7.2 Corner 1

This re-entrant corner is equal to a rectangular box with a 100 per cent opening. The relief time is taken as

$$t = \frac{3 (L_1 + H)}{U} \quad (3.40)$$

since the rarefaction waves have to cover an additional distance  $L_1$  from the free edge to relieve the pressures in the cavity. This relief time is longer than that for the front wall (see Eq. 3.38). The symbolic loading is also shown in Fig. 3.21. The pseudo-steady-state pressure,  $f_{os}(t)$ , is the same as that given by Eq. 3.38.

#### 3.4.7.3 Corner 2

The loading in this corner of height  $H$  and width  $W_2$  is analogous to a front wall of height  $W_2$  and width  $H$ . The pressure drops from the instantaneous reflected pressure,  $p_r$ , to pseudo-steady-state pressure

$$f_{os}(t) = p_o(t) + \frac{3}{4} p_d(t)$$

in the time

$$t = \frac{3 W_2}{U} \quad (3.41)$$

Since this corner is two-dimensional, it is quite possible that a vortex originating from the front wall will reach the corner after the pressure there is relieved to pseudo-steady state. In this case, the loading which is predicted to follow the pseudo-steady-state curve can be considered an upper bound (minimum turbulence case), Fig. 3.22.

#### 3.4.7.4 Corner 3

The corner as a whole is two-dimensional, and the average loading is not corrected for three-dimensionality near the top. The loadings are deduced from the Princeton double block and are similar to those for the shielded structure shown in Figs. 3.11 and 3.12. The loading on the upstream face builds up almost instantaneously to  $p_{rc}$ , derived previously, which is for this case approximately equal to

$$f_0(t) = \frac{p_o(0) + p_r}{2} \quad (3.42)$$

at

$$t = \frac{L_2 + L^* + L_3}{U}$$

and then drops to pseudo-steady state in an additional  $8 W_3/U$  time units, differing from the loading on the shielded wall (Fig. 3.12) which was corrected for three-dimensionality. From that time on, it follows the pseudo-steady-state curve

$$f_{os}(t) = p_o(t) + \frac{3}{4} p_d(t) \quad (3.43)$$

The loading on the downstream face builds up to

$$b_0(t) = f_0(t) \quad (3.44)$$

at

$$t = \frac{6 W_3}{U} + \frac{L_2}{U}$$

and then drops to the pseudo-steady state,  $b_{os}$ , in an additional  $4 W_3/U$  time unit. The pseudo-steady-state values are taken, as in Fig. 3.11, as

$$b_{os}(t) = p_\sigma(t) - \frac{1}{2} p_d(t) \quad (3.45)$$

It follows this value to the end of the first positive phase Fig. 3.13.

#### 3.4.7.5 Eaves

(a) Outside Pressures. The outside pressure,  $r_0(t)$ , builds up to the pseudo-steady-state pressure,  $r_{os}(t)$ , at the time where  $t = L_1/U$

$$r_{os}(t) = p_\sigma(t) - 0.55 p_d(t) \quad (3.46)$$

(b) Inside Pressures. The inside pressure is equal to outside pressure until the time  $t = L_1/U$ , after this time it builds up to  $p_r$  in an additional  $L_1/U$  units, because the wave is reflected from the front wall,

$$r_i(t) = p_r \quad (3.47)$$

at

$$t = \frac{2 L_1}{U}$$

It then drops to pseudo-steady-state front pressure, i.e.,  $r_{is}(t) = f_{os}(t)$ , at the time given in Eq. 3.40, i.e., in  $3(L_1 + H)/U$  time units and follows this value until the time  $t = t_0$

$$r_{is}(t) = p_\sigma(t) + \frac{3}{4} p_d(t) \quad (3.48)$$

from this time on, the net pressure on the eaves is

$$r_{is}(t) - r_{os}(t) = 1.25 p_d(t) \quad (3.49)$$

acting in an upward direction.

#### 3.4.8 Loading in Region of Regular Reflection, Structures 3.1s and t (Shot 9)

General methods for computing loadings on a closed building whose width is equal to or greater than twice its height are given in the *Planning Program for Air Force Structures Tests*, Final Report, Part V. By using this method, charts have been prepared which facilitate loading computations for the case of an atmospheric pressure equal to 14.7 psi. These charts were presented in Phase Report III, *Ad Hoc Analytical Services*, [Contract No. AF33(600)-25583]. An explanation of these charts and their use is given below. In order to compare regular reflection region loading with Mach region loading, a method for computing loadings on closed

buildings in the Mach region when the atmospheric pressure is equal to 14.7 psi is also included in Fig. 3.28.†

The flow field which results when a blast wave strikes a horizontal surface obliquely is presented in Fig. 3.25. Region 0 is the ambient gas at rest which is being overrun by the incident shock wave of velocity  $U$ . Region 1 is the typical free-space blast wave region, which has a peak over-pressure  $p'_\sigma(0)$  immediately behind the shock wave.

The incident shock wave, which strikes the ground (horizontal surface) at an angle  $\alpha$ , is reflected as another shock wave (the reflected shock wave) which moves upward into region 1 and creates behind it a region 2. The peak overpressure in region 2 is  $p_\sigma(0)$  and exists immediately behind the reflected shock wave. The reflected overpressure, as measured along the ground, is assumed to vary according to the law:

$$p_\sigma(t) = p_\sigma(0) e^{-ct/t_0} \frac{1-t}{t_0}$$

which is the same as a typical blast wave in the Mach region. The wave shape factor,  $c$ , is shown on Fig. 5.5, as a function of scaled height and scaled distance from Ground Zero.

The relation of  $\xi$ ,  $\alpha$ , and  $p_\sigma$  is shown on Fig. 3.29. The scheme of Fig. 3.28 applies until the limiting angle of regular reflection is reached. This angle is given in Fig. 3.30 as a function of shock strength,  $\xi$ .

† Although the atmospheric pressure at the test site is 13.2 psi, the loading schemes do not introduce any appreciable errors, since  $14.7 - P_0 \ll 1/14.7$ . The drag pressures, however, are computed for the actual value of the atmospheric pressure  $P_0 = 13.2$  psi.



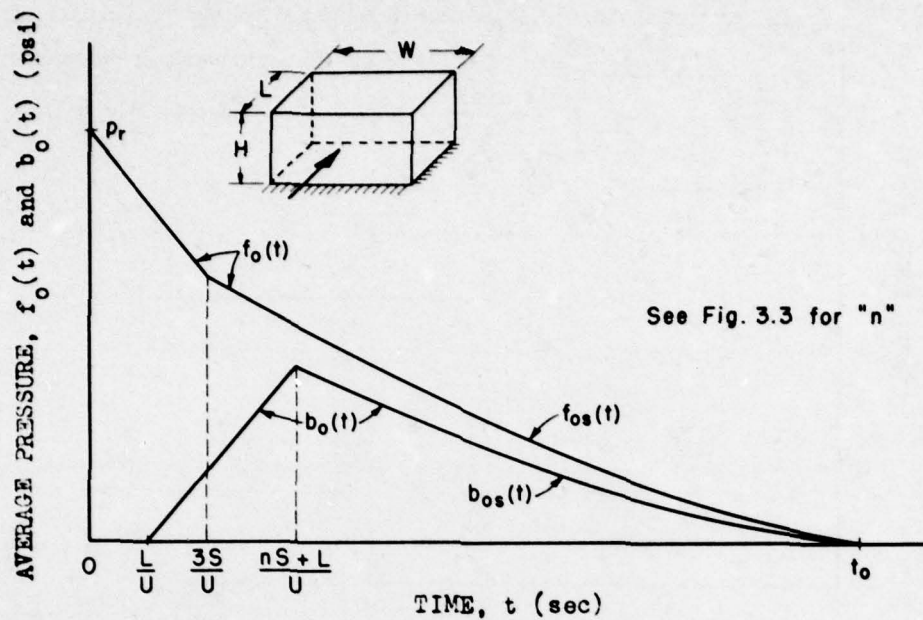


Fig. 3.1—Average pressure on front and rear of Structures 3.1a to c, e, f, i, s, and t.

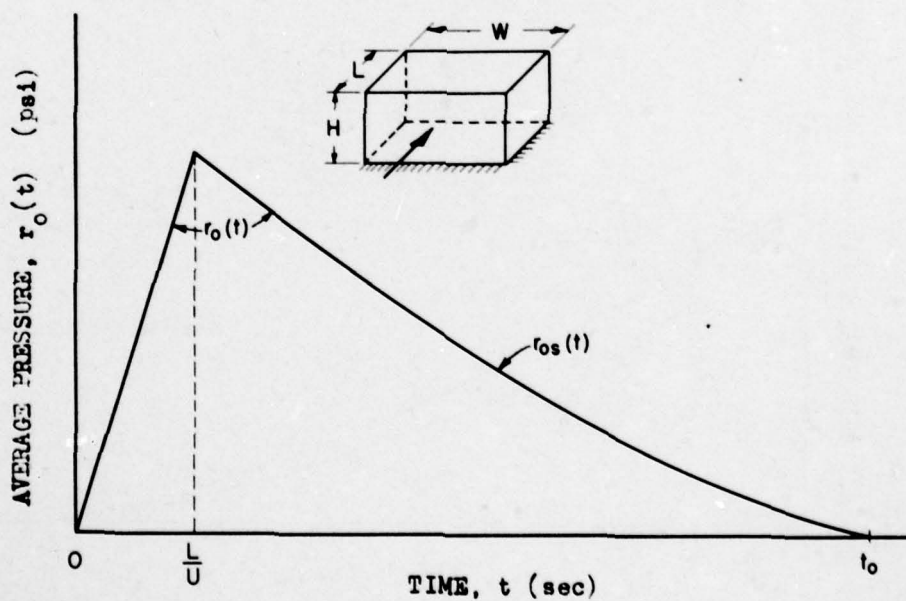


Fig. 3.2—Average pressure on top of Structures 3.1a to c, e, f, i, s, and t.

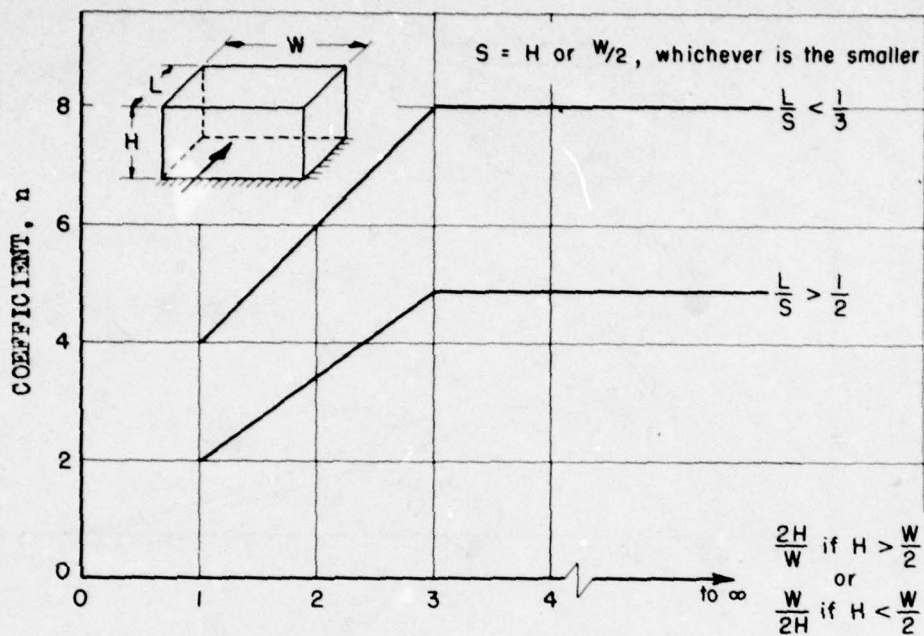


Fig. 3.3—Three-dimensional effect of pressure build-up on rear surface.

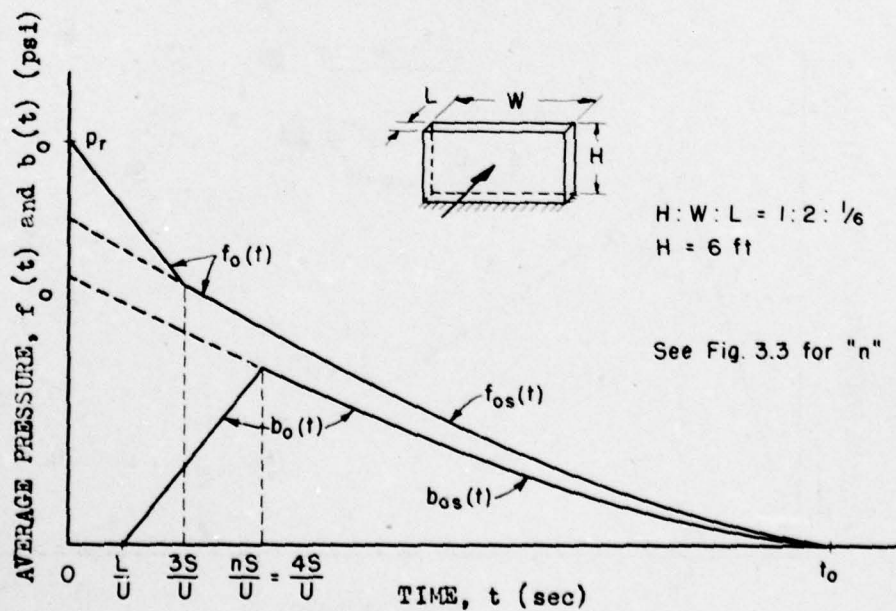


Fig. 3.4—Average pressure on front and rear of Structure 3.1d and first wall of Structure 3.1n.

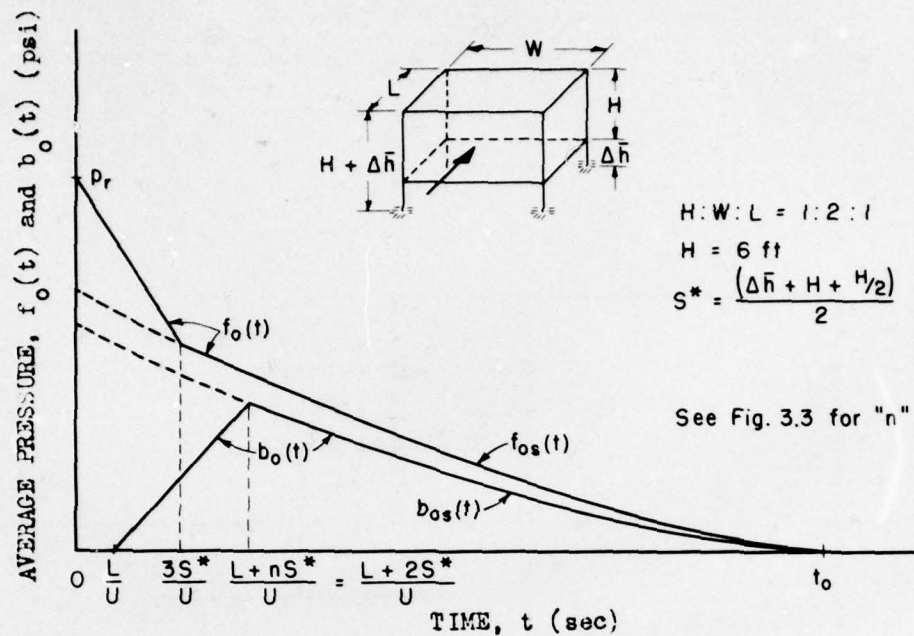


Fig. 3.5 — Average pressure on front and rear of Structures 3.1o and p.

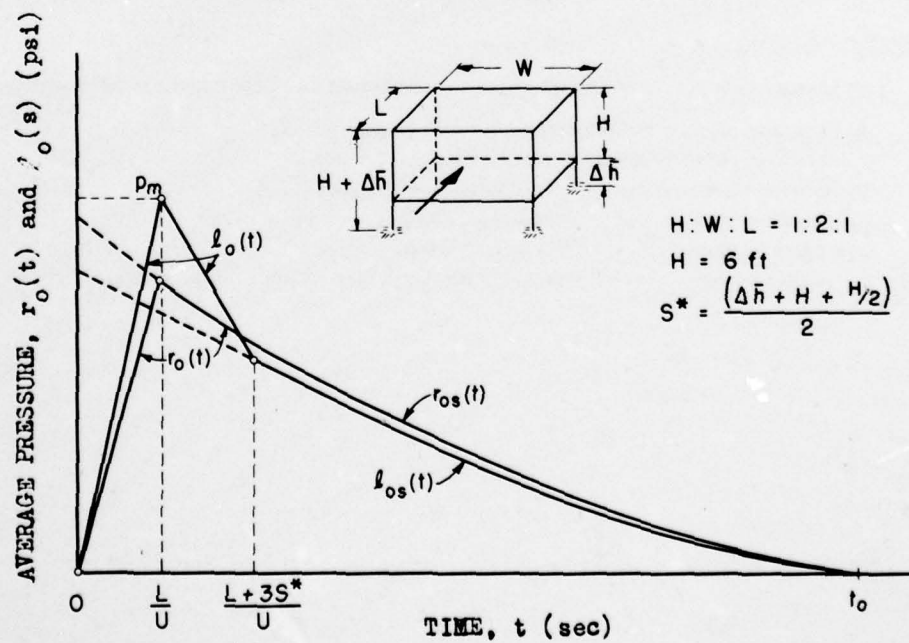


Fig. 3.6 — Average pressure on top and bottom of Structures 3.1o and p.



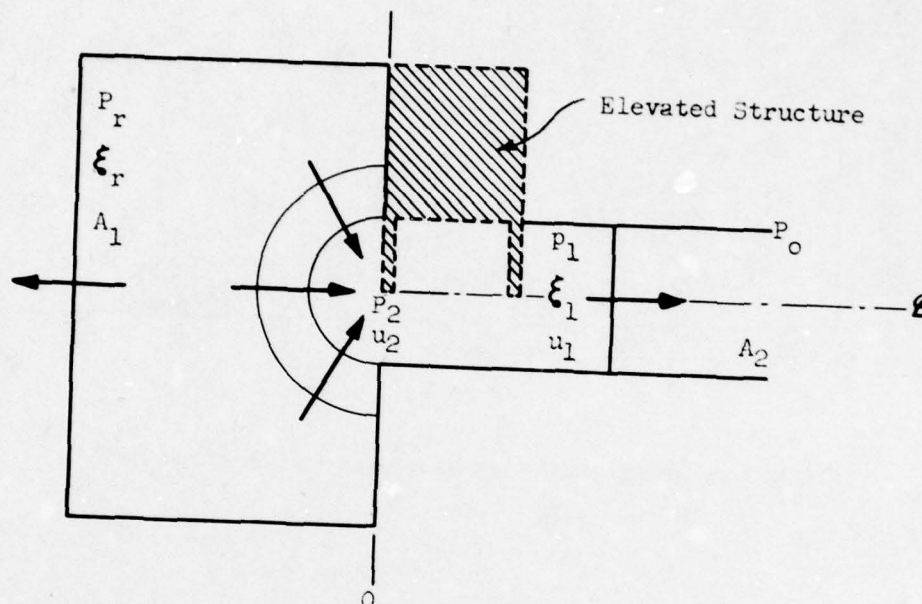


Fig. 3.7—Analogy between flow through channel contraction and flow under elevated structures:

- $P_r$  = absolute pressure behind reflected shock of strength,  $\xi_r$
- $P_2$  = absolute pressure behind rarefaction wave
- $P_1$  = absolute pressure behind transmitted shock of strength,  $\xi_1$
- $u_1$  = particle velocity behind transmitted shock
- $u_2$  = particle velocity behind rarefaction wave
- $A_1, A_2$  = cross-sectional area of wide and narrow channel sections, respectively.

AD-A073 468

DEFENSE ATOMIC SUPPORT AGENCY WASHINGTON DC

F/G 15/6

OPERATION UPSHOT-KNOTHOLE, NEVADA PROVING GROUNDS, MARCH - JUNE--ETC(U)

JUL 55 E V GALLAGHER, T H SCHIFFMAN

UNCLASSIFIED

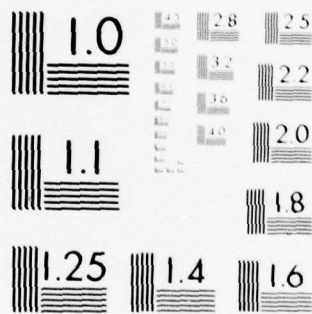
DASA-WT-721

NL

2 OF 4

AD  
A073468





MICROCOPY RESOLUTION TEST CHART  
NATIONAL BUREAU OF STANDARDS-1963-A



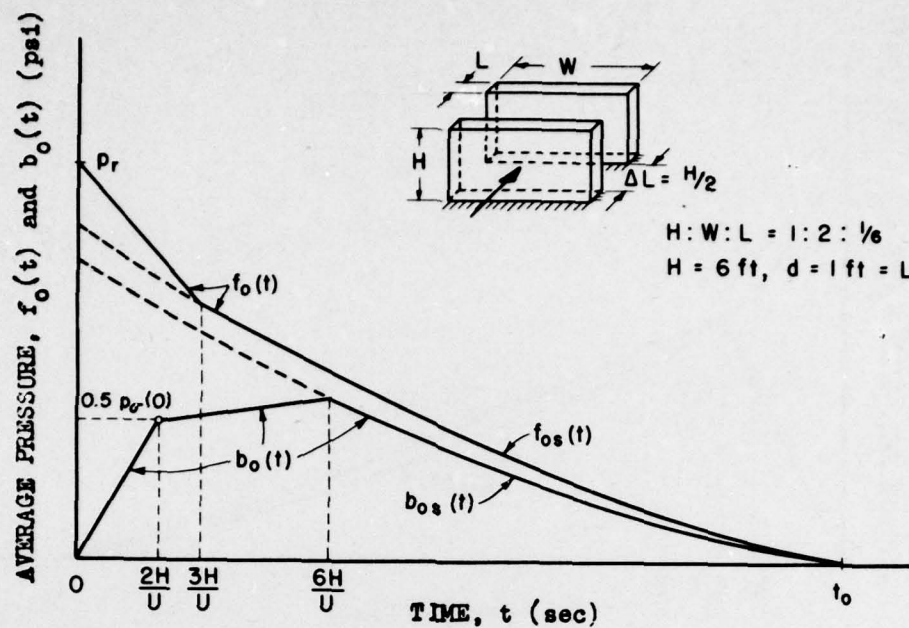


Fig. 3.8—Average pressure on front and rear of first wall of Structure 3.11.

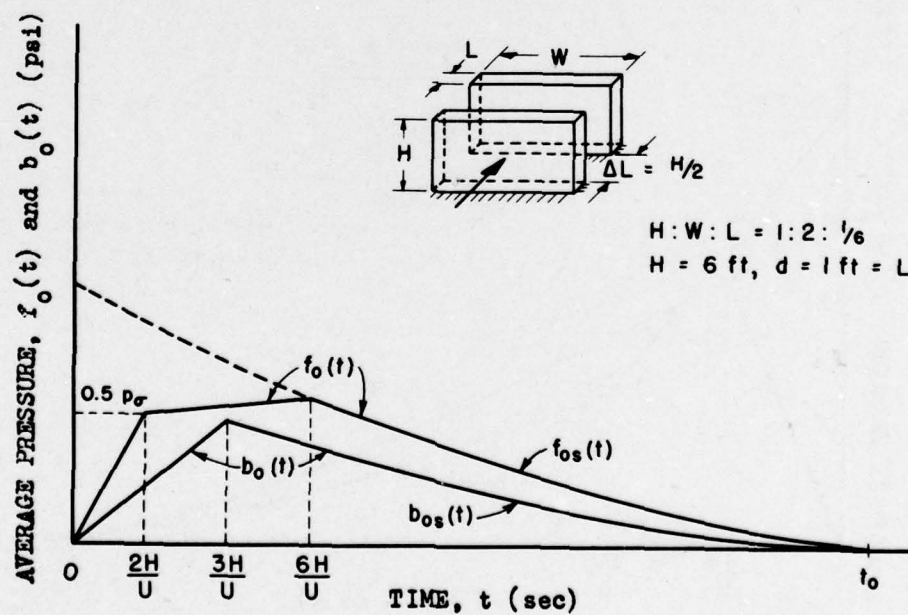


Fig. 3.9—Average pressure on front and rear of second wall of Structure 3.11.

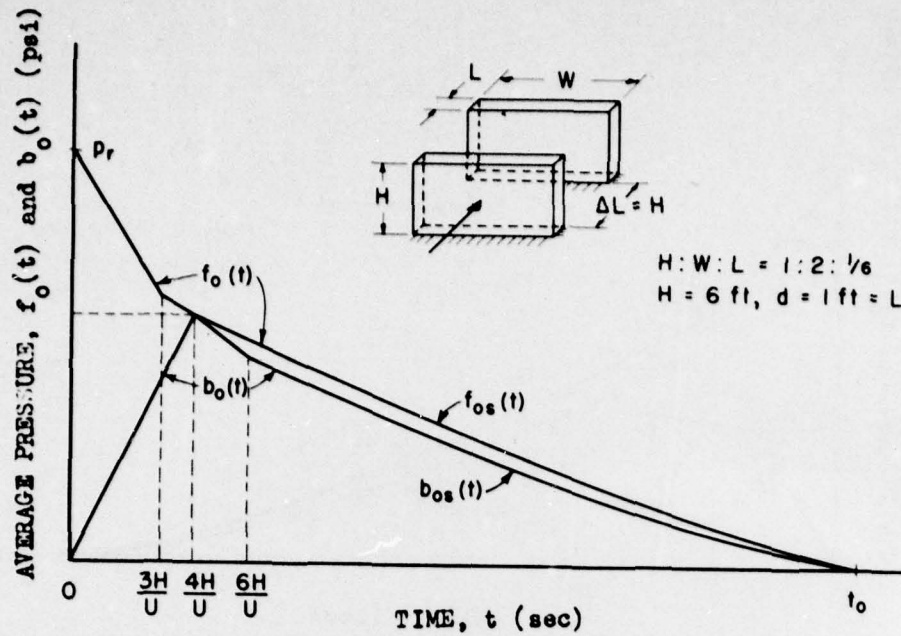


Fig. 3.10—Average pressure on front and rear of first wall of Structure 3.1m.

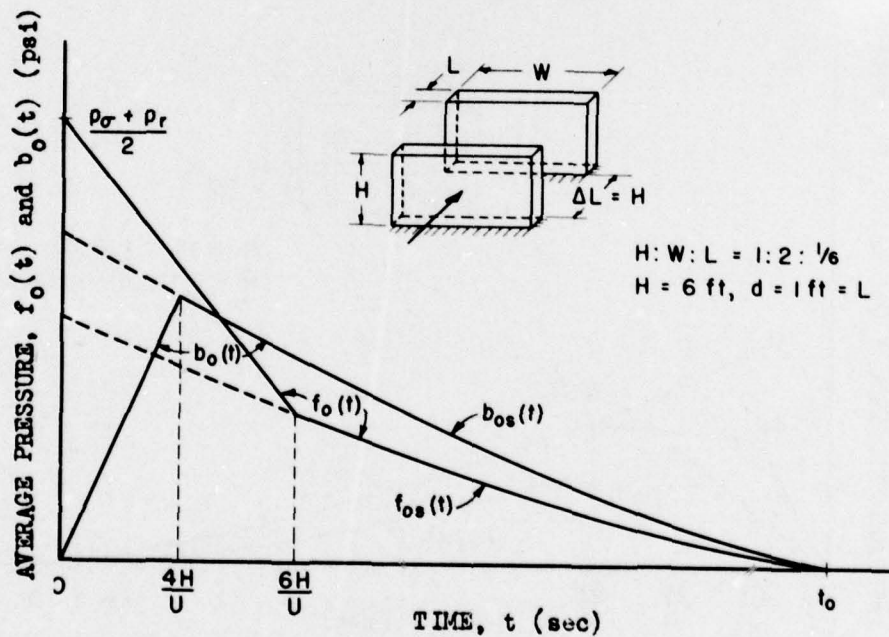


Fig. 3.11—Average pressure on front and rear of second wall of Structure 3.1m.

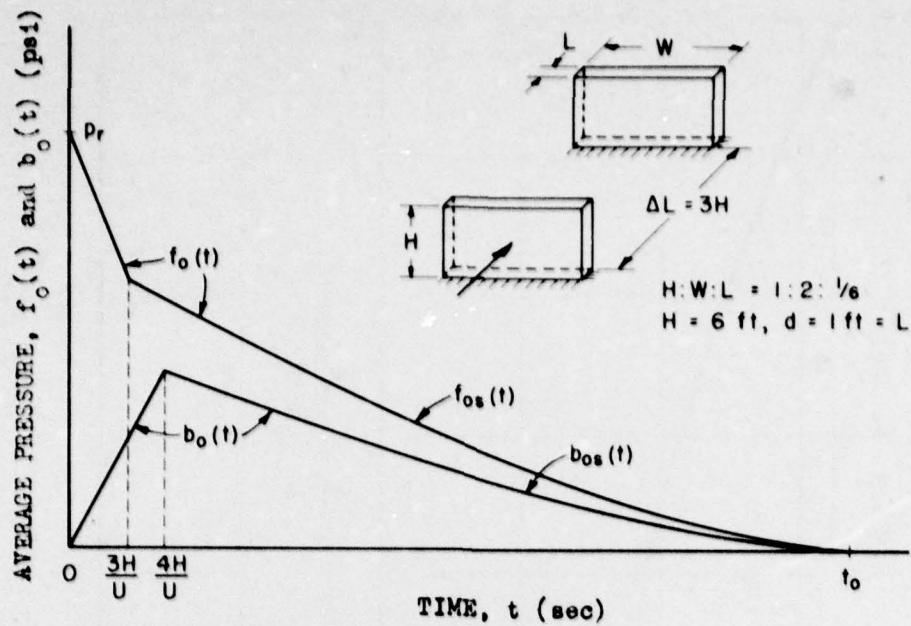
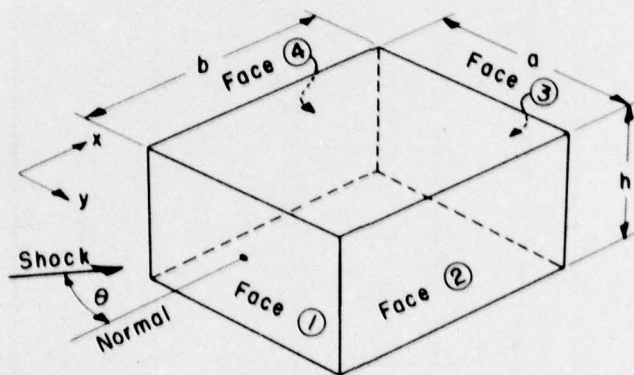


Fig. 3.12—Average pressure on front and rear of second wall of Structure 3.1n.



Notes:

1.  $0 \leq \theta \leq \pi/2$  and is measured in horizontal plane (x-y).
2. Shock front is a vertical plane front.
3.  $a < b$  (hence,  $\theta$  is measured from the narrower face).

Fig. 3.13—Geometry of problem for shock loading predictions on block at various orientations.



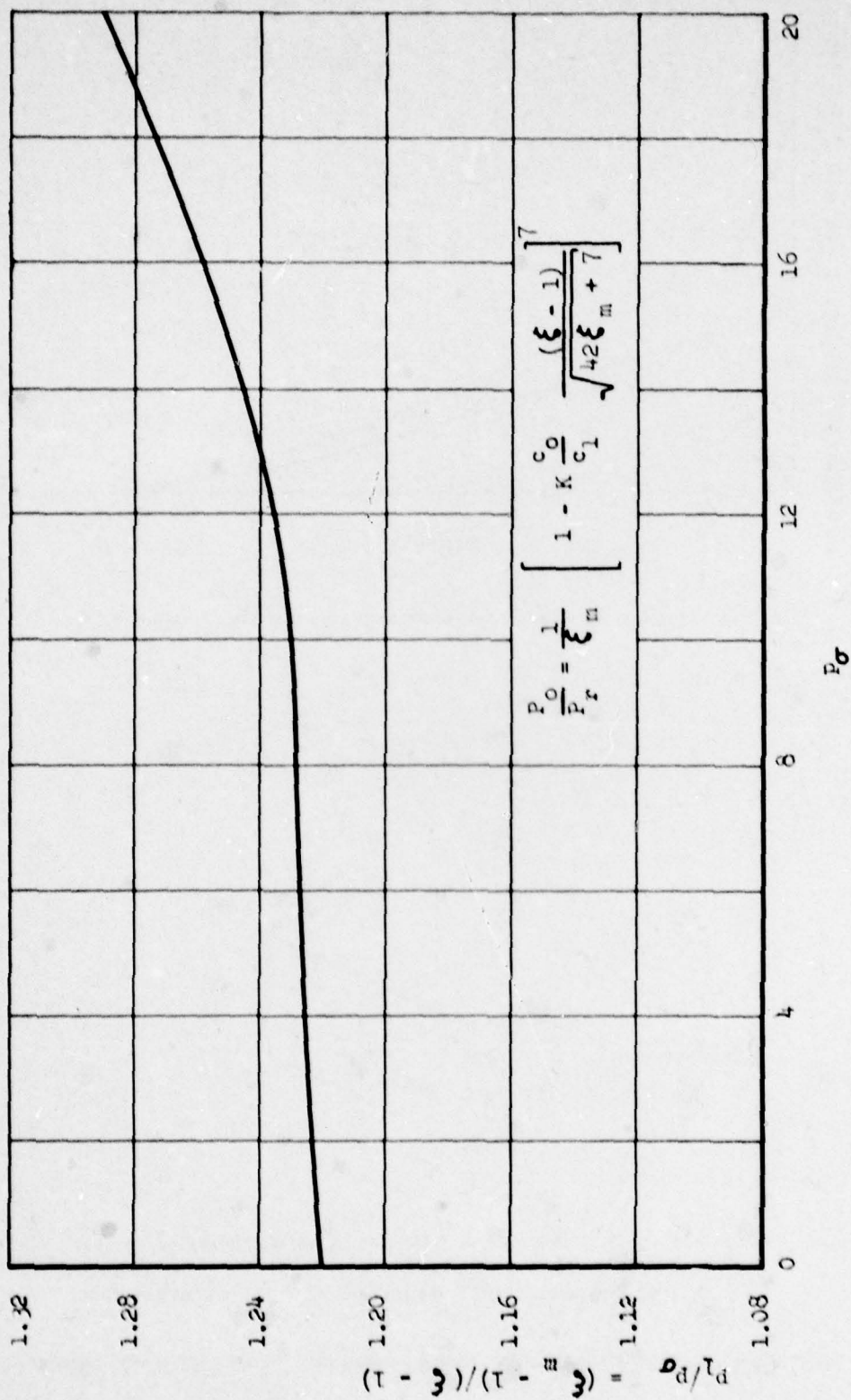


Fig. 3.14—Peak pressure in reduced channel.

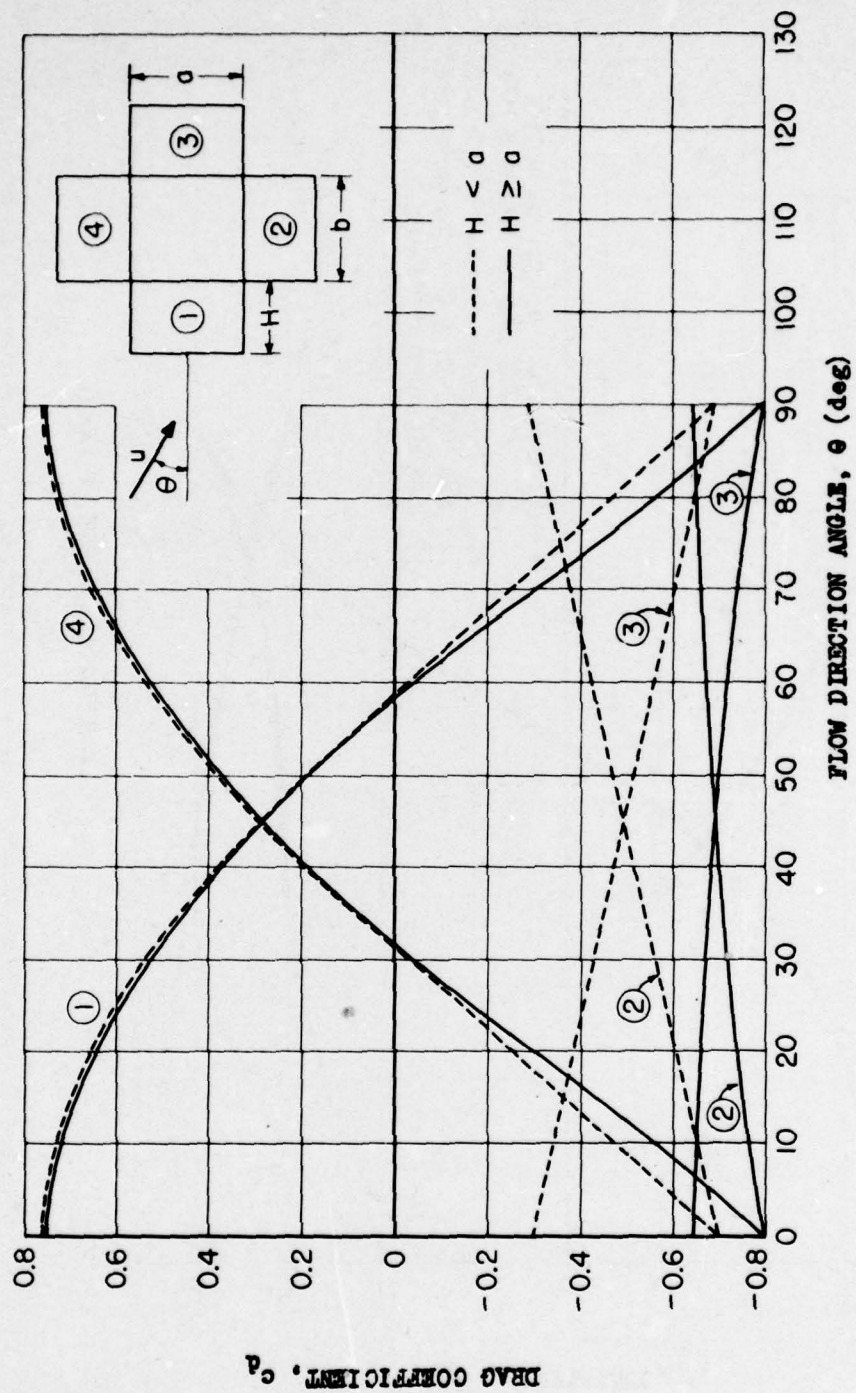


Fig. 3.15—Drag coefficient for each face vs the flow direction angle for solid rectangular blocks which are approximately square in plan.

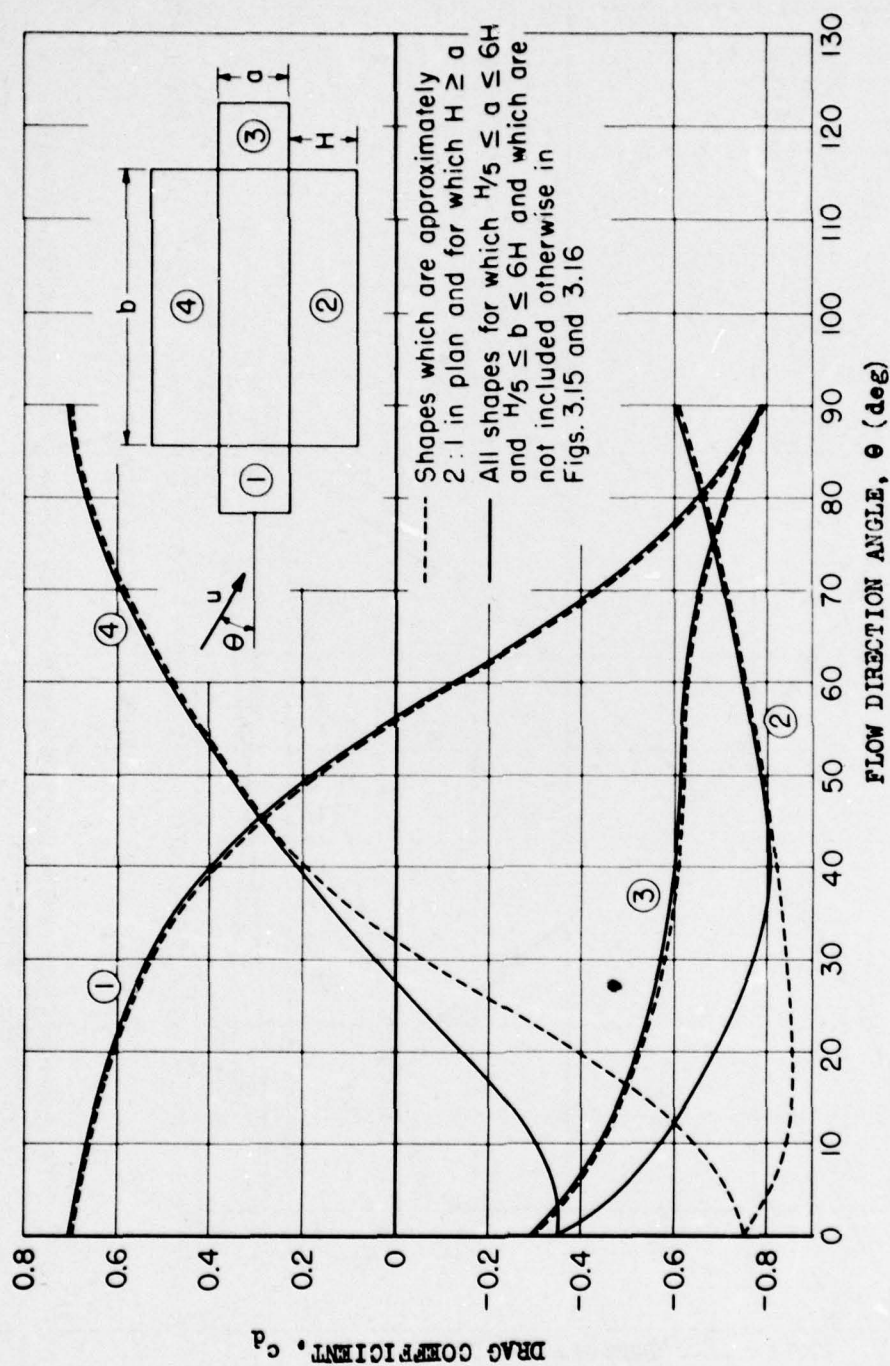


Fig. 3.16—Drag coefficient for each face vs the flow direction angle for solid rectangular blocks which are not square in plan.



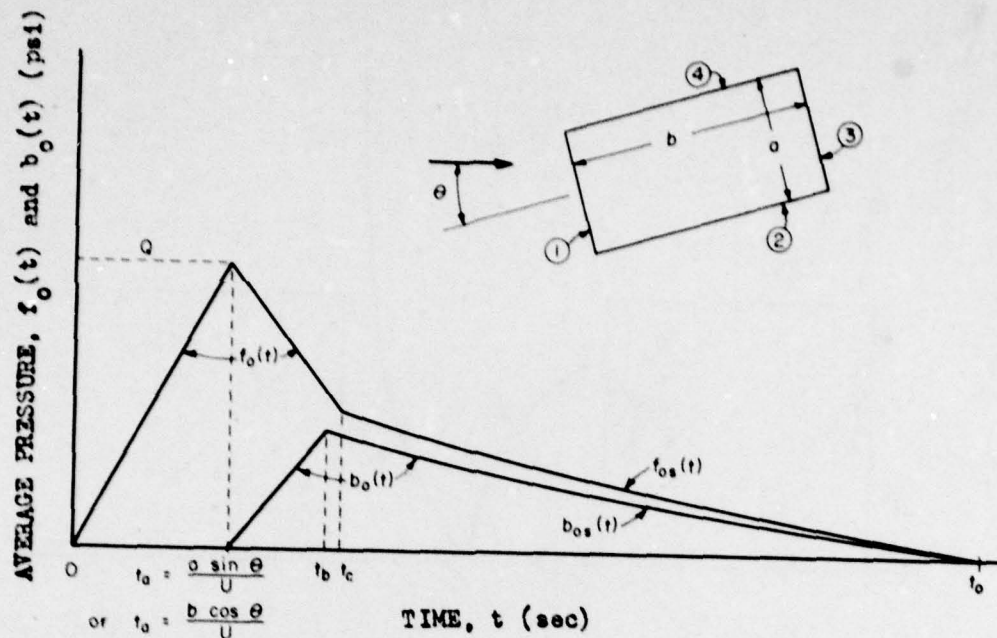


Fig. 3.17—Diffraction loading predictions for vertical walls of Structures 3.1g and h.

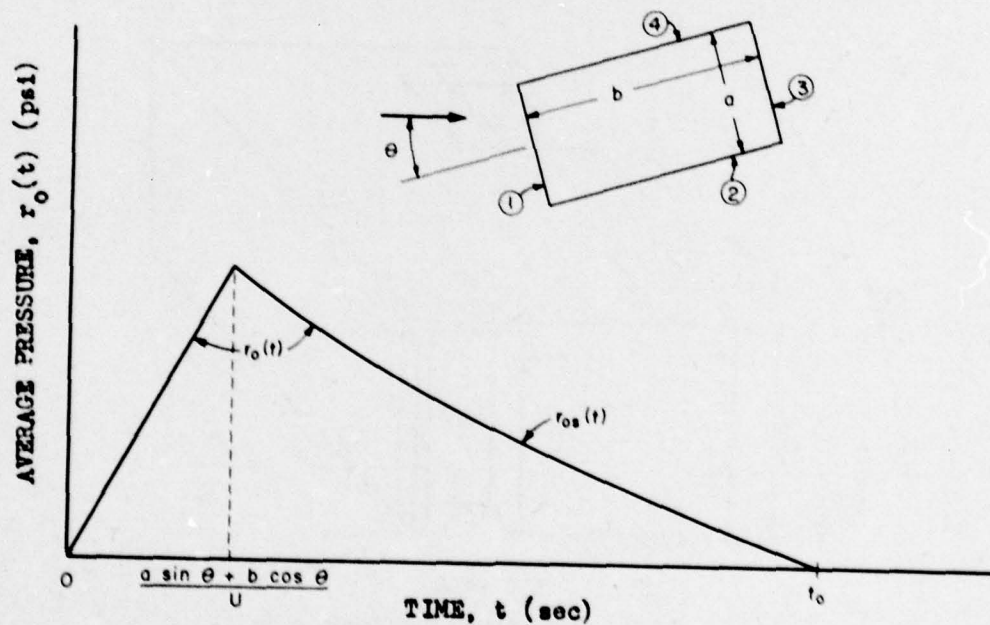


Fig. 3.18—Average pressure on top of Structures 3.1g and h.

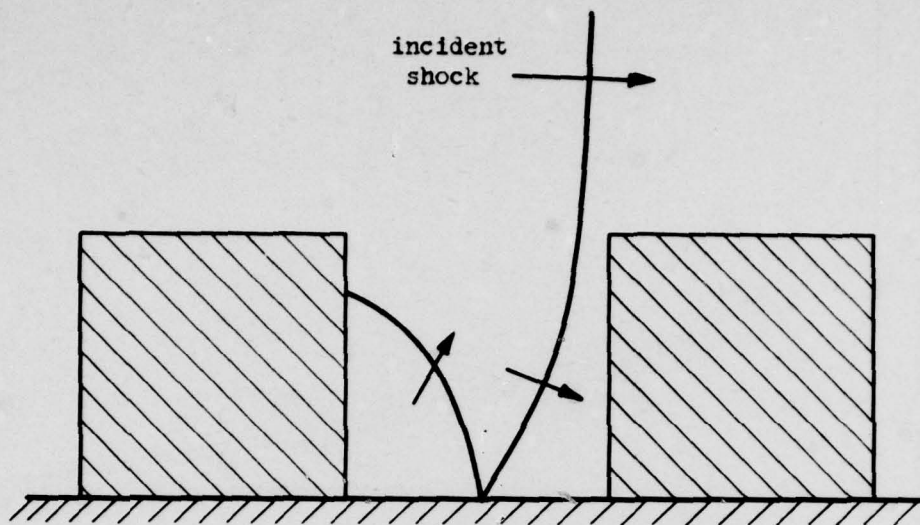


Fig. 3.19—Shock entering true re-entrant corner.

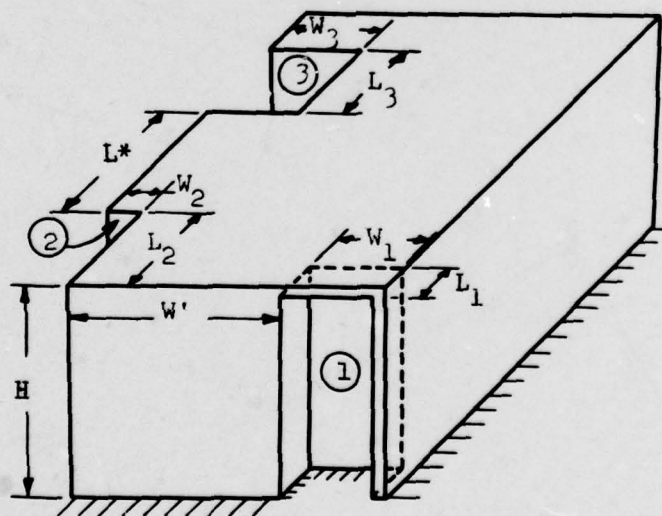


Fig. 3.20—Nomenclature for Structure 3.1q.

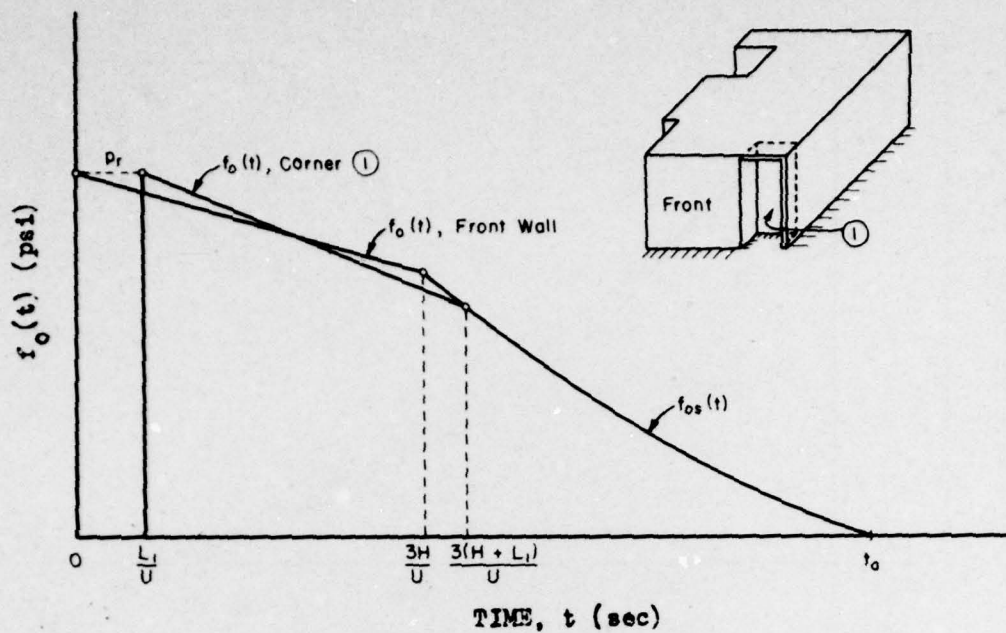


Fig. 3.21—Average pressure on front wall and corner 1 of Structure 3.1q.

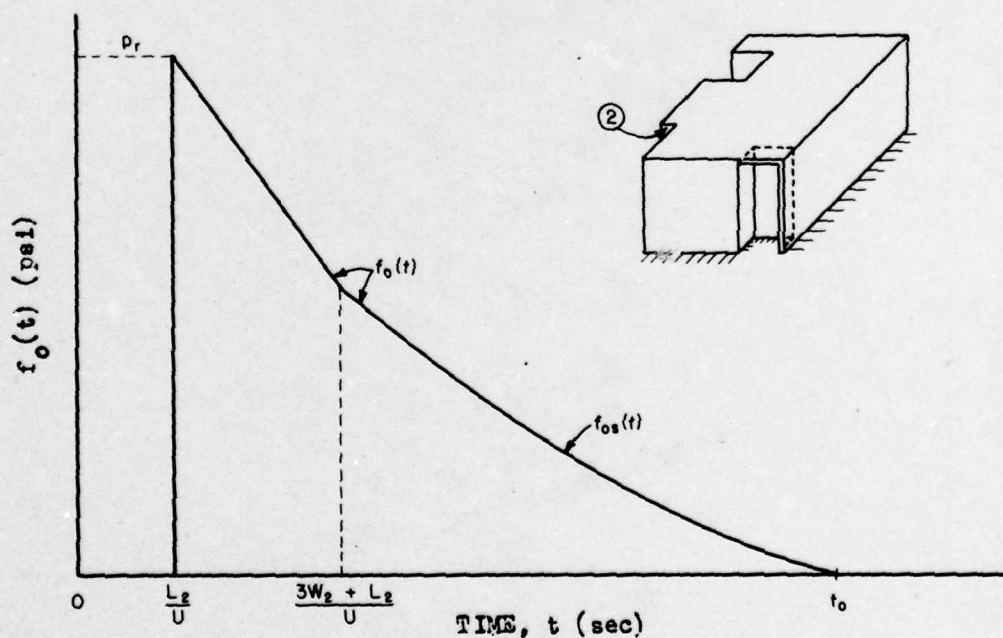


Fig. 3.22—Average pressure in corner 2 of Structure 3.1q.



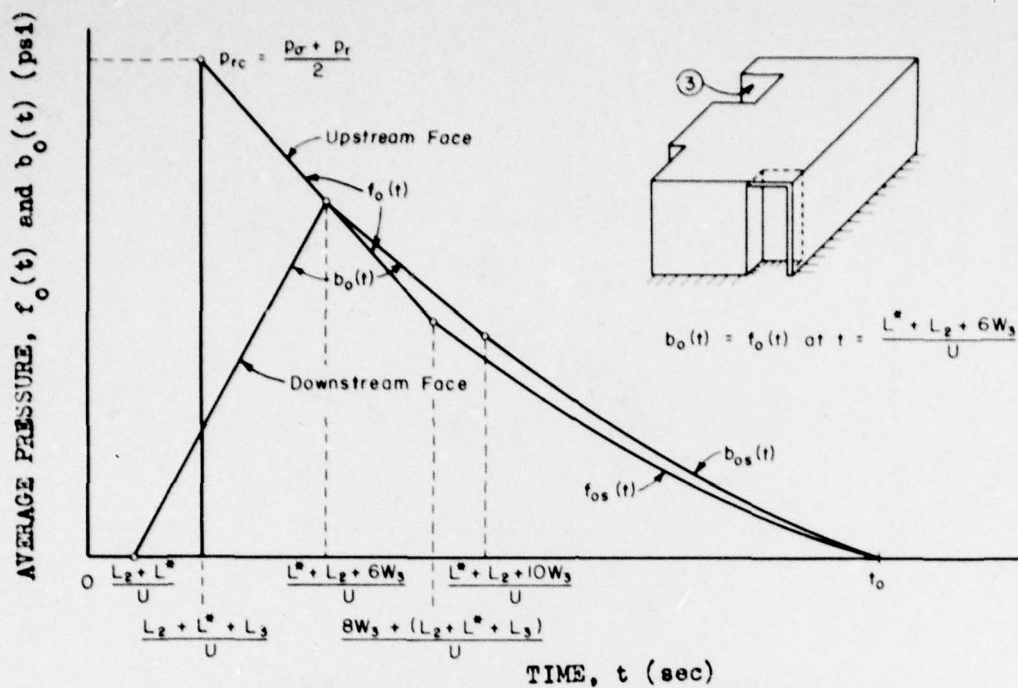


Fig. 3.23—Average pressure in corner 3 of Structure 3.1q.

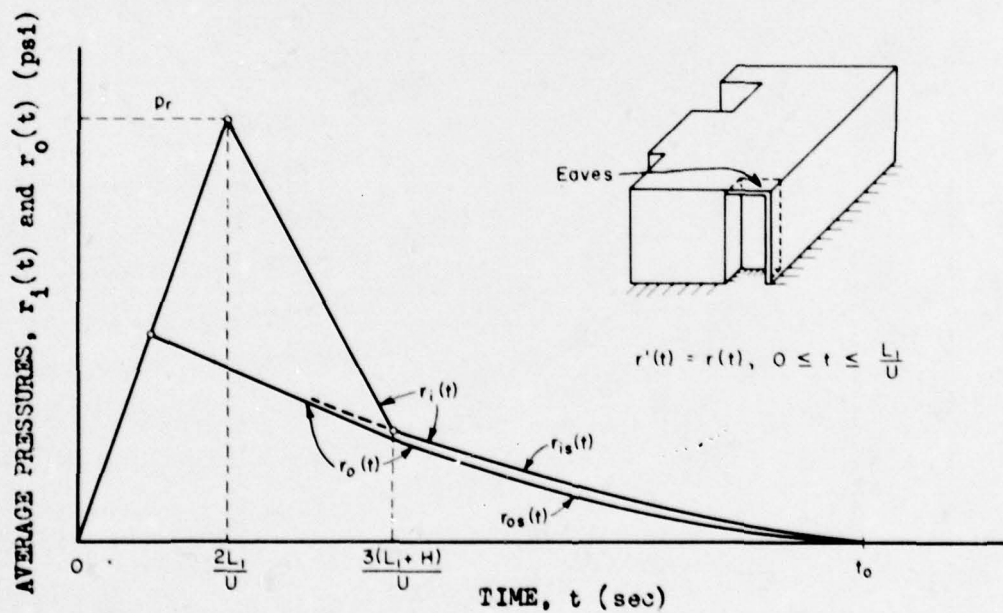


Fig. 3.24—Average vertical pressure on eaves of Structure 3.1q.

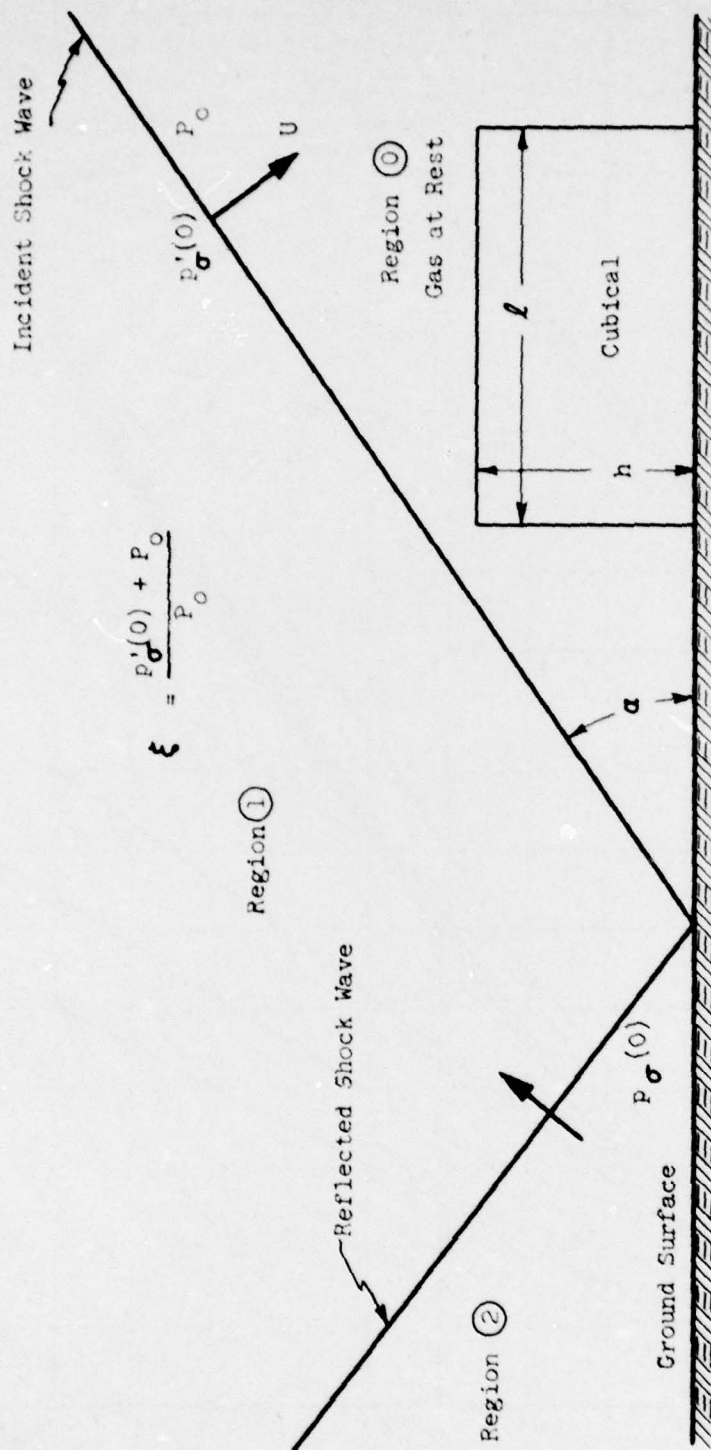


Fig. 3.25 — Initial shock wave configuration.

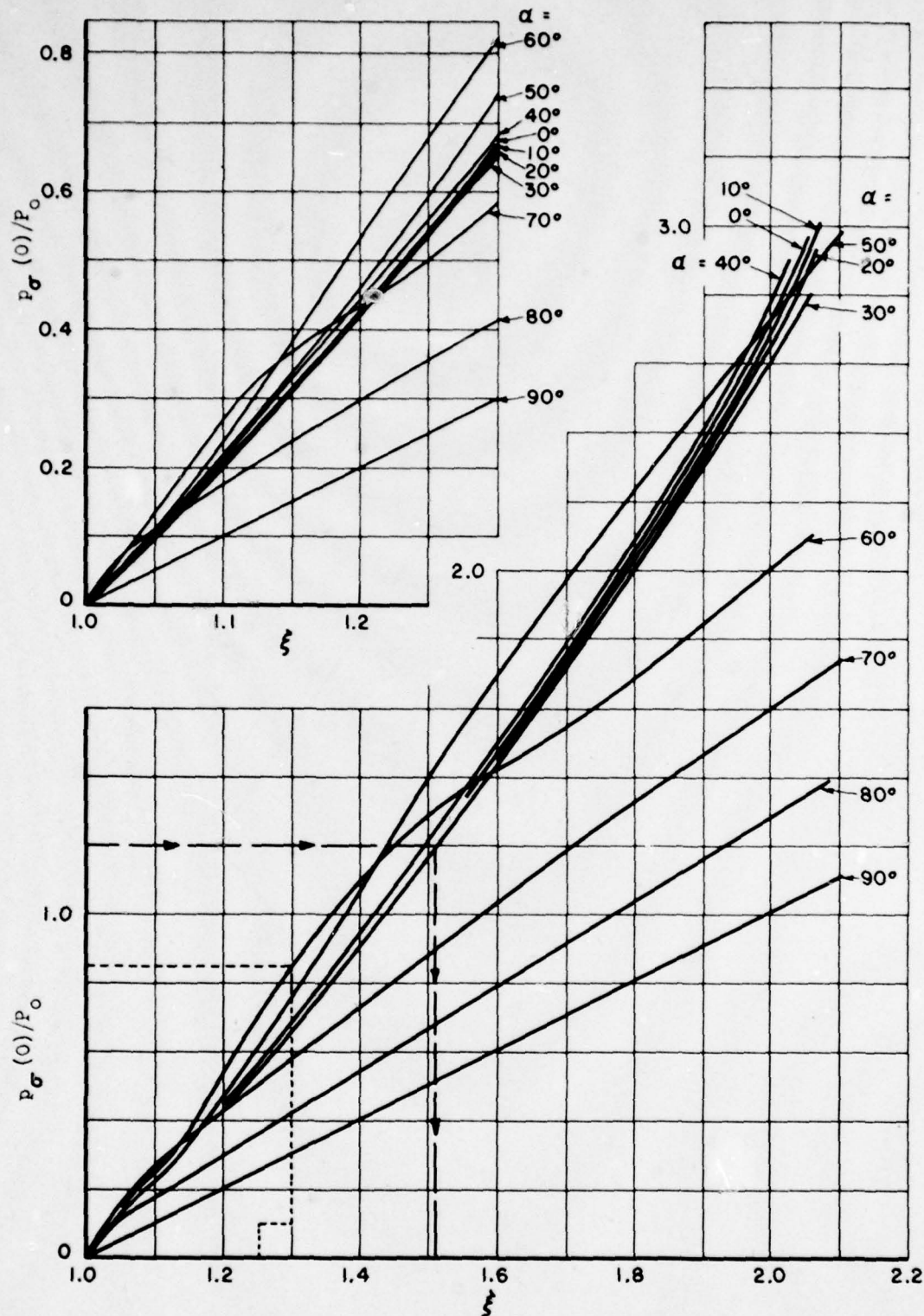


Fig. 3.26—Reflected pressure as a function of shock strength.



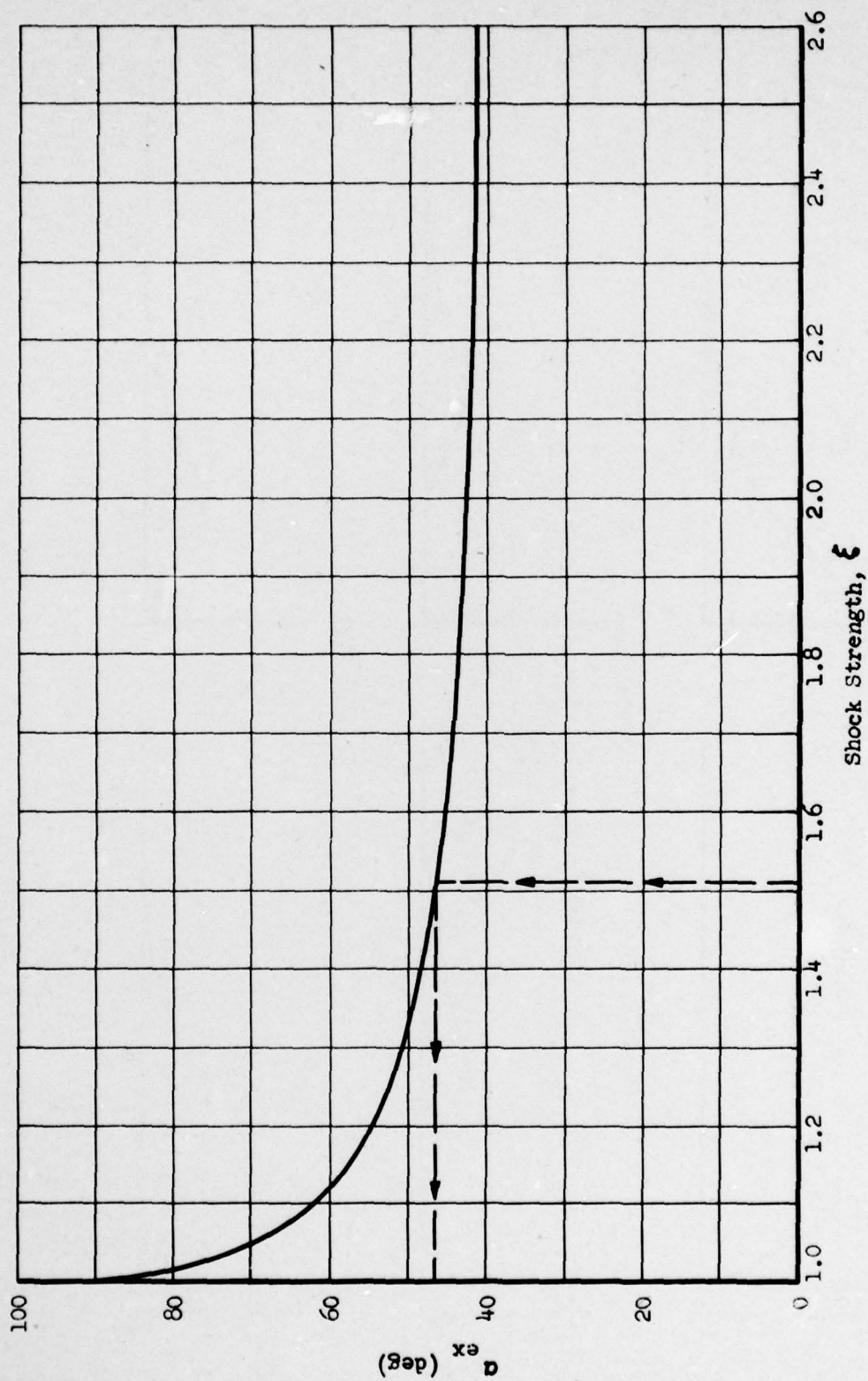


Fig. 3.27 —  $\alpha_{ex}$  as a function of shock strength.

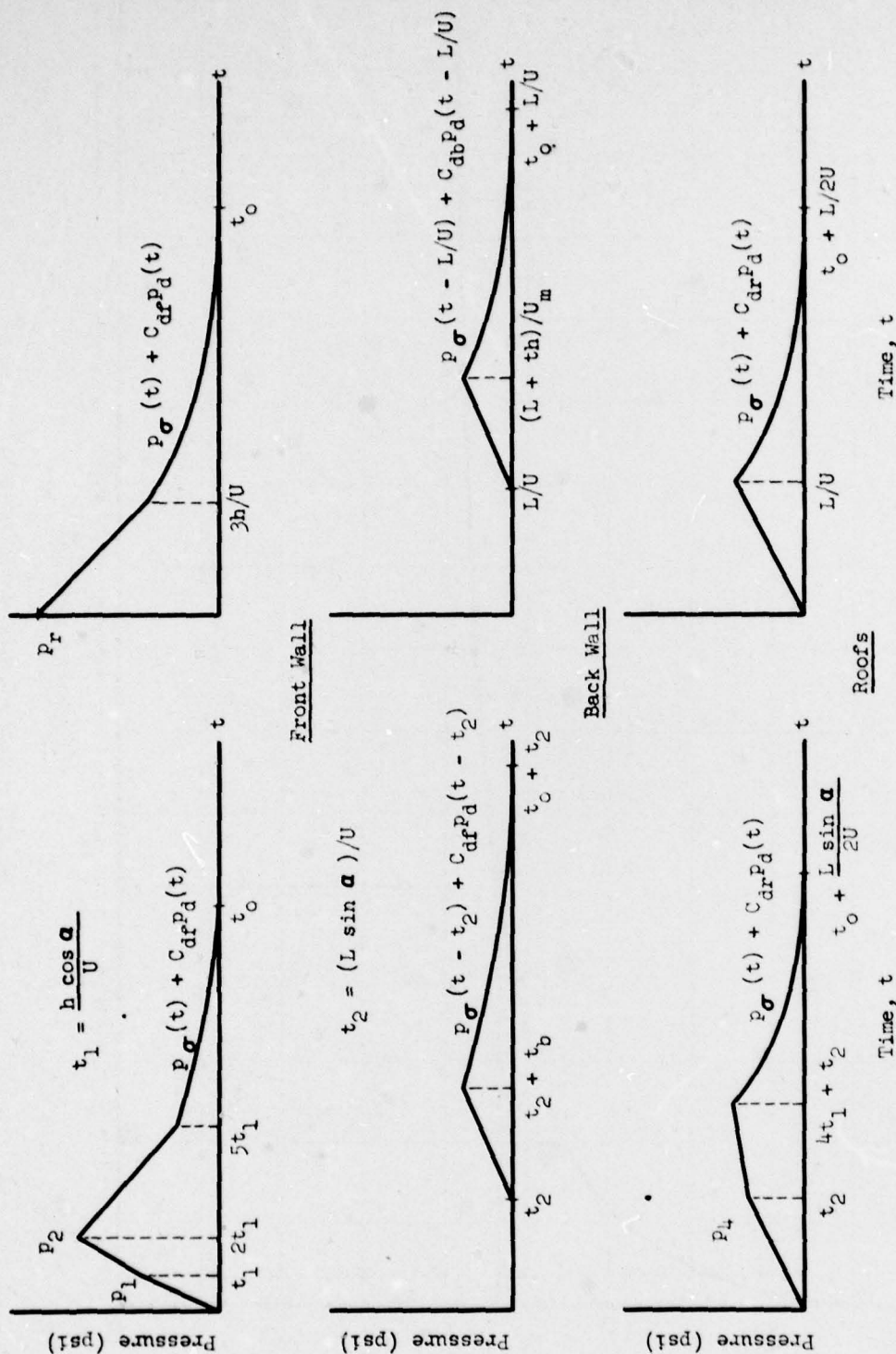


Fig. 3.28—Net loading on closed buildings in regular reflection region and Mach reflection region.

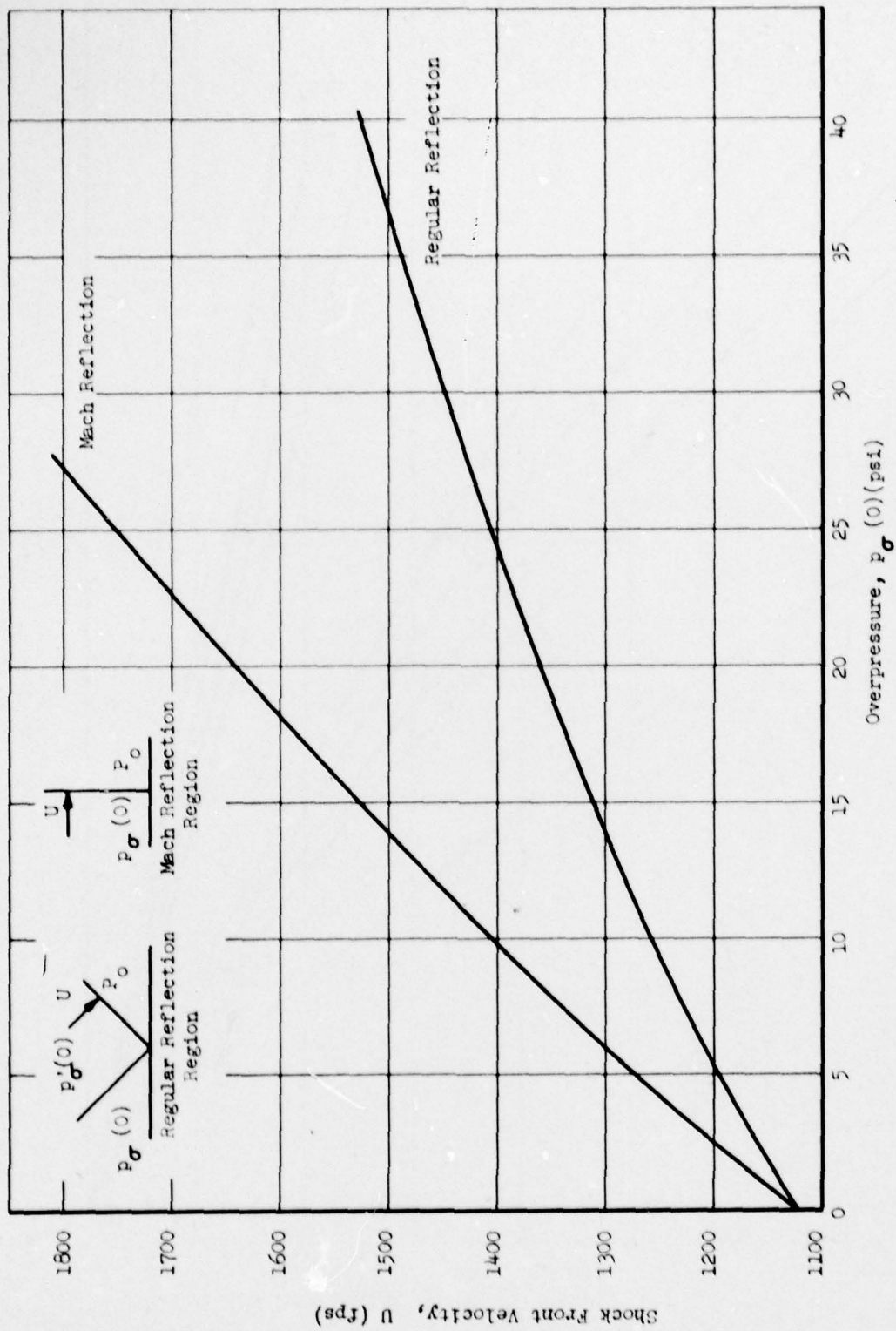


Fig. 3.29—Velocity of shock front vs overpressure ( $P_0 = 14.7$  psi).



UNCLASSIFIED

~~SECRET~~

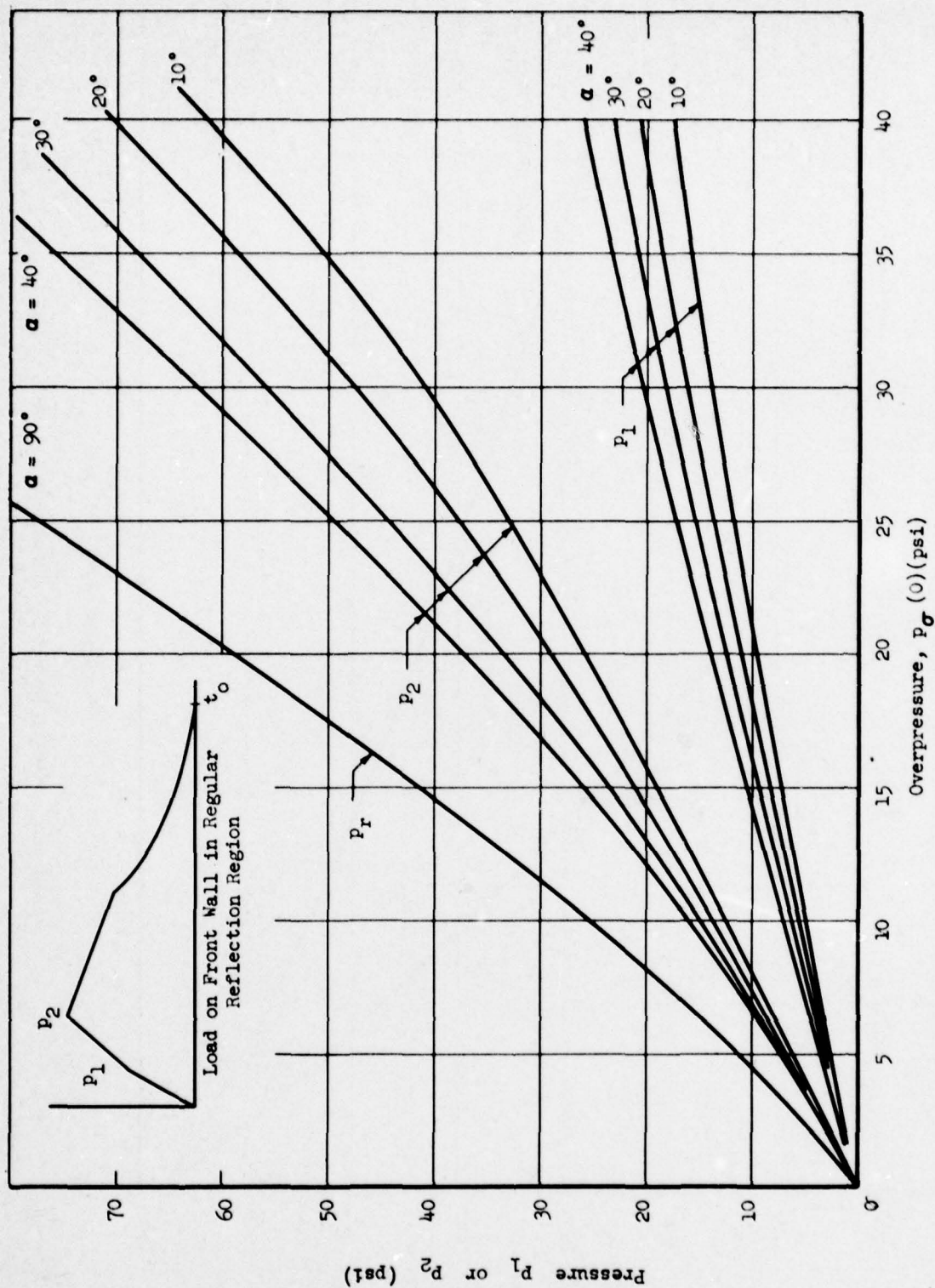


Fig. 3.30—Pressures  $P_r$ ,  $P_1$ , and  $P_2$  vs overpressure for closed buildings ( $P_0 = 14.7$  psi).

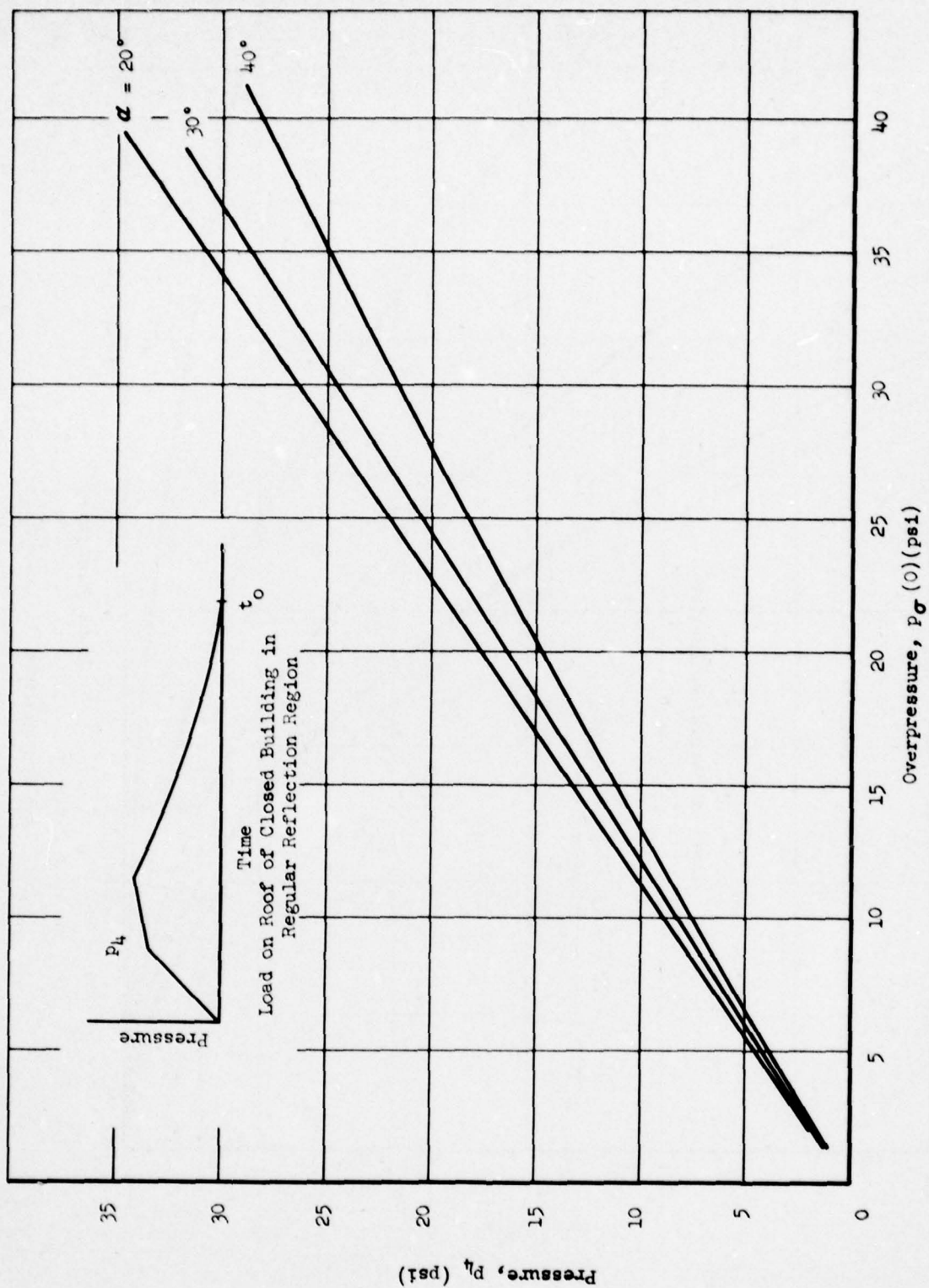


Fig. 3.31— $p_4$  vs overpressure closed buildings ( $P_0 = 14.7$  psi).

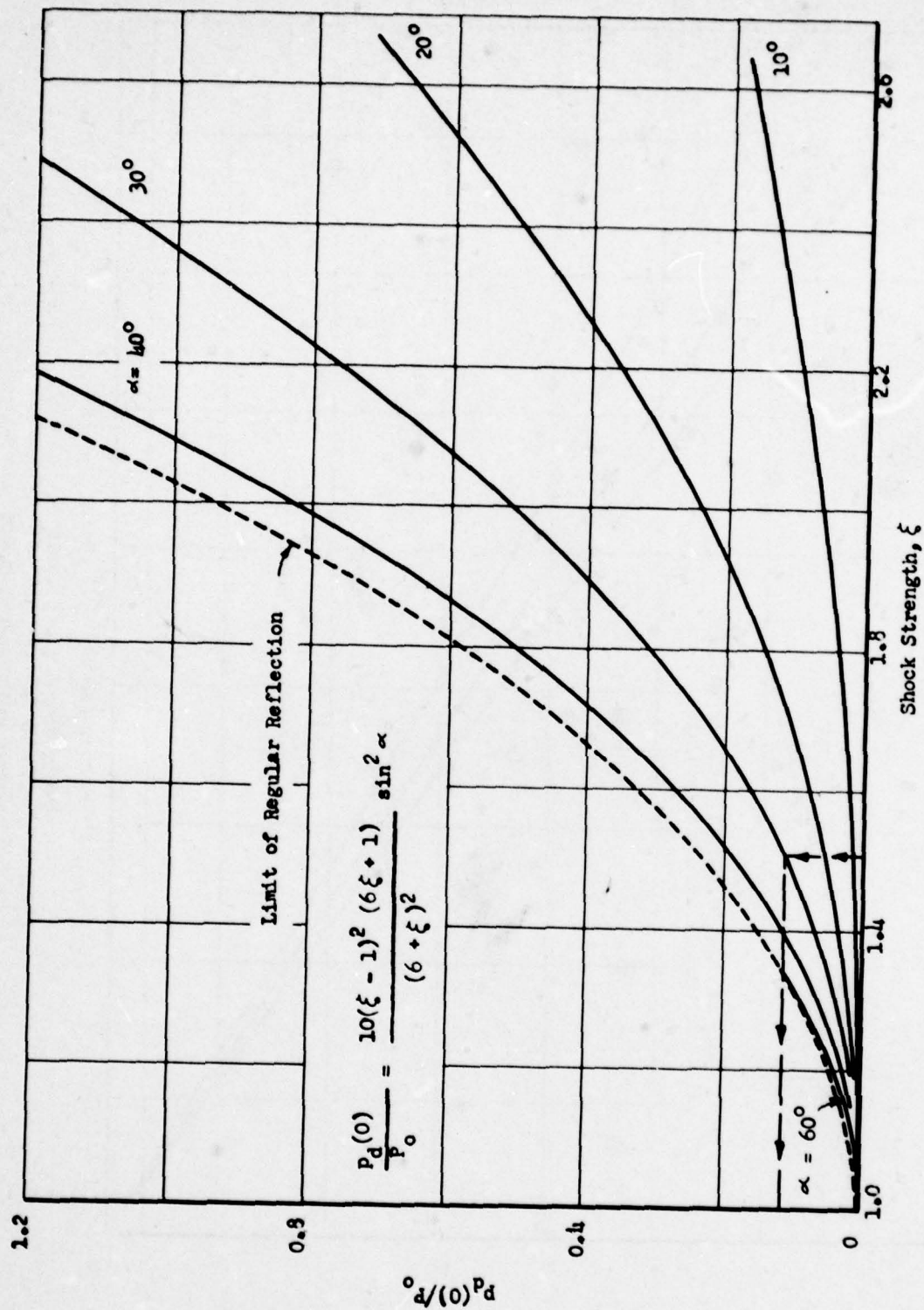


Fig. 3.32—Drag pressure as a function of shock strength.



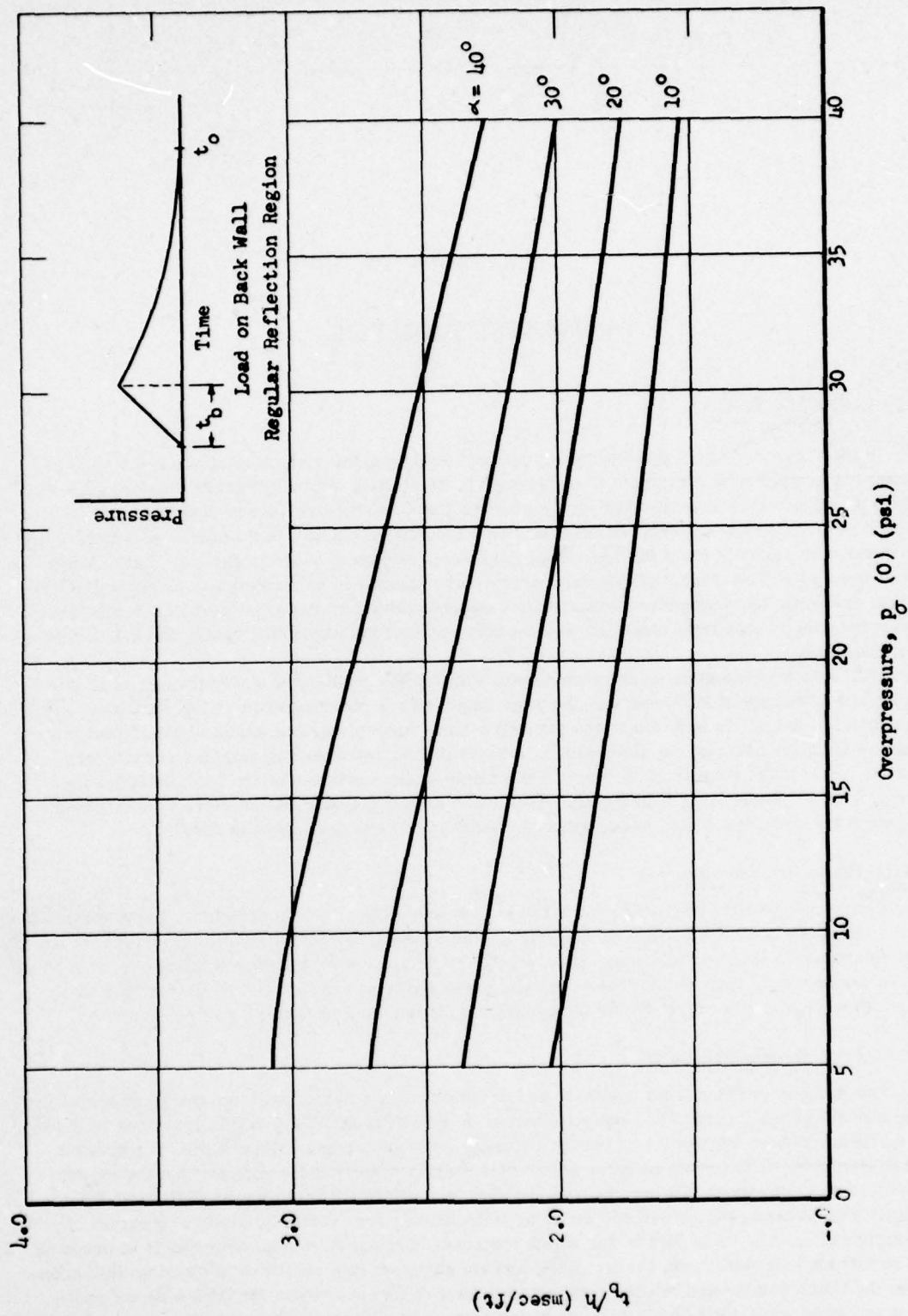


Fig. 3.33—The quantity,  $t_b/h$ , vs overpressure ( $P_0 = 14.7$  psi).

## CHAPTER 4

### POST-TEST ANALYSIS

#### 4.1 INTRODUCTION

In this chapter, which presents the post-test analysis, the reduction of data into special forms for comparison with pretest predictions is discussed. Basic pressure curves, such as free stream or side-on pressures, and computed forms of the dynamic pressures are discussed before dealing with the records of gages located on the test buildings. The evolution of pressure-time curves from the individual gage records into average pressures, net average pressures, and other forms of normalized pressure-curves is presented and discussed. Comments are made upon graphical comparisons between pressure records from shock tube tests and other large scale field tests, as well as between various gages throughout the 3.1 series of structures.

Diffraction phenomena on the structures, such as the build-up of pressures on rear surfaces, the influence of vortices, and the time required for clearing of the front surfaces, are discussed in detail. In addition to the pressure-time curves, various types of quantities, depending upon the phenomena under study, such as diffraction and drag impulse curves, are used to present the results of the test. The effects of the variation of the individual parameters, such as width, length, and size, which were among the original objectives of this test, are each treated separately, and additional observations are discussed in detail.

##### 4.1.1 Basic Pressure Curves

Chapter 3 gave loading predictions for the various structures in schematic form applicable to a wide range of shock conditions. In this chapter the experimental results are studied and are compared to those predictions. It is necessary to determine numerical values for the shock parameters, such as side-on pressure, wave shape and duration, and orientation or shock direction, from which all the necessary quantities used in Chap. 3 can be computed.

##### 4.1.2 Free Stream Pressure

The side-on pressure, wave shape, and duration were determined from the readings of the free stream gages located near the structures. Figures 2.1 and 2.2 give the locations of these free stream gages. Figure 2.1 indicates the position of the actual Ground Zeros for Shots 9 and 10 from which the orientation or shock direction is readily determined. There were five free stream gages located along the arc at a distance of 4900 ft from intended Ground Zero, spaced well between the structures so as to be relatively free from the disturbing effect of possible reflections. For Shot 9, for which the actual Ground Zero was over 800 ft to one side of the intended Ground Zero, the five free stream gages on this arc were at varying distances from the bomb source and might be expected to give different results for both side-on pressure and wave shape; for Shot 10, these gages were, for all practical purposes, equally distant from actual Ground Zero.

The pressure-time records for the free stream gages at ground level, on both Shots 9 and 10, are given in Figs. 4.1 and 4.3. These figures show the deviation of free stream pressures among the gages BA, BB, BC, BD, and BE to be less for Shot 9 than Shot 10 (about 0.3 psi for Shot 9 and about 0.6 psi for Shot 10). In fact, except for the first 15 msec, the difference in pressure between gages is not too much greater than local fluctuations in pressure measured by the individual gages. The curve for Shot 10 shows a very slow rise in pressure for gage BB during the first 100 msec such that it differs by from 20 to 50 per cent from the average of the remaining four gages. Therefore the reading of this gage was disregarded.

In addition to these free stream gages located at the ground, some gages were located at elevations up to 10 ft above ground at these same locations. Table 4.1 gives values of peak pressure at various heights. Figure 4.2 typifies the relation of pressure readings to the elevations of the gages. The initial side-on pressure was from 1.0 to 1.5 psi higher for an increase in elevation of 10 ft above ground level.

TABLE 4.1—Peak Pressure in Vicinity of  
3.1 Structures at Various Elevations\*

Peak pressure (psi)	Height above ground (ft)
6.35	0
6.4	2
7.4	5
7.8	10

\* Operation UPSHOT-KNOTHOLE, Preliminary Report, Summary Report of the Technical Director, Programs 1-9 (1953), WT-782.

The duration of the positive phase,  $t_0$ , used throughout this analysis was 0.92 and 0.88 sec for Shots 9 and 10, respectively, except for Structures 3.1s and t. Figures 4.1 and 4.3 show the variation of pressure during only the first 0.7 sec of the duration since, beyond this time, no significant features of the loading phenomena on the buildings were observed. Figure 4.2 uses the expanded time scale for a more detailed analysis of the early stages of the blast waves. The finite rise time of roughly 2 msec is the result of the response time of the gages. (It can be seen from the subsequent figures that an equivalent time is required to reach the maximum recorded pressures also for gages on normally oriented surfaces undergoing head-on reflection.)

It is interesting to observe in Fig. 4.2 the minor variation of pressure recorded almost simultaneously by the gages—approximately at the time  $t = 0.035$  sec. The gages at 2 and 5 ft above the ground were mounted on the same pole and recorded this peak simultaneously, whereas the gage at 10 ft above the ground recorded this peak a few milliseconds later.

#### 4.1.3 Side-on Pressure Curves

The free stream pressure curves shown in Figs. 4.1 and 4.3 were used to determine the variation of side-on pressure with time. Two alternate methods of expressing side-on pressure were considered (either through an equation or graphically).

The method, referred to in Chap. 3, utilizes a mathematical expression such as is given in Sec. 3.3.1, determining the value of the constant  $c$  as the number which gives a shape most closely resembling that of the free stream curves in Figs. 4.1 and 4.3. However, in matching the curves given by an equation to the measured pressure curves, there was no reason to prefer any one of the measured curves, and a value of  $c$  was chosen, which fitted the average of the entire group of measured curves. The best fit that can be obtained by trying various values of the exponential coefficient  $c$  in Eq. 3.1 may be in error during some portions of the first



positive phase. A better job of curve fitting can be done for certain experimental wave shapes, using equations of a different form. However, since the validity of any equation, used to denote the variation of side-on pressure, is judged by how well it matches the average of the free stream pressure readings, one might just as well use this free stream average, obtained graphically, without use of any equations, as the definition of side-on pressure.

In Fig. 4.4 the side-on pressure curves for Shots 9 and 10, obtained by sketching through the center of the band of free stream curves, are shown. In drawing these curves, during the first 20 msec when the reading is rising rapidly, the shape of the curve was obtained as follows:

The portion of the curve beyond the time  $t = 20$  msec was sketched-in first and then extended backward, smoothly, to the time  $t = 0$ . Thus, the value of side-on pressure,  $p_o(0)$ , was, in effect, obtained by extrapolation from the shape of the pressure curve later in the duration and is slightly in error. However, since the pressure at every time during the rest of the duration is defined independently by the curve, the only practical reason for giving some specific pressure in psi, corresponding to the time  $t = 0$ , is that of convenience in referring to the shock strength in the conventional manner.

#### 4.1.4 Drag Pressure

##### 4.1.4.1 Rankine-Hugoniot Curves

Drag pressure is defined throughout the entire positive phase for the purposes of this chapter, using the extended form of the Rankine-Hugoniot equation as given in Eq. 3.3, i.e.,

$$p_d(t) = \frac{2.5 p_o(t)^2}{7P_0 + p_o(t)}$$

This equation is based on the assumption that the kinetic energy,  $\frac{1}{2} \rho u(t)^2$ , of the moving fluid equals the dynamic head,  $p_d(t)$ , at every time,  $t$ , during the positive phase of the blast wave. The value of  $P_0$  must be taken as 13.2 psi for both Shots 9 and 10. The values of  $p_o(t)$  for use in Eq. 3.3 are obtained from Fig. 4.4. Curves corresponding to Eq. 3.3 are presented in Figs. 4.8 and 4.9. Equation 3.3 and its corresponding assumption need not be introduced in the analysis if reliable dynamic pressure measurements, applicable to the vicinity of the items loaded, are available. Although no such measurements were available for the 3.1 structures, adjustment of the nearest pressure measurements were used as discussed below.

##### 4.1.4.2 Measured Dynamic Pressure Curves

Dynamic pressures obtained from the Sandia q-gage records *Dynamic Pressure Time and Supporting Air Blast Measurements*, Sandia Corporation, were used as an alternate form of expressing drag pressures. No q-gages were located in the immediate vicinity of the 3.1 group of structures. By interpolating linearly between the readings of q-gages located at distances of 4075 and 6545 ft from intended Ground Zero, dynamic pressure curves were obtained for the region of the 3.1 structures. These derived curves showed higher peak values for both Shots 9 and 10 than obtained from Eq. 3.3 at the time  $t = 0$ . In addition, the shape of these curves indicated a less rapid decay throughout the positive phase. The higher peak values may have been the result of interpolating linearly. The value of peak drag pressure,  $p_d(0)$ , obtained from Eq. 3.3, was believed to be more reliable than the interpolated values. The curves labeled Sandia q-gages in Figs. 4.8 and 4.9 were obtained from the interpolated curves using a constant (with respect to time) correction factor. This correction factor was chosen such that the adjusted magnitude of the interpolated curve at the time  $t = 0$  would be equal to  $p_d(0)$  obtained from Eq. 3.3. A separate correction factor was therefore used for Shots 9 and 10.

## 4.2 DISCUSSION OF DATA AND FORMS FOR PRESENTING RESULTS

### 4.2.1 Records

The large amount of pressure data obtained from the various 3.1 structures was received by Armour Research Foundation in the form of nonlinear pressure-time plots, punched card stacks, and tabulations obtained by reading these plots. These punched card stacks were plotted in linear form.

Some difficulty was experienced with the BRL information in that no zero time was provided with the records. Now, zero time is defined as the time when the shock front first impinges on a structure. In order to synchronize the individual pressure gages on a given face for averaging, the proper time delay had to be estimated. The procedure was to subtract the number of milliseconds from the arbitrary zero to the first significant rise of the curve. The correct gage time delay as computed by  $d/U$  ( $d$  being the distance from the first point of impingement of the shock front to the gage in question, as measured along a line perpendicular to the shock front,  $U$  = shock front velocity) was added to the point where the first pressure rise was seen on the gages. With this information, the individual gage records of BRL, SRI, and NOL were plotted.

Average pressure-time curves were computed from the individual gage records. The averaging was accomplished by means of an IBM Card Program Calculator. The individual gage records were multiplied by appropriate weighting factors (see Sec. 4.2.5) and summed at assigned time intervals. If no card reading was available at the assigned time, a linear interpolation was performed.

### 4.2.2 Individual Pressure-Time Records

The individual pressure-time records for some typical gages of the 3.1 group are plotted in Figs. 4.10 to 4.17. As-built locations of the gages on these structures are given in Figs. 2.13 to 2.44. The individual pressure records for all the gages would be too voluminous for presentation here. Examples of gage records on structures representing the best and worst cases of gaging have been presented. Individual gage records for gages located on the same surface have been plotted on one set of coordinate axes in Figs. 4.10 to 4.17 for Shots 9 and 10, up until the time  $t = 0.7$  sec.

Structure 3.1a was the control structure for the entire group and, unfortunately, also represents the poorest example for comparison of individual gage records within one surface. Structure 3.1c, on the other hand, represents an example of gage records which compare very favorably. In addition to the gage records, the side-on pressure curve has been included for Shots 9 and 10 with the records on the front surfaces of Structure 3.1a.

It is impossible to make a statement of gage accuracy in terms of a single number, or even in terms of a reasonable range of percentages (which applies under field conditions). Using check gages (see Sec. 4.2.3), gage accuracy can be expressed in the form shown in Table 4.2. However, even in this form the accuracy of any particular gage still is not known. In the absence of any specific statement of gage accuracy, it is at least pointed out that the pretest estimate of gage accuracy was much better than that found in the field. An important aspect of instrumentation deficiencies in this test is that the readings on the control structure were the least reliable of any in the group. Readings on this structure were more vital in attaining the objectives of the test than those of any other single structure.

The plots of the individual gage records are given in Figs. 4.10 to 4.17. A general picture of the band of variation which existed between gages is used in obtaining each average which will serve as a means of estimating the accuracy with which net loads could be computed. That is to say, for surfaces such as the rear of Structure 3.1a, for which the individual gages differ by roughly from 0.6 to 1.5 psi, values of the net pressure obtained by subtracting loads on the back from those on the front are of this same order of magnitude, and, therefore, the pressure magnitudes are of questionable accuracy. However, since the differences in individual gage readings are of a random nature, it should not be expected that effects showing

consistent trends would be attributed to errors in instrumentation. In fact, it can be assumed that any effect studied (such as peak pressure and rise time) which shows a consistent trend among the various structures is not greatly affected by instrumentation errors. The band of pressures between the gages on a given surface is, in general, for most of the structures, much smaller than that given for Structure 3.1a. The band is, generally speaking, more similar to those shown for Structure 3.1c. Furthermore, it can be observed from these graphs that the worst deviations exist for gages located on the top surfaces and in the early phases of the loading cycle where differences are to be expected from the pressure phenomena. With regard to the validity of average pressures derived and used later in this report, the spread in the pressures read on Structure 3.1a, as shown by Figs. 4.10 to 4.14, is the result of including in this picture records which are the obvious result of gage calibration errors, e.g., gages a4 and a7.

TABLE 4.2 — Field Conditions\*

Scale Factors			Shot 9	Shot 10		
Ambient pressure at burst point	11.9 psi	12.8 psi				
Ambient pressure at ground	13.2 psi	13.2 psi				
Height of burst	2453 ft	524 ft				
Scaled height of burst	760 ft	201 ft				
Scale factor	0.314	0.384				
Side-on Pressures and Durations for 3.1 Program						
Structure	Peak side-on pressure		Distance from actual GZ		Positive phase duration	
	Shot 9 (psi)	Shot 10 (psi)	Shot 9 (ft)	Shot 10 (ft)	Shot 9 (sec)	Shot 10 (sec)
3.1a-q	5.7-6.4	3.1-3.4	4900-5300	4900	0.92	0.88
3.1s	16	37	1280	860	0.68	0.29
3.1t	11.5	8.8	2240	2200	0.76	0.60

\* Operation UPSHOT-KNOTHOLE, Preliminary Report, Summary Report of the Technical Director, Programs 1-9 (1953), WT-782.

It can be seen from Fig. 4.11, which shows the gage records on the front surface of Structure a, Shot 9, using an expanded time scale, that minor variations in pressure occur simultaneously and have proportional magnitude between the miscalibrated gages and the remainder of the group. It was attempted to correct these miscalibrated curves, using some fixed point of reference such as peak pressure or the ratio of pseudo-steady-state pressures from the later phases of the duration. The corrected curves compared favorably with the others throughout the positive phase but, nonetheless, were not used in the average.

#### 4.2.3 Comparison of SRI and BRL Check Gages

Check gages were placed approximately 6 in. apart at various gage locations throughout the 3.1 group of structures as a means of measuring the validity of the records. The exact locations of all these check gages is given in Figs. 2.13 to 2.44, where check gage numbers followed by the letter A are SRI gages. Typical examples of the pressures recorded by these check gages are given in Figs. 4.18 to 4.24 for both Shots 9 and 10, together with the side-on pressure curve. Figures 4.19, 4.20 and 4.22 to 4.24 use an expanded time scale which exhibits diffraction phenomena.

UNCLASSIFIED

~~SECRET RESTRICTED DATA~~



Since the confidence which one can place in any of the pressure records will be based largely upon the comparison of these check records, it is desirable to formulate a statement in terms of percentage error in addition to observing the general relation from the graphs. However, as can be seen from these figures for any given pair of check gages, the agreement of pressures varies with time. In some cases the pressure records have the same time history except for a slight phase difference. It is not possible to compute the percentage of error in a form which is both concise and meaningful. By computing the error at representative points and averaging these values, a rough estimate was obtained and is given in Table 4.2. The largest error, obtained for check gage a17, is obviously the result of a gage miscalibration.

#### 4.2.4 Wave Duration

The duration of the positive phase was, as given in the *Summary Report of the Technical Director*, WT-782,  $t = 0.92$  sec and  $t = 0.88$  sec for Shots 9 and 10, at the 4900-ft station, respectively, as listed in Table 4.3. Considerable deviation from these accepted values was

TABLE 4.3—Comparison of SRI and BRL Check Gages

Difference in reading of check gages*	Occurrence (%)
Less than 5%	25
5–10%	50
Greater than 10%	25
Extreme case gives an error of 30–50%.	

\*Difference in Gage Reading computed as a percentage of the lower gage readings.

found to exist for the individual gage records. Some of these are given in Table 4.4. The values given in this table appear to indicate that the duration,  $t_0$ , was not known accurately. This is because the pressure-time curves are nearly horizontal at the end of the duration and small errors in pressure readings lead to considerable errors in duration. In most cases an error of about 0.2 psi, which is only a small percentage of initial side-on pressure, would result in an error of  $\pm 0.1$  sec in the duration, which is a considerable portion of the accepted value.

#### 4.2.5 Average Pressures on Surfaces

As pointed out in Sec. 4.2.1, average pressure-time curves were obtained for those surfaces having more than one gage. The method of obtaining the average pressure on a face of a structure consisted essentially of applying a weighting factor to each of the individual gage records and adding them, starting each at the common zero time. Each gage record was first scrutinized to determine its validity by judging if it had a reasonable shape and peak value for the particular face on which it recorded. Second, as stated above, the pseudo-steady-period pressures were checked by comparing it with the side-on pressure envelope for the arc on which the structures were placed.

The weighting factors were determined by first laying out the face with the valid gages in position. Next, straight lines were drawn from each gage location to each of its nearest neighbors and perpendicular bisectors were erected on these lines. These bisectors then formed the boundaries of the areas for which each gage was assumed to be effective. Physically, each point on a structure face has one gage to which it is in closest proximity. This point is then considered to be in the effective area of that gage. These individual areas divided by the total area of the face were the weighting factors applied to their respective gages.

TABLE 4.4—Duration of Positive Phase for Individual Gages on Structures (Shot 9 Only)

Structure	Gage	Duration, $t_0$ (sec)	Structure	Gage	Duration, $t_0$ (sec)	Structure	Gage	Duration, $t_0$ (sec)	Structure	Gage	Duration, $t_0$ (sec)
3.1a	1	0.88	3.1b	11	0.86	3.1g	18		3.1m	1	1.06
3.1a	2	1.2	3.1b	12	0.98	3.1g	19	0.97	3.1m	2	0.94
3.1a	3	1.14	3.1b	13	0.98	3.1h	3	0.612	3.1m	3	0.99
3.1a	4	0.78	3.1b	14	0.78	3.1h	4	0.88	3.1m	4	1.07
3.1a	6	0.85	3.1b	15		3.1h	5	1.00	3.1m	5	0.99
3.1a	7	0.92	3.1b	16	0.92	3.1h	6	1.05	3.1m	6	1.04
3.1a	8	0.92	3.1e	1	0.99	3.1h	7a	.96	3.1n	1	1.4
3.1a	10	0.90	3.1e	2	1.06	3.1h	7b		3.1n	2	0.89
3.1a	11	1.02	3.1e	3	0.96	3.1h	8a		3.1o	2	0.96
3.1a	12	1.1	3.1e	4	0.89	3.1h	9		3.1o	3	0.92
3.1a	13	0.98	3.1e	5	0.91	3.1h	10		3.1o	4	0.94
3.1a	14	0.90	3.1e	6	1.00	3.1h	11		3.1o	5	1.01
3.1a	15	0.95	3.1g	1	0.96	3.1h	12	0.0855	3.1o	6	0.86
3.1a	16	0.98	3.1g	2	0.85	3.1h	13a		3.1o	7	1.01
3.1a	17	0.97	3.1g	3	1.05	3.1h	13c	0.86	3.1p	1	0.94
3.1a	18	0.72	3.1g	4	1.05	3.1h	14a	0.89	3.1p	2	0.95
3.1a	19	0.94	3.1g	6	0.94	3.1h	14b	0.91	3.1p	3	
3.1a	20	0.85	3.1g	7		3.1h	15	0.84	3.1p	4	
3.1a	21	1.05	3.1g	8		3.1h	16a		3.1p	6	1.06
3.1a	22	1.05	3.1g	9		3.1h	16b		3.1p	7	0.682
3.1a	24	0.96	3.1g	10		3.1h	17		3.1q	1	1.00
3.1a	26	0.91	3.1g	11	1.70	3.1h	18	0.91	3.1q	2	1.00
3.1a	26	0.95	3.1g	12	1.01	3.1h	19	0.95	3.1q	3	1.00
3.1a	28	0.96	3.1g	13a	1.01	3.1i	1	0.94	3.1q	4	1.08
3.1b	1	1.02	3.1g	13b	1.01	3.1i	2	0.88	3.1q	5	1.07
3.1b	2	1.04	3.1g	13c	0.95	3.1i	3	1.20	3.1q	6	1.16
3.1b	3	1.03	3.1g	14a	0.90	3.1i	4	1.02	3.1q	7	1.11
3.1b	4	1.02	3.1g	14b	1.03	3.1i	5	0.97	3.1q	8	1.04
3.1b	5	0.80	3.1g	15	1.01	3.1i	1	0.98	3.1q	10	1.01
3.1b	6		3.1g	16a	0.86	3.1i	2	1.02	3.1q	11	1.07
3.1b	7		3.1g	16b		3.1i	3	0.98	3.1q	12	1.00
3.1b	8		3.1g	17	0.57	3.1i	4	1.54	3.1q		
3.1b	10	0.98	3.1g	18		3.1i	5	0.83	3.1q		

Average pressure curves corresponding to the individual gage records of Figs. 4.10 to 4.17 are given in Figs. 4.25 to 4.28. Average pressures are given for those structures whose individual gages are not presented here in Figs. 4.29 to 4.48. It can be seen from Figs. 4.25 to 4.28 that the deviation in average pressure on similar surfaces of different structures is of a smaller magnitude than that shown in Figs. 4.10 to 4.17, which gives the individual gage readings for a given surface. Thus differences in average pressure on corresponding surfaces of different structures cannot very well be attributed to the variations of their geometric parameters since each of these average pressure curves is derived from individual gage readings, which vary widely. On the other hand, had the individual gage readings on the same surface agreed closely with one another, the average pressure curve would be considered accurate, and differences between average pressure curves could be associated with variations in the geometric parameters of the structures. These average pressures are studied in more detail in the subsequent sections of this chapter. In summary, it is exceedingly doubtful that correlation of surface pressures can be established as a function of variations in height, width, length, etc., during the drag period of loading.

The relation between the average pressures on the front and rear surfaces and the side-on pressure are shown in Figs. 4.29 to 4.44. In terms of the schematic loadings given in Chap.

3, some surprising trends are seen to occur. According to the schematic loadings, average pressures on the front surfaces should, in the pseudo-steady state, approach the value given by side-on pressure with the difference between the two curves decaying exponentially. Contrary to this prediction, the pressure on the front surface usually coincides with, and in some cases falls below, the side-on pressure immediately following relief of reflected pressures. After this time, the pressure on the front usually rises above side-on pressure by an increasing amount during the pseudo-steady state.

In relation to side-on pressure, the pressures on the rear behave similar to those for the front surfaces, i.e., after the initial build-up to a value of slightly less than side-on, they either rise above side-on or run parallel to it. This trend is even more surprising than that found on the front surfaces since pressures on the back should usually be below side-on. The pressures on the front are at least in the right direction above side-on but by a surprising amount.

The reason for this cannot be determined and may result from errors in the reading of gages located on the structures. If, on the other hand, the gage readings are reasonably correct, this subject is certainly worthy of extensive study in future tests since the results obtained herein are extremely different from those obtained from all other tests to date. The above-mentioned deviations from previous theories may be due to a shift in the base line. It is also possible that there is some undetermined characteristic of the gages causing the higher pressures in the later phases of the loading cycle. It is noteworthy, however, that some minor variations in pressure can be observed occurring at corresponding times between Shots 9 and 10. The front surface of Structure 3.1a shows the pressure curve bulging above side-on in the time interval between 10 and 20 msec on both Shots 9 and 10. As another example, a minor increase in pressure on both the front and rear surfaces of Structure 3.1a is observed on Shot 9 at the time  $t = 0.36$  sec. This could be due to the variation in side-on pressure due to height.

In summary of the loadings of front and rear surfaces given here, it can be stated that they would be best related to a slightly different wave shape from that obtained by the free stream pressure gages on both Shots 9 and 10. A wave shape having higher pressures after the time  $t = 0.4$  sec would be more closely related to these pressures on the structures. An additional explanation of the high values of surface pressure is discussed in Chap. 5 in connection with the net loadings obtained from them.

#### 4.2.6 Net Pressure Curves

The net horizontal pressure per unit area is obtained by subtracting the average pressure on the rear surface from that on the front. Net loadings on the 3.1 structures are shown in Figs. 4.29 to 4.48, together with the loadings on the front and rear surfaces just discussed. These net pressure curves are considerably higher than was predicted. They are not discussed in detail in this chapter but, instead, are treated rather exhaustively in Chap. 5, dealing with the subject of increased net loadings and drag trends. However, it is pointed out here that the credibility of these high net loads is affected by the possibility of errors in the average pressure curve discussed above. Errors in choosing the zero time for either front or back gages, which is equivalent to translating the front loading curve to the right or the back loading curve to the left, were considered as an additional possible cause for the high values of pressure in the computed net curves. This appears to be a plausible argument, at least from a qualitative point of view. However, a quantitative investigation indicates that errors in determining zero time, even if assumed to be as large as 5 msec, could only cause the net pressures to vary by a maximum of 10 per cent for most of the structures. If one were to assume an across the board reduction of 10 per cent in all experimentally determined net pressures, the resulting net loads would still be greater than the predicted nets by the same order of magnitude as before such a reduction. Thus the increase in net loads observed here can not reasonably be attributed to errors in the determination of the zero time.

In addition to those structures for which front and rear loadings were available for computation of the net pressures, the pairs of thin walls designed to determine the effects of



shielding and multiple reflections were treated by assuming that their ungaged surfaces experienced pressure variations identical to those on corresponding surfaces of Structure 3.1d, the isolated thin wall.

Net loadings for thin walls were thus computed and are shown in Figs. 4.49 to 4.57. In these figures two time scales are used, one reaching the time  $t = 0.7$  sec and the other the time  $t = 0.18$  sec. This has been done throughout this chapter in order to study the diffraction and pseudo-steady-state phase separately. In Sec. 4.4 the effects of shielding distance on the net loads on these walls will be discussed.

#### 4.2.7 Average Pressures on Strips of Surfaces

As mentioned earlier in Sec. 4.2.2, in addition to averaging the pressures of the individual gages over an entire surface, curves were constructed giving the average pressures of individual gages which were laid out in the form of strips running parallel to and transverse to the shock direction. These averages were obtained with less accuracy than those for entire surfaces in that they did not weigh the tributary areas for the individual gages. An additional weakness is that since the gage layout was not specifically designed for this type of averaging the pressures really represent smaller sections of the surface than the strip would indicate. Nonetheless, by taking strips running in the two perpendicular directions, it was hoped that the differences in pressure along edges from those in the center of the surface or near to the ground might be detected.

In Figs. 4.58 to 4.66 linearized pressure-time curves along the various strips are shown, together with the side-on pressure curve for Shots 9 and 10. Although these figures do not afford a great accuracy, they simplify the comparison. The pressures are given until the time  $t = 0.7$  sec and therefore do not show loading details during the diffraction phase due to compressed time scale. Although most of the strips have a width roughly equal to  $\frac{1}{3}$  of the width or height of the structure, in many cases only two curves are available for comparison. This is unavoidable since, as can be seen in Figs. 2.13 to 2.44, most of the surfaces have all their gages on one side. If gages were available on each side, the added influence of a slight misorientation of the blast wave (9 deg on Shot 9) might be considered.

These curves for the pressures along strips will be referred to subsequently in Sec. 4.4. They were of use in preparing Figs. 4.101 to 4.113 in connection with the relation between such variables as the clearing time, the build-up time, the vortex activity, and the positions of the strips for which they are computed.

#### 4.2.8 Graphical Comparisons Between Pretest Predictions and Experimental Average Pressures

One of the most useful means of interpreting the experimental results is by direct comparison to the already established pretest predictions of Chap. 3. This technique is of most value during the early stages of loading, when the pressures vary most rapidly and are closely related to various parameters of the blast and the structure such as the time values of the build-up and the clearing periods and the peak reflected pressure. In Figs. 4.67 to 4.100, the comparisons are made until the time  $t = 0.16$  sec for the various surfaces of the 3.1 structures. These figures will be discussed in detail whenever necessary later in this chapter. They may be useful in the future, in connection with other data for possible revision of the pretest predictions, wherever discrepancies exist between schematic loadings and the experimental results.

### 4.3 CRITERIA FOR USE IN THE POST-TEST ANALYSIS

This short discussion of the basic tools used in performing the post-test analysis is intended to give an over-all view of the form of these analyses.

The primary means of reducing data is in terms of the pressure-time curves by comparing experimental values of peak pressures, variations of the pseudo-steady-state curves, and

the clearing and build-up times as well as time phase delays. Frequently, experimental curves, whose pressure values at some given time differ widely from the pretest predictions, are considered to be in good agreement by making linearizations which preserve the areas under the pressure-time curves. In addition, the loading can be interpreted entirely in terms of impulses which are subdivided logically into that for the diffraction and the drag phases.

#### 4.4 DIFFRACTION AND DRAG PHENOMENA

The original objectives of the 3.1 test are primarily concerned with the diffraction phase of the loading. The peak pressures on upstream surfaces and their relief times, along with the build-up of pressure on rear surfaces and their build-up times, are worthy of special discussion before dealing with the individual objectives of the whole test program. In this section the nature of the loading on the front and rear surfaces is discussed separately. Attempts to relate the clearing time,  $t_c$ , and the build-up time,  $t_b$ , with ratios of structural parameters are dealt with. In addition, the effect of vortices on various portions of surfaces are discussed in detail.

##### 4.4.1 Relief of Reflected Pressures on Upstream Surfaces

The subject of reflected pressures is discussed in Chap. 3. Schematic loadings given there show an instantaneous rise to reflected pressure at the time  $t = 0$ , followed by a linear decrease in pressure, to pseudo-steady-state values. This decrease in pressure is referred to as the "relief," and the time interval during which it takes place is called the "relief time." Although the schematic loading indicates that pressure variation is clearly defined between critical points on a curve, these schematic loadings are actually idealizations of slightly more irregular phenomena. The field records show that neither the beginning nor the end of the relief time is sharply defined.

The peak pressure reached by a gage is almost always somewhat less than the predicted value of reflected pressure  $p_r$ . How much lower it may be depends on how far relief of pressures has progressed before the gage has fully responded to the sudden increase in pressure. It is believed that recorded pressure reaches its peak value at a point which lies on, or very nearly on, the relief line of the pretest prediction.

The field records usually show that the end of the relief period is characterized by the gradual rounding off of pressures from the steep relief lines to the pseudo-steady-state curve. This leaves the time at which relief is completed somewhat open to arbitrary choice, which can result in differences of about 25 per cent between two possible values. In measuring diffraction impulses, the analyst must exercise careful judgement in choosing the time at which the diffraction period is considered to be ended. Every attempt was made to follow consistent rules even though in some cases they lead to unexpected results.

##### 4.4.2 Build-up of Pressure on Rear Surfaces

In order to determine  $n$ , the number of  $S/U$  time units for the build-up of pressure on the rear surface of the structure, it is necessary to find both the time at which the build-up began and also the time at which the build-up is completed. Difficulty is encountered in choosing both these time values from experimental curves. The more familiar the analyst is with the phenomena, the better are his chances of picking these time values properly. Therefore the following discussion is included before the analysis of specific structures is begun.

The beginning of the build-up was determined by working with individual gage records, as well as the average on the surface. The time at which the average pressure begins to build up from a zero value should be (see Chap. 3) equal to  $L/U$ . The average pressure on the rear surface utilizes the results of several gages, which, because they are at different distances from the edges of the rear wall, have different absolute times for which the pressure begins to increase from zero. The absolute time scale for a structure was established by computing



the time elapsed between the time when the shock struck the front face of the structure and a particular gage in question and by calling zero time the time when the first rise is seen on a gage minus the computed time lapse for this gage.

If one observes the average pressure curves on the rear surface of structures, it is seen that the curve is rounded off near the end of the build-up period. The value chosen for the time at which the build-up is completed depends upon the judgement of the analyst. The following discussion is intended to give the reader some understanding of the nature of this build-up.

One might expect that the build-up time for the average pressure on the rear surface would be much larger than for any of the individual gages. The average pressure builds up as the shock front sweeps across the surface encountering the various gages. Upon examining the data, one sees that the build-up time for most of the individual gages is almost as large as that for the average pressure on the surface, e.g., the build-up times for the average pressure on the rear surface of buildings on Shots 9 and 10 range from 7 to 17 msec, whereas for most of the individual gages the build-up time is roughly from 5 to 12 msec.

Examination of the loadings on rear surfaces indicates that the initial build-up consisted of two distinct phases. By correlating the shape of the build-up curve for individual gages with the position of these gages relative to the free edges and the reflecting surface at the ground, the reason for the two phase build-up of certain individual gages becomes evident.

Consider a gage (such as d2)<sup>†</sup> which is near the upper edge of the rear face and well removed from both the side edges and the ground line below. Its first phase results from the wave coming down from the roof and the second from the wave, reflected from the ground, coming back up the wall. The time lapse between the two increases as pressure becomes less and as the position of the gage is brought nearer to the ground. For gages not close to any side edge but near the ground (such as gages a16, 17, d5, and i6, all of which are 1½ ft or less from the ground), the initial build-up time is very short since the two phases almost merge into one. For gages near the ground but also near a side edge (such as gages a15, a4, and i5), the two stage effect of the initial build-up is obscured by the wave coming from the sides. Gage 15 on Structure 3.1b is near the ground but is 18 ft from the nearest side edge; the effects of the wave coming from around the side are not felt until long after the first two phases mentioned above have been completed, making it possible to observe that they nearly coincide for this gage.

Gage b10, which is located at the center of a wall 36 ft wide and 6 ft high, demonstrates the absence of three-dimensional effects near an upper edge of a rear surface which is free from the influences of a wave coming around the side. Three-dimensional effects are most noticeable for gages in a corner formed by the intersection of two free edges, e.g., gages d1 and i2. For these gages the initial pressure build-up is very quick (about 2 msec to the full value). For gage i2, the pressure builds up in two phases. The first phase, which takes 2 msec, is, in a sense, the true initial build-up time for this gage because the pressure increases only slightly during the next 10 msec.

#### 4.4.3 Dimensionless Relief and Build-up Time as a Function of the Various Geometric Parameters

The shock parameters which determine the diffraction loadings are critical pressure values and critical time values.

The critical pressure values, reflected pressure  $p_r$ , and pseudo-steady-state pressures,  $f_{os}(t)$  and  $b_{os}(t)$ , are well known near the time  $t = 0$ .

The critical time values, namely,  $t_c$ , the relief time on front, and  $t_b$ , the build-up time on the back, cannot be calculated by analytical means, and their pretest value has been deduced from two-dimensional shock tube tests which already included the effect of length. So far only a single large-scale field test (GREENHOUSE Structures 3.1.1 and 3.3.8a) existed from which modifications for the effect of width were drawn.

<sup>†</sup>For brevity, in this chapter a gage such as P2 on Structure 3.1d is designated as d2.



Therefore the following brief summary of how  $t_c$  and  $t_b$  vary with the various geometric parameters on UPSHOT-KNOTHOLE Shots 9 and 10 is instructive, even if no definite conclusions can be drawn as yet, as to whether the pretest loading schemes should be retained or modified as a result of this test.

Figures 4.101 to 4.107 present the dimensionless relief and build-up time,  $Ut_c/S$  and  $Ut_b/S$  ( $U$  = shock front velocity and  $S$  is the characteristic relief or build-up distance, normally the height or half width, whichever is smaller), as a function of the geometric parameters, namely, width, length, size, ground proximity, orientation, and shielding distance. The effect sought and the choice of independent variables are tabulated in Table 4.5.

TABLE 4.5—Data for Figs. 4.101 to 4.107

Fig. No.	Effect	Varying parameter or ratio	Constant parameters	Structure No.
4.101	Width	$W/H$	$L, H$	3.1a-c
4.102	Length	$L/H$	$W, H$	3.1a, d, i
4.103	Scale	$H/H_a$	$W, H, L$	3.1a, e, f
4.104	Ground Proximity	$\Delta H/H$	$W, H, L$	3.1o, p
4.105	Orientation	$\theta$	$W, H, L$	3.1a, g, h
4.106-4.107	Shielding	$\Delta/H$	$W, H, L$	3.1d, l, m, n

- \*  $W$  = Width.
- $H$  = Height.
- $H_a$  = Length of Structure 3.1a.
- $\Delta H$  = Elevation above ground.
- $\theta$  = Angle of Orientation.
- $\Delta$  = Separation between walls.

The relief time for the entire front surface was obtained by averaging individual gages such as shown in Figs. 4.108 and 4.109.

Summarizing, in most cases the relief time on front is somewhat lower than the value of three-dimensionless time units that was predicted, and the build-up time on back of a three-dimensional thin wall is closer to two-dimensionless time units, rather than four as was anticipated. The potential effect of this change in time units, i.e.,  $t_b U/S$ , on the diffraction impulse can be seen in Fig. 5.3. The effect of the change in  $t_c U/S$  is roughly one-half of that for  $t_b U/S$ .

#### 4.4.4 Effect of Vortex Activity

The effect of vortex activity is elusive and quite difficult to define since lowering of pressure might be due to expansion phenomena and general lower pseudo-steady-state values in addition to the turbulent (vortex) effects. In previous weapon effects work, the most outstanding vortex effects were observed on roofs of two-dimensional models which were placed in the shock tube and were observed by means of interferometry. These tests demonstrated that the larger the ratio of height to length the more pronounced was the vortex activity in terms of average roof pressures. How this activity depended on the width of an actual (rather than a two-dimensional) structure was observed in only one large-scale field test (Structures 3.1.1 and 3.3.8a of GREENHOUSE, *Blast Loading and Response of Structures*, WT-87, where it was shown that the more two-dimensional a structure is the more severe is the lowering of roof pressures near the loading edge. This present test demonstrated, as did the GREENHOUSE test, that for three-dimensional structures, such as the 3.1 models of 9 and 10, the vortex activity can be neglected in pretest roof loading schemes.

The experimental results of Shots 9 and 10 verified this assumption, i.e., if vortex activity,  $V$ , is defined by the following ratio (see Fig. 4.110)

$$V = \frac{\int_0^{t_0} [r(t) - r_{os}(t)] dt}{\int_0^{t_0} r_{os}(t) dt} \quad (4.1)$$

then  $V$  is indeed at most equal to a few per cent of the total roof loading. However, in order to study the phenomena locally more in detail, one can observe the roof vortex on three structures of different width along longitudinal (parallel to flow direction) and transverse strips and thus determine the dependence of vortex strength on the nearness of front, side, and back edges. For quantitative measurements, it is also convenient to redefine the vortex activity

$$V' = \frac{\int_{t_i}^{t_f} [r(t) - r_{os}(t)] dt}{\int_{t_i}^{t_f} r_{os}(t) dt} \quad (4.2)$$

where  $t_i$  is the initial time of the vortex activity when the roof pressure starts dropping after the initial build-up to pseudo-steady-state pressure and  $t_f$  is the time at which the roof pressure reaches its pseudo-steady-state value again. (In terms of entire roof surfaces or along longitudinal strips,  $t_i$  is defined as  $L/U$  and  $t_f$  would equal  $t^*$ , the end of the diffraction period. For transverse strips,  $t_i$  would be equal to  $y/U$ , where  $y$  is the distance from the front edge to the particular strip under study, and  $t_f$  would again roughly equal  $t^*$ .)

TABLE 4.6—Gages Which Were Not Used to Evaluate Vortex Activity

Structure	Gage No.	
	Shot 9	Shot 10
3.1a	21, 23, 25	23, 27
3.1b	4, 5, 9	5, 9
3.1c		2, 1

With this frame of reference in mind, Figs. 4.110 to 4.113 present a study of vortex strengths as a function of the proximity to the free edges with total structure width as parameters.

Figures 4.110 and 4.111 exhibit vortex strength along three longitudinal strips up to the midpoint, and Figs. 4.112 and 4.113 present a study of vortex strength in three transverse strips spaced between the front and back edge of Structures 3.1a, b, and c. The resulting values of  $V'$  are connected by curves for an estimate of the continuing function.

As can be seen from Figs. 4.110 and 4.111, vortices seem to be just as severe at  $x/W \approx 0.2$  as at 0.5 (the center longitudinal strip) although the widest structure (3.1b) still maximizes the vortex activity as anticipated.

From Figs. 4.112 and 4.113 one confirms that in transverse strips vortices are most severe near the leading edge ( $Y/L \approx 0.2$ ) although there does not seem to be any marked dependence on total building width.

Quantitatively, the vortices in the above adopted reference frame constitute up to 30 per cent of the roof loading up to the time the pseudo-steady-state value is reached. In terms of roof loading until the end of the positive phase, they are not significant enough to warrant a change in average roof loadings to include their effect.



#### 4.4.5 Drag Phase Loads and Net Loading

It can be recalled from the discussion in Chap. 3, which dealt with loads of the drag phase, that the values of the drag coefficient,  $C_d$ , were expected to be constant. In Sec. 3.4.3 the drag coefficients are defined for several surfaces. These drag coefficients are used in the schematic loadings given at the end of Chap. 3. Based upon these pretest predictions, one would expect the loading on front, top, and rear surfaces to be of a form which is equal to side-on pressure plus some constant times drag pressure, i.e.,

$$f_{os}(t) = p_o(t) + C_{df} p_d(t) \quad (4.3)$$

for the front surface, and similarly for the top and rear surfaces,  $r_{os}(t)$  and  $b_{os}(t)$ , respectively.

It is convenient to rearrange the terms of the equations and solve for the drag coefficients as follows: [using  $C_{df}(t)$  in place of  $C_{df}$  and using  $F(t)$ , the measured average loading, in place of  $f_{os}(t)$ , the predicted values]

$$C_{df}(t) = \frac{F(t) - p_o(t)}{p_d(t)} \quad (4.4)$$

It is in this form that drag coefficients are determined experimentally from the test data. Although the drag coefficient is shown as a time dependent quantity in the above equation, the value should not vary during the loading if it is to be in agreement with the predictions of Chap. 3. Minor local variations of the drag coefficients, say plus or minus 20 to 30 per cent, can be ignored if a good average line can be drawn such that the average remains constant. It was expected that if one solved for the drag coefficient,  $C_d$ , using the experimental values of  $F(t)$  and  $p_o(t)$  —  $F(t)$  denotes the average pressure on a front surface and  $p_o(t)$  the average of free stream gages — and the computed value of drag pressure as given by the Eq. 3.3, constants in agreement with those given in Chap. 3 would be obtained.

Graphically speaking, this means that the difference in ordinates, between the curves  $f_{os}(t)$  and  $p_o(t)$ ,  $b_{os}(t)$  and  $p_o(t)$ ,  $r_{os}(t)$  and  $p_o(t)$ , if plotted as a function of time, should have the same shape as the curves given in Figs. 4.8 and 4.9. As stated in Sec. 4.2, inspection of Figs. 4.29 through 4.44 shows that this is not the case for front and rear surfaces. Although this condition is approached for top surfaces, there is still a considerable deviation from the pretest predictions.

The experimentally determined values of the drag coefficients are nothing like those given by the pretest predictions. It is surprising that instead of remaining constant, at values less than or equal to one, they increase to values of ten or greater, when computed from Eq. 4.4, using  $p_o(t)$  and  $p_d(t)$  from Figs. 4.4, 4.8, and 4.9.

The physical meaning of these increased drag coefficients is not thoroughly understood. The explanation may be that the drag coefficients are neither constant (with respect to time) nor of the magnitude indicated in Chap. 3. It is doubtful, however, that they actually should reach values as high as ten. The explanation may also lie in the values assigned from the drag pressure-time curve,  $p_d(t)$ , Eq. 4.4. The subject of "increased drag trends" is discussed in detail in Chap. 5.

Experimentally determined curves showing the drag coefficients computed as a function of time,  $C_d(t)$ , are given for the front and rear surfaces in Chap. 5. The drag coefficient curves in Chap. 5 offer a good comparison, in that three different forms for expressing the denominator of Eq. 4.4 were used in computing them. The three forms are: (1)  $p_d(t)$ , as defined by Eq. 3.3, and shown graphically in Figs. 4.8 and 4.9; (2) the adjusted form for the Sandia q-gage records discussed in Sec. 4.1.4 and also shown in Figs. 4.8 and 4.9; and (3)  $p_d(t)$ , the dynamic pressure, as discussed in Chap. 5 and shown in Fig. 5.7 to decay at the same rate as side-on pressure. Similar curves for the top surfaces are given in this chapter in Figs. 4.114 to 4.116. Chapter 5 offers a possible explanation for these increased drag loads.



TABLE 4.7—Values of "n" for Build-up Time Units

Structure	Build-up distance, (S) (ft)	Shot No.	Measured build-up		
			Time, (nS/U), (sec)	"n" Measured (nS/U) + (S/u)	"n" Predicted (See Fig. 3.3)
3.1a	6	Shot 9	0.010	2.17	2
3.1a	6	Shot 10	0.011	2.24	2
3.1b	6	Shot 9	0.013	2.82	5
3.1b	6	Shot 10	0.017	3.47	5
3.1c	3	Shot 9	0.008	3.47	3.5
3.1c	3	Shot 10	0.007	2.85	3.5
3.1d	6	Shot 9	0.009	1.95	4
3.1d	6	Shot 10	0.012	2.45	4
3.1e	18	Shot 9	0.034	2.45	2
3.1e	18	Shot 10	0.031	2.11	2
3.1f	12	Shot 9	0.031	3.35	2
3.1f	12	Shot 10	0.022	2.24	2
3.1g	6	Shot 9	0.005	1.08	2
3.1g	6	Shot 10	0.014	2.86	2
3.1h	6	Shot 9			2
3.1h	6	Shot 10	0.017	3.47	2
3.1i	6	Shot 9	0.008	1.73	2
3.1i	6	Shot 10	0.010	2.04	2
3.1o	5.34	Shot 9	0.015	3.65	2
3.1o	5.34	Shot 10	0.009	2.06	2
3.1s	6	Shot 9	0.012	2.60	2
3.1s	6	Shot 10			2
3.1t	6	Shot 9	0.006	1.30	2
3.1t	6	Shot 10			2

These results are unexpected in that either the assumptions for the variation of drag pressures with respect to time,  $p_d(t)$ , or the magnitude and form of the drag coefficient, or both, do not check with pretest conditions. The significance of these unexpected results are, with regard to this chapter, twofold. First, from a purely empirical point of view, they change the shape of the net loading curve to a linearly decreasing quantity, instead of the rapidly decreasing exponential decay presented in Chap. 3. Secondly, from an analytic point of view, they thwart any attempt to check the experimental results against the pretest predictions during the pseudo-steady-state phase in a routine manner.

#### 4.5 EFFECTS OF WIDTH

The main effects of width were expected to be shown in the build-up time on the rear wall and the intensity of the vortex on the top surface. No effects were expected to be shown on the front or side surfaces. Structure 3.1b had no gages on either the front or side surfaces; Structure 3.1c had no gages on the side surfaces; and Structure 3.1a had one gage on each side surface. Figures 4.67 to 4.70, 4.77 to 4.82, and 4.87 to 4.92 present a graphical comparison of the pretest prediction to the experimental pressure-time curves. Figures 4.101, 4.110, and 4.111 show the effect of width variations on clearing time, build-up time and vortex intensity.

#### 4.5.1 Rear Surfaces

The effects of width, on the 3.1 cubicles, are determined from the experimental loading on the rear surface. From these experimental results measured values of "n" are obtained for comparison with the pretest predictions. The loading on the rear surfaces of Structures 3.1a to c throughout most of the positive phase is given in simplified form for Shots 9 and 10 in Figs. 4.117 and 4.118. The results of these two figures, with respect to the loading during this later phase, are inconclusive.

It can be seen from Figs. 2.13 and 2.16 that the gages on the rear surfaces of Structures 3.1a and c are located so as to give an average pressure which is representative of the entire surface, whereas the gages on the rear surface on Structure 3.1b will tend to overemphasize the measurements of pressures near the sides of the structure and underemphasize those near the center.

The number of S/U time units denoted by "n," required for the pressure to build up on the rear surfaces of Structures 3.1a to c, are listed in Table 4.7. This table shows the values computed using the pretest method of prediction and those values determined experimentally on Shots 9 and 10. (For Structures 3.1a to c the predicted values of "n" are equal to 2, 5, and 3.5, respectively.) The experimental values are roughly 2.2 for Structure 3.1a and 3.25 for Structures 3.1b and c. The computed values of "n" for Structures 3.1b and c are considerably higher. For Structure 3.1c on Shot 9, the value of "n" = 3.47 compares very well with the predicted value of 3.5. Although these values of "n" cannot be determined with extreme accuracy, they at least indicate the proper trend. Both Structures 3.1b and c have a slower build-up on the rear than does Structure 3.1a, as was predicted.

A better understanding of how the values of "n," given in Table 4.7, are related to the actual pressure-time curves during the diffraction phase can be obtained from Figs. 4.119 and 4.120. In these figures the average pressure on the rear surfaces of each of the three structures for both Shots 9 and 10 is plotted as function of time in H/U units. It must be remembered that for Structure 3.1c,  $S = \frac{1}{2} H$ , and, therefore, the time  $H/U = 1$  corresponds to 2 S/U units for Structure 3.1c. It is also easy to see from this figure that the value of "n," determined experimentally, could easily be changed by assuming a slightly different value of pressure for the fully built-up value. The average pressure vs time curves for each of these structures on both Shots 9 and 10, up until the time,  $t = 0.16$  sec, is given in Figs. 4.87 thru 4.92.

#### 4.5.2 Top Surfaces

In order to study the variations of loading on the top of cubicles in relation to variation of the width, gages were placed on the roof of Structures 3.1a to c, as shown in Figs. 2.13, 2.15, and 2.16. The distribution of gages on the roof of these three structures was about the same as for their rear surfaces, with regard to the ability of the pattern of gages to measure the average pressure.

Simplified average pressure-time curves on the top surfaces of Structures 3.1a to c, for Shots 9 and 10, are given in Figs. 4.117 and 4.118, respectively. These figures exhibit a greater vortex effect as width increases. This vortex effect, known previously to exist for purely two-dimensional structures, was not considered in the pretest schematic loading for the three-dimensional structure. The earlier phase of the loading, shown in Figs. 4.77 through 4.82, together with the computed curve for the pretest prediction is presented as the comparison of the loading on the top surface of a two-dimensional structure to those of three-dimensional structures. These are the average pressures before simplification and give more detail up until the time  $t = 0.16$  sec.

Any attempt to revise the schematic load prediction for these top surfaces, which would be based upon the observation of the simplified average pressure-time curves of Figs. 4.117 and 4.118 and Figs. 4.77 to 4.82, would also probably incorporate a quantitative relation between the ratio of width to height and the minimum pressures resulting from the vortex. It must be remembered that the gage patterns on these three surfaces are not equivalent. From the figures that show individual gage records on the top surfaces, it can be seen that the vor-

tex is most intense immediately behind the front edge. The effect of the vortex is almost negligible at the rear edge, having decreased gradually from front to back. The roof of Structure 3.1a has gages near the front, center, and back portions of the roof, whereas Structure 3.1b has gages near the front and in the center, and Structure 3.1c has gages near the front and back only. Thus, the average for the top of Structure 3.1b does not include any measurements near the back edge and overemphasizes the sharp vortex in the upstream portion of the roof. The top of Structure 3.1c has gages near the front and rear, ignoring the area midway, and perhaps gives a relatively good average effect. It is not certain how much of the increased vortex effect on Structure 3.1b is due to its greater width and how much is due to the location of the gages. This uncertainty prohibits any immediate revision of the schematic loadings on the top surfaces.

The determination of the loading on strips of surfaces referred to in Secs. 4.3 and 4.4.4 was motivated partly by the desire to gain new information regarding the distribution of loads for use in damage analysis and partly by the need for some reliable rules which would enable one to extrapolate the loadings on one portion of a surface from those measured on another. If this attempt had been more fruitful, perhaps the revisions discussed above could have been made. However, as it turned out, this strip analysis is just a convenient means for expressing the results of this test quantitatively and should not be considered an attempt to develop general loading relationships.

#### 4.5.3 Princeton Shock Tube Comparisons

Since there is considerable shock tube information on the Structure 3.1b type of model ( $L:H = 1:1$ ) from the Princeton II-11 report, it is instructive to make comparisons with those results.

Plots of the individual pressure records, as taken from gages 1, 2, 10, and 15 on Structure 3.1b, were compared to Princeton shock tube results. The pressures on the roof of Structure 3.1b, midway between the sides, match those of the Princeton shock tube two-dimensional model prior to and during the action of the vortex which decreases pressure sharply. After the diffraction phase, there is little consistency between the two. Normalized pressures on the center of the back wall of Structure 3.1b are slightly lower than those for the Princeton shock tube model in this comparison.

#### 4.5.4 Conclusions on Width Effects

The objective of width effects studies was to determine the type of loading on the top and rear surfaces of three-dimensional models as compared to that on two-dimensional models. This objective was satisfactorily fulfilled.

##### 4.5.4.1 Rear Surfaces

Revised values of "n" are given to account for quicker build-up time as related to width. (See Figs. 3.3 and 4.125.)

##### 4.5.4.2 Top Surfaces

Vortex intensity increases with width. Quantitative revisions are recommended for future.

##### 4.5.4.3 Shock Tube Comparison

For  $H:W:L = 1:6:1$ . Diffraction loading at center of top and rear surface for the field test model is the same as those of the Princeton shock tube model ( $L:H = 1:1$ ).

#### 4.6 EFFECTS OF LENGTH

The effects of length on loadings studied here consist in checking the pretest schematic loads with the experimental pressure-time records for the rear and top surfaces. In addition,



a comparison of two structures having identical height to width to length ratios is made. No effects of length upon the loading of the front and side surfaces of these cubicles were expected. Structure 3.1i had no gages on the front surface. Structures 3.1a and d had gages on the front surfaces, but these gages were not intended for the purpose of measuring the effects of length (3.1a was the control structure for the entire test group, and 3.1d was the control structure for the three pairs of thin walls). Structure 3.1i had no gages on the sides and only one on the top.

Structure 3.1i, having a height of 6 ft, and GREENHOUSE Structure 3.3.8a, having a height of 7 ft, are compared at the end of this section since both of these structures had an identical height to width to length ratio.

The simplified pressure-time curves for Structures 3.1a, d, and i are shown in Figs. 4.121 and 4.122. These curves show no significant difference in the pseudo-steady-state phase which can be related to length of structure.

#### 4.6.1 Rear Surfaces

Values of "n" for the experimental build-up time on the back is compared to the pretest prediction in Table 4.7. The predicted values of "n" given in this table for Structures 3.1a, d, and i, are 2, 4, and 2, respectively, and the experimental values are roughly  $n = 2$  for all three structures. The build-up of pressure on the rear of each of these surfaces is shown in Figs. 4.123 and 4.124, which express time in  $H/U$  units. These curves have been translated horizontally to remove the time phase delay before the shock reaches the rear surface at the time  $t = L/U$ . The build-up of pressure on the back of each of the three structures is almost identical from beginning to end and has a rather clearly defined shape so that there is little doubt in choosing the time at which the build-up is completed. Vortices, which occur on Shot 9 but not on 10, mentioned above, are seen more clearly here. Structure 3.1d, whose build-up time was predicted to be twice as long as the experimental, due to the presence of a vortex, is seen to have the sharpest vortex effect of the three structures. If 3.1d were a two-dimensional thin wall, shock tube results indicate that the pressure build-up would not have been completed until the time  $t = 8 H/U$ . The experimentally determined value of "n" is only 2. However, a faster build-up is to be expected since Structure 3.1d has a finite width allowing the shock to sweep around the sides. Nonetheless, some effects of the vortex are still shown, terminating at a time roughly equal to  $5 H/U$  units.

The pressure-time curves for the backs of these three structures for Shots 9 and 10, covering both the diffraction phase and the initial stages of pseudo-steady-state phase are shown in Figs. 4.87, 4.88, 4.93, 4.94, 4.99, and 4.100.

#### 4.6.2 Loading on Top Surfaces

The data available for comparing the loading on the top surfaces to determine the effects of structure length, i.e., where length is the only variable changed within the group, are very limited. There was only one gage on the top of Structure 3.1i, and there were nine gages on the top of Structure 3.1a, as shown in Figs. 2.13 and 2.27, which give the as-built gage locations for these structures. Structure 3.1d is the thin wall.

In Figs. 4.121 and 4.122 the simplified average pressure-time curves are compared for the top surfaces of Structures 3.1a and i for both Shots 9 and 10. With the exception of a short interval of time (between  $t = 0.15$  sec and  $t = 0.21$  sec during which the average pressure on the top of Structure 3.1a, as given by the gage readings for Shot 9, seems to behave erratically), the curves given by these two figures exhibit a consistent trend. In each case the pressure rises initially to a value in the neighborhood of side-on pressure, drops sharply, reaching a minimum value, and then rises sharply before leveling off in a gradual decay which causes the pressure to coincide with side-on pressure somewhere between the time  $t = 0.2$  and  $t = 0.4$  sec. The first peak value of pressure is higher for Shot 9 in each case, and the subsequent stages occur at later times than for Structure 3.1a. It must be remembered, however, that there is only one gage on the top of Structure 3.1i, and it, therefore, does not represent a good average.

Rather than compare the average pressure of the top of Structure 3.1a to the single gage on the roof of 3.1i, two individual gages on Structure 3.1a were selected and compared to gage 1 on Structure 3.1i. As can be seen from Figs. 2.13 and 2.27, gage i1 is located a distance of 3 ft (one-sixth of the length) from the front edge along the longitudinal centerline. Gage a26 is at a distance of 3 ft (one-half the length) from the front edge, whereas gage a27 is a scaled distance of one-sixth the length (but a distance of only 1 ft) from the front edge.

A comparison of these individual gage readings is given in Fig. 4.126 for Shot 9, and Fig. 4.127 gives the comparison for Shot 10. From the above discussion of gage locations, with distances given both in feet and as a scaled percentage of the length, one might expect the reading on gage i1 to be somewhere between the pressures of a26 and a27. (The pressure record for gage a27 is no good on Shot 10). However, it can be seen from Fig. 4.126 that gage i1, while matching the pressures on Structure 3.1a rather well in the pseudo-steady state, is considerably higher during the diffraction phase, showing no effects of the vortex action near the front edge of 3.1a (i.e., at gage a27). These results appear to indicate that for structures of this type having the same height and width, the increased length tends to weaken the vortex, acting at some per cent of the length from the front edge. It is probably true that increased pressures, due to the weakening of this vortex, are felt over the entire top surface, but, strictly speaking, the above discussion applies only to the upstream portions of the roof.

#### 4.6.3 Comparisons of Structures 3.1i (UPSHOT-KNOTHOLE) to Structure 3.3.8a (GREENHOUSE)

The two cubicles, Structures 3.1i of UPSHOT-KNOTHOLE and 3.3.8a of GREENHOUSE (*Blast Loading and Response of Structures*, WT-87) both having height to width to length ratios equal to 1:2:3 and heights of 6 and 7 ft, respectively, are compared as a means of relating Program 3.1 of UPSHOT-KNOTHOLE to GREENHOUSE. The average pressure vs time curves on the top and back surfaces are compared in Figs. 4.128 and 4.129. The gage arrangement on rear surfaces of Structures 3.1i and 3.3.8a was almost identical; however, the roof of Structure 3.3.8a was more extensively instrumented than the roof of Structure 3.1i. The pressures on top surfaces are similar, except that Structure 3.1i shows an unproportionately high initial peak pressure on Shot 9. Furthermore, Shot 9 of UPSHOT-KNOTHOLE had a different wave shape than for Shot 10 or the GREENHOUSE Test, the latter two being nearly alike. In addition to the difference in wave shapes, the initial overpressures were different in each of the three cases, namely  $p_o(0) = 10, 6.0,$  and  $3.2$  psi for GREENHOUSE, Shot 9, and Shot 10, respectively. The free stream side-on pressure variation for GREENHOUSE is shown in Fig. 4.132, both as the experimental curve and the theoretical curve.

A more useful comparison of the pressures on these two structures is obtained by normalizing surface pressures with respect to the free stream pressure. The durations were approximately equal for the three shots ( $t_0 = 0.88$  sec for GREENHOUSE and Shot 10 of UPSHOT-KNOTHOLE, and  $t_0 = 0.92$  sec for Shot 9), and thus a comparison could be made without normalizing with respect to time. Figures 4.130 and 4.131 express the loading on the top and rear surfaces as a percentage of side-on pressure as a function of time. In connection with these curves, one must observe that on Fig. 4.132 the experimental free stream pressure at GREENHOUSE differed from the theoretical curve between the time,  $t = 0.3$  and  $t = 0.5$  sec. This characteristic of the free stream curve at GREENHOUSE was not as pronounced as the surface pressures. The free stream gages there were not as well spaced, with respect to Structure 3.3.8a of GREENHOUSE, as in Program 3.1.

It is seen from Figs. 4.130 and 4.131, which give the normalized pressures on the top and rear surfaces, that the curves for the three blast waves compare very favorably. The curves interwind and never vary by more than 10 per cent (based on the GREENHOUSE theoretical curve). Beyond the time  $t = 0.4$  sec, the three normalized curves diverge. During the first 25 msec, the curves for the top surface of Structure 3.1i reach a peak value greater than  $p_o(0)$ . This does not occur for the GREENHOUSE structure.

A comparison of the normalized average pressure on the rear surfaces between Shot 10 and GREENHOUSE, which had nearly identical wave shapes, gives an excellent comparison

~~SECRET - RESTRICTED DATA~~

UNCLASSIFIED



until the time  $t = 0.4$  sec. Shot 9, for which the wave shape decayed much more rapidly, compares very well after the time  $t = 0.1$  sec. For the roof and the rear surfaces, the experimental GREENHOUSE curve shows an erratic deviation from the UPSHOT-KNOTHOLE tests.

#### 4.6.4 Conclusions on Length Effects

Within the intended scope, the objectives of length effects were fulfilled.

##### 4.6.4.1 Rear Surfaces

Build-up on the back of three-dimensional thin wall was completed in 2 S/U instead of 4 S/U time units. (See Figs. 3.3 and 4.125.)

##### 4.6.4.2 Top Surface

Loading on the top surface appears to be related to the ratio of width to length. Further exploration (in the shock tube) is definitely recommended. Insufficient data were available for the determination of rules governing this variation.

##### 4.6.4.3 GREENHOUSE Comparison

Normalized pressures on the top and rear surfaces of nearly identical structures in the UPSHOT-KNOTHOLE and GREENHOUSE programs compared favorably.

#### 4.7 SIZE EFFECTS

Structures 3.1a, e, and f, grouped to measure the effect of increased size of structure, are shown in Figs. 2.13, 2.14, and 2.19 through 2.22, which give the building dimensions and gage locations. For a special scaling comparison, Fig. 4.133 illustrates the relation between certain gage locations on Structures 3.1a, e, and f.

##### 4.7.1 Pressures on Scaled Structures

The pressure records of gages located in identically scaled positions on Structures 3.1a, e, and f are compared in Figs. 4.134 through 4.143. In these figures the time values for gages on Structure 3.1a are multiplied by 2 when compared to a gage on Structure 3.1f and by 3 when compared to a gage on Structure 3.1e. Some of these gages on Structures 3.1a and e were also SRI check gages (gages a8, a10, and e5). It can be seen from these figures, which use the expanded time scale for the smaller size structures to measure scaling, that the pressure values throughout compare at least as well to the SRI and BRL check gages shown in Figs. 4.18 through 4.24. In addition to those curves shown, comparisons were made in a similar fashion between Structures 3.1e and f. Those exhibited here are typical for the entire group.

##### 4.7.2 Peaked Shock Effect

As discussed in Chap. 3, a peaked shock effect, tending to reduce the load on the front surface and to increase the loads on the rear surface, was expected to occur for larger structures. This effect, due to a deceleration of flow, is not thoroughly understood, but it was observed here in a purely empirical fashion. In Fig. 4.35, which shows the loading on the front and rear surfaces of Structure 3.1e for Shot 9 together with the side-on pressure curve and the net load for this structure, the effect referred to in Chap. 3 is clearly observable on front surface loading which is well below side-on pressure throughout the pseudo-steady state. Although this front loading is that of a single gage, it appears unlikely that miscalibration accounts for the low reading since the peak reflected pressure is not abnormally low compared to those for other structures of this test. The lowered front loading results in a negative net pressure throughout the entire pseudo-steady-state period. A tendency toward this same effect is shown for Structure 3.1e on Shot 10. Here the net pressure is zero throughout most of



the pseudo-steady-state phase, as shown in Fig. 4.36. Structure 3.1f, whose size is between that of 3.1a and 3.1e, is shown in Figs. 4.37 and 4.38, for Shots 9 and 10, respectively. It can be seen from these figures that the net pressure during most of the pseudo-steady-state phase is zero on Shot 9. However, the net pressure is positive on Shot 10 (i.e., a net loading in the downstream direction). The wave shape for Shot 9 is more peaked than that for Shot 10, and the tendency seems to be that the larger the structure and the more peaked the shock, the stronger the tendency is toward a negative net load. In neither of these cases was the structure long enough in comparison to the wave duration to allow for the pressure at the rear at any given time to be larger than that at the front, due simply to their relative positions with respect to the wave length.

#### 4.7.3 Conclusions on Size Effects

The objectives of size effects studies were to investigate time-scaling and check for the occurrence of the peaked shock effect. These objectives were fulfilled.

##### 4.7.3.1 Relation of Pressures on Geometrically Similar Structures

The pressure-time curves on the top and rear surfaces of geometrically similar structures can be satisfactorily obtained from one another by multiplying time scales by the corresponding ratios of structure sizes.

##### 4.7.3.2 Peaked Shock Effect of Structure Height

Peaked shock effects resulting in negative net loads were observed for a structure having  $\tau_0 = Ut_0/H = 66$ . This is primarily due to lowering of pressures on the front surface. No analytic treatment was attempted.

#### 4.8 EFFECTS OF ORIENTATION

Structures 3.1a, g, and h were grouped in order to measure orientation effects. The intended orientations and as-built dimensions of these structures are given in Chap. 2. They are shown in Figs. 2.6, 2.13, 2.14, and in 2.23 through 2.26. However, both Shots 9 and 10 were slightly misoriented from the intended Ground Zero. The actual angles of orientation are shown for the various surfaces of Structures 3.1g and h in Table 4.8.

The comparisons given in the following paragraphs were made to measure orientation effects.

##### 4.8.1 Variation of Peak Pressure on Obliquely Loaded Surfaces

The pretest prediction for variation of peak obliquely reflected pressure,  $Q$ , with angle or orientation,  $\theta$ , for obliquely loaded semifront surfaces is given in Table 3.1 and Fig. 3.17. Experimentally determined values of this peak pressure for various surfaces of Structures 3.1a, g, and h are plotted as a function of orientation angle,  $\theta$ , in Fig. 4.144. The values of the theoretical peak pressure,  $Q$ , defined in Chap. 3, and used in connection with Fig. 4.171 have been computed for the actual conditions present at Shots 9 and 10 and are plotted next to the measured values of peak pressure. Although the measured values are in every case lower than those predicted, they compare favorably since it will be recalled that, even under normal orientation, measured values of peak pressure are usually lower than the predicted reflected pressures, due to the response time of the gages. It is believed that the value of true peak pressure is very closely approximated by a single straight line connecting the end points of the pretest prediction curve of Fig. 4.144.

##### 4.8.2 Impulses on Obliquely Loaded Surfaces

The angle of orientation for various surfaces is defined in Table 4.8. Numerical values of  $\theta$  for semifront surfaces are also given. Areas under the pressure-time curves during the

diffraction phase were measured and compared to the areas under the corresponding pretest prediction curves. Figure 4.145 summarizes the results of this analysis and indicates that the diffraction impulse decreases continuously as the angle of orientation  $\theta$  increases from 0 to 90 deg., i.e., from normal reflection to parallel flow. A post-test development indicates that the diffraction impulse on semifront surfaces can be obtained using the pretest method of prediction with a correction factor of  $[1 - \frac{1}{2}(\theta/90)]$ , where  $\theta$  is expressed in degrees. Actually, the straight line approximation through the experimental points of Fig. 4.145 would yield a correction factor of  $[0.95 - (0.47\theta/90)]$ . However, since about the same degree of accuracy is obtained using either of the above correction factors, the former expression has been chosen because it is simpler. The pressure-time curves used as a basis for constructing Fig. 4.145 are presented in Figs. 4.146 through 4.152.

TABLE 4.8—Actual Angles of Incidence,  $\theta$ , for Obliquely Loaded Structures 3.1g and h

Surface	Shot 9		Shot 10	
	$\theta_g$ (deg)	$\theta_h$ (deg)	$\theta_g$ (deg)	$\theta_h$ (deg)
Front	13 $\frac{1}{2}$	36	21	43 $\frac{1}{2}$
Right Side	76 $\frac{1}{2}$	54	69	46 $\frac{1}{2}$
Left Side	103 $\frac{1}{2}$	126	111	133 $\frac{1}{2}$
Rear	166 $\frac{1}{2}$	144	159	136 $\frac{1}{2}$

#### 4.8.3 Conclusions on Orientation Effects

The effects of orientation were only partially fulfilled since the drag coefficients, which were treated in great detail in the pretest prediction, could not be checked and considerable instrumentation difficulties were encountered on the oriented structures.

##### 4.8.3.1 Peak Pressures

Satisfactory agreement exists between the experimental values and pretest predictions for peak pressure on obliquely loaded surfaces. Peak pressure,  $Q$ , varies linearly with angle of incidence,  $\theta$ , between normal and parallel orientation (at least for overpressures up to 6 psi).

##### 4.8.3.2 Diffraction Impulse

The pretest prediction of diffraction impulse on obliquely loaded surfaces gave values which were higher than measured impulses. A correction factor to be applied to the pretest prediction is recommended, namely, the factor  $[1 - \frac{1}{2}(\theta/90)]$ .

#### 4.9 EFFECTS OF SHIELDING

Structures 3.11 to n, which are pairs of thin walls similar to the isolated thin wall of Structures 3.1d, separated by a varying distance (3, 6, and 18 ft, respectively), were studied here to determine the effects of shielding. Sketches of these pairs of thin walls are shown in Figs. 2.9 and 4.153. The as-built gage locations are shown in detail in Figs. 2.28 through 2.33. Structure 3.1d, the isolated thin wall, which is also shown in Fig. 4.153 for the purpose of comparing gage locations on its surfaces to corresponding surfaces of the pairs of thin walls of Structures 3.11 to n, has its as-built gage locations and dimensions given in detail in Figs. 2.17 and 2.18. Comparisons between shielding and shielded walls and an isolated free wall have been made as described in the following paragraphs.

#### 4.9.1 Comparison to Isolated Thin Walls — Assumptions Required to Obtain Net Loads

The variations in pressure on any surface of these walls resulting from the proximity of the thin wall is negligible compared to the total pressure on that surface. However, compared to the net load on either shielding or shielded wall, these same variations in pressure are significant. By assuming that the front surface of Wall No. 1, for Structures 3.1l and m, has the same pressure-time curve as the front of Structure 3.1d and that the rear surfaces of Wall No. 2, for Structures 3.1l and m, have the same pressure-time curves as for the rear surface of Structure 3.1d, net loads were computed for each of these walls.

The net average pressure-time curves for Structure 3.1d and for both walls, Nos. 1 and 2 (i.e., the shielding and shielded walls) of Structures 3.1l and m, are shown in Figs. 4.33, 4.34, and 4.49 through 4.56. The diffraction phase of loading is shown by an expanded time scale,  $t = 0$  to 0.16 sec in Figs. 4.53 through 4.57, and the pseudo-steady-state range of loading is shown until the time  $t = 0.7$  sec in Figs. 4.49 through 4.52.

TABLE 4.9 — Ratio of Net Impulses on Structures 3.1l to n to Impulse on Structure 3.1d (Shot 9)

	Time of impulse, $t_f$ (sec)	Impulse of net surface Impulse of 3.1d
Front of Structure 3.1d minus rear of Wall No. 1 of Structure 3.1l	0.091	1.073
Front of Structure 3.1d minus rear of Wall No. 1 of Structure 3.1m	0.090	0.718
Front of Structure 3.1d minus rear of Wall No. 1 of Structure 3.1l	0.680	1.376
Front of Structure 3.1d minus rear of Wall No. 1 of Structure 3.1m	0.560	0.263
Front of Wall No. 2 of Structure 3.1l minus rear of Structure 3.1d	0.125	0.218
Front of Wall No. 2 of Structure 3.1m minus rear of Structure 3.1d	0.120	0.397
Front of Wall No. 2 of Structure 3.1l minus rear of Structure 3.1d	0.680	1.067
Front of Wall No. 2 of Structure 3.1m minus rear of Structure 3.1d	0.520	0.591

By taking the areas under these curves, net impulses can be computed during any desired interval of time. By arbitrarily choosing the end of the diffraction phase to be that time at which the curve begins to smooth off and become less jagged, ratios of the impulses on these shielding and shielded walls with respect to the net impulse on Structure 3.1d, the isolated thin wall, were computed and are entered in Table 4.9. Each of these impulses was computed by taking the area under the curve until some time,  $t_f$ , shown in this table, with all the areas beginning from time equal to zero. Curves relating net impulse on the wall for the shielding and shielded walls to the distance separating them are shown in Figs. 4.155 and 4.156. In these figures, the ordinates represent the ratio of the net impulse on any given wall to the net impulse on Structure 3.1d, while the abscissa represents the ratio of the distance between walls to the wall height. The curves are based on very limited data and are not considered to be suitable for use in future loading predictions. The following discussion is intended to clarify the relation between these curves and the experimental data.

Wall d, which is isolated, is also represented by the case wherein there are two walls infinitely far apart. Therefore, the ordinate approaches a value of 1.0 asymptotically as the abscissa goes to infinity. Intuitively, one feels that for any given wall, the effects of the other wall are insignificant at some finite distance of separation. Aside from the above-mentioned asymptote as the abscissa goes to infinity, only two experimental points are known for each curve of Figs. 4.155 and 4.156. These experimental points indicate only the general direction of the curves. A solid line indicates the most probable shape of a curve in the vicinity of experimental points, whereas the dashed lines are more approximate since they apply to those regions of the figure for which no experimental points are available.

It is interesting to observe in Table 4.9 that for both walls, Nos. 1 and 2, in Structure 3.1l, separated by a distance of one-half the height, the total impulse is higher than for an isolated thin wall. For Structure 3.1m, where the walls are separated by a distance of one



height unit, the total impulse is lower than for an isolated thin wall on both the shielding and shielded wall. In addition to the net loads studied above, pressure-time curves for individual gages in similar locations on the walls of Structures 3.11 to n were compared to similar gages on Structure 3.1d. The impulses, i.e., the areas under the pressure-time curves, for gages located on surfaces of the pairs of thin walls were normalized by the impulses of similar gages on Structure 3.1d. No conclusions could be drawn on the basis of these impulses, and they are not presented here.

Structure 3.1n was very lightly gaged, having only one gage on each of two surfaces, and these gages were located in re-entrant corners, making this structure of little interest in dealing with either net average pressures or average pressures on a surface. However, it is pointed out here that the pretest assumption, namely, that no reflected pressure would be felt on the rear surface of wall No. 1, Structure 3.1n, due to the large separation ratio of 3 times the height, was incorrect. These gages, in fact, show the highest reflected pressures found on any of the 3.1 structures in this overpressure region. Perhaps this is due to the fact that the wave reflected from the second wall strikes the first wall head-on, rather than obliquely as is the case at the shorter separating distances.

#### 4.9.2 Conclusions on Shielding Effects

This objective of the test is only partially fulfilled. The main reason was that the pretest predictions were much simpler than the field records. The results of this test are not adequate for deriving an accurate method of prediction.

For pairs of thin walls separated by a distance of one-half the height, the net diffraction impulse on each wall is greater than on an identical isolated wall. At a separation distance of one height unit, the net diffraction impulse is less than that of a free wall.

Reflections from the shielded wall affect the loading of the shielding wall significantly at separation distances of three and even more height units. In the range of shielding distances between one-half and three height units, the loading on the back of the shielding wall appears to increase as the walls are placed farther apart.

#### 4.10 EFFECT OF ELEVATION ABOVE GROUND (GROUND PROXIMITY)

As was anticipated, no significant effects of elevation could be detected during the pseudo-steady state. Simplified pressure-time curves for the front and rear surfaces are presented in Figs. 4.157 and 4.158. Although there was one gage on the front surface of Structure 3.1o, the records were not good and are not included in this comparison. Pressures on the bottom surfaces are discussed separately below.

The effect of elevation above ground can best be studied from Figs. 4.159 to 4.162, which show the pressures at the gages located at the bottom faces, together with the pretest predictions. The most outstanding difference between the pretest predictions and the test results is the fact that the predictions do not take into account the vortex effects, which are quite pronounced in the case of a bottom surface. On the other hand the comparison for peak value indicates fair agreement, as shown in Table 4.10. One can conclude from this table that, at the lower overpressures, the pressure multiplication can be neglected.

The measured averages on the rear surfaces (see, for example, Fig. 4.164 or 4.165 for Structures 3.1o, Shots 9 and 10) agree with predicted initial build-up slopes and final pseudo-steady-state values, but they exhibit larger final build-up times, due to the effect of vortices.

##### 4.10.1 Conclusions on Effects of Elevation Above Ground

The elevation effects objectives were only partially fulfilled. Inconclusive results were obtained regarding the values of the clearing distances and build-up distances on the front and rear surfaces.

#### 4.10.1.1 Net Impulse

No effect.

#### 4.10.1.2 Pressure Increase on Underface

For Shot 10 the pressure increase was 3.5 psi. No effect was observed. For Shot 9 the pressure increase was 6 psi, approximately as predicted (see Figs. 4.159 to 4.162).

#### 4.10.1.3 Loading on Rear Surfaces

Vortex effects led to predicted rear build-up and pseudo-steady state but delayed final build-up time. Good agreement exists between predicted and measured values of pressure during the pseudo-steady-state phase. A vortex, which results in significant lowering of pressures, was observed but not predicted. It occurred immediately after the peak pressure was reached.

TABLE 4.10—Ratio of Peak Pressures to Side-on Pressure at Bottom of Elevated Structures

	Predicted	Measured
Shot 9		
3.1o	1.21	1.23
3.1p	1.19	1.29
Shot 10		
3.1o	1.21	1.00
3.1p	1.19	1.02

#### 4.11 IRREGULARLY SHAPED RECTANGULAR STRUCTURE 3.1q

Structure 3.1q is the only model considered in studying the effects of irregularity in shape of these cubicles. The difference in shape between Structure 3.1q and the other structures was discussed in Chaps. 1, 2, and 3. The schematic loadings were given in Chap. 3, and in this section frequent reference is made to Chaps. 1, 2, and 3. Experimental data are compared to the pretest predictions, as well as to shock tube results. Although no revisions of pretest predictions are made in this section, conclusions are drawn from which future revisions can be based.

##### 4.11.1 Relation Between Pretest and Post-test Analysis

The specific reasons for studying a structure such as Structure 3.1q were discussed in Chap. 1. It was pointed out in that chapter that the effects of loading in cavities, setbacks, and re-entrant corners are of interest since, in dealing with actual structures, such irregularities of shape from the idealized models are frequently encountered. Figure 2.10 exhibits the specific type of shape irregularities under study here. Figure 2.12 shows some of these shape characteristics photographically. Detailed dimensions, giving the gage locations, are presented in Figs. 2.38 through 2.40, together with the as-built dimensions of the structure. The pretest prediction of loadings on various surfaces of Structure 3.1q are given in Sec. 3.4.7, together with the schematic loading diagrams of Figs. 3.21 to 3.23. As pointed out in Chap. 3, the structure is designed especially to measure pressure multiplication in re-entrant corners. In addition, it studies the changes in relief time in such corners.

The post-test analysis of this section consists of (1) checking pretest predictions against the experimental pressure-time curves on the various surfaces and (2) comparing shock tube pressure-time curves of the Princeton double block to individual gage records placed on the surface of the open ended notch (formed by Sections A-A and B-B). Comments are made on each of these graphical comparisons.



#### 4.11.2 Presentation of Data

As can be seen from Figs. 2.38 through 2.40, gages were strategically placed on Structure 3.1q to measure special effects, as described below.

On Section A-A, 3 gages were placed near the open end of a surface which is similar to the front of the second block of the Princeton double block model. Gages q1 and q2 indicate the initial effects of a wave entering through the opening at the roof. Higher reflected pressures should be felt near the opening than at points nearer to the ground (such as at gage q3). Gage q4 is located on a surface similar to the back of the first block of the Princeton double block shock tube model and gages q8 and q10 are on a surface analogous to the floor between the two blocks. The pressure-time curves for these gages are normalized into percentage of side-on pressure, and the time values are expressed in  $H/U$  or  $L/U$ , instead of seconds, for direct comparisons to the Princeton data.

On Section C-C of Structure 3.1q, gages q5, q6, and q7 are situated so as to measure the relief time at a point which is very near to one free edge but set back from the other free edge. Gage q11 measures the effects of relief of reflected pressures on a surface parallel to the direction of flow, so that it will experience both the initial shock front and the reflected wave returning from a reflecting surface located downstream. Gage q12 measures the relief time on a surface frequently found in real structures.

Comparison of gage records to the pretest prediction pressures are shown only until the time  $t = 0.12$  sec, for the purpose of observing details of the diffraction loading. In comparing gage records to shock tube pressure-time curves, the plot is continued only until a time varying between 10 to 15 of the dimensionless time limits, because the shock tube pressure-time curves were available only until this time.

#### 4.11.3 Comparison of Individual Gages on the Same Surface

Average pressure-time curves were compared to the individual gage readings. In addition, individual gage readings were plotted together during the pseudo-steady state of the loading but are not presented here. Instead of presenting these individual gage readings, the following qualitative discussion is given below. Gages q1, q2, and q3, discussed above, were compared during the diffraction phase. For both Shots 9 and 10 higher pressures were experienced for gages nearer to the ground than for those near the roof. (Gages q1 and q2 are near the roof, and gage q3 is near the ground.) No similar trend was observed for gages q5, q6, and q7 on the setback surface of Section C-C nor for gages q8 and q10 on the left elevation. For all the above-mentioned gages, during the pseudo-steady-state phase, the shape of the pressure-time curve was similar to those of upstream or downstream surfaces not located within a notch.

#### 4.11.4 Comparison of Pretest Predictions to Pressure Records

In Fig. 4.166 gages q1, q2, and q3, on Section A-A, are compared to the pretest prediction for the average pressure on this surface. Zero time is referred to as the time at which the shock strikes the front of the structure which accounts for the time phase delay. Although these three gage readings are nearly identical after the time  $t = 0.015$  sec, they differ before this time in that the reflected pressure on gage q1 is never as high as for gage q2 or q3, but it shows that two peak values occur. Gage q2 is located near gage q1 but closer to the re-entrant corner and shows a higher value for the first reflected pressure. Gage q3 shows the highest value of reflected pressure with the longest time required for relief. Gage q3 is really representative of pressures over most of this surface and would compare favorably with the pretest prediction if a change in the shape of the pressure curve is made without changing the area beneath the curve, that is, maintaining the same diffraction impulse. On both Shots 9 and 10 the experimental loadings deliver impulses which are roughly equal to those of the pretest predictions, although much more jagged curves are observed for the field records. At extremely high overpressures the field records may indicate greater impulses, and perhaps this prediction should be revised after shock tube studies on these structures are completed.



Gage q4 represents a similar case to that just discussed above, in that the predicted and experimental impulses are roughly equal, and the experimental peak reflected pressures are considerably higher than the predicted values, and their curves are more jagged.

Gages q5, q6, and q7 show that immediate relief from the nearby free edge reduces reflected pressures to about 125 per cent of side-on and that relief to the expected pseudo-steady-state values from this higher value is delayed somewhat by the presence of the wall from the setback.

Gage q12, located on the front surface in a cavity similar to that of a usual doorway (surface 1), shows a peak pressure much higher than predicted and is believed to be a miscalibrated gage. (The experimental reflection coefficient would be equal to three,  $p_r/p_o = 3.0$ .) This gage record also shows a very rapid relief to a pressure less than side-on before reaching the pseudo-steady-state value. The diffraction impulse is somewhat higher than was predicted, but this is to be expected from a miscalibrated gage whose pressure readings are too high.

#### 4.11.5 Comparison with Shock Tube Results

Figure 4.174 shows the relation between the notch in the side of Structure 3.1q and that of the Princeton double block. The Princeton double block is purely two dimensional, having both ends of the notch closed by the shock tube walls, whereas the notch of Structure 3.1q has one end closed at the ground surface and the other end open at the roof. In Figs. 4.175 through 4.179, which show the pressure-time curves on various surfaces of these two similar notches, the following observations are made: Fig. 4.175, which compares the pressure record of gage q3 on Shots 9 and 10 to that of the front surface of the block, shows that the field records have higher reflected values and shorter relief times. This may be due to the nature of the Princeton pressure-time curve, which was derived by averaging pressures throughout the surface instead of at some particular point, as for gage q3. The comparison between Shots 9 and 10 is very good in this normalized form, showing the peak reflected pressure to be slightly greater than two times side-on. It can also be seen that, by preserving areas, the impulses determined from the field records can be made equivalent to that of the shock tube model.

The average of gages q1, q2, and q3, obtained graphically, is compared to the Princeton model for Shots 9 and 10 in Fig. 4.177. This figure shows that, after averaging these three gage records, the reflected pressure is very nearly the same as for the shock tube model, but that no appreciable increase in impulse is obtained from lengthening of the relief time. This can be expected for two reasons, namely: (1) the diffraction impulse averaged over the surface should be slightly less for the Structure 3.1q notch because one end is open, allowing for quicker relief, and (2) the averaging of pressures between gages q1, q2, and q3 did not consider "weighting of areas" for the gages and therefore overemphasize the effects of gages q1 and q2 near the opening at the roof.

Figure 4.178 compares the loading on the rear of the first block of the two similar notches described above. For the Structure 3.1q notch the ratio of length to height is equal to one, whereas length to height equals 1.5 for the Princeton shock tube notch. It was not immediately obvious which dimensionless time unit should be chosen,  $L/U$  or  $H/U$ . For the loading on this surface, as can be seen from Fig. 4.178, a better comparison is obtained using  $L/U$  as the dimensionless time unit. This was tried for Figs. 4.175 and 4.177, but it did not give a favorable comparison for the surface treated in those figures.

The pressure on the floor of the notch between the Princeton blocks is compared to the surface marked left elevation in Fig. 3.50, containing gages q8 and q10, and to the gage on the ground between walls 1 and 2 of Structure 3.1m. These three cases represent a notch with both ends closed, one end closed, and both ends open, except that the geometry in the upstream and down-stream direction from these notches differs. (The shock tube uses blocks 3.1q as a notch in a much larger block and Structure 3.1m is formed by two thin walls.) For the average of gages q8 and q10 of the notch, the diffraction impulse is nearly the same as that on the floor between the blocks in the shock tube. On the ground surface between the two

walls of Structure 3.1m, the impulse is much higher than on corresponding surfaces of either of the above cases (Structures 3.1q and the Princeton double block) for both Shots 9 and 10.

#### 4.11.6 Conclusions on Effects of Irregularly Shaped Rectangular Structure

The intended objectives of loading on irregularly shaped objects were completely fulfilled.

The loadings on the surfaces of Structure 3.1q in general had the same diffraction impulses, but higher reflected pressures and faster relief times, than were given in the pretest predictions.

Normalized pressure-time curves on surfaces of the notch at the sides were also compared to loadings on corresponding surfaces of the Princeton double block. Here, again, higher peak (re-entrant corner) pressures and shorter relief times were observed on Structure 3.1q than on the Princeton double block, but the diffraction impulses were roughly the same.

#### 4.12 REGULAR REFLECTION EFFECTS, STRUCTURES 3.1s AND t (SHOT 9)

The load predictions for structures in the regular reflection region, Structure 3.1s and t, Shot 9, were given in detail in Chap. 3, Figs. 3.1 and 3.2.

The basic constants to be used for the pretest predictions on structures 3.1s and 3.1t are

Structure 3.1s	Structure 3.1t
$p_o(0) = 16 \text{ psi}$	$p_o(0) = 11.5 \text{ psi}$
$P_0 = 13.2 \text{ psi}$	$P_0 = 13.2 \text{ psi}$
$c \text{ (Fig. 5.5)} = 0.98$	$c \text{ (Fig. 5.5)} = 1.33$
$t_0 = 0.76 \text{ sec}$	$t_0 = 0.68 \text{ sec}$
$\alpha = 30 \text{ deg}$	$\alpha = 44 \text{ deg}$
Angle of orientation	Angle of orientation
$\delta = 30 \text{ deg}$	$\delta = 16 \text{ deg}$

The net load predictions are given in Figs. 4.180 to 4.183, and the corresponding experimental results are given in Figs. 4.45 to 4.48. Considering that Structure 3.1s was probably located in a pseudo Mach stem region due to a thermal layer (Appendix C) and that there was some orientation effect (see also Sec. 4.14), the agreement is fair.

##### 4.12.1 Conclusions on Regular Reflection Effects

The regular reflection objectives were only partially fulfilled. The rather elaborate pretest predictions given in Chap. 3 could only be tested in two instances of incidence angles of 30 deg (Structure 3.1s) and 44 deg (Structure 3.1t). In the former both peak pressures and pseudo-steady-state values were somewhat overestimated, whereas on the latter they were somewhat underestimated, but on the whole the agreement is fair (see Figs. 4.180 to 4.183).

#### 4.13 PRECURSOR EFFECTS, STRUCTURES 3.1s AND t (SHOT 10)

On the basis of the discussion in Appendix A, a schematic loading scheme which yields the entire net loads for block like structures in a precursor region may be constructed. (There are no diffraction loads on Structure 3.1t.) For the conditions of Shot 10 this scheme would consist of a linear rise from zero pressure to a peak value equal to the product of the drag coefficient for the structure times the ideal surface dynamic pressure at this ground range, i.e.,  $C_d p_d(t)$ . This peak is followed by a linear decay to zero pressure at the end of the positive duration of the wave. To extrapolate this loading picture to other bomb yields, one



method would be to multiply the time of the peak pressure by the cube root of the ratio of this bomb yield to 15 kt, i.e., by  $(W/15)^{1/3}$ , to give the new time of maximum pressure, with decay to zero pressure occurring at the time of the positive phase for the new yield. This schematic loading scheme is shown in Fig. A.29 and is reproduced in Fig. 4.184 for the conditions on Structure 3.1t.

The loads given in Fig. A.29 represent a smooth variation in net pressure. To this loading scheme, in order to represent the actual loading conditions, a random oscillation must be superimposed. This oscillation should range in magnitude up to 50 per cent of the peak as given in Fig. A.29. It is felt that the response of the structure may be considerably altered by these random oscillations, even if the net impulse remains constant since such factors as wall breakage may be strongly affected by their presence. Thus a true response picture of the structure would give some average computed deflection (assuming the building resistances are completely known) with some distribution of deflection about this average.

Although this loading scheme probably represents the best possible current picture for block like structures, there are many uncertainties inherent in it (see Appendix A), and a great deal of further investigation should be performed to resolve these uncertainties. For realistic target structures that are partially open, it is felt that the loading scheme presented here gives an overestimate of the loads since the wave entering the interior may well have a much smaller concentration of dust. In this case the average net pressure experienced by the building could be closer to the drag pressures computed by means of the Rankine-Hugoniot relations from the pressures actually occurring in the blast wave. The blast conditions over other types of surfaces may also result in much smaller over-all loads.

The loading scheme presented in Fig. A.29 has been obtained on the basis of the conditions in the precursor for UPSHOT-KNOTHOLE Shot 10. It is possible that the peak pressures acting on a structure for a bomb of very high yield might be considerably larger; therefore for large yield bombs the loading method presented may yield an underestimate of the actual loads which a structure may undergo.

It must be emphasized that the scheme of Fig. A.29 which was obtained from data on Shot 10 is based on the theory that the precursor rise time should scale like a hydrodynamic variable. Therefore, in order to apply it to other shots, it is expected that one should preserve (1) the same scaled height of burst and (2) the same type of surface. Thus the scheme would not be applicable to large yield weapons exploded in the Pacific Proving Grounds where both above conditions were violated. For weapons comparable in yield to Shot 10 in the Pacific Proving Grounds, the predictions of Fig. A.29 should be fairly applicable, despite the difference in surface conditions.

With these reservations the following conclusions apply: The pressure records obtained by NOL on Structure 3.1t in the precursor region of Shot 10 are valid. On the basis of these records it may be stated that the loads on the structure were of unusually high magnitude compared with loads computed on the basis of peak pressures in the blast wave. Superimposed on these loads were random oscillations of large magnitudes.

The effects noticed upon Structure 3.1t may be attributed, in all likelihood, to a large amount of dust present in the air which is carried along by the blast wave. This dust loading not only has an effect on the loads experienced by a target, but it also influences intimately the structure of the precursor itself.

A method of computing loads in a precursor is presented in Fig. A.29. It is felt that this scheme for predicting loads is probably about as accurate as can be developed at present. The loads predicted on the basis of this method approximate the drag loads which would be obtained if the bomb were exploded over an ideal surface.



#### 4.13.1 Conclusions on Precursor Effects

##### 4.13.1.1 Pressure Records

NOL records on Structure 3.1t in the precursor region of Shot 10 are valid. Loads are high when compared to loads computed on basis of peak side-on pressure. Superimposed are large random oscillations.

##### 4.13.1.2 Dust Effects

The effects noticed on Structure 3.1t may be attributed, in all likelihood, to a large amount of dust present in the air which is carried along by the blast wave. This dust loading not only has an effect on the loads experienced by a target but also influences intimately the precursor itself.

##### 4.13.1.3 Loading Scheme for Precursor, Shot 10

A method of computing loads in a precursor is presented in Fig. A.29. It is felt that this scheme for predicting loads is probably about as accurate as can be developed at present. The loads predicted on the basis of this method approximate the drag loads which would be obtained if the bomb were exploded over an ideal surface.

##### 4.13.1.4 Applicability to Other Precursor Shots

It is assumed that the rise time scales like a hydrodynamical variable

$$\text{Rise time} = 100 (W/15)^{1/3}$$

that is, one must preserve the same scaled height of burst and the same type of surface.

The most outstanding result from this post-test analysis is the fact that, with few exceptions, there is no reason at this time to modify the pretest predictions if correct wave shapes and correct drag pressures are taken into account. This will be discussed later in the general conclusions. The most important exception is the post-test build-up coefficient "n" given in Fig. 4.125. The modifications indicate that "n" is the same for three-dimensional thin walls as for finite blocks.  $W/2H = 1$ , and the rising slope to two dimensionality extends to the ratio  $W/2H = 5$ , rather than 3.

#### 4.14 EFFECTS OF ORIENTATION DUE TO DIFFERENCES BETWEEN ACTUAL AND DESIGNATED GROUND ZEROS

Owing to differences between actual and designated ground zeros on Shots 9 and 10, there was a deviation from the normal side-on loading. These deviations extended up to orientations of 10 deg for items located in the Mach region and up to 36 deg for items in the regular reflection region. It is felt that these orientation effects can be neglected for the following reasons:

In the Mach region of Shot 9 when the shock first contacts the obstacle, the pressure on the front wall would ordinarily rise to  $p_r$ , instantaneously. The orientation effect introduces a finite rise time on the front surface, i.e., instead of having an instantaneous rise in pressure from zero to the reflected value, a build-up of average pressure takes place as the shock front sweeps across the surface. This rise time,  $t_{\text{rise}}$ , is

$$t_{\text{rise}} = \frac{W \sin \theta}{U} \quad (4.5)$$

$W$  is the width of the surface under consideration,  $\theta$  is the angle of incidence, and  $U$  is the shock front velocity. The quantity  $t_{\text{rise}}$  is small compared to the diffraction period time for the structure

$$t^* = \frac{L + 5S}{U}$$

(4.6)

since for the values of  $\theta$  encountered here,  $W \sin \theta$  is small compared to the quantity  $L + 5S$  (where  $L$  = length and  $S$  = build-up distance on back surface) and is entirely negligible compared to the positive phase duration,  $t_0$ . This relation has been observed in ARF shock tube tests on obstacles of  $H:W:L = 1:2:3$  for the Effects of Orientation Program. Thus the ratio of rise time to diffraction period (for  $\theta = 15$  deg) is only 10 per cent, and the diffraction impulses are practically identical with those of head-on orientation,  $\theta = 0$ .

For items situated in the regular reflection region of Shot 9, the pressure on the front wall reaches its peak value at  $t = (2H \cos \alpha / U)$  which is of the same order of magnitude as  $W \sin \theta / U$  for the test conditions of Shot 9, namely,  $30 \text{ deg} \leq \alpha \leq 44 \text{ deg}$ ;  $16 \text{ deg} \leq \theta \leq 30 \text{ deg}$ ; and  $W/H = 2$ . For the extreme limit, where the orientation rise time is two-thirds of the regular reflection rise time (Structure 3.1s), the diffraction impulse is probably the same as if  $\theta$  were taken as zero since the effect of a decreased peak pressure and an increased diffraction period tend to cancel when computing their product which is proportional to the diffraction impulse. Thus the effect of orientation can again be neglected for the items in the regular reflection region of Shot 9.

In the case of Shot 10 the maximum value of  $\theta$  is only 4 deg and therefore negligible in computing the loads on the test items of Project 3.1.

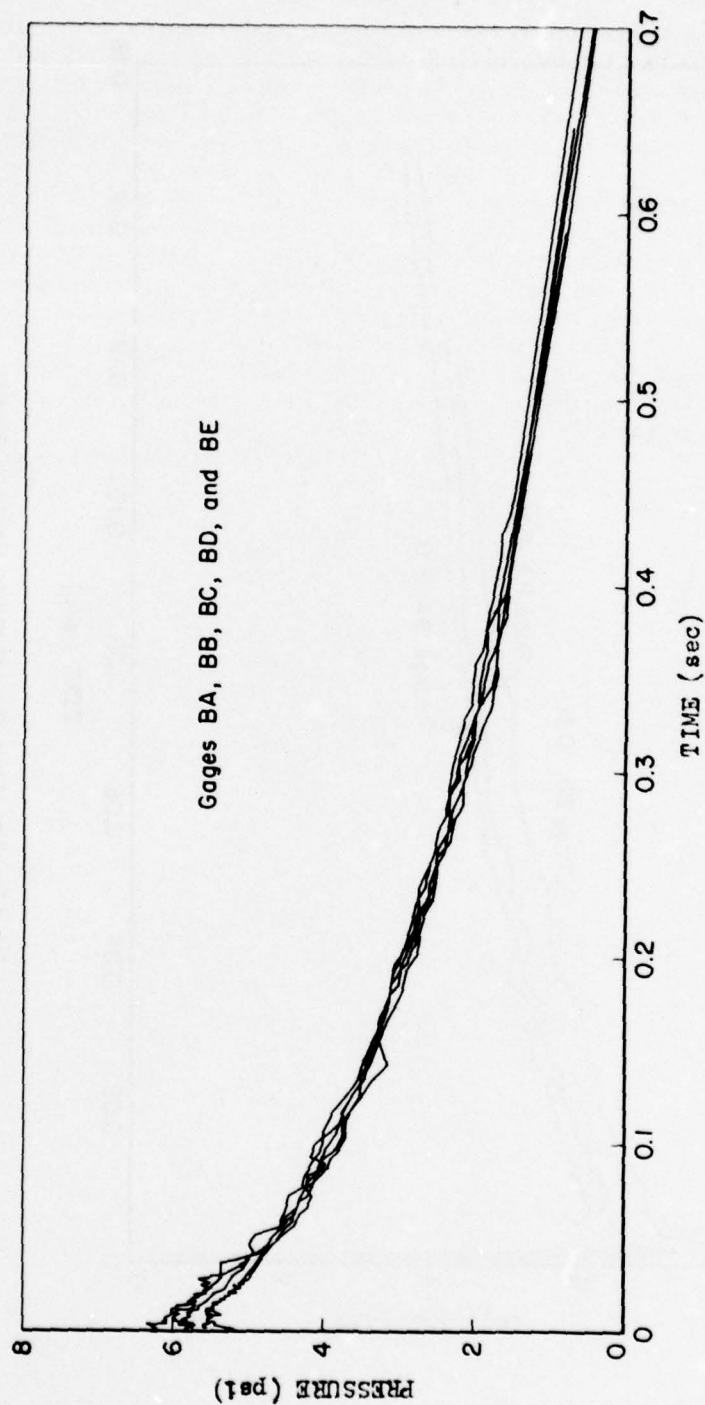


Fig. 4.1 — Free stream gages at ground level, Shot 9.



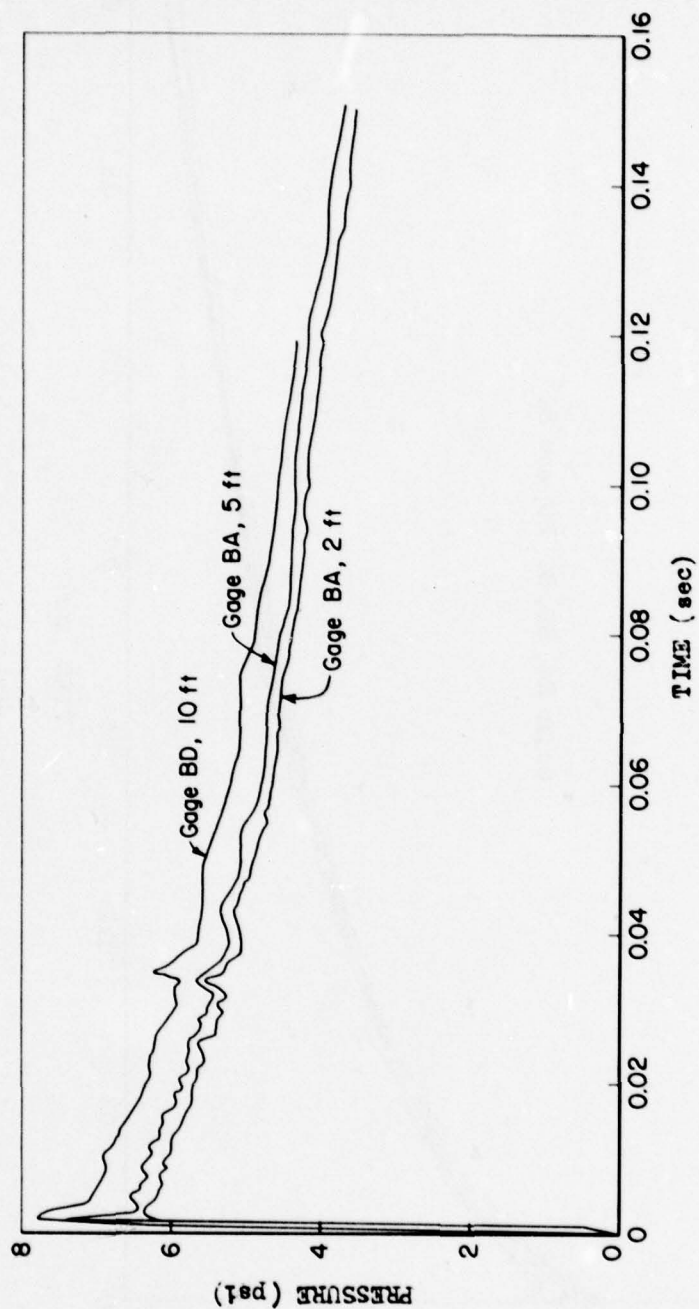


Fig. 4.2—Free stream gages at various elevations, Shot 9.

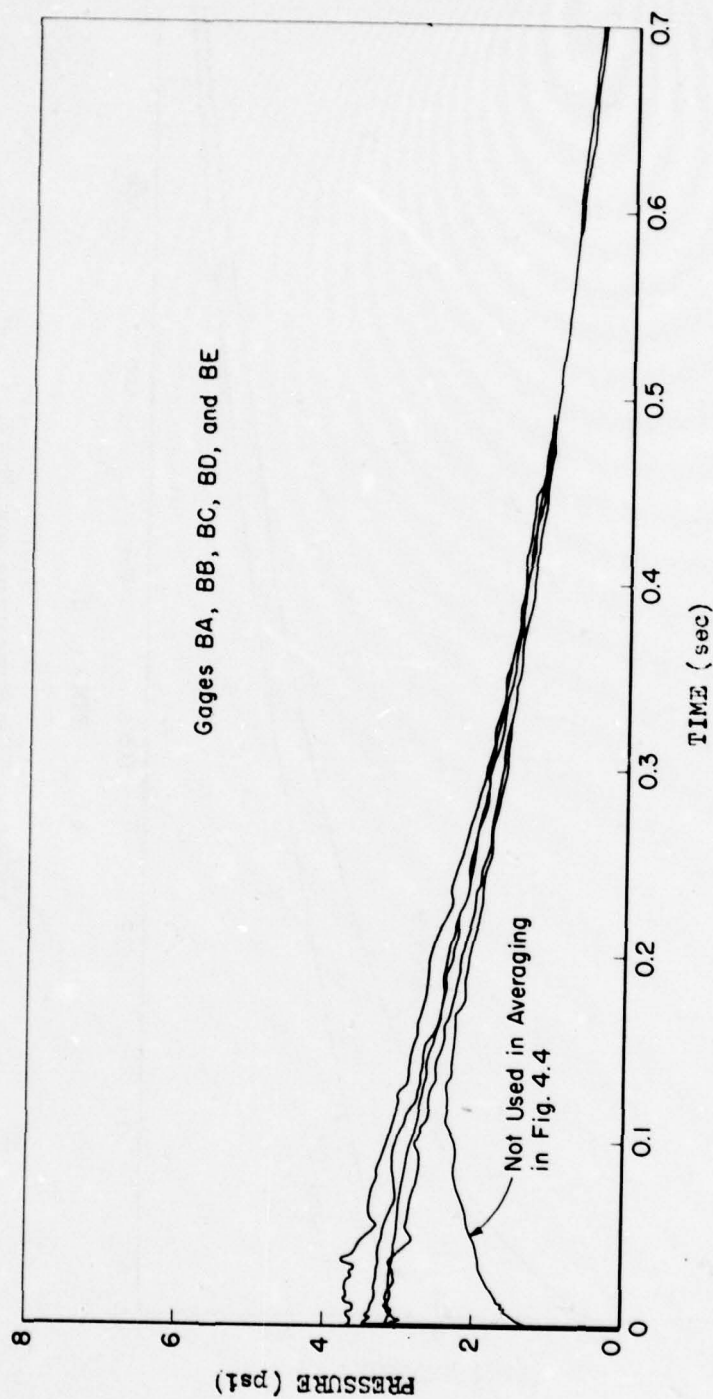


Fig. 4.3—Free stream gages at ground, Shot 10.

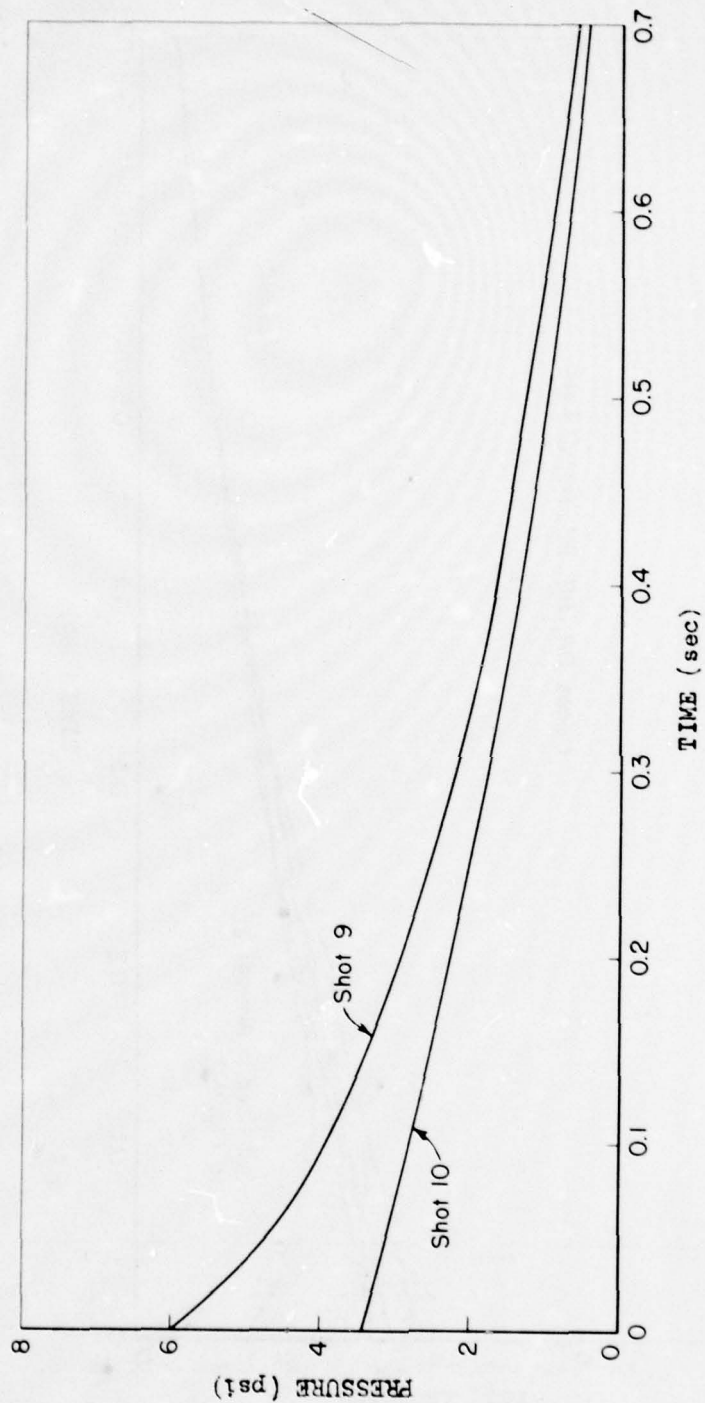


Fig. 4.4--Average of free stream gages, Shot 9.



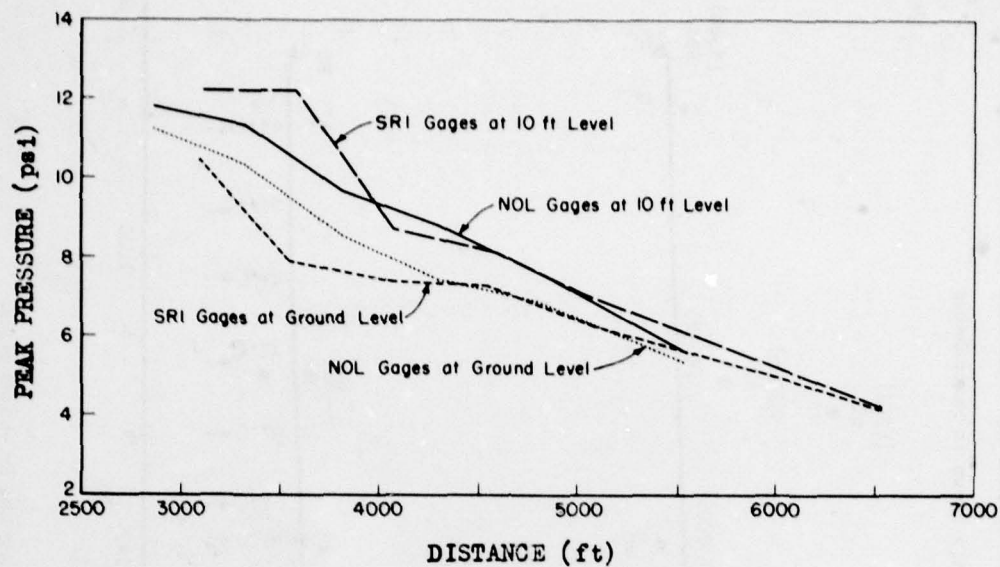


Fig. 4.5—Peak pressure vs distance from Ground Zero, Shot 9.

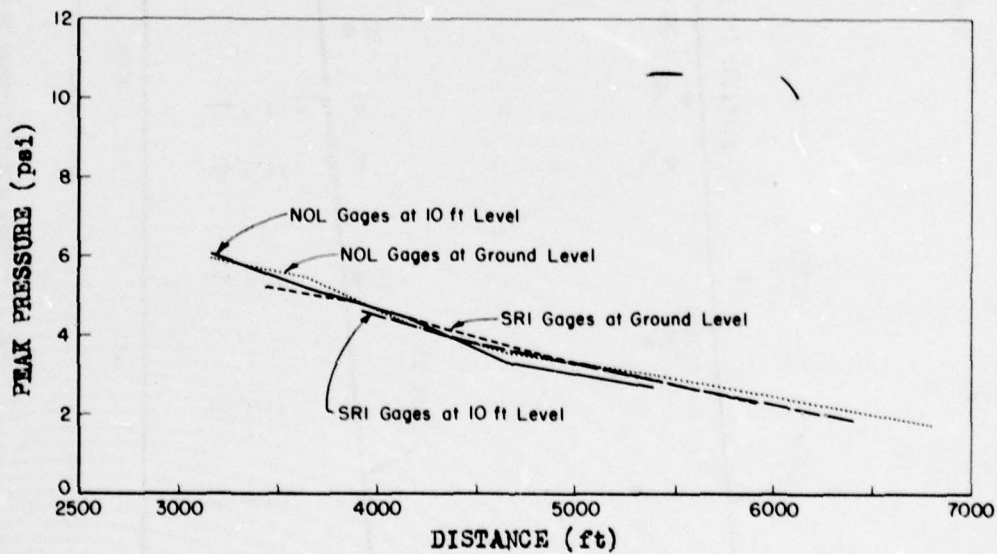


Fig. 4.6—Peak pressure vs distance from Ground Zero, Shot 10.

UNCLASSIFIED

~~SECRET RESTRICTED DATA~~

152

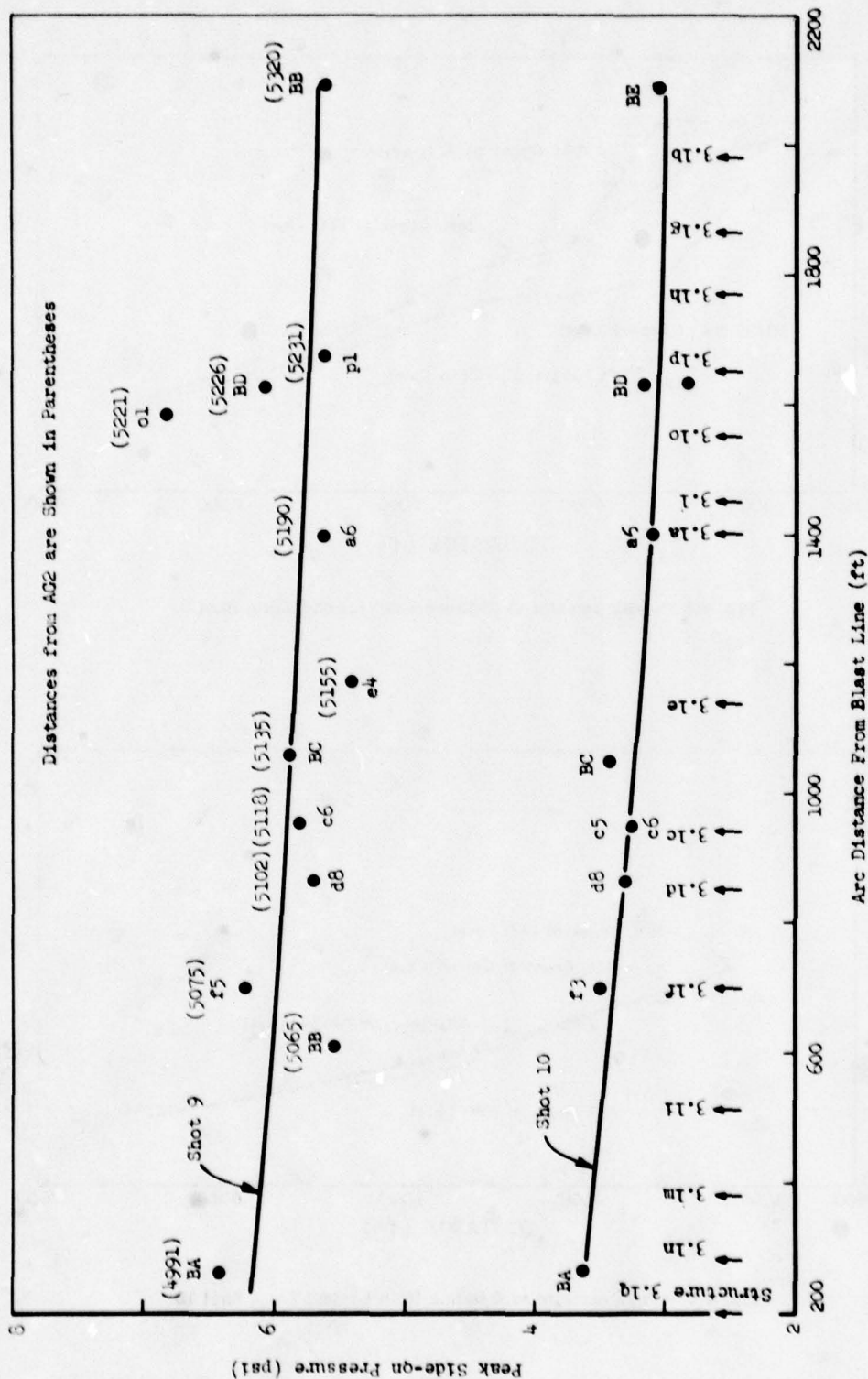


Fig. 4.7—Peak side-on pressure vs arc distance from blast line for various gages.

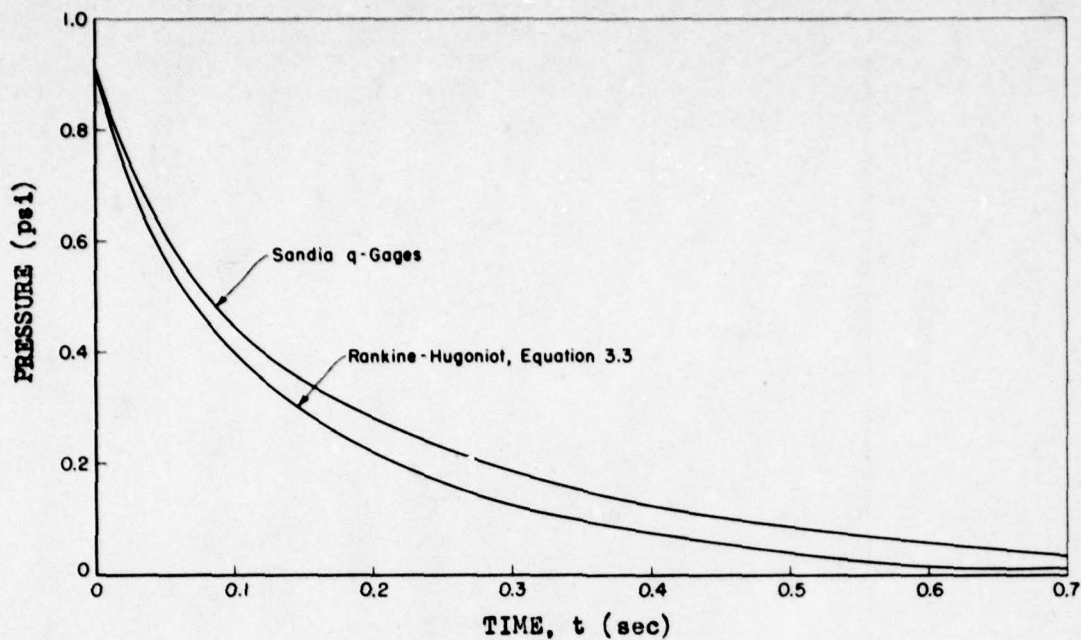


Fig. 4.8—Free stream dynamic pressure, Shot 9.

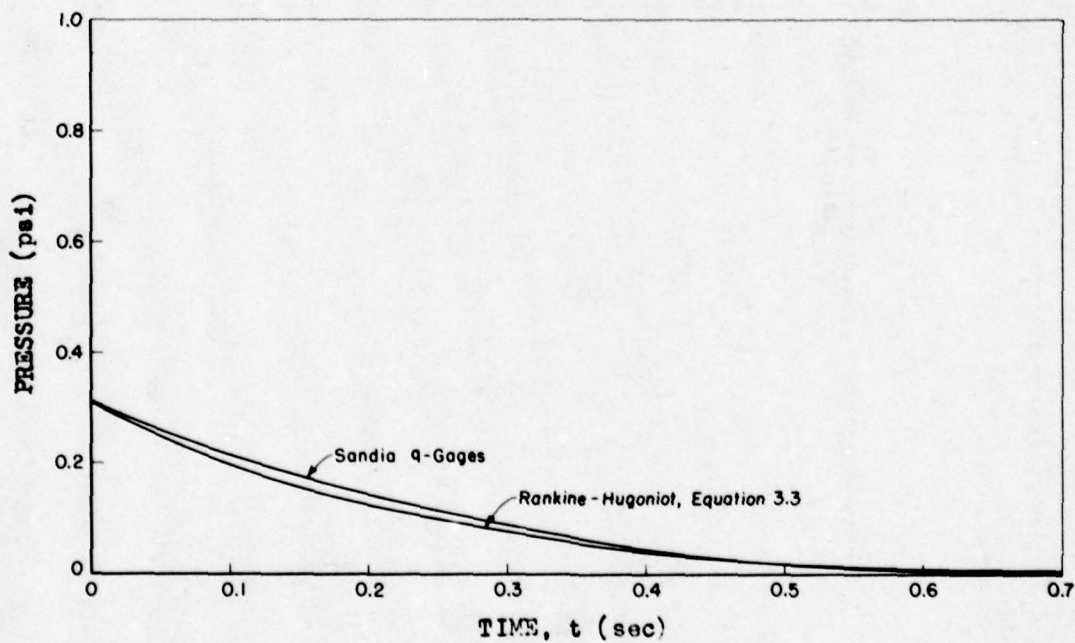


Fig. 4.9—Free stream dynamic pressure, Shot 10.



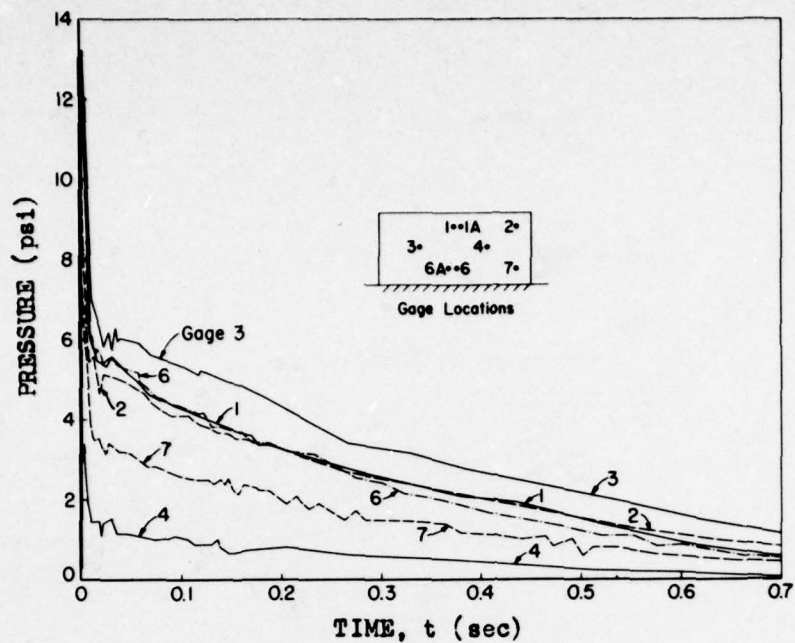


Fig. 4.10—Individual gage records, Structure 3.1a, front surface, Shot 9.

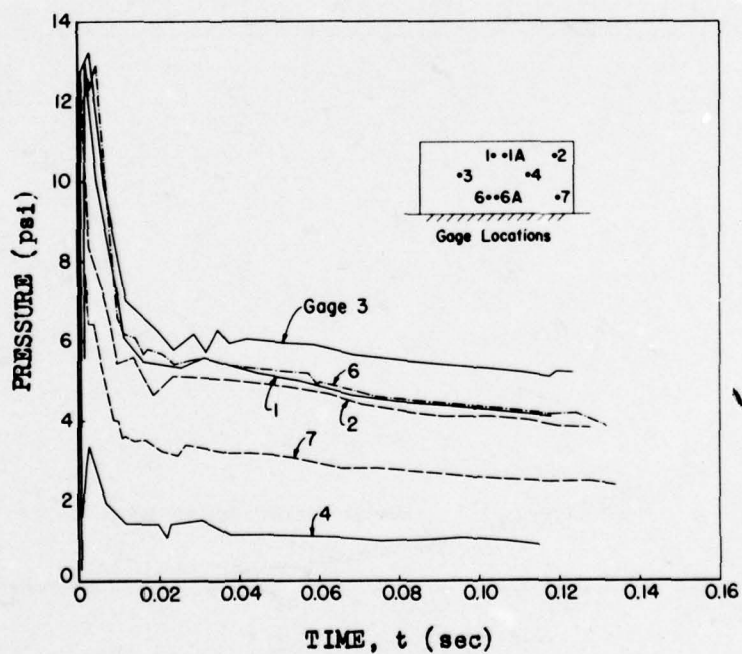


Fig. 4.11—Individual gage records, Structure 3.1a, front surface, Shot 9.

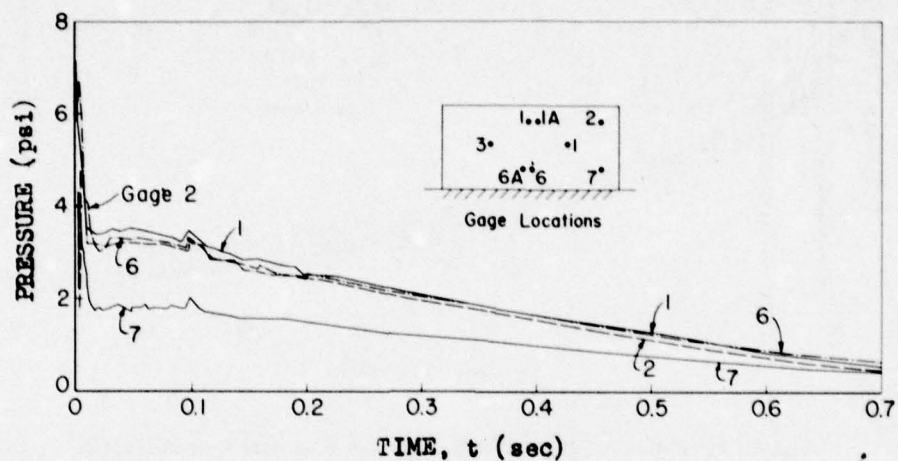


Fig. 4.12—Individual gage records, Structure 3.1a, front surface, Shot 10.

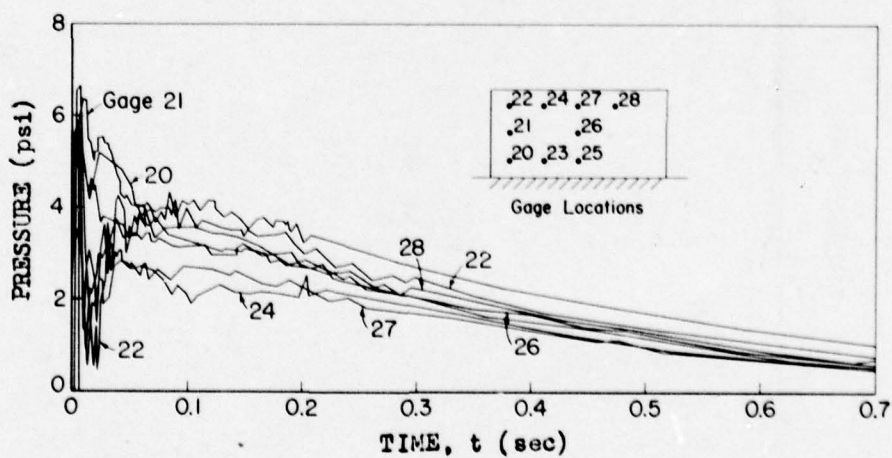


Fig. 4.13—Individual gage records, Structure 3.1a, top surface, Shot 9.

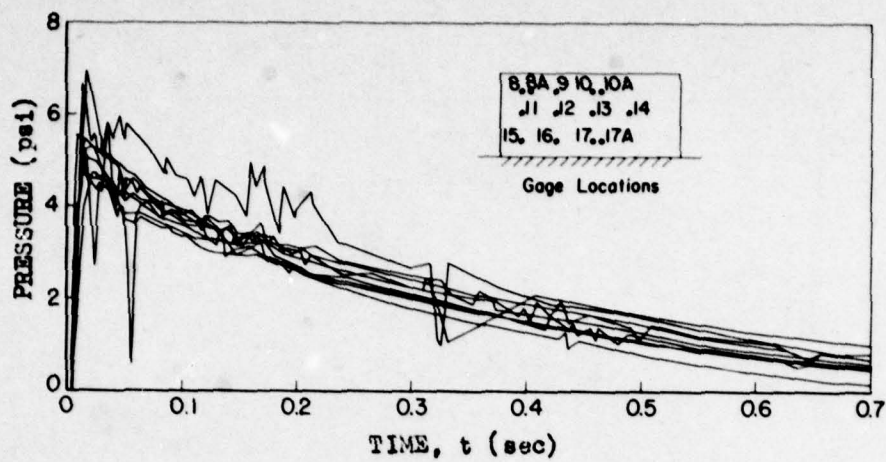


Fig. 4.14—Individual gage records, Structure 3.1a, rear surface, Shot 9.

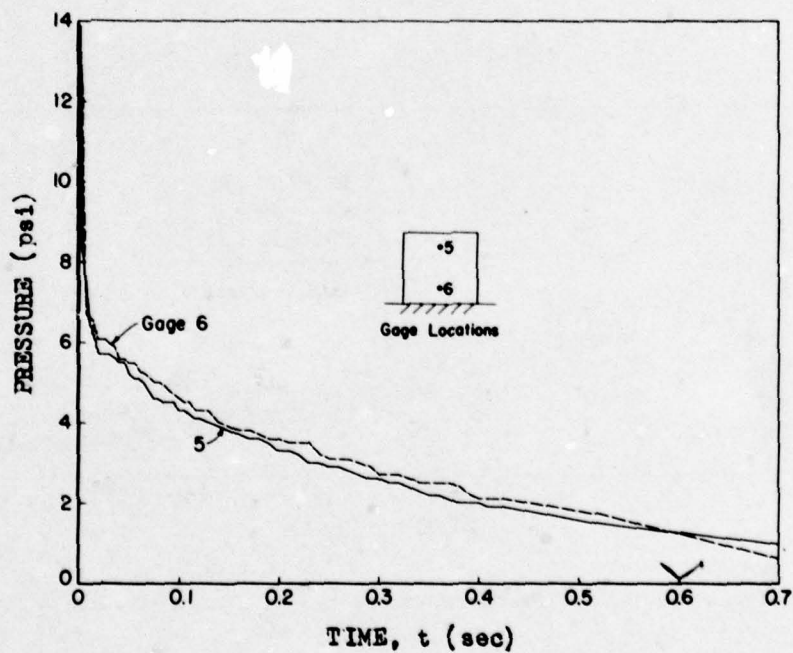


Fig. 4.15—Individual gage records, Structure 3.1c, front surface, Shot 9.



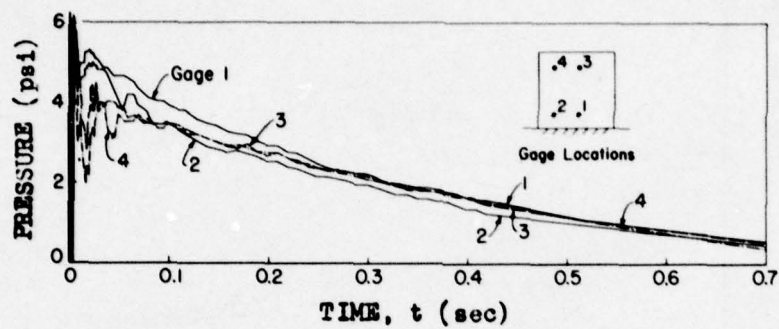


Fig. 4.16—Individual gage records, Structure 3.1c, top surface, Shot 9.

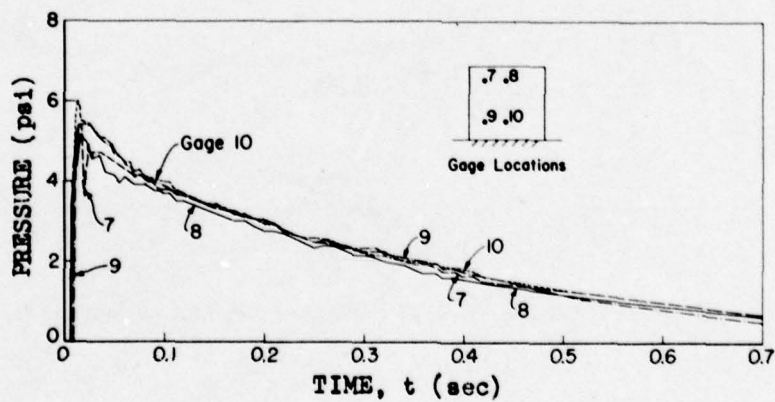


Fig. 4.17—Individual gage records, Structure 3.1c, rear surface, Shot 9.

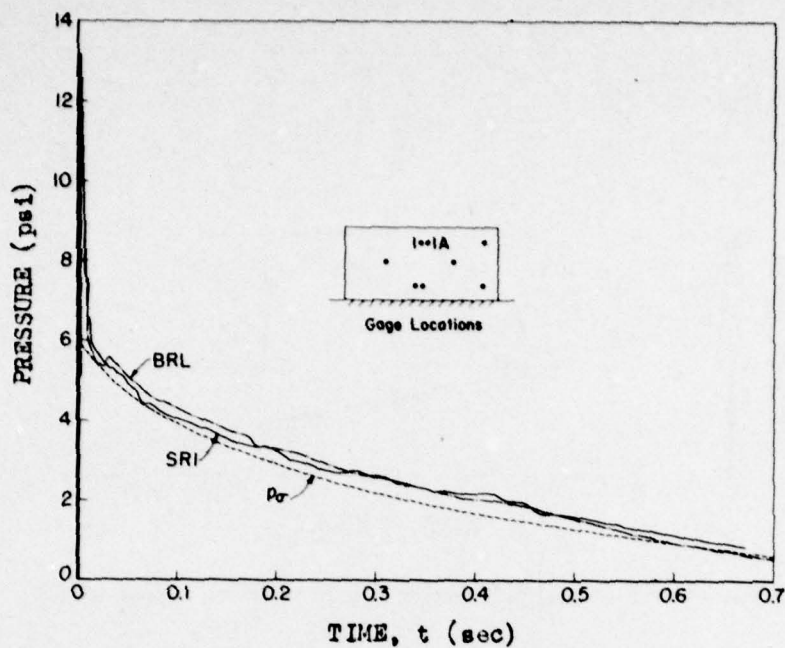


Fig. 4.18—Comparison of SRI and BRL check gages, Structure 3.1a, gages 1 and 1a, Shot 9.

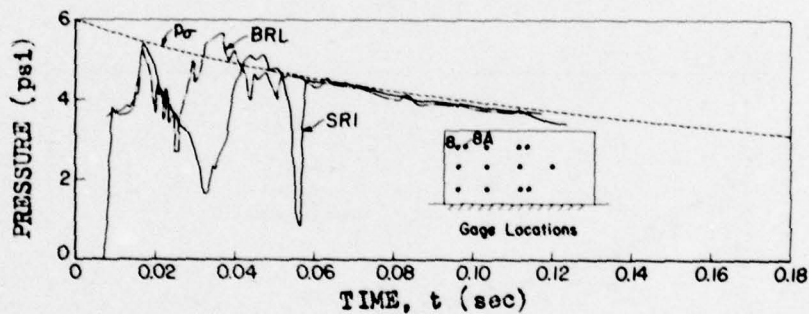


Fig. 4.19—Comparison of SRI and BRL check gages, Structure 3.1a, gages 8 and 8a, Shot 9.

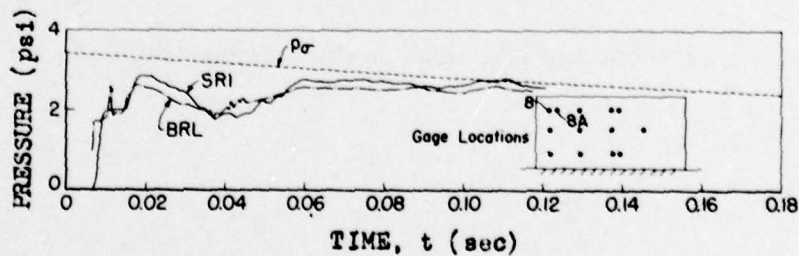


Fig. 4.20—Comparison of SRI and BRL check gages, Structure 3.1a, gages 8 and 8a, Shot 10.

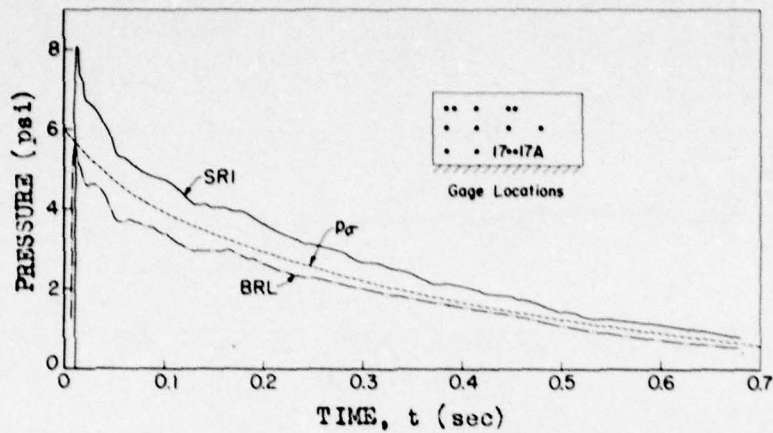


Fig. 4.21—Comparison of SRI and BRL check gages, Structure 3.1a, gages 17 and 17a, Shot 9.

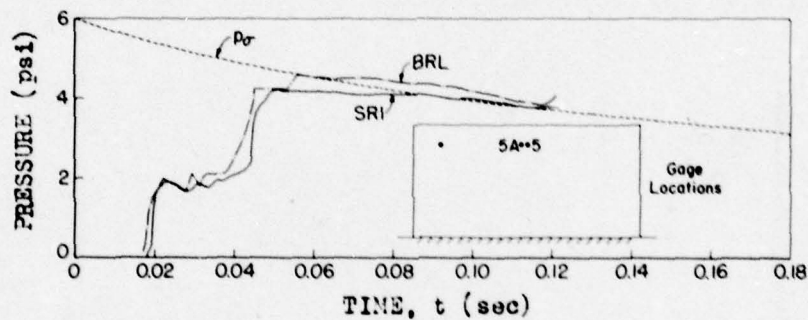


Fig. 4.22—Comparison of SRI and BRL check gages, Structure 3.1e, gages 5 and 5a, Shot 9.

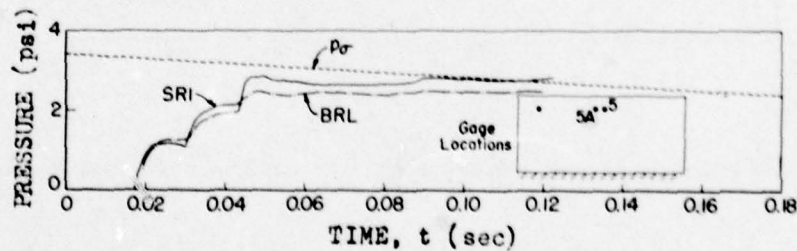


Fig. 4.23—Comparison of SRI and BRL check gages, Structure 3.1e, gages 5 and 5a, Shot 10.



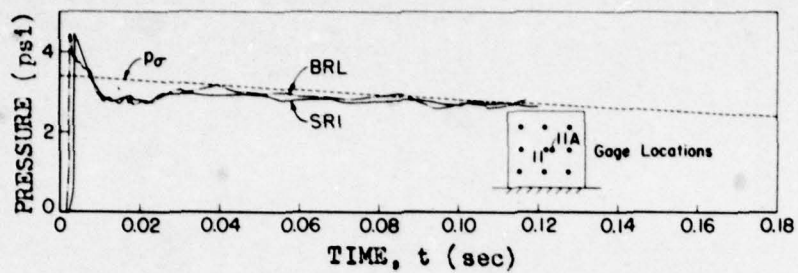


Fig. 4.24—Comparison of SRI and BRL check gages, Structure 3.1g, gages 11 and 11a, Shot 10.

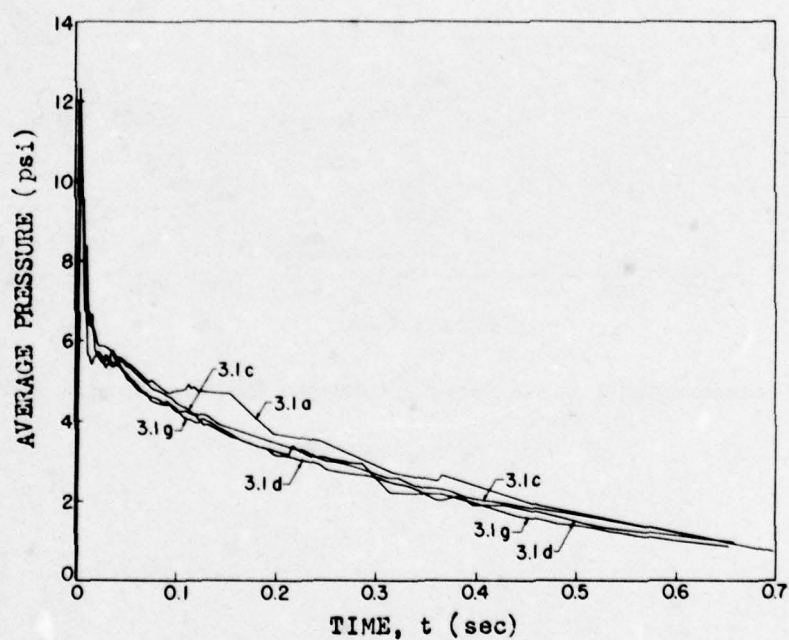


Fig. 4.25—Average pressure on front surfaces, Structures 3.1a, c, d, and g, Shot 9.

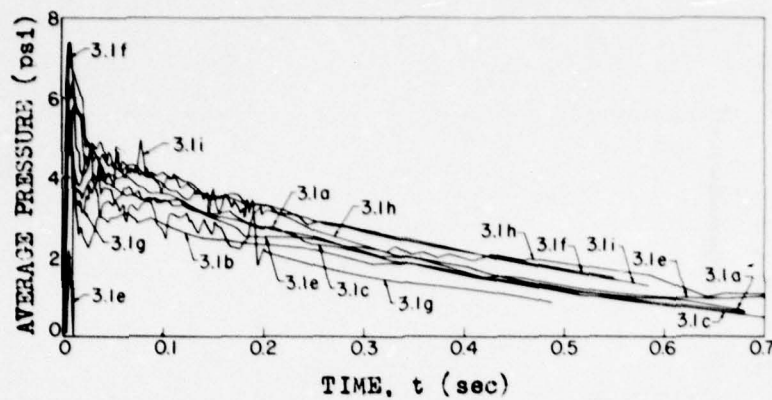


Fig. 4.26 — Average pressure on top surfaces, Structures 3.1a to c and e to i, Shot 9.

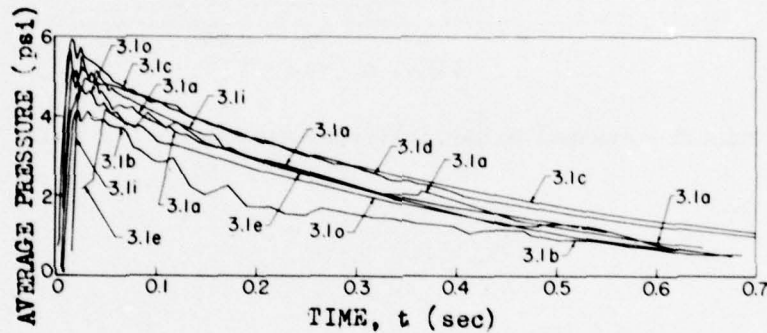


Fig. 4.27 — Average pressure on rear surfaces, Structures 3.1a to e, i, and o, Shot 9.

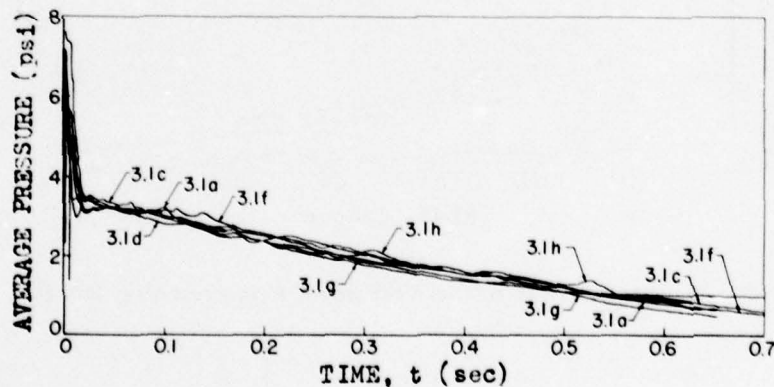


Fig. 4.28 — Average pressure on front surfaces, Structures 3.1a, c, d, and f to h, Shot 10.

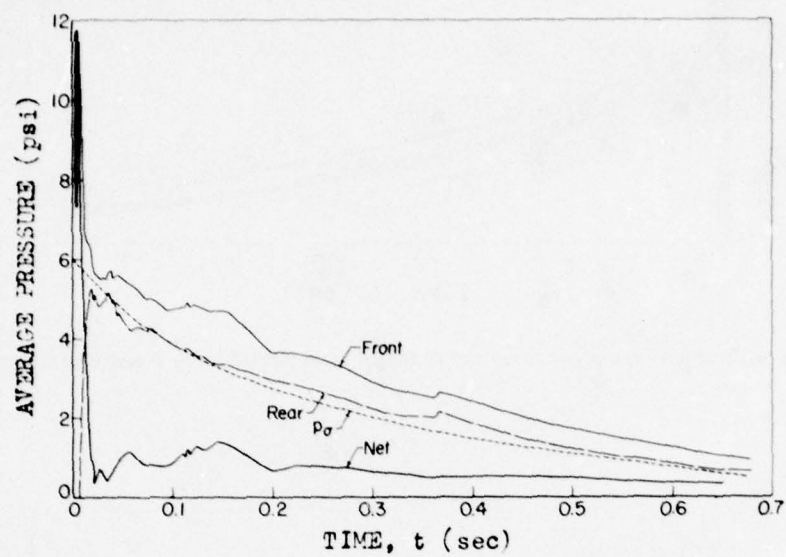


Fig. 4.29 — Average front, rear, and net pressures, Structure 3.1a, Shot 9.

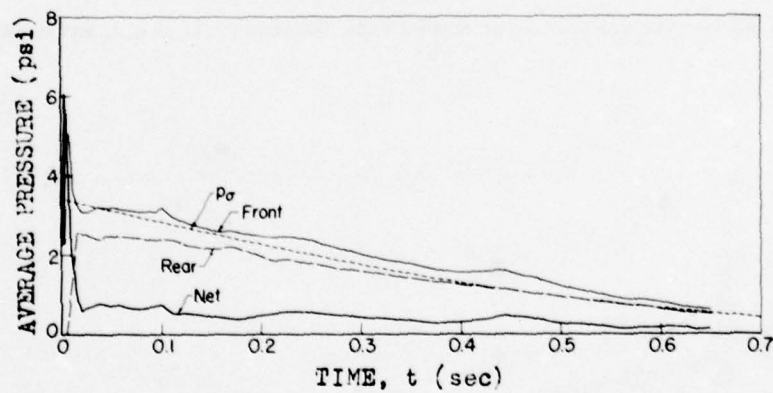


Fig. 4.30 — Average front, rear, and net pressures, Structure 3.1a, Shot 10.

UNCLASSIFIED

~~SECRET RESTRICTED DATA~~



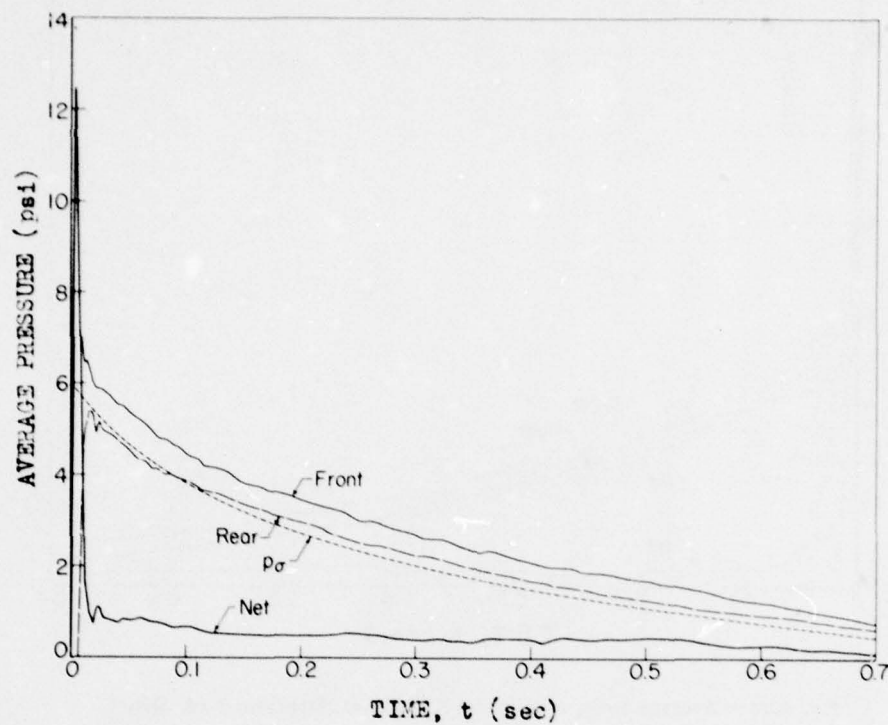


Fig. 4.31 — Average front, rear, and net pressures, Structure 3.1c, Shot 9.

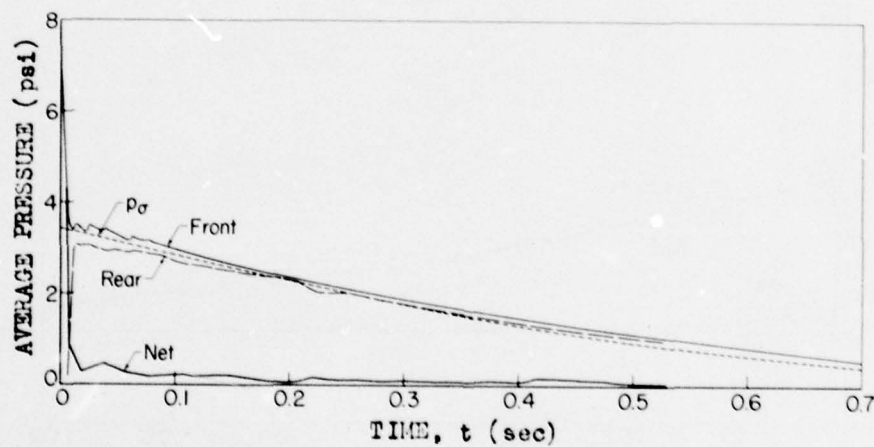


Fig. 4.32 — Average front, rear, and net pressures, Structure 3.1c, Shot 10.

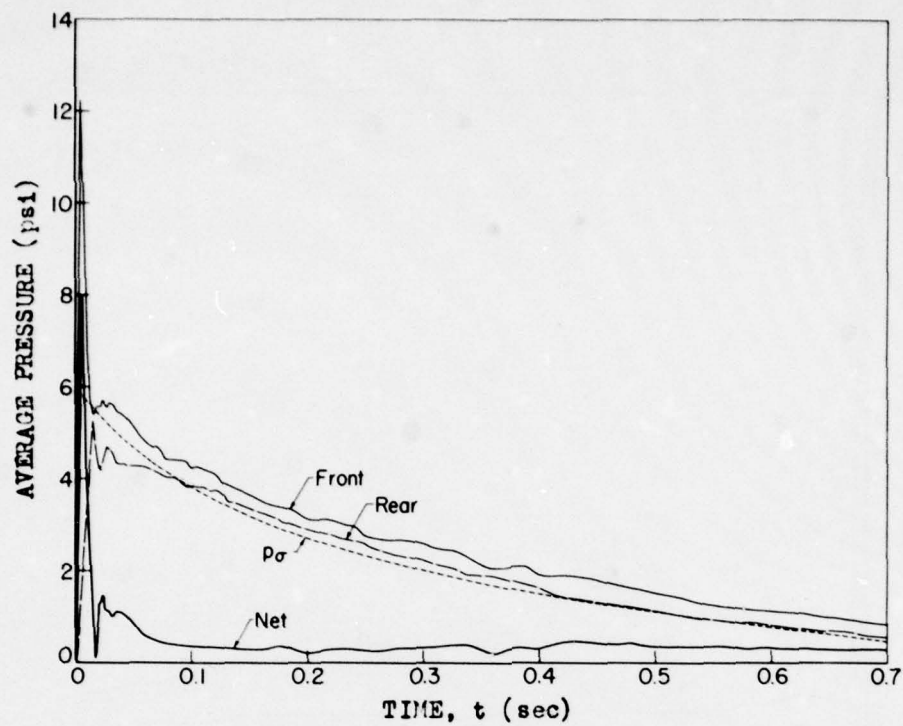


Fig. 4.33—Average front, rear, and net pressures, Structure 3.1d, Shot 9.

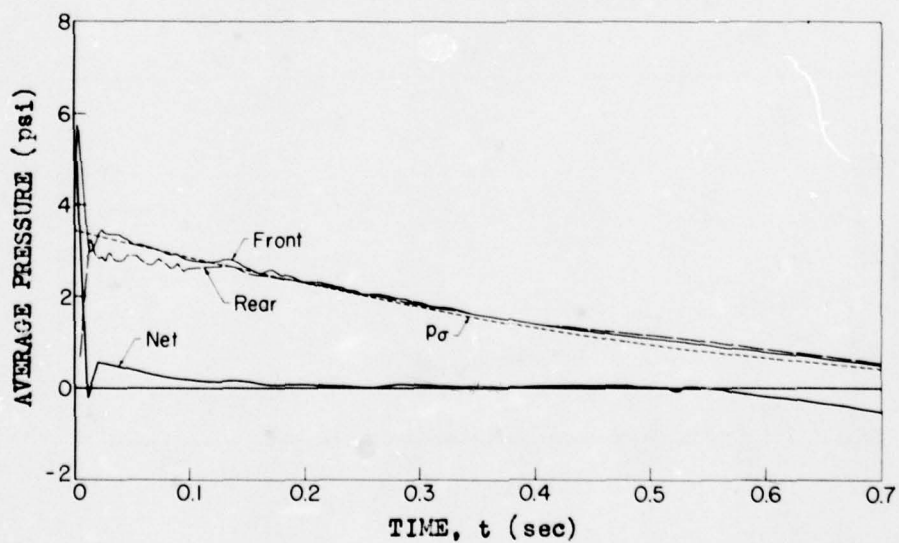


Fig. 4.34—Average front, rear, and net pressures, Structure 3.1d, Shot 10.

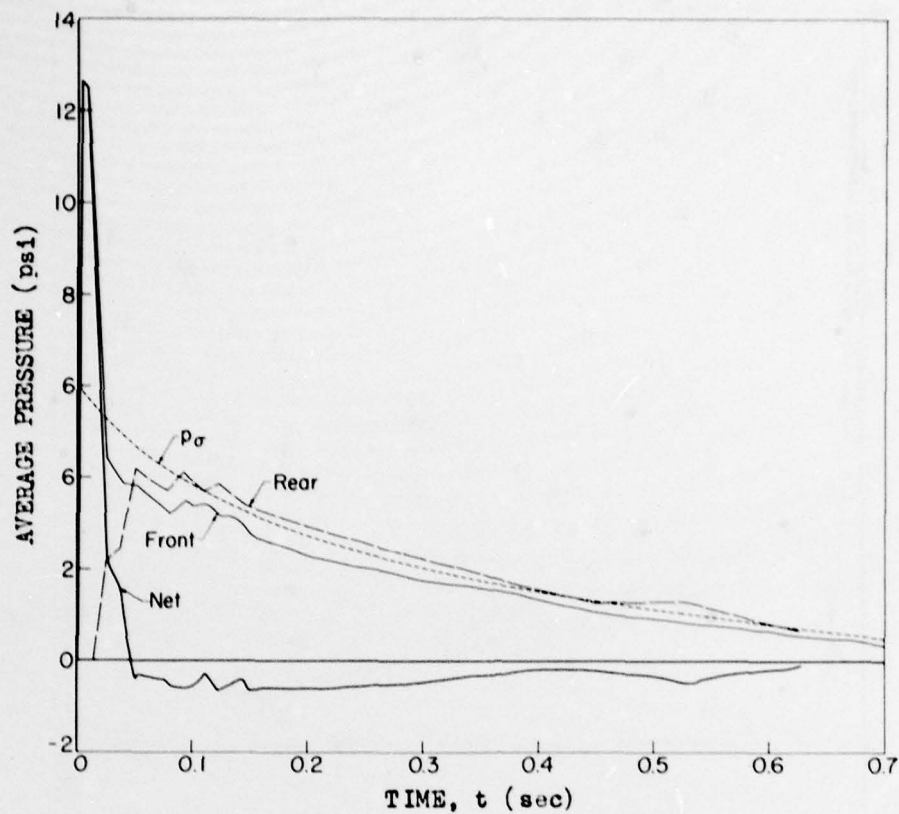


Fig. 4.35—Average front, rear, and net pressures, Structure 3.1e, Shot 9.

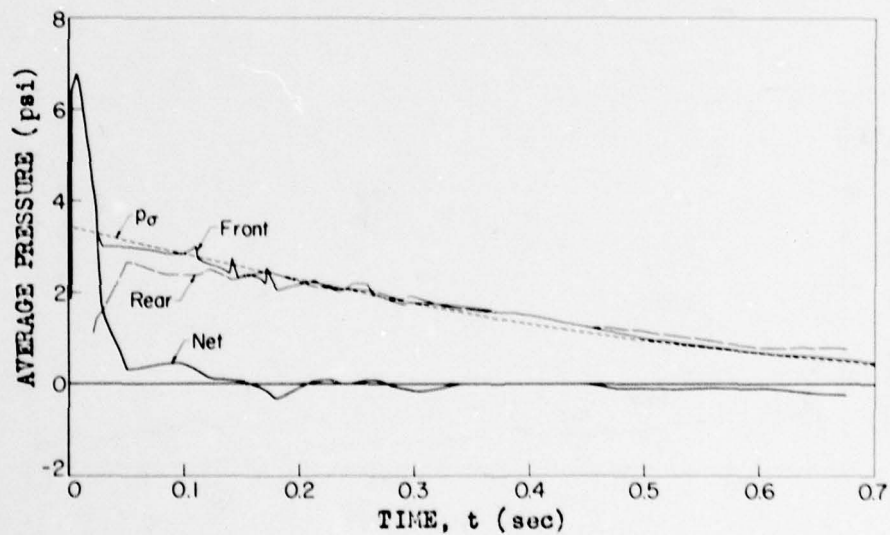


Fig. 4.36—Average front, rear, and net pressures, Structure 3.1e, Shot 10.



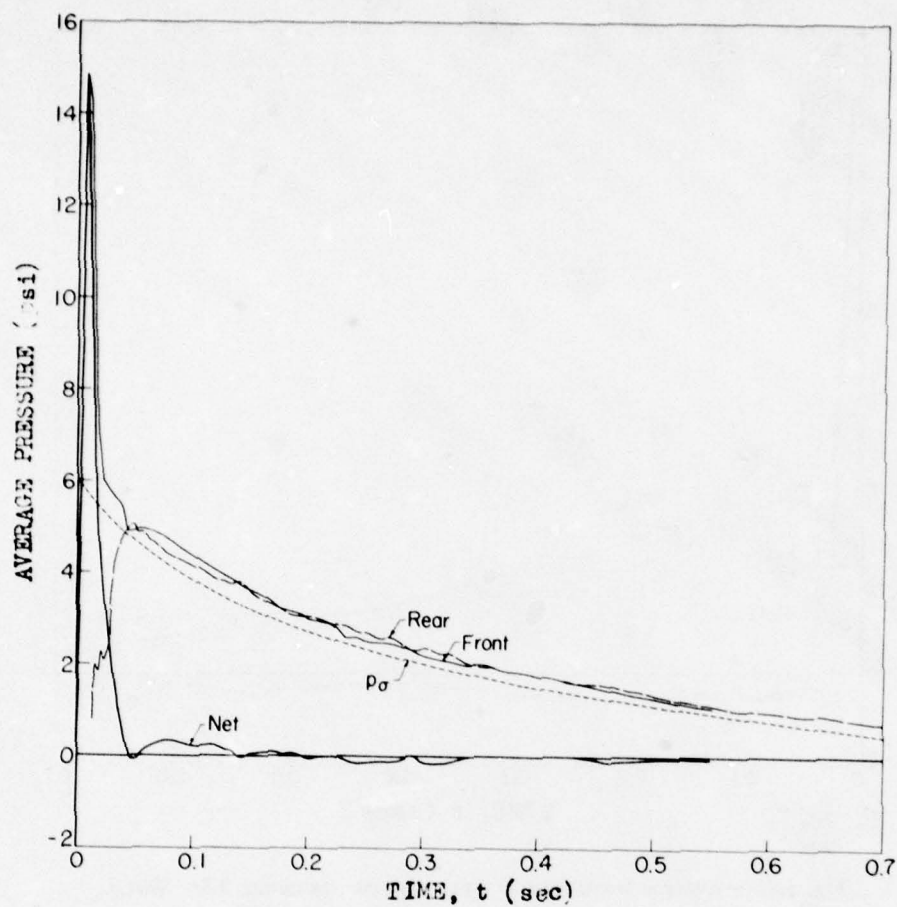


Fig. 4.37—Average front, rear, and net pressures, Structure 3.1f, Shot 9.

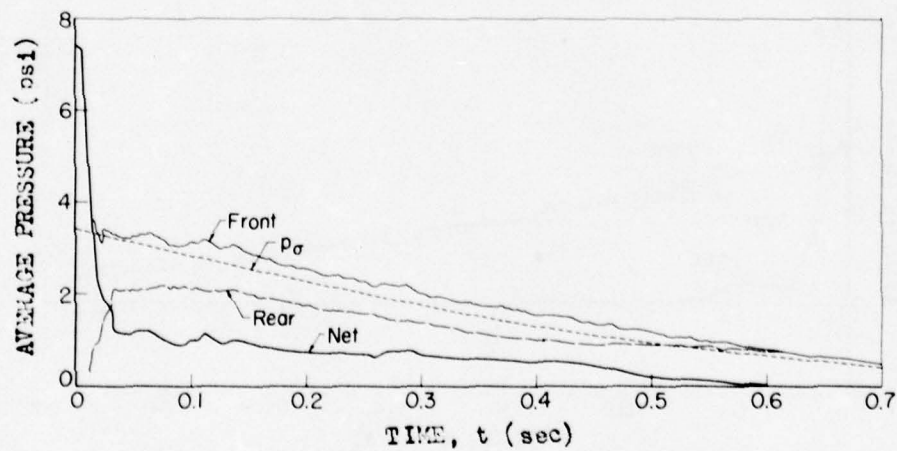


Fig. 4.38—Average front, rear, and net pressures, Structure 3.1f, Shot 10.

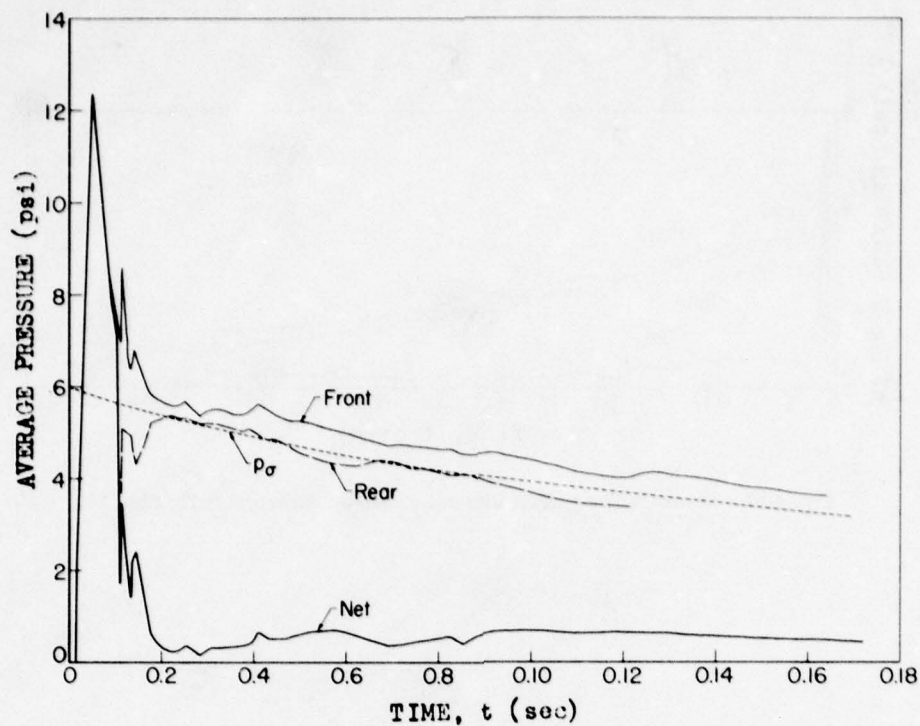


Fig. 4.39—Average front, rear, and net pressures, Structure 3.1g, Shot 9.

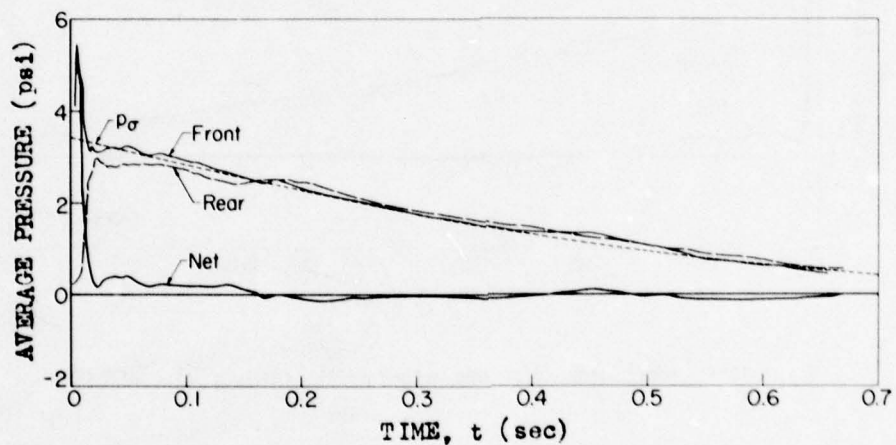


Fig. 4.40—Average front, rear, and net pressures, Structure 3.1g, Shot 10.

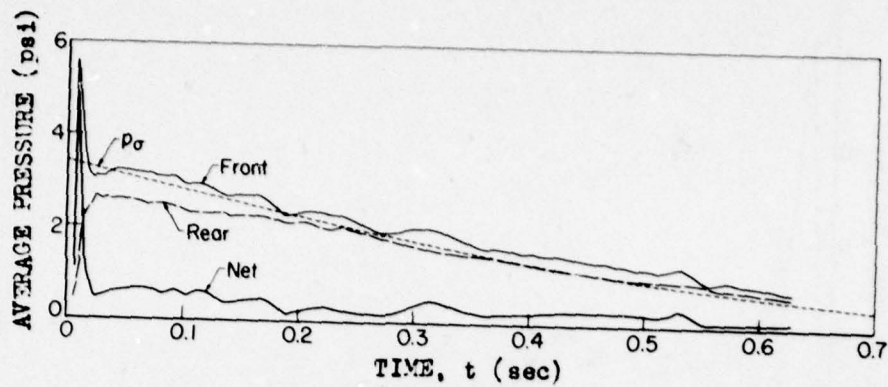


Fig. 4.41 — Average front, rear, and net pressures, Structure 3.1h, Shot 10.

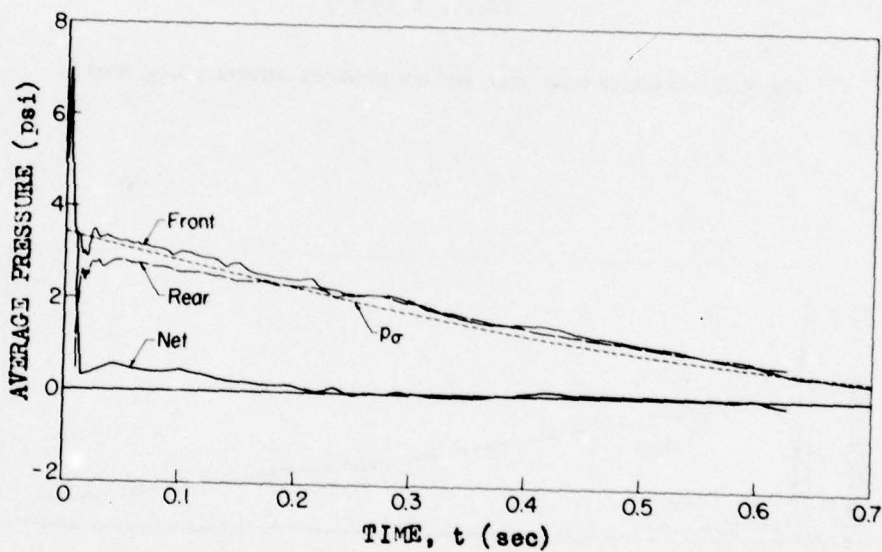


Fig. 4.42 — Average front, rear, and net pressures, Structure 3.1o, Shot 10.



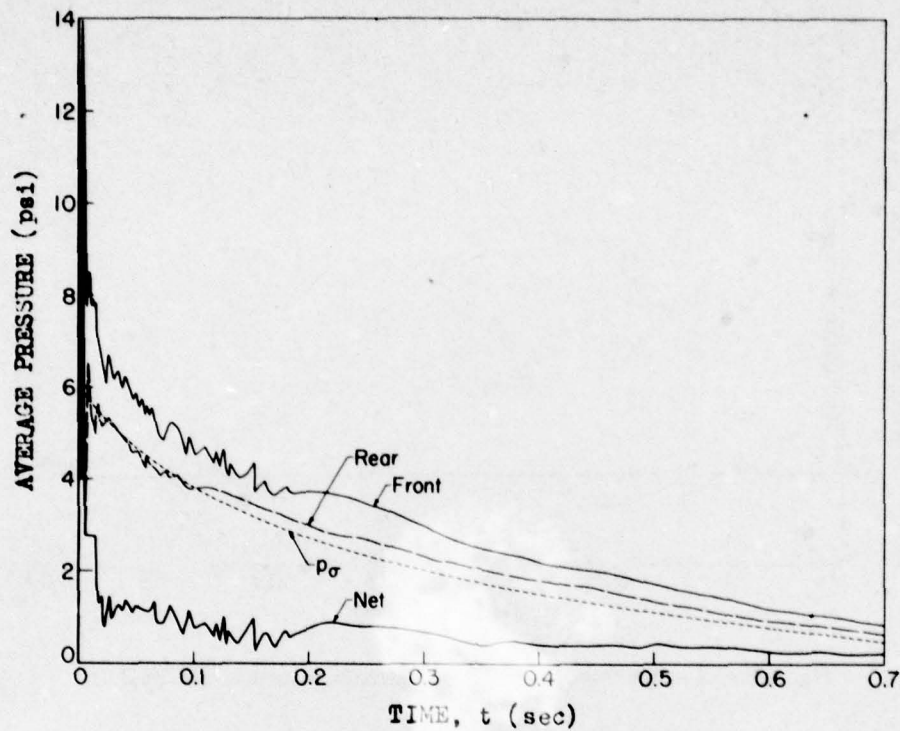


Fig. 4.43—Average front, rear, and net pressures, Structure 3.1p, Shot 9.

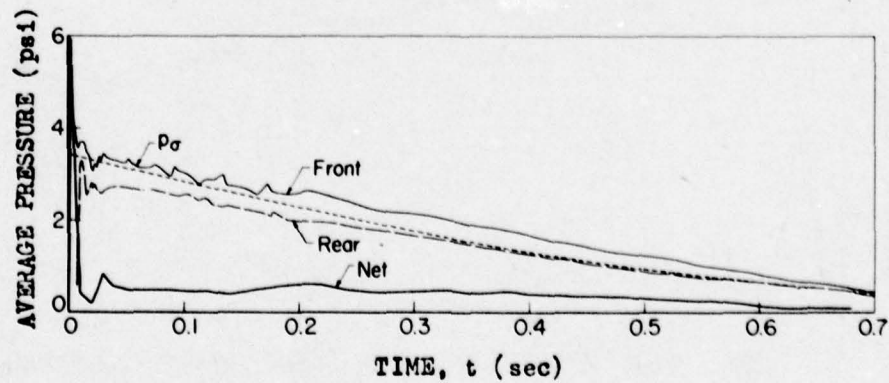


Fig. 4.44—Average front, rear, and net pressures, Structure 3.1p, Shot 10.

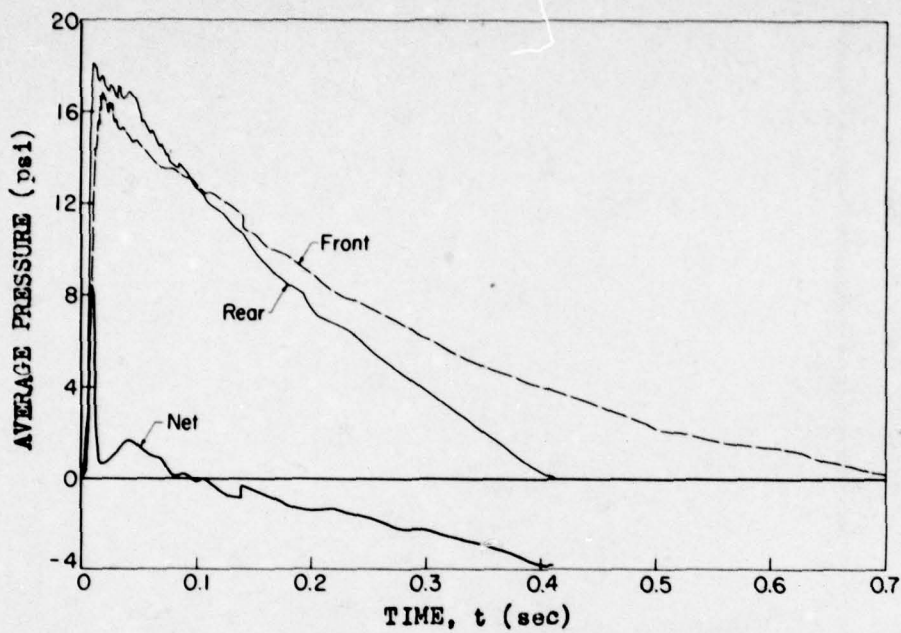


Fig. 4.45—Average front, rear, and net pressures, Structure 3.1s, Shot 9.

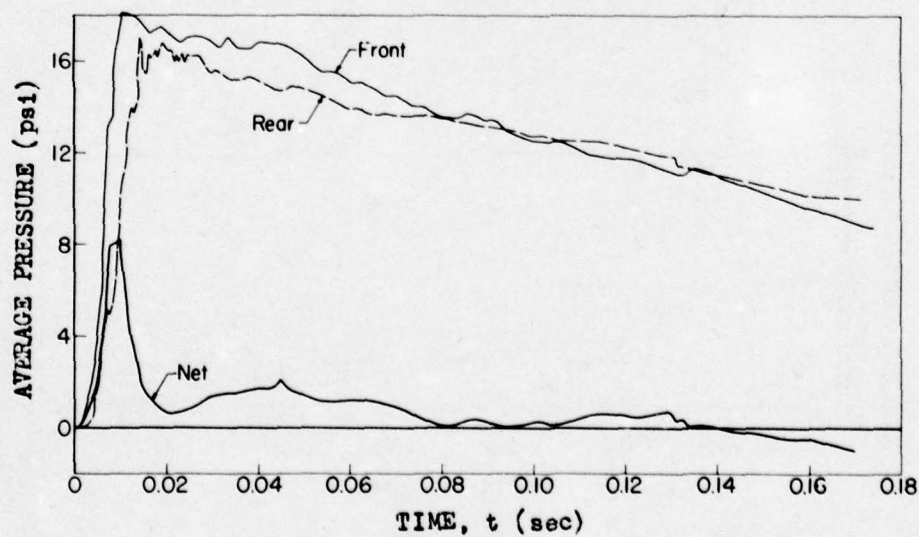


Fig. 4.46—Average front, rear, and net pressures, Structure 3.1s, Shot 9.

UNCLASSIFIED

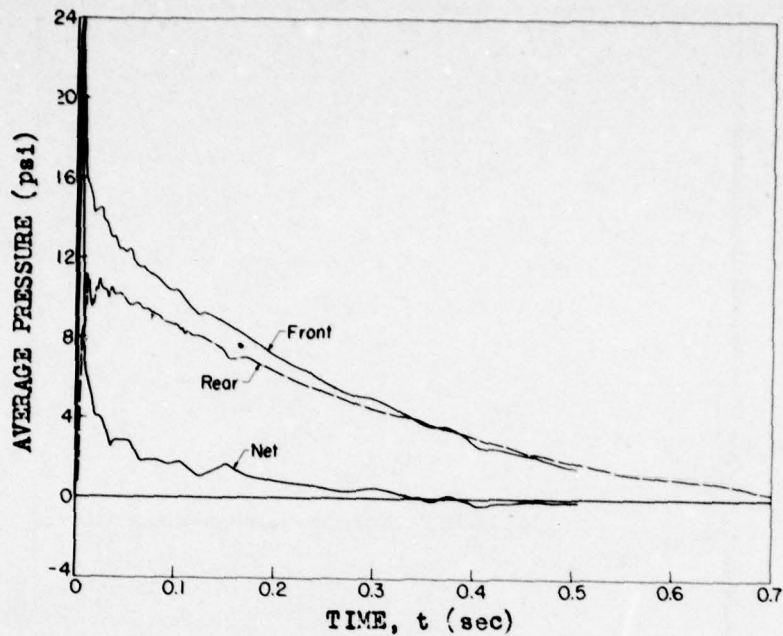


Fig. 4.47—Average front, rear, and net pressures, Structure 3.1t, Shot 9.

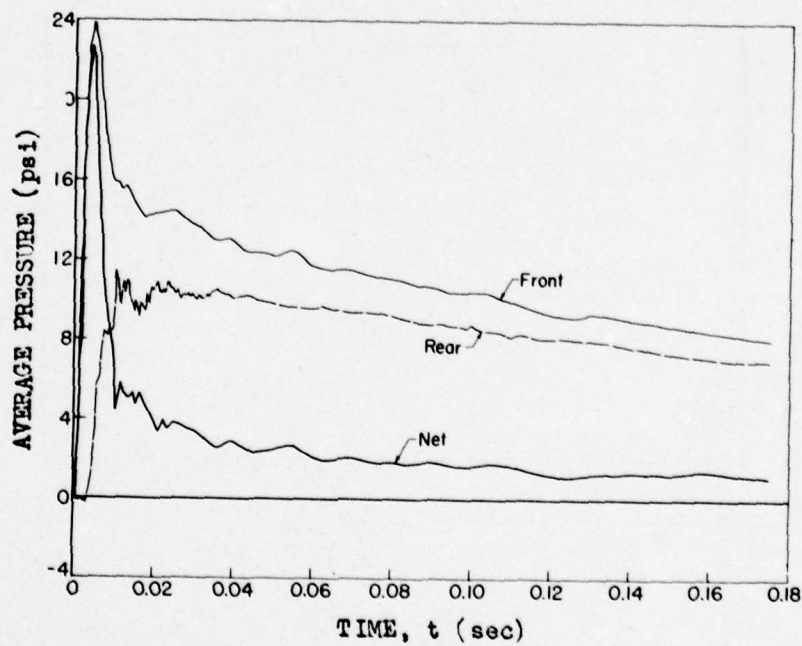


Fig. 4.48—Average front, rear, and net pressures, Structure 3.1t, Shot 9.



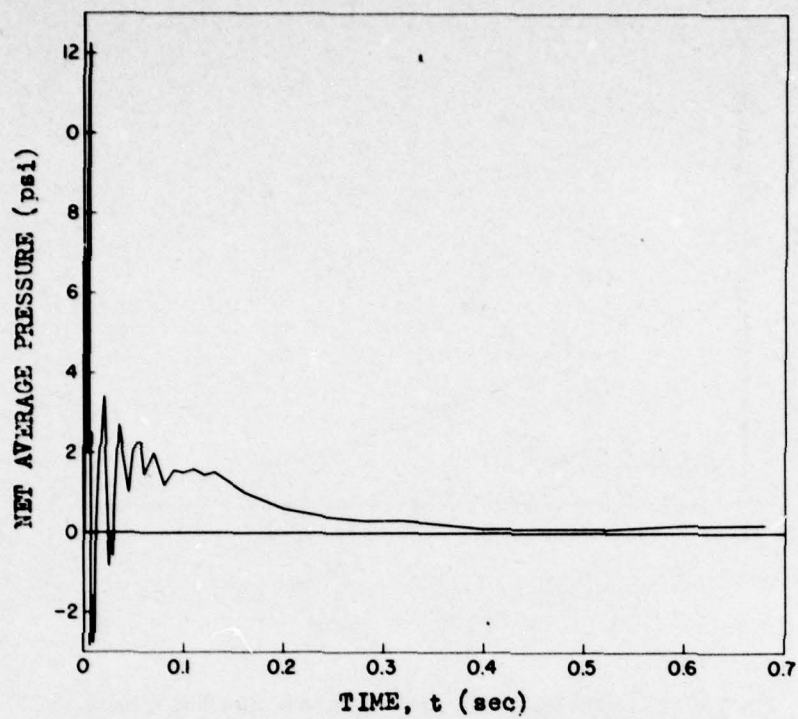


Fig. 4.49—Net average pressure, Structure 3.1l, shielding wall, Shot 9.

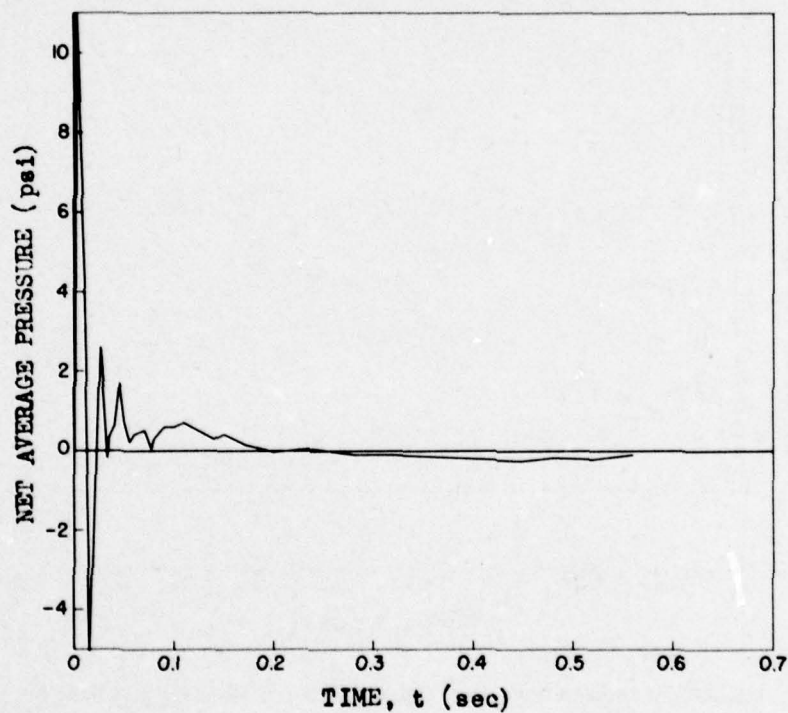


Fig. 4.50—Net average pressure, Structure 3.1n, shielding wall, Shot 9.

**UNCLASSIFIED**

~~SECRET RESTRICTED DATA~~

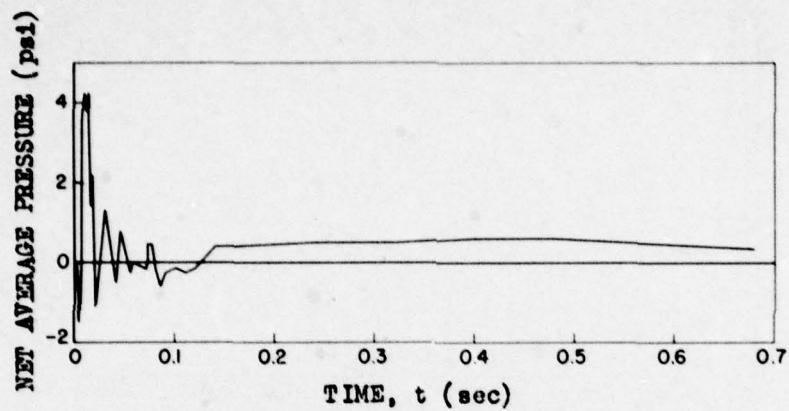


Fig. 4.51 — Net average pressure, Structure 3.11, shielded wall, Shot 9.

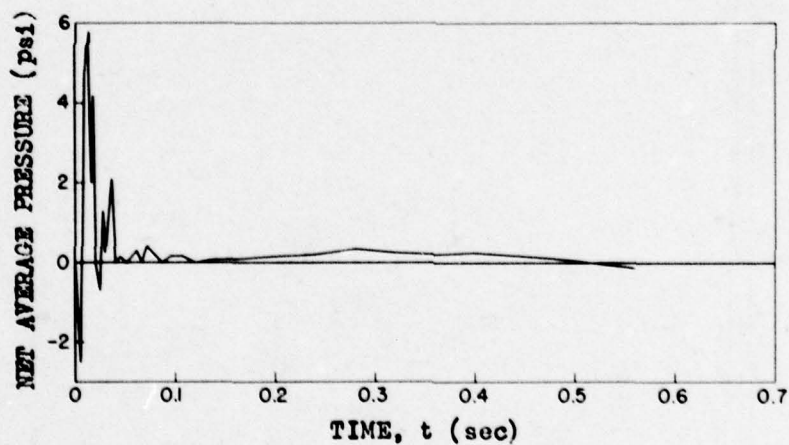


Fig. 4.52 — Net average pressure, Structure 3.1m, shielded wall, Shot 9.

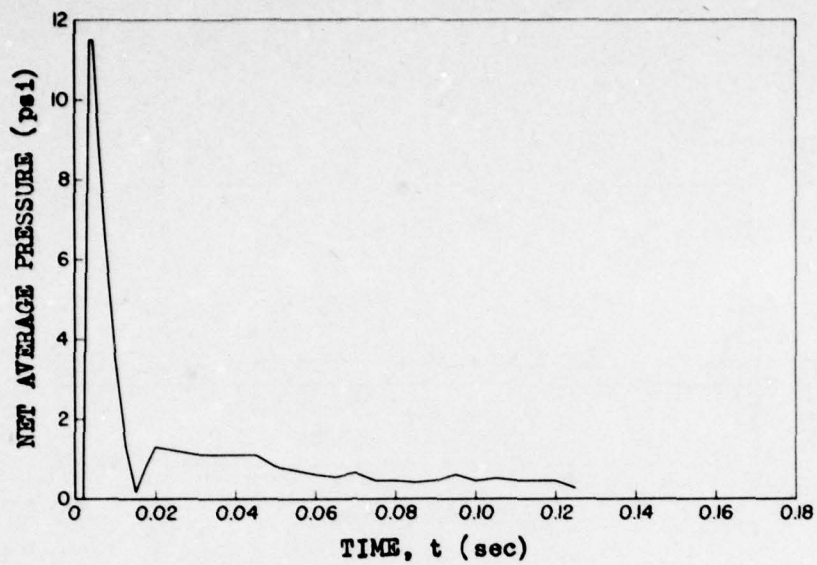


Fig. 4.53—Net average pressure, Structure 3.1d, Shot 9.

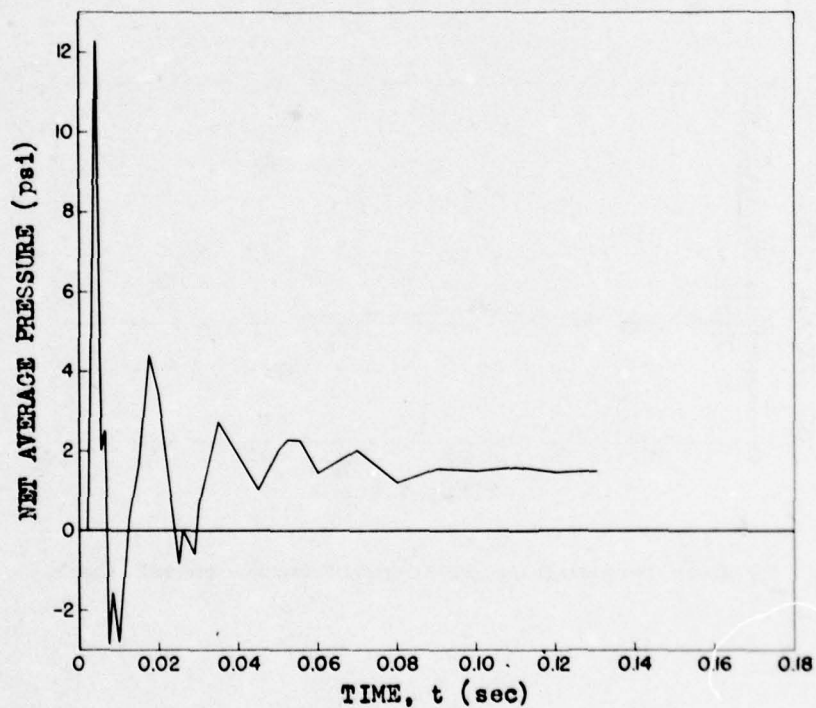


Fig. 4.54—Net average pressure, Structure 3.11, shielding wall, Shot 9.



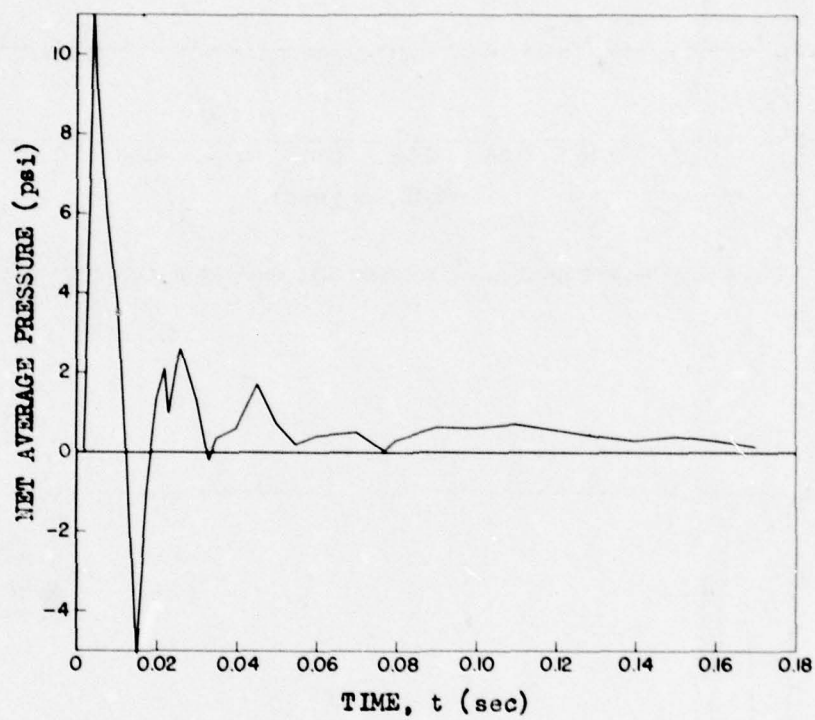


Fig. 4.55—Net average pressure, Structure 3.1m, shielding wall, Shot 9.

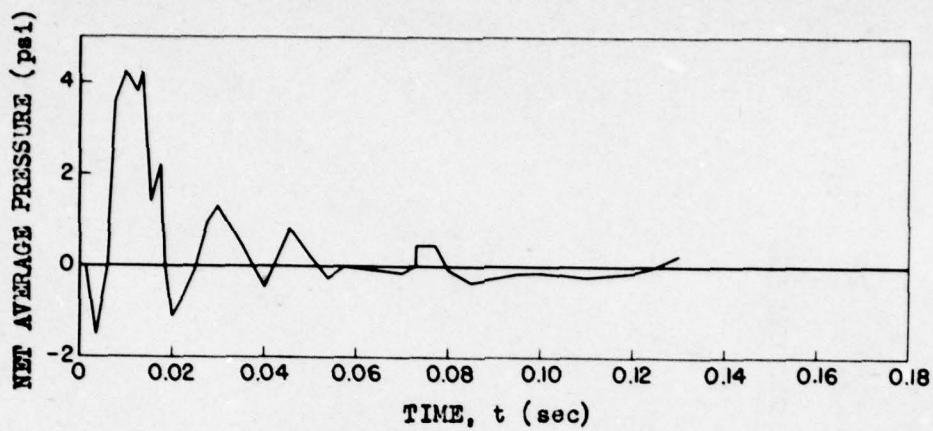


Fig. 4.56—Net average pressure, Structure 3.11, shielded wall, Shot 9.

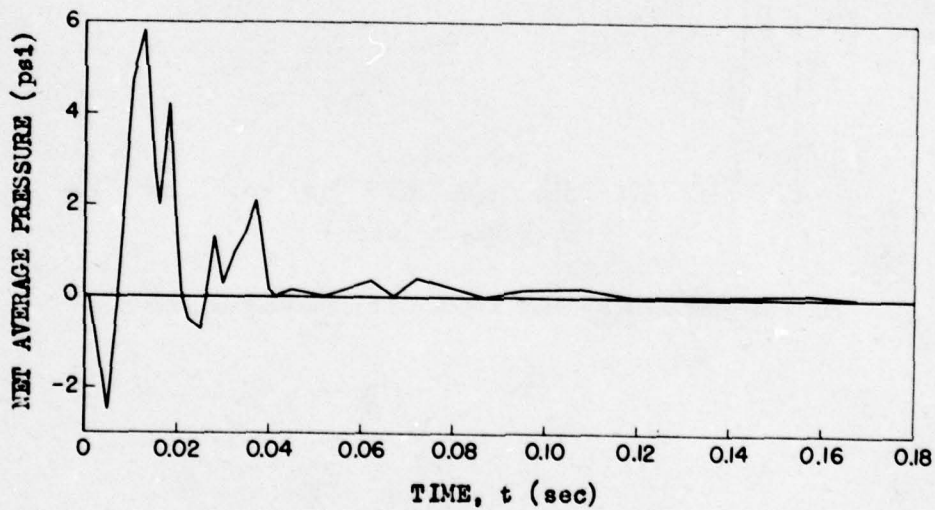


Fig. 4.57—Net average pressure, Structure 3.1m, shielded wall, Shot 9.

UNCLASSIFIED

~~SECRET RESTRICTED DATA~~

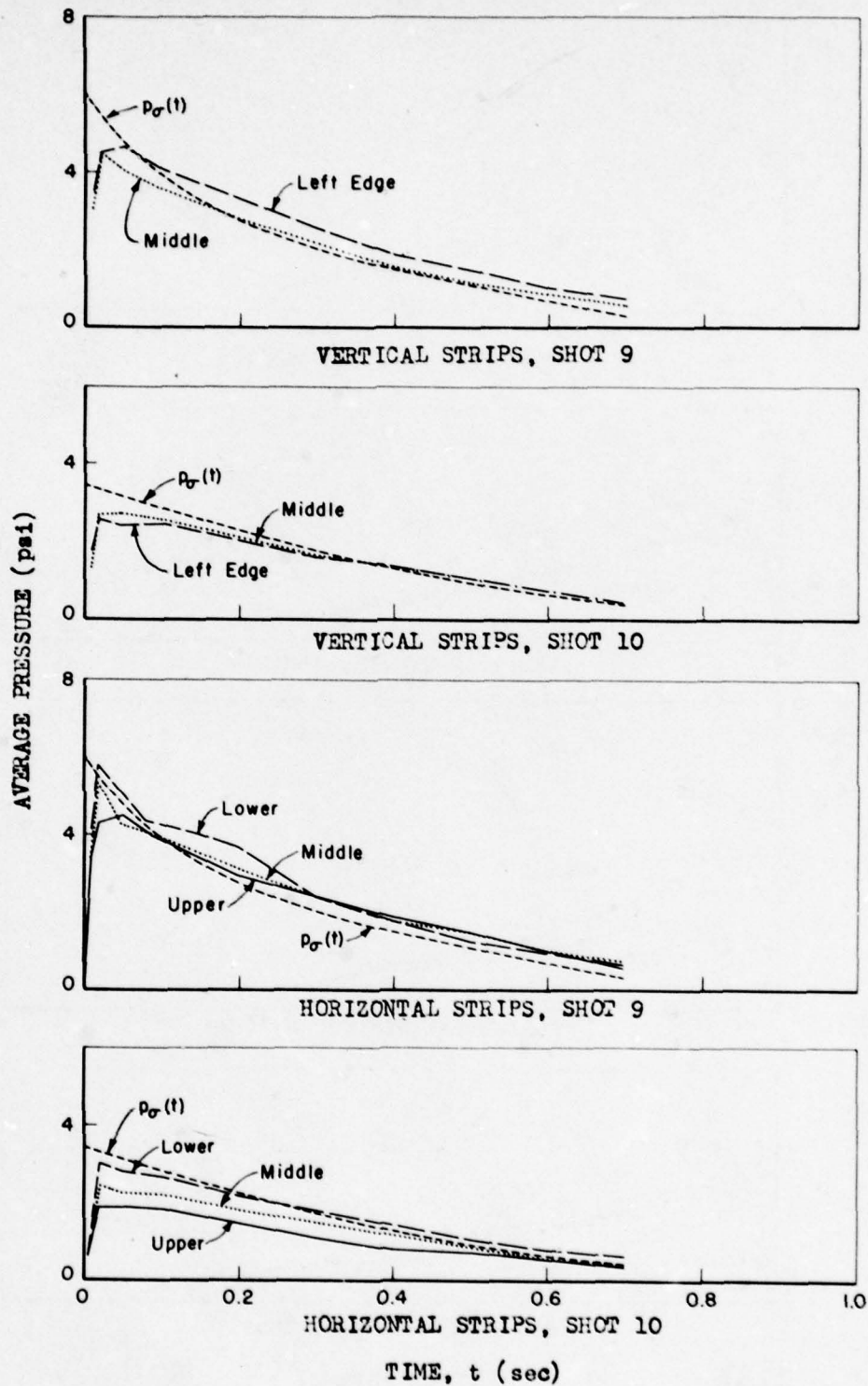
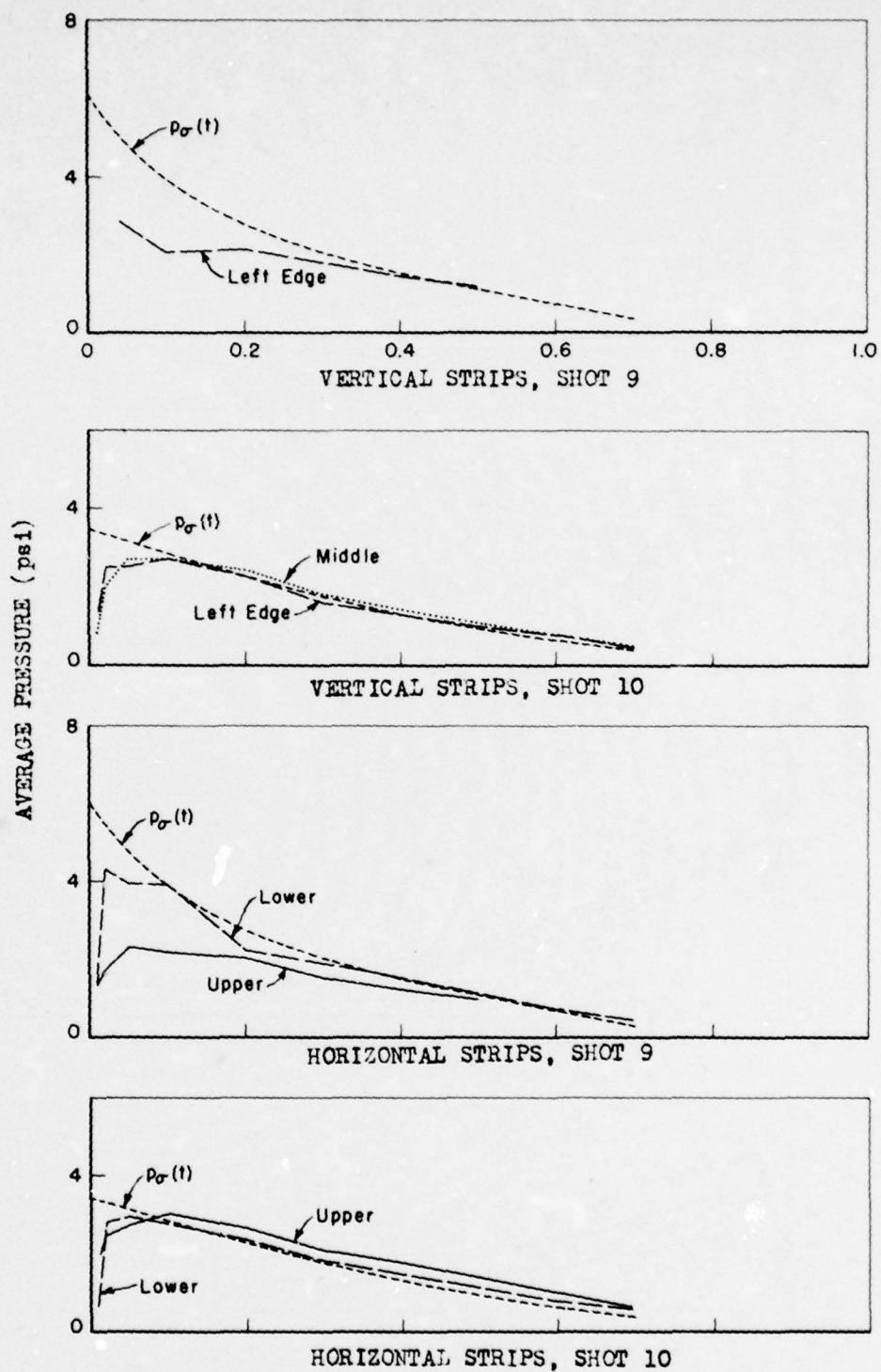


Fig. 4.58 — Average pressures on strips of rear surface, Structure 3.1a.





UNCLASSIFIED

TIME,  $t$  (sec)

Fig. 4.59 — Average pressures on strips of rear surface, Structure 3.1b.

UNCLASSIFIED

~~SECRET RESTRICTED DATA~~

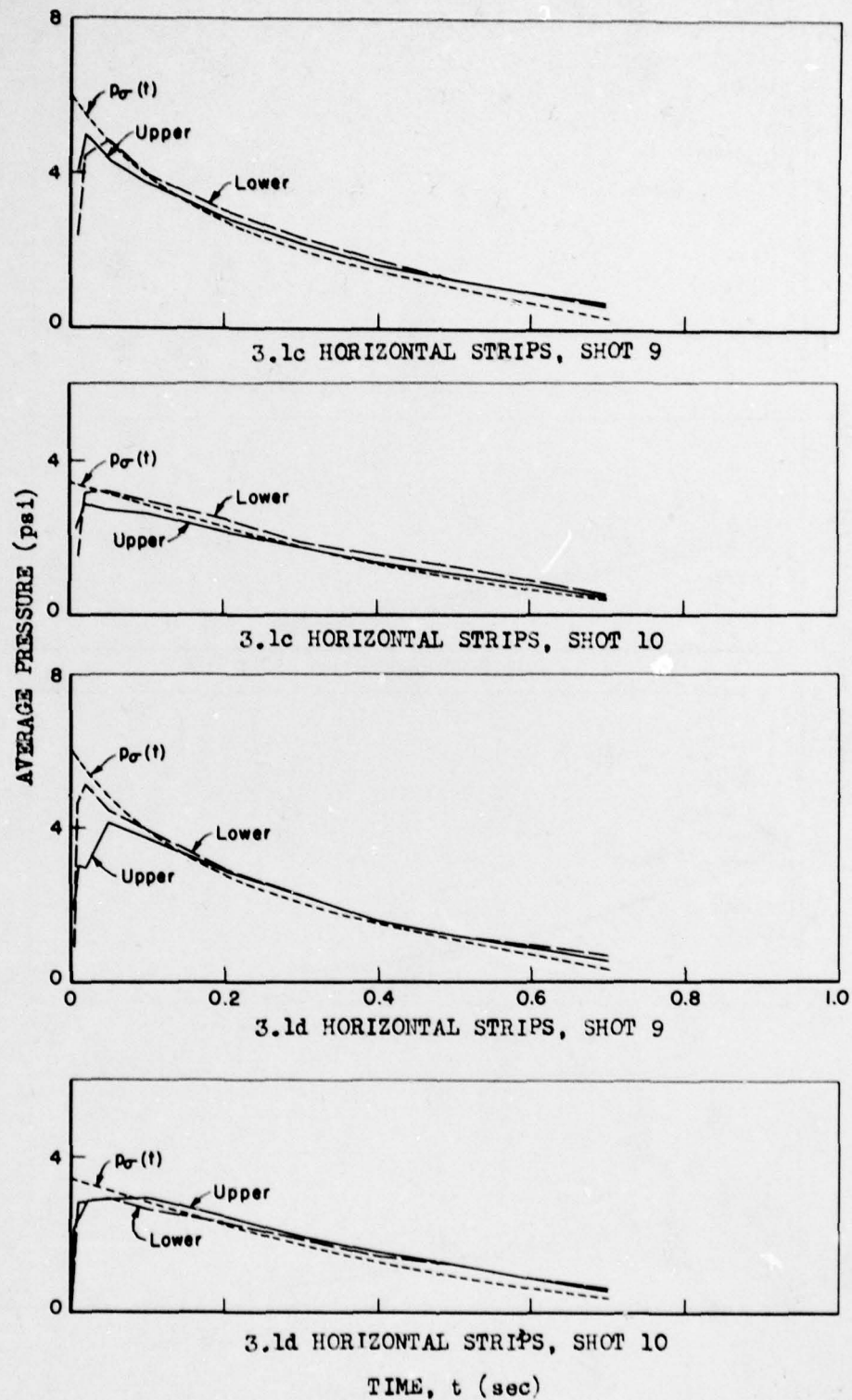


Fig. 4.60 — Average pressures on rear surfaces of Structures 3.1c and d.

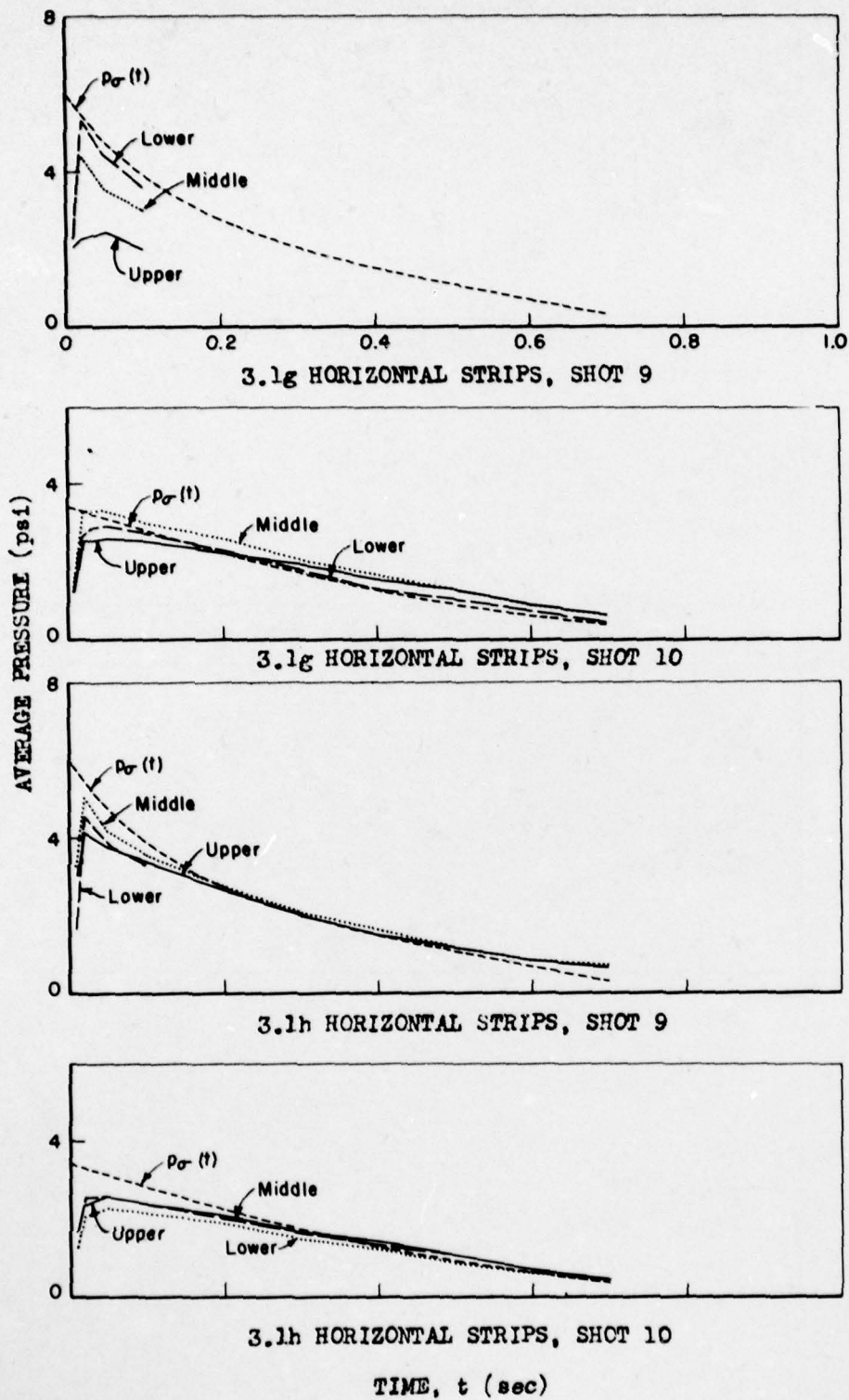


Fig. 4.61 — Average pressures on rear surfaces of Structures 3.1g and h.



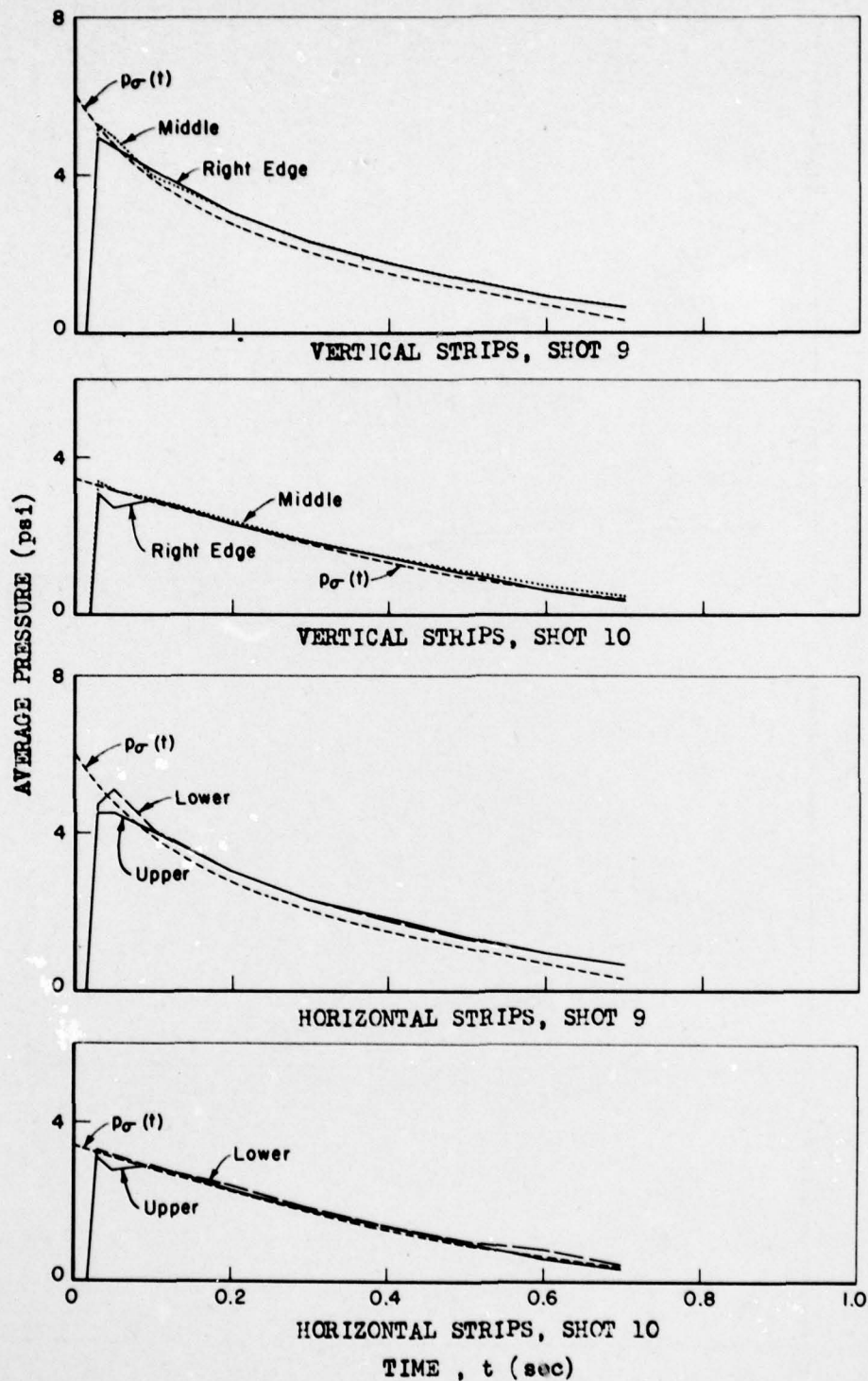


Fig. 4.62—Average pressures on strips of rear surface, Structure 3.1i.

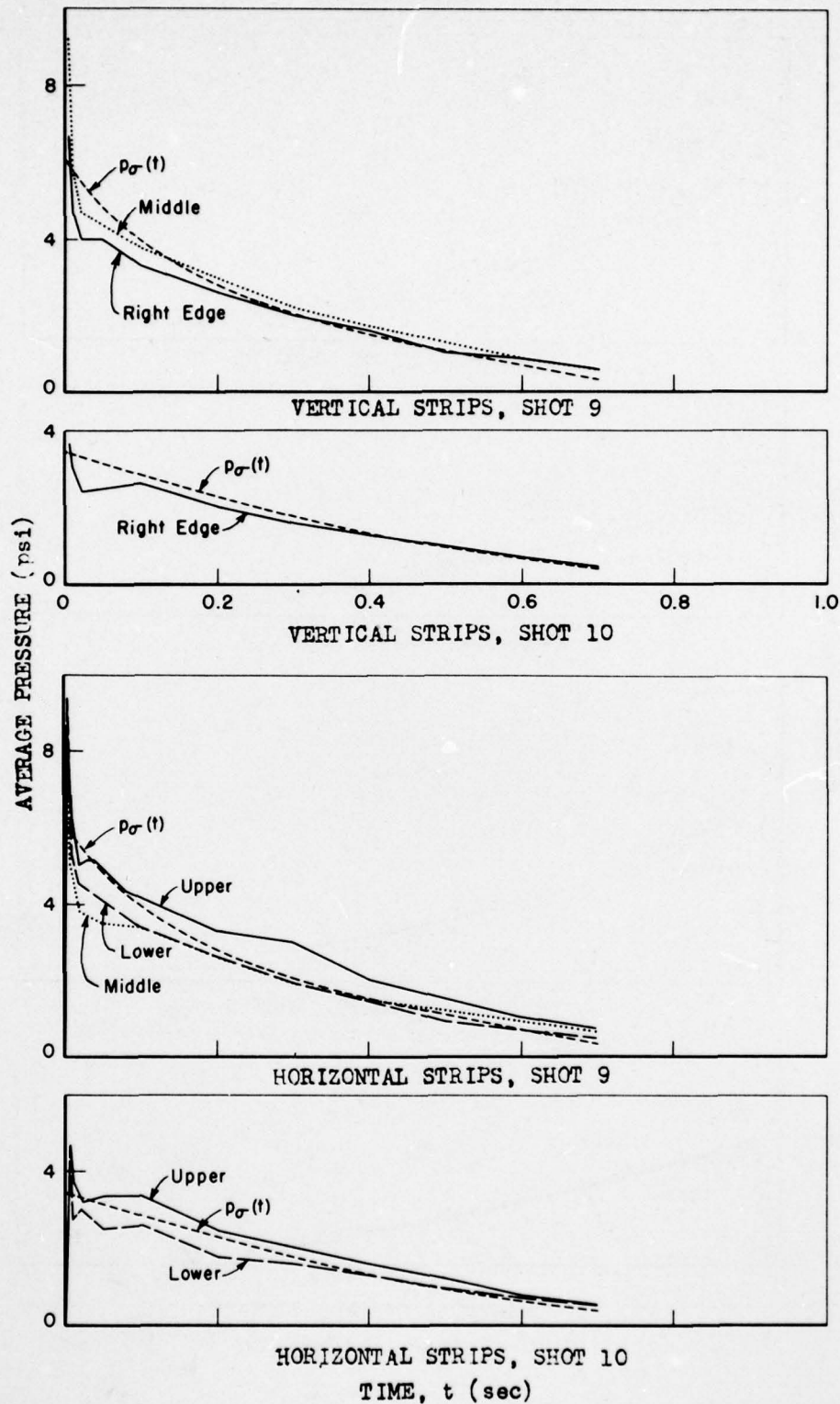


Fig. 4.63—Average pressure on strips of front surface, Structure 3.1a.

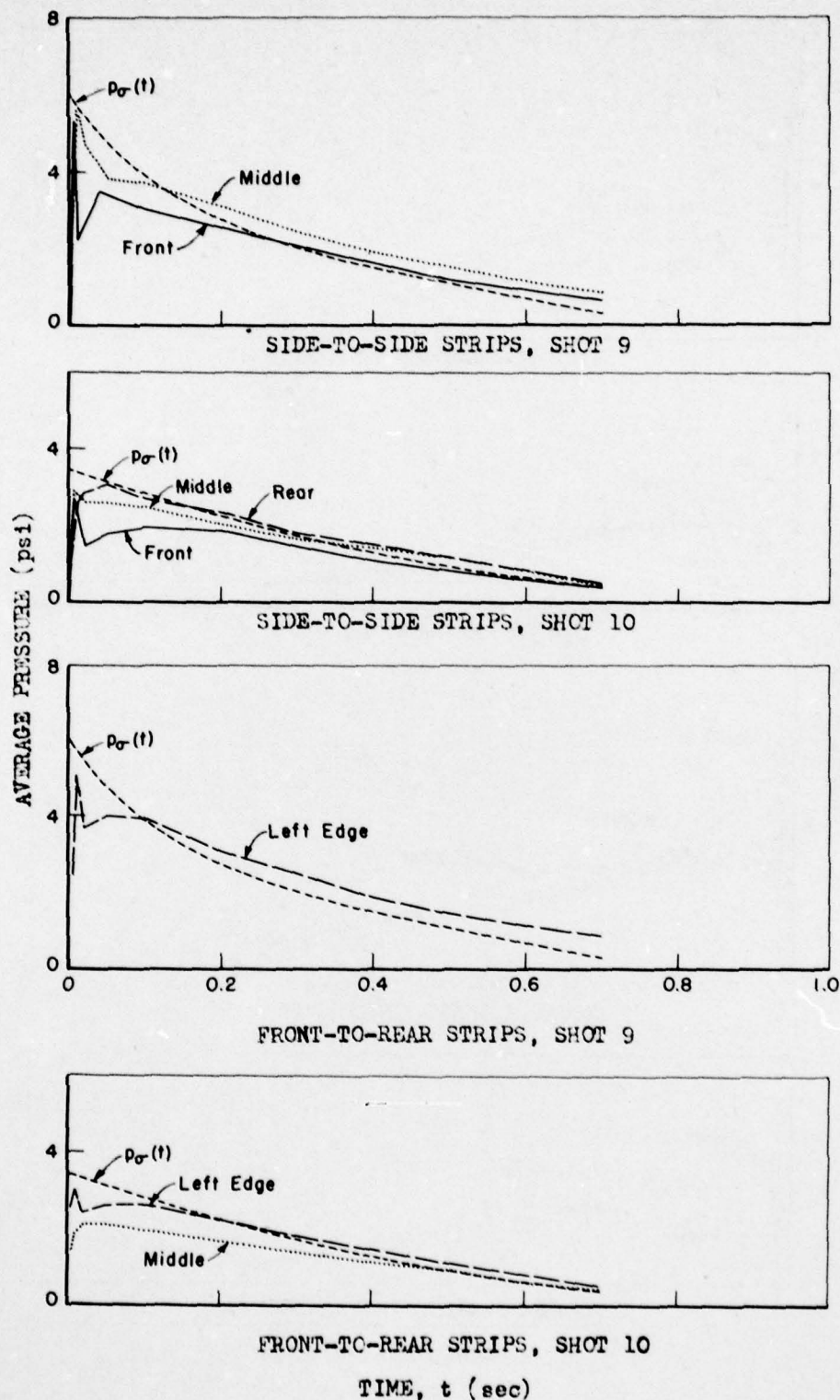


Fig. 4.64—Average pressure on strips of top surface, Structure 3.1a.



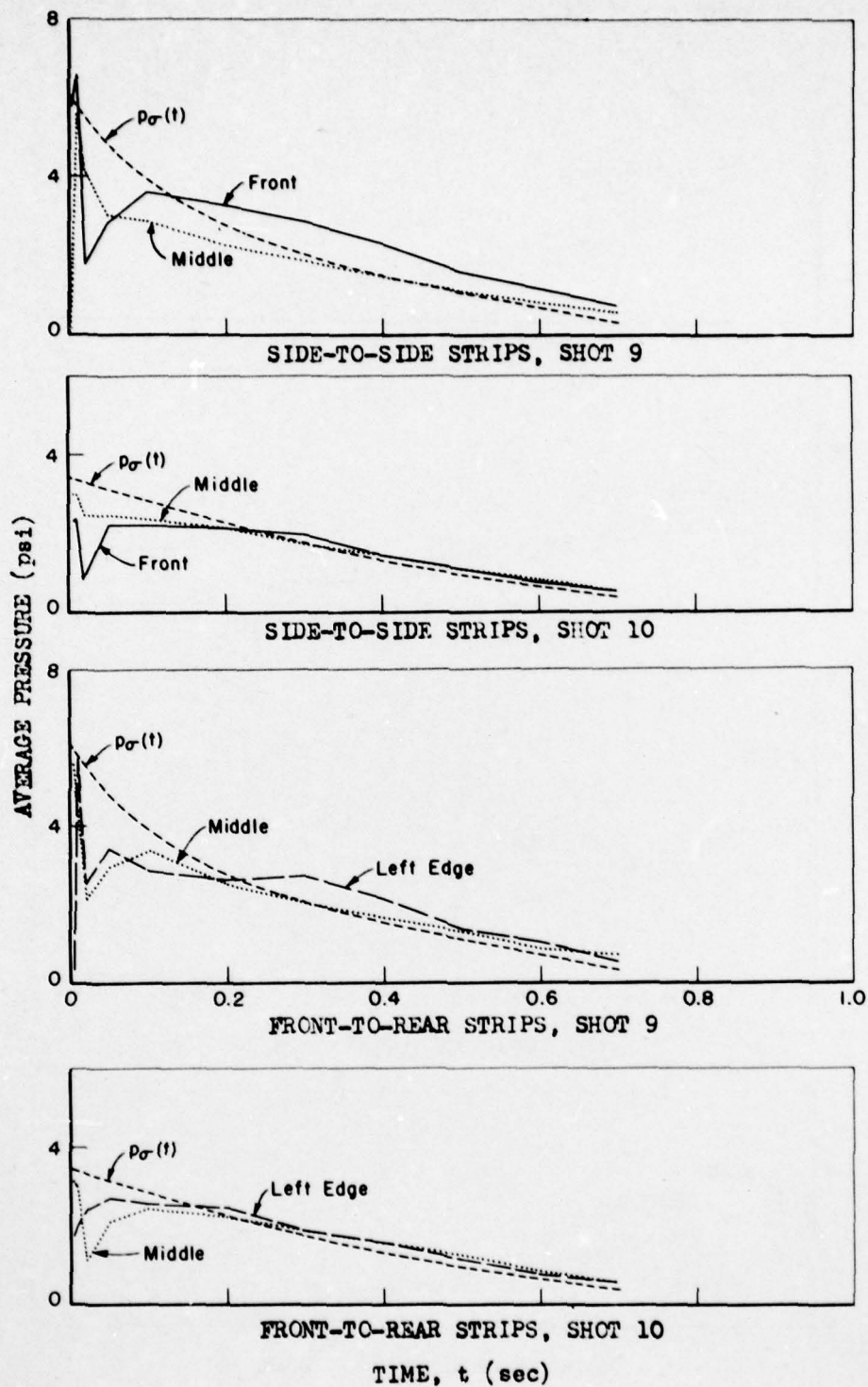


Fig. 4.65 — Average pressure on strips of top surface, Structure 3.1b.

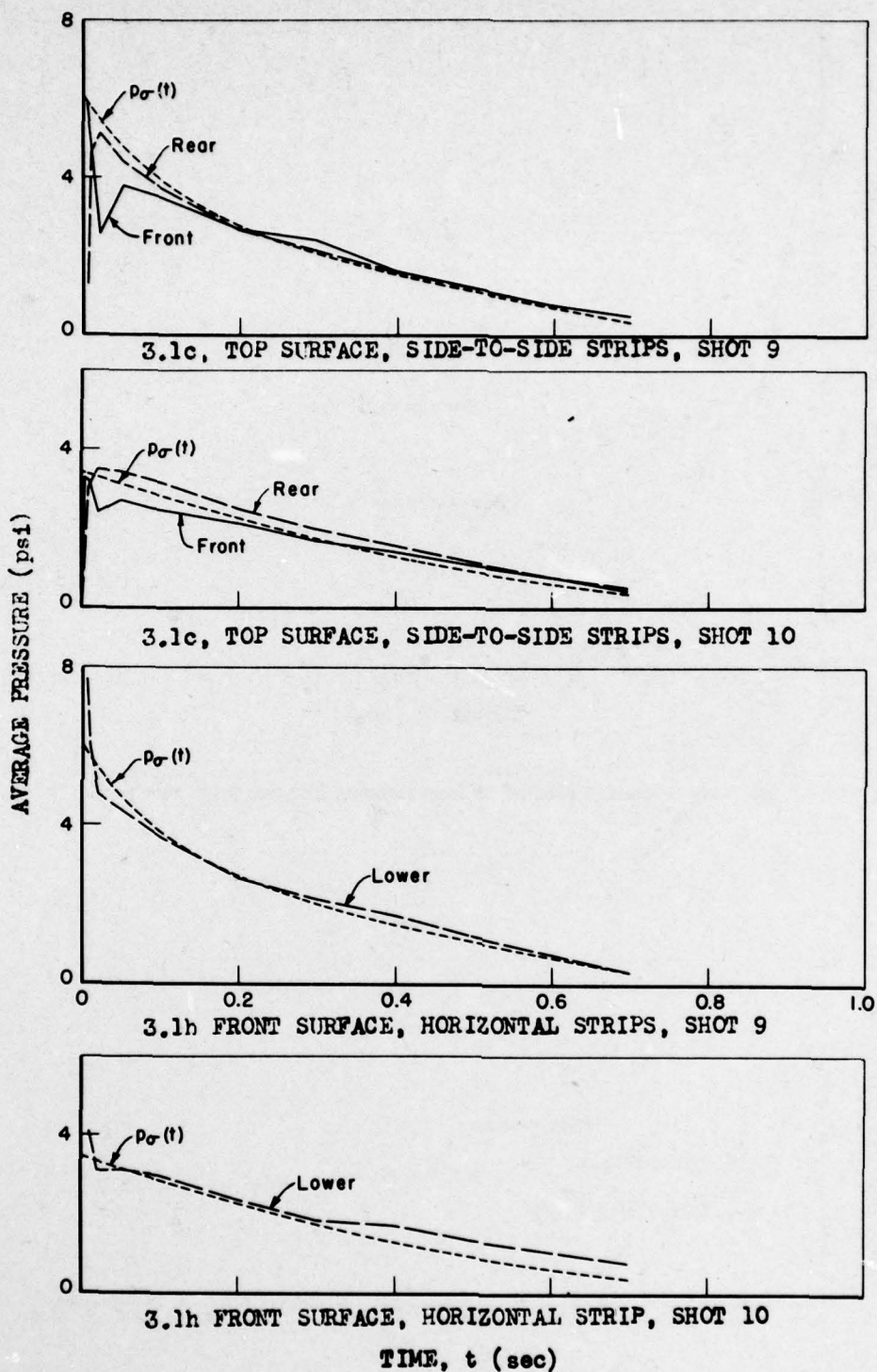


Fig. 4.66—Average pressure on strips of top surface, Structure 3.1c, and front surface, Structure 3.1h.

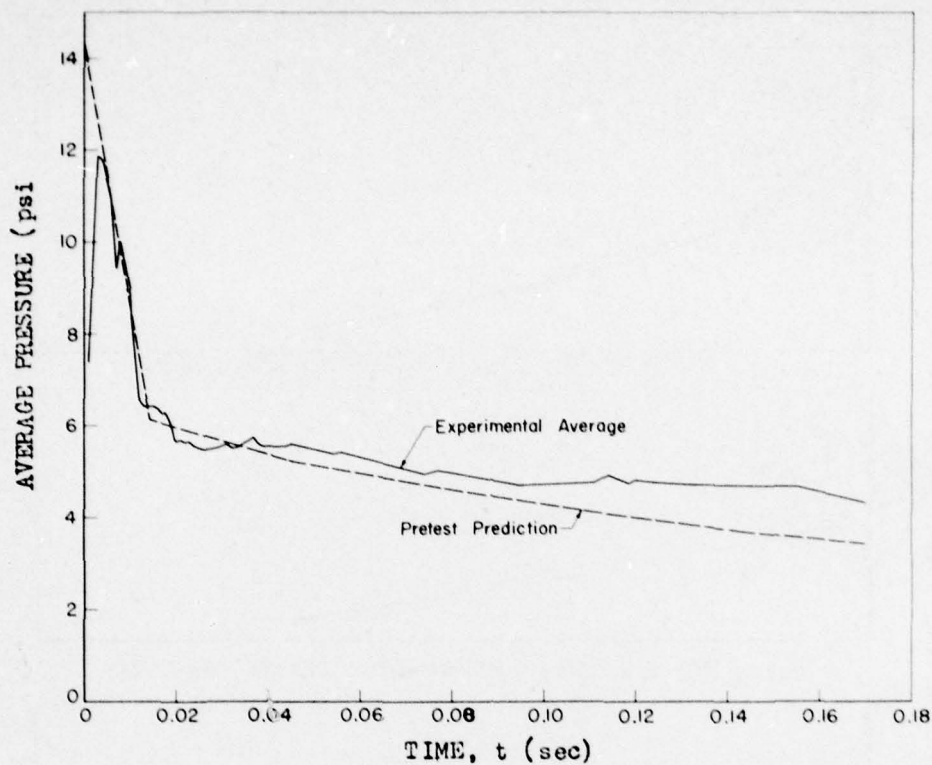


Fig. 4.67—Average pressure on front surface, Structure 3.1a, Shot 9.

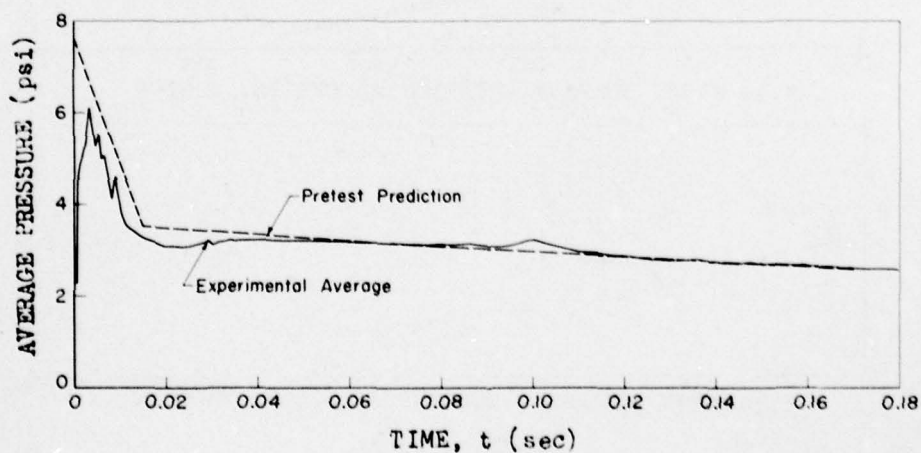


Fig. 4.68—Average pressure on front surface, Structure 3.1a, Shot 10.



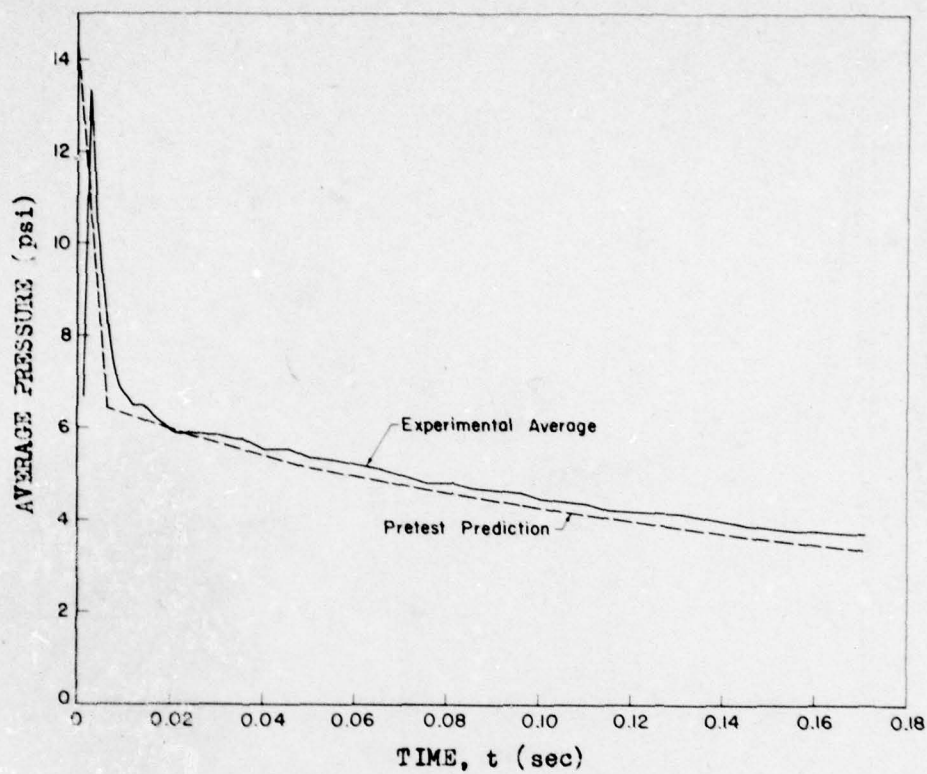


Fig. 4.69—Average pressure on front surface, Structure 3.1c, Shot 9.

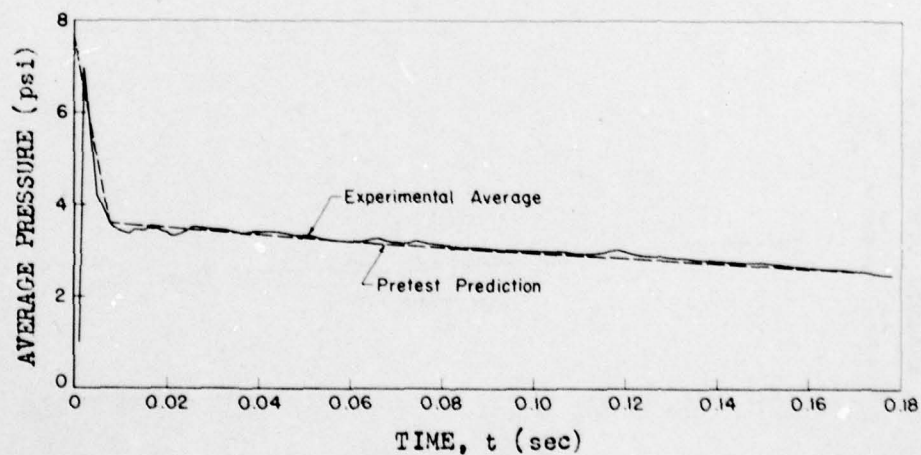


Fig. 4.70—Average pressure on front surface, Structure 3.1c, Shot 10.

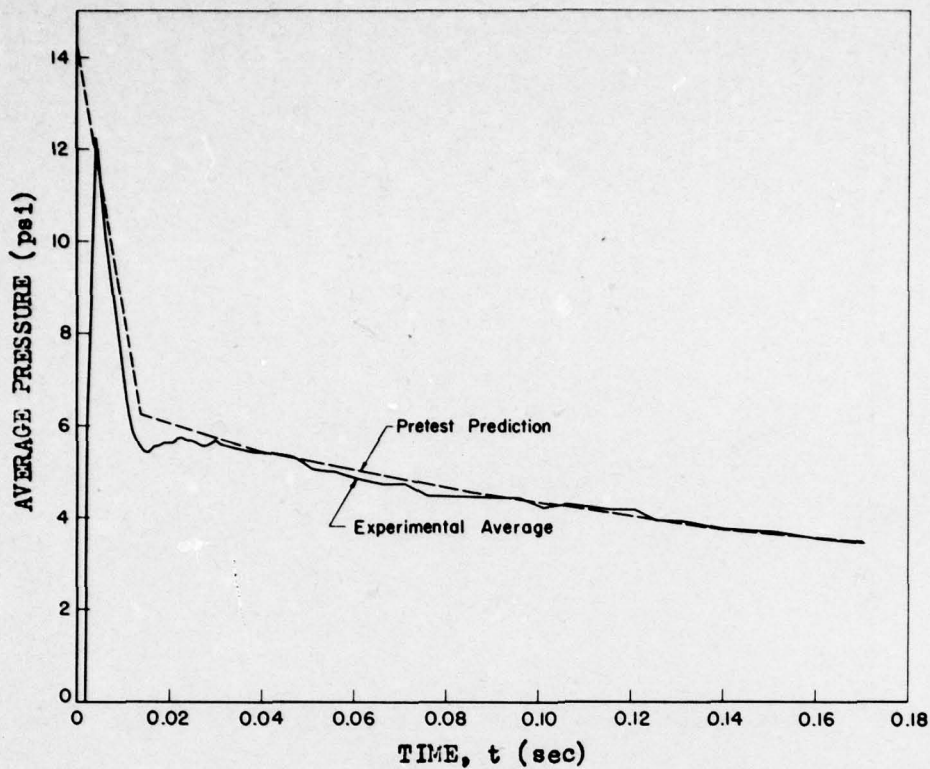


Fig. 4.71 — Average pressure on front surface, Structure 3.1d, Shot 9.

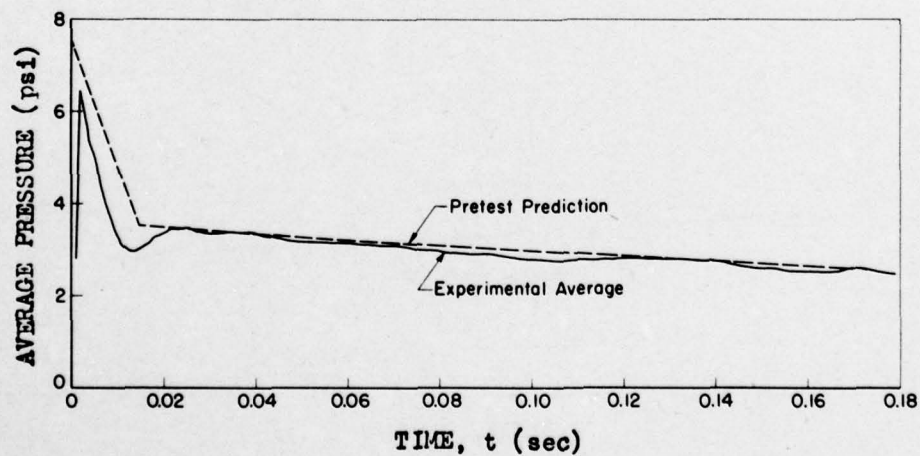


Fig. 4.72 — Average pressure on front surface, Structure 3.1d, Shot 10.

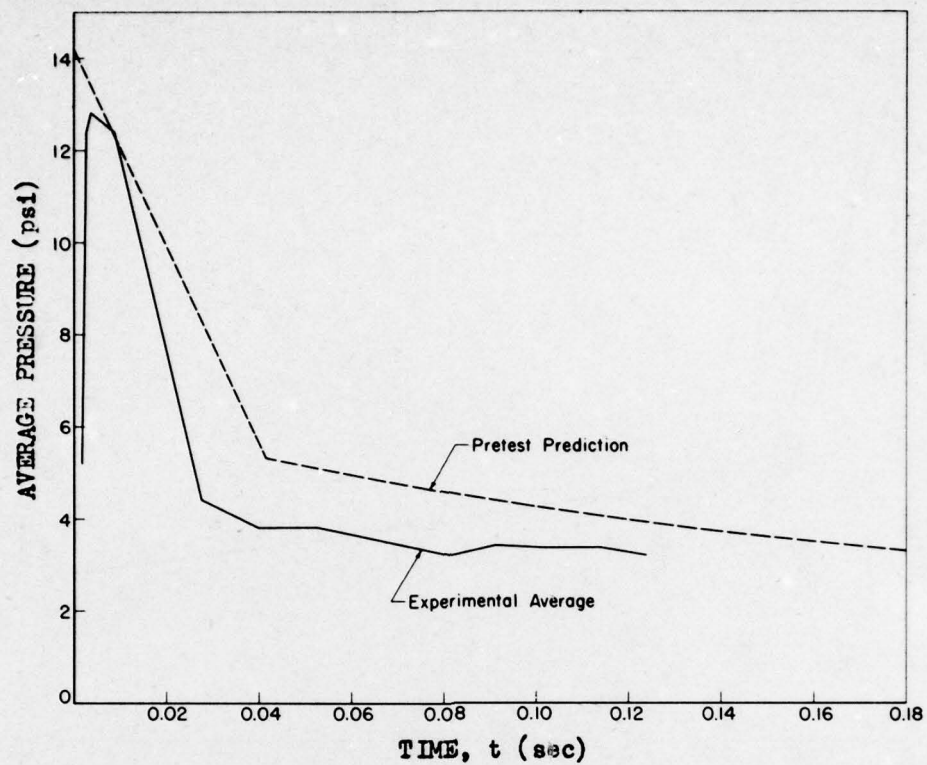


Fig. 4.73—Average pressure on front surface, Structure 3.1e, Shot 9.

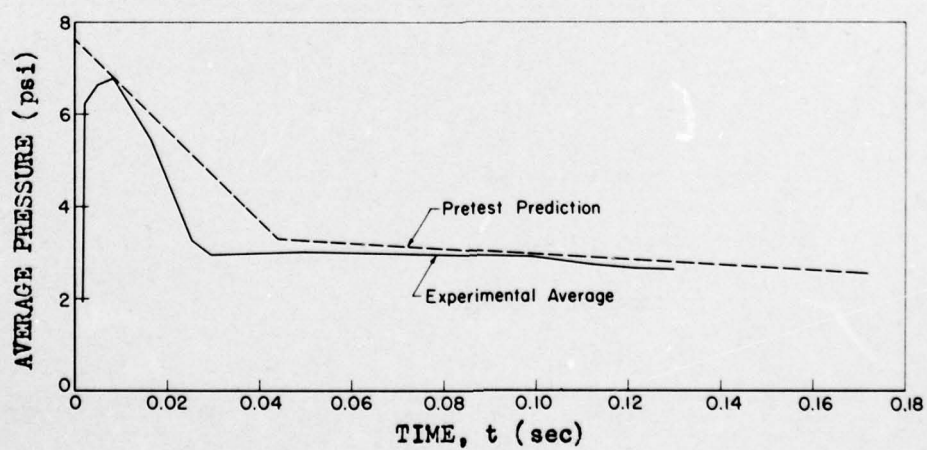


Fig. 4.74—Average pressure on front surface, Structure 3.1e, Shot 10.



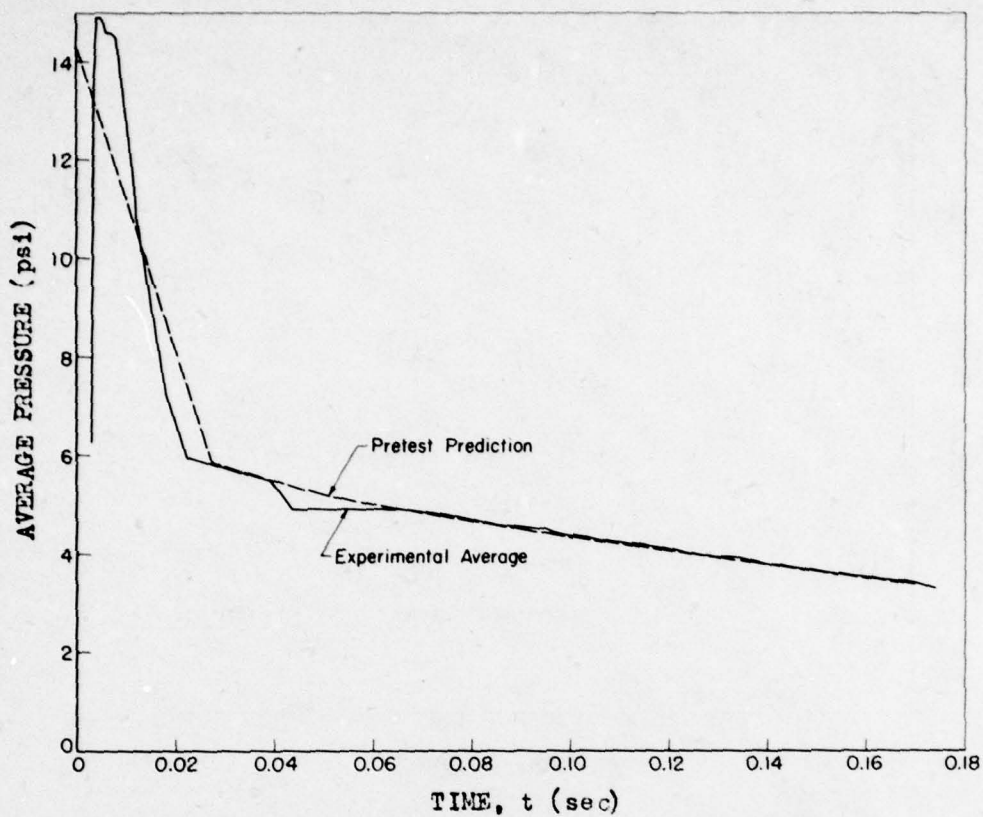


Fig. 4.75—Average pressure on front surface, Structure 3.1f, Shot 9.

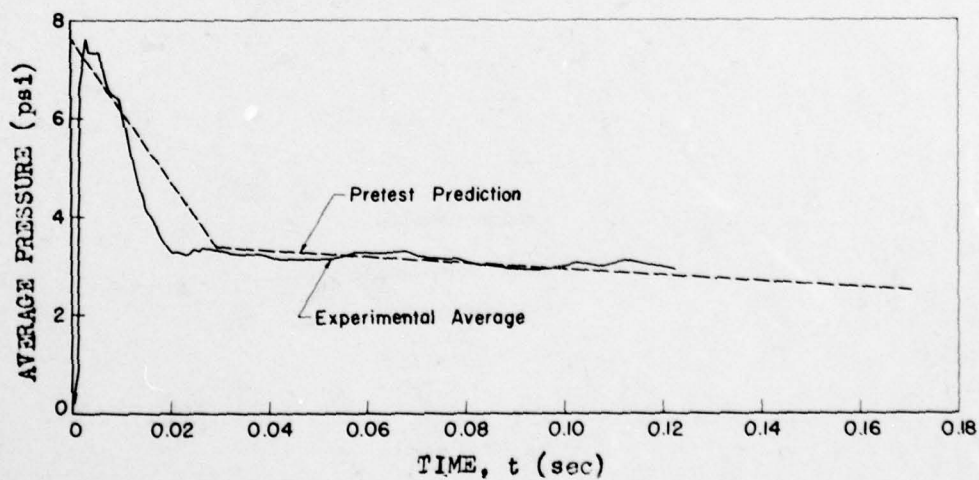


Fig. 4.76—Average pressure on front surface, Structure 3.1f, Shot 10.

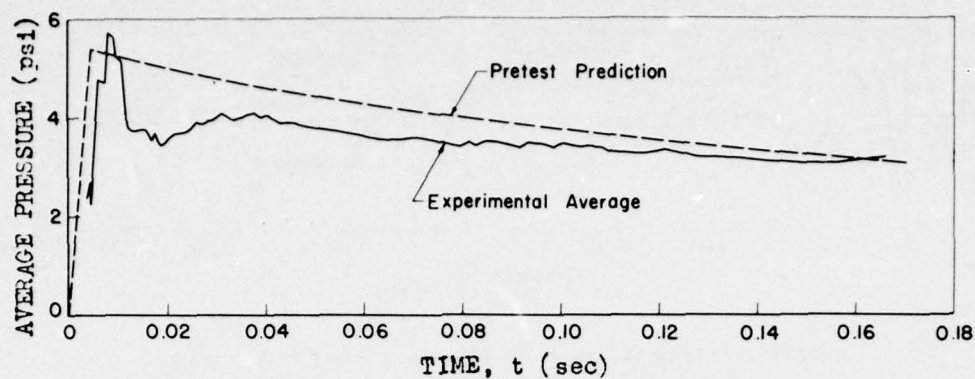


Fig. 4.77—Average pressure on top surface, Structure 3.1a, Shot 9.

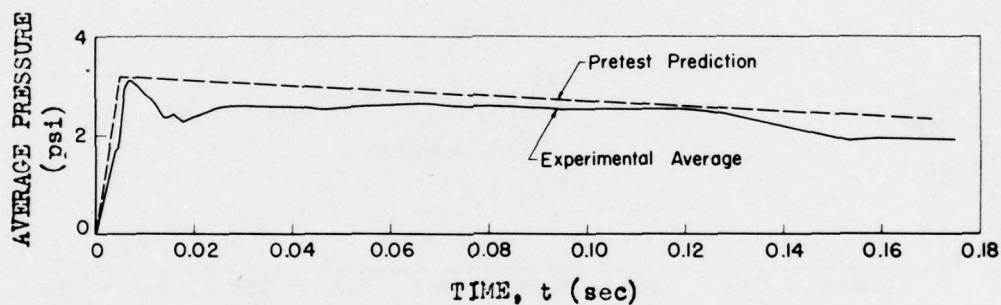


Fig. 4.78—Average pressure on top surface, Structure 3.1a, Shot 10.

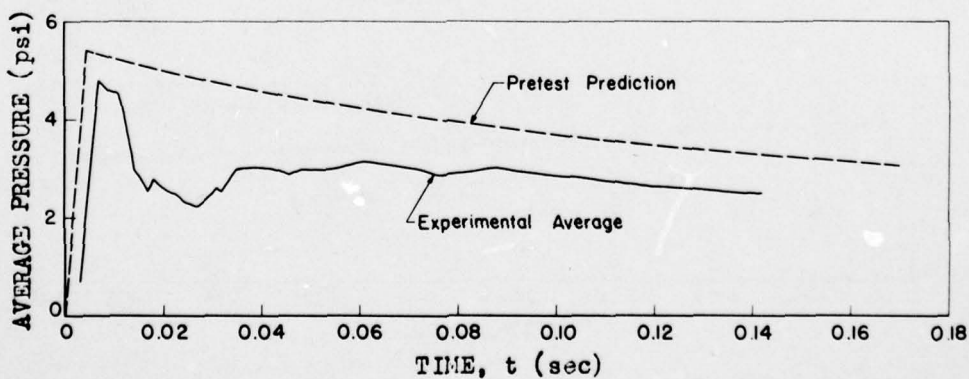


Fig. 4.79—Average pressure on top surface, Structure 3.1b, Shot 9.

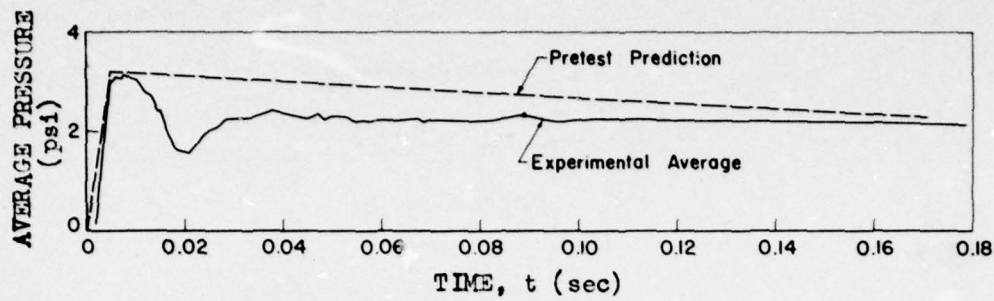


Fig. 4.80 — Average pressure on top surface, Structure 3.1b, Shot 10.

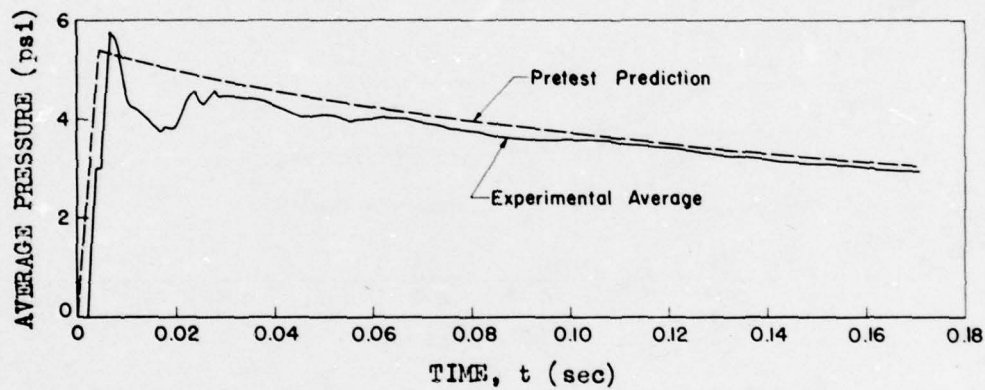


Fig. 4.81 — Average pressure on top surface, Structure 3.1c, Shot 9.

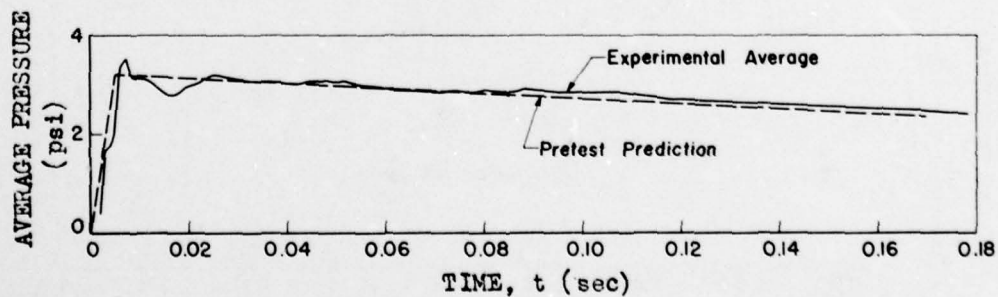


Fig. 4.82 — Average pressure on top surface, Structure 3.1c, Shot 10.



AD-A073 468

DEFENSE ATOMIC SUPPORT AGENCY WASHINGTON DC  
OPERATION UPSHOT-KNOTHOLE, NEVADA PROVING GROUNDS, MARCH - JUNE--ETC(U)  
JUL 55 E V GALLAGHER, T H SCHIFFMAN

F/G 15/6

UNCLASSIFIED

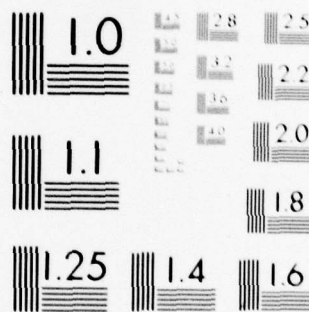
DASA-WT-721

NL

3 OF 4

AD  
A073468





MICROCOPY RESOLUTION TEST CHART  
NATIONAL BUREAU OF STANDARDS-1963-A

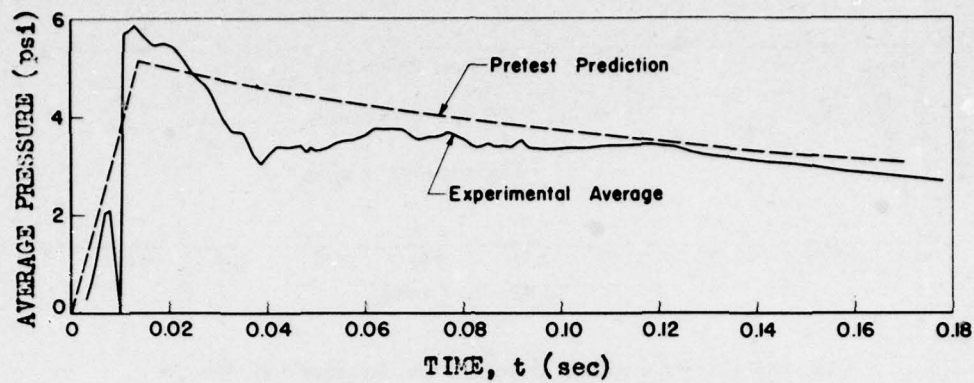


Fig. 4.83—Average pressure on top surface, Structure 3.1e, Shot 9.

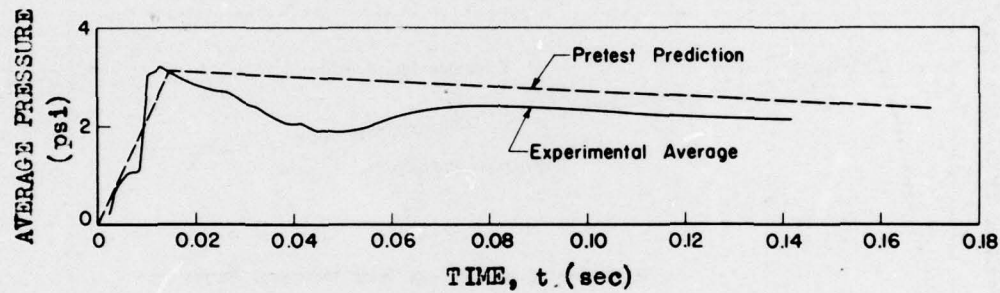


Fig. 4.84—Average pressure on top surface, Structure 3.1e, Shot 10.

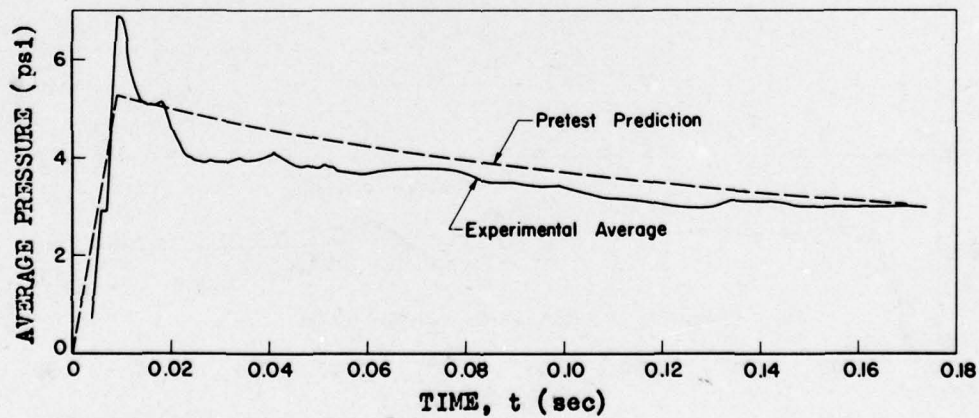


Fig. 4.85—Average pressure on top surface, Structure 3.1f, Shot 9.



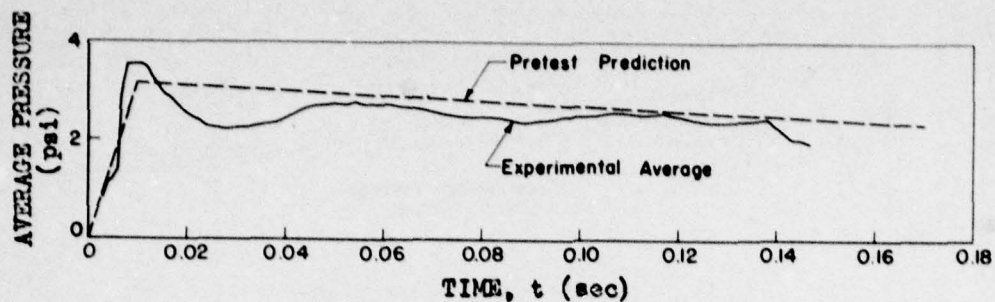


Fig. 4.86 — Average pressure on top surface, Structure 3.1f, Shot 10.

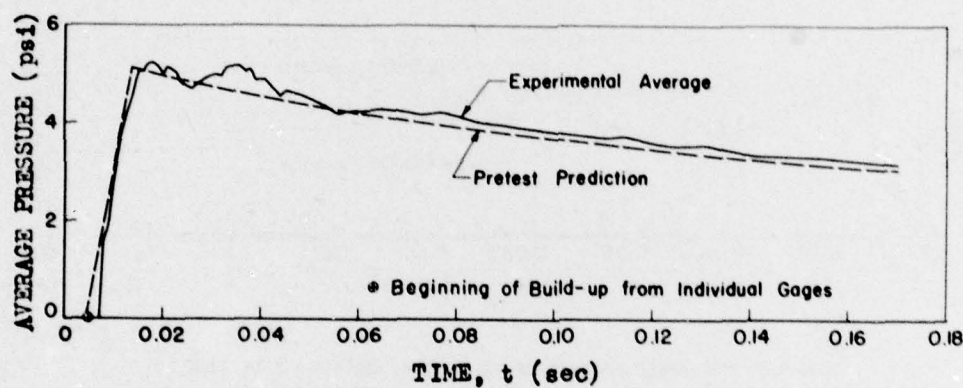


Fig. 4.87 — Average pressure on rear surface, Structure 3.1a, Shot 9.

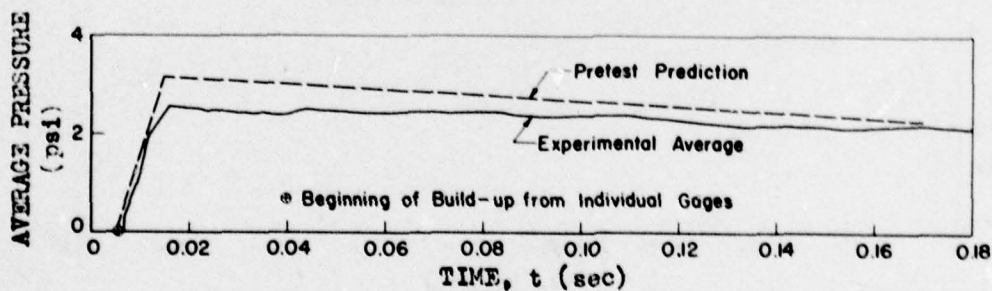


Fig. 4.88 — Average pressure on rear surface, Structure 3.1a, Shot 10.

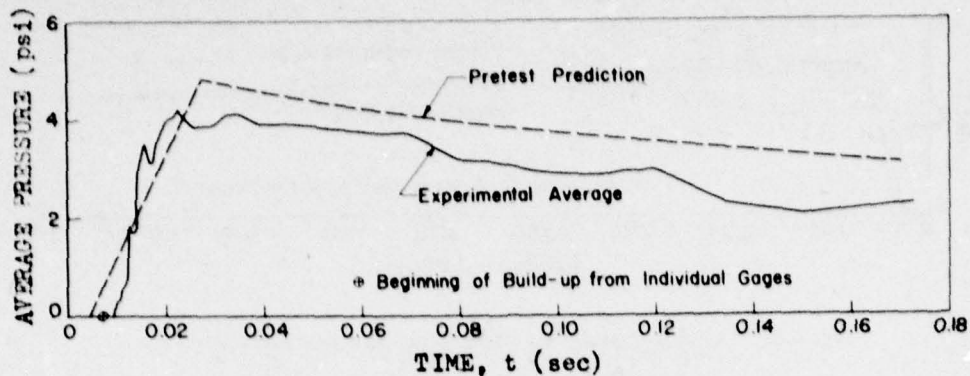


Fig. 4.89—Average pressure on rear surface, Structure 3.1b, Shot 9.

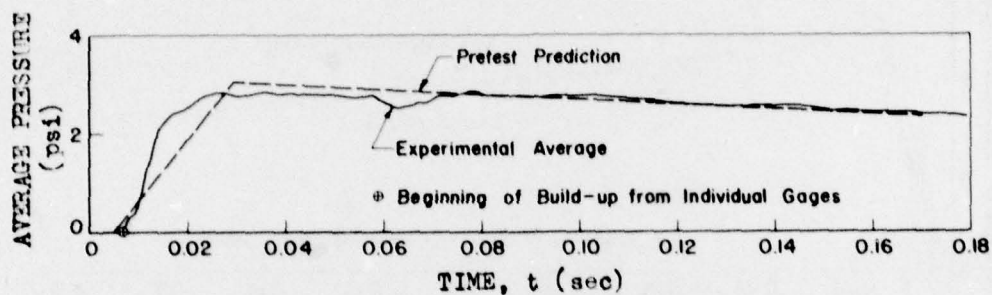


Fig. 4.90—Average pressure on rear surface, Structure 3.1b, Shot 10.

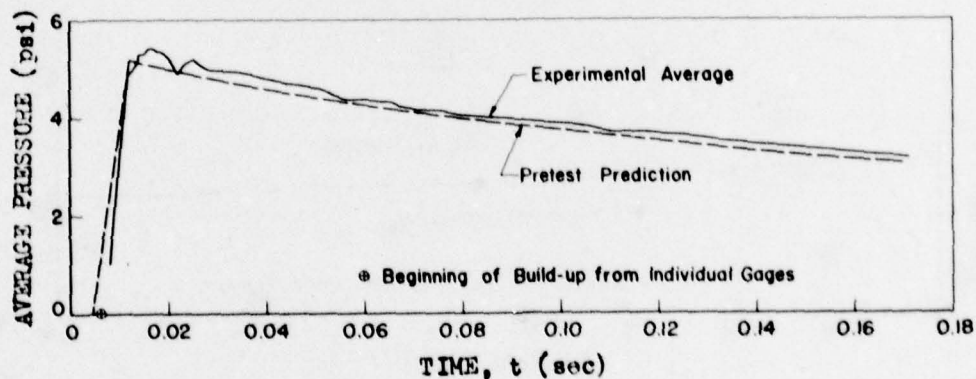


Fig. 4.91—Average pressure on rear surface, Structure 3.1c, Shot 9.

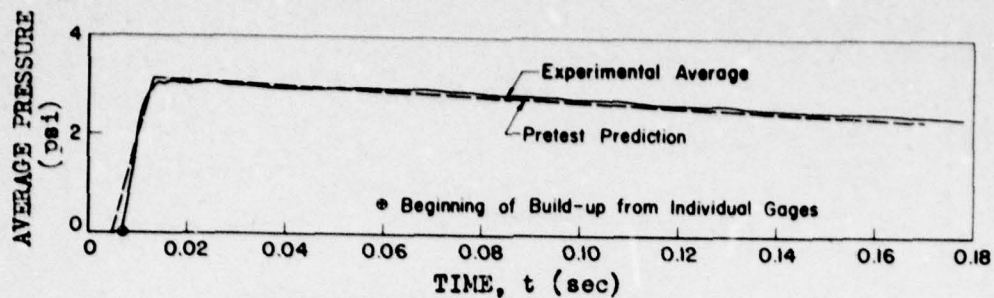


Fig. 4.92—Average pressure on rear surface, Structure 3.1c, Shot 10.

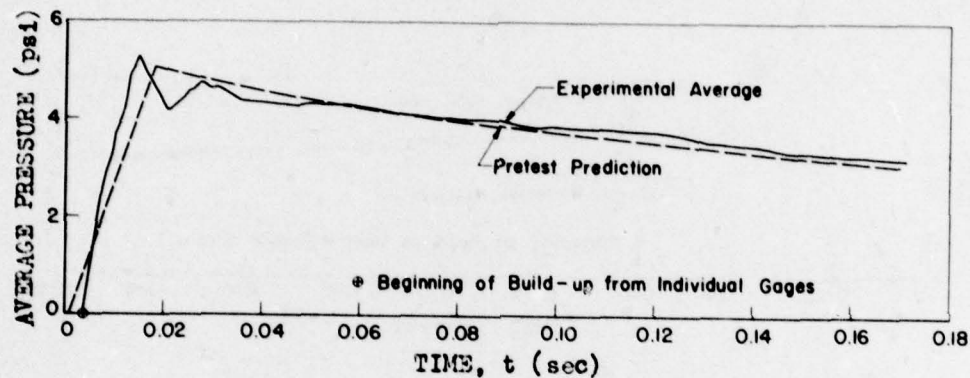


Fig. 4.93—Average pressure on rear surface, Structure 3.1d, Shot 9.

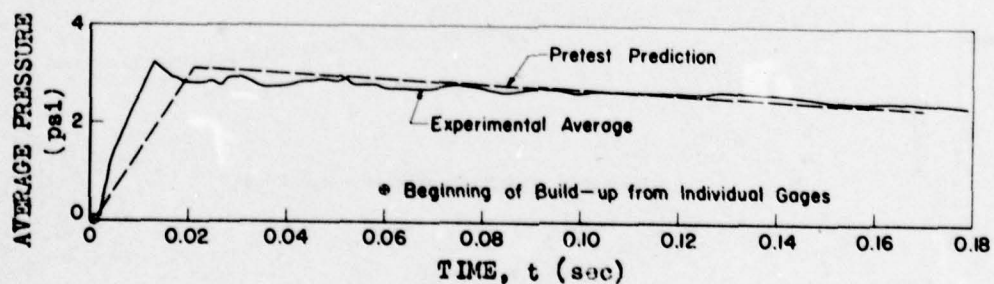


Fig. 4.94—Average pressure on rear surface, Structure 3.1d, Shot 10.



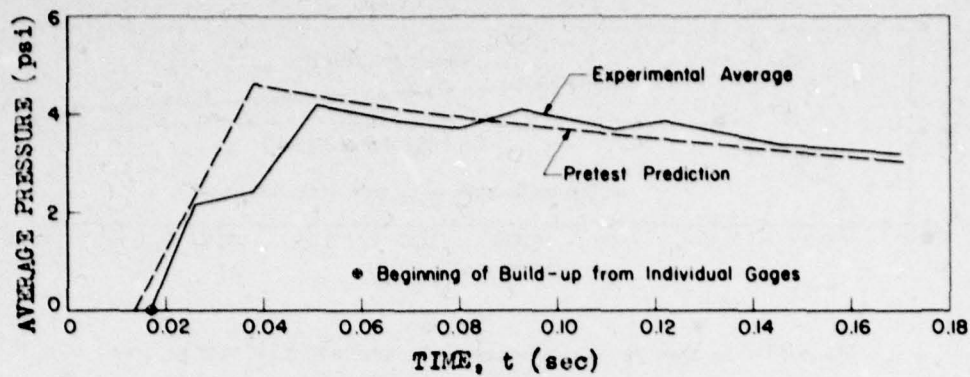


Fig. 4.95—Average pressure on rear surface, Structure 3.1e, Shot 9.

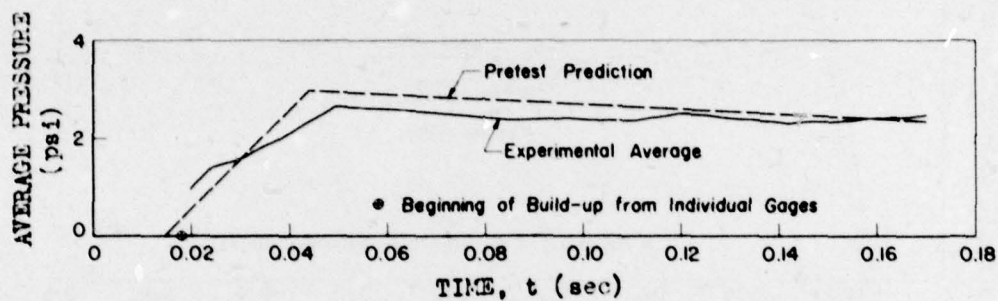


Fig. 4.96—Average pressure on rear surface, Structure 3.1e, Shot 10.

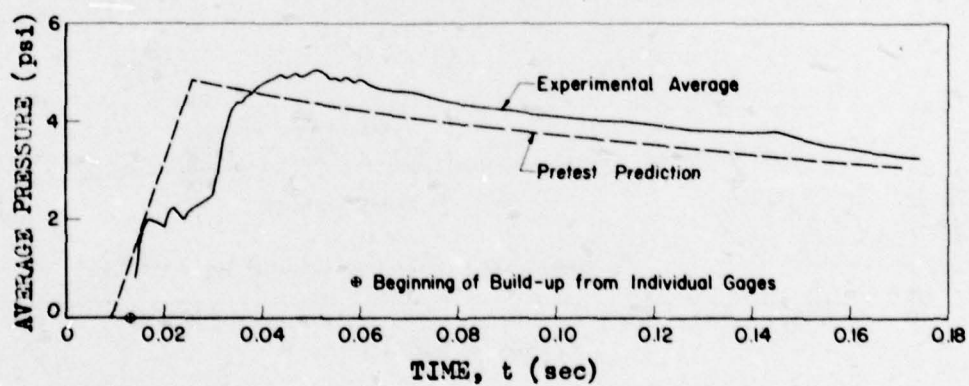


Fig. 4.97—Average pressure on rear surface, Structure 3.1f, Shot 9.

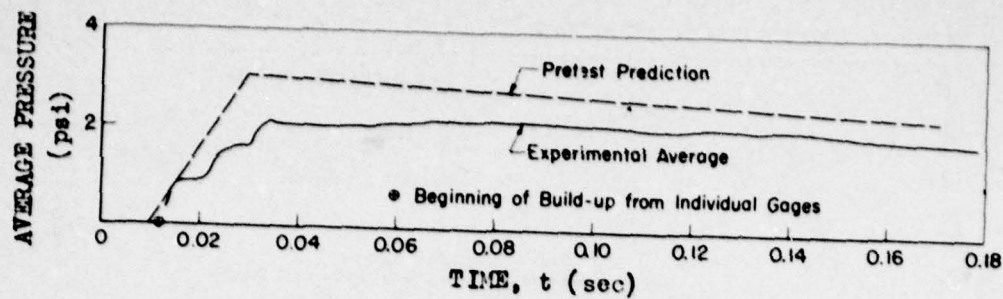


Fig. 4.98 — Average pressure on rear surface, Structure 3.1f, Shot 10.

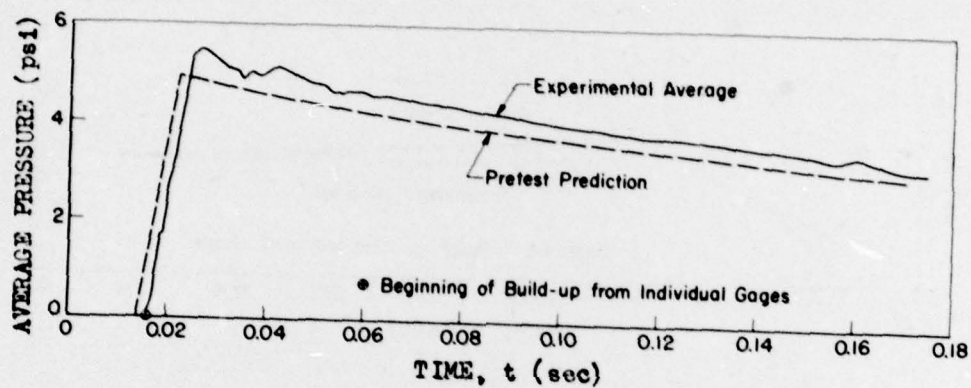


Fig. 4.99 — Average pressure on rear surface, Structure 3.1i, Shot 9.

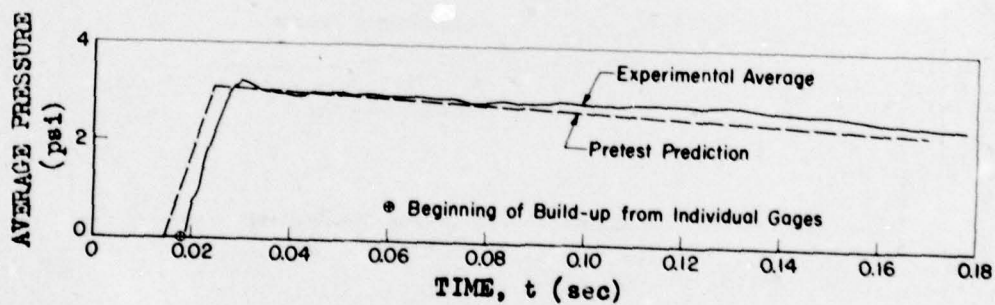


Fig. 4.100 — Average pressure on rear surface, Structure 3.1i, Shot 10.

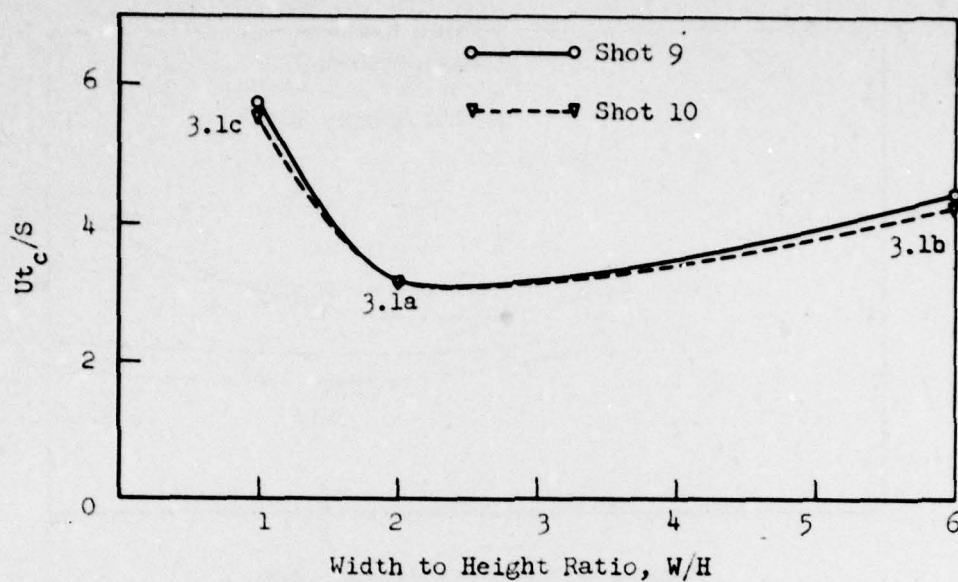


Fig. 4.101 — Effect of width ( $L$  and  $H$  constant).

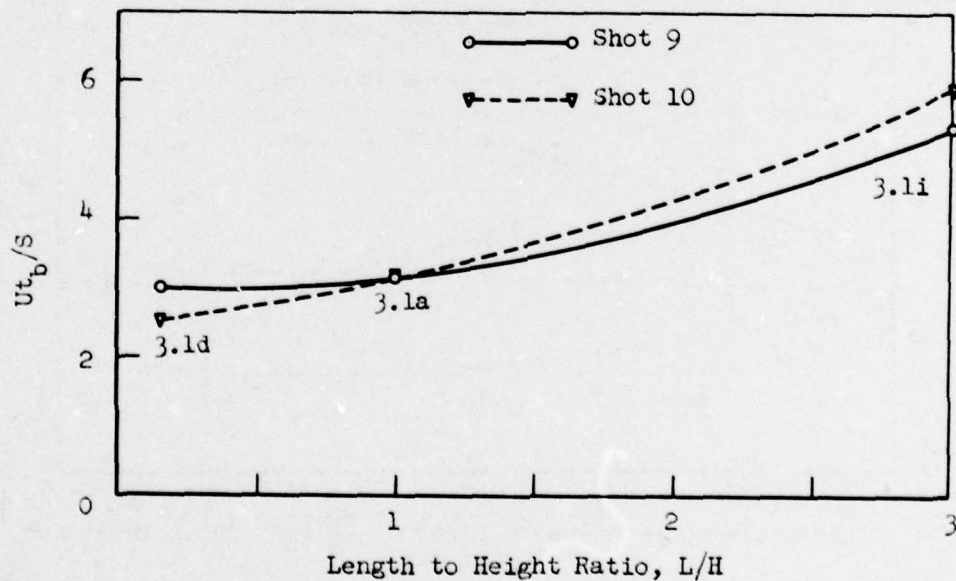


Fig. 4.102 — Effect of length ( $W$  and  $H$  constant).



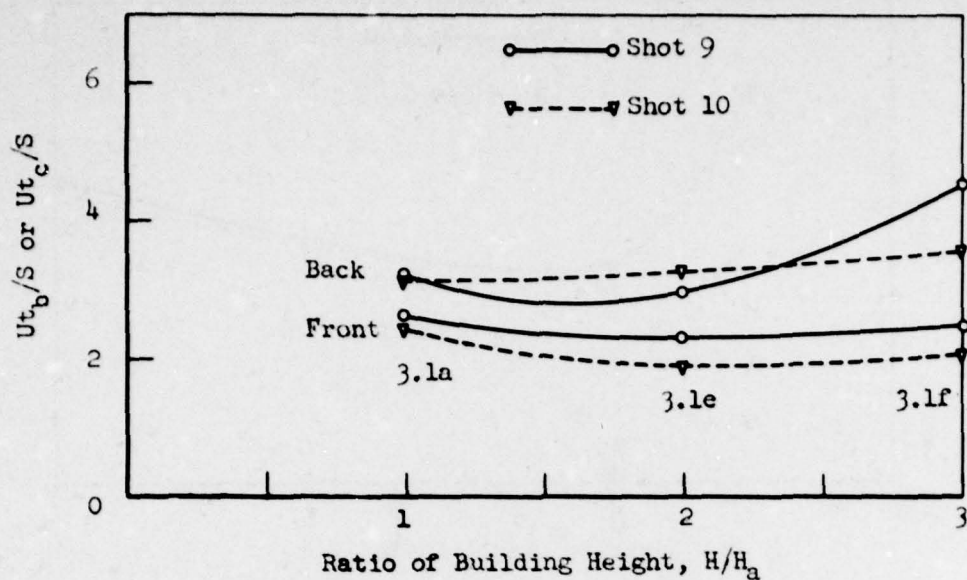


Fig. 4.103—Effect of size (ratio  $W:H:L = \text{constant}$ ).

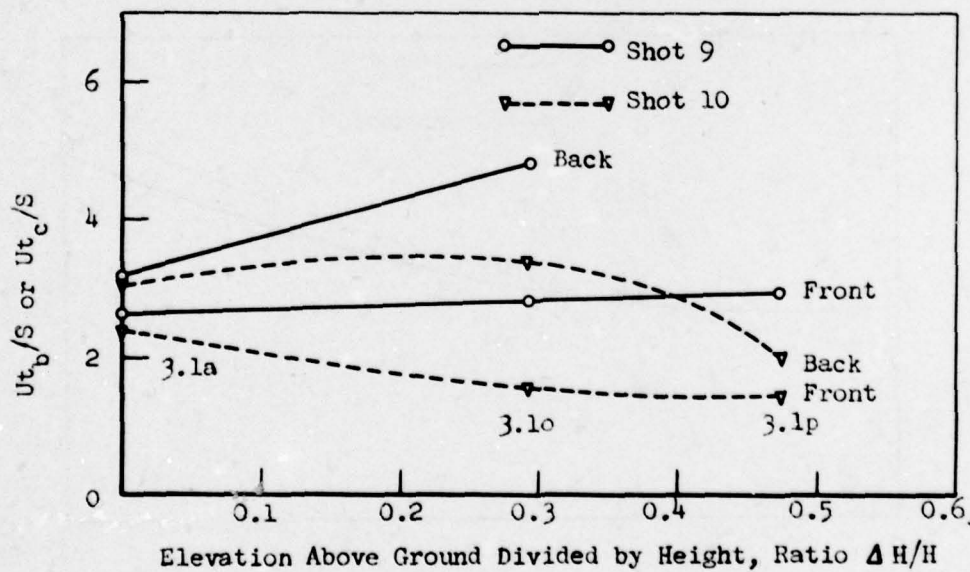


Fig. 4.104—Effect of ground proximity ( $L, W, \text{ and } H \text{ constant}$ ).

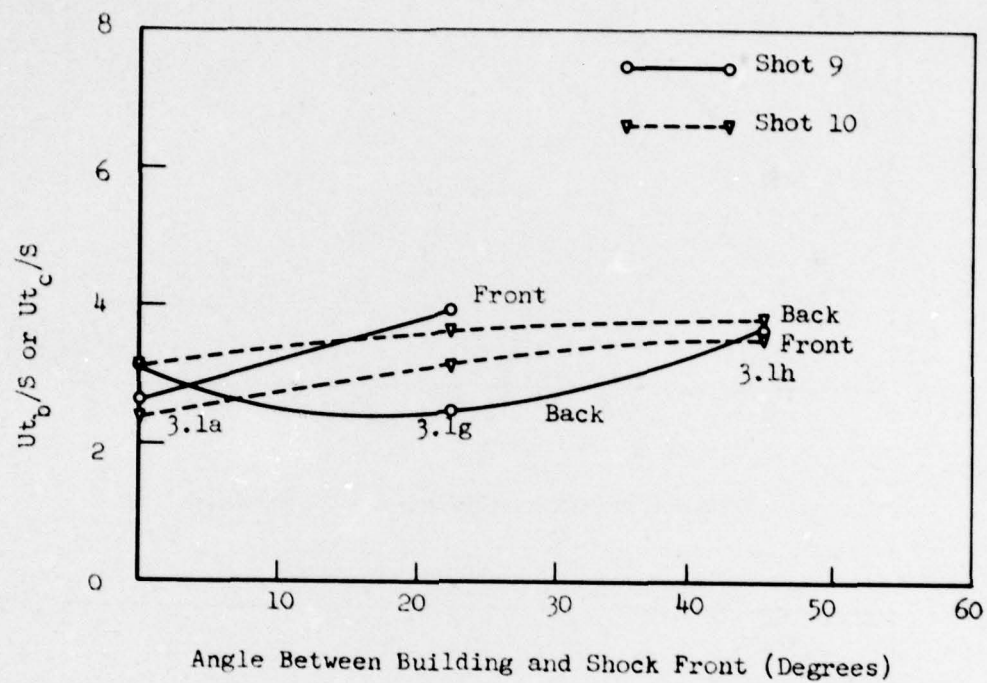


Fig. 4.105 — Effect of orientation (L, H, and W constant).

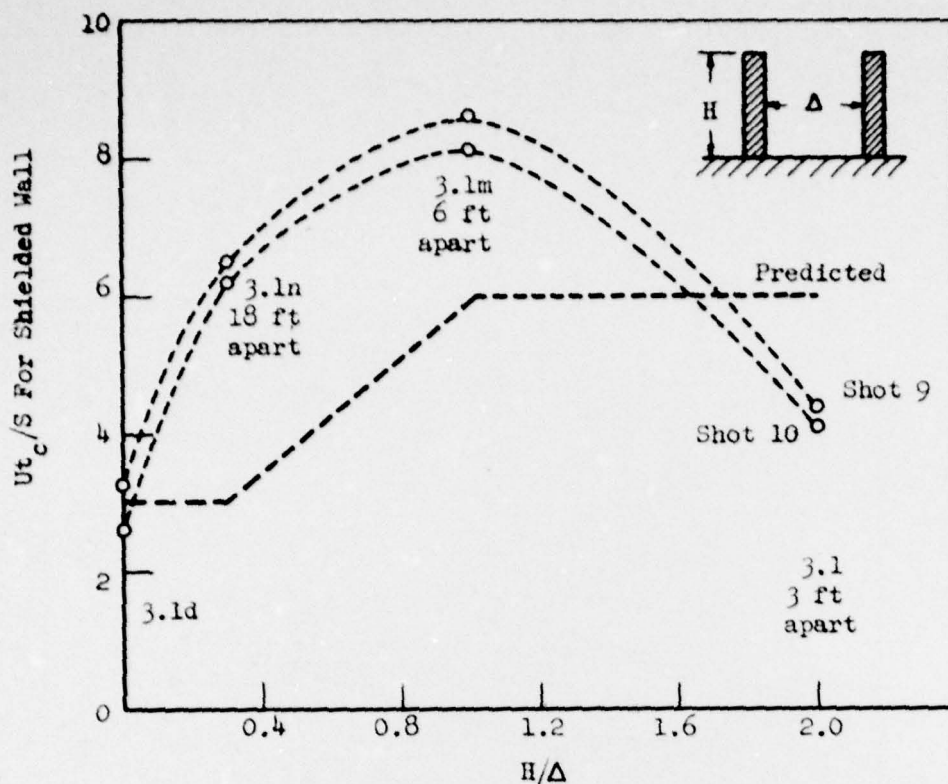


Fig. 4.106—Effect of shielding on relief time ( $W; H; L = \text{constant}$ ).

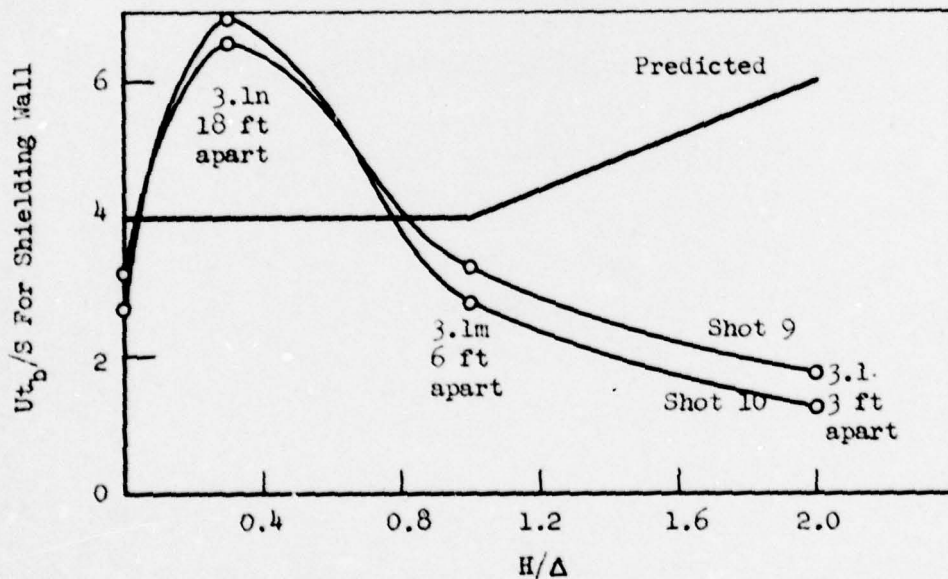


Fig. 4.107—Effect of shielding on build-up time ( $W; H; L = \text{constant}$ ).



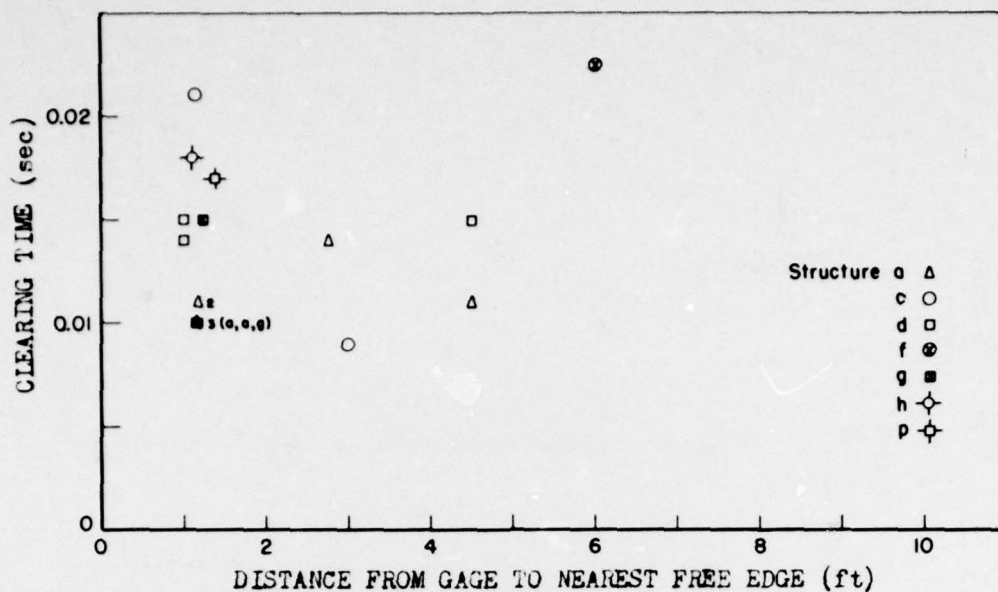


Fig. 4.108—Clearing time vs clearing distance for typical gages, Shot 9.

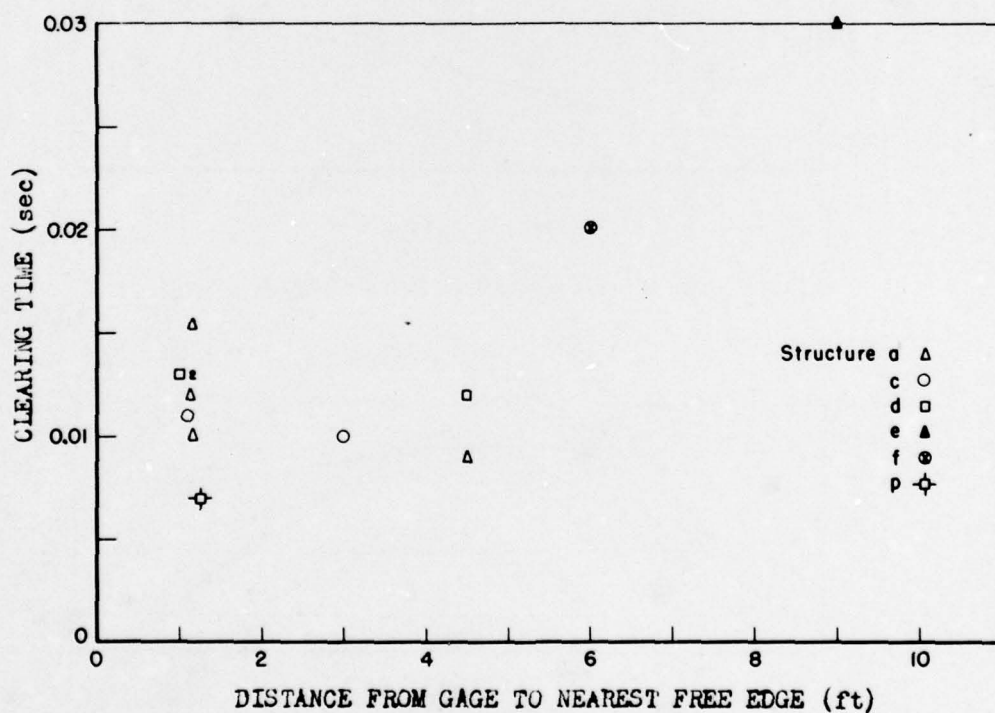


Fig. 4.109—Clearing time vs clearing distance for typical gages, Shot 10.

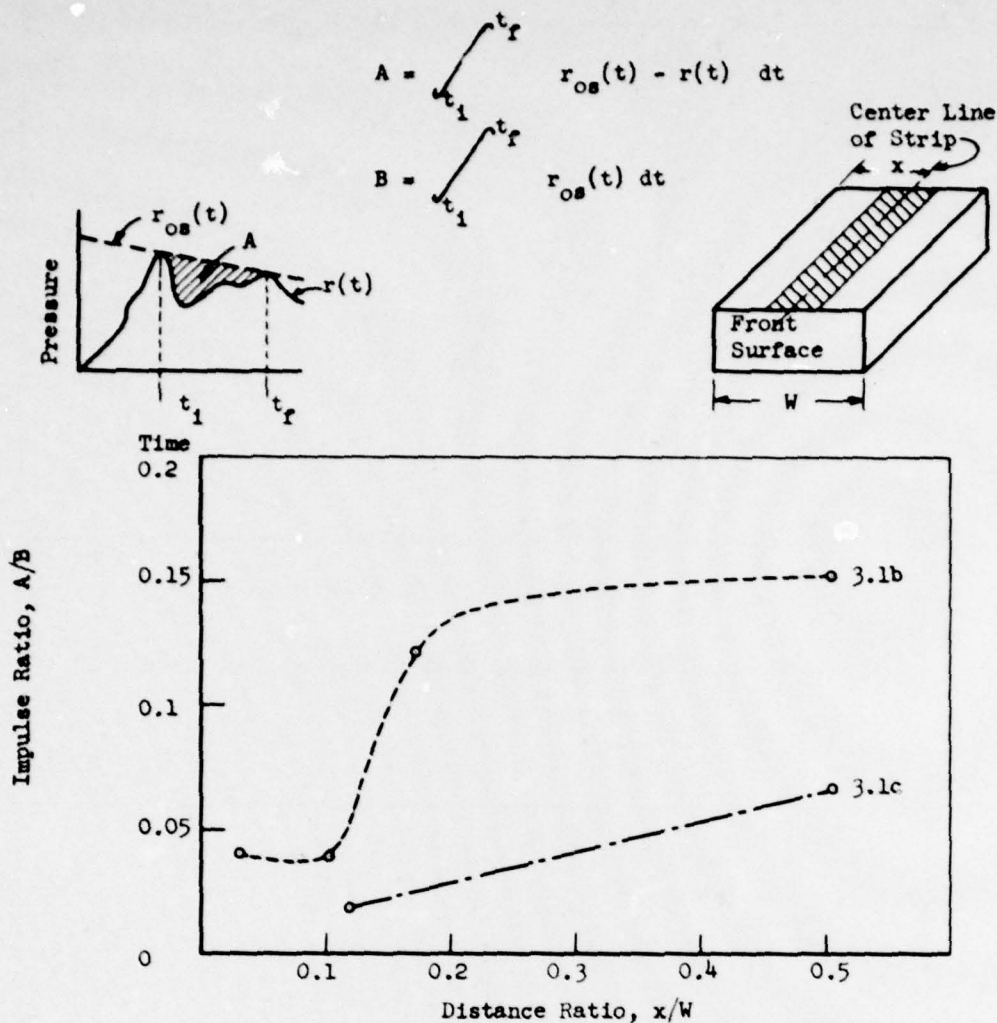


Fig. 4.110 — Effect of vortex on top surface, Structures 3.1b and c, Shot 9.

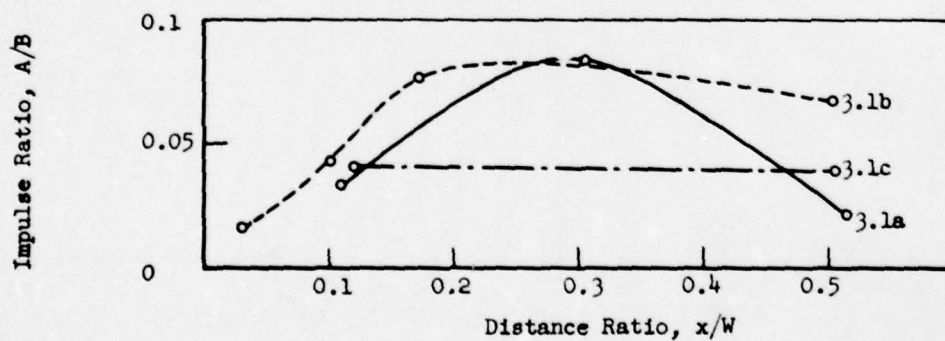


Fig. 4.111 — Effect of vortex on top surface, Structures 3.1a to c, Shot 10.

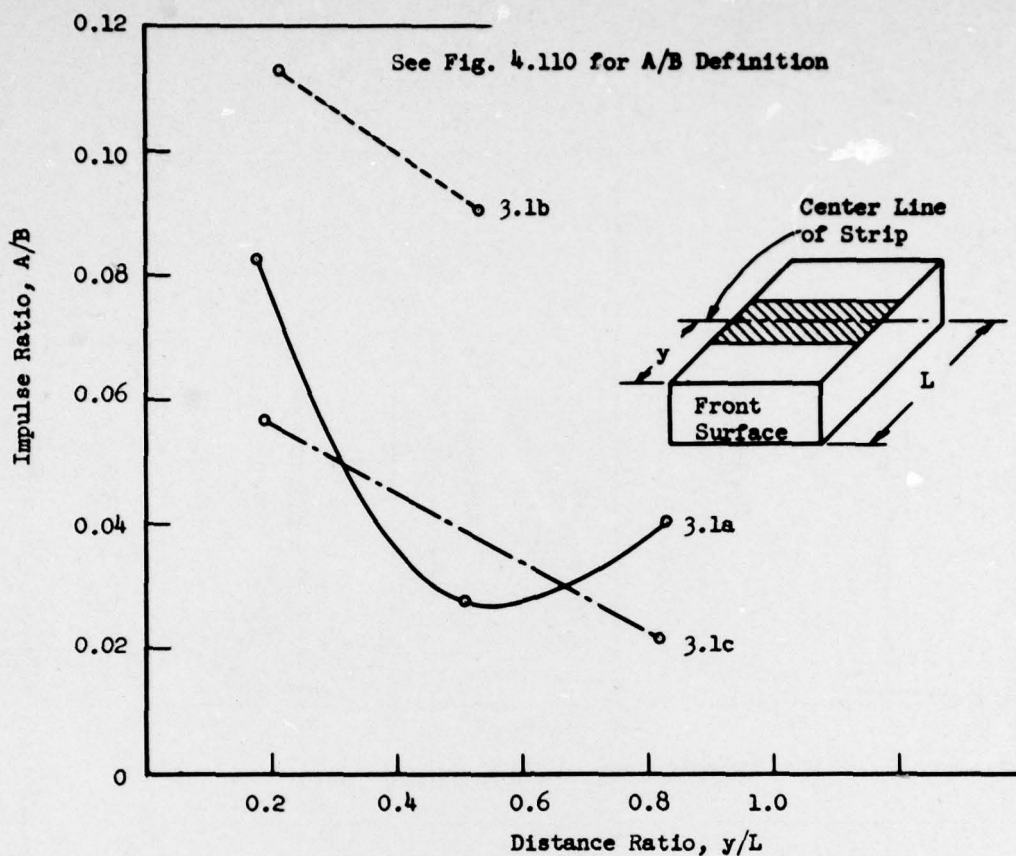


Fig. 4.112—Effect of vortex on top surfaces, Structures 3.1a to c, Shot 9.

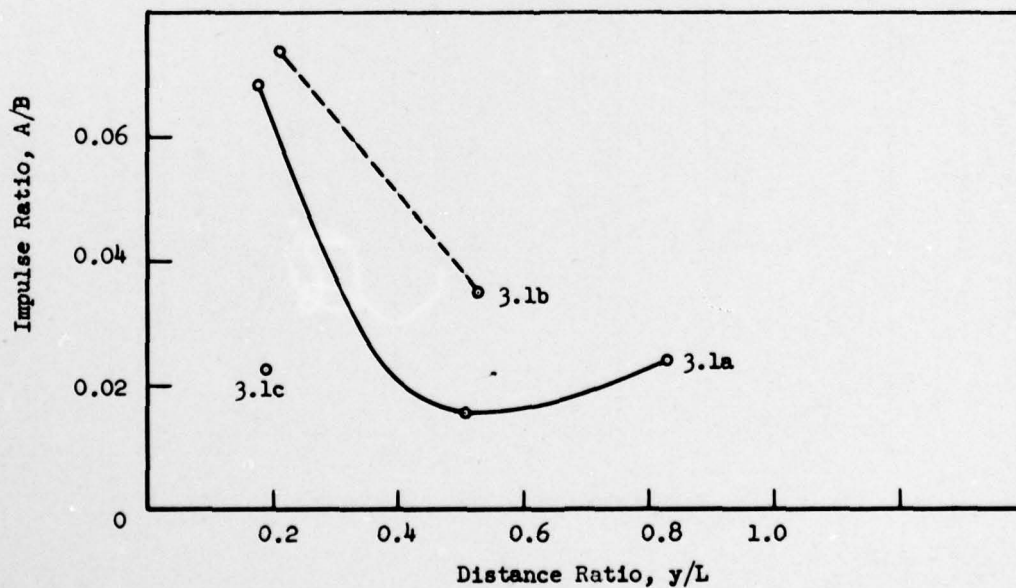


Fig. 4.113—Effect of vortex on top surfaces, Structures 3.1a to c, Shot 10.



UNCLASSIFIED

~~SECRET RESTRICTED DATA~~

206

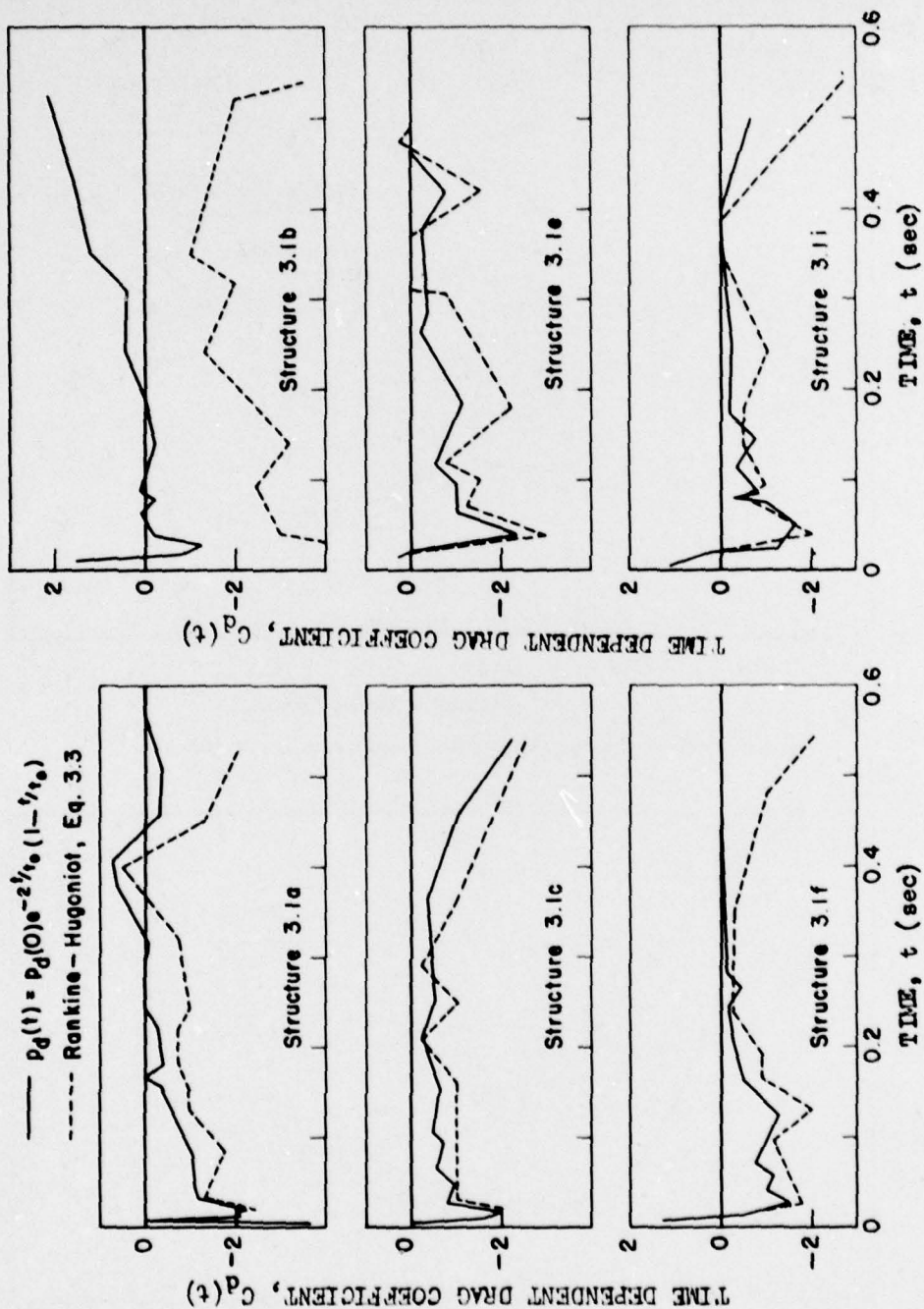


Fig. 4.114 — Time-dependent drag coefficients, top surfaces, Structures 3.1a to c, e, f, and i, Shot 9.

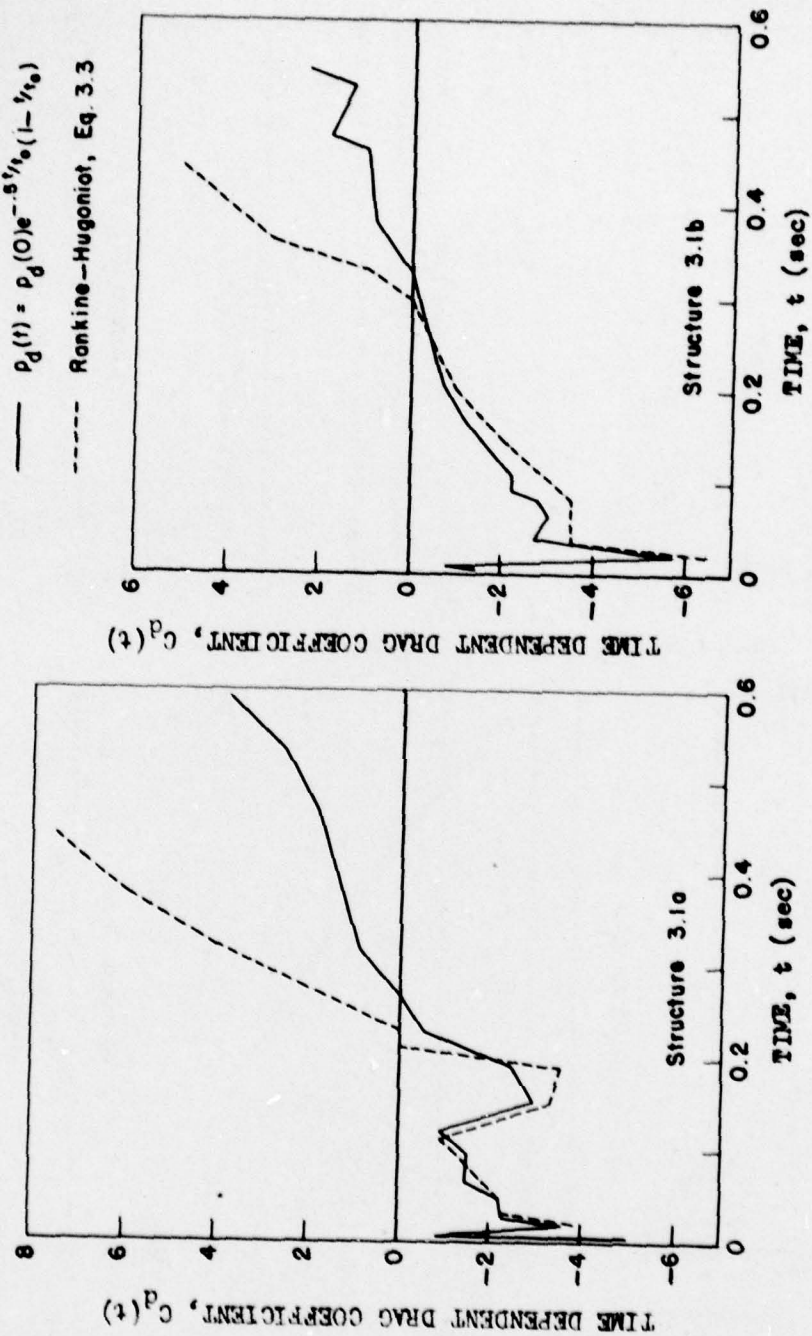


Fig. 4.115—Time-dependent coefficient, top surfaces, Structures 3.1a and b, Shot 10.

UNCLASSIFIED

~~SECRET RESTRICTED DATA~~

208

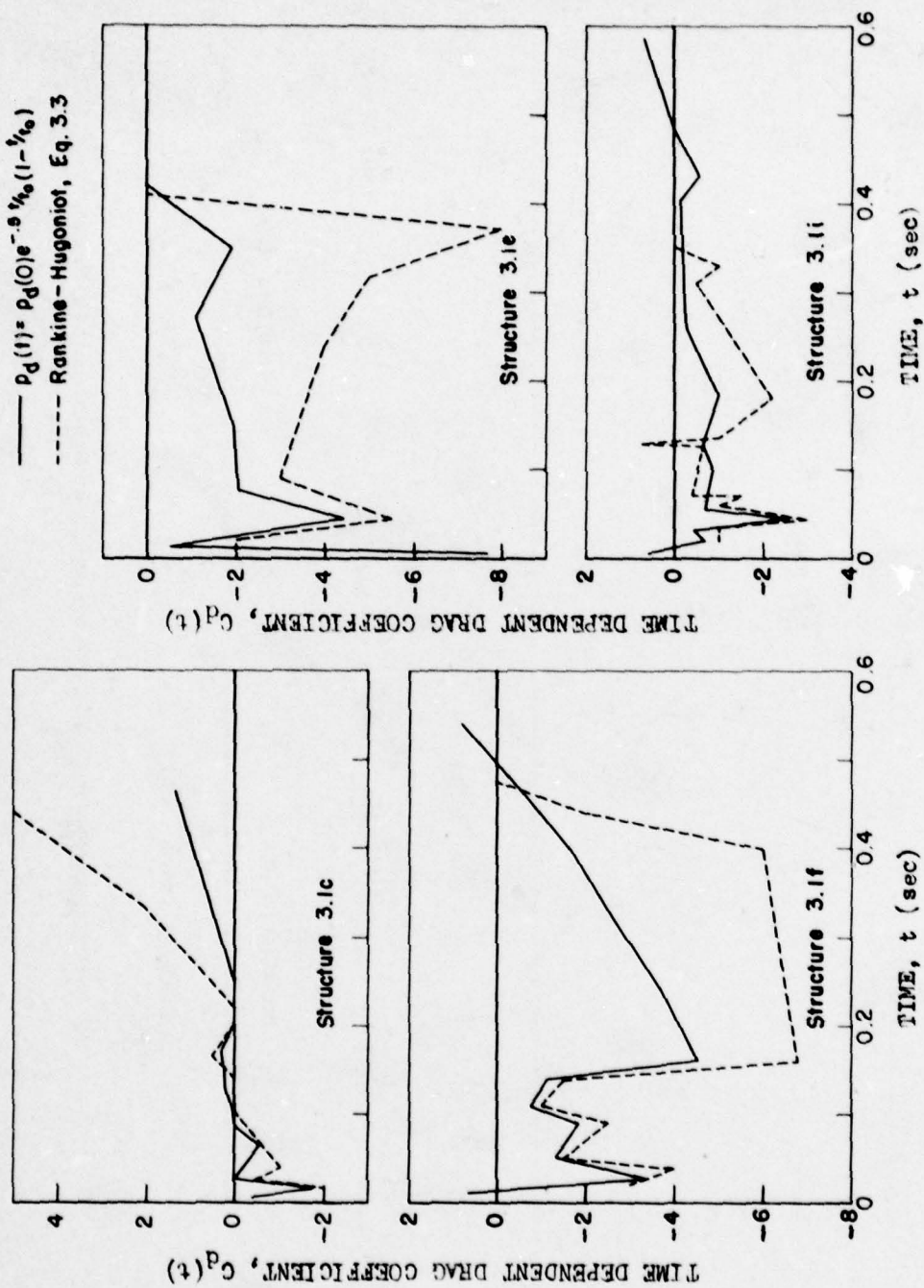


Fig. 4.116 — Time-dependent drag coefficients, top surfaces, Structures 3.1c, e, f, and i, Shot 10.



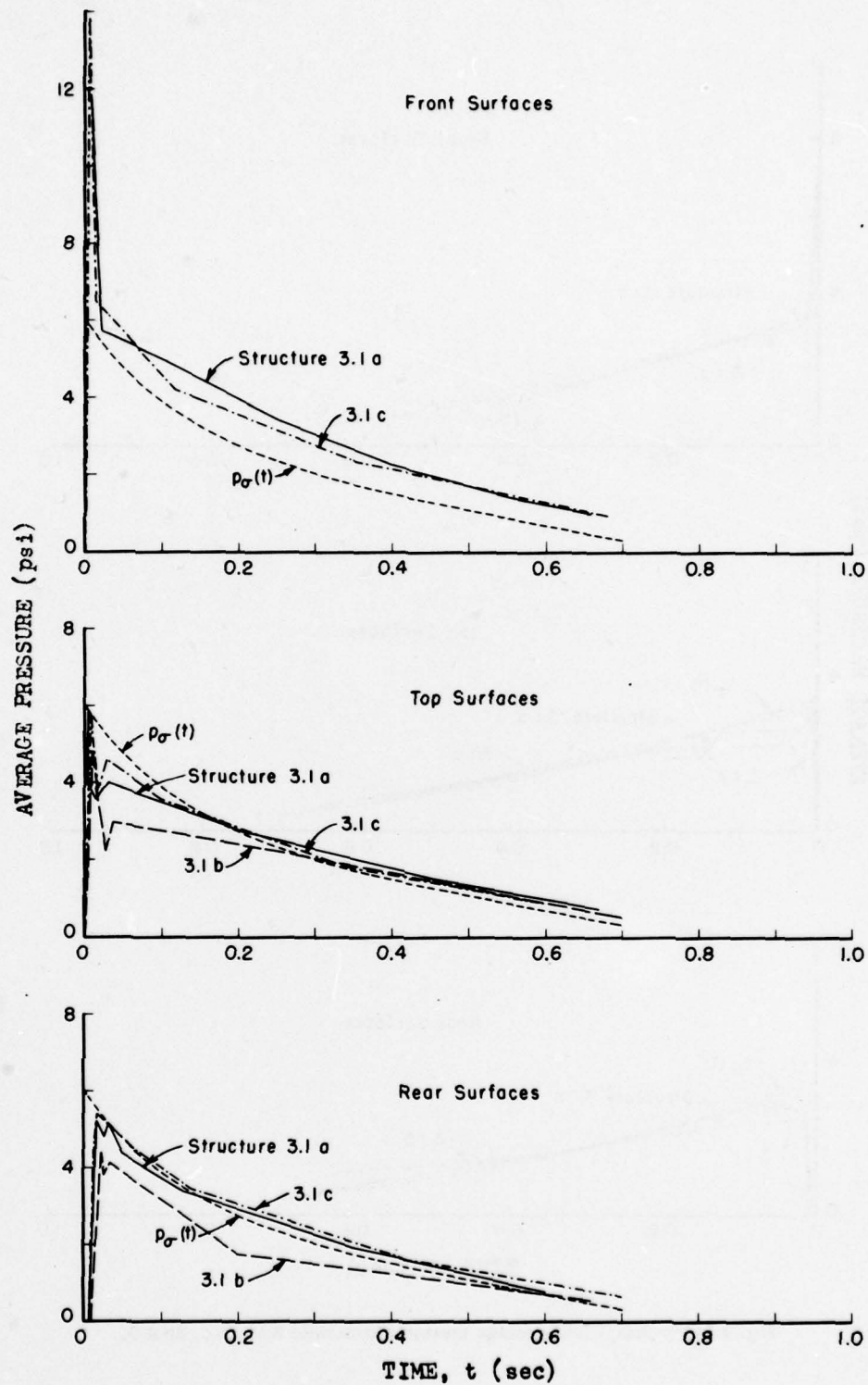


Fig. 4.117—Simplified average pressure, Structures 3.1a to c, Shot 9.

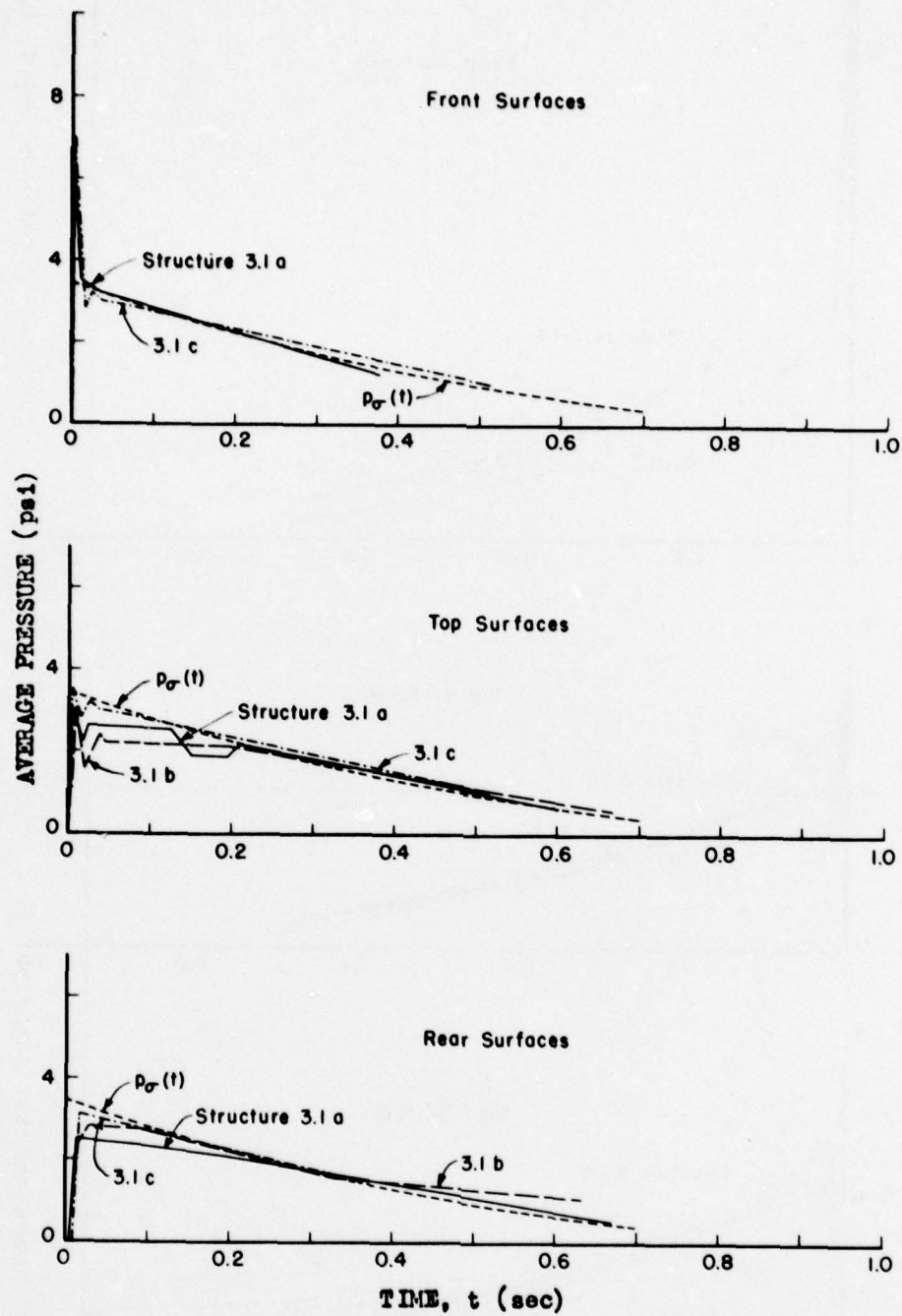


Fig. 4.118—Simplified average pressure, Structures 3.1a to c, Shot 9.

UNCLASSIFIED

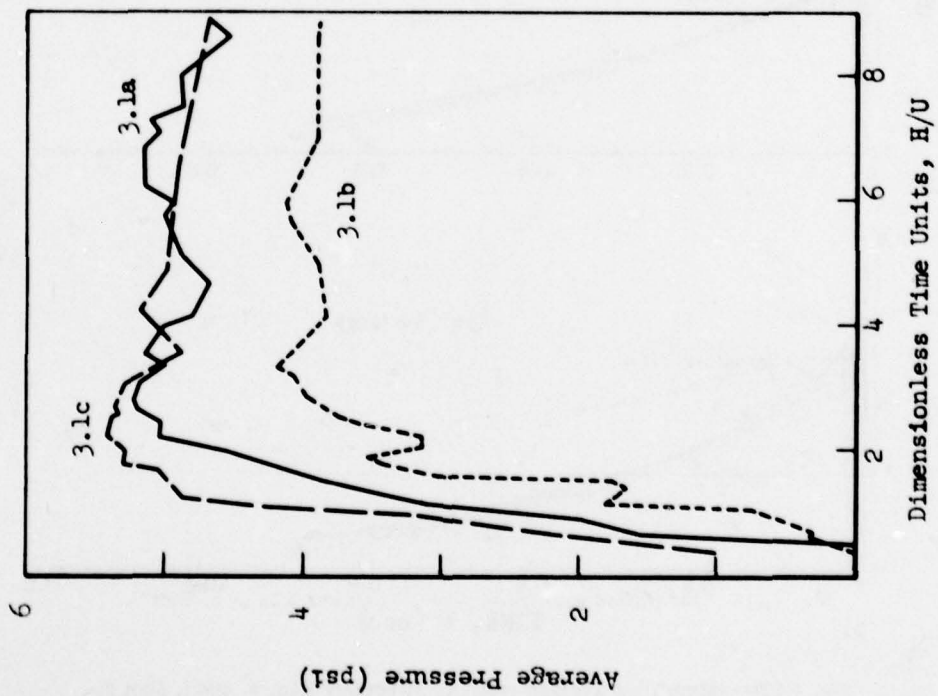


Fig. 4.119—Effect of width on build-up time on rear surface, Shot 9.

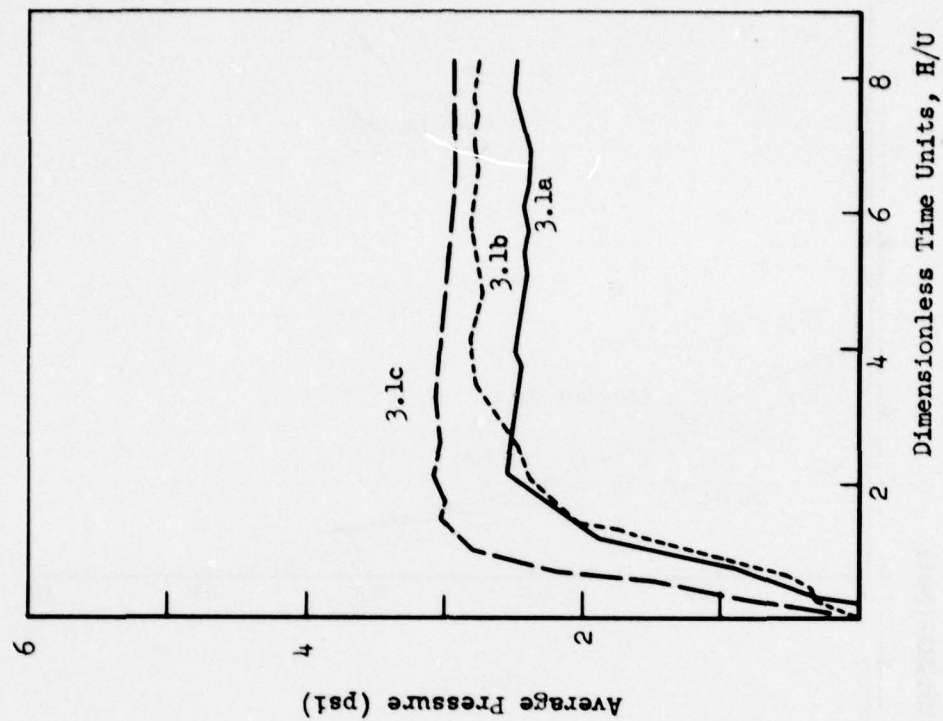


Fig. 4.120—Effect of width on build-up time on rear surface, Shot 10.



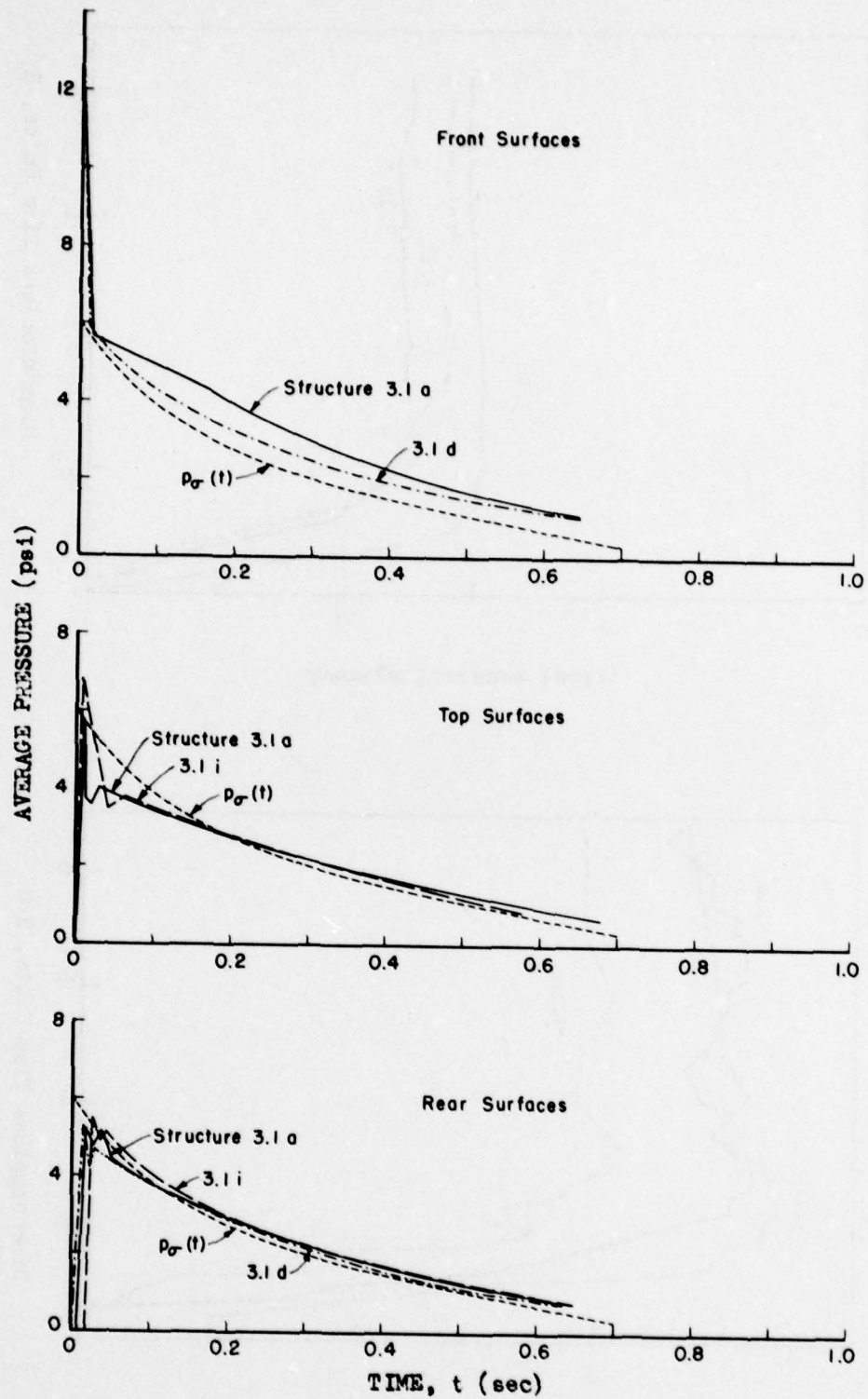


Fig. 4.121 — Simplified average pressure, Structures 3.1a, d, and i, Shot 9.

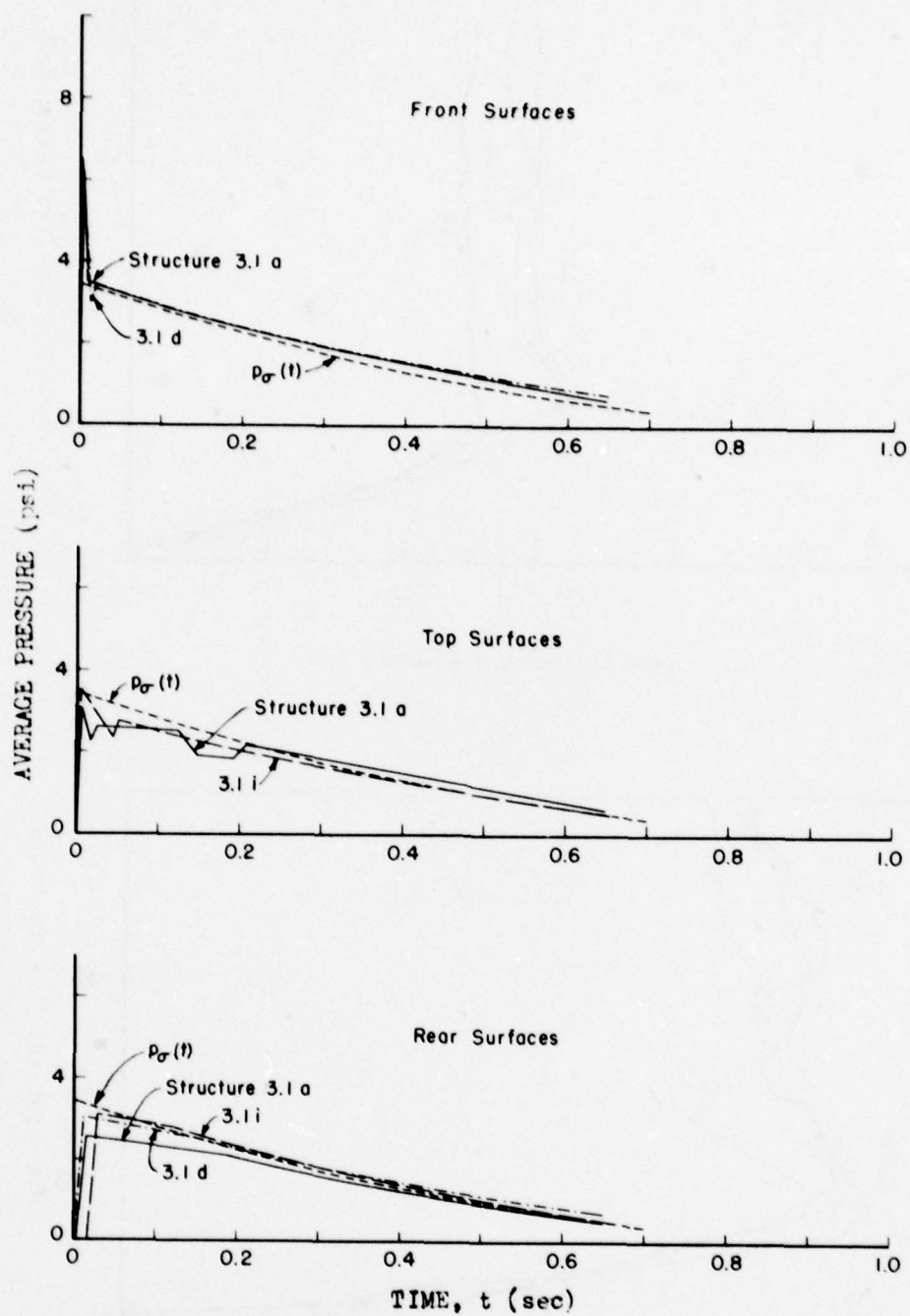


Fig. 4.122—Simplified average pressure, Structures 3.1a, d, and i, Shot 10.

UNCLASSIFIED

214

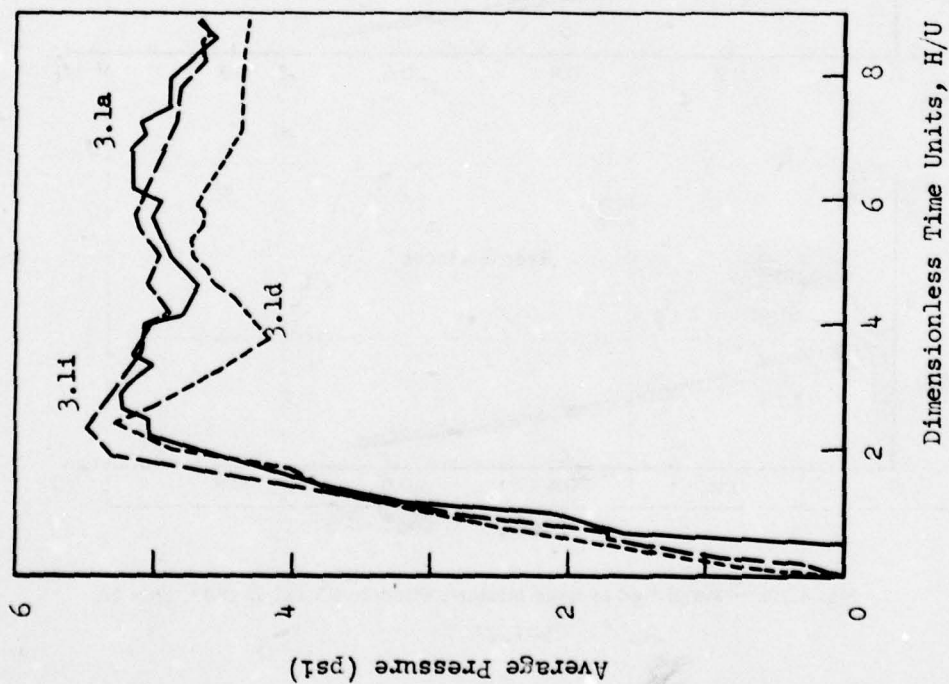


Fig. 4.123 — Effect of length on build-up time on rear surface, Shot 9.

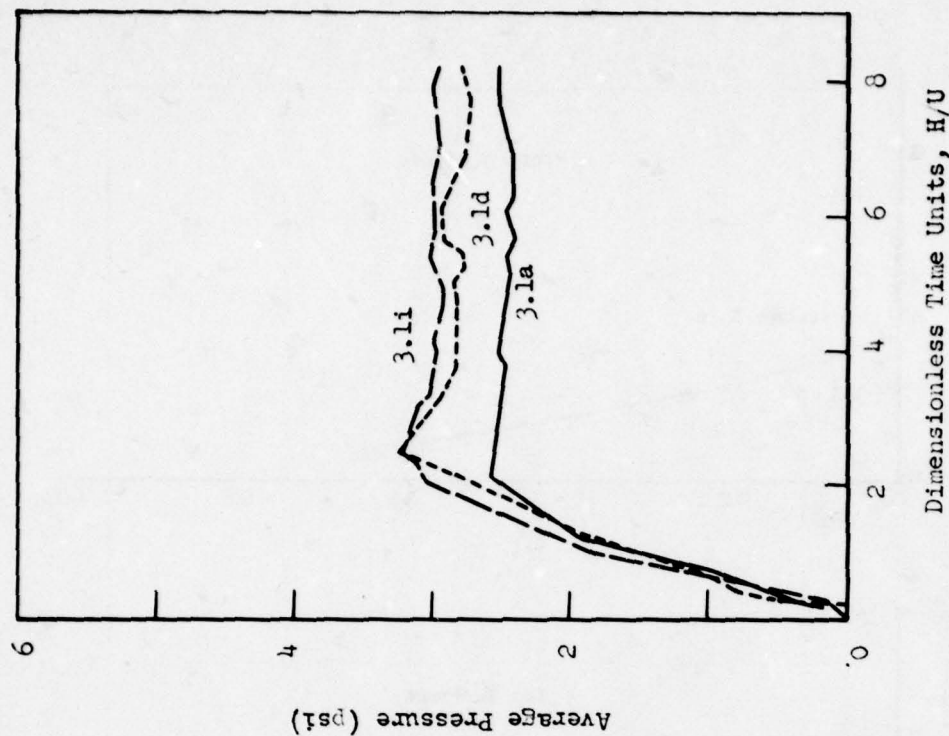


Fig. 4.124 — Effect of length on build-up time on rear surface, Shot 10.



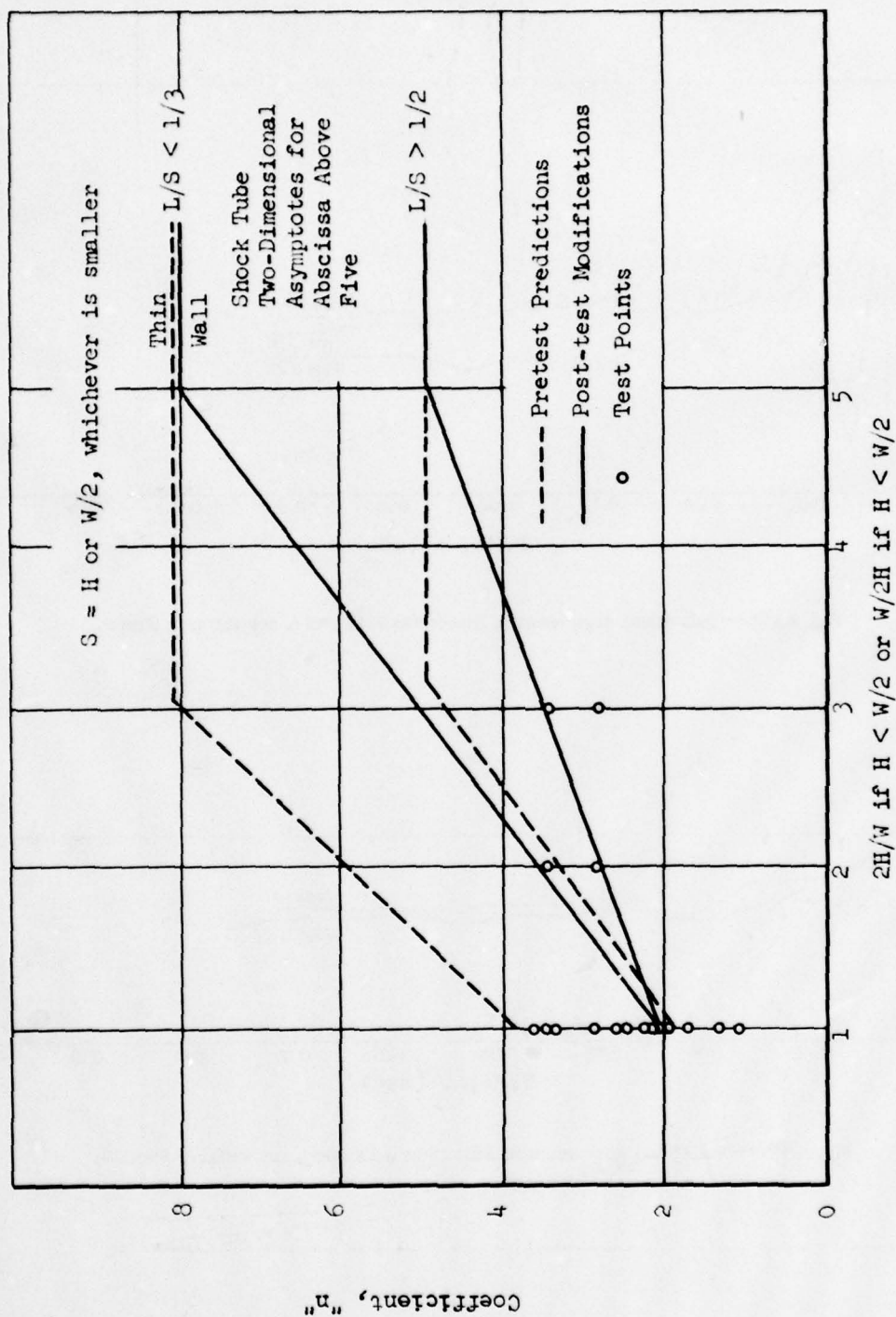


Fig. 4.125—Rear build-up coefficient "n."

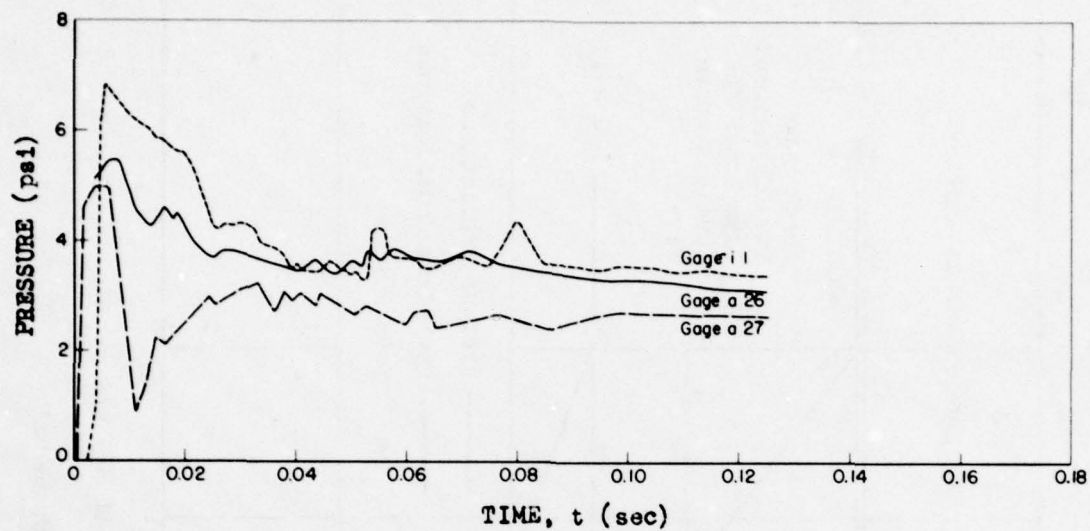


Fig. 4.126 — Individual gage records, Structures 3.1a and i, top surface, Shot 9.

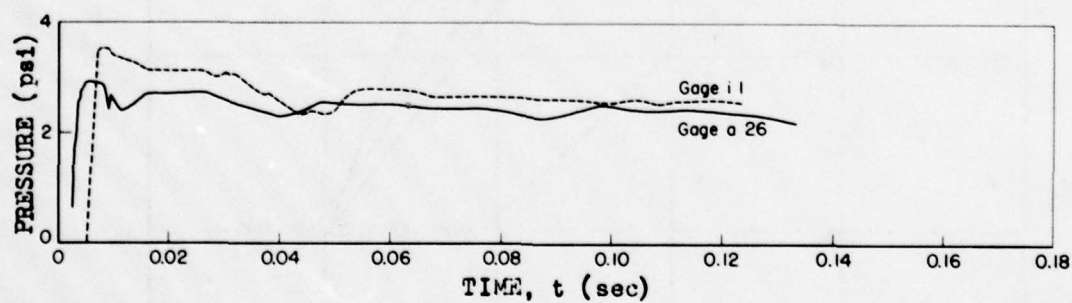


Fig. 4.127 — Individual gage records, Structures 3.1a and i, top surface, Shot 10.

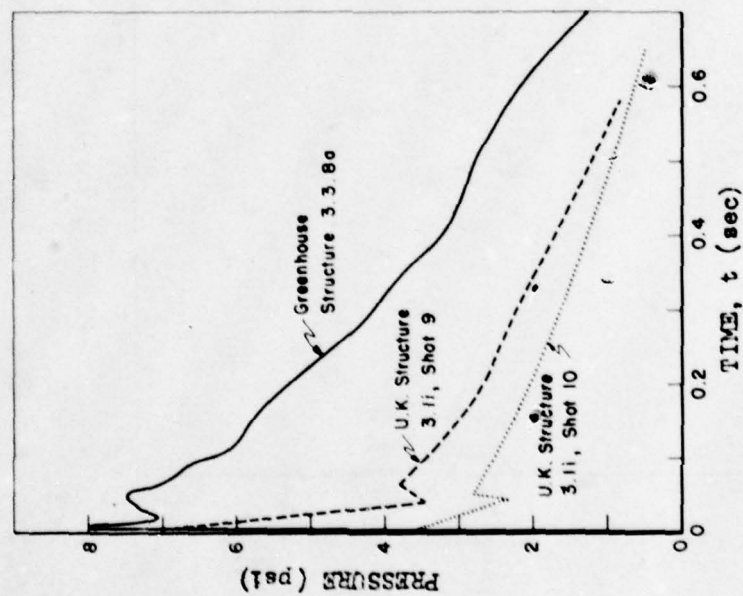


Fig. 4.128 — Comparison of UPSHOT-KNOTHOLE to GREENHOUSE, top surface pressures.

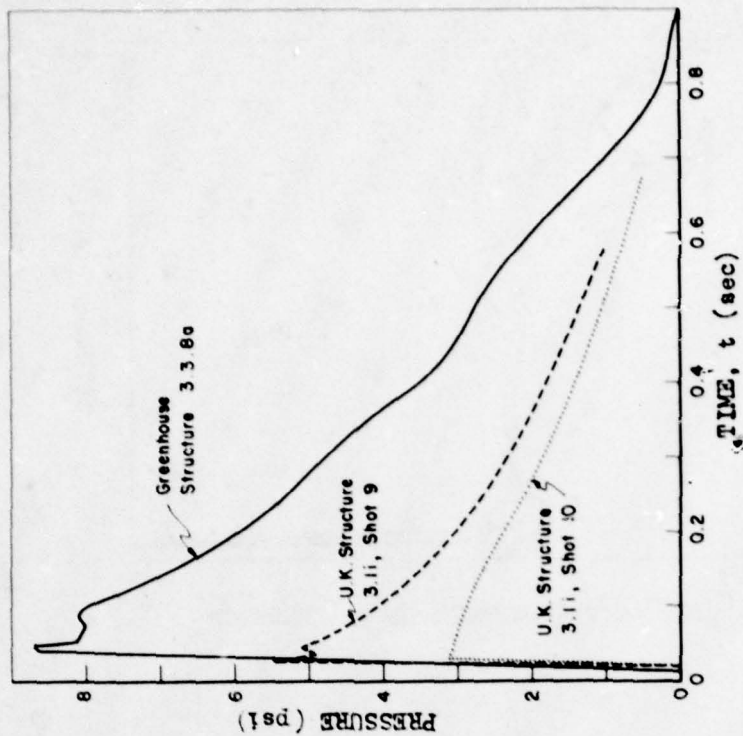


Fig. 4.129 — Comparison of UPSHOT-KNOTHOLE to GREENHOUSE, rear surface pressures.



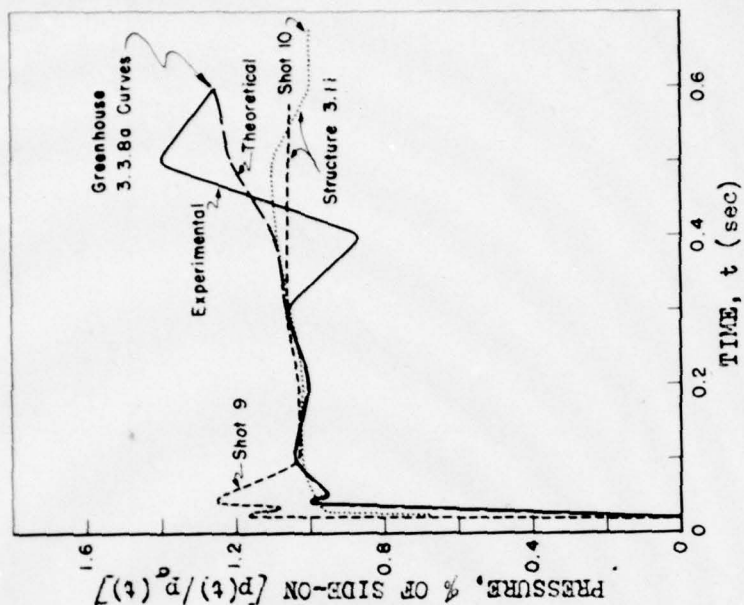


Fig. 4.131 — Comparison of UPSHOT-KNOTHOLE to GREENHOUSE, rear surface normalized pressures.

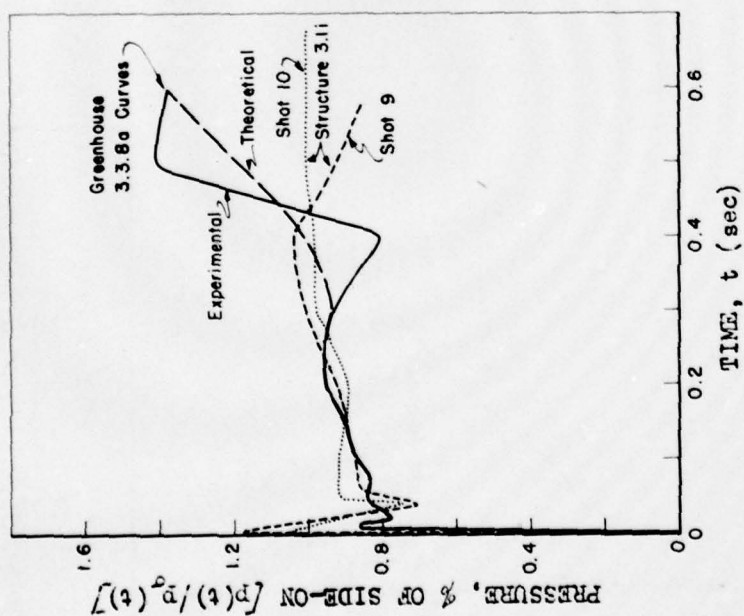


Fig. 4.130 — Comparison of UPSHOT-KNOTHOLE to GREENHOUSE, top surface normalized pressures.

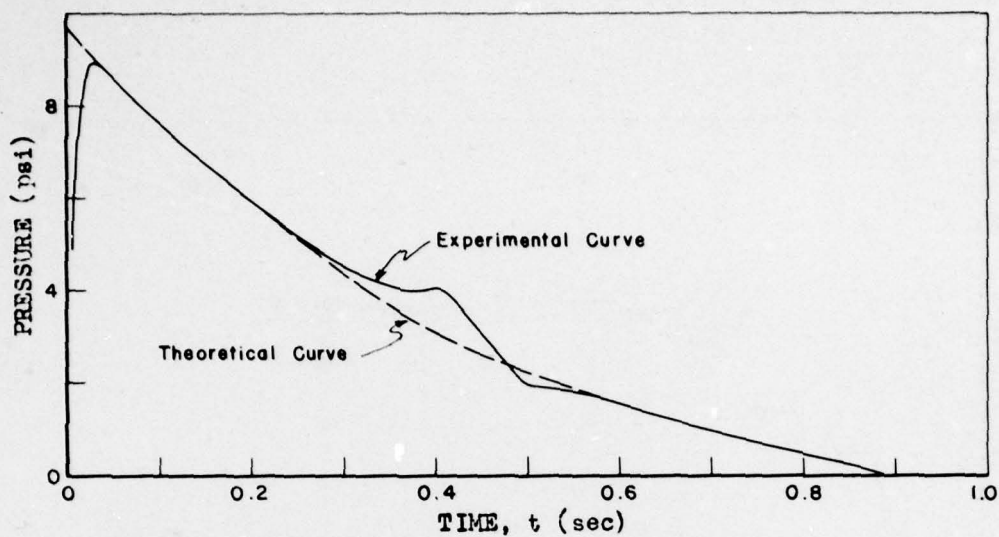


Fig. 4.132—GREENHOUSE free stream pressure.

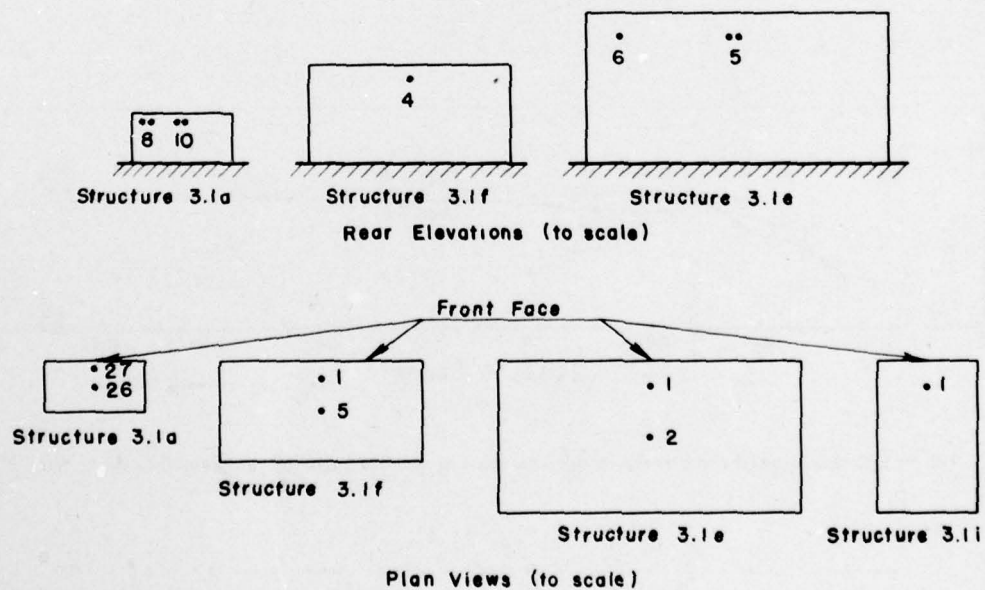


Fig. 4.133—Gage locations on Structures 3.1a, e, f, and i.

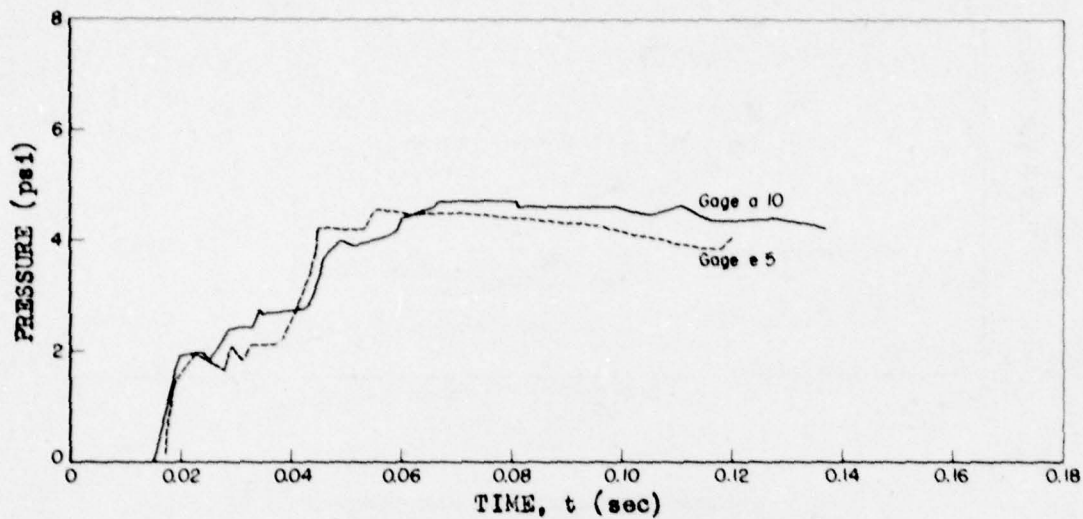


Fig. 4.134 — Individual gage records showing time scaling on rear surfaces, gages a10 and e5, Shot 9.

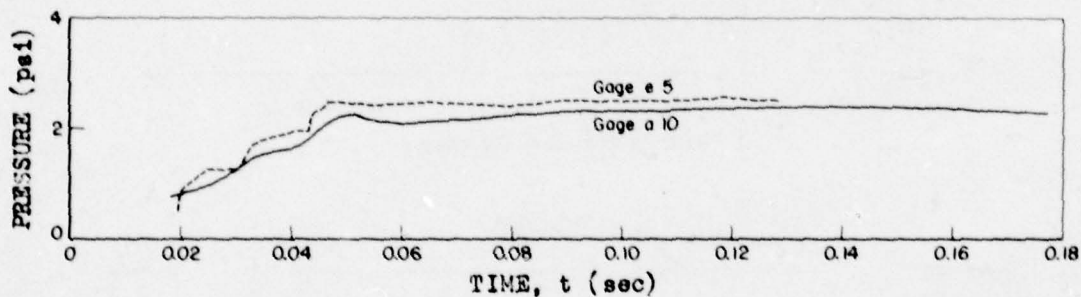


Fig. 4.135 — Individual gage records showing time scaling on rear surfaces, gages a10 and e5, Shot 10.

UNCLASSIFIED

~~SECRET RESTRICTED DATA~~



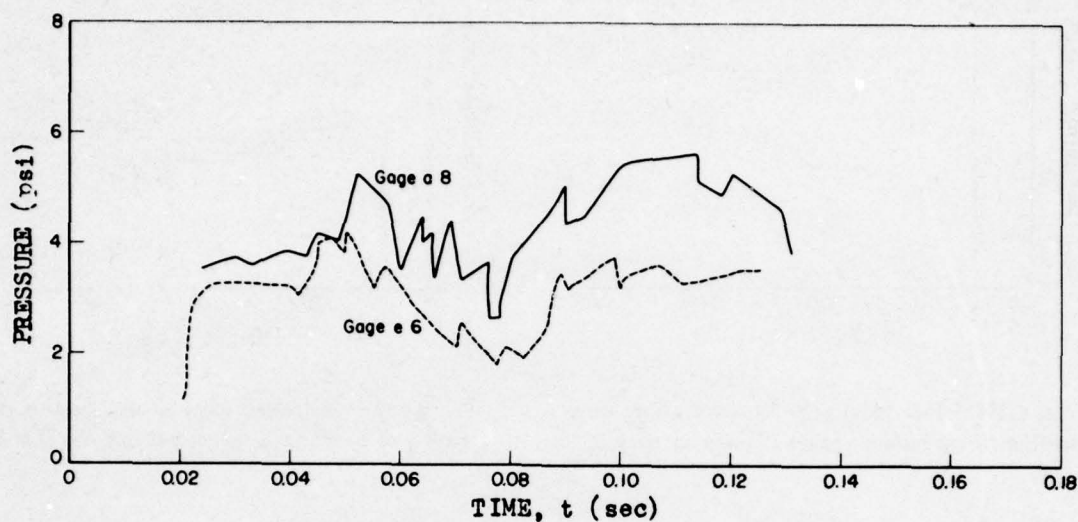


Fig. 4.136 — Individual gage records showing time scaling on rear surfaces, gages a8 and e6, Shot 9.

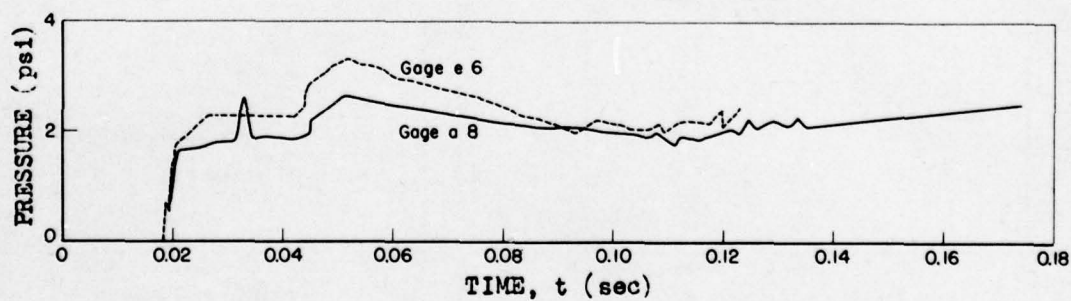


Fig. 4.137 — Individual gage records showing time scaling on rear surfaces, gages a8 and e6, Shot 10.

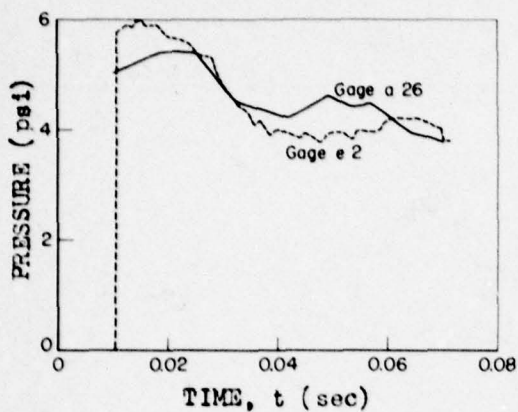


Fig. 4.138—Individual gage records showing time scaling on top surface, gages a26 and e2, Shot 9.

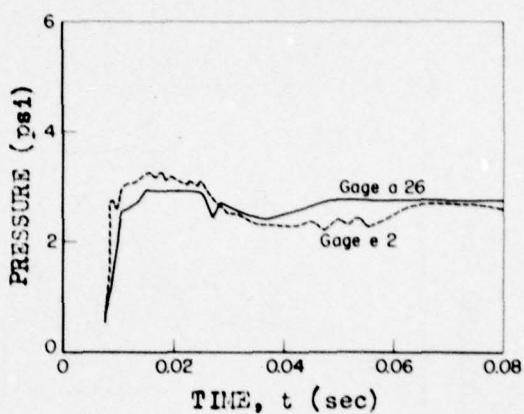


Fig. 4.139—Individual gage records showing time scaling on top surface, gages a26 and e2, Shot 10.

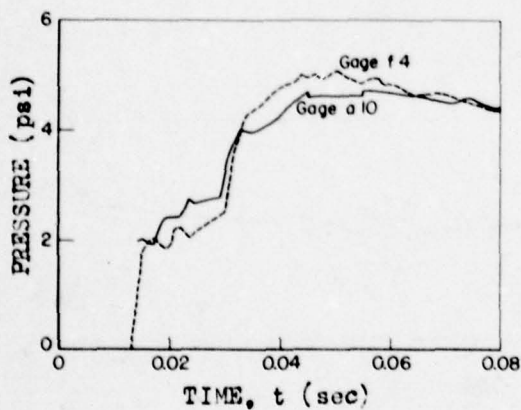


Fig. 4.140—Individual gage records showing time scaling on rear surface, gages a10 and f4, Shot 9.

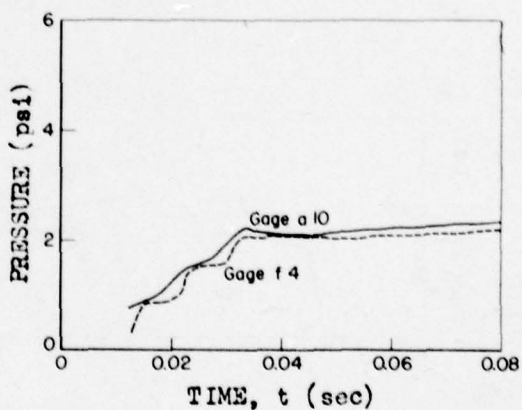


Fig. 4.141—Individual gage records showing time scaling on rear surface, gages a10 and f4, Shot 10.

UNCLASSIFIED

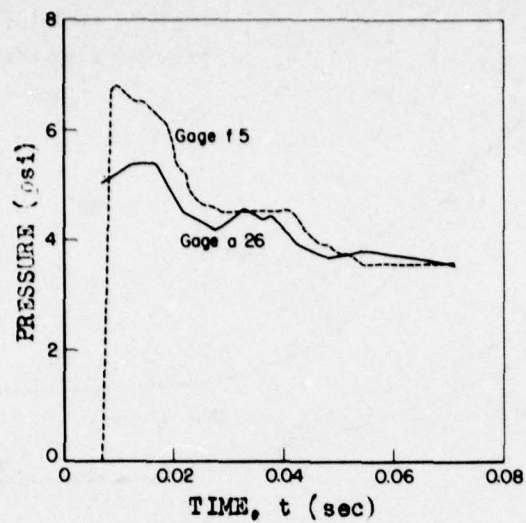


Fig. 4.142—Individual gage records showing time scaling on top surface, gages a26 and f5, Shot 9.

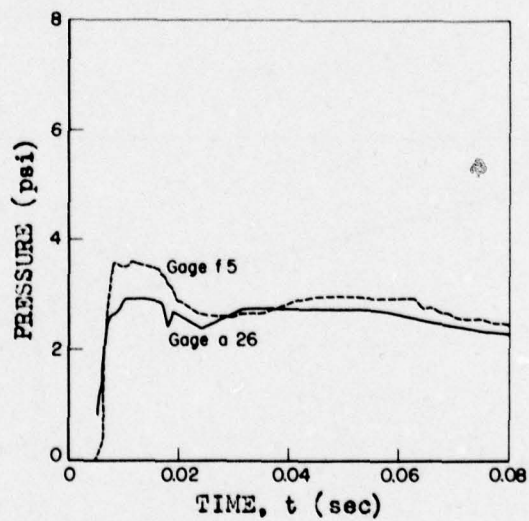


Fig. 4.143—Individual gage records showing time scaling on top surface, gages a26 and f5, Shot 10.



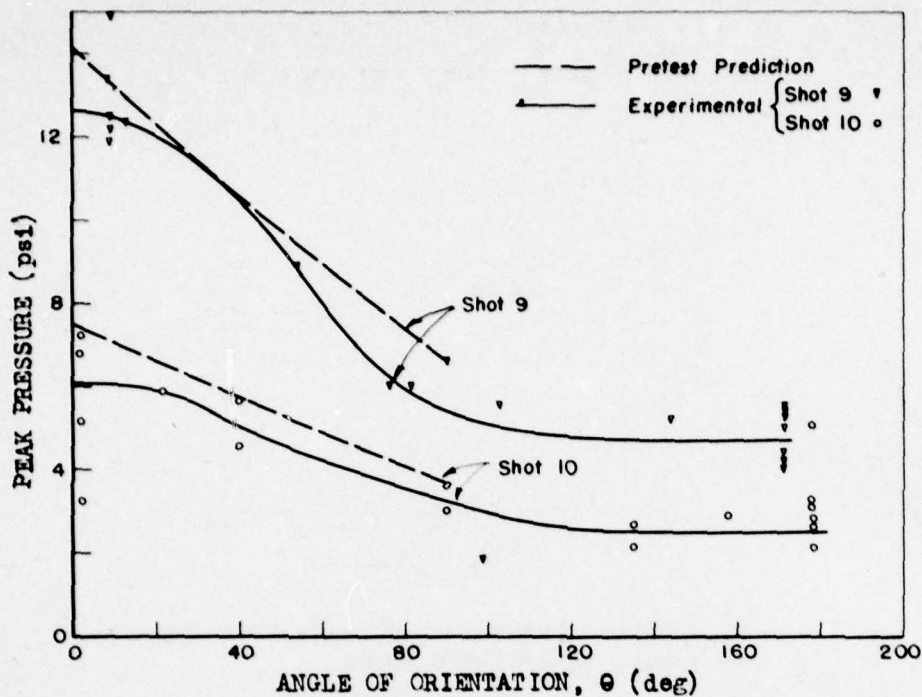


Fig. 4.144—Peak pressure as a function of surface orientation.

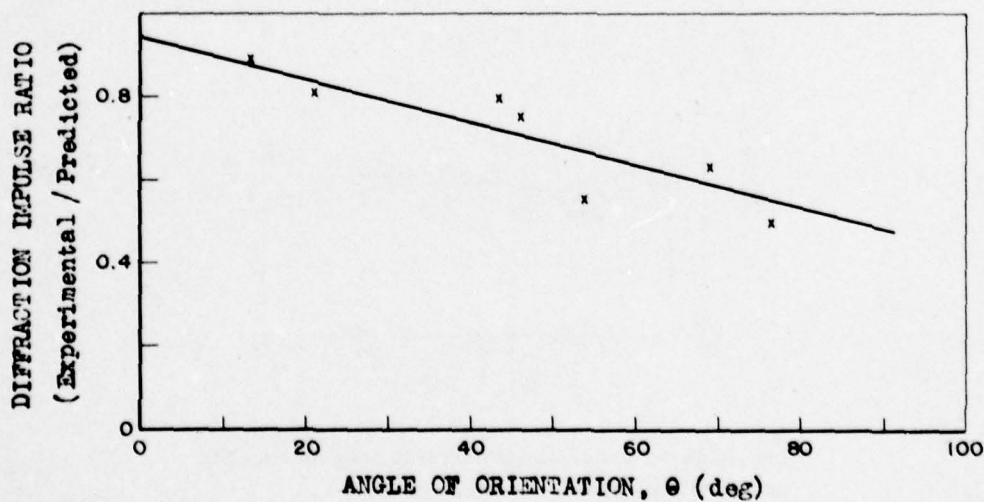


Fig. 4.145—Comparison of experimental to predicted diffraction impulse on obliquely loaded semi-front surfaces.

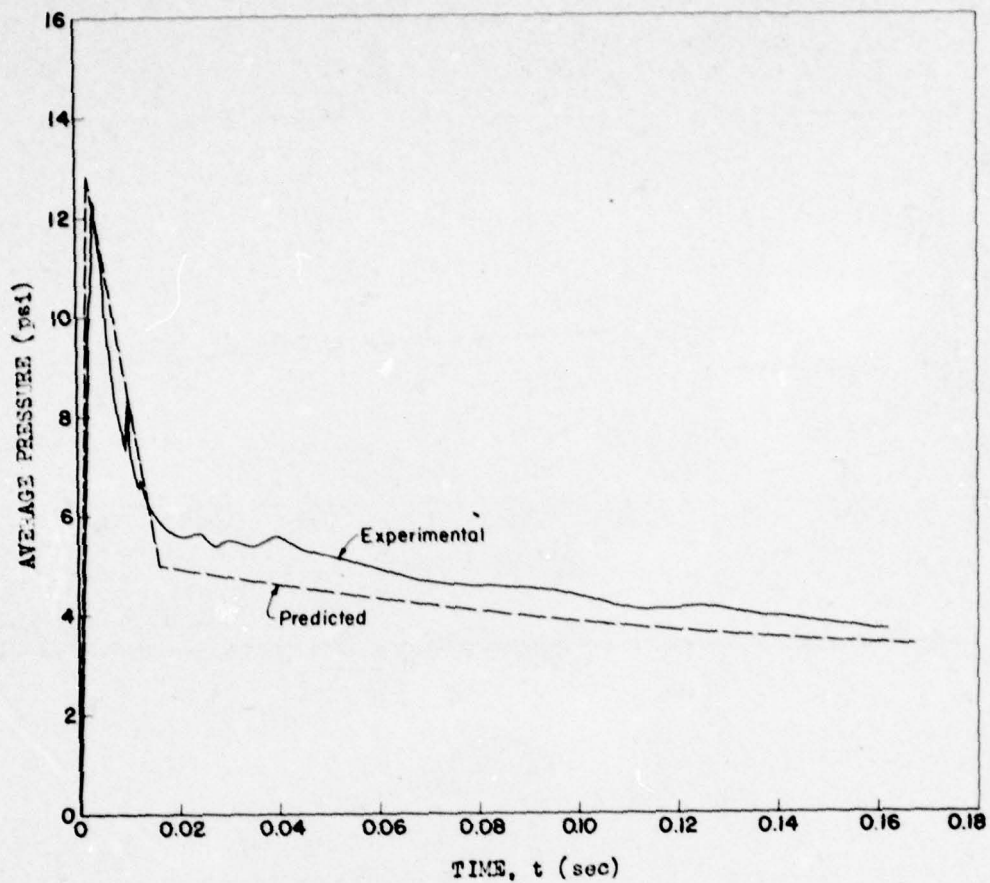


Fig. 4.146—Comparison of predicted to experimental pressure on front surface, Structure 3.1g, Shot 9.

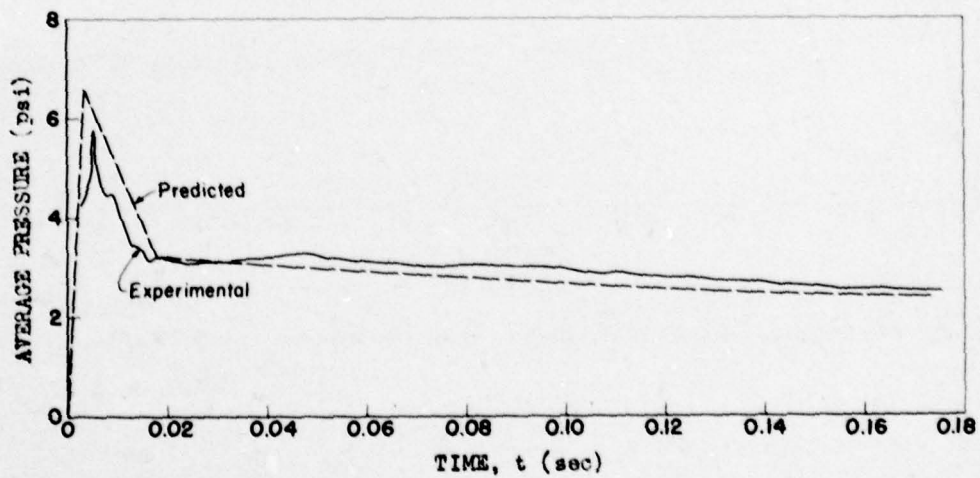


Fig. 4.147—Comparison of predicted to experimental pressure on front surface, Structure 3.1g, Shot 10.

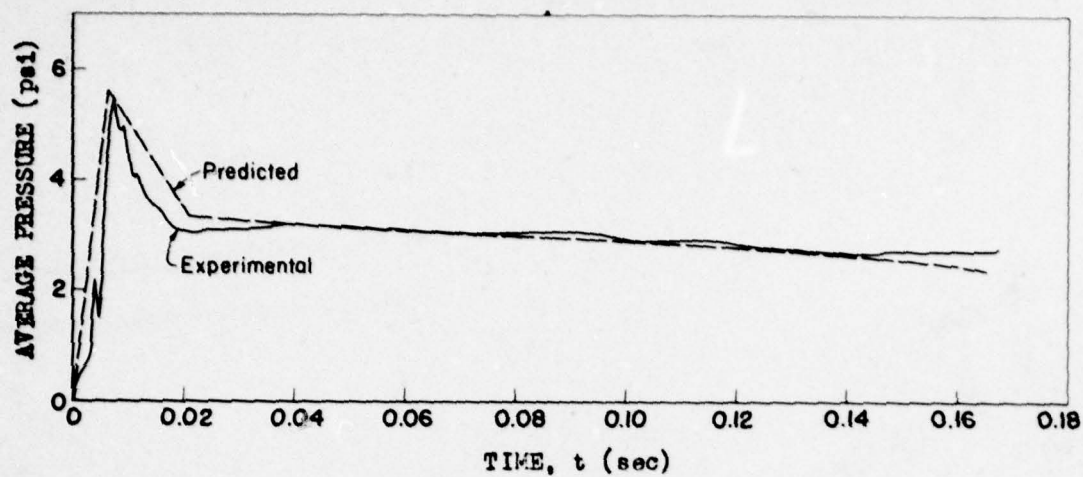


Fig. 4.148 — Comparison of predicted to experimental pressure on front surface, Structure 3.1h, Shot 10.

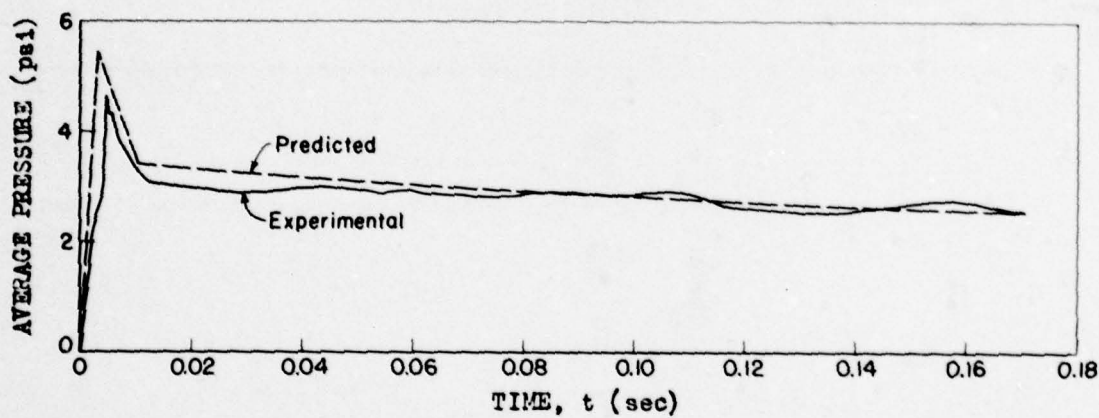


Fig. 4.149 — Comparison of predicted to experimental pressure on right side surface, Structure 3.1h, Shot 10.

UNCLASSIFIED

226

~~SECRET RESTRICTED DATA~~



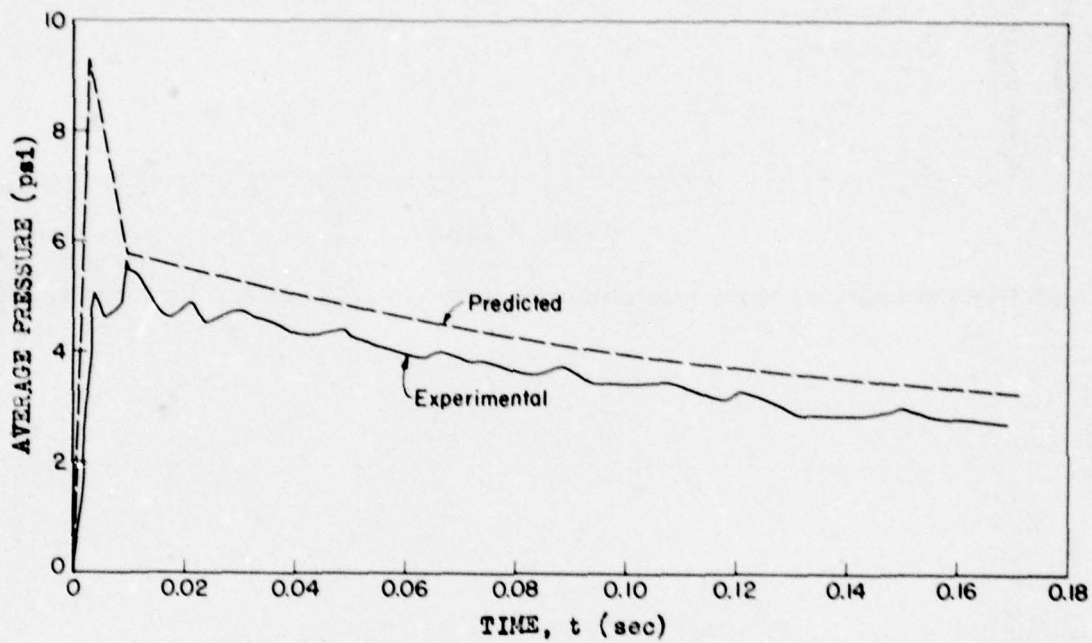


Fig. 4.150—Comparison of predicted to experimental pressure on right side surface, Structure 3.1h, Shot 9.

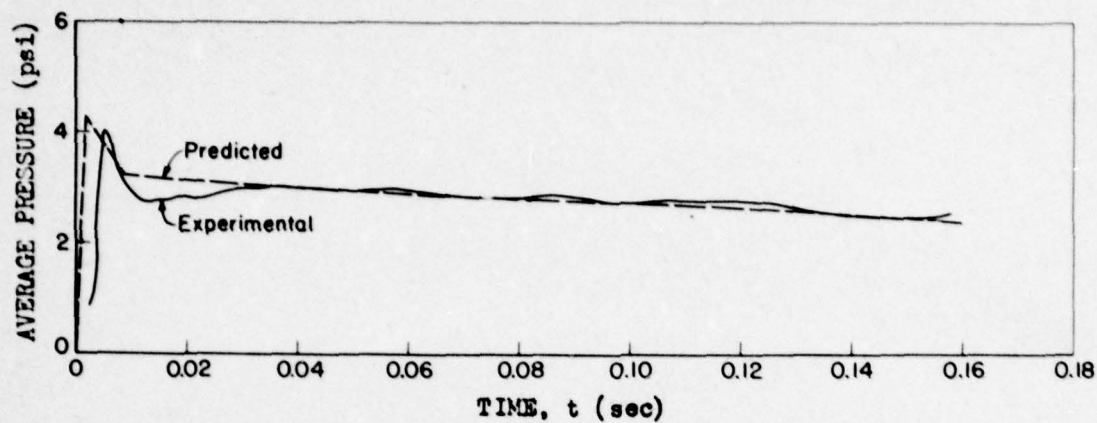


Fig. 4.151 — Comparison of predicted to experimental pressure on right side surface, Structure 3.1g, Shot 10.

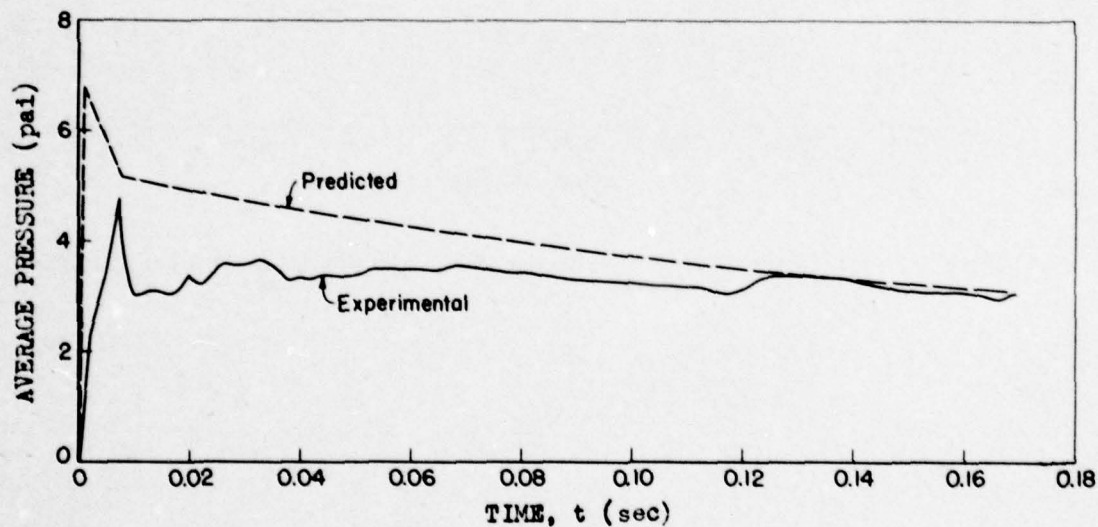


Fig. 4.152 — Comparison of predicted to experimental pressure on right side surface, Structure 3.1g, Shot 9.

UNCLASSIFIED

~~SECRET RESTRICTED DATA~~

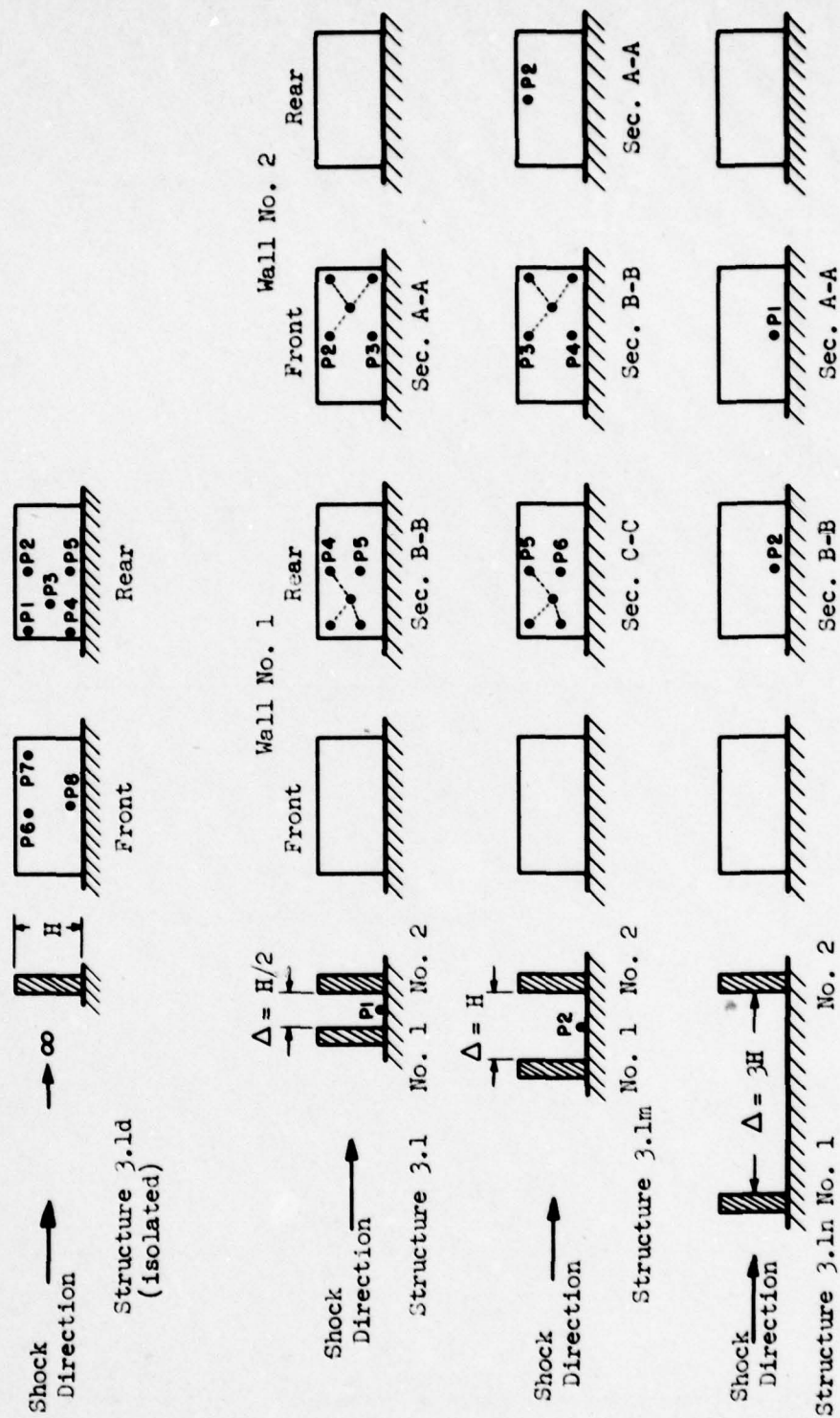


Fig. 4.153—Shielding effects.



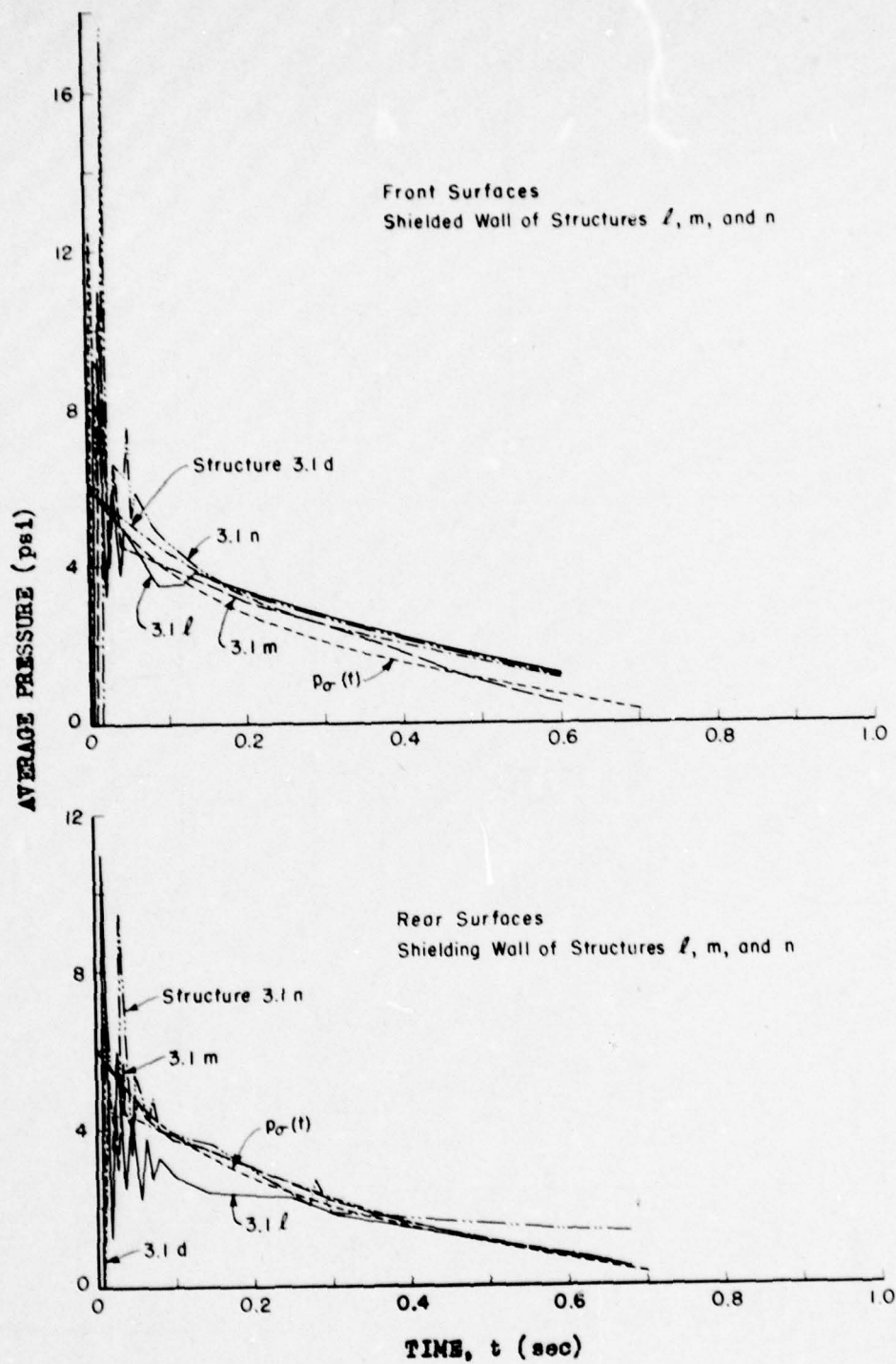


Fig. 4.154—Simplified average pressure, Structures-3.1d, l, m, and n, Shot 9.

UNCLASSIFIED

230

~~SECRET-RESTRICTED DATA~~

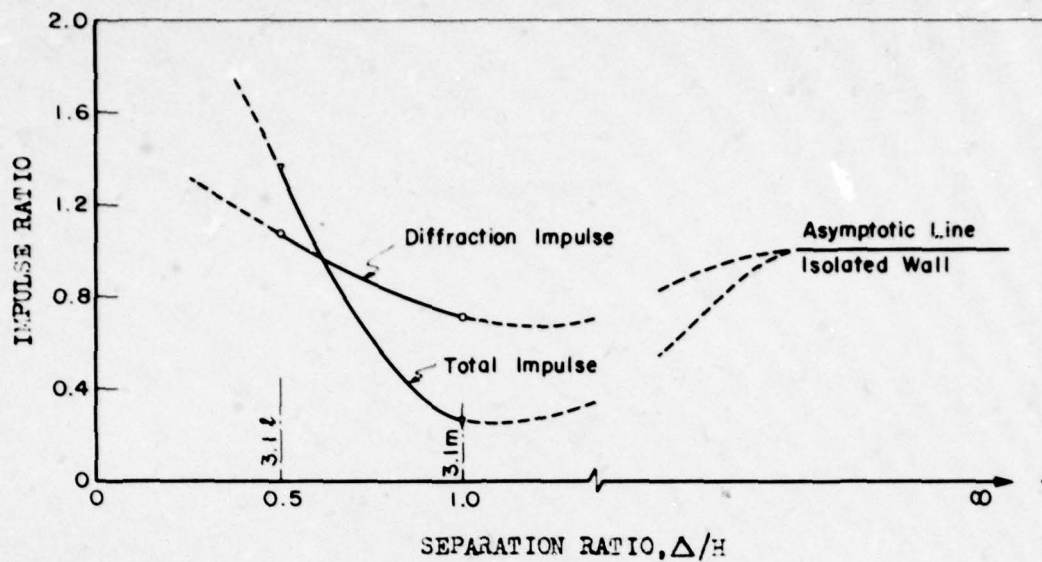


Fig. 4.155 — Ratio of net impulse on shielding walls (Structures 3.11 and m) to that on isolated wall (Structure 3.1d), Shot 9.

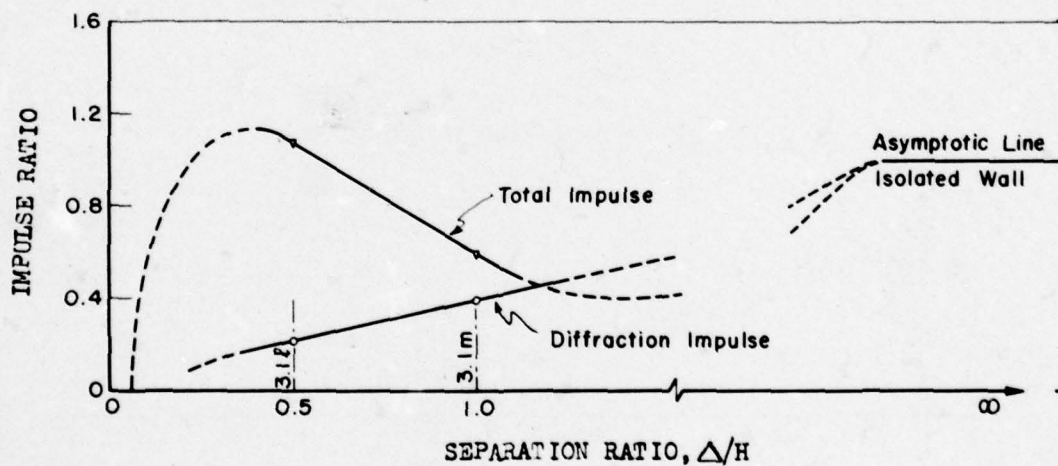


Fig. 4.156 — Ratio of net impulse on shielding walls (Structures 3.11 and m) to that on isolated wall (Structure 3.1d), Shot 10.

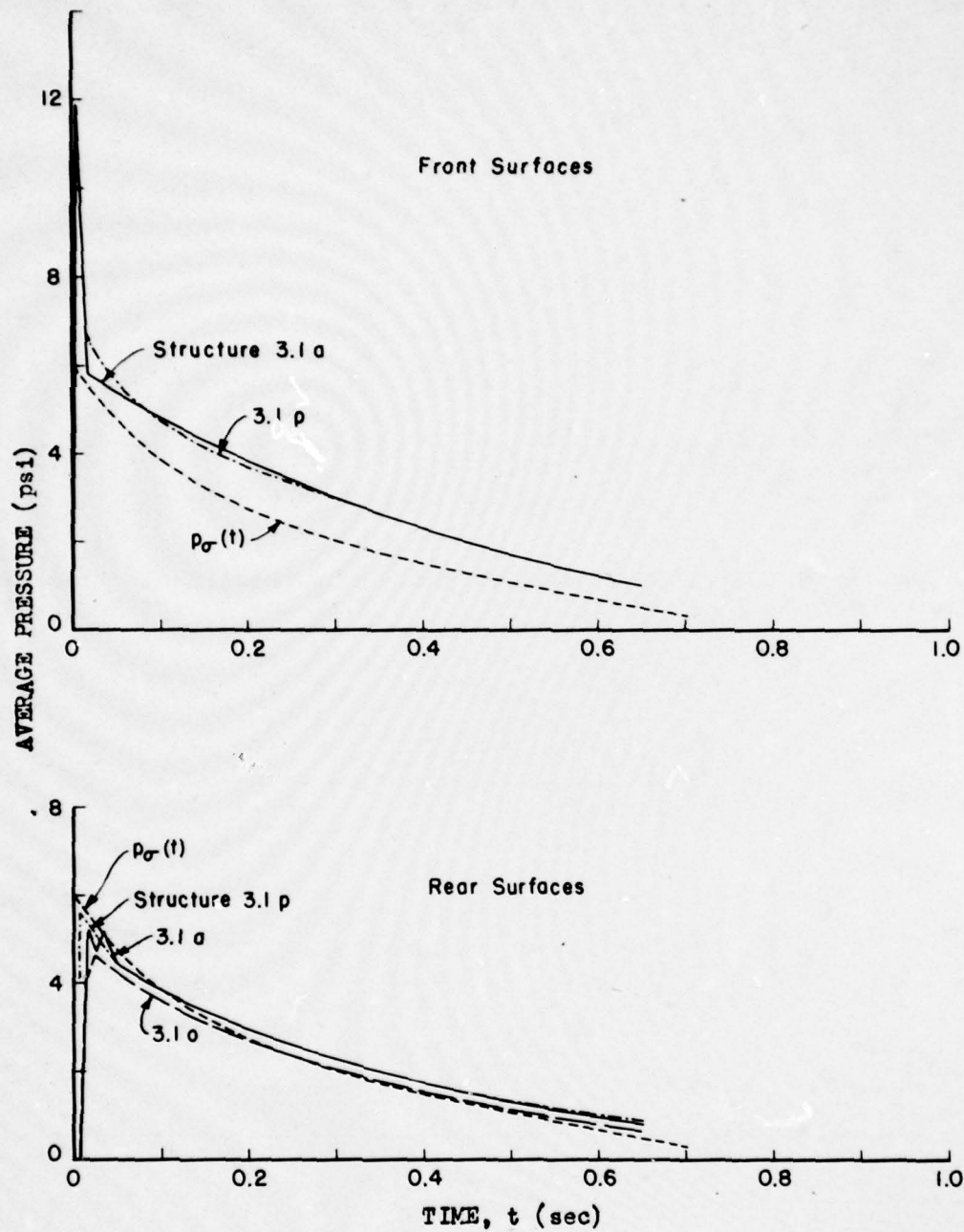


Fig. 4.157 — Simplified average pressure, Structures 3.1a, o, and p, Shot 9.

UNCLASSIFIED

~~SECRET - RESTRICTED DATA~~



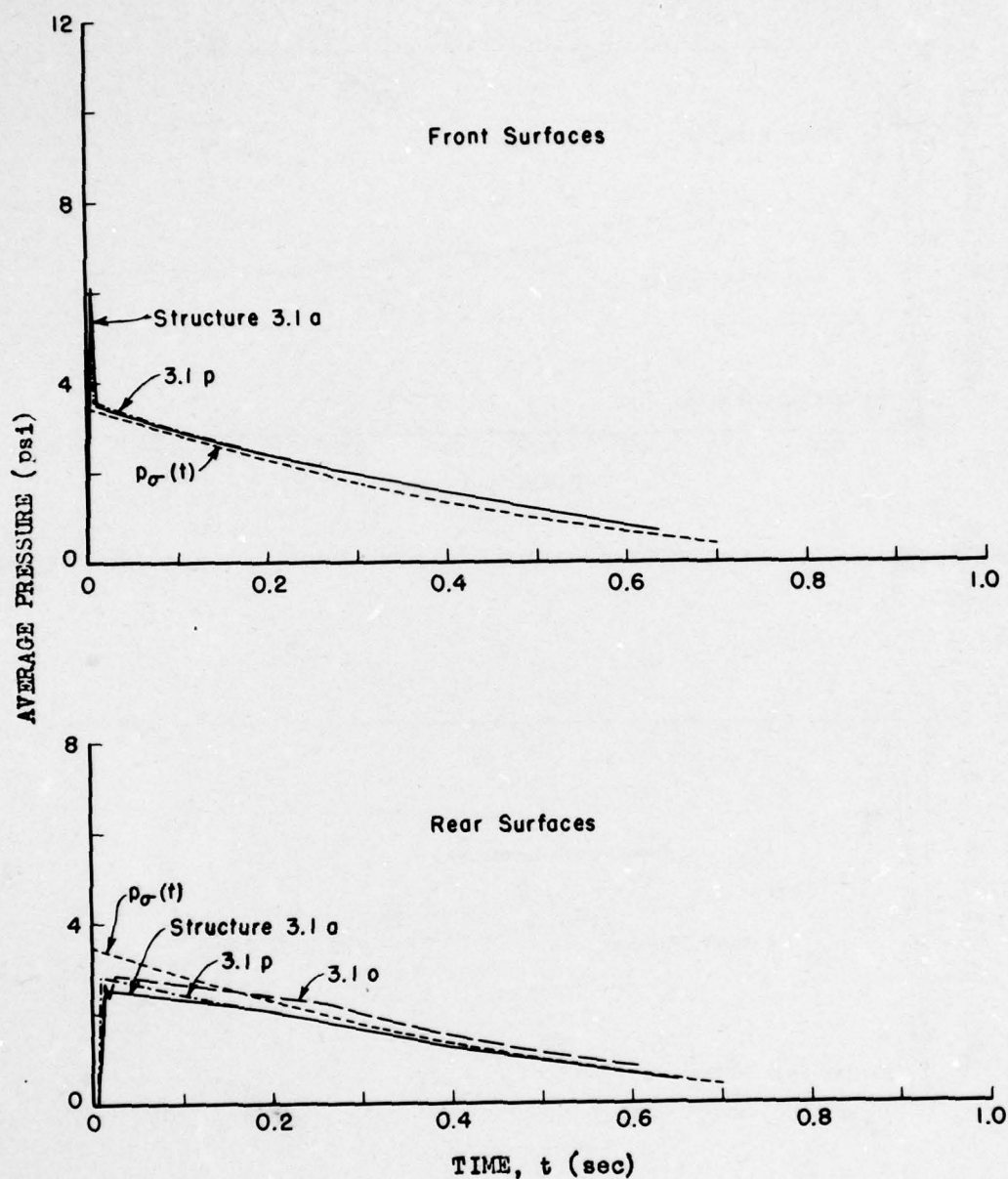


Fig. 4.158 — Simplified average pressure, Structures 3.1a, o, and p, Shot 10.

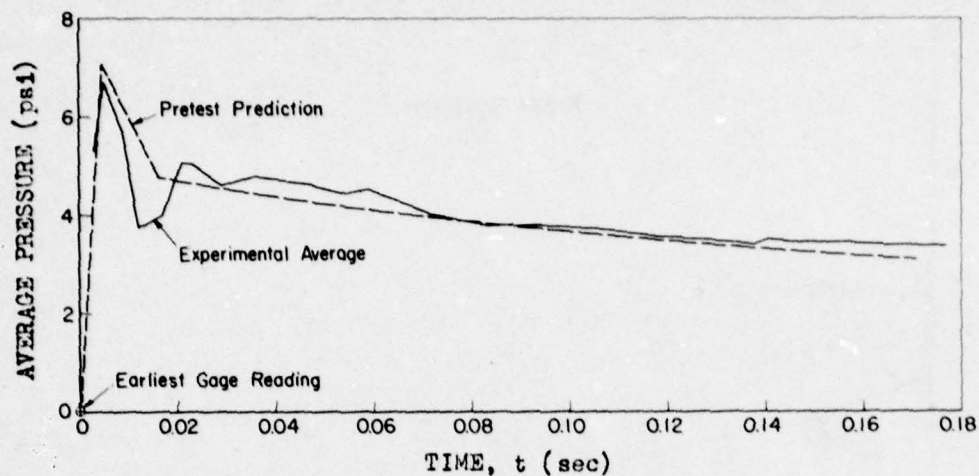


Fig. 4.159—Comparison of pretest prediction to experimental pressure on underside of Structure 3.1o, Shot 9.

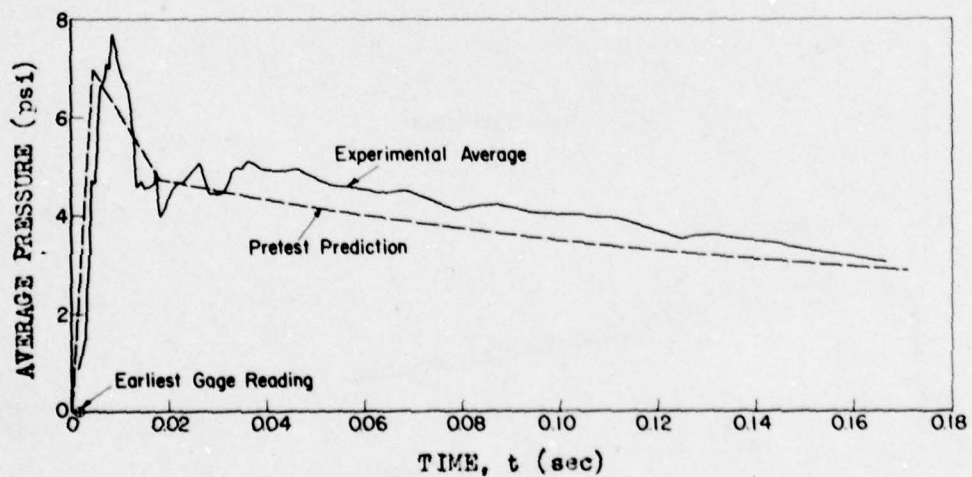


Fig. 4.160—Comparison of pretest prediction to experimental pressure on underside of Structure 3.1p, Shot 9.

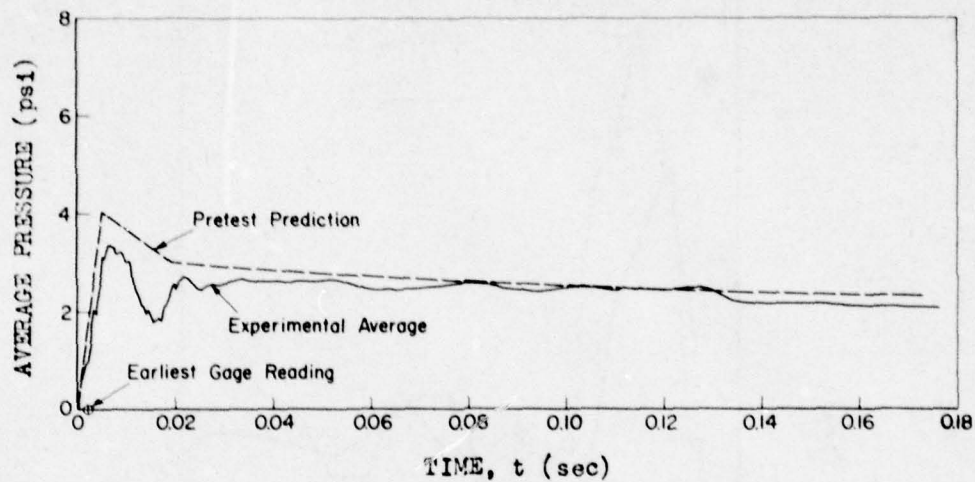


Fig. 4.161 — Comparison of pretest prediction to experimental pressure on underside of Structure 3.1o, Shot 10.

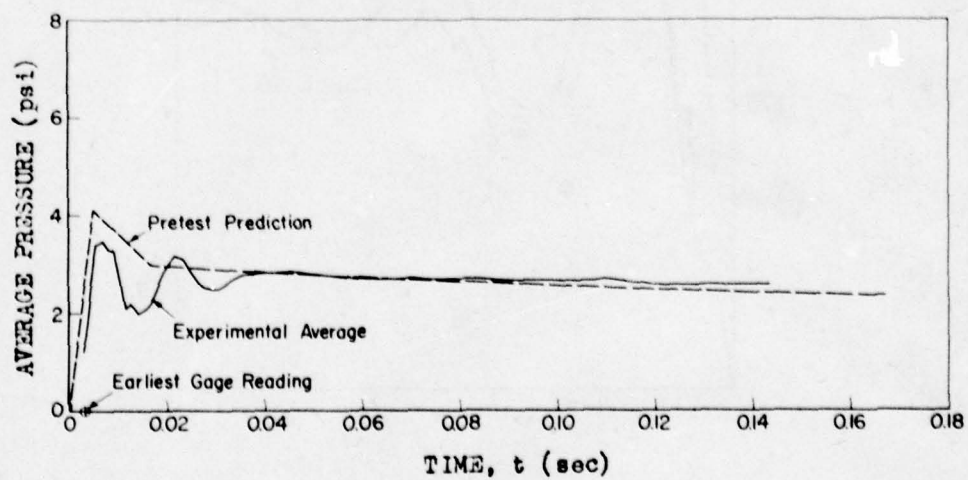


Fig. 4.162 — Comparison of pretest prediction to experimental pressure on underside of Structure 3.1p, Shot 10.



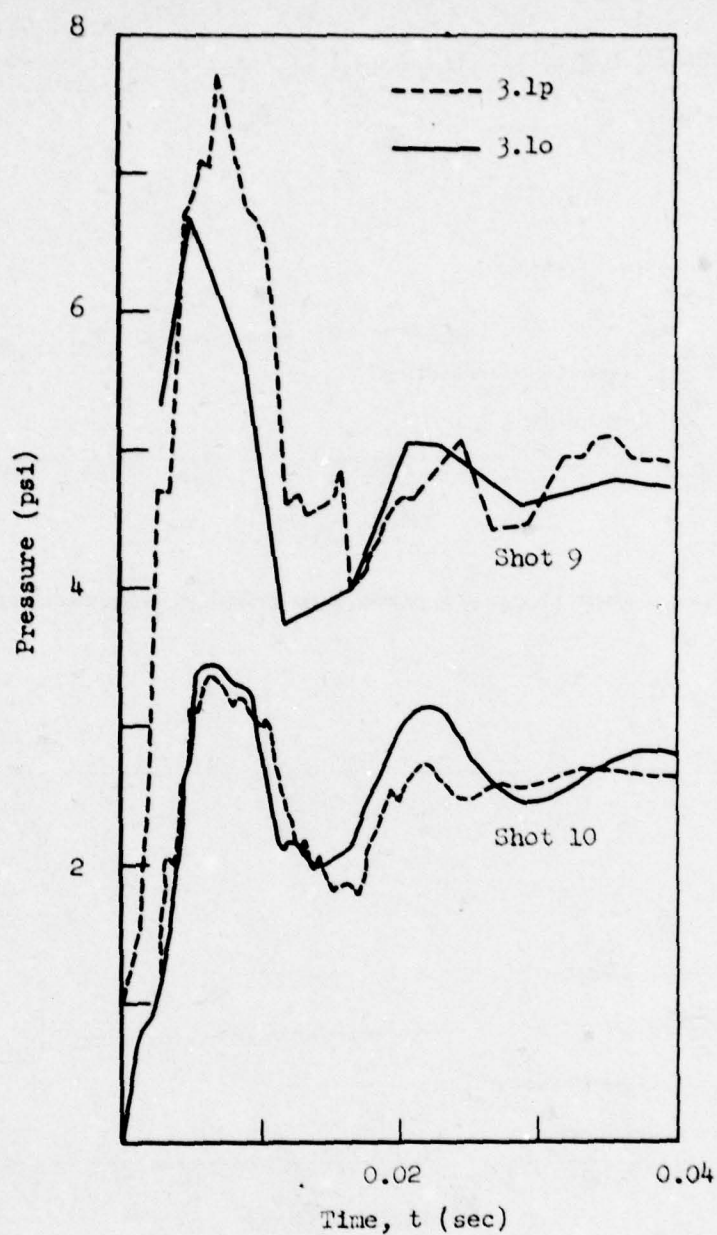


Fig. 4.163—Diffraction loading on underside of elevated cubicles, Structures 3.1o and p.

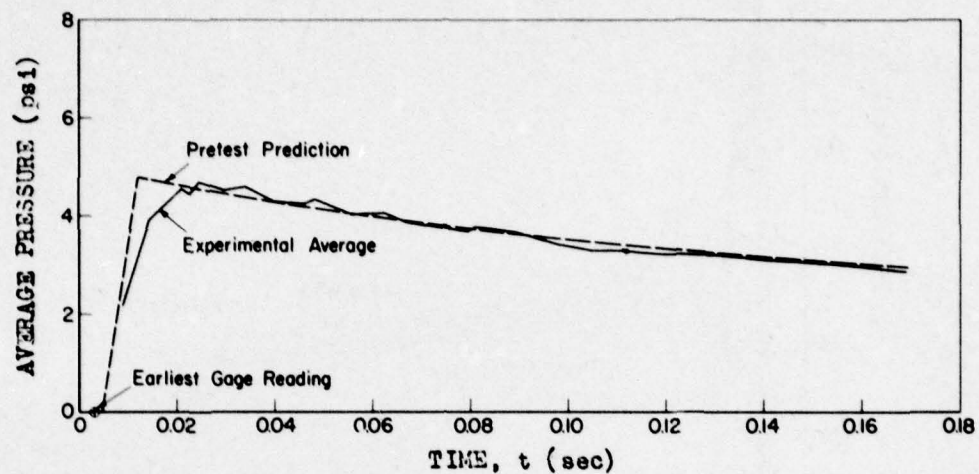


Fig. 4.164 — Comparison of pretest prediction to experimental pressure on rear surface, Structure 3.1o, Shot 9.

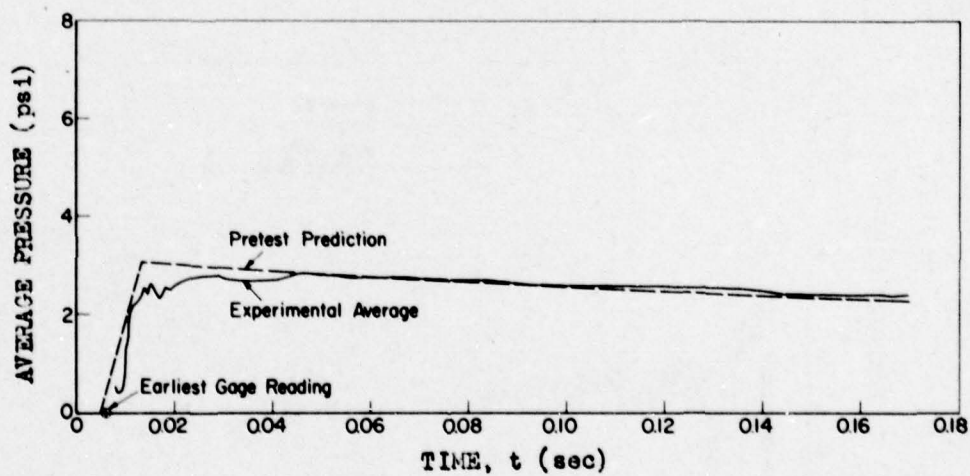


Fig. 4.165 — Comparison of pretest prediction to experimental pressure on rear surface, Structure 3.1o, Shot 10.

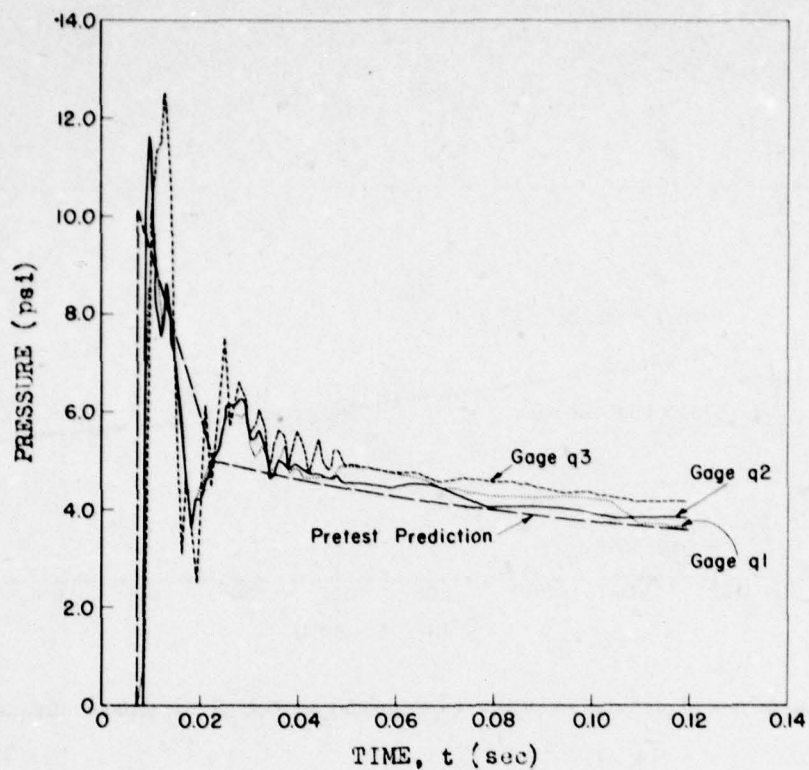


Fig. 4.166—Comparison of pretest prediction to experimental pressure, Structure 3.1q, Section A-A, Shot 9.

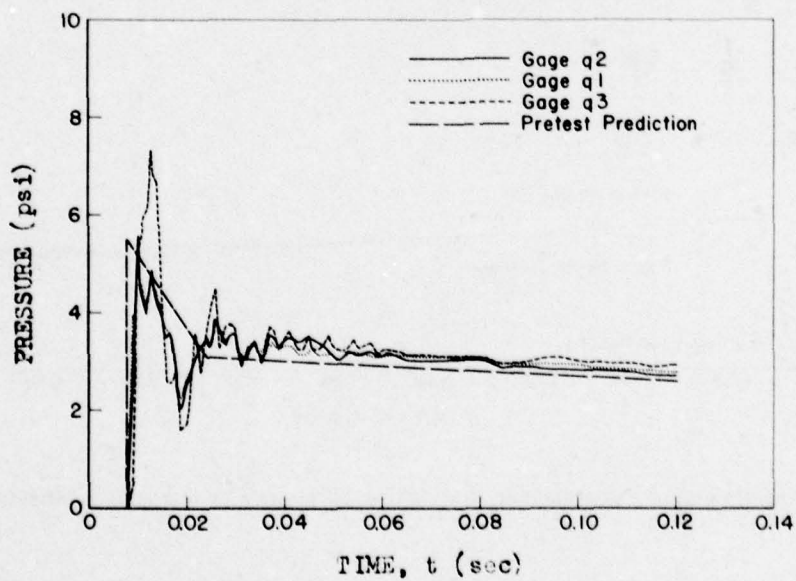


Fig. 4.167—Comparison of pretest prediction to experimental pressure, Structure 3.1q, Section A-A, Shot 10.



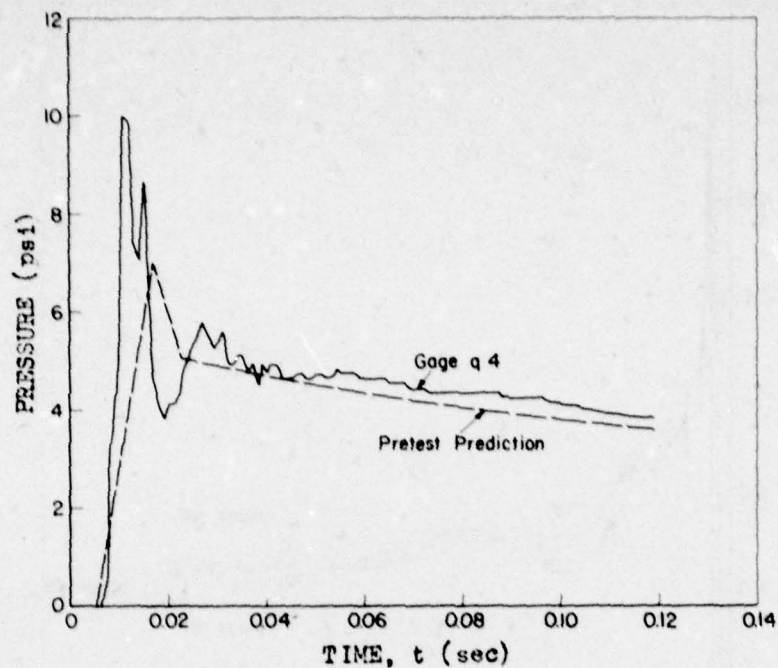


Fig. 4.168 — Comparison of pretest prediction to experimental pressure, Structure 3.1q, Section B-B, Shot 9.

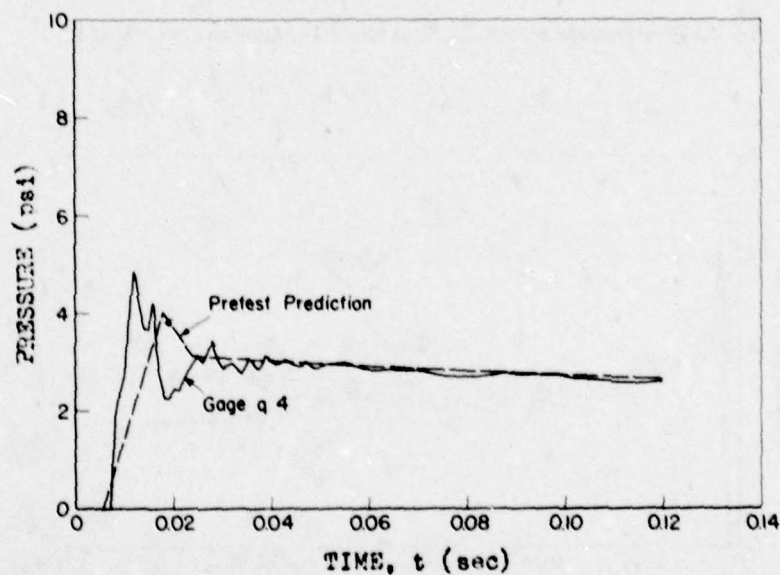


Fig. 4.169 — Comparison of pretest prediction to experimental pressure, Structure 3.1q, Section B-B, Shot 10.

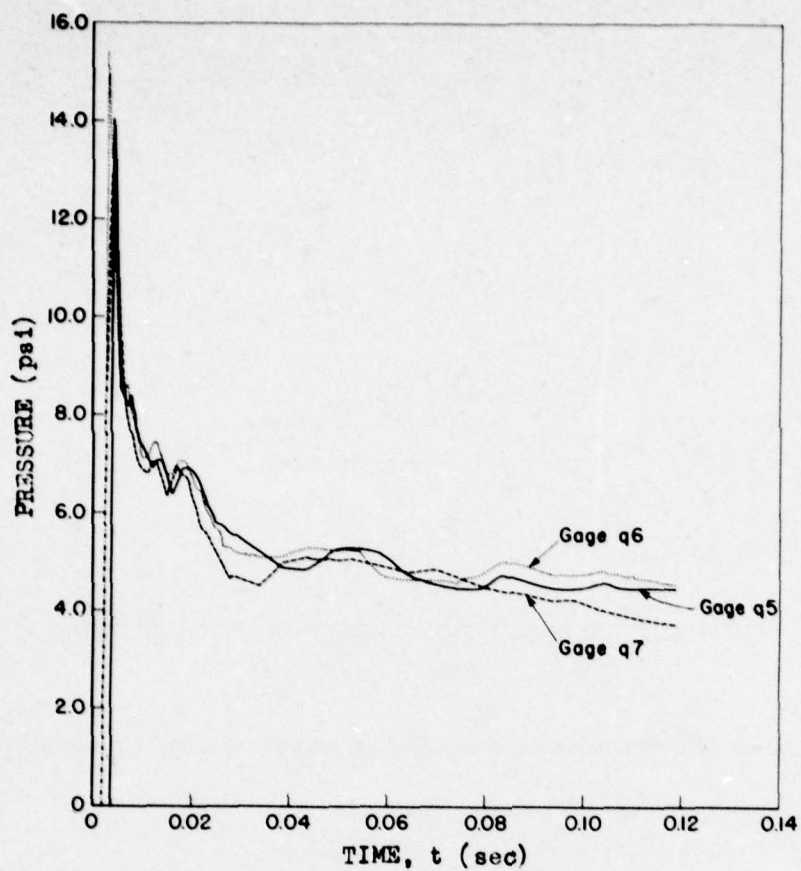


Fig. 4.170 — Pressure records on Structure 3.1q, Section C-C, Shot 9.

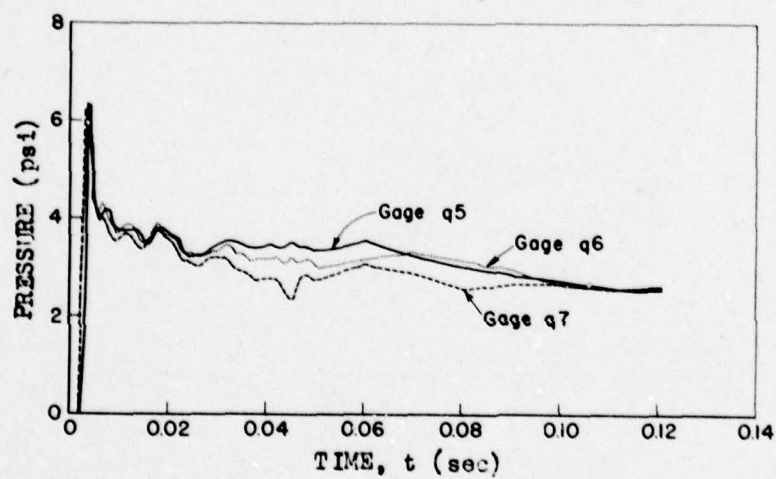


Fig. 4.171 — Pressure records on Structure 3.1q, Section C-C, Shot 10.

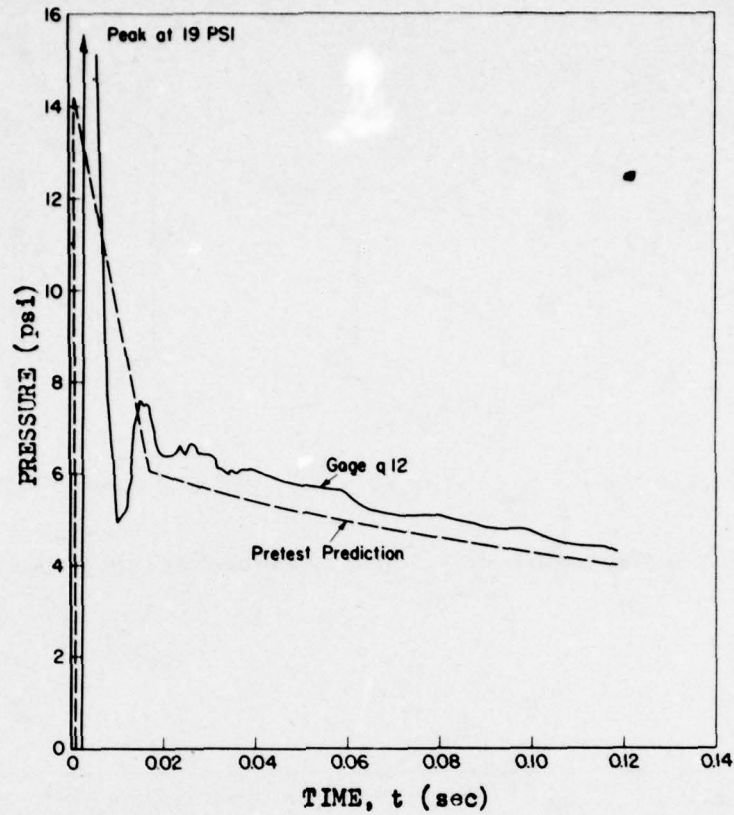


Fig. 4.172 — Comparison of pretest prediction to experimental pressure, Structure 3.1q, corner 1, Shot 9.

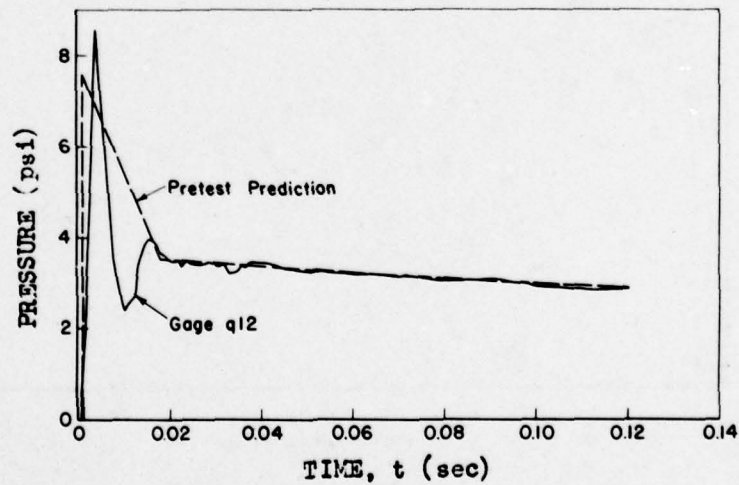


Fig. 4.173 — Comparison of pretest prediction to experimental pressure, Structure 3.1q, corner 1, Shot 10.



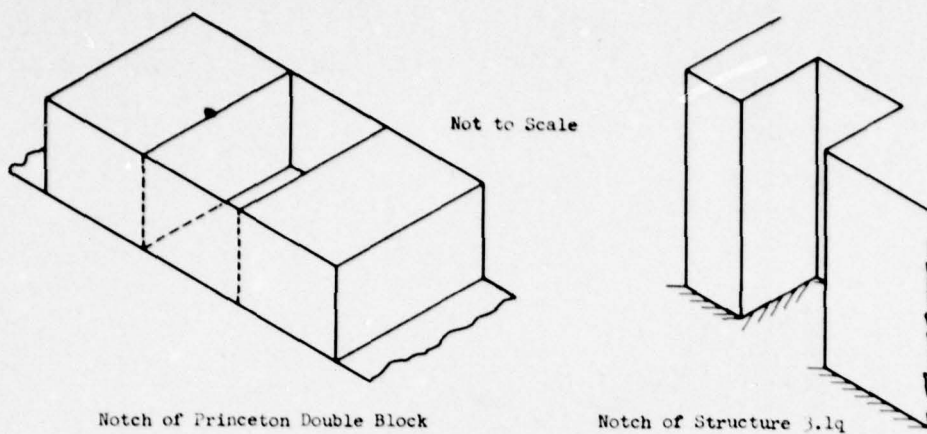


Fig. 4.174—Comparison of geometry of Princeton double block and notch, Structure 3.1q.

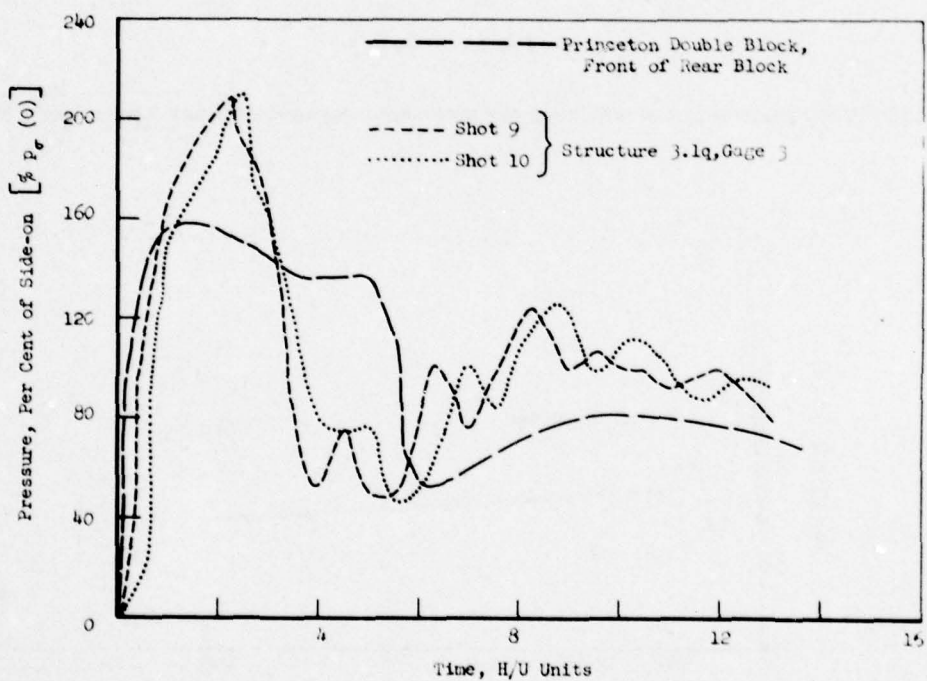


Fig. 4.175—Comparison of Princeton double block pressures to gage 3, Structure 3.1q.

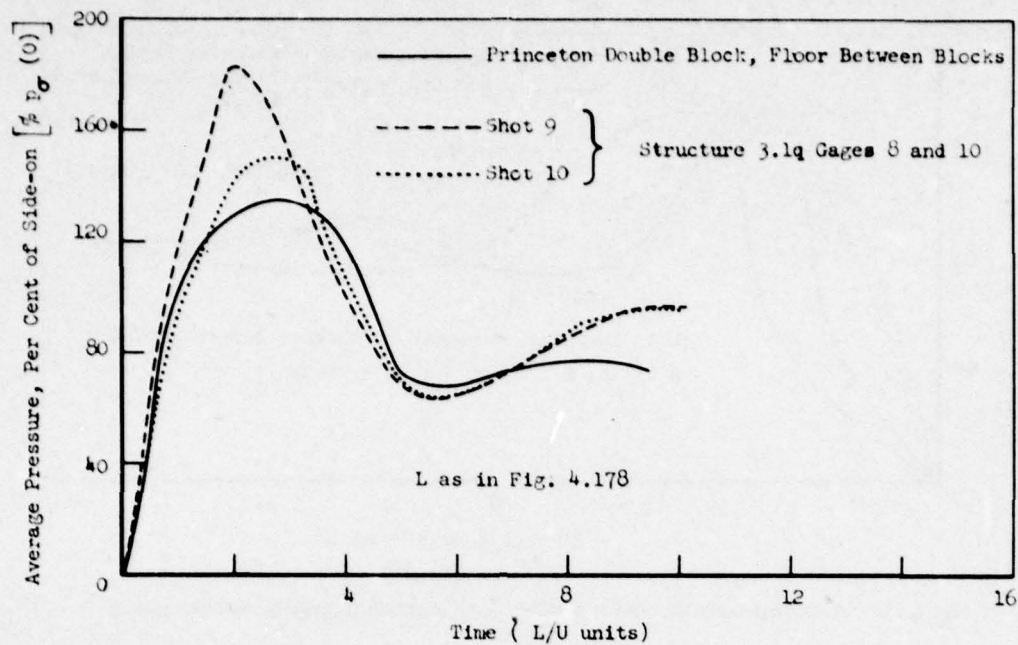


Fig. 4.176 — Comparison of Princeton double block pressures to gages 8 and 10, Structure 3.1q.

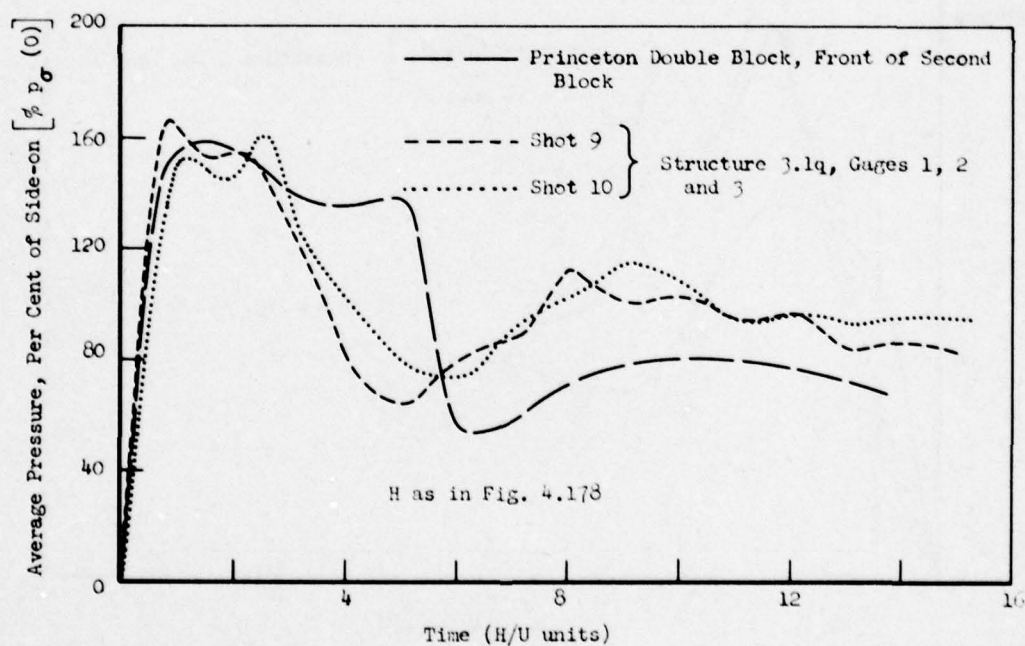


Fig. 4.177 — Comparison of Princeton double block pressures to gages 1 to 3, Structure 3.1q.

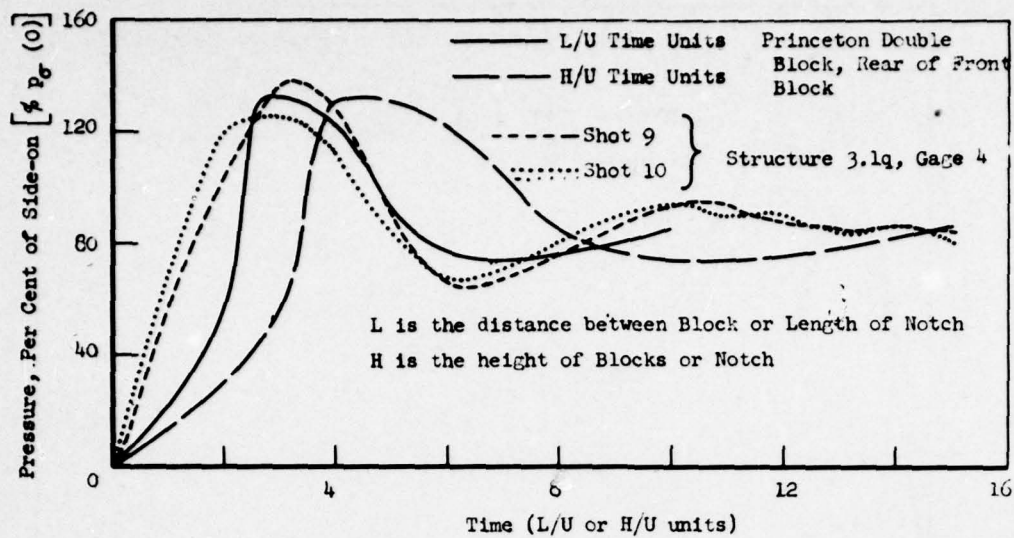


Fig. 4.178—Comparison of Princeton double block pressure to gage 4, Structure 3.1q.

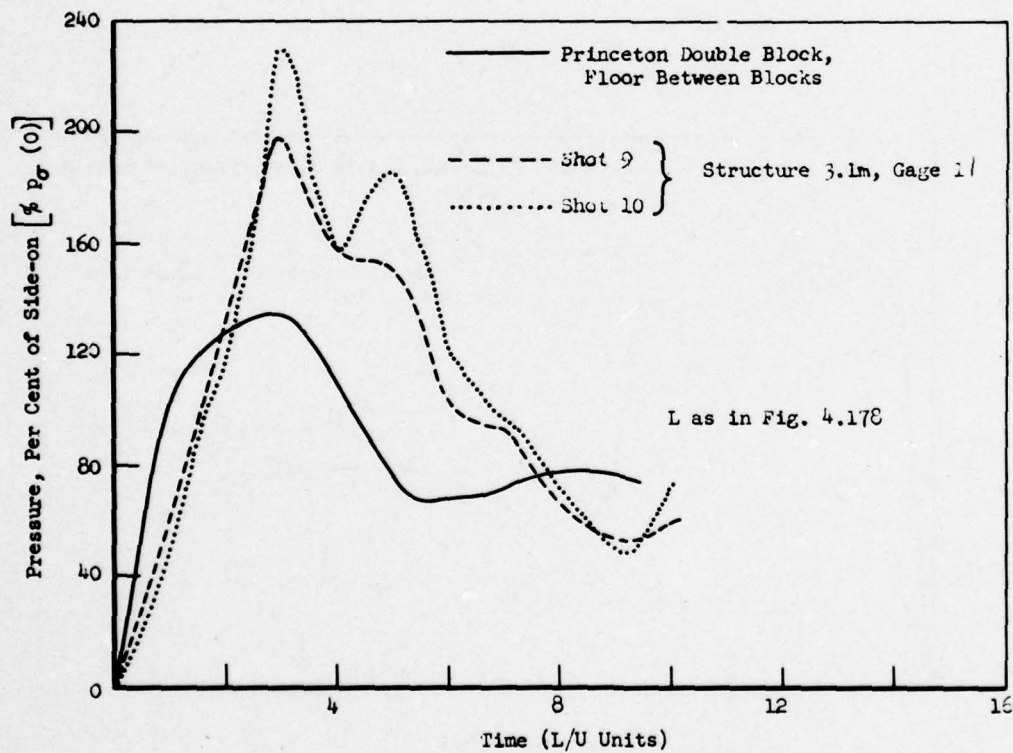


Fig. 4.179—Comparison of Princeton double block pressures to gage 1, Structure 3.1m.

UNCLASSIFIED



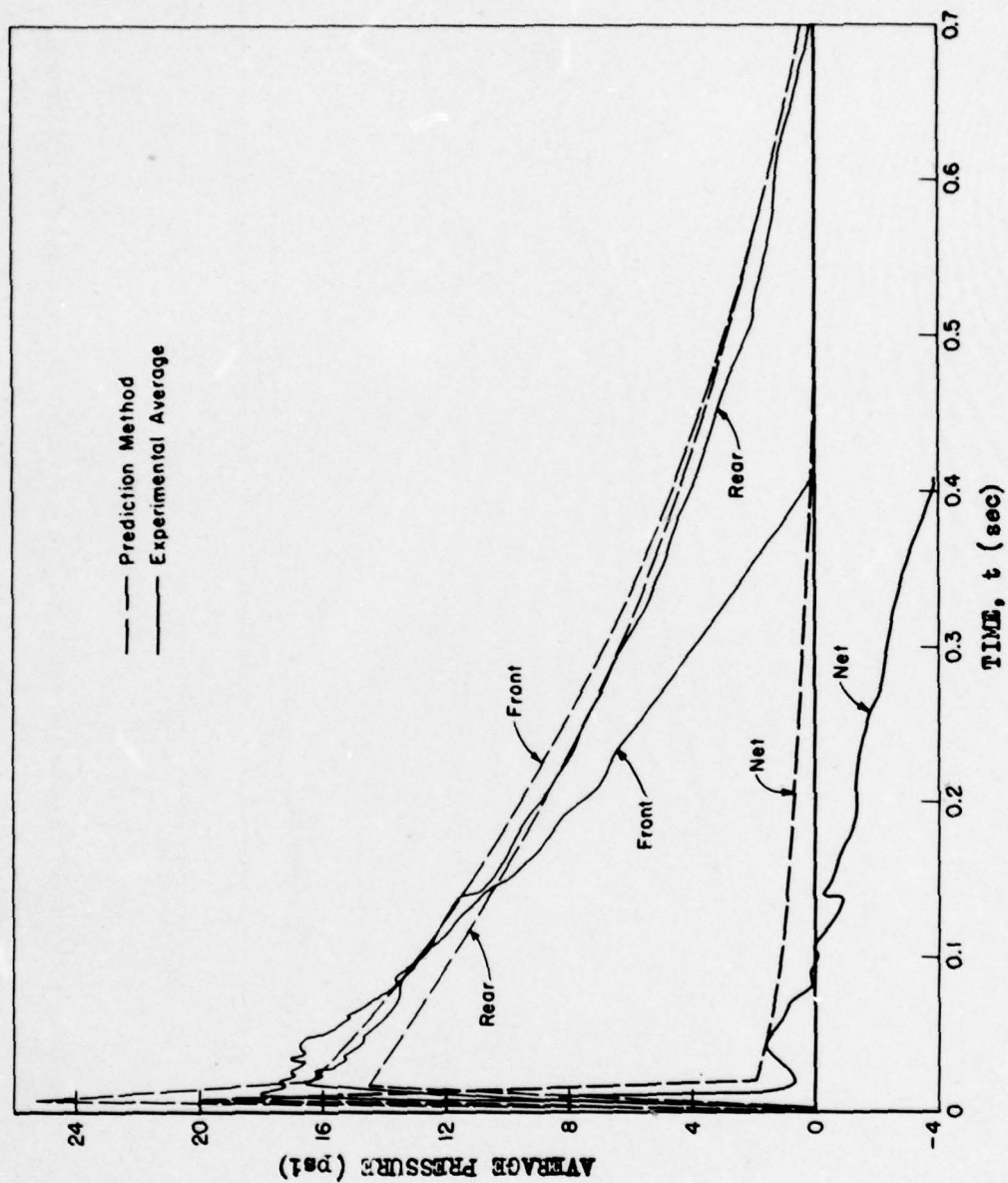


Fig. 4.180 — Comparison of predicted to experimental average pressures; front, rear, and net; Structure 3.1a, Shot 9.

UNCLASSIFIED

246

~~SECRET RESTRICTED DATA~~

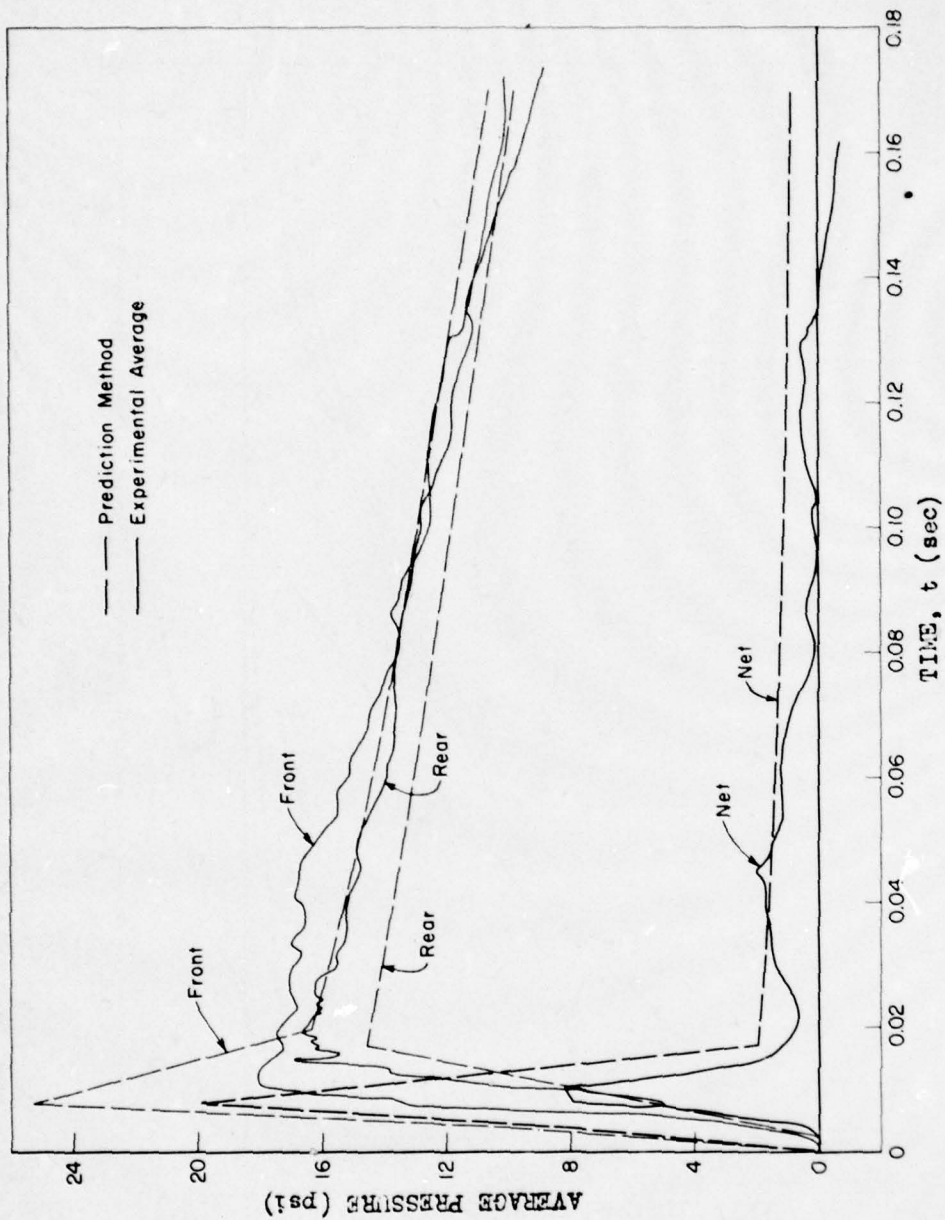


Fig. 4.181 — Comparison of predicted to experimental average pressures; front, rear, and net; Structure 3.1s, Shot 9.

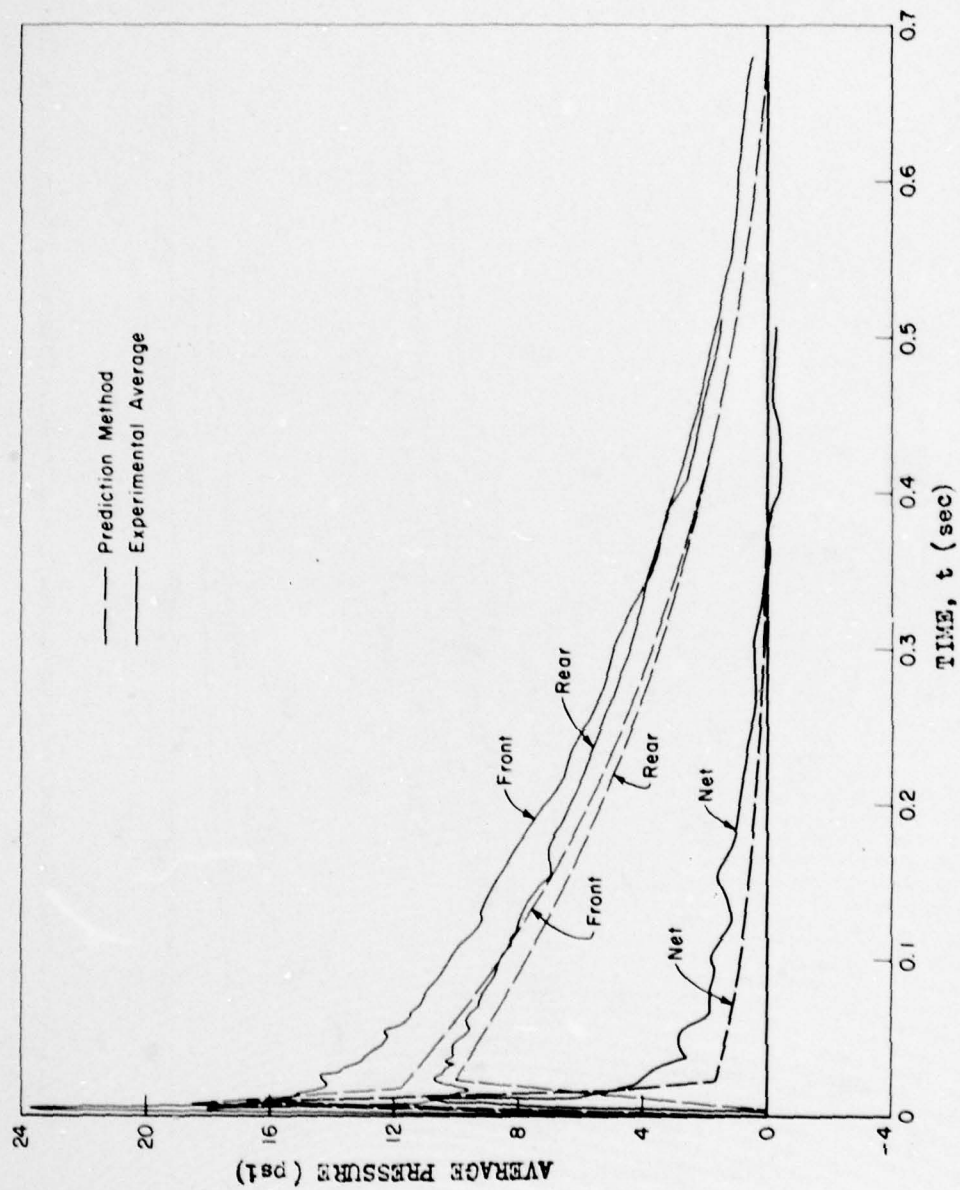


Fig. 4.182 — Comparison of predicted to experimental average pressures; front, rear, and net; Structure 3.1t, Shot 9.

UNCLASSIFIED



UNCLASSIFIED

248

~~SECRET RESTRICTED DATA~~

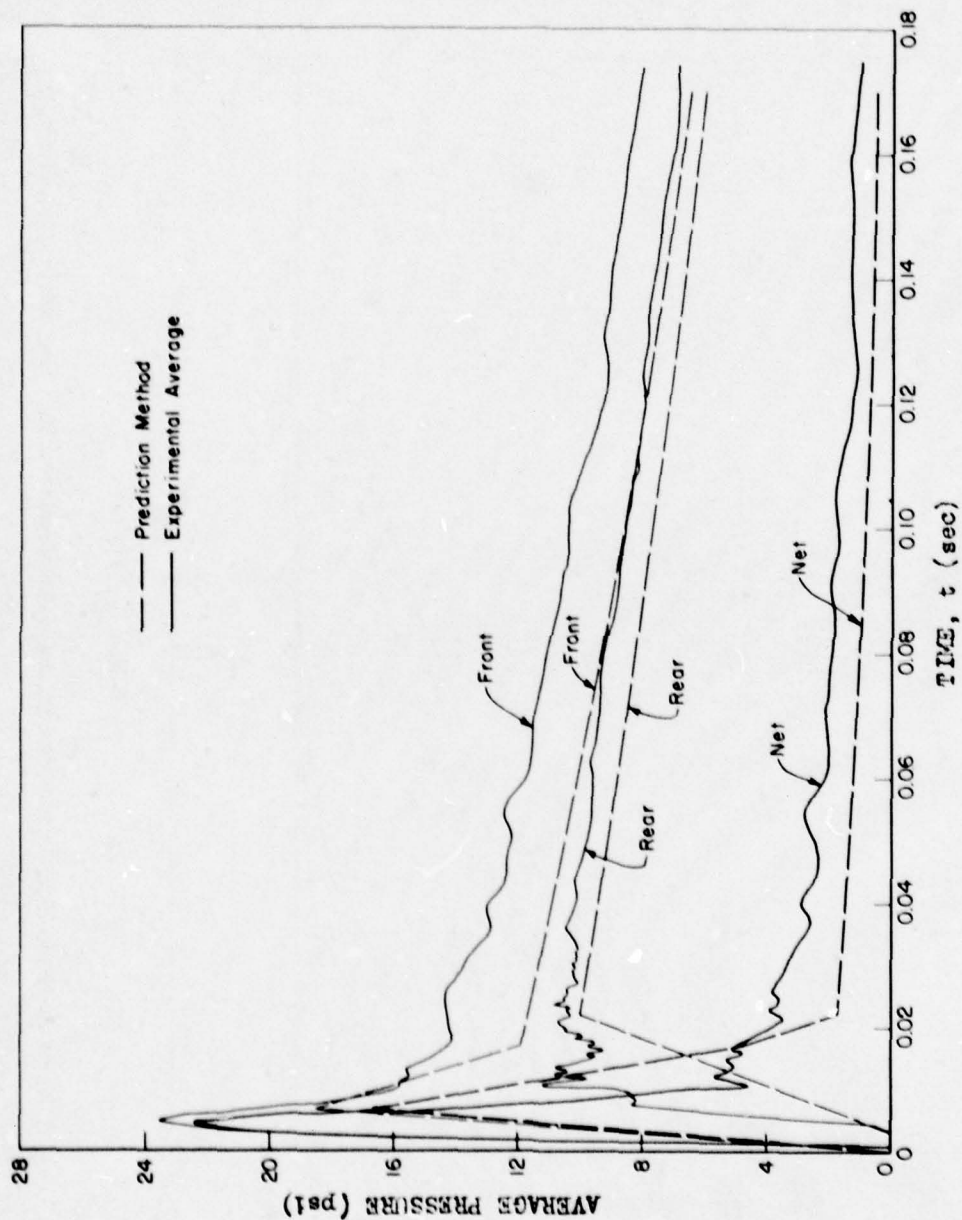


Fig. 4.183—Comparison of predicted to experimental average pressures; front, rear, and net; Structure 3.1t, Shot 9.

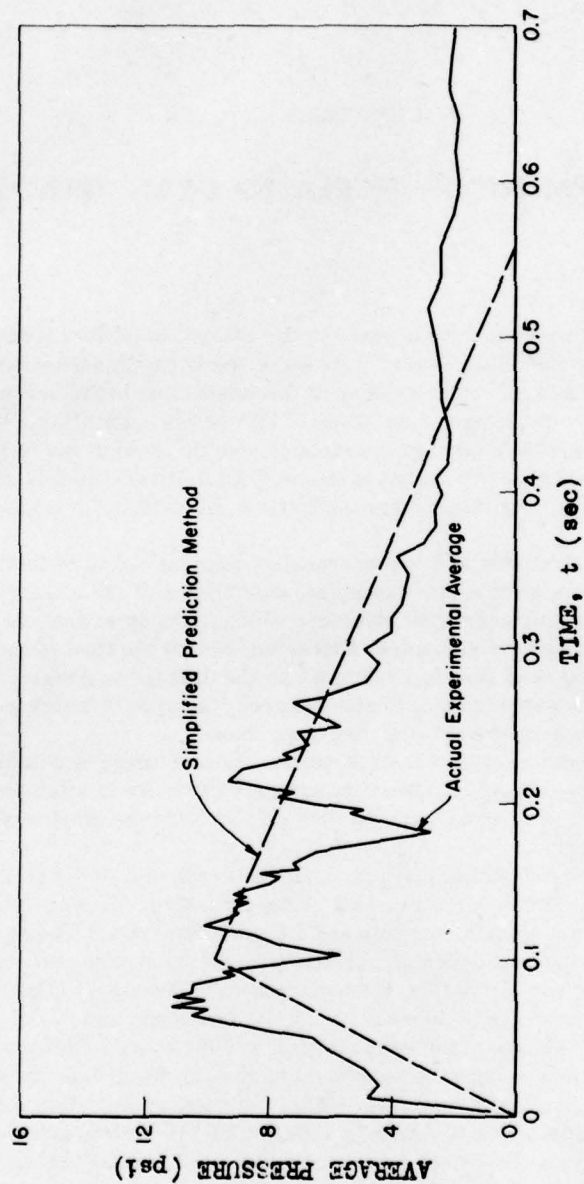


Fig. 4.184 — Comparison of experimental average net pressure on Structure 3.1t (Shot 10) to that of simplified prediction method for precursor loading.

## CHAPTER 5

# DEVELOPMENT OF INCREASED DRAG TRENDS

### 5.1 INTRODUCTION

Vast strides have been made in recent years in the estimation of force-time functions for targets exposed to long duration blast waves. This work has been almost exclusively of an empirical nature, guided by a meager understanding of the interaction between a region of fluid in which conditions are rapidly changing and an obstacle immersed in that fluid. Wherever deemed accurate, these investigations have utilized concepts of long standing in the field of steady-state fluid dynamics. It is believed that this adoption of steady-state flow concepts should be evaluated more closely by means of the latest large-scale field test results in Operation UPSHOT-KNOTHOLE.

The blast loading of a structure is a highly transient process which is briefly described in the following steps (see Chap. 3 for a more complete description of the loading): First, the blast front reflects from the surface of the structure which faces upstream, and then this shock front moves through and around the structure, diffracting so that the flow is carried to all surfaces. A period of development of flow follows in which the diffraction pressures decrease, and a flow pattern develops which approaches, to some degree, the pattern which would exist if the structure were exposed to a steady wind, i.e., the drag phase.

The development of a loading theory for structures whose damage is principally due to drag loading has, however, been severely hampered by extreme difficulty in attempts to correlate forces on the structure with pressures and with flow velocities in the blast wave during the drag or pseudo-steady-state phase.

In the past the most common correlation method was to attempt to define a "drag coefficient" (a constant) for each surface or component of the structure. This coefficient is multiplied by the dynamic pressure ( $\frac{1}{2}\rho u^2$ ), as computed from the Rankine-Hugoniot conditions, extended throughout the duration, and added algebraically to the blast wave side-on pressure to yield the average pressure (and ultimately, the force) on each structural surface or component. Such coefficients are determined from three sources: (1) full-scale and model field tests using explosives, (2) wind-tunnel (steady-state) experiments, and (3) shock tube tests. The drag coefficients determined from these sources have, however, been in disagreement, and there has often been disagreement among various studies within each source (see Fig. 5.10). The latest large-scale field test data just add a few more points to a highly controversial field. Briefly, one finds in these tests an increased drag force, over that predicted by pretest methods, which assumed that the Rankine-Hugoniot relation (see Eq. 3.3) determines the drag pressure throughout the entire period of the decaying blast wave and not only at the shock front. Whether this increase in drag force is to be ascribed to the coefficient  $C_d$  or to the dynamic pressure ( $\frac{1}{2}\rho u^2$ ) is debatable.

UNCLASSIFIED



## 5.2 NET LOADINGS

Although in the planning phase for UPSHOT-KNOTHOLE Shots 9 and 10 the loadings on individual surfaces were of greater interest than the net loadings, the latter can be obtained from the test results as a bonus. A fair knowledge of these net loadings, i.e., the difference between front and back loadings, does not necessarily require an exact knowledge of individual front and back loadings. From a phenomenological point of view the net loadings can be divided into two phases, namely, the diffraction and drag phases. During the diffraction phase the pressure rises instantaneously to reflected pressure, and after a short time, short depending on the ratio of building dimensions to positive wave length,  $Ut_0$ , it drops to the drag pressure. During the drag phase the net load decreases monotonically to zero. In some applications the time integrated net loads, i.e., the net impulse, are of interest. This impulse has been predicted for many simple shapes in conjunction with other weapons effects programs, and a summary of this impulse for some of these shapes, obtained from a forthcoming final report, *Compendium on Air Blast Effects* (Directorate of Intelligence, USAF), is presented in Figs. 5.1 to 5.4.

Figure 5.1 repeats the symbolic loading schemes on front and back walls as described in detail in Chap. 3, Figs. 3.1 and 3.2. The number of build-up time units on the back wall,  $n$ , as a function of width, height, and length is given in Fig. 5.2. The net horizontal impulses, i.e., the integrals associated with these pressure-time loadings, are obtained from Fig. 5.1 and are presented in Figs. 5.3 and 5.4. Figure 5.3 represents the reduced diffraction impulse per unit area per unit clearing distance  $I_{DF}/\bar{h}$ , whereas Fig. 5.4 presents the reduced drag impulse per unit area per unit positive wave duration per unit drag coefficient,  $I_{DR}/t_0 C_d$ . These impulses and portions thereof are defined on Fig. 5.1.

In order to use these charts, the following parameters must be given: width in feet,  $W$ ; height in feet,  $H$ ; length (in flow direction) in feet,  $L$ ; side-on pressure psi,  $p_0$ ; positive wave duration in seconds,  $t_0$ ; and a wave shape factor "c" to be obtained from Fig. 5.5. The discussion of the significance of the factor "c" is deferred until the next section. The quantity,  $\bar{h}$ , is found as follows:

In applying this chart to a block on the ground, take  $\bar{h} = H$  or  $W/2$ , whichever is smaller. If the block is suspended in air a distance  $d \geq H$  above ground, take  $\bar{h} = H/2$  or  $W/2$ , whichever is smaller. If  $d \leq H$ , interpolate linearly in terms of  $d/H$ , i.e., take  $\bar{h} = H[1 - (d/2H)]$  or  $W/2$ , whichever is the smaller. One obtains  $\beta$ ,  $\gamma$ , and  $\delta$  from Figs. 5.3(a) and (b) and 5.4, as follows:

$$\beta = \frac{I_\beta}{\bar{h}} \quad \text{as a function of } p_0 \text{ and } n, \text{ Fig. 5.3(a)}$$

$$\gamma = \frac{I_\gamma}{L} \quad \text{as a function of } p_0 \text{ only, Fig. 5.3(b)}$$

$$\delta = \frac{I_{DR}}{t_0 C_d} \quad \text{as a function of } p_0 \text{ and "c," Fig. 5.4}$$

For the 3.1 structures,  $C_d = 1.25$  (pretest predictions based mainly on steady-state wind-tunnel experiments). The diffraction impulse is computed as  $I_{DF} = (\bar{h}\beta + L\gamma)$ , lb-sec/ft<sup>2</sup>, while the drag impulse is  $I_{DR} = C_d t_0 \delta$ , lb-sec/ft<sup>2</sup>.

Two fundamental assumptions regarding the drag phase were used in these pressure-time and impulse predictions, namely: (1) that the drag coefficients are constant and are the same as those obtained from steady-state wind-tunnel tests, for the particular shapes under consideration, although they are applied to transients of less than one-second duration, and (2) that the drag pressure can be expressed in terms of overpressures at each instant of time according to Eq. 3.3. (This equation is theoretically valid only at the shock front, i.e., for  $t = 0$ .) This assumption leads to the conclusion that the drag pressure should vanish simultaneously with overpressures, i.e., at the end of the positive wave duration.

In the light of experimental values of net loadings obtained from the 3.1 structures on Shots 9 and 10, these assumptions have been critically reviewed. The second assumption was

found to be inadequate from theoretical considerations. These considerations (treated in detail in Appendix B) are summarized in the next section. Their significance, in terms of the test conditions of Shots 9 and 10, can best be understood by stating that drag impulses, in terms of the revised predictions approach, are up to twice the value calculated by the assumed Rankine-Hugoniot equation, which essentially assumed an isentropic relation in the decaying blast wave.

The measured net loadings for Structures 3.1a to p are presented in Figs. 4.8(a) and (b). One notes immediately that they tend to decay almost linearly, rather than exponentially, which is the first indication of increased drag trends.

### 5.3 SIDE-ON PRESSURES

Although at various points throughout the space free stream infinite atmosphere side-on pressures have quite similar wave shapes in the overpressure regions of practical interests, the reflected pressures (near the ground) have a wave shape dependent on the position of the bomb release with respect to the target location. These wave shapes can be computed approximately from data published by L. J. Vortman on peak overpressures, durations, and impulses (Sandia Corporation, *Prediction of Incident Pressure-Time Curves for Nuclear Explosions*), by assuming that the side-on pressure-time relation can be approximated analytically by the expression

$$p_{\sigma}(t) = p_{\sigma}(0) e^{-ct/t_0} (1 - t/t_0) \quad (5.1)$$

where  $p_{\sigma}(0)$  is the initial side-on pressure (at the shock front) and  $t_0$  the first positive phase duration (for side-on pressures). The wave shape factor "c" describes the decay of the wave.

By integrating Eq. 5.1 between the limits  $t = 0$  and  $t = t_0$  and setting the analytic expression for impulse equal to the measured impulse values

$$I_{p_{\sigma}} = \int_0^{t_0} p_{\sigma}(t) dt = \begin{cases} p_{\sigma}(0) \cdot t_0 \cdot \frac{e^{-c} + c - 1}{c^2}, & c \neq 0 \\ p_{\sigma}(0) \cdot t_0 \cdot \frac{1}{2}, & c = 0 \end{cases} \quad (5.2)$$

one obtains from the measured  $p_{\sigma}(0)$  and  $t_0$  values a chart of "c" contours as a function of scaled height and distance (see Fig. 5.5). Although this chart was not based on data from UPSHOT-KNOTHOLE Shots 9 and 10, the "c" values

$$c \approx 2.0 \text{ for Shot 9} \quad (5.3)$$

$$c \approx 0.5 \text{ for Shot 10} \quad (5.4)$$

lead to wave shapes which agree remarkably well with blast line results at distances from Ground Zero corresponding to the 3.1 structures (approximately 5000 ft). Table 5.1 presents numerical values of

$$I_{p_{\sigma}}/p_{\sigma}(0) \cdot t_0$$

as a function of "c" obtained from Eq. 5.2.

This table indicates that one should expect more reduced "side-on impulse" for conditions of Shot 10, Eq. 5.4 than for Shot 9, Eq. 5.3. Note that for the conditions of the GREENHOUSE large-scale field test, the coefficient "c" was nearly equal to 1.0, which justified the fact that the UPSHOT-KNOTHOLE pretest load-prediction methods were based on the analytic expression

$$p_{\sigma}(t) = p_{\sigma}(0) e^{-t/t_0} (1 - t/t_0) \quad (5.5)$$

UNCLASSIFIED

TABLE 5.1—Reduced Side-on Impulse\* for Various Values of the Decay Coefficient, "c"

c = 0	0.5	1.0	1.5	2.0	2.5
$I_{p\sigma}/p_{\sigma}(0) \cdot t_0 = 0.50$	0.426	0.368	0.321	0.284	0.253

\* Reduced impulse refers to the dimensionless quantity obtained by dividing the impulse by the product of peak pressure times wave duration, e.g.,  $[I_{p\sigma}/t_0 p_{\sigma}(0)]$  is the reduced side-on impulse and  $[I_{DG}/t_0 \cdot p_d(0)]$  is the reduced drag impulse.

The actual free stream side-on curves for Shots 9 and 10 were obtained by analyzing blast line test results at ground levels along the 5000-ft arc from ground zero, corresponding to the location of the 3.1 structures. These curves are given in Fig. 5.6. Figure 5.6 (a) represents the adopted average for Shot 9, and Fig. 5.6 (b) gives that for Shot 10. Note that for Shot 9, at early times, these curves are slightly below that shape given by Eq. 5.1, but in later portions of the pressure-time cycle they are slightly above that shape given by Eq. 5.1. Although all analyses with regard to the calculation of dynamic pressures and dynamic pressure coefficients will be based on the use of the actual free stream average for side-on pressure, analytic expressions for side-on pressure decay can be developed which fit the experimental curve better than does Eq. 5.1. For Shot 9, a good fit was obtained using the relation

$$p_{\sigma}(t) = p_{\sigma}(0) \frac{1 - (t/t_0)^2}{1 + 5(t/t_0)} \quad (5.6)$$

and for Shot 10, Eq. 5.5 was satisfactory.

The impulse obtained by integrating Eq. 5.6 between  $t = 0$  and  $t = t_0$ ,  $I_{p\sigma} = 0.284 p_{\sigma}(0) \cdot t_0$ , agrees exactly with that given by Eq. 5.2 for  $c = 2.0$ , as can be seen from Table 5.1. Therefore the predicted wave shape, Eq. 5.1, preserves, in the mean, the free stream impulse, and thus verifies the validity of the "c" chart, Fig. 5.2, for Shot 9 test conditions, although, in deriving this chart, no Shot 9 test data were included.

#### 5.4 DRAG PRESSURES

The dynamic pressure—or drag pressure—results from the kinetic energy of the moving fluid and is defined as the product of one-half the density times the square of the particle velocity, namely,

$$p_d(t) = \frac{1}{2} \rho(t) [u(t)]^2 \quad (5.7)$$

where  $\rho(t)$  is the density-time and  $u(t)$  the particle velocity-time relation. These state variables are related at the shock front by means of the Rankine-Hugoniot relations to the side-on pressure and absolute pressure,  $P_0$ , namely,

$$p_d(0) = \frac{1}{2} \rho(0) [u(0)]^2 = \frac{2.5[p_{\sigma}(0)]^2}{7P_0 + p_{\sigma}(0)} \quad (5.8)$$

By means of assumption 2 in Sec. 5.2, one obtains

$$\frac{1}{2} \rho(t) [u(t)]^2 = \frac{2.5[p_{\sigma}(t)]^2}{7P_0 + p_{\sigma}(t)} \quad (5.9)$$

The quantity  $p_{\sigma}(t)$  for the evaluation of Eq. 5.9 is the average experimental pressure-time curve of Fig. 5.6. It can be presented analytically by the approximation, Eq. 5.6. The resulting

~~SECRET~~ ~~RESTRICTED~~ DATA

UNCLASSIFIED



dynamic pressure-time curves for Shot 9 are given in Fig. 5.7(a) and are given for Shot 10 in Fig. 5.7(b). For future work, where, however, complete side-on time relations are not available from test results, the calculations of roughly the same shape, as given in Figs. 5.7(a) and (b), can be accomplished by means of Eq. 5.1, supplemented by the "c" chart, Fig. 5.5, as follows:

For weak and moderate shock strengths (for example, the condition of Shots 9 and 10 near the 3.1 structures) the denominator in Eq. 5.9 is a slowly varying function compared to the numerator, and, hence, the following simplification is indicated

$$p_d(t) = p_d(0) \left[ \frac{p_\sigma(t)}{p_\sigma(0)} \right]^2 \quad (5.10)$$

where  $p_d(0)$  is given by Eq. 5.8 and the reduced side-on pressures  $p_\sigma(t)/p_\sigma(0)$  are obtained from Eq. 5.1. Hence the application of the Rankine-Hugoniot relations leads to the result that dynamic pressure decays faster than side-on pressure, approximately as the squared value.

The drag impulse is found by integrating Eq. 5.10 between the limits 0 to  $t_0$

$$I_{DG} = \int_0^{t_0} p_d(t) dt = \begin{cases} p_d(0) \cdot t_0 \cdot \frac{2c^2 - 2c + 1 - e^{-2c}}{4c^3}, & c \neq 0 \\ p_d(0) \cdot t_0 \cdot \frac{1}{3}, & c = 0 \end{cases} \quad (5.11)$$

where the wave shape factor "c" is obtained from Fig. 5.5.

Table 5.2 presents numerical values of  $I_{DG}/p_d(0) \cdot t_0$  as a function of "c" obtained from Eq. 5.11.

TABLE 5.2—Reduced Drag Impulse\* for Various Values of the Decay Coefficient, "c"

	c = 0	0.5	1.0	1.5	2.0	2.5
$I_{DG}/p_d(0) \cdot t_0 = 0.333$		0.264	0.216	0.181	0.156	0.136

\* Reduced impulse refers to the dimensionless quantity obtained by dividing the impulse by the product of peak pressure times wave duration, e.g.,  $[I_{p0}/t_0 p_p(0)]$  is the reduced side-on impulse and  $[I_{DG}/t_0 \cdot p_d(0)]$  is the reduced drag impulse.

It follows from the assumption that the Rankine-Hugoniot relations apply throughout the decaying blast wave, Eqs. 5.9 and 5.10, that the drag pressure varies roughly as the square of the side-on pressure. Hence their integrated values, i.e., the reduced drag impulse (the dimensionless quantity obtained by dividing the drag impulse by the product of drag pressure times wave duration) is always smaller than the reduced side-on impulse (the side-on impulse divided by the product of side-on pressure times wave duration). This results from the fact that for  $0 < t < t_0$  and  $0 < c < 2.5$ ; the integrands satisfy the following inequality:

$$[e^{-ct/t_0} (1 - t/t_0)]^2 \leq [e^{-ct/t_0} (1 - t/t_0)]$$

It should be noted that, if the actual side-on curve, Fig. 5.6, had been used in Eq. 5.9 and the first part of Eq. 5.11—this statement is equivalent to the use of Eqs. 5.6, 5.9 and 5.11—one would obtain  $I_{DG} = 0.139 p_d(0) \cdot t_0$  which agrees with that given by Eq. 5.11 for  $c = 2.4$ , as can be seen from Table 5.2. Therefore the predicted wave shape, Eq. 5.1, leads also to dynamic pressure-time curves which roughly preserve the drag impulse in addition to side-on impulse. The ratios of these respective impulses, obtained by comparing Tables 5.1 and 5.2, are summarized in Table 5.3.

From Table 5.3 it is seen that the drag to side-on impulse ratio for Shot 9 and Shot 10 test conditions based on the admittedly incorrect Rankine-Hugoniot assumption, Eq. 5.9, varies from 1.61 to 1.84.

It is believed that the particle velocity, and hence dynamic pressure, do not go to zero at the same time the overpressure vanishes. By assuming that the Rankine-Hugoniot relations apply throughout the decaying blast wave, i.e., postulating that dynamic and side-on pressure vanish simultaneously, an obvious error is introduced. Yet in previous weapons effects studies, this error was assumed to be unimportant as far as its effect on drag pressures and impulses was concerned due to lack of more pertinent theoretical and reliable experimental data. However, a recent theoretical investigation based mainly on free stream data indicated quantitatively the large error which results in dynamic pressures and impulses by assuming the Rankine-Hugoniot relation to apply throughout the decaying blast wave or energies from the solution of

TABLE 5.3—Ratio of Reduced Side-on Impulse to Reduced Drag Impulse for Various Values of the Decay Coefficient, "c"

c = 0	0.5	1.0	1.5	2.0	2.5
$\frac{I_{ps} p_d(0)}{I_{bs} p_e(0)} = 1.5$	1.61	1.70	1.77	1.82	1.86

the IBM M problem (completed in 1946). This theory is presented in detail in Appendix B. The results can be summarized with the statement that all the ratios given in Table 5.3 should be roughly equal to 1, independent of "c." Thus the quantity  $u^2$  and the dynamic pressures decay roughly like the first power of the side-on pressures and not as the square, as was assumed previously, i.e.,

$$p_d(t) \approx p_d(0) e^{-ct/t_0} (1 - t/t_0) \quad (5.12)$$

Hence in the case of the 3.1 structures exposed to Shot 9, one would, by such a theory as presented in Appendix B, predict 84 per cent more drag impulse than by the present methods and in the case of Shot 10, roughly 60 per cent more.

Measured values of Shots 9 and 10 drag pressures were obtained by interpolating between Sandia q-gage wave shapes at 4075 and 6500 ft, and for the 3.1 structures at 5000 ft. These data were given in the UPSHOT-KNOTHOLE report, *Dynamic Pressure Vs Time and Supporting Air Blast Time Measurements, WT-714*. Although there was some uncertainty with respect to a slight shift in the base line associated with the 6500-ft distance in Shot 9, the interpolation in wave shape, combined with the computed Rankine-Hugoniot value at the shock front, places the measured value between that given by the Rankine-Hugoniot theory, Eq. 5.9 and that by the theory presented in Appendix B, Eq. 5.12. As seen in Figs. 5.7(a) and (b), this measured q value is much closer to the curve obtained by the Rankine-Hugoniot approach. It is very difficult to evaluate the reliability of this test result, particularly since the latest theory predicts a dynamic pressure positive wave length duration,  $t_2$ , roughly 60 per cent larger than the side-on pressure wave length duration,  $t_0$  (see Appendix B). This effect was not borne out by test results, although the magnitude of dynamic pressures for  $t_2 \leq t \leq t_0$  were perhaps too small to be detected. On the other hand, the value of  $p_d(0) = \frac{1}{2}\rho(0) [u(0)]^2$ , theoretically well-known, checks only within 20 per cent at the two locations which form the bounds for the interpolation in wave shapes near the 3.1 structures.

## 5.5 DRAG COEFFICIENTS

The drag coefficients are obtained by taking instantaneous values on the net curves for Structures 3.1a to 3.1p, Figs. 5.8a and 5.8b, and dividing them by the dynamic pressure values,

Figs. 5.7(a) and (b), at the same instant of time. The three values of  $C_d$  thus obtained are shown in Figs. 5.9a and b and correspond to the three values of dynamic pressures given in Figs. 5.7(a) and (b), namely, the highest value of drag coefficient corresponds to the dynamic pressure as given by the Rankine-Hugoniot approach and the lowest value corresponds to that given by the latest theory (Appendix B). The drag coefficients, as given by the measured values of the Sandia q-gages, are fairly high too, but they are not as high as would have been anticipated by the Rankine-Hugoniot approach. Note that for points near the ground, to account for the increase in side-on pressure with altitude (which is roughly 0.1 psi per ft), and for an average structure height of 6 ft, the increase in initial net drag pressure is only about 20 per cent. However, although the net pressure does not change appreciably, an increase in altitude above the ground level would easily shift the bulk of  $C_d$  from the front drag coefficient to the rear drag coefficient, where the front drag coefficient,  $C_{df}$  is defined as

$$C_{df} = \frac{f(t) - p_{\sigma}(t)}{p_d(t)} \quad (5.13)$$

and the rear drag coefficient,  $C_{db}$  as

$$C_{db} = \frac{b(t) - p_{\sigma}(t)}{p_d(t)} \quad (5.14)$$

The quantities  $f(t)$  and  $b(t)$  are the average loadings on front and rear surfaces, respectively, on all 3.1 structures. The dynamic pressures  $p_d(t)$  are given in Figs. 5.7(a) and (b). It was found that at the ground level, Shot 9, where  $p_{\sigma}(0) = 6$  psi,  $C_d \approx C_{df}$ ,  $C_{db} \approx 0$ , whereas, at the 6-ft level, one would obtain  $C_d \approx -C_{db}$ ,  $C_{df} \approx 0$  for  $p_{\sigma}(0) = 6.6$  psi.

Thus the transient drag coefficients given in Figs. 5.9(a) and (b) correspond also to the front drag coefficients for side-on pressures at ground level as reference. Note that the drag coefficients remain constant, roughly until the time,  $t = 0.3$  sec and then rise rapidly, reaching very large values when computed in terms of the Rankine-Hugoniot theory. This might indicate some peculiar transient phenomena.

## 5.6 DRAG IMPULSE COEFFICIENTS AND TOTAL IMPULSE RATIO

Although the drag coefficients expressed as a function of time are important for the study of the over-all phenomenon in practical applications, the values of the drag coefficients averaged to predict drag impulse and total impulse is often of great importance.

The measured total impulse defined by Eq. 5.15

$$I_{TM} = \int_0^{t_0} [f_0(t) - b_0(t)] dt \quad (5.15)$$

can be split into a diffraction and drag impulse as follows:

$$I_{DFM} = \int_0^{t^*} [f_0(t) - b_0(t)] dt \quad (5.16)$$

defines the measured diffraction impulse and

$$I_{DGM} = \int_{t^*}^{t_0} [f_0(t) - b_0(t)] dt \quad (5.17)$$

defines the measured drag impulse, where  $t^*$  is the time associated with the end of the diffraction period and is determined experimentally as a sharp break in the net curve (for example, see Fig. 5.8).

The calculated total impulse is obtained by the methods given in Sec. 5.2, Figs. 5.1 to 5.4, with values of "c" obtained from Fig. 5.5. In Eqs. 5.15 and 5.16  $f_0(t)$  is assumed to start with



a value of computed reflected pressure at the time,  $t = 0$ , and varies linearly until it reaches the measured value of peak pressure. This increases the impulse above that obtained by using the pressure record directly for the value of  $f_0(t)$  throughout the entire duration of loading. This increased impulse is more accurate than that obtained directly.

$$I_{DFC} = \bar{h}\rho + L\gamma + 1.25 p_d(0) \cdot t^* \quad (5.18)$$

while the computed drag impulse is given by

$$I_{DGC} = 1.25 \left[ \int_0^{t^*} p_d(t) dt - p_d(0) \cdot t^* \right] \quad (5.19)$$

where  $t^*$  is the same value as used in Eqs. 5.16 and 5.17,  $p_d(0)$  is given by Eq. 5.8 and  $\int_0^{t^*} p_d(t)$  by Eq. 5.11. The drag coefficient 1.25 has been retained as the pretest estimate for the particular shapes of the 3.1 structures obtained from various steady-state wind tunnel tests.

TABLE 5.4—Predicted and Measured Net Impulses

Shot No.	Structure	Computed diffraction impulse (psi-sec)	Computed drag impulse (psi-sec)	Measured diffraction impulse (psi-sec)	Measured drag impulse (psi-sec)	Measured total impulse (psi-sec)	Computed total impulse (psi-sec)	$\bar{C}_d = \frac{1.25 I_{DGM}}{I_{DGC}}$	Total impulse ratio $\frac{I_{TM}}{I_{TC}}$
		$I_{DFC}$	$I_{DGC}$	$I_{DFM}$	$I_{DGM}$	$I_{TM}$	$I_{TC}$	$I_{DGC}$	$I_{TC}$
9	a	0.1188	0.1275	0.1168	0.4400	0.5568	0.2463	4.33	2.26
9	c	0.0906	0.1275	0.0928	0.3194	0.4122	0.2181	3.13	1.89
9	d	0.1182	0.1323	0.0928	0.3413	0.4341	0.2505	3.22	1.73
9	e*	0.2475	0.1090	0.2510	-0.2335	0.0175	0.3565	-2.68	0.049
9	f*	0.1650	0.1124	0.2336	-0.0006	0.2330	0.2774	-0.007	0.84
9	p	0.0918	0.1330	0.1306	0.2900	0.4206	0.2248	2.73	1.87
10	a	0.0666	0.0760	0.0566	0.2852	0.3418	0.1426	4.69	2.40
10	c	0.0490	0.0768	0.0512	0.1026	0.1538	0.1258	1.67	1.22
10	d	0.0577	0.1188	0.0342	0.0271	0.0613	0.1765	0.28	0.35
10	e*	0.1425	0.1044	0.1652	-0.0135	0.1517	0.2469	-0.16	0.61
10	f*	0.1333	0.0698	0.1371	0.3581	0.4952	0.2031	6.41	2.44
10	h*	0.0702	0.0637	0.0381	0.1955	0.2336	0.1339	3.84	1.74
10	o*	0.0743	0.1176	0.0452	0.0742	0.1194	0.1919	0.79	0.623
10	p	0.1567	0.1196	0.0306	0.2554	0.2860	0.2763	2.67	1.04

\*Structures which are not considered to be meaningful with respect to drag computations (see Sec. 5.7 and Table 5.5).

Table 5.4 presents the estimated and computed diffraction, drag and total impulses in lb-sec/in.<sup>2</sup> for several structures in Shots 9 and 10 where meaningful net load (and impulse) could be measured.

An average drag impulse coefficient (in terms of measured and predicted drag impulses) is defined as

$$\bar{C}_d = \frac{\left[ \int_{t^*}^{t^*} [f(t) - b(t)] dt \right]_{\text{measured}}}{\left[ \int_{t^*}^{t^*} p_d(t) dt \right]_{\text{calculated}}} = \frac{1.25 I_{DGM}}{I_{DGC}} \quad (5.20)$$

Values for  $C_d$  are given in Column 9 of Table 5.4. The damage to a structure depends, however, on total impulse, rather than drag impulse alone and therefore in Column 10, Table 5.4, there is a ratio of measured to predicted impulses (as calculated by Eq. 5.11), the total impulse ratio. For the 3.1 structures, it was anticipated that diffraction and drag impulses would be

roughly equal, but the measured to computed drag impulses (compare Columns 6 and 4) differ by an average ratio of 3:1 (and extreme ranges from 1:3:1 to 5:1) and thus lead to total impulses at least twice as high as were expected. The impact of these findings on future drag and total impulse predictions is deferred until the next section.

## 5.7 DISCUSSION OF RESULTS AND CONCLUSIONS

Thus far, an increase in net loads, relative to pretest predictions has been discussed. The net loads during the drag phase can be looked upon as the product of two terms, namely,

$$f(t) - b(t) = C_d(t) p_d(t)$$

where, with different assumptions for the dynamic pressures  $p_d(t)$ , the time dependent drag coefficient,  $C_d(t)$ , assumes values ranging from nearly constant and of nearly the same order of magnitude as in wind tunnel test data to variations which begin with constant behavior and then at 0.3 sec (60-80 H/U units, where the period of stabilization has been reached) rise to extremely high values (up to four times as high as the wind tunnel value). This behavior is also mirrored in case these coefficients are averaged for preserving the measured impulse:

$$\bar{C}_d = \frac{\int_{t^*}^{t_0} f(t) - b(t) dt}{\int_{t^*}^{t_0} p_d(t) dt} \quad (5.21)$$

where the interval of integration  $t^*$  to  $t_0$  describes the drag phase. The value of  $\bar{C}_d$  in Eq. 5.21 varies by a ratio of 1.85:1, depending on the method by which  $p_d(t)$  is calculated. For the Rankine-Hugoniot method,  $\bar{C}_d$  is 85 per cent larger than for the latest method given in Appendix B.

Therefore, the question of whether the increased forces and impulses should be accounted for by increased  $C_d(t)$  and  $\bar{C}_d$  or by increased  $p_d(t)$  and  $\int_{t^*}^{t_0} p_d(t) dt$ , respectively, is to some degree arbitrary on the basis of present evidence. In fact, Eq. 5.21 can be looked upon as a means of defining  $\bar{C}_d$ . Since most previous weapons effects predictions are based on elementary Rankine-Hugoniot theory, the results in these reports could be expressed by retaining that method of computing drag pressures, and any necessary modifications of drag forces could be incorporated by increasing the time dependent and average drag coefficient. In terms of this reference frame, one obtains from the test results a considerable increase in drag force over the present prediction, even if one chooses the drag coefficient as  $\bar{C}_d = 2.33$  (i.e., the value found from Structure 3.3.8a of the GREENHOUSE large-scale field test). The drag impulse coefficients for the 3.1 structures, Shots 9 and 10, are shown in Table 5.4, Column 9.

In Fig. 5.10, values of drag coefficients are presented for several different situations. The value of " $C_d$ " for the UPSHOT-KNOTHOLE field test is obtained by taking a constant value which will preserve the drag impulse computed from  $\frac{1}{2}\rho u^2$  by means of the conventional Rankine-Hugoniot equations.

Drag pressure coefficients or drag impulse coefficients could not be computed for some of the structures because their net loadings were not available. For other structures, the results, listed in Table 5.4, are not considered to be valid in such a drag analysis; these structures are denoted by the asterisk in Table 5.4. The subject, namely which structures have and have not been used in studying these drag coefficients, is discussed below and summarized in Table 5.5.

The basic requirement of any given structure to be used in studying the net drag coefficients is that an average pressure-time curve is available for both front and rear surfaces. Preferably, the average pressure curve should be obtained from more than one single gage on the surface. If the reading of one gage is used as the average, obvious miscalibration errors for this gage would disqualify the entire structure for that shot. Where there is good reason

TABLE 5.5—Summary of Treatment Given Various 3.1 Structures in Net Drag Analysis

Status of structures regarding computation of net drag coefficients of Table 5.4						
Computed in Table 5.4						
Shot No.	Structure No.	Statement of validity			Not computed in Table 5.4	Remarks
		Good	Fair	Poor		
9 & 10	a		X			Both front and rear surfaces gaged adequately — poor gages, not used. Considerable differences existed among those individual gages which were used.
9 & 10	b				X	No gages on front surface.
9 & 10	c	X				Front and rear surfaces gaged adequately, individual gages in good agreement.
9 & 10	d	X				Measures peaked shock effect lightly gaged.
9 & 10	e			X		
9 & 10	f			X		
9	g				X	Record good only until $t = 0.17$ sec. oblique incidence actual $\theta = 13\frac{1}{2}^\circ$ .
10	g				X	Oblique incidence, actual $\theta = 21^\circ$ .
9	h				X	Oblique incidence, actual $\theta = 36^\circ$ .
10	h			X		Oblique incidence, actual $\theta = 43\frac{1}{2}^\circ$ .
9 & 10	i				X	No gages on front surfaces.
9 & 10	l				X	Each wall has only one surface gaged, also
9 & 10	m				X	for those average pressures available
9 & 10	n				X	multi-reflection effects conceal drag pressure loadings.
9	o				X	Record of single gage on front no good.
10	o			X		Obviously miscalibrated, adjusted curve used to compute drag coefficients.
9 & 10	p		X			Lightly gaged (1 on front, 2 on back).
9 & 10	q				X	No gages on front or rear.
9	s & t				X	Located in regular reflection region.
10	s & t				X	Located in precursor region.

to expect that the loadings during the drag phase will differ from those on most of the other structures, due to causes other than a difference in drag coefficient, this structure should also be eliminated from an analysis leading to conventional drag coefficients. Table 5.5 is best examined with the above criteria in mind.

It can be seen from Table 5.5 that Structures 3.1b, i, l, m, n, and q could not be included in the study of drag coefficients, since they did not meet the requirement that at least one gage each be located on both the front and rear surfaces.

Structures 3.1e and f were specifically designed to measure peaked shock effects which represent a deviation from the normal drag loading conditions and, therefore, these structures, too, should not be considered in the drag analysis. For either of these structures a negative impulse is not to be interpreted as resulting from a negative drag coefficient, but rather as resulting from a peaked shock effect.

Structures 3.1g and h are designed to test effects of oblique incidence and should not be averaged in with the computation of drag coefficients under normal loading.

Structures 3.1s and t cannot be used, because in Shot 9 they were in the regular reflection—pseudo-Mach stem region—and in Shot 10 in a heavy precursor region.

Structures 3.1o and p, the elevated structures, should be included in the analysis from the standpoint of effect expected, but they are of limited value from the standpoint of instrumenta-

~~SECRET RESTRICTED DATA~~ UNCLASSIFIED



tion adequacy. Each of these structures had but one gage on the front surface, which had to be used to obtain the average pressure. On Shot 9 this gage on the front surface did not produce a readable record; on Shot 10 it was obviously miscalibrated. Therefore, due to this instrumentation difficulty, Structure 3.10 is not considered in the drag loading analysis. However, a net loading curve was obtained from Structure 3.10, using the method of adjustment which changes pressure ordinates of the miscalibrated gage by the ratio of

$$\frac{(p_r)_{av.}}{(p_r)^0}$$

where  $(p_r)_{av.}$  is the measured average value of reflected pressures determined from the other structures and  $(p_r)^0$  is the peak pressure measured by the miscalibrated gage. This derived net curve is of little use in drawing any positive conclusions. It is presented merely to indicate that, following such a procedure, one will obtain curves for the net loading which have at least the same over-all shape as the other net loading curves but which are of very uncertain magnitude.

In evaluating increased drag trends, after rejecting these various structures, there are still eight cases left, namely, Structures 3.1a, c, d and p, for both Shots 9 and 10.

All the above statements are based on the assumption that the increased measured drag loadings are real and not the result of systematic gage instrumentation, calibration, or data reduction and plotting errors. Furthermore, in some instances, the average on a surface was calculated from individual gages whose critical time values seemed reasonable but whose amplitudes differ as much as 30 per cent.

The effects of those uncertainties and changes, on a formal error estimate, are very difficult to predict and their effect on the final conclusions, namely, the existence of increased drag forces, is even more uncertain. Only a few comparisons of SRI and BRL gages at roughly the same location are available. The average error between those gages is of the order of 5 to 10 per cent and the maximum error about 30 to 50 per cent (see Table 4.3 and Figs. 4.18 to 4.24).

The uncertainties in the adapted side-on pressure curve can be estimated, for example, in Shot 9, by comparing the complete envelope of the blast line gages BA to BE to the average given by Eq. 5.6 and shown on Fig. 5.6. It is found that the width of this over-all envelope is roughly 0.3 psi, independent of time. A comparison with most net loadings indicates that, after 0.4 sec, the net average pressure on these surfaces falls below this value of 0.3 psi. In this case, this number (0.3 psi) represents an envelope of gages which well may be in variance by an appreciable percentage of this 0.3 psi, so that the time of 0.4 sec, when the error in reading pressure as given by the envelope is equal to the net force, is probably not realistic. Rather, it is an indication that, here, one deals with phenomena whose absolute values easily may be of the same order of magnitude as various gage errors if these errors should accidentally combine such as to give the observed paradoxically high drag results. On the other hand, the explanation offered in Appendix B is believed to be physically plausible and ascribes the increased drag force to increased  $\frac{1}{2}\rho u^2$  values.

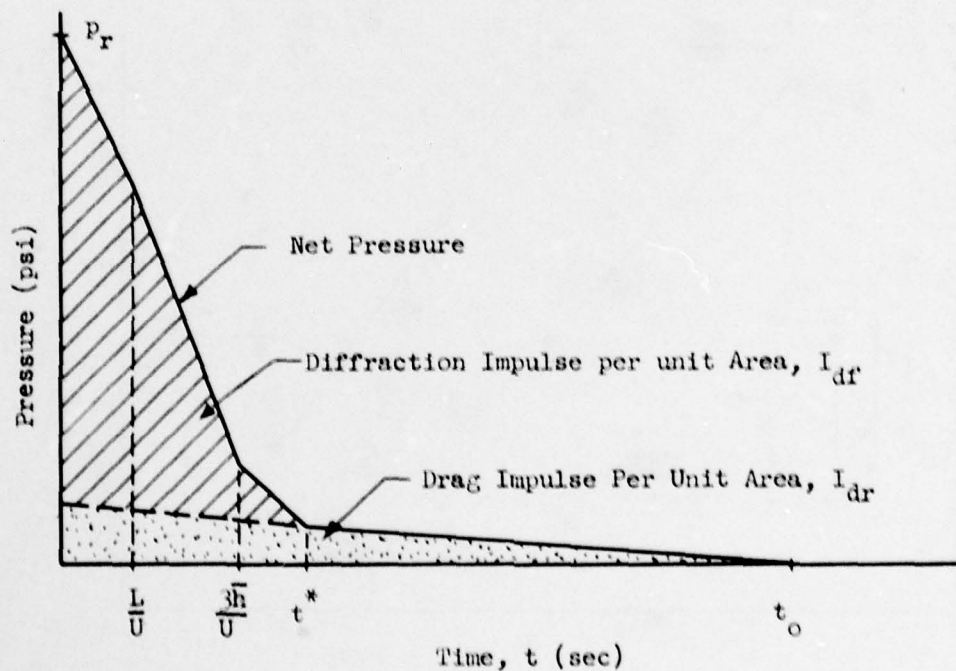
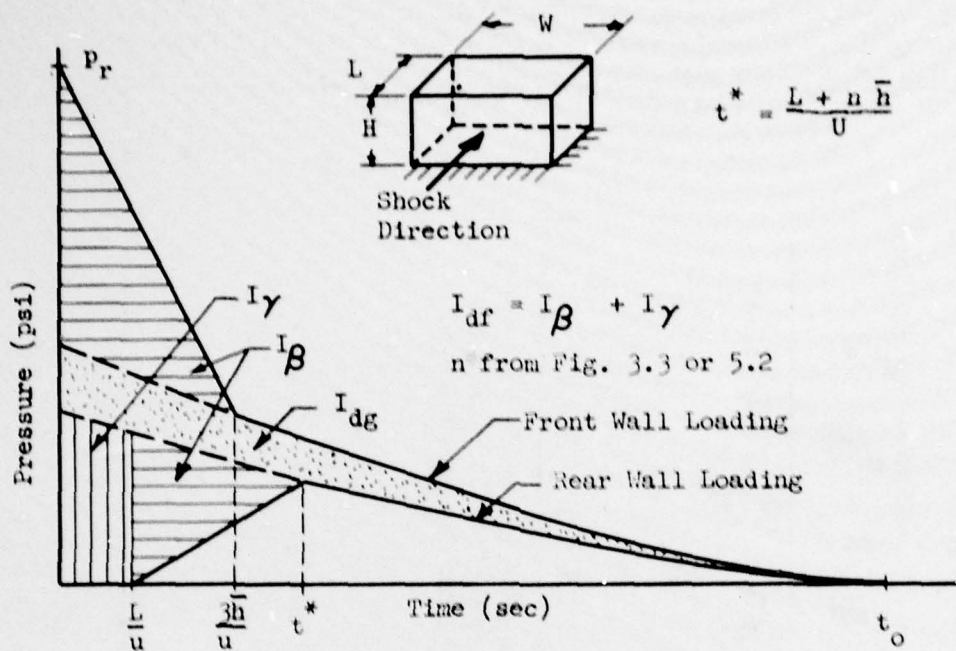


Fig. 5.1 — Definition of diffraction and drag impulses.

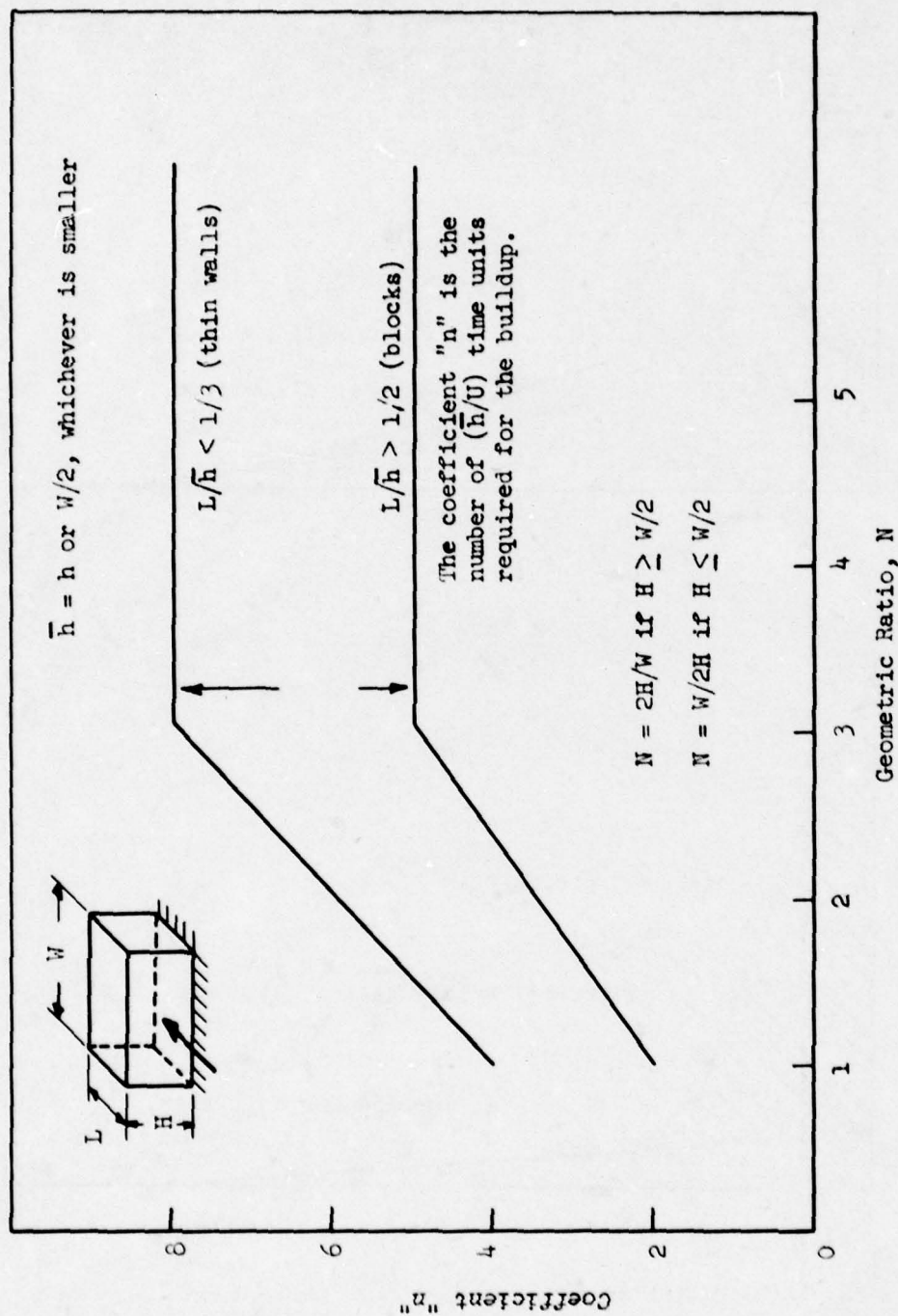


Fig. 5.2—Three-dimensional effect of pressure build-up on a rear surface.



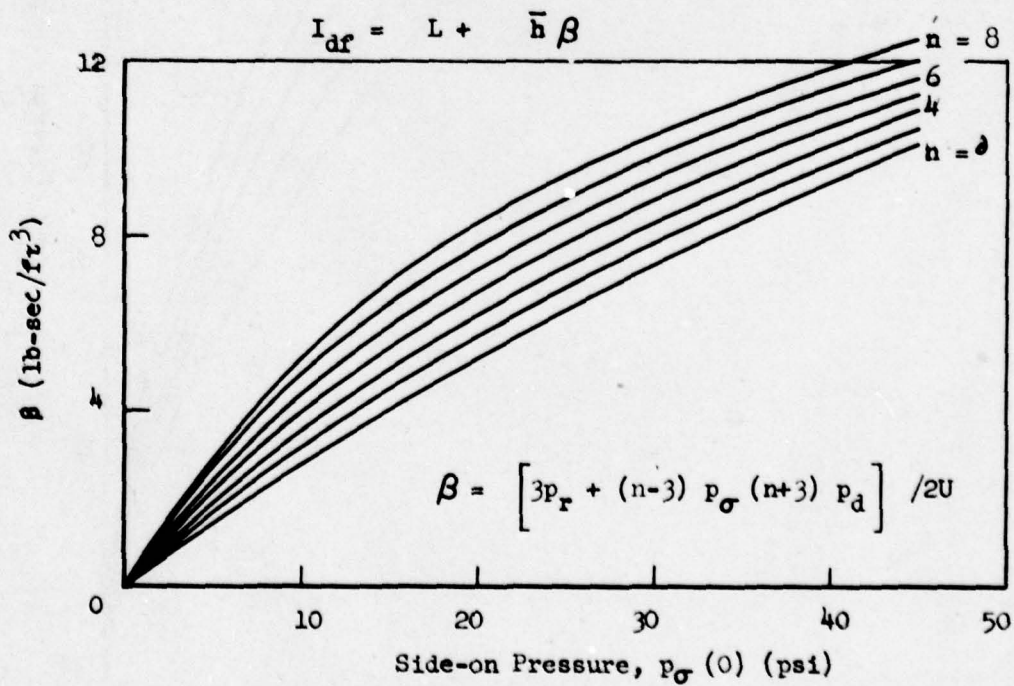
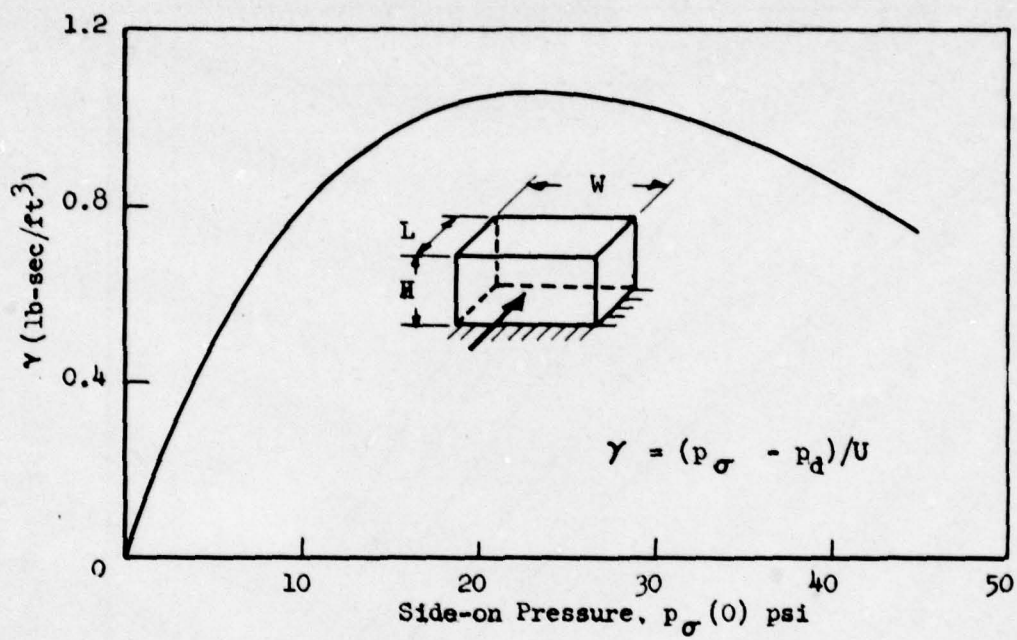


Fig. 5.3—Coefficient,  $\beta$  and  $\gamma$ , for computing diffraction impulse  $I_{df}$ .

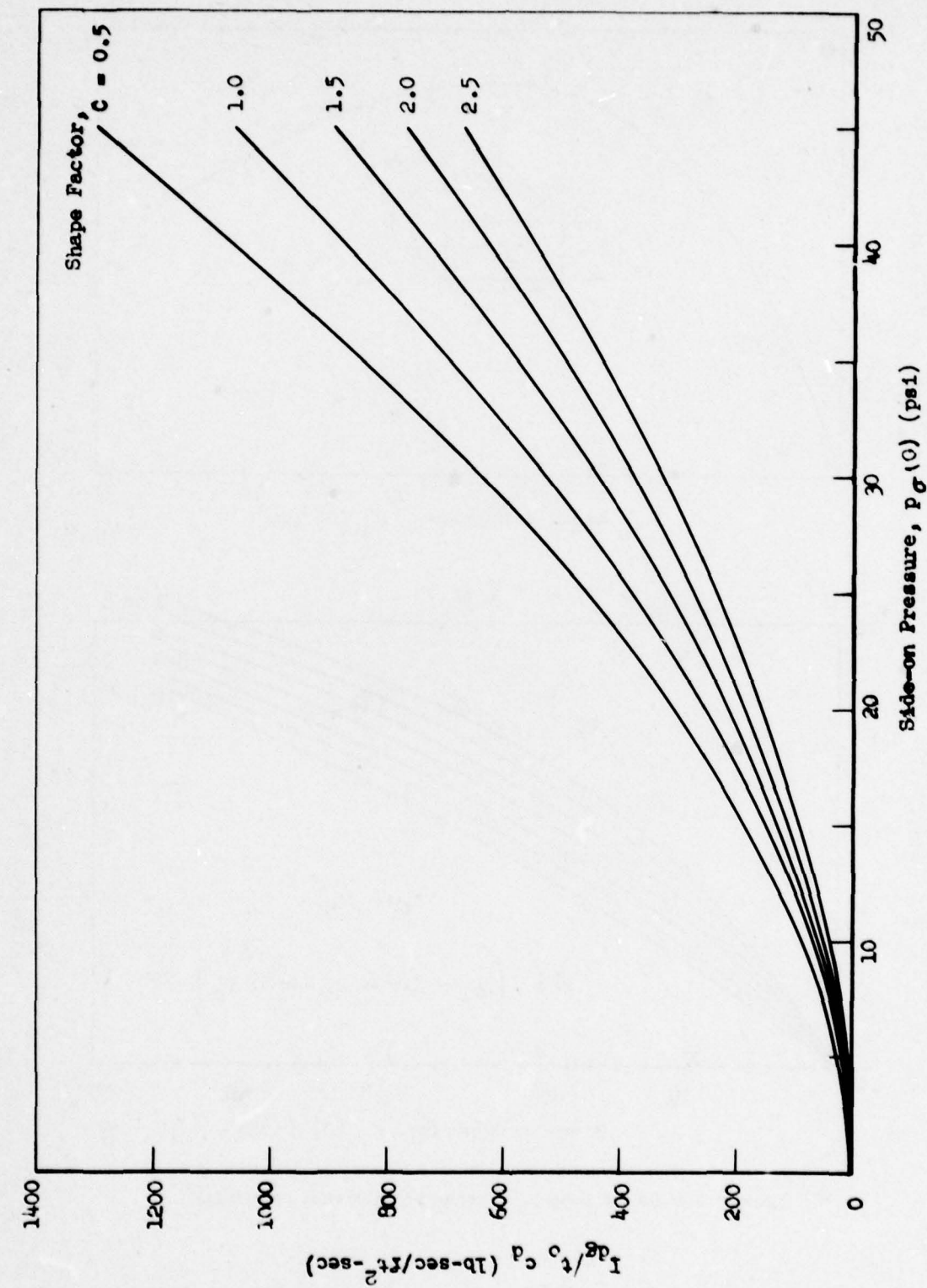
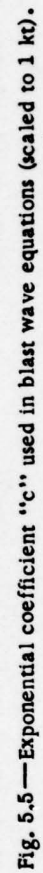


Fig. 5.4—Reduced drag impulses as a function of side-on pressure for various values of shape factors.





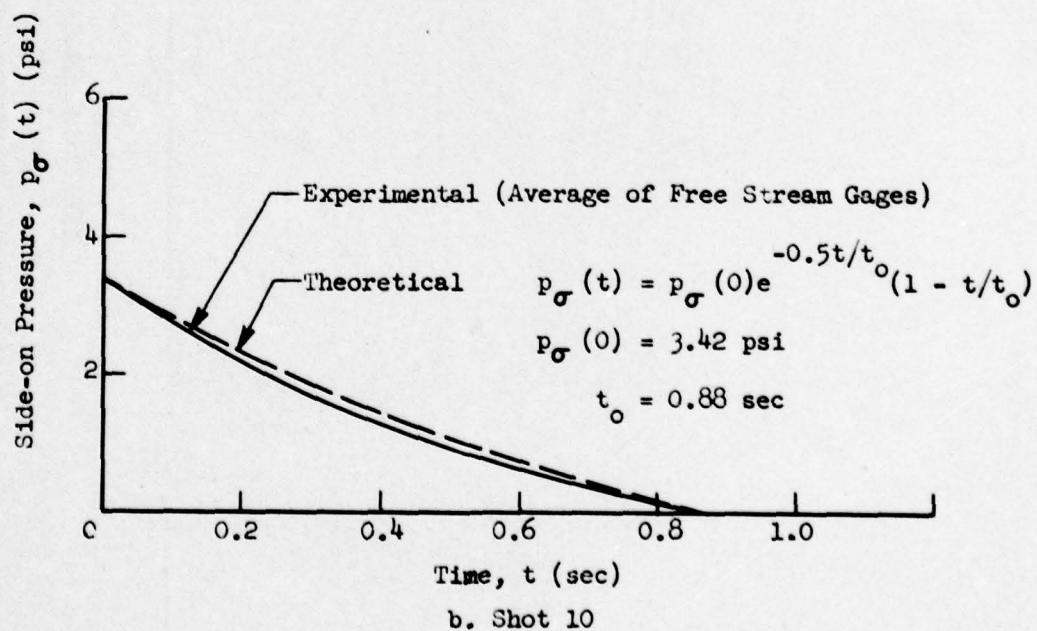
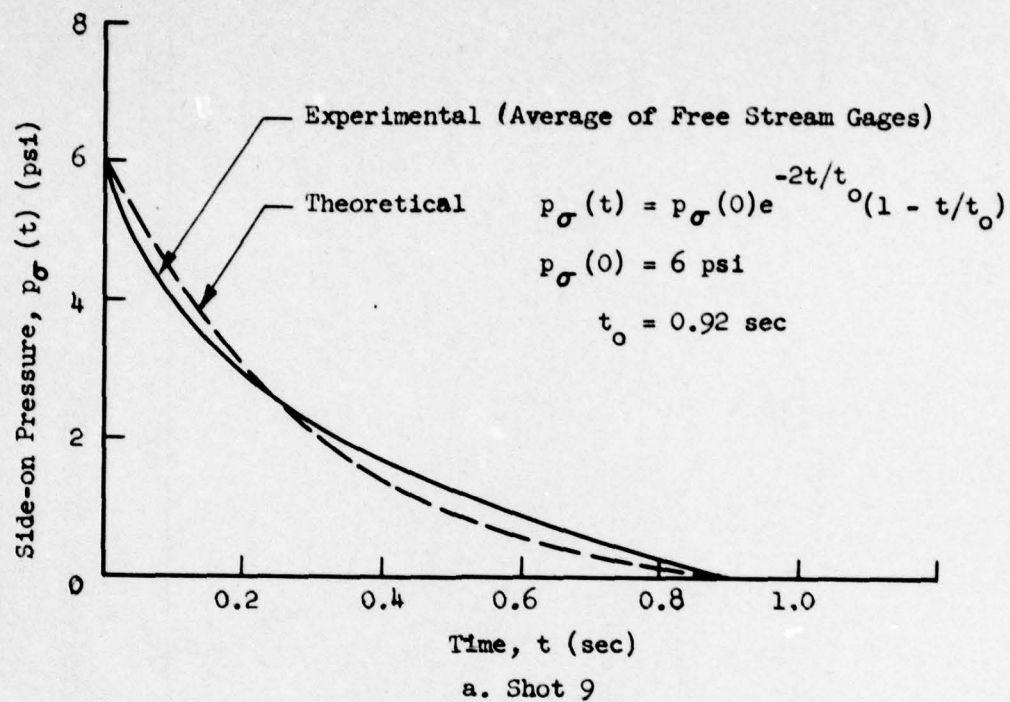


Fig. 5.6—Side-on pressure time relations. (a) Shot 9. (b) Shot 10.

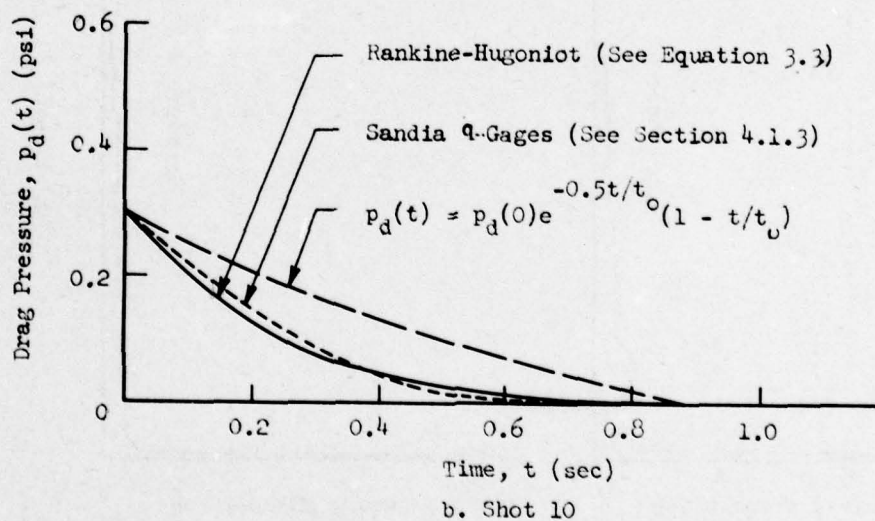
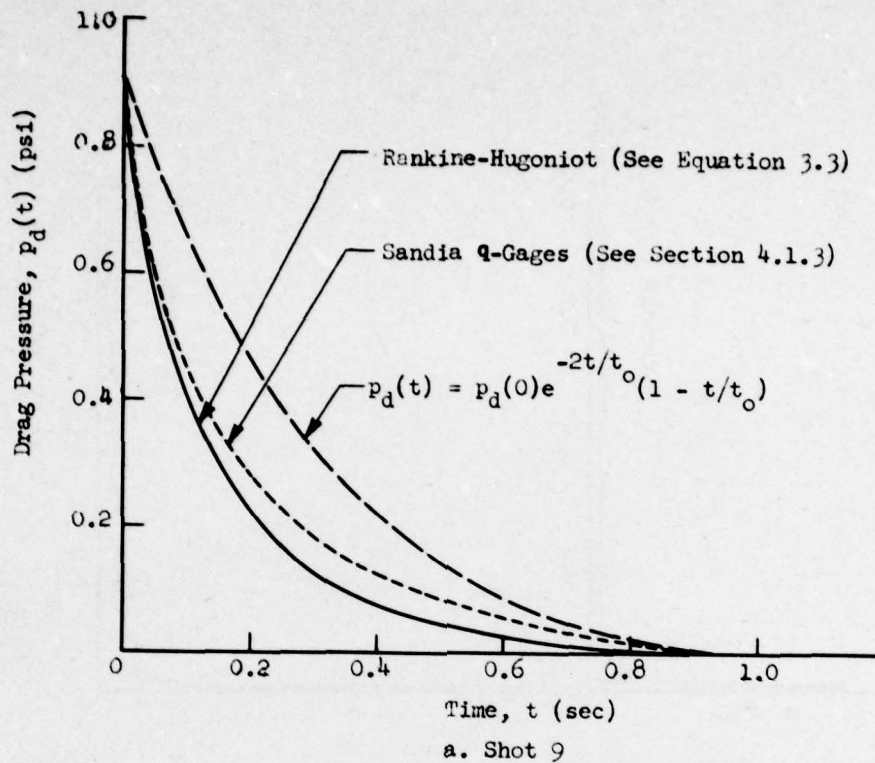


Fig. 5.7—Dynamic pressure time relations. (a) Shot 9. (b) Shot 10.

UNCLASSIFIED

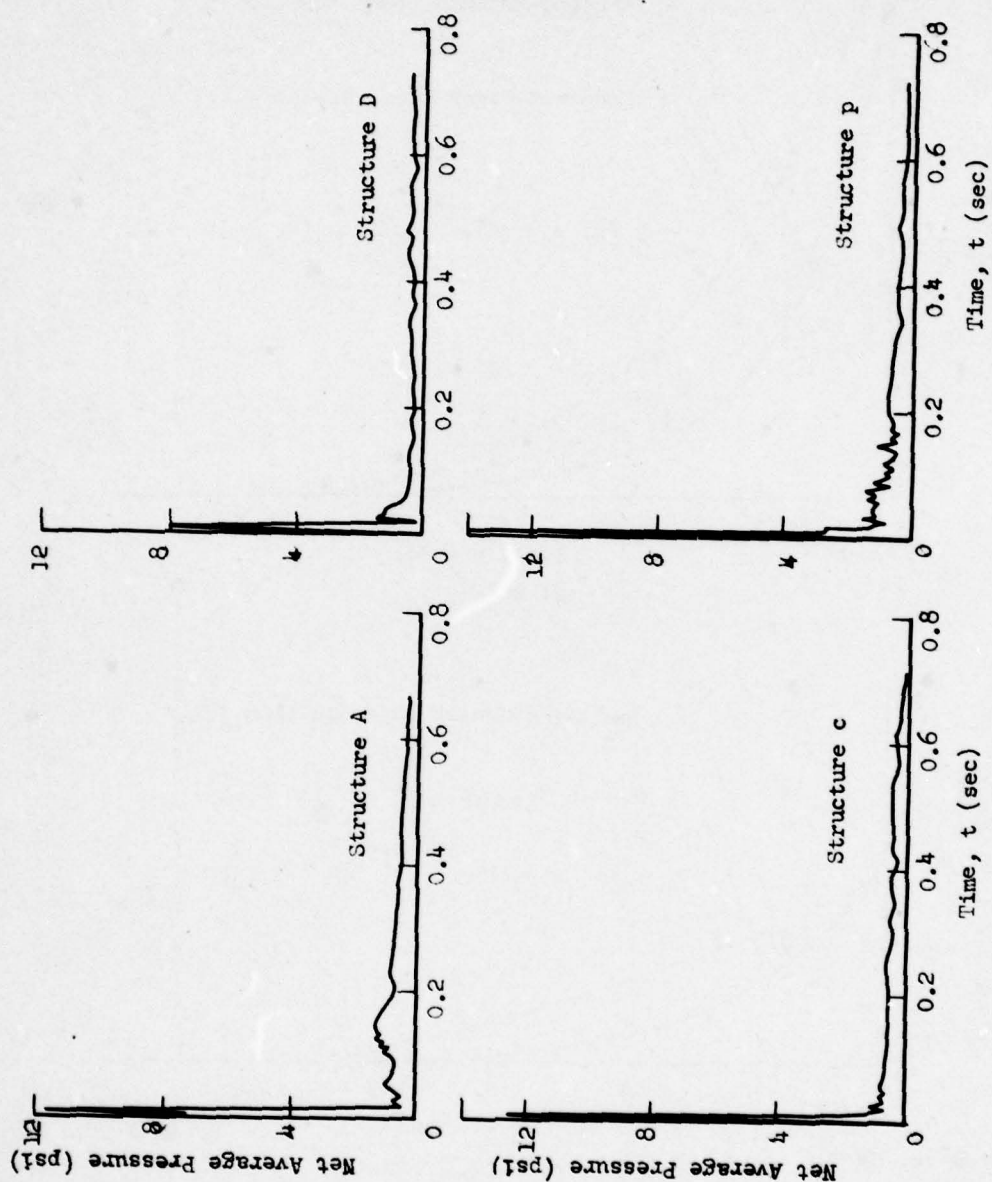
~~SECRET RESTRICTED DATA~~

Fig. 5.8a—Net forces on Structures 3.1a, c, d, and p, Shot 9.

UNCLASSIFIED

~~SECRET RESTRICTED DATA~~



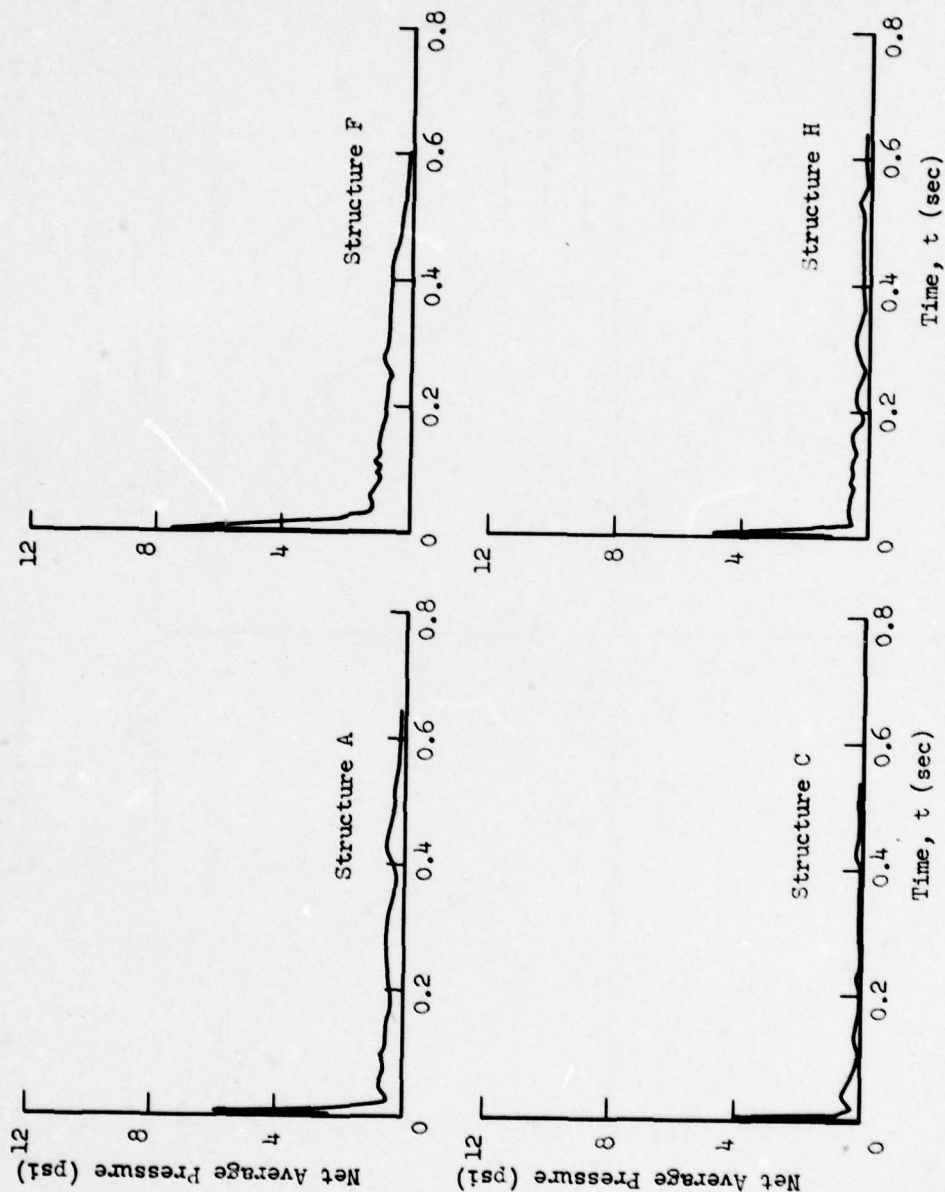
~~SECRET~~ UNCLASSIFIED

Fig. 5.8b—Net pressures on Structures 3.1a, c, f, and h, Shot 10.

~~SECRET RESTRICTED DATA~~

UNCLASSIFIED

UNCLASSIFIED

~~SECRET RESTRICTED DATA~~

270

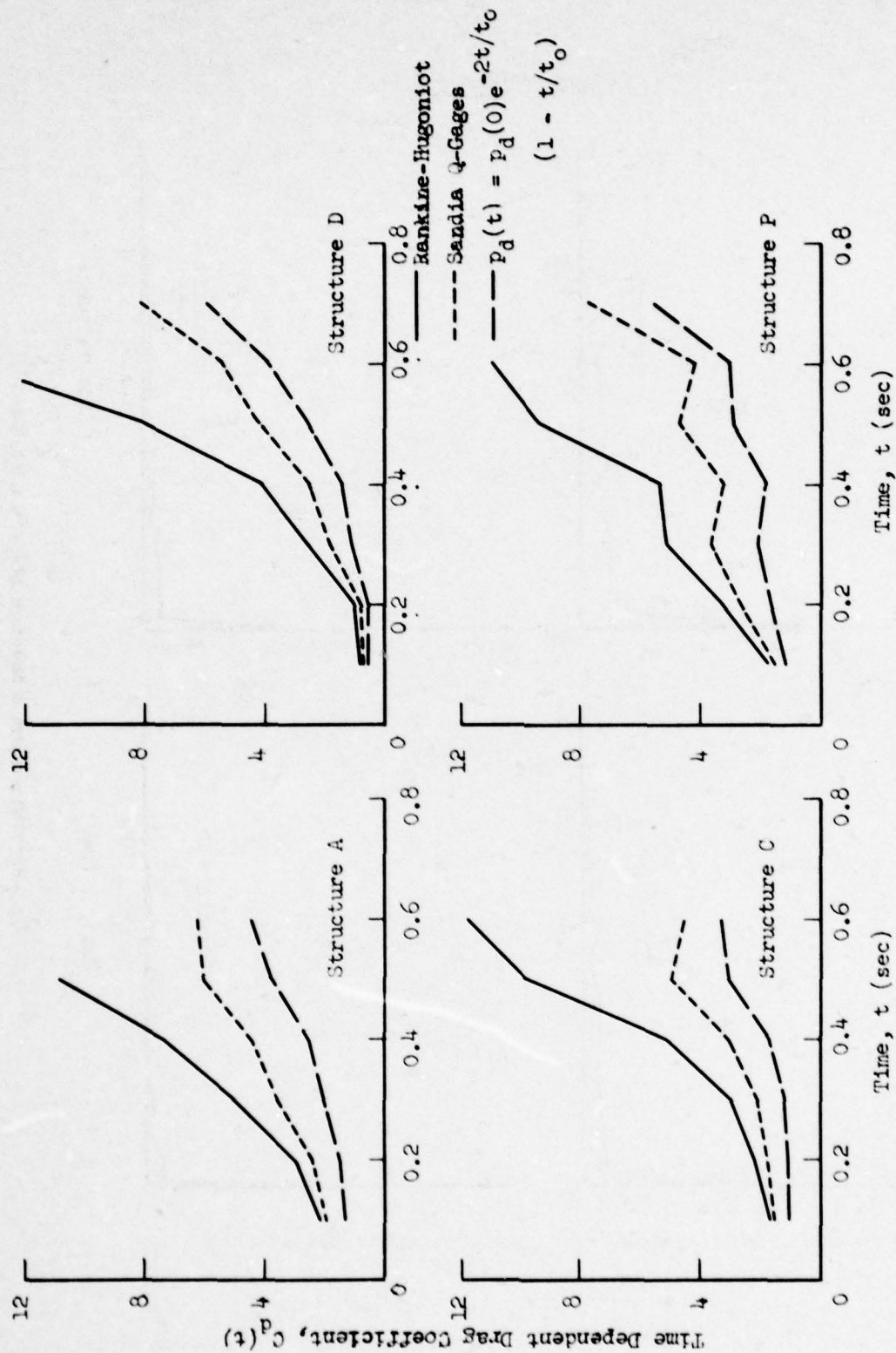


Fig. 5.9a—Drag coefficients on Structures 3.1a, c, d, and p, Shot 9.

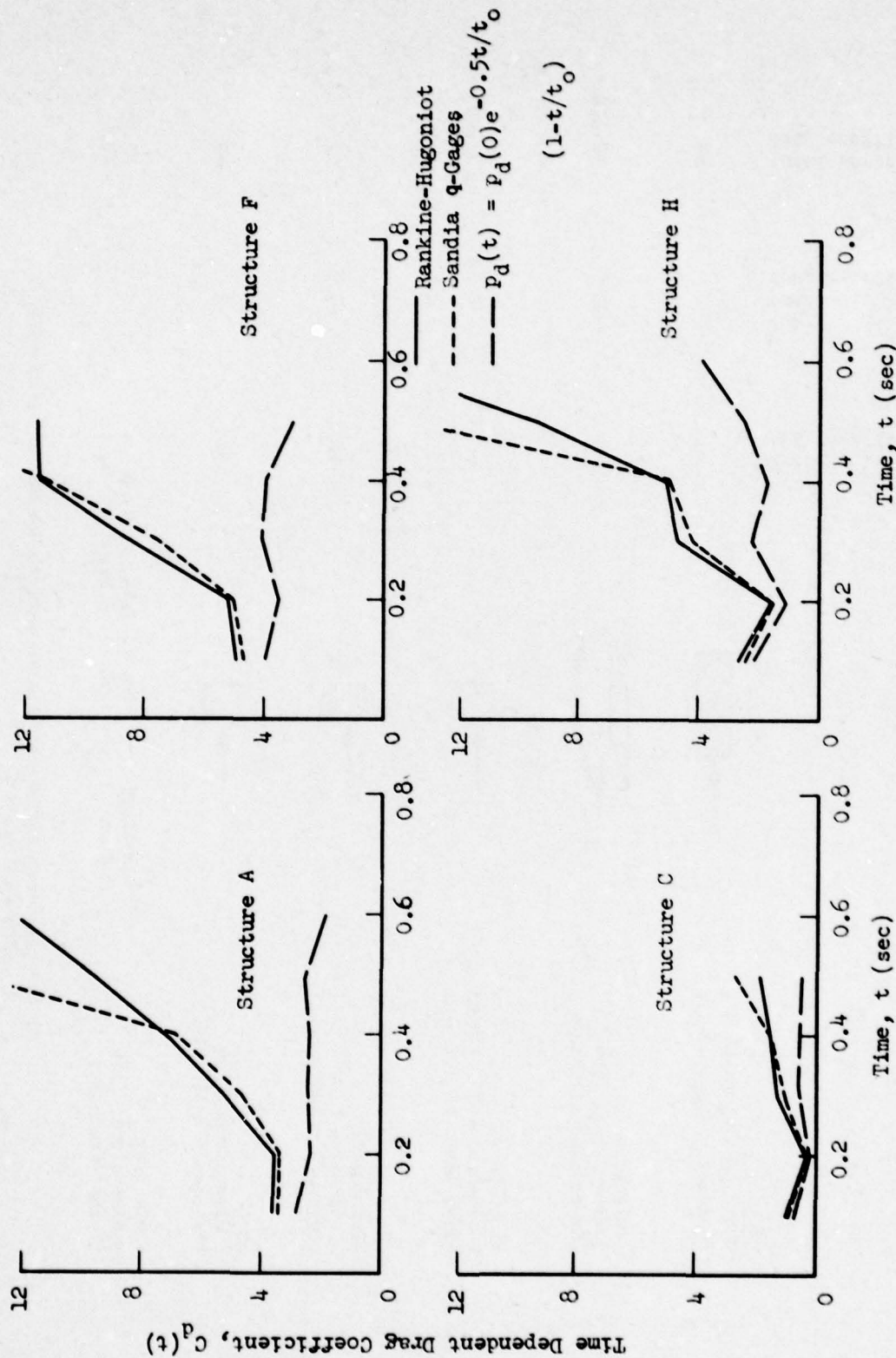


Fig. 5.9b—Drag coefficients on Structures 3.1a, c, f, and h, Shot 10.



	$C_{dr}$ drag coefficient front wall	$C_{db}$ drag coefficient back wall	$C_d$ total horizontal drag coefficient
Shock Tube 2 dimensional flow (Princeton Rept. II-11)	+1	-1	+2
Field Test 3 dimensional flow (Greenhouse structure 3.3.8a)	+2	-1/3	+2-1/2
Wind Tunnel 2 dimensional flow approx. (Iowa Inst. of Hydr. Res.)	+0.75	-0.65	+1.40
Wind Tunnel 2 dimensional flow (Irminger & Møkkentved)	+2/3	-1/3	+1
Shock Tube 2 dimensional flow (Princeton Rept. II-11)	+1	-1	+2
Field Test 3 dimensional flow (Upshot-Knothole)	Average From Shot 9, 3.1a, c, d, p Shot 10, 3.1a, c, d, o, p		+3.35 +4.0

Fig. 5.10—Comparisons between wind tunnel drag coefficients and those found in the shock tube and in field tests.

~~SECRET RESTRICTED DATA~~

UNCLASSIFIED

## CHAPTER 6

## SUMMARY AND CONCLUSIONS

In a program of the type described in this report, the conclusions, of necessity, come solely from instrument records. In Program 3.1 certain questions have arisen, concerning the performance of the instrumentation, which strongly affect the validity of the conclusions. As is discussed later, it is difficult, if not impossible, to give formal expressions representing the validity of the instrument performance. A qualitative assessment of the records is presented, but this gives rise to the unfortunate circumstance that a number of the conclusions are ultimately based on subjective treatment of the data and that others evaluating the data might draw different conclusions than those contained herein.

It is felt that the conclusions concerning the diffraction period of the flow are, in the main, rather well substantiated by the data. It was realized in the original test design that information about the forces on a structure during the drag phases of the flow would be difficult to determine, since the magnitude of the expected forces were of the same order as the errors that could be reasonably expected in the instrumentation. In the post-test analysis of the records, certain interesting trends toward increased drag forces (increased with respect to the pre-test predictions) were found. Although very many questions as to the validity of the trends should justifiably be raised, this report presents a rather extensive treatment of the results due to the potential importance of this information in the determination of damage. Since the theory contained in Appendix B makes these increased drag trends not only possible, but quite probable, it is felt that it would be improper to dismiss too readily those indications of increased drag which are contained in the data. Although it may be premature to base vulnerability predictions on these findings, they are valuable, nevertheless, in drawing attention to certain deep uncertainties in the drag loading prediction schemes.

The authors of this report hope that the analysis contained herein is accepted in the spirit in which it is written; not as a discussion which must be accepted as valid but as an attempt to obtain all the information possible from Program 3.1.

The conclusions can be subdivided into over-all conclusions of a general nature and specific conclusions for individual test objectives. The specific conclusions were derived, in the main, by comparing the pretest predictions presented in Chap. 3 with the post-test analysis presented in Chap. 4.

A summary of Chaps. 2 and 3, followed by specific conclusions in the form of brief summaries for Chaps. 4 and 5, and Appendixes A to C, is given below.

#### 6.1 TEST ITEMS AND INSTRUMENTATION

With the gages on the test items averaged in the manner as explained in Sec. 4.2, the maximum information was obtained by grouping the structures as shown in Table 2.1 and thus

~~SECRET RESTRICTED DATA~~

UNCLASSIFIED

UNCLASSIFIED

~~SECRET, RESTRICTED DATA~~

obtaining three variations of each particular geometric parameter. The lack of front gages on some cubicles prevented the obtaining of net loadings, but in one instance the latter was estimated by assuming standard front loadings and subtracting the measured rear loadings. Structures 3.1s and t were in a severe precursor on Shot 10, which caused Structure 3.1s to overturn.

The instrumentation was disappointing with respect to calibration accuracy, but it was fairly satisfactory with respect to time values (rise time, 2 to 3 msec.). Individual gages differed by as much as 100 per cent of side-on pressure in the extreme case of obvious calibration errors (see Fig. 4.10), whereas the average discrepancy was much lower. Check gages between BRL and SRI agreed on the average of between 5 and 10 per cent (see Table 4.3).

## 6.2 PRETEST PREDICTIONS

Average pressures were predicted on front, roof, and rear walls of various structures in order to deduce the loading method in Mach and regular reflection regions for correlations with previously known shock-tube, wind-tunnel, GREENHOUSE, and Sandia data. These pretest predictions are given in Chap. 3. A comparison of pretest predictions and UPSHOT-KNOTHOLE test results is presented in detail in Chap. 4.

## 6.3 POST-TEST ANALYSIS

The original test objectives, namely the effect of change of various shock and geometric parameters on the loading (note that the term "loading" has many interpretations, e.g., net loads, impulses, etc.) has been subdivided into the individual tasks given in Table 2.2 and discussed below. In addition to fulfilling the original test objectives, three bonus findings emerged, namely: (1) the establishment of a wave shape factor "c," different from unity, to be used in the incident side-on curve

$$p_{\sigma}(t) = p_{\sigma}(0) e^{-cx} (1 - x), \quad x = t/t_0$$

The value of "c," which depends on scaled height of burst and scaled distance from Ground Zero (see Fig. 5.5), is roughly 2.0 for Shot 9 and 0.5 for Shot 10, rather than 1.0 as anticipated in the pretest predictions; (2) increased drag forces, which will be discussed in the next section; and (3) a detailed study of the precursor effects for structure 3.1t, Shot 10.

### 6.3.1 Width Effects

The objective of width effects studies was to determine the type of loading on the top and rear surfaces of three-dimensional models as compared to that on two-dimensional models. This objective was satisfactorily fulfilled.

(a) Rear Surfaces. Revised values of "n" given to account for quicker build-up time as related to width. (See Figs. 3.3 and 4.125.)

(b) Top Surfaces. Vortex intensity increases with width. Quantitative revisions recommended for future.

(c) Shock Tube Comparisons. For H:W:L = 1:6:1. Diffraction loading at center of top and rear surfaces for the field test model are the same as those of the Princeton Shock Tube Model (L:H = 1:1).

### 6.3.2 Length Effects

Within the intended scope, the objectives of length effects were fulfilled.

UNCLASSIFIED

~~SECRET, RESTRICTED DATA~~



(a) Rear Surfaces. Build-up on back of three-dimensional thin wall completed in  $2S/U$ , instead of  $4S/U$ , time units. (See Figs. 3.3 and 4.125.)

(b) Top Surfaces. Loading on the top surface appears to be related to the ratio of width to length. Further exploration (in the shock tube) is definitely recommended. Insufficient data were available for determination of rules governing this variation.

(c) Greenhouse Comparison. Normalized pressures on the top and rear surfaces of nearly identical structures in the Upshot Knothole and Greenhouse programs compared favorably.

#### 6.3.3 Size Effects

The objectives of size effects studies were to investigate time-scaling and check for the occurrence of the peaked shock effect. These objectives were fulfilled.

(a) Relation of Pressures on Geometrically Similar Structures. The pressure-time curves on the top and rear surfaces of geometrically similar structures can be satisfactorily obtained from one another by multiplying time scales by the corresponding ratios of structure sizes.

(b) Peaked Shock Effect of Structure Height. Peaked shock effects resulting in negative net loads were observed for a structure having  $t_0 = Ut_0/H = 66$ . This is primarily due to lowering of pressures on the front surface. No analytic treatment attempted.

#### 6.3.4 Orientation Effects

The effects of orientation were only partially determined, since the drag coefficients, which were treated in great detail in the pretest predictions, could not be checked, and considerable instrumentation difficulties were encountered on the oriented structures.

(a) Peak Pressures. Satisfactory agreement exists between the experimental values and pretest predictions for peak pressures on obliquely loaded surfaces. Peak pressure,  $Q$ , varies linearly with angle of incidence,  $\theta$ , between normal and parallel orientation (at least for overpressures up to 6 psi).

(b) Diffraction Impulse. The pretest prediction of diffraction impulse on obliquely loaded surfaces gave values which were higher than measured impulses. A correction factor to be applied to the pretest prediction is recommended, namely, the factor  $1 - \frac{1}{2} (\theta/90)$ .

#### 6.3.5 Shielding Effects

This objective of the test was only partially fulfilled. The main reason was that the pretest predictions were much simpler than the field records. The results of this test are not adequate for deriving an accurate method of prediction.

For pairs of thin walls separated by a distance of one-half the height, the net diffraction impulse on each wall is greater than on an identical isolated wall. At a separation distance of one height unit, the net diffraction impulse is less than that of a free wall.

Reflections from the shielded wall affect the loading of the shielding wall significantly at separation distances of three and over height units. In the range of shielding distances between one-half and three height units, the loading on the back of the shielding wall appears to increase as the walls are placed farther apart.

#### 6.3.6 Effect of Elevation

The elevation effects objectives were only partially fulfilled. Conclusive results were obtained regarding the values of  $S^*$ , the clearing distances and build-up distances on the front and rear surfaces.

(a) Net Impulse. No effect.

Pressure Increase on Underface: Shot 10 (3.5 psi). No effect observed. Shot 9 (6 psi) pressure increase approximately as predicted (see Figs. 4.159 to 4.162).

(b) Loading on Rear Surfaces. Vortex effects leading to predicted rear build-up and pseudo-steady-state, but delayed final build-up time. Good agreement exists between predicted and measured values of pressure during the pseudo-steady-state phase. A vortex, which results in significant lowering of pressures, was observed but not predicted. It occurred immediately after the peak pressure was reached.

#### 6.3.7 Irregularities of Shapes, Cavities, Setbacks, Etc.

The intended objectives of loading on irregularly shaped objects were completely fulfilled.

The loadings on the surfaces of Structure 3.1q in general had the same diffraction impulse but higher reflected pressures and faster relief times than given in the pretest predictions.

Normalized pressure-time curves on surfaces of the notch at the sides were also compared to loadings on corresponding surfaces of the Princeton double block. Here, again, higher peak (re-entrant corner) pressures and shorter relief times were observed on Structure 3.1q than on the Princeton double block, but the diffraction impulses were roughly the same.

#### 6.3.8 Regular Reflection Effects

The regular reflection objectives were only partially fulfilled. The rather elaborate pretest predictions, given in Chap. 3, could only be tested in two instances of incidence angles of 30 deg (3.1s) and 44 deg (3.1t). In the former, both peak pressures and pseudo-steady-state values were somewhat overestimated, while on the latter they were somewhat underestimated, but on the whole the agreement is fair (see Figs. 4.180 to 4.183).

#### 6.3.9 Precursor Effects

(a) Pressure Records. NOL Records on Structure 3.1t in the precursor region of Shot 10 are valid. Loads are high when compared to loads computed on the basis of peak side-on pressure. Superimposed are large random oscillations.

(b) Dust Effects. The effects noticed on Structure 3.1t may be attributed, in all likelihood, to a large amount of dust present in the air which is carried along by the blast wave. This dust loading not only has an effect on the loads experienced by a target, but it also influences intimately the precursor itself.

(c) Loading Scheme for Precursor, Shot 10. A method of computing loads in a precursor is presented in Fig. 3.34. It is felt that this scheme for predicting loads is probably about as accurate as can be developed at present. The loads predicted on the basis of this method approximate the drag loads which would be obtained if the bomb were exploded over an ideal surface.

(d) Applicability to Other Precursor Shots. It is assumed that the rise time scales like a hydrodynamic variable,  $\text{rise time} = 100 (W/15)^{1/3}$ , that is, one must preserve the same scaled height of burst and the same type of surface.

#### 6.3.10 Effects of Shock Strength

This objective of the test was not fulfilled since those structures intended for studying Mach loading with higher shock strengths were actually located in a region of regular reflection.

The most outstanding result of the post-test analysis is the fact that, with few exceptions, there is no reason at this time to modify the pretest predictions if correct wave shapes and correct drag pressures are taken into account. This will be discussed later in the general conclusions. The most important is the post-test build-up coefficient "n", given in Fig. 4.125.

The modifications indicate that "n" is the same for three-dimensional thin walls as for finite blocks.  $W/2H = 1$ , and the rising slope to two-dimensionality extends to the ratio  $W/2H = 5$ , rather than 3.

#### 6.4 INCREASED DRAG TRENDS

It was found that increased drag forces existed, unless instrumentation uncertainties combined accidentally in such a manner to give this result on many obstacles (see Table 5.1). The nature of these increases is as follows: At the beginning of the drag phase the loading starts with an anticipated value obtained by Rankine-Hugoniot theory, but then the decay is nearly linear, unlike the double exponential that would be predicted from Rankine-Hugoniot theory extended to apply throughout the entire duration as in Eq. 3.3. These increased drag forces can be accounted for in two ways, namely, by means of a transient drag coefficient as given by Eq. 4.4 (Sec. 4.4.5), which assumes very large values during the later portion of the loading period (Fig. 5.7) or by increased dynamic pressure values or  $\frac{1}{2}\rho u^2$  (Appendix B), which possess a less rapid decay than given by the assumption of the Rankine-Hugoniot theory. Either of these views and/or a combination of them could explain the drag forces observed, although it seems probable that high values of  $\frac{1}{2}\rho u^2$  are the proper explanation of the effects. A specific decision is deferred on the variation of drag coefficients until some confirmation can be obtained from results of scaled shock tube tests, which ARF is, at present, undertaking on scaled models on Contract No. AF33(616)-2540. At any rate, the pretest value of 1.25 seems too low, and, if, for purposes of comparison, the Rankine-Hugoniot theory is retained to calculate drag forces, the new drag coefficient is roughly 3.35 (Shot 9) and 2.33 (Shot 10). In terms of the new theory for calculating  $\frac{1}{2}\rho u^2$ , presented in Appendix B, where drag pressure decays roughly at the same rate as side-on pressure, the average values of drag coefficients which preserve the total drag impulse (these are actually drag impulse coefficients) are 1.8 (Shot 9) to 1.45 (Shot 10). This is slightly lower than the GREENHOUSE (*Blast Loading and Response of Structures*, WT-87) field result, which shows that the drag pressure coefficient is  $C_D = 2.33$  but uses the Rankine-Hugoniot theory extended throughout the duration to compute dynamic pressure. However, the important distinction between the GREENHOUSE and UPSHOT-KNOTHOLE drag coefficients which must be emphasized is that the GREENHOUSE coefficient is a ratio of drag pressures, and the UPSHOT-KNOTHOLE coefficient is a ratio of drag impulses.

#### 6.5 PRECURSOR THEORY

The loading in the precursor region (Appendix A) has no diffraction phase if the height  $H$  and the length  $L$  are small compared to the wave length  $U/t_0$ . The net pressure rises linearly to the nonprecursor drag pressure (i.e., as if no precursor were present)  $C_d p_d(0)$  in 100 msec for Shot 10 test conditions and then decays linearly to zero at  $t_0$  (see Fig. A.34). To apply this loading scheme to other shots, it is assumed that the rise time scales like a hydrodynamic variable, i.e.,  $t_{\text{rise}} = 100 (W/15)^{1/3}$ , and that, therefore, both scaled height of burst and the same type of surface must be preserved.

#### 6.7 WAVE SHAPE THEORY

Two main conclusions are derived (Appendix B): (1) the positive duration material velocity is from 1.5 to 2.5 times the positive duration of the pressure wave and corresponds roughly to the absolute minimum on the pressure wave and is illustrated in Fig. B.2 (for a reflected wave, the material velocity duration is that of a free wave of twice the yield); and (2) the rate of decay of the material velocity,  $U(t)/U(0)$ , is proportional to the square root of the rate of decay of side-on  $\sqrt{p_{\sigma}(t)/p_{\sigma}(0)}$  rather than to  $p_{\sigma}(t)$ , and, therefore,  $\frac{1}{2}\rho u^2$  decays roughly like side-on pressure. In particular, one obtains for the impulse ratio



$$\frac{I_{p_o}}{I_{\frac{1}{2}\rho u^2}} = \frac{\int_0^{t_0} p_o(t) dt}{\int_0^{t_0} \frac{1}{2}\rho(t) [u(t)]^2 dt} = \frac{p_o(0)}{\frac{1}{2}\rho(0) [u(0)]^2}$$

which suggests an equipartition of static and dynamic pressures on a normalized basis, namely, the impulse delivered through static or dynamic pressure must always bear the same relationship to the peak values, considering different positive durations.

## 6.7 REGULAR REFRACTION THEORY

The problem of a shock wave striking a gaseous interface (Appendix C) (thermal boundary layer) has been previously solved numerically (see H. Polachek and R. J. Seeger, "On Shock Wave Phenomena," in NOL Memorandum 9971 and *Physical Review*). In Appendix C solutions are obtained by means of engineering approximations, and these solutions could be combined with those of a shock wave striking a solid interface to solve the pseudo Mach stem problem, which was believed to be present at Structures 3.1s and t, Shot 9. The simple engineering solutions compare favorably with the complex exact solutions of Polachek and Seeger, which have been obtained by means of the IBM Selective Sequence Electronic Calculator for the Oxygen-Nitrogen Refraction and Nitrogen-Oxygen Refraction Problem (Figs. C.3 to C.6). It should be noted that thermal boundary layers can be simulated, using gases with different specific heat ratios,  $\gamma$ . This theory is applied to UPSHOT-KNOTHOLE, Shot 9, at the 837-ft ground range station, both at ground level and at 10-ft elevation. Assuming a constant thermal layer of  $3\frac{1}{2}$  ft height, one obtains good comparison between measured and calculated wave shapes, maximum and minimum pressures, and delay times between incident and reflected shocks. The increased dynamic pressure at the 2100-ft station, too, can be calculated by regular refraction theory, rather than assuming a pseudo Mach stem (involving a single triple point).

## 6.8 GENERAL CONCLUSIONS

This section presents the general conclusions reached as a result of the analysis of the test data presented in this report:

1. The test objectives were generally attained, inasmuch as useful information was obtained with regard to the effect of various geometric and shock parameter changes on the diffraction and drag loadings. With few exceptions diffraction phenomena checked pretest predictions. Drag coefficients were not found to be constant. It is difficult to summarize in a few sentences the many various conclusions on the effects of length, width, and other changes; therefore, the reader is referred to Sec. 6.4 for the detailed conclusions.

2. Although the form of the equation is probably not rigorous on theoretical grounds, the incident side-on pressure may be represented practically by an equation of the form

$$p_o(t) = p_o(0) e^{-ct/t_0} \left(1 - \frac{t}{t_0}\right)$$

where the shape factor "c" is given in Fig. 5.5.

3. The decay in drag forces seems to be nearly linear, and, as a consequence, drag coefficients are larger during the later portions of the positive phase duration than would be predicted by the conventional transformation from side-on to dynamic pressures using the Rankine-Hugoniot relation between pressure and material velocity; this also leads to larger drag impulses and, hence, larger total impulses. If this effect is the real and not the accidental combination of instrumentation uncertainties, it could be ascribed either to a "transient" drag coefficient or to larger dynamic pressures. The latter point of view is adopted in a study in Appendix B by F. B. Porzel, wherein it is shown that drag pressures should decay more nearly as the first power of side-on pressure and not as the square, as would be predicted by Rankine-

Hugoniot convention. It is felt that the hydrodynamic argument in Appendix B is probably the correct explanation for the majority of the drag effects observed and that, on the basis of its inherent validity, combined with the measurements obtained, this theory gives the best description of drag loadings in terms of the current state of knowledge. On the other hand, if the dynamic pressure is calculated from the extended Rankine-Hugoniot theory (i.e., Eq. 3.3), the side-on pressure being referred to the ground-on level and if an increased drag coefficient is adopted as the explanation for net drag pressures being higher than previously expected, then such drag coefficients would be roughly equal to the front wall drag coefficient and the back wall drag coefficient would be nearly zero.

4. In terms of the new form factor for side-on pressure in Conclusion 2 above and the increased drag forces discussed in Conclusion 3 above, there is reasonable agreement between prediction and test results on nearly all test objectives. However, it should be pointed out that primary emphasis was placed on the study of diffraction phenomena since the pressure gage data were not expected to be sufficiently accurate to resolve the relatively small drag forces. A comparison between measured and predicted diffraction loads served to confirm certain aspects of the pretest load prediction methods and led to revisions of others. In the remaining instances, the form of the data was inadequate to either confirm or revise the methods. This latter category includes those cases in which the test data clearly disagreed with predictions but were too sparse to warrant revision of the prediction scheme.

One of the few cases, however, where revisions were clearly indicated concerned the rear build-up coefficient "n" (see Fig. 4.125).

5. Pretest diffraction impulse predictions, based on all entries of Table 5.4, are on the average of 40 per cent too high, with a standard deviation of 100 per cent. The worst discrepancies between prediction and test results occur for Structures 3.1h, o, and p, Shot 10. If Structure 3.1p, Shot 10, would be excluded from Table 5.4, the predictions would be 12 per cent too high, with a standard deviation of 35 per cent, and if Structures 3.1o and p are excluded, the predictions are, on the average, only 1 per cent too high with a standard deviation of 25 per cent. Post-test diffraction impulse predictions are already presented in terms of "n" (the dimensionless build-up time or rear surface) and, hence, easily modified if further data become available.

## APPENDIX A

### LOADING IN PRECURSOR REGION†

By L. A. Schmidt

#### A.1 INTRODUCTION

In Operation UPSHOT-KNOTHOLE Shot 10, as was expected, there was a well-developed precursor which extended out to about 2500 ft from Ground Zero. Thus, Structures 3.1s and t were included well within the precursor region. It turned out that these were the only two structures in the precursor region of any shot which were extensively instrumented. Because the damage which occurred in the precursor region of Shot 10 was much higher than had been expected on the basis of the usual peak pressure criteria, there was a general feeling that undetermined phenomena had occurred. Since the effect was so pronounced and would have considerable consequence in the determination of damage criteria, it is evidently important to determine the nature of these phenomena. Therefore, one expects that the records from these two structures would contain valuable information.

As will be seen later, the information contained in these pressure records bears not only upon the loadings of a structure in a precursor, but also upon the incident free stream conditions because the tests on these structures turned out to contain interesting diagnostic information about the free stream conditions.

#### A.2 TEST ARRANGEMENT

The locations of the two test structures are shown in Fig. A.1. For Shot 10, these structures were located at distances of 1047 and 2106 feet from actual Ground Zero. The maximum angular deviation of these structures from parallel to the shock front was less than 4 deg, which is considered negligible.

These two structures were instrumented by NOL. See the Final Report on Project 3.28.2 prepared by NOL for a description of the instrumentation used. On Shot 10 records were obtained from all 24 gages on Structure 3.1s and from 23 gages on Structure 3.1t. The general performance of the instrumentation appeared to be good, and apparently the records adequately reproduced the pressures upon the gages (on Structure 3.1s there were some spurious effects, see Sec. A.3.4.1). In a few cases, there were apparent inaccuracies in the calibration factors, but these inaccuracies were too few to invalidate the results. The locations of the gages on these two structures are shown in Fig. A.2.

---

† This is a specific discussion of Structures 3.1s and t in Shot 10.



In addition to the gages upon the structures themselves, there were a number of additional pressure gages placed by NOL near Structure 3.1t. These pressure gages formed Program 3.1u of Operation UPSHOT-KNOTHOLE and have been very useful in the analysis of the present results. The locations of these pressure gages are given in Fig. A.3.

### A.3 DESCRIPTION OF TEST RESULTS

#### A.3.1 Introduction

A direct indication of extensive damage is found in Structure 3.1s. This structure was severed from its base, overturned, and thrown back about 20 to 25 ft. In Fig. A.4 the depression in the left foreground shows the initial location of the structure. Apparently the structure was inadequately keyed to its foundation for the loads exerted since the reinforcing steel rods pulled out and failed in tension. It is not known at what time the structure began to move during the shock wave so that there is uncertainty as to the orientation of the structure throughout the blast wave. The gage cables broke at between 250 and 800 msec, but acceleration effects could be seen before this time. On Structure 3.1t, there were no indications of any structural damage.

There appears to be, upon first examination of the pressure records from Structures 3.1s and t, a large amount of irregularity present in the records. Of the two sets, the records on Structure 3.1t appear better. Moreover, there was no uncertainty as a result of structural failure in the 3.1t records; there were also a number of additional 3.1u pressure gages placed in its vicinity. Accordingly, the pressures upon 3.1t will be discussed more extensively here.

Due to the apparently irregular fluctuations of the records of Structure 3.1t, it would be hard to see, initially, what occurred in terms of pressure phenomena. It is best to consider the records upon 3.1t as a set of isolated records and obtain whatever comparisons are possible on the records, independent of the physical phenomena. If some correlations of this type can be obtained, then the records can be interpreted in terms of physical phenomena. Although this procedure is somewhat different than that usually followed in an analysis of this type, it appears safest, due to the nature of the phenomena, to regard the gage records as a closed body of information which may be studied by itself. Once conclusions have been made as to the nature of these records, then the physical meaning of this information may be discussed and reasonably sound conclusions may be drawn.

#### A.3.2 Incident Blast Wave Pressures

##### A.3.2.1 Blast Line Pressure Records

The peak pressure in the blast wave as a function of distance from Ground Zero is given in Fig. A.5. The pressure plotted is the maximum in the blast wave, regardless of the time at which it occurs, and is read from ground level gages only.

At the 3.1s location, the pressure level is about 50 psi and decays very rapidly with distance. The shape of the free stream pressure wave consists in a rise to an initial peak pressure of about 15 psi, this is followed by a decay to about half this pressure at a time of 70 msec after which there is a rise to a peak of 50 psi in about 30 msec. Figure A.6 shows the estimated time variation of side-on pressure that was incident on Structure 3.1s at ground level. This estimate of pressure was obtained by interpolation from ground level gage records at the nearest blast line pressure stations.

At the 2100-ft ground range (Structure 3.1t), the peak pressure in the blast wave is almost constant with distance. The pressure-time curve also changes slowly as a function of distance from Ground Zero (Fig. A.5). The general shape of the side-on pressure incident on Structure 3.1t is shown in Fig. A.7. In this figure, there is a fairly sharp rise in pressure to about 6 psi which occurs near 40 msec, followed by a gradual rise to a peak of about 8 psi at 120 msec and a gradual decay to zero pressure at about 500 msec.

#### A.3.2.2 Structure 3.1u Pressure Records

The general shape of the time variation of side-on pressure, as shown in Fig. A.7, is an average not only of the side-on pressure records from the blast line but also of the diffraction gages from the NOL 3.1u study. The NOL gages were placed in fairly close proximity to Structure 3.1t, and it is therefore reasonable to question their value in a determination of side-on pressures since it is not known how much of their record characteristics were caused by diffraction effects from the structure and how much were the result of variations within the main blast wave. A good indication of these diffraction effects can be obtained from the 3.1u records on Shot 9. In these records, it appeared that, except for possibly positions 1, 2, and 5 (Fig. A.3), the diffraction effects on the gages are quite negligible.

This same general conclusion was borne out by shock tube tests performed at ARF in conjunction with a study on the *Effects of Orientation on the Blast Loading of Structures*, performed under Air Force Contract AF33(616)-166. In these shock tube tests, it was found that a pressure gage placed in the wall of the tube in a position relative to the model comparable to that of the 5-ft gage at position 5 of the Program 3.1u would show a fairly small pressure spike of fairly short duration and no other evident diffraction effects. Thus, it is felt that for a shock wave the majority of the diffraction effects of the 3.1u gages would be small.

For a compression wave, as occurred at Structure 3.1t on Shot 10, it is felt, however, that these diffraction effects would be still less since there is no initial shock to be reflected and any wave reflections would have to occur over a long time period. An inspection of the 3.1u records would certainly show no consistent phenomena occurring which could be attributed to diffraction effects from the structure, with the probable exception of the ground level gages at positions 1 and 2.

The side-on pressure incident on Structure 3.1t (Fig. A.7) is essentially the shape of the pressure as given by the ground level gage in position 5. The pressure read by this gage, however, was about 1 psi lower than the pressures on nearby gages. This pressure difference is within the tolerances of the measuring system and, hence, is not believed to be real. Therefore, the pressure levels on this gage were raised to agree with the pressure level observed on the next nearest gage, that at position 6, to obtain the curve in Fig. A.7. (If a possible Bernoulli effect was causing the lower pressures, so that the 1 psi pressure difference was real, this pressure would still have to be corrected in the same way to give free stream conditions.)

There is some correspondence between the oscillations present for the ground level gage at position 5 and those at positions 6 and 7. It might be expected that the difference in the correlation between these gages is representative of the difference between the pressure shown in Fig. A.7 and the actual pressure incident upon the structure. This would mean that there is a reasonable chance that many of the oscillations present in this record are also incident upon the structure.

#### A.3.3 Pressure Records on Structure 3.1t

##### A.3.3.1 General Appearance of the Pressure Records

The individual records on Structure 3.1t are given in Chap. 4 and summarized in Figs. A.30 to A.33. A cursory inspection of these records will reveal apparently much random oscillation. Furthermore, it appears that the magnitude of the oscillations on the front face of the structure, gage numbers p8 to p15 inclusive, is larger than on any of the other faces. The magnitude of the oscillations on the top and side wall gages is next in order, and the magnitude of the oscillations in the rear gages is the least.

##### A.3.3.2 Appearance of Average Pressures

The pressures on the several faces have been averaged and are given in Figs. A.8 to A.11. In these figures, it may be seen that considerable oscillation is retained in these averages. If the oscillations in the individual gage records were of a purely random nature, one would expect that the magnitude of oscillations in the average would be considerably reduced. (The



ratio of the remaining to the original oscillations would be in the order of the reciprocal of the square root of the number of gages averaged, or 0.4 for the front, top and rear, and 0.6 for the side.) Since this is not the case, one concludes that the oscillations in these records are not purely random but represent systematic fluctuations common to the records from several gages placed on the same face. The oscillations must be due to some real phenomenon and cannot be simply "hash" in the electronic recording.

It is hard to see how acceleration could account for this type of signal. An inspection of the original playbacks of the 3.1t records does not indicate any signals (as are seen on the 3.1s records) which have the appearance of acceleration signals. Low-frequency signals from either the wall or structure moving as a whole would not produce the type of signals present. Moreover, there is a slow rise time of the pressure wave which tends to eliminate ringing. On Structures 3.1s and t, which were struck by clean shocks of 18 and 13 psi, on Shot 9, one would expect comparable acceleration effects. Acceleration effects were small on these records. Thus, one concludes that these signals can only be caused by actual pressure upon the side of the structure.

#### A.3.3.3 Pressures on Individual Faces

(a) Front Face Records. As can be seen upon inspection of Fig. A.8, the average pressure on the front face of Structure 3.1t began rising fairly smoothly until it reached a peak of about 15 psi around 60 msec after the blast first struck this face. After this time, there were three large oscillations in the records. The first oscillation occurred around 80 msec, the second around 120 msec, and the third round 22 msec after the blast wave struck the building. Each of these large oscillations was in the order of 4 psi in pressure and 60 msec in duration. After these three large oscillations occurred, the average pressure apparently became smoother during the decay to zero.

The individual gage records on the front face (gages p8 to p14) show that these general features are well reproduced in each of the individual locations. The similarity in general appearance is even more strongly confirmed by observing the original playbacks where there is a very definite contrast between the smoothness of the initial rise during the first 60 msec and during the decay of the wave after 250 msec in comparison with the general hashiness in the intermediate period. In fact, there are actually more common features in the records which can be identified than were shown in the average pressures given in Fig. A.8. For example, in pressure record p8 there is a definite break in the slope 11 msec after shock arrival which is also identifiable on all the records for this face. By an inspection of copies of the original NOL slow-speed playbacks, an approximate absolute time of arrival of the blast wave on a pressure gage after the time of bomb detonation was established. From this time basis, it is seen that this break in slope comes at the same absolute time on all the pressure records for the front face to within the accuracy of measuring times of arrival from the NOL slow playbacks. It may also be noticed that the initial portion of the wave arrives at different absolute times on the front face. This would indicate that the blast wave front is not vertical but slants backwards. Certain features of the oscillations on these records are apparently identifiable on each individual gage record but do not appear in the average because they occur at slightly different times in the records and are therefore washed out in the averaging process. An example of such a reproducible oscillation might be that occurring between 110 to 130 msec on gage p10; this also can be seen on several other records, such as p8, p11, and p13.

(b) Roof Records. The average pressures on the roof of Structure 3.1t are shown in Fig. A.10. As is the case with the front face, the oscillations appearing on the various individual gage records are well reproduced in the average. It appears that traces of a vortex shed off the front of the roof can be seen in records p6 and p7. A surprising thing is that the strength of the vortex at the corner of the roof is considerably greater than at the center.

(c) Side Face Records. The correlation of the pressure records on the side face is good. The records of gages p16 and p18 are in especially good agreement during the initial periods, whereas, there is a depression in p17 apparently caused by a vortex. Around 50 msec, a



depression also occurs on both p16 and p18 which may be the result of vortex or may be a random oscillation. Until this time, these two records reproduce well the value for side-on pressure, which is given in Fig. A.7. The relatively early occurrence of the vortex on gage p17 may be due to an upward component of flow which would not allow a vortex to be swept over gages p16 and p18. The record p17 appears to be somewhat intermediate in appearance between p6 and p7 which would not be too unexpected since the distance of p17 to an edge of the structure parallel to the flow is intermediate between that of p6 and p7.

(d) Rear Face Records. Very little oscillation is apparent on the average of the rear face records shown in Fig. A.9. This is the case for the several individual gage records as well. The pressure rises fairly rapidly to a value of about 5 to 6 psi and then remains nearly constant until about 200 msec. There is an apparent vortex on p23 and some indications of one on p19. The rise time on record p24 is much faster than that of any other pressure record. This is due either to the blast wave tending to "shock up" as it travels in a clear region down the rear or due to a superposition of waves from over the top and around the sides that builds up the pressure more rapidly in a position similar to a reflection process.

#### A.3.3.4 Scale of Oscillation on Records

There are at least three large-scale "bumps" evident and identifiable upon all the front-face records and upon most of the records on the other faces. Each of these bumps is of the order of 60 msec in duration and about 4 psi in magnitude on the front face. There are also correlations between bumps of smaller magnitudes which are identifiable on these records. For example, on the front face gages it is possible to correlate the bumps on gage p10 with those on several other gages. By suitable examination, one is able to arrive at some correlation between the area under an individual bump and its probable extent in space: the probability of observing correlated bumps on adjacent gages is higher as the area under each individual bump increases. Moreover, for fairly small bump sizes (for instance, for bumps with impulses of the order of 60 psi/msec) it is also seen that there is a higher probability of correlation for gages at separations of about 6 ft. This tendency for a difference in correlation as the distance between gages is increased seems to decrease with bump size until sizes of about 130 psi/msec are reached, when the probability of correlation for all appears about the same.

These oscillations have all the appearance of turbulent cells of some type, which exist in the air and are blown over the structure. As the size of the turbulent cell increases, there is greater probability that several gages will feel its effect. The duration is of the order of 60 msec and represents the length of time that a turbulent cell might be acting on a gage. Since these cells should be propagating with air velocity, about 300 ft/sec, the length of these cells in the direction of flow might be in the order of 18 ft. This typical dimension is not inconsistent with the size of cell which might be expected to engulf all the gages on one face of the structure with fairly high probability.

#### A.3.3.5 Agreement of Oscillations on Averages from Several Faces

The average pressures for the several faces are plotted together in Fig. A.12, together with the side-on pressure of Fig. A.7. On these plots, one notes a tendency for downward dips in the averages on back, side, and roof gages at the same time that there are upward swings in the averages for the front wall gages. These dips in the averages, moreover, tend to be fairly independent of oscillations in the side-on pressure. The differences between the average pressure on a certain face and the side-on pressure are given in Fig. A.13. In this figure there is fairly good agreement in the tendency toward oscillations in one direction or another on the several faces. It also appears evident that, on those faces where the difference in pressure from side-on pressure is the least, the magnitude of oscillation is also small. The records can be brought into reasonable qualitative agreement both in magnitudes of pressure difference and of oscillation by multiplying the differences on the rear roof and side faces by a constant factor to bring on agreement with the front faces. These factors are 2 for the side face, 2 for the roof, and  $3\frac{1}{2}$  for the rear face.

#### A.3.4 Pressure Records on Structure 3.1s

##### A.3.4.1 General Appearance of the Pressure Records

The records on Structure 3.1s are given in Chap. 4. In general, the features observed on Structure 3.1t are magnified on Structure 3.1s but this magnification occasionally results in unrecognizability. There are many oscillations in the records which are probably not real phenomena. The NOL Final Report for Program 3.28.2 states that the gages used have two natural frequencies of from 700 to 1200 cycles/sec and 300 to 500 cycles/sec for the twisted Bourdon tube, oscillating in torsion or as a cantilever beam. These frequencies, especially the higher one, can be readily identified from an inspection of the original playbacks. However, the nature of the other oscillations is more subtle. As in Structure 3.1t, there is a tendency for the largest oscillations to occur on the front face, with smaller magnitude oscillations occurring on the side and roof faces and practically no oscillations on the rear face gages. The appearance of the rear face gages tends to rule out accelerations of the structure as a rigid body as the cause of the oscillations. On each of the faces there appear to be similarities in the oscillations present, although certain oscillations may be absent on several gages. If the face as a whole were accelerated, the accelerations should be present on all the gages, and, depending upon the mode of the acceleration, it should be possible to observe effects upon the edges of the block different from those near the center. Although this tends to rule out also nonrigid body accelerations, the possibility of very serious acceleration effects still remains in the records.

Another effect must be considered in an evaluation of the gage reliability. After about 120 msec, the gages on the front wall of the structure generally go to large negative values of gage pressure, far greater than 13 psi and below zero pressure absolute. It appears from the original playbacks that the base line is drifting greatly because these values are reached even though the trace is quite smooth. The pressures on the other faces also reach large negative values at times of about 70 msec after the blast arrives. The values of these pressures are also very low, often reaching almost a vacuum. However, once this valley of negative pressures is past, positive phase durations can be identified, and the values of negative pressure obtained thereafter are approximately the same as those obtained along the blast line.

The high thermal radiation might cause the readings observed upon the front face. In this shot, the gages were initially shielded from the thermal radiation by an aluminum foil. After the foil was either blown away or melted, it was possible that the gages might have been heated by the thermal radiation. However, the base line shift would probably have been in the opposite direction from Shot 9, where this effect was also noticed on these gages, and it is also doubtful that much thermal radiation could penetrate the dust cloud generated by the blast wave front.

About the only mechanisms which are left open to explain the negative pressures on the front wall gages are either some unknown gage effect (such as could be generated by dust impinging on the gages) or an effect due to the motion of the gage leads in the structure. In either case, it would be difficult to assess the importance of this effect upon the value of the earlier portions of the front wall records or upon all of the other records. (There are also base line shifts in the front face 3.1t records, but these are of sufficiently small magnitude as to not affect seriously the conclusions obtained from the record.)

Due to possible acceleration effects and base line shifts, the 3.1s records must be interpreted with caution. It is possible that more detailed analysis of the records may give better indications of their validity, but at present it can only be said that there are errors in the records and it is not known whether or not these errors are large enough to render the records useless. Nevertheless, values of the averages of the gages on the several faces are given, along with a short discussion of the appearance of the averages.

##### A.3.4.2 Appearance of Average Pressure

The average pressures on the front, roof, rear, and side surfaces are given in Figs. A.14 to A.17. The pressures on the front face seem fairly well in agreement with the general features observed in the average pressures on Structure 3.1t. Considering the amount of filtering of the



oscillations which should have occurred, it is surprising to have such well-defined large oscillations remaining in the average pressures. It is felt that there is good probability that the peaks occurring at 35, 65, and 85 msec are real occurrences.

On the rear face, the pressure goes below ambient at a time about 65 msec after the blast wave first strikes the building and remains there until about 90 msec. By referring to the estimated ground level pressure-time curve shown in Fig. A.6, it can be seen that a minimum of about 6 psi occurs in the pressure at about this time. In fact, until about 90 msec it seems that the average pressure on the rear face is about 10 psi lower than is the side-on pressure. This general tendency to be lower than blast wave pressure is also repeated on the roof and the side gages.

### A.3.5 Possible Explanation of Phenomena

#### A.3.5.1 High Values of Net Pressure

On both Structures 3.1s and t the net pressure is much higher than could be explained by conventional loading theory. The pressure varies in the blast wave sufficiently slowly so that there cannot be much variation in phenomena from steady-state values. Thus, the majority of the difference in net pressure between the front and rear faces must be explained by abnormally high values of the product of the drag coefficient times the dynamic pressure  $C_d \times \frac{1}{2}\rho u^2$ .

It is hard to see how the drag coefficient could vary extensively from conventional values. If one assumes a value of drag coefficient equal to 2, the net pressure obtained on the structure is low by a factor of about 4, when this pressure is computed by means of the dynamic pressure which would conventionally be associated with the blast wave at the measured pressure level. Any values of drag coefficient much higher than 2 would be unrealistic for a cubicle of the shape used, since these values already represent the highest values possible on the basis of well-established loading theory in a clean shock wave.

Thus, it is necessary to assume that the value of dynamic pressure itself is abnormally high. This anomalously high value can, of course, be attributed either to the density or to the particle velocity. There were no direct successful measurements of either the density or the particle velocity in the precursor of Shot 10. Thus, on an *a priori* basis one cannot say which of the two variables account for the major portion of the effect, although it shall be shown that high values of density are in all likelihood the cause of the greater portion of the effects observed.

#### A.3.5.2 Explanation of High Values of Drag Pressure in Terms of Precursor Phenomena

The most direct indication that large variations in density of the air are causing most of the effect come from measurements of the density by a beta densitometer (see WT 610, P. Florcruz, LASL, Program 6) in Operation IVY which gave air densities 8 times the normal values. These densities could only be caused by the presence of large quantities of dust. The presence of large oscillations in the dynamic pressure without associated variations in static pressure are another indication. If these large oscillations in dynamic pressure were caused by the variations in particle velocity only, it would be necessary to have large variations in static pressure to cause them. For example, a certain variation in particle velocity, which would cause twice the variation in dynamic pressure, would also require a comparable variation in static pressure. Static pressure oscillations of this order of magnitude do not appear to be present where many large variations in dynamic pressure are observed.

Another indication that variations in density cause the variations in dynamic pressure can be obtained from an inspection of the dynamic pressure records obtained on Project 1.1d by the Sandia Corp. These records begin to rise at a fairly slow rate but suddenly have a well-defined break in slope and go to values which considerably exceed not only the expected dynamic pressures but even the range of the gages. In Fig. A.18, the time necessary after the blast wave starts for these heavy loads in dynamic pressure to reach the gage is plotted as the function of the height of the gage above the ground at two ground ranges. From all indications, this time is a linear function of the height beginning at the origin. This phenomenon could be



explained by assuming that the blast wave front is picking up dust from the ground and convecting it upwards at a constant velocity. An explanation in terms of high particle velocities would necessitate, at the least, new descriptions of the flow field in a precursor.

In Figs. A.19 to A.23, the blast line pressures as measured by SRI are given. These pressures were determined by tracings of the original playbacks made available by SRI at NPG during the test operation. The height of the gage above the ground is plotted as the ordinate and absolute times after bomb detonation on the abscissa with contours of constant pressure plotted as a parameter. These contours give the time at which a certain pressure arrives at some specific height above the ground. If the entire blast wave is traveling outward from Ground Zero with no strong variations in the flow pattern, these pictures present a spacewise function of the blast wave, but it is felt that the main features of them are probably correct. In order to clarify some points on these figures, and since they are of interest in themselves, some comments will be included for each figure. For purposes of clarity, it is probably best to describe first the farthest gage stations and then proceed toward Ground Zero.

The pressures at 2916 ft from Ground Zero are shown in Fig. A.23. At this distance the wave form has become clean with little or no hash in the records; the initial blast front is a clean shock, which gives the peak pressure in the blast wave. The decay of the wave following the shock front is quite regular. The contours, as plotted, have a considerable bowing forward at the 10-ft level which might be real or might represent simply a small error in the calibration of the gage. If the phenomenon is real, the boundary layer effects along the ground could well account for the reductions in pressure. It would be necessary to look at gage stations farther out along the blast line to determine the reality of this bowing out. The dotted lines in Fig. A.23 simply indicate a possible configuration of the contours if the gage calibrations are varied.

The pressures at 2416 ft from Ground Zero exhibit more interesting features. This station is about at the limit of the precursor. The initial wave front rises to a pressure of about 4 psi and maintains this value for around 60 msec before rising to the peak in the blast wave. The initial plateau is evidently the remains of the precursor region of the blast, and the second wave front is the arrival of the main blast itself. For both wave fronts, the rise along the ground is not a sharp shock but a compression wave. The first front is probably toed forward as the result of the presence of a thermal layer which appears to extend for not more than 10 ft and represents, in a small region, characteristics typical of weak precursor action, as such. The second shock front does not reach the ground surface. There is none of the toeing-out of the pressure contours typical of precursor action caused by a thermal layer. It is hard to visualize any other mechanism besides the presence of a strong dust layer which could serve to produce such an effect. If the wave front were approaching the ground at a smaller angle, then one would expect that the presence of a heavy dust layer would serve somewhat as a reflecting layer, and since the dust-laden air is more dense than the air alone, one would expect that at least the pressures behind the main air shock would reach the ground. But since the wave front is more nearly vertical, the primary effect is probably not one of turning the flow velocity as it is for steeper incidence but is one of simply imparting a greater magnitude to the velocity in a direction parallel to the ground. If this is the case, the dust would act as an absorbing medium because of its greater inertia. The apparent absence of any reflected wave front also tends to support this statement. Since Shot 10 was at a burst height of 500 ft, a Mach stem is formed at this distance of 2416 ft, and the wave front at 1040 msec is undoubtedly a Mach stem. The fact that this Mach stem is bent back is a further indication that dust must be influencing the hydrodynamics. Another interesting effect to observe is the toeing forward of the contours at 1070 and 1120 msec. This toeing forward during a time of pressure decay could possibly be explained again by the dust strongly absorbing energy from the flow within a layer 10 ft above the ground.

The next station at which contours are plotted is at 1916 ft and is well within the precursor. In Fig. A.21, the times of arrival of heavy dynamic pressures indicated by the Sandia q-gages is shown by the dashed line which is labeled "dust front." A problem occurred in drawing the pressure contours from the values of pressure indicated by the gages. The configuration given

is one possible arrangement of these contours, but the topology of the problem is such that other configurations would be possible. It is felt, however, that the configuration in the initial portion of the wave and the bending forward of the contours around the 9 to 11 psi pressure region observed just behind the dust front are realistic.

There is a definite toeing out of the shock which is observed on the 50-ft gages. This could be caused by a thermal layer which existed in the air before the arrival of the blast front. It would be helpful to look at the shock photography in order to more definitely discuss this blast front. If the effects observed are caused by the presence of a thermal layer, then the initial blast front could be inclined as a result of a strong feeding of energy along the ground. This feature will be discussed more fully later. Probably the most noteworthy portion of Fig. A.24 is the tendency for the contours of constant pressure to be parallel to the dust front. This indicates first that the high values of drag pressure measured by the Sandia q gages (and thus, in all probability, high values of dust loading of the air) are connected with the pressures observed in the blast wave. This indicates, in turn, that a consideration of precursor phenomena cannot be made without intimately connecting it with these dynamic pressure considerations. A second conclusion that could be drawn from these contours just behind the dust front is that it appears likely that there is a flow of energy near the dust front. The presence of these pressures on the order of 11 psi which are observed just behind the dust front are quite difficult to explain since the only other possible source of pressures of this order of magnitude would be from above at from between 700 and 730 msec. These high pressures could not be readily fed from farther behind in the wave, since the wave is attenuating here.

The pressure contours at 1417-ft ground range are given in Fig. A.20 where, as before, the beginning of high dust loadings are indicated by the dashed line labeled "dust front." The heavy dashed line labeled "record failure" indicates time at which the records from all the above-ground gages begin showing large erratic signals. It seems quite likely that this time is the beginning of the failure of the gage tower. All the gages read quite regularly up to this time, with the exception of the gage at the 10-ft height which has some fairly large variations which may or may not be real. One interesting feature of this figure (which will be more accentuated at 924 ft) is the appearance of the initial wave front. The contours giving the rise in pressure across this wave front are more spread out at higher elevations than they are at the 10-ft elevation. This effect is precisely the opposite from that which is observed due to the presence of a thermal layer preceding the blast wave. It seems as if there is a more sharply delineated driving mechanism for the wave near the ground than for that higher in the air. As at the 1916-ft station, there is a strong tendency for the contours near the dust front to be parallel to it.

The dust front at the 1417-ft station is steeper than at the 1916-ft station. This could be explained by assuming that the dust is convected up from the ground in a direction perpendicular to the blast wave front. An inspection of the pressures at 1417 and 1916 ft enables one to make the further assumption that the sound speed is constant with height above ground since the wave front is straight (the toeing-out of the front in the first 10 ft which indicates a higher sound velocity in this region can be neglected here). This conclusion of constant sound speed implies that the angle of the wave front with the ground is roughly constant with distance from Ground Zero, which appears to be approximately correct for these ranges. The velocities of propagation of the blast wave parallel to the ground,  $V$ , can be computed from the time of arrival measurements and are found to be about 2500 ft/sec at the 1417-ft station and 1600 ft/sec at the 1916-ft station. Under these assumptions the configuration in Fig. A.24 is obtained. In a time  $\Delta t$  the wave front will have progressed  $2500\Delta t$  along the ground from point A. Meanwhile the compression wave front, traveling at sonic velocity, will have traveled  $c_0\Delta t$  in a direction perpendicular to the wave front. Since the time interval,  $t_1$ , for the wave to arrive at a gage some height,  $H$ , above the ground after passing the same position on the ground can be measured (Fig. A.24), the angle of the wave front with the ground can be determined by the relation  $t_1 = H/\tan \theta$ . These angles are 37 deg for the 1417-ft station and 43 deg for the 1916-ft station. The sound speed can be found by  $c_0 = V \sin \theta$ . The sound speed is calculated as 1690 ft/sec at 1417 ft. and 1100 ft/sec at 1916 ft. (These values are probably as good as the NEL

AD-A073 468

DEFENSE ATOMIC SUPPORT AGENCY WASHINGTON DC  
OPERATION UPSHOT-KNOTHOLE, NEVADA PROVING GROUNDS, MARCH - JUNE--ETC(U)  
JUL 55 E V GALLAGHER, T H SCHIFFMAN

F/G 15/6

UNCLASSIFIED

DASA-WT-721

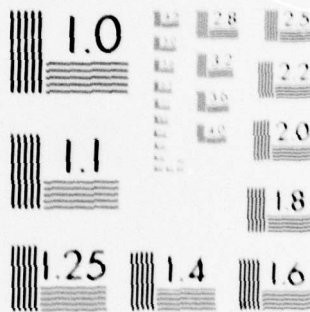
NL

4 OF 4

AD  
A073468







MICROCOPY RESOLUTION TEST CHART  
NATIONAL BUREAU OF STANDARDS-1963-A

sound speed measurements and are not inconsistent with them. The value at 1916 ft can only be taken to mean that the air heating at this distance is negligible.) Once  $c_0$  has been determined, the particle velocity,  $u$ , can be computed from the overpressure behind the wave front. Values of 11 psi at 1417 ft and 8 psi at 1916 ft were used. The angle of the dust front,  $\alpha$ , can be computed by  $u/V = \tan \alpha$ , giving values of  $\alpha = 17$  deg at 1417 ft and 14 deg at 1916 ft. The time interval,  $t_2$ , necessary for the dust front to arrive at a height,  $H$ , over the ground after the blast wave has passed this point can then be computed by  $t_2 = H/\tan \alpha$  and then be compared with the measured values from the Sandia q gages. The ratios of the measured to the computed values of  $t_2$  are 1.2 at the 1417-ft station and 1.5 at the 1916-ft station. The agreement seems reasonable when the possible corrections necessary to the assumptions and the possible errors in the measurements are considered.

It may be mentioned that the values of 2500 and 1600 ft/sec for the wave front velocity along the ground require explanation when the sound velocities, in general, are of the order of 1690 and 1100 ft/sec for the air above a 10-ft elevation. One possible explanation would be the presence of a thermal shock traveling outward at this velocity. Another possible explanation would be a thermal layer near the ground, hot enough to cause sonic velocities of this magnitude. If it is assumed that there is a strong, sharply defined thermal layer of not more than a 10-ft height above the ground before the blast, then this thermal layer will be convected upward by the flow velocity. The sharp break in the 7 psi contour at 660 msec at the 1916-ft station would mark the possible boundary of this thermal layer and is strongly suggestive of this type of action. There would then be a high-sonic-speed channel in which the blast wave could sweep forward as is suggested by the forward bending of the pressure contours. The bending back of the pressure contours near the ground could be due to the presence of a very heavy dust layer confined to a layer near the ground. The sudden rise on the Sandia q gages could conceivably be explained by a contact discontinuity, with the high pressures occurring when the gages were exposed to the high-velocity air on the underside of the discontinuity. However, the sharp bending back of the same 7 psi contour when the dust front is reached seems to indicate that the high drag pressures are due to heavy dust loading, with the role of the thermal channel confined to that of a mechanism of feeding the blast front. It is quite possible that the peak pressures might be beneath the dust front since the energy density transported by the blast wave is given by

$$E = \frac{1}{2} \rho u^2 + \frac{1}{\gamma - 1} P$$

and a greater amount of energy could be transported beneath the dust front in the region of higher density for a smaller peak pressure. This type of action is in accord with the principle of least pressures of F. B. Porzel, who states that, in a hydrodynamic situation where two flow patterns are possible, the pattern actually realized is that which gives the lowest pressure, (*Height of Burst for Atomic Bombs*). The flow pattern discussed at the 1417-ft station is of the same general nature as that for the 1916-ft station, although there is more of a tendency for the peak pressures to be above the dust front. A rotation of the dust front upward would bring the two pictures into better agreement and would not be ruled out by the accuracy of the experimental data.

The high flow velocities in the thermal channel feeding the wave front, if such is the case, would not be inconsistent with the assumption made above, that the particle velocity convecting the dust front upward is perpendicular to the blast front since the majority of the upward flow would have to occur before the thermal channel could be established. This would be the case since the thermal layer itself is apparently under 10 ft in height.

The presence of the thermal channel feeding energy to the blast front at a fairly low elevation could explain the presence of the steeper compression front near the ground than at higher elevations. It is possible on the 1417-ft station to see a tendency toward a radial expansion of pressure centered at about 370 to 380 msec at the 10-ft elevation.

The pressures obtained at 924 ft from Ground Zero are shown in Fig. A.19. The only records obtained were at the ground level and at the 50-ft elevation. There were two gages at the 10-ft elevation, but they were contradictory, therefore, neither of the two gage records was used here.

The most noteworthy feature about Fig. A.19 is the appearance of the two blast fronts. The first front is a compression wave at the 50-ft elevation and a shock front on the ground, reaching a value of 14 psi immediately. The main blast front is a compression wave on the ground, but at 50 ft it is a shock going from a value of 10 to a value of 55 psi. The action of the main blast wave is not contrary to expectations, but the action of the first precursor front is quite unusual. One mechanism to explain the presence of such a strong shock front on the ground may be the thermal channeling effect discussed above tending to feed energy rapidly forward near the ground. The feeding could not be from too low a level or the low pressures on the ground at 240 msec would not have been observed. Some mechanism connected with the dust action, such as an overshoot due to its inertia and a subsequent retardation of the other pressure waves, would have to be postulated. The presence of a thermal shock is a more likely explanation of the pressure picture. The lack of good gage records between 0 and 50 ft strongly affects the understanding of the phenomena occurring.

One gets the feeling upon observing the series of flow contours that the whole pattern of the precursor grows in height as the distance from Ground Zero increases. At the 924-ft station the main blast front is clearly visible, and the slow rise of the precursor pressure wave indicates that there has not been much tendency for the wave to "shock up," which would indicate that the whole phenomena is of fairly recent origin. At the 1417-ft station the bending forward of the 11 and 12 psi contours around 390 msec at the 50-ft gage elevation would tend to indicate a feeding of energy from a higher level. This process may have resulted in the actual formation of a shock at the 1916-ft station, which is undoubtedly the bottom portion of the precursor fronts seen in fireball pictures. The bending toward horizontal of the steep shock front at the 50-ft elevation and 1916 ft from Ground Zero indicates that now the main feeding of energy to the precursor is from a lower level. At the 2416-ft, station the pattern is nearly vertical. The main blast front is evident and the precursor front is running itself out as is expected in a clean pressure wave. A close inspection of the blast photography pictures for this shot should help considerably in an understanding of the phenomena occurring at higher altitudes and their relation to the ground level phenomena.

From the above discussion of the precursor phenomena it should be clear that high values of dust loading in the air are intimately tied in with a description of the flow patterns in the precursor. At the present time it appears that the most reasonable assumption that could be made is that the high values of dynamic pressure are due to high dust loading in the air and that this dust loading of the air is of a highly irregular nature, having the appearance of an average dust loading of the air as a function of time with large turbulent fluctuations (of the order of possible 50 per cent of the mean value at Structure 3.1t) superimposed on the mean.

From the fluctuations on all the faces of the Structure 3.1t, and not on just the front face of the structure, as well as the large values of  $C_d \frac{1}{2}\rho u^2$  on each face, it must be assumed that the function of the dust is to cause real variations in the dynamic pressure.

#### A.4 VALUES OF DRAG PRESSURES DETERMINED FROM TEST RESULTS

##### A.4.1 Magnitudes of Drag Loadings

Once the general nature of the phenomena occurring over Structure 3.1t has been determined, the problem remains of considering the values of pressures measured for the purposes of assigning numerical values to the loadings and incorporating them into a computational scheme.

The net pressure on Structure 3.1t (the difference in average pressure between the front and rear faces) is given in Fig. A.25. In Fig. A.26, the net impulse as a function of time



$$I(t) = \int_0^t p_{\text{net}}(\tau) d\tau$$

is presented. On the same figure, the net impulse, as a function of time, that would have been received by this structure had it been placed on an ideal surface is also plotted. The values of the hydrodynamic variables which would occur over an ideal surface at this ground range are given in Fig. A.27. These values for an ideal surface were obtained from *Theoretical Height of Burst Curves* by F. B. Porzel, issued by LASL in May and August of 1953. In Fig. A.28 the loads on Structure 3.1t from this ideal surface wave were drawn. These loadings were obtained by the methods described in Sec. A.3.4.2 of this report.

It is seen that the net impulse received by Structure 3.1t over this real surface was, if anything, a little higher than the loadings which would have occurred over an ideal surface. In the document just referred to, it was predicted that the loads obtained in a precursor would approximate the loadings on an ideal surface, and this general type of action has been confirmed by Structure 3.1t.

In Sec. A.3.4.2, the ratios of the differences between average pressure on a face and side-on pressure were presented. If the action causing these pressure differences is due to high values of drag pressure, then the distribution of drag coefficients between these several surfaces can be obtained. If one takes an over-all value of the drag coefficient equal to 2, then the drag coefficient for the front face is 1.5, for the top and side faces it is 0.75, and for the rear face it is -0.5. This distribution of drag coefficients is in accord with what would be expected for a clean blast wave. The product of drag coefficient times dynamic pressure observed on Structure 3.1t reached a value of about 8. The peak dynamic pressure over an ideal surface with an initial side-on pressure of 14 psi is equal to 4.5 psi. If this dynamic pressure is multiplied by the drag coefficient of 2, a net pressure of 9 psi is obtained. This is about the net pressure which was actually measured on the structure, and in view of the inaccuracies of the measurement and the necessity of extrapolating to other regions of the precursor, the peak dynamic pressure may be taken as the peak dynamic pressure over an ideal surface. However, this peak pressure is not reached at the beginning of the blast wave but at some later time. This time may be best estimated as being about 100 msec after the blast front arrives.

#### A.4.2 Schematic Loading Method

On the basis of the foregoing discussion, a schematic loading scheme which yields the entire net loads for block-like structures in a precursor region may be constructed. For the conditions of Shot 10, this scheme would consist in a linear rise from zero pressure to a peak of the product of the drag coefficient for the structure times the ideal surface dynamic pressure at this ground range. (There are no diffraction loads on the structures.) This peak is followed by a linear decay to zero pressure at the end of the positive duration of the wave. To extrapolate this loading picture to other bomb yields, one method would be to multiply the time of the peak pressure by the cube root of the ratio of this bomb yield to 15 kt to give the new time of maximum pressure, with decay to zero pressure occurring at the time of the positive phase for the new yield. This schematic loading scheme is shown in Fig. A.29 and is reproduced in Fig. A.25 for the conditions on Structure 3.1t.

The loads given in Fig. A.29 represent a smooth variation in net pressure. To this loading scheme, in order to represent the actual loading conditions, a random oscillation must be superimposed. This oscillation should range in magnitude up to 50 per cent of the peak as given in Fig. A.29. It is felt that the response of the structure may be considerably altered by these random oscillations, even if the net impulse remain constant, since such factors as wall breakage may be strongly affected by their presence. Thus, a true response picture of the structure would give some average computed deflection (assuming the building resistances are completely known) with some distribution of deflection about this average. Although this loading scheme probably represents the best possible current picture for blocklike structures there are many uncertainties in it, and a great deal of further investigation should be performed to resolve these uncertainties. For realistic target structures which are partially open, it is felt that the loading scheme presented here gives an overestimate of the loads since the wave

entering the interior may well have a much smaller concentration of dust. In this case, the average net pressure experienced by the building could be closer to the drag pressures computed by means of the Rankine-Hugoniot relations from the pressures actually occurring in the blast wave. The blast conditions over other types of surfaces may also result in much smaller over-all loads.

The loading scheme presented in Fig. A.29 has been obtained on the basis of the conditions near the limits of the precursor for Shot 10 and is strictly valid only for the shot conditions. It is possible that the peak pressures acting on a structure for a bomb of very high yield might be considerably larger. Thus, for large-yield bombs, the loading method presented may yield an underestimate of the actual loads which a structure may undergo.

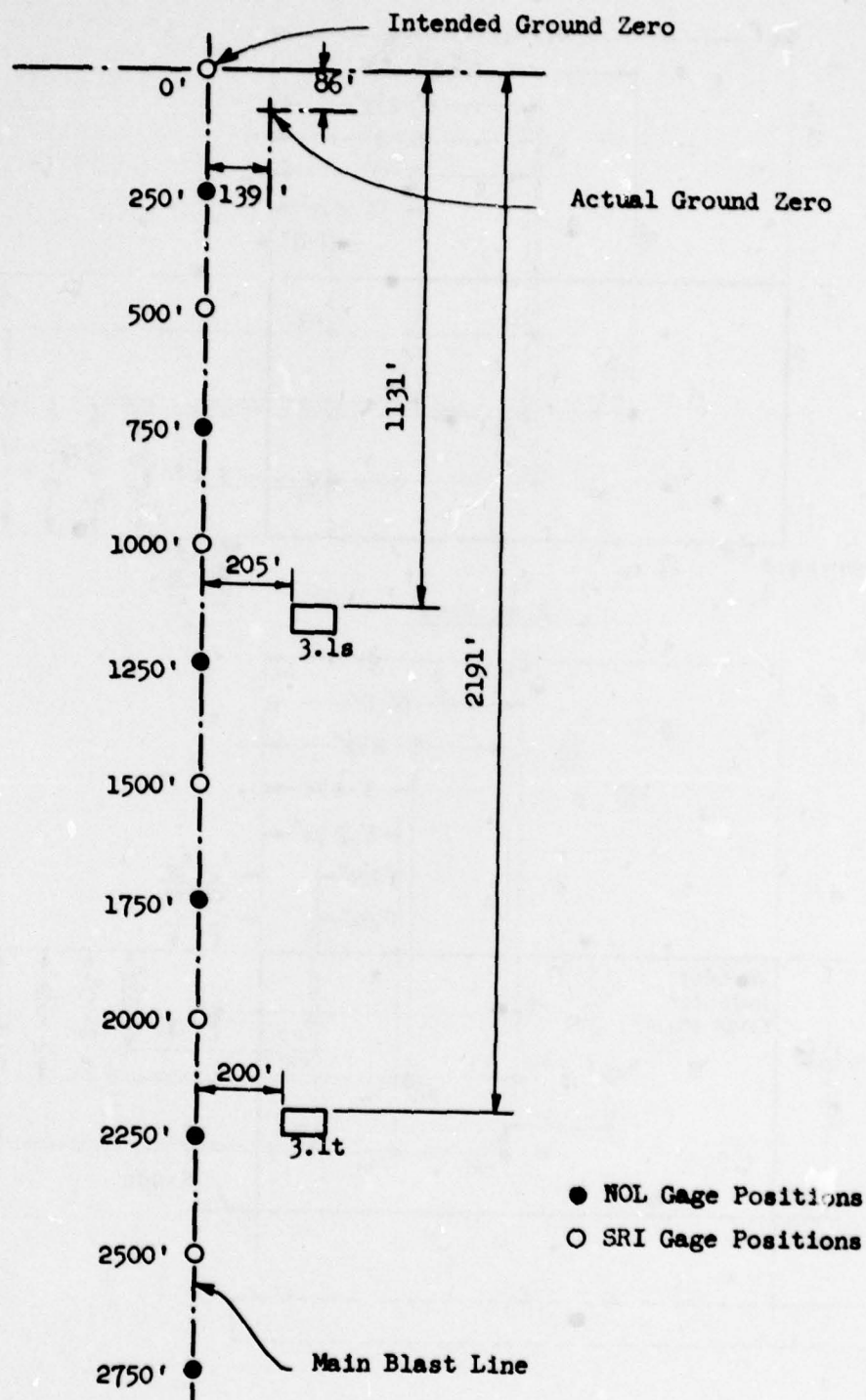


Fig. A.1 — Location of Structures 3.1s and t and blast line gages.



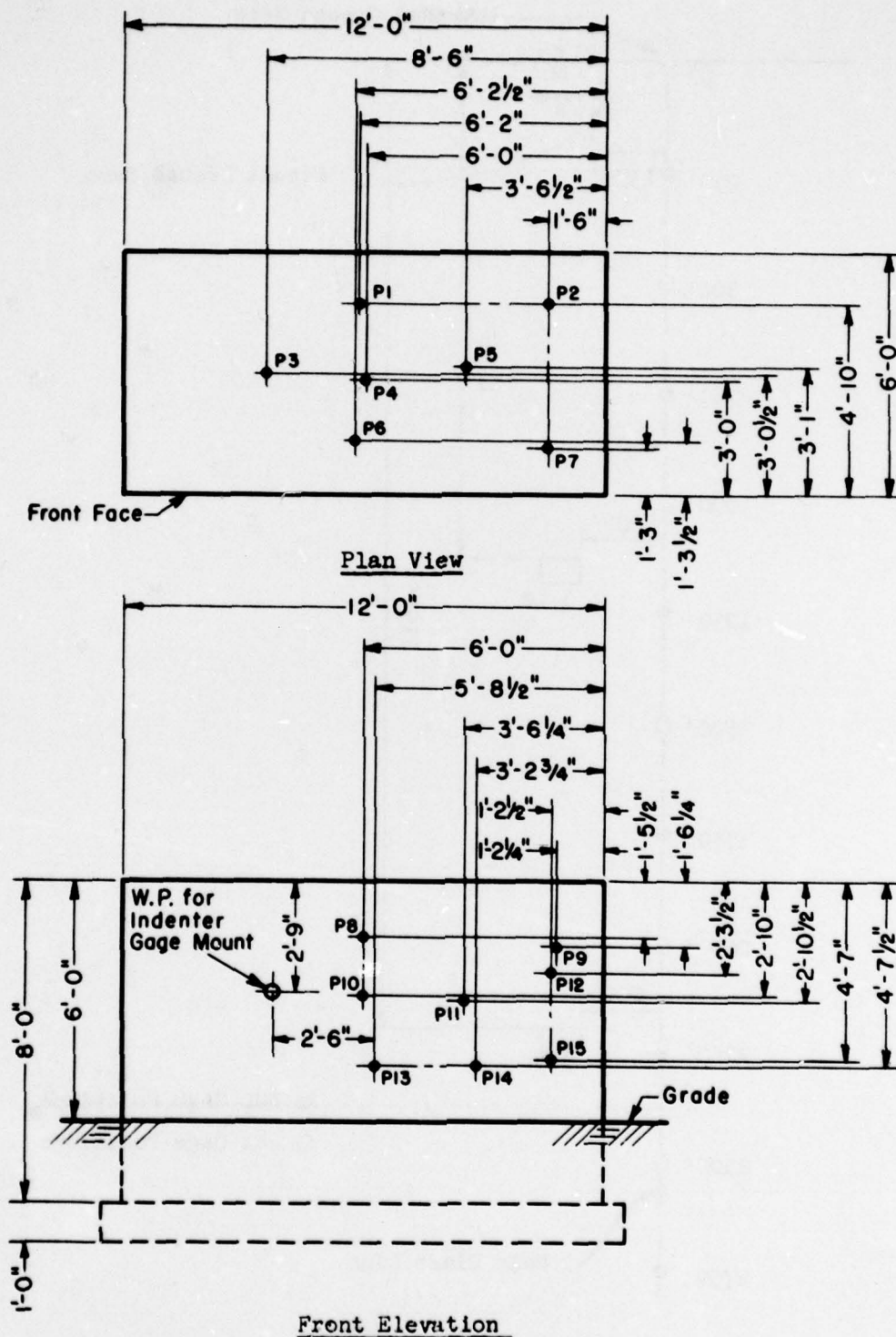
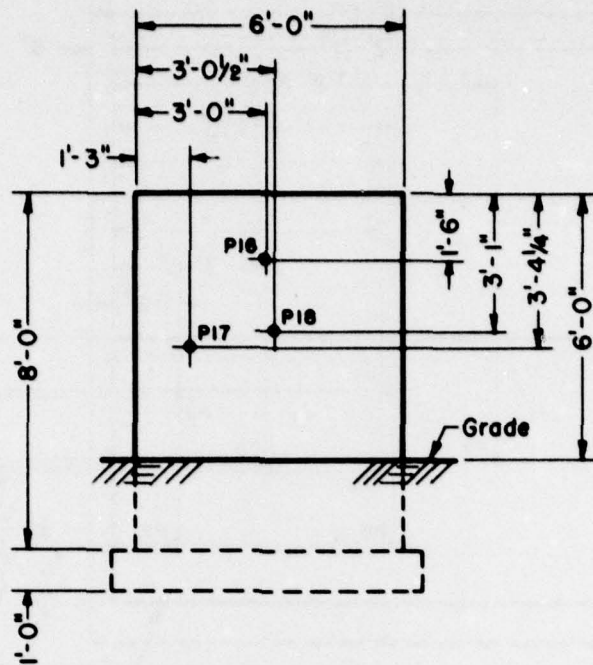
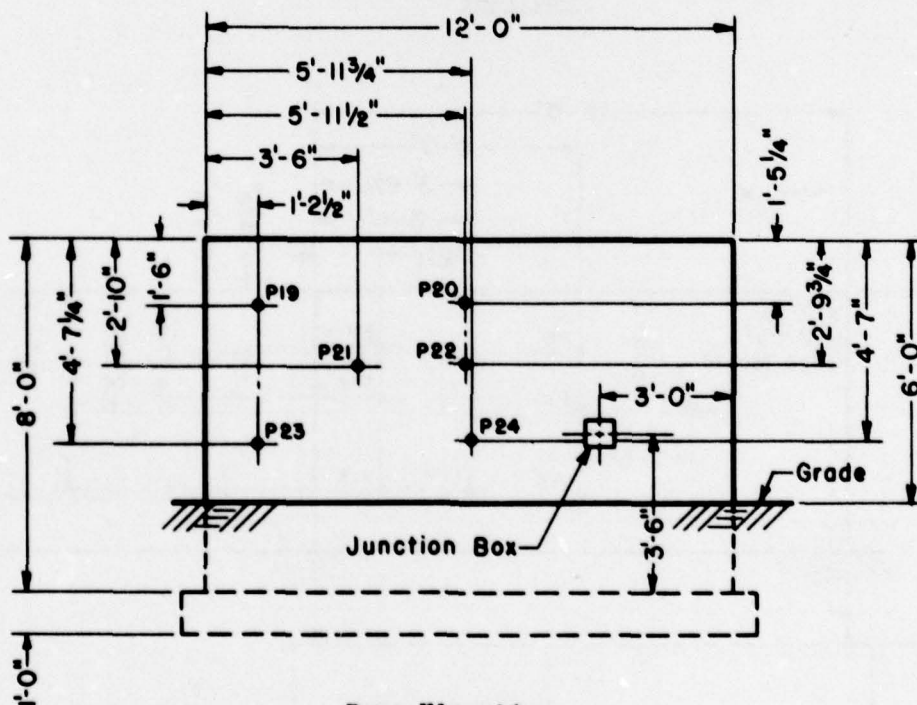


Fig. A.2a — Structure 3.1t, plan view and rear elevations.



Right Elevation



Rear Elevation

Fig. A.2b—Structure 3.1t, right and rear elevations.

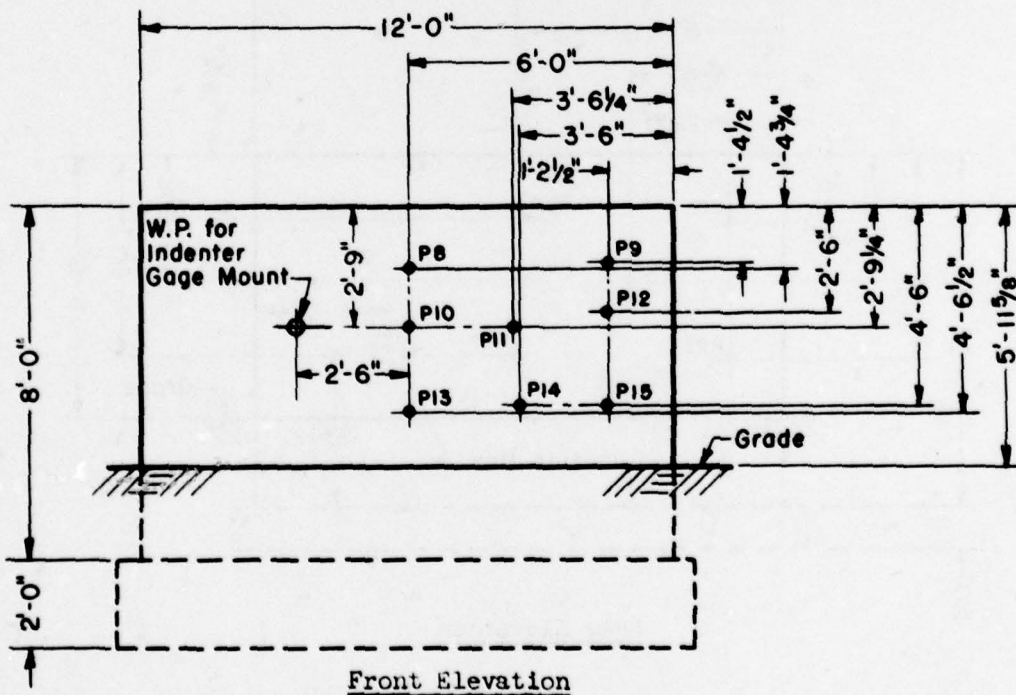
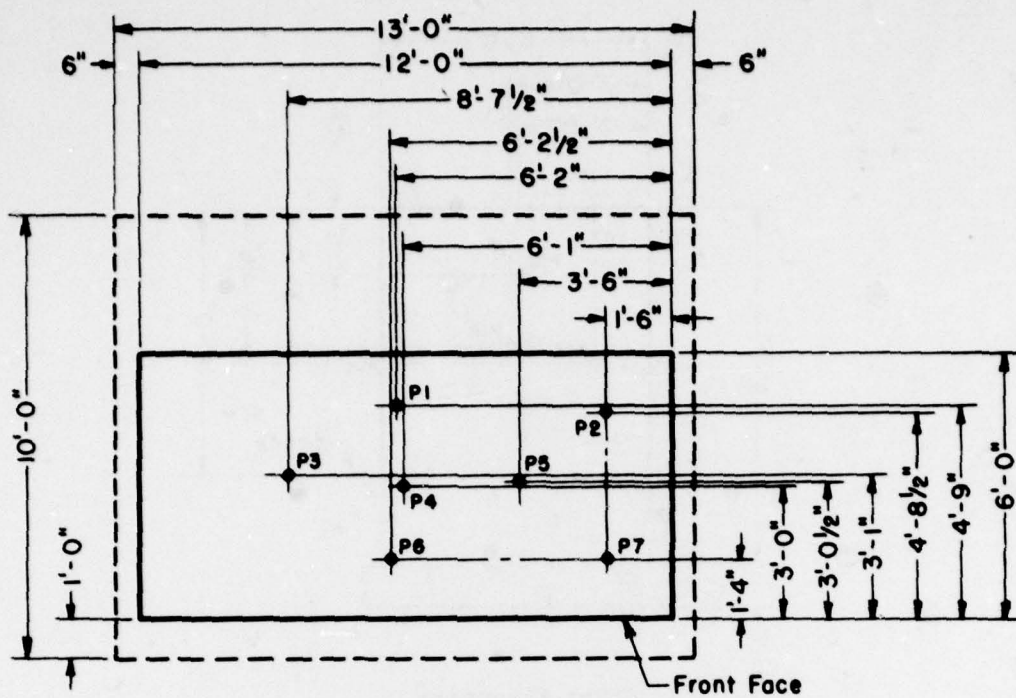


Fig. A.2c—Structure 3.1s, plan view and front elevations.



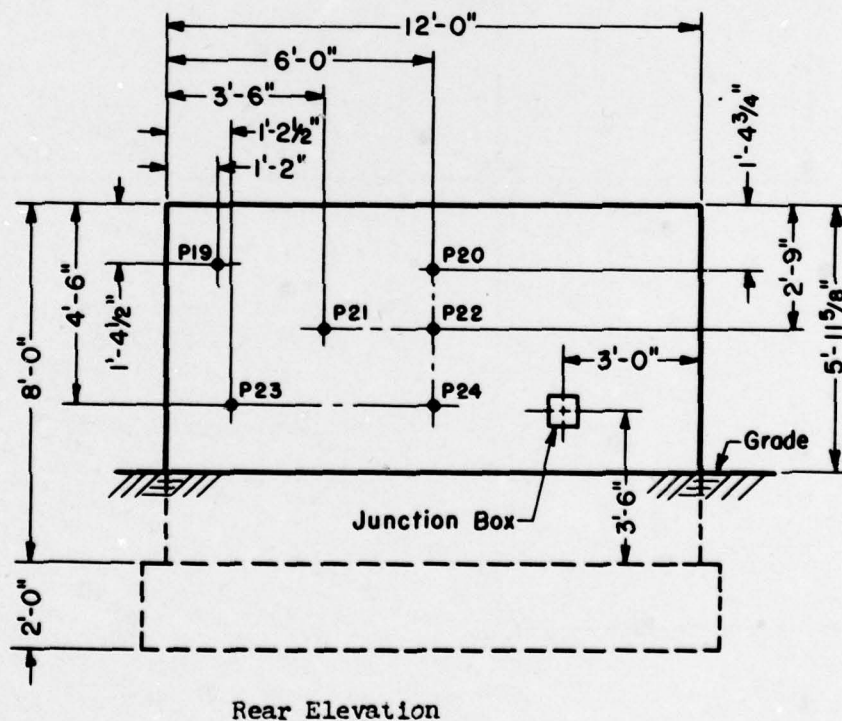
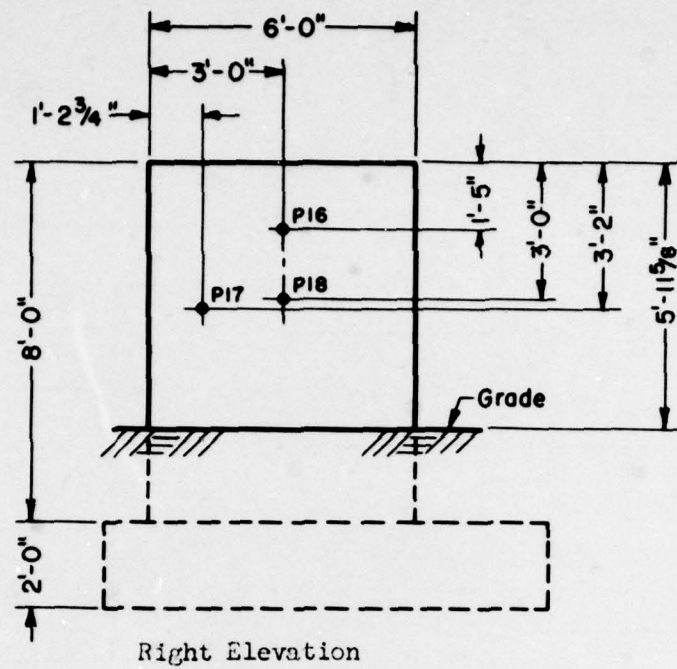


Fig. A.2d—Structure 3.1s, right and rear elevations.

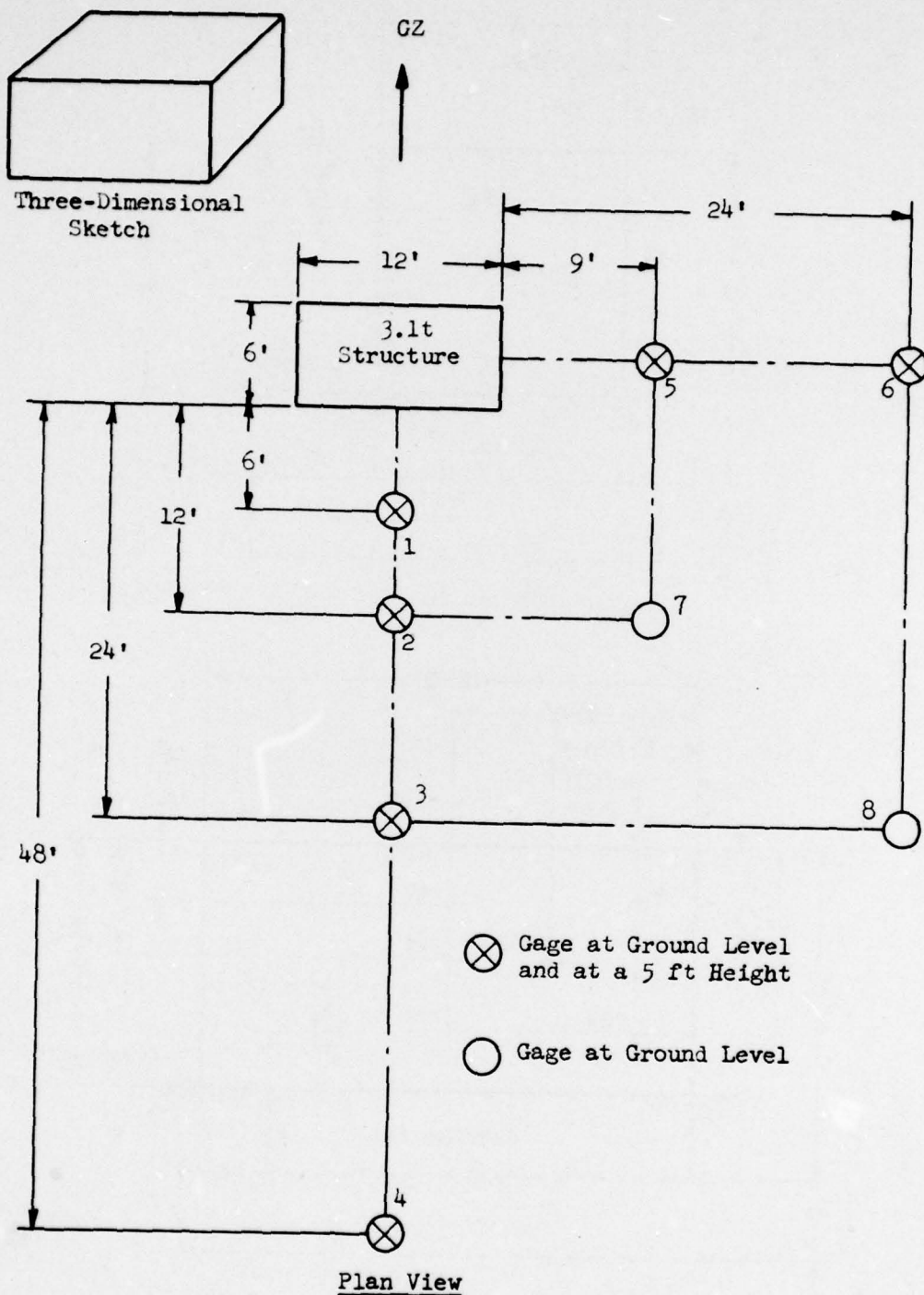


Fig. A.3—Location of pressure gages for Program 3.1u.



Fig. A.4—Postshot photograph of Structure 3.1s.



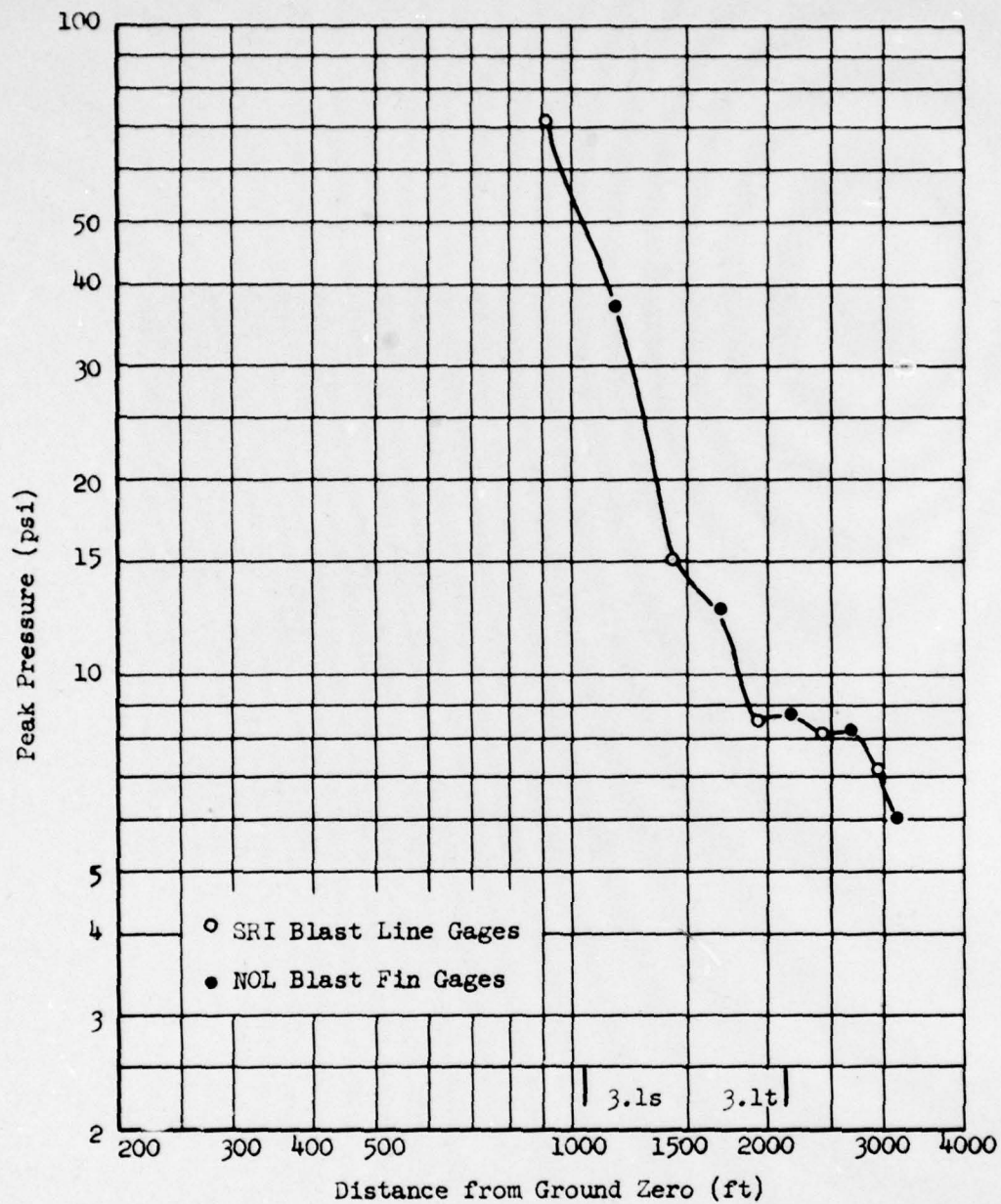


Fig. A.5—Ground level peak pressure as a function of distance from Ground Zero, Shot 10.

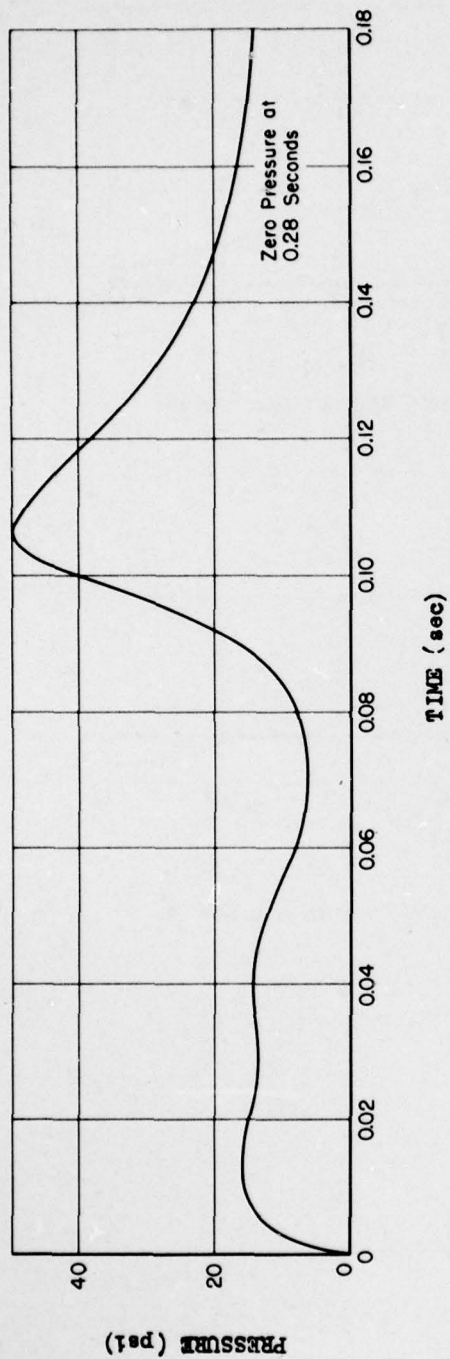


Fig. A.6—Estimated ground level pressure incident on Structure 3.1s, Shot 10.

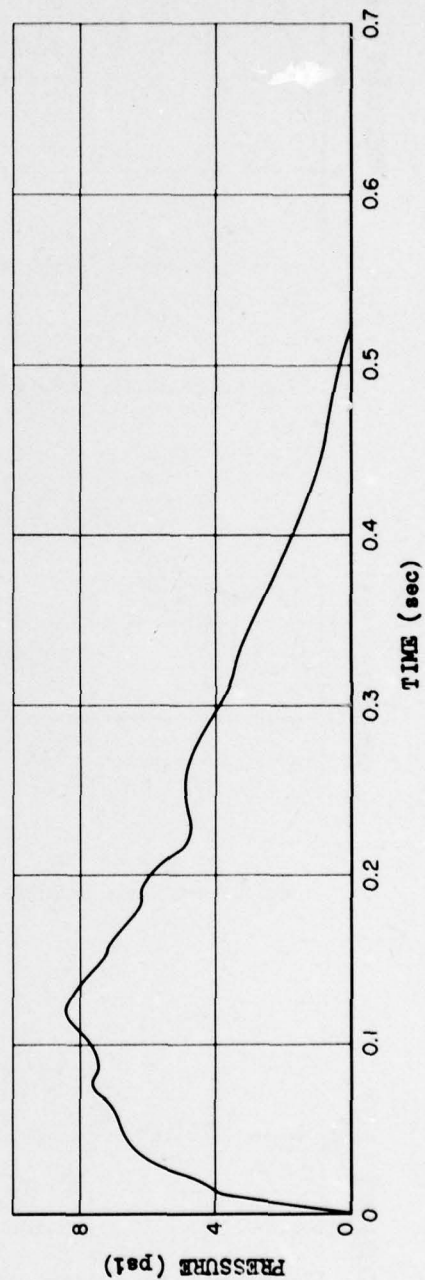


Fig. A.7—Estimated ground level pressure incident on Structure 3.1t, Shot 10.

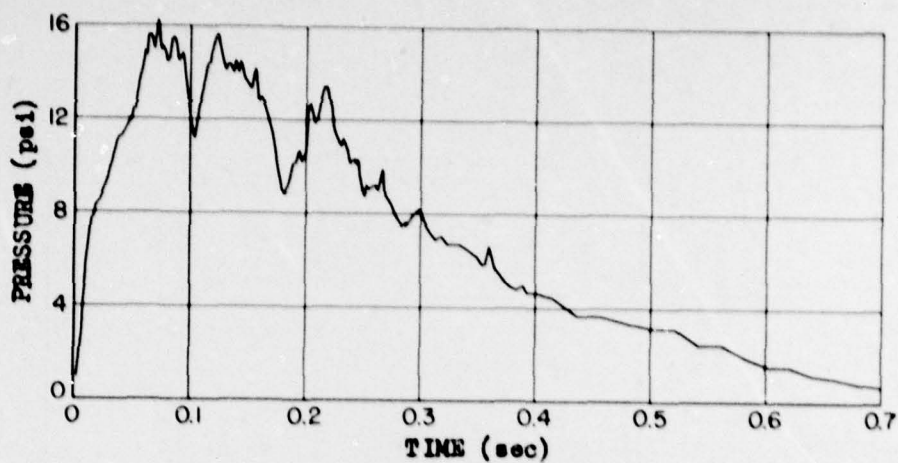


Fig. A.8—Average pressure on the front face of Structure 3.1t, Shot 10.

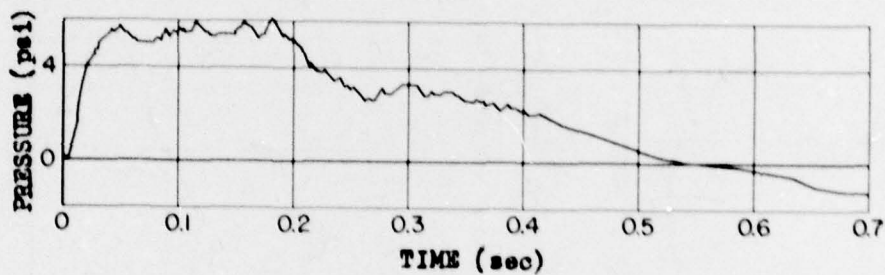


Fig. A.9—Average pressures on the rear face of Structure 3.1t, Shot 10.

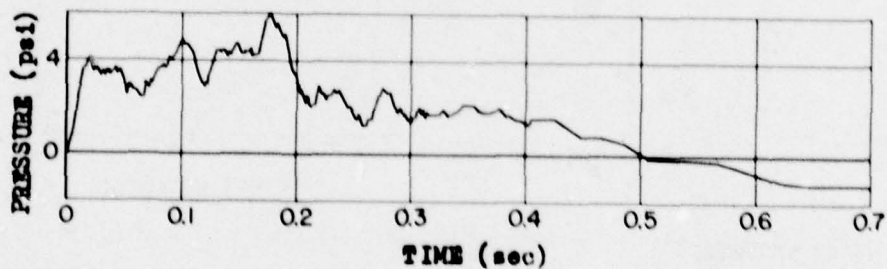


Fig. A.10—Average pressures on the top face of Structure 3.1t, Shot 10.

UNCLASSIFIED



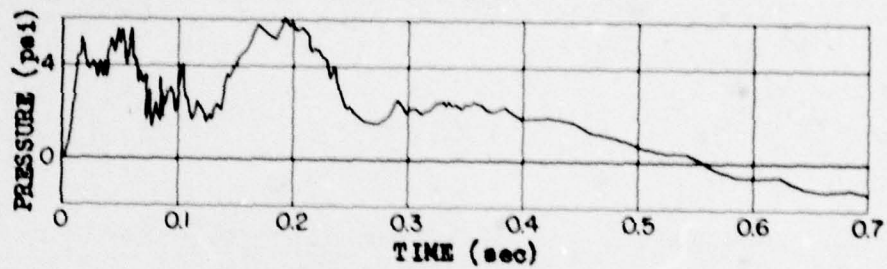


Fig. A.11 — Average pressure on the side face of Structure 3.1t, Shot 10.

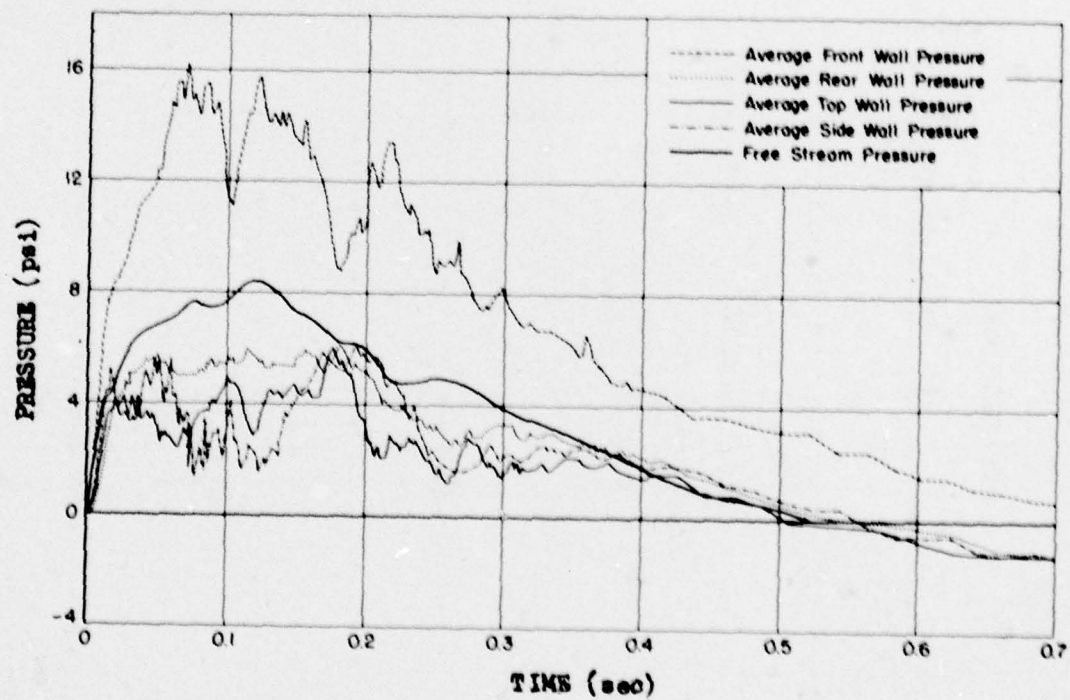


Fig. A.12 — Average pressures on all faces of Structure 3.1t, Shot 10.

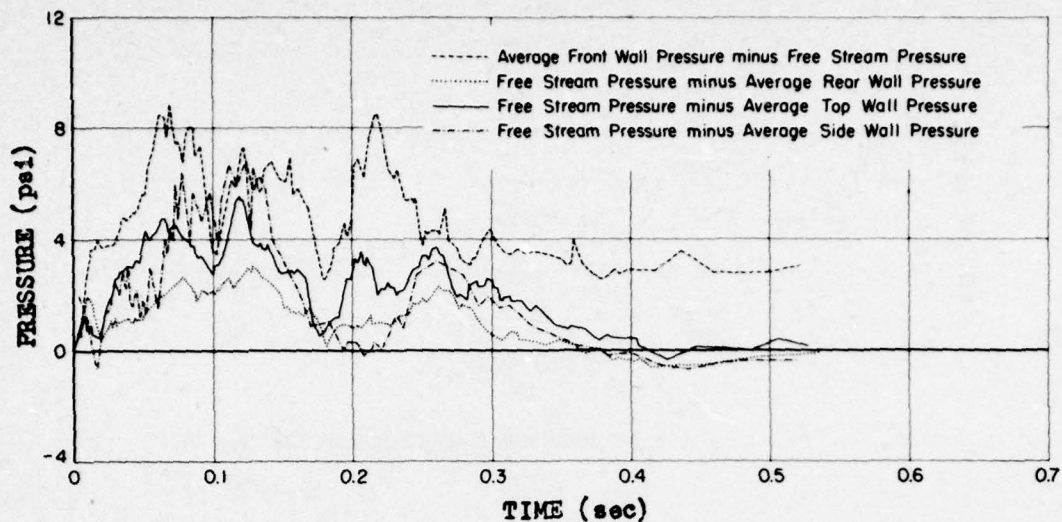


Fig. A.13—Difference between free stream pressure and the average pressure on the faces of Structure 3.1t.

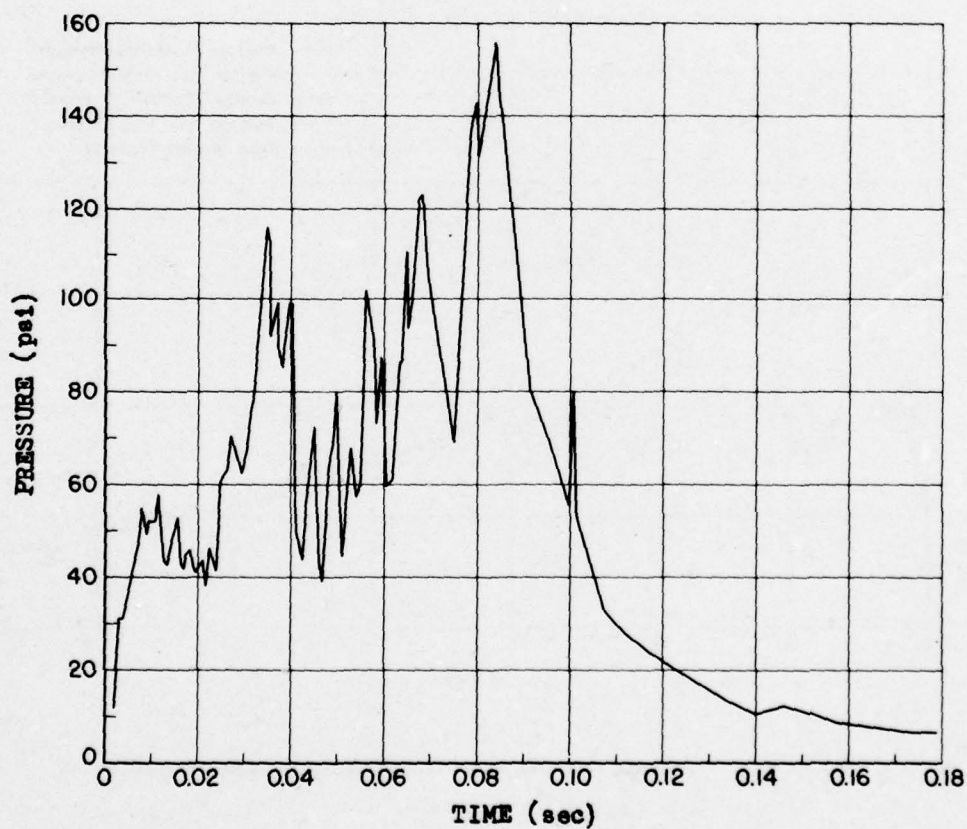


Fig. A.14—Average pressure on front surface of Structure 3.1s, Shot 10.

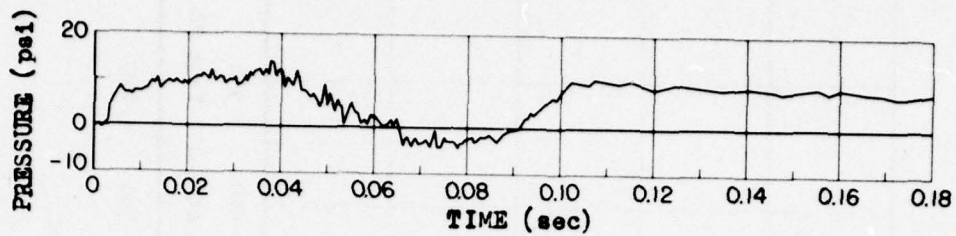


Fig. A.15—Average pressure on rear surface of Structure 3.1s, Shot 10.

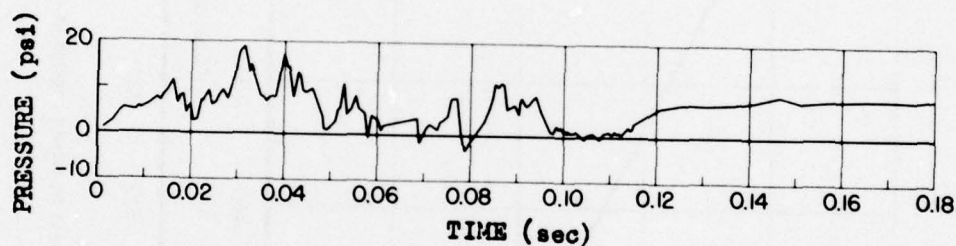


Fig. A.16—Average pressure on top surface of Structure 3.1s, Shot 10.

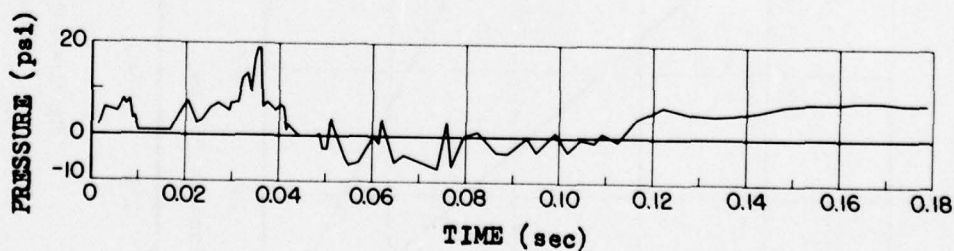


Fig. A.17—Average pressure on side surface of Structure 3.1s, Shot 10.



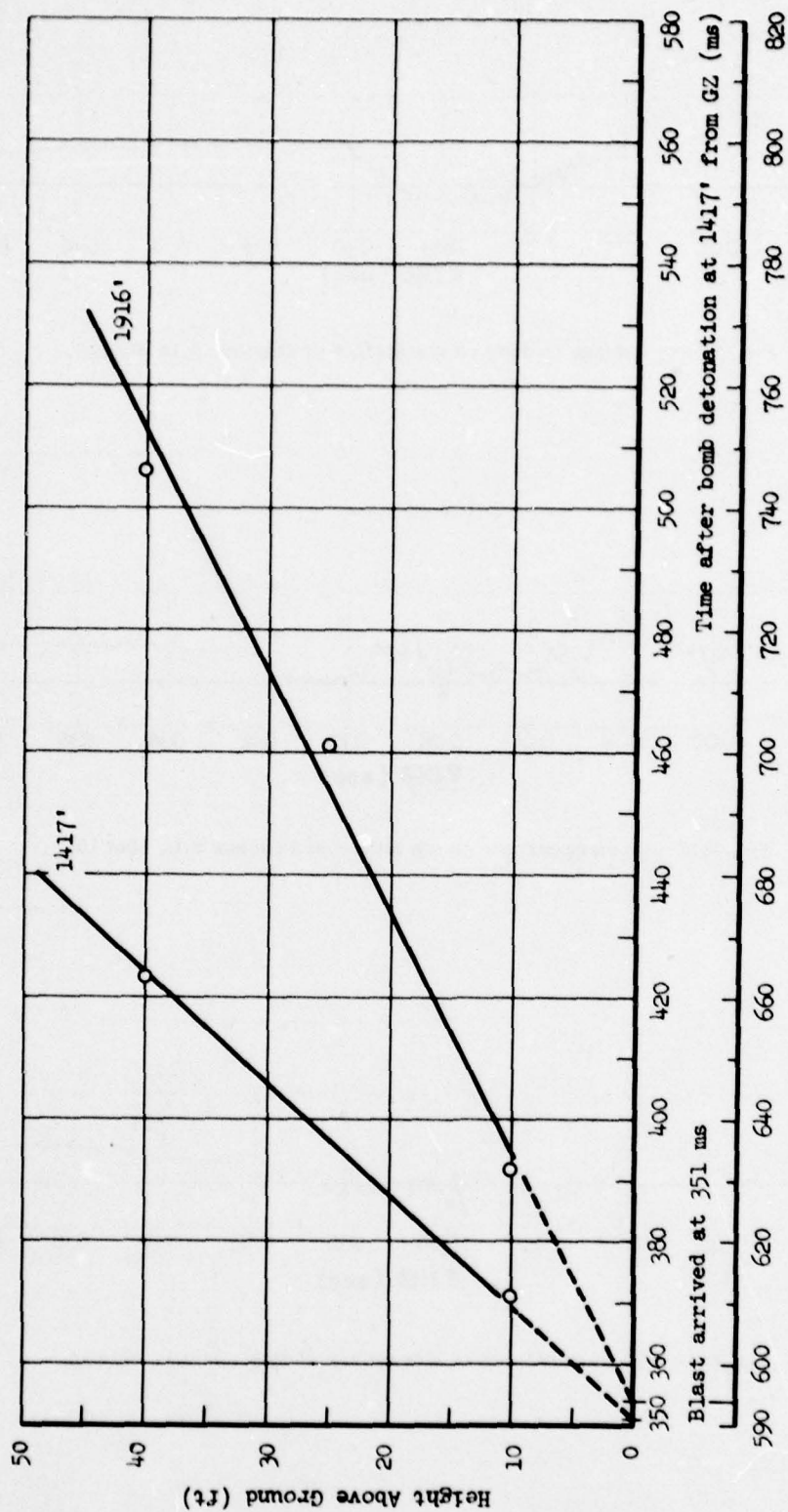


Fig. A.18—Time of arrival of heavy dust loads on Sandia q-gages at various elevations above ground.

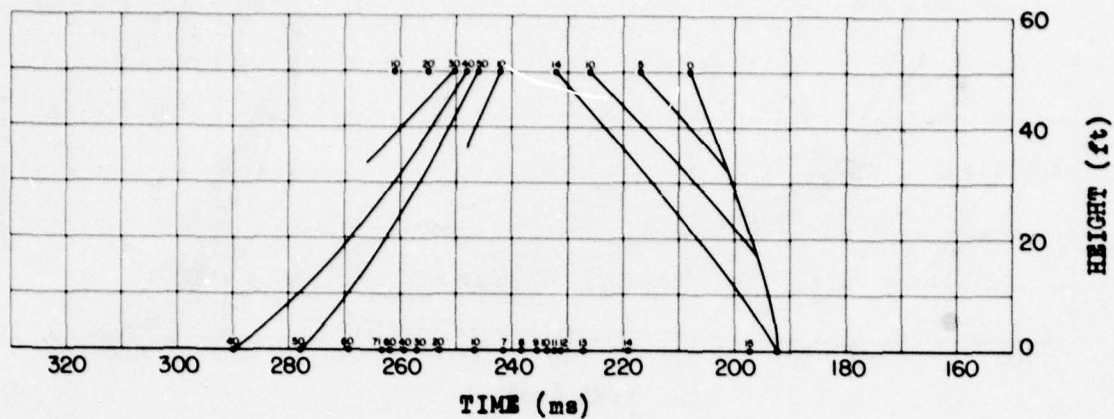


Fig. A.19—Constant pressure contours from blast line as a function of gage height and absolute time at 924 ft from Ground Zero.

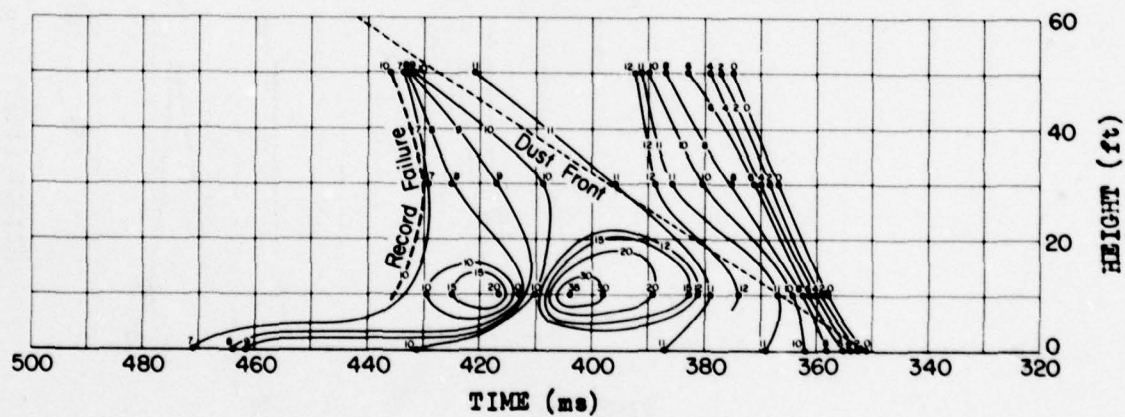


Fig. A.20—Constant pressure contours from blast line as a function of gage height and absolute time at 1417 ft from Ground Zero.

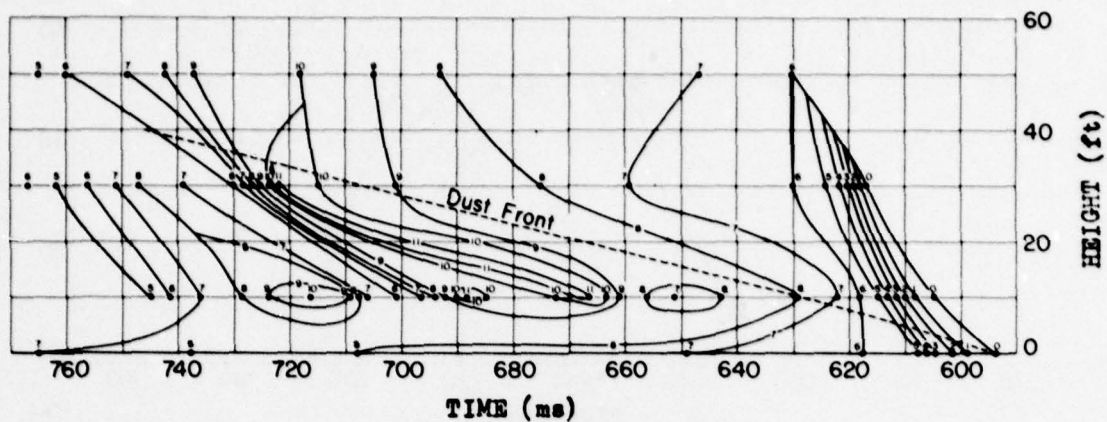


Fig. A.21—Constant pressure contours from blast line as a function of gage height and absolute time at 1916 ft from Ground Zero.

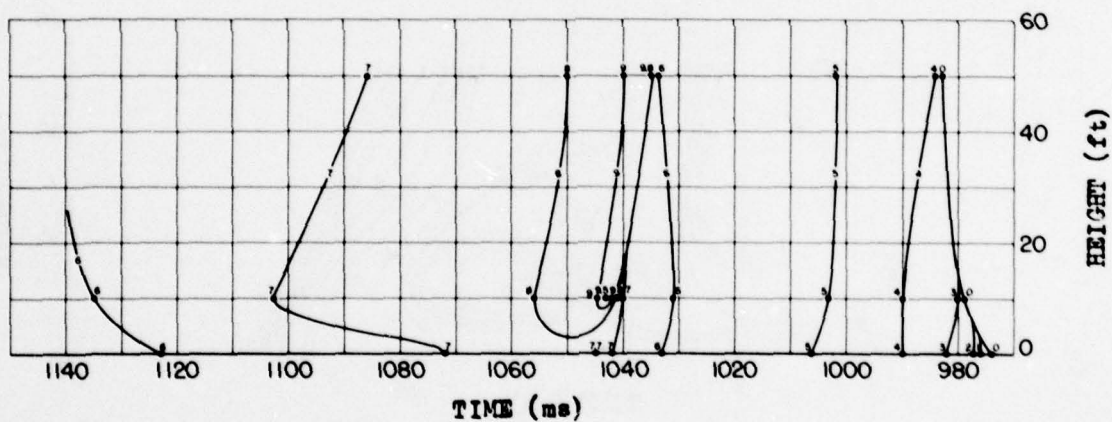


Fig. A.22—Constant pressure contours from blast line as a function of gage height and absolute time at 2416 ft from Ground Zero.

UNCLASSIFIED

308

UNCLASSIFIED



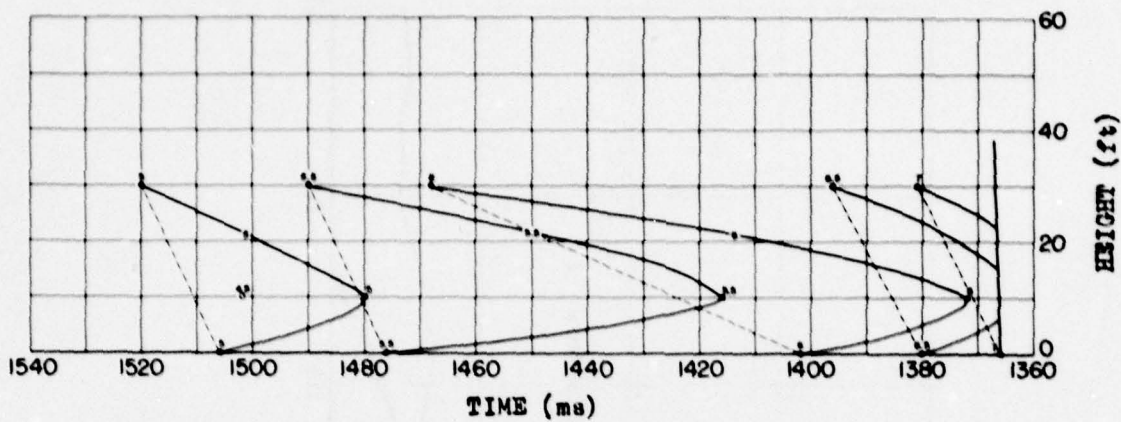


Fig. A.23—Constant pressure contours from blast line as a function of gage height and absolute time at 2916 ft from Ground Zero.

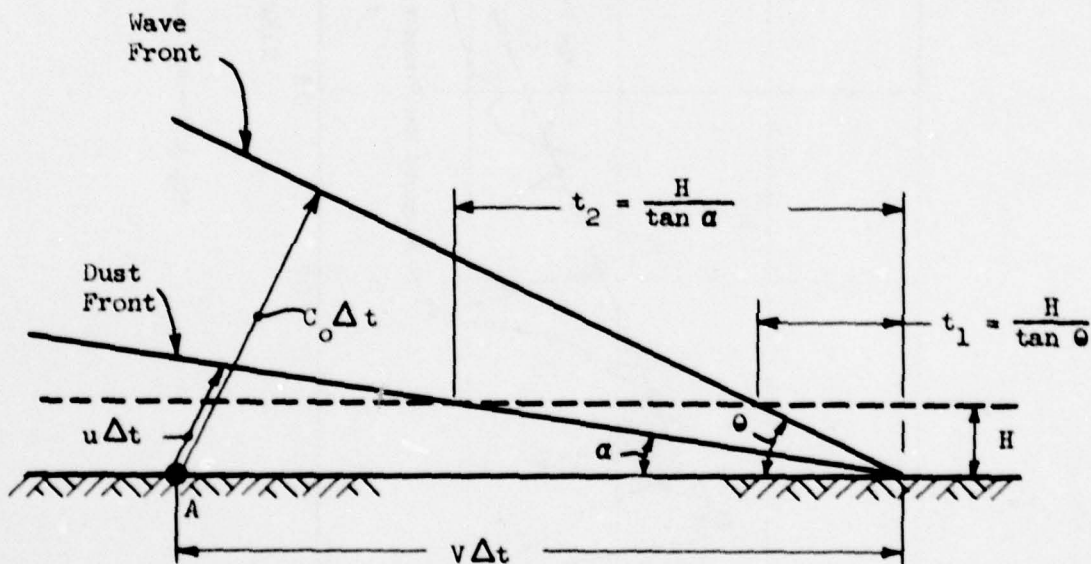


Fig. A.24—Schematic drawing of blast and dust fronts in precursor region.

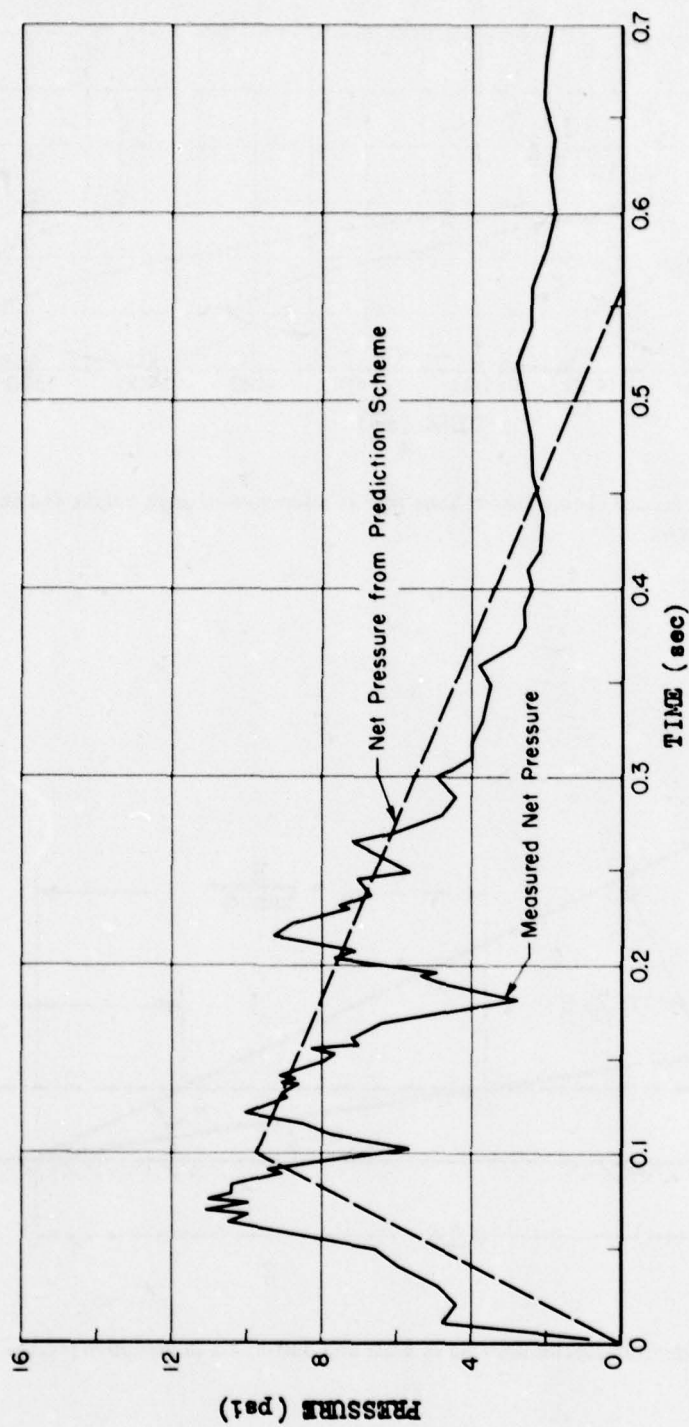


Fig. A.25 — Net pressure on Structure 3.1t.

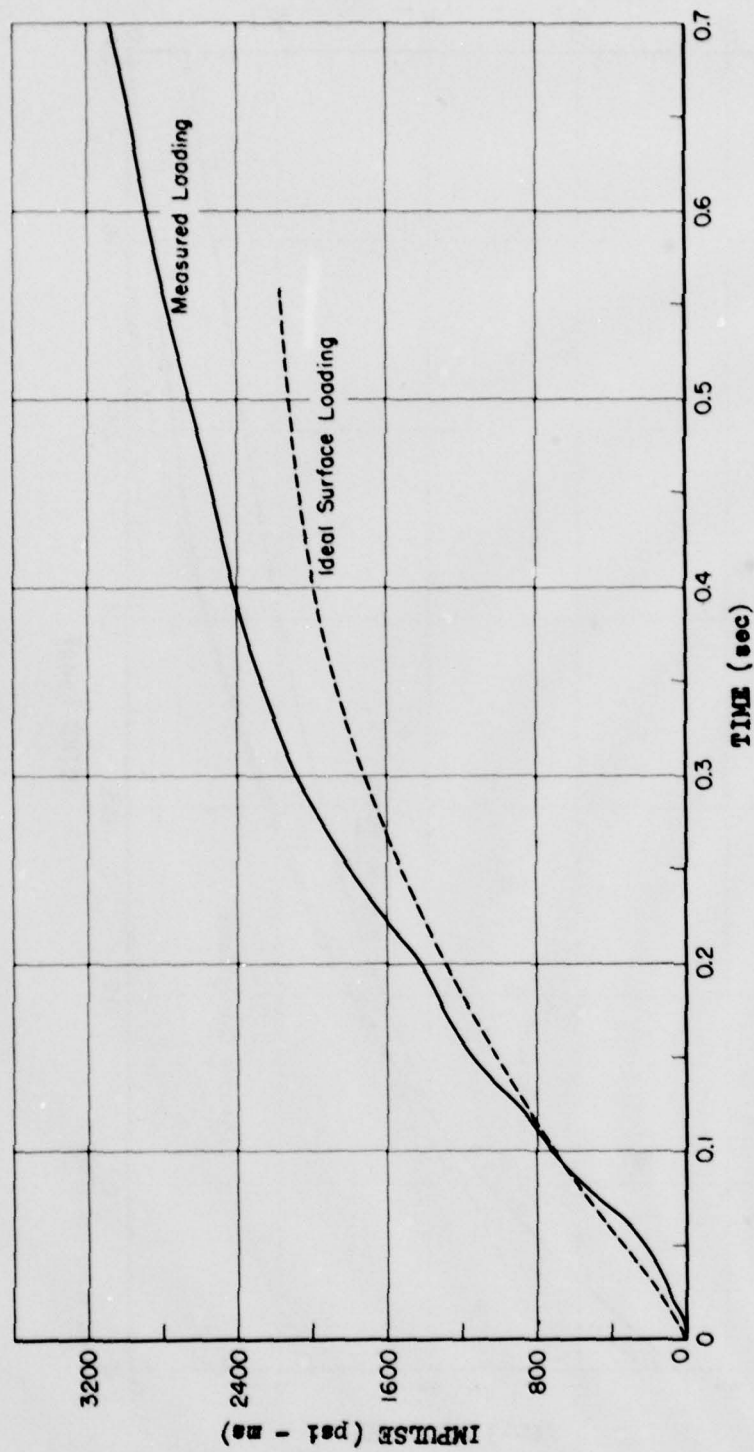


Fig. A.26 — Net impulse as a function of time on Structure 3.1t, Shot 10.



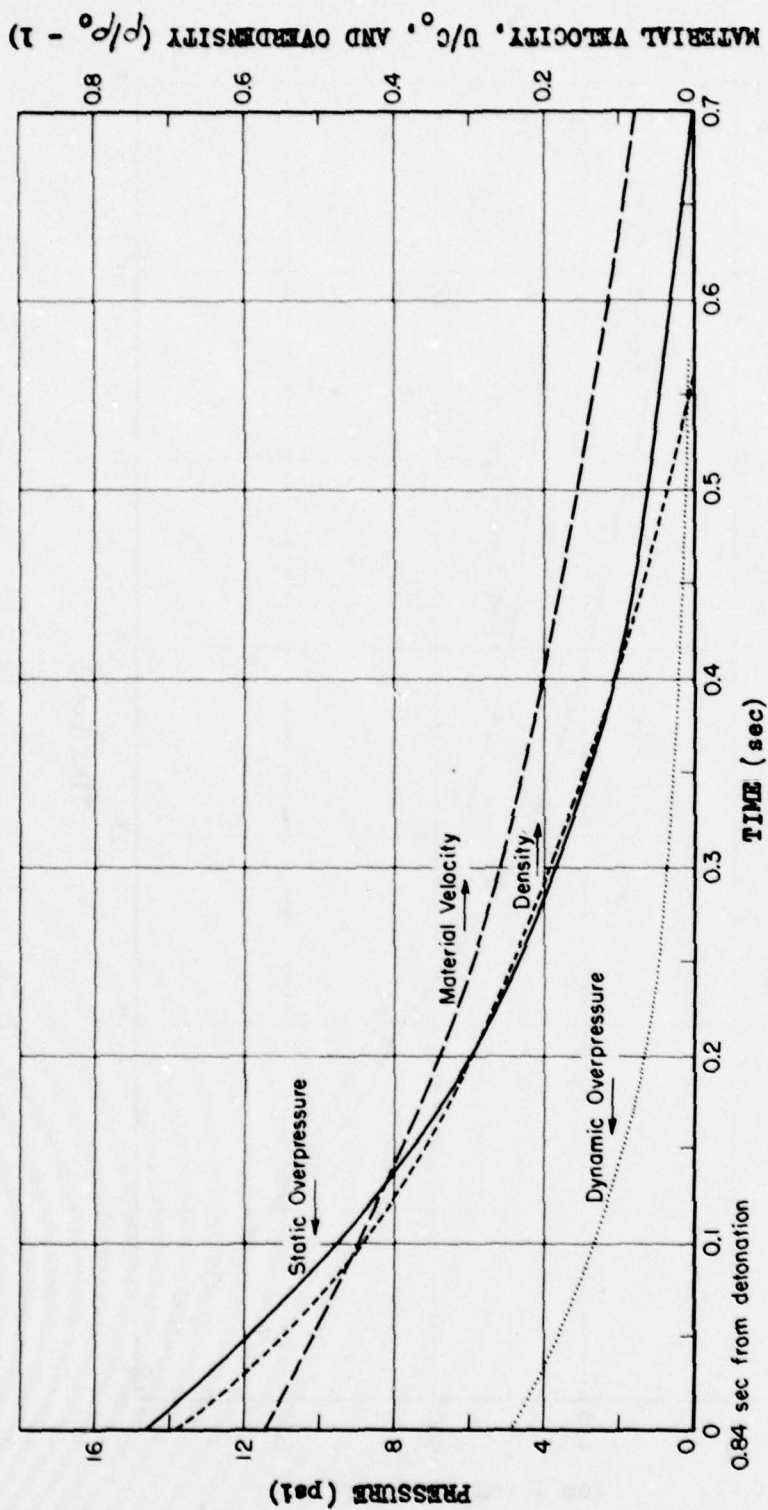


Fig. A.27 — Predicted hydrodynamic variables over an ideal surface for Structure 3.1t.

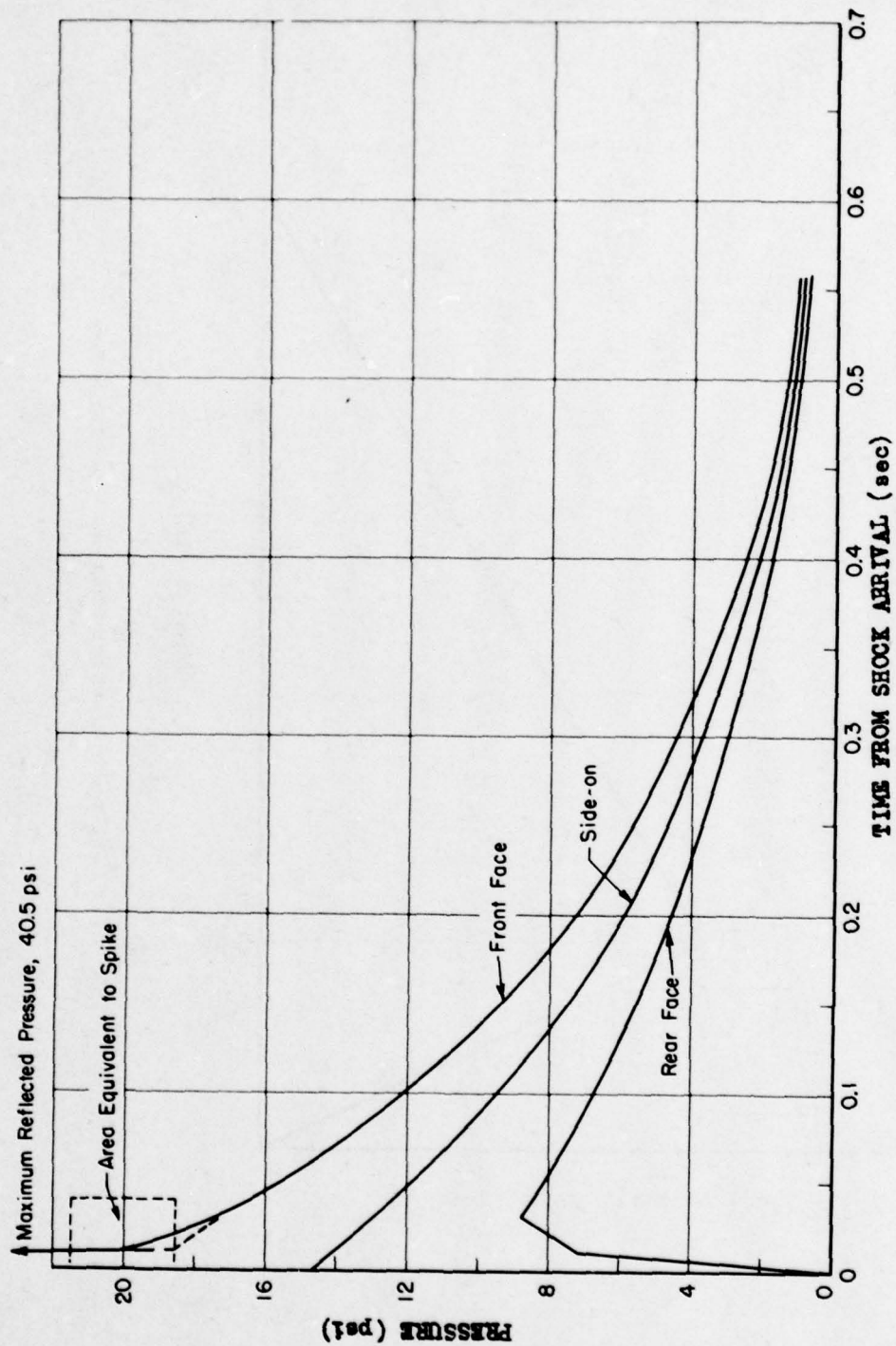


Fig. A.28—Ideal surface loadings for Structure 3.1t.

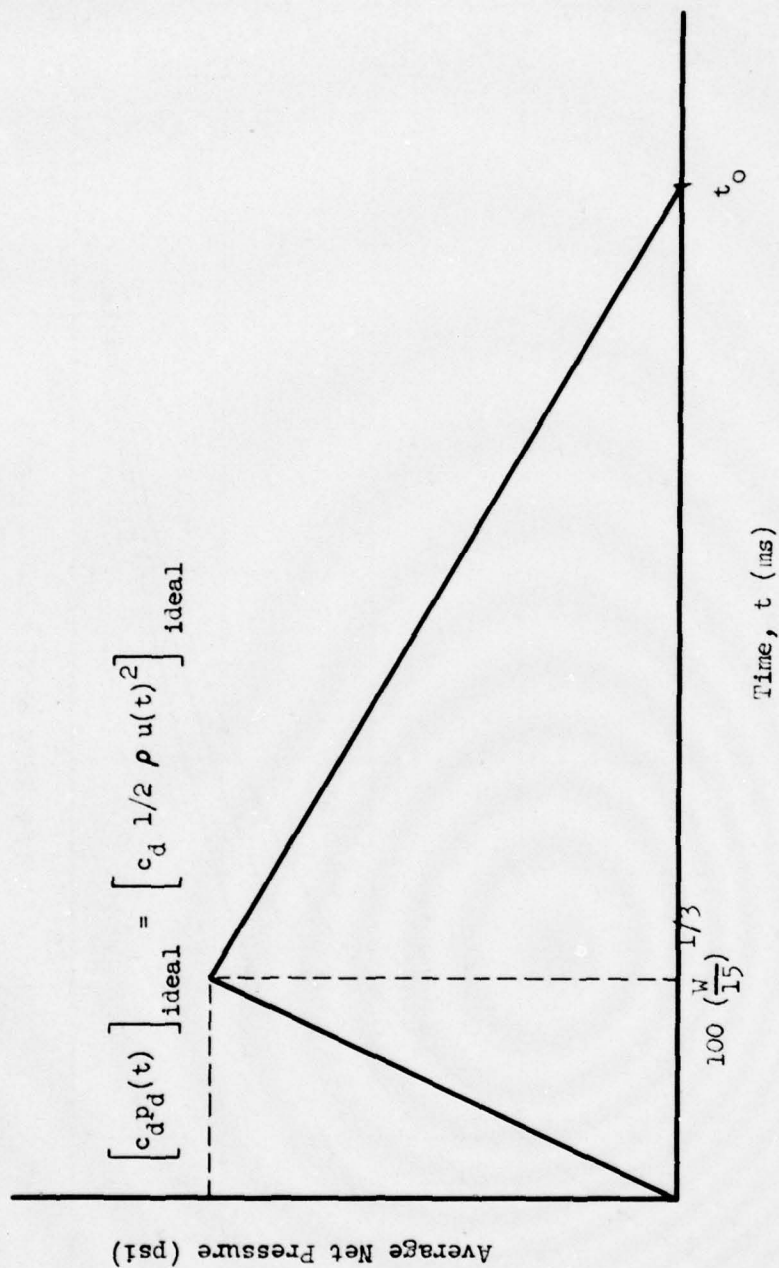


Fig. A.29—Schematic loading scheme in a precursor.



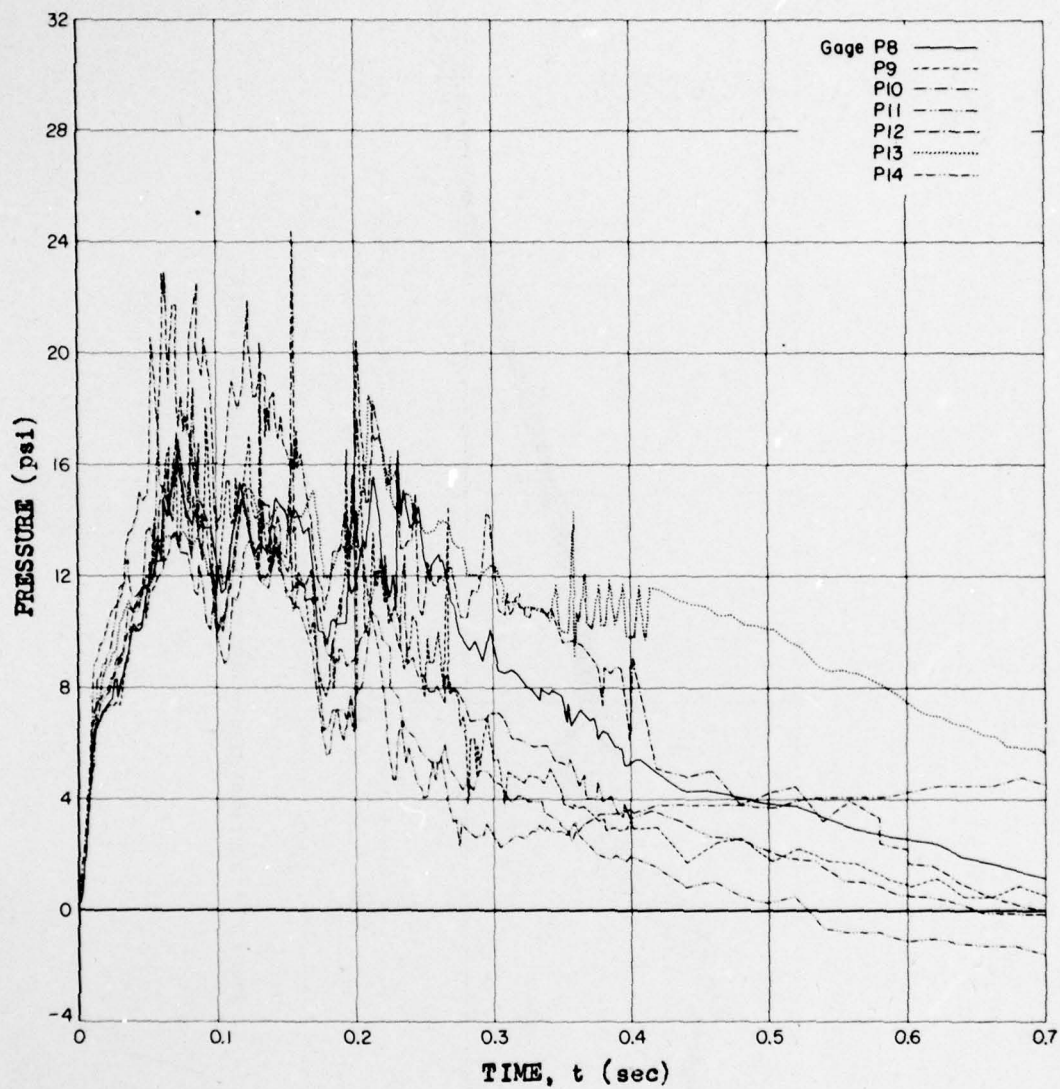


Fig. A.30—Individual gage records, front surface, Structure 3.1t, Shot 10.

UNCLASSIFIED

316

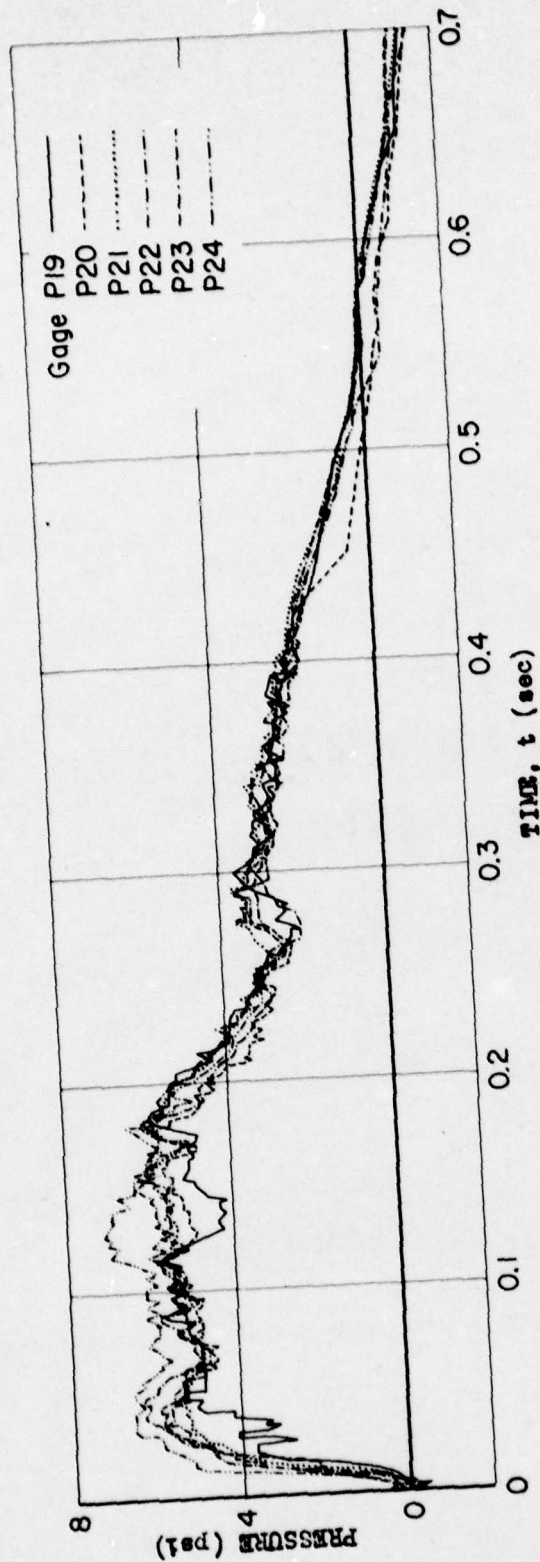


Fig. A.31 — Individual gage records, rear surface, Structure 3.1t, Shot 10.

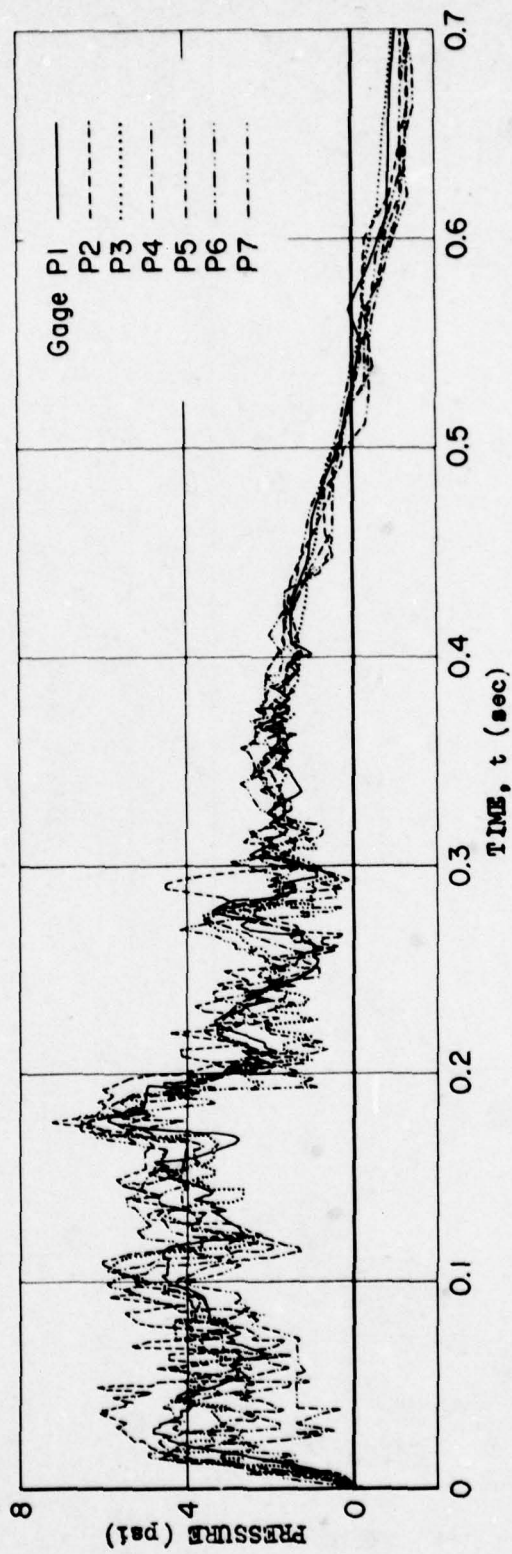


Fig. A.32—Individual gage records, top surface, Structure 3.1t, Shot 10.



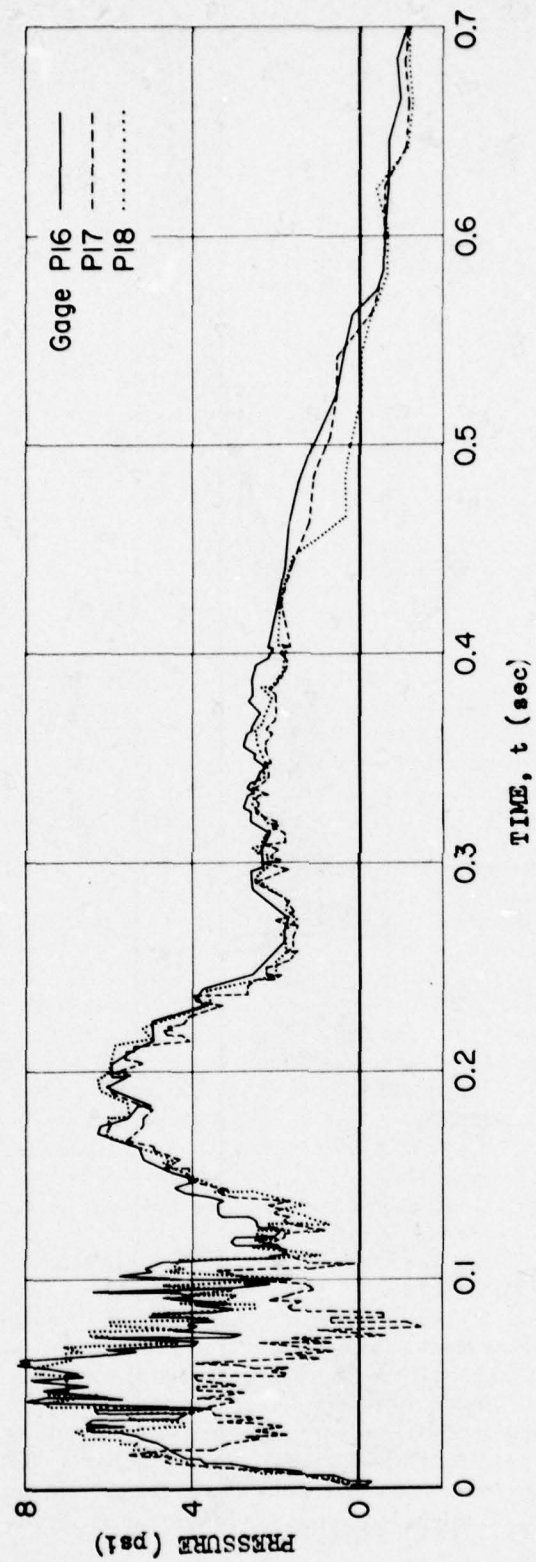


Fig. A.33—Individual gage records, right side, Structure 3.1t, Shot 10.

## APPENDIX B

# COMPARISON OF WAVE FORMS FOR STATIC AND DYNAMIC PRESSURES

By F. B. Porzel

### B.1 STATEMENT OF THE PROBLEM

#### B.1.1 Purpose

The purpose of this appendix is to investigate current methods of determining dynamic pressure as a function of time from the blast wave of a nuclear explosion and, if possible, to suggest improvements in methods for predicting dynamic pressure. In most cases, either reliable measurements of dynamic pressure are lacking or a transformation is required to extrapolate measured results to different yields, heights of burst, and surface conditions. Because of the relative abundance and good reliability of pressure-time records, it would be especially desirable to provide a method of predicting dynamic pressure from them.

#### B.1.2 Customary Procedure

At present there is a procedure, which can almost be described as "standard procedure" by which the velocity-time curve is constructed from the pressure-time curve. At the shock front, there is no question that the material velocity is related to the peak pressure by the Rankine-Hugoniot equation; in this customary procedure the Rankine-Hugoniot relation is assumed to hold on the interior of the wave, and, at successive times on the pressure-time curve, the material velocity is calculated from the corresponding pressure.

As a result, the positive duration for material velocity is necessarily identical to the positive duration for the pressure wave, and, by virtue of the Rankine-Hugoniot equation, the initial decay of material velocity is more severe than is the pressure decay at the shock front. In calculating the dynamic pressure from  $\frac{1}{2}\rho u^2$ , the density-time curve is also concave upward, and after squaring the material velocity, the decay of dynamic pressure is several times greater than the decay of peak pressure.

This method has the obvious advantage of giving the correct value for the material velocity at the shock front, but unfortunately the procedure is justified only at the shock front. There is no reason *a priori* to believe the positive durations are the same. No allowance is made for the way in which divergence of the blast wave may affect the shape of the velocity wave in comparison with the shape of the pressure wave. In any given pressure-time curve, all mass particles on the interior of a shock wave were initially shocked at higher pressures than the current peak and thereby suffered greater entropy changes than the mass points currently at the shock front. A fundamental deficiency of the customary method is that the velocity is calculated as if entropy change were necessarily less than at the current shock front. The simplest kind of approximation might just retain the relative shape of the pressure and velocity

curves, taking the ratio of material velocity to its peak value to be the same as the ratio of pressure to its peak. The deficiency of this method, using the Rankine-Hugoniot equations, even as an approximation is that it actually reduces such a normalized velocity-time curve below the normalized pressure-time curve, which is just opposite in direction to the correction expected by the shock hydrodynamics.

### B.1.3 Plan of Attack

In the subsequent sections the behavior of the velocity wave forms and dynamic pressure wave forms in comparison with the overpressure wave form are investigated. For the case of the blast wave in free air and, as a necessary consequence, for a surface burst over an ideal surface, this problem can be considered completely solved through a machine integration of the hydrodynamic equation for a point source explosion in air, which was done in Los Alamos, IBM Problem M under direction of Fuchs. These results were correlated in Report J-17837, dated May 25, 1953, and Report J-19704, dated Aug. 20, 1953. The title of these reports, *Theoretical Height of Burst Curves*, was an excerpt from a more comprehensive description which is given in Report LA-1644, *Height of Burst for Atomic Bombs*, LASL. These documents contain curves that give a complete description of the wave form for pressure, material velocity, density, and dynamic pressure on the interior of a wave from which the corresponding curves of dynamic pressure vs time and static overpressure vs time are readily calculated. From the work in Report LA-1665, which is the second of the series starting with LA-1664, there is good assurance that the same ideas may be extended to scaled heights of burst which are less than 100 ft as well as to all type surfaces.

For scaled heights of burst in excess of 100 ft, the only really adequate approach is to repeat this calculation for the case of the bomb burst at a finite distance from a rigid plane. But even in this ideal case, such an approach will be nearly impossible for several years to come, partly because even the best modern calculation machines are not capable of handling the hydrodynamic problem for the case of several space variables and partly because no complete theoretical description is available to furnish the boundary conditions for the behavior of the reflected wave near the triple point of the Mach stem. In addition to these difficulties, practical interest is always concerned with real surfaces, in which case the hydrodynamic variables near the shock front are violently altered from the ideal case by virtue of the interaction of the surface with the shock wave itself.

On the basis of work presented in Reports LA-1406, LA-1664, and LA-1665, it is possible to arrive at a reasonable compromise for practical purposes. These papers showed that, whereas the peak pressure is strongly reduced by virtue of surface effects (primarily due the thermal effects), the same reduction by no means applies to the wave form as a whole. In fact, such theoretical and empirical evidence as does exist tends to support the view that the pressure impulse over a real surface is practically identical with the pressure impulse over an ideal surface. With regard to dynamic pressures, the situation is even more favorable. The peak dynamic pressure is not appreciably reduced over a real surface, and, to a first approximation, it remains at the same value as over an ideal surface. There are further theoretical reasons for believing that the peak dynamic pressure may actually be enhanced. Furthermore, positive durations are not expected to decrease over a real surface from their corresponding value over an ideal surface and this, together with the impulse arguments, is good assurance for the reasonable applicability of the ideal wave form to an impulse criterion.

The plan to be followed here is as follows: The relative wave forms for pressure and material velocity will be considered on the basis of hydrodynamic arguments alone without regard to further theoretical and empirical evidence. From this, a general behavior for single shocks can be formulated, which will then be tested with the IBM results for free air wave forms. At that time, we will be in a position to make the necessary conditions for a compromise solution for the wave forms for overpressure and dynamic pressure as functions of time together with their impulses.



## B.2 ARGUMENT FROM SPHERICAL DIVERGENCE

Consider a mass particle of air labeled by the band,  $dr$ , in the radius-time plot in the upper half of Fig. B.1. This particle was first struck by the shock at time  $t_s$ . The curved band describes its subsequent position  $r$  at later times  $t$ ; the slope of the band is, in fact, the material velocity

$$u = \frac{dr}{dt}$$

If this be a spherical shock, then the material within the band labeled  $dr$  represents a spherical shell of material whose mass is given by

$$\text{Mass} = 4\pi\rho r^2 dr$$

If this thickness of the shell is denoted by  $dr$ , conservation of mass requires that

$$\rho r^2 dr = \text{constant on the path } u$$

If there are no secondary shocks or compression waves within the positive phase, then, by definition, the velocity at a given time is an increasing function with radius within the positive phase. This means that the outer line of the banded particle is moving with a higher velocity than is its inner limit and that the thickness,  $dr$ , must be increasing on a linear plot. Because the velocity gradients are themselves nearly linear,  $dr$  is nearly proportional to  $r$ . When this same plot is with log-radius-vs-log-time scales, then experience shows that the logarithmic spacing, which is  $dr/r$ , tends to remain constant. Rewriting conservation of mass in the form

$$\rho r^3 \frac{dr}{r} = \text{constant}$$

it follows that

$$\rho r^3 = \text{constant on the path } u$$

This equation states that density will be a minimum when the radius is a maximum. Following the usual assumption that the changes in state are adiabatic behind the shock, then for a given mass particle, the absolute pressure  $P$  is related to the density through its absolute shock pressure  $P_s$  and density at  $t_s$  by the adiabatic law:

$$P = P_s \left( \frac{\rho}{\rho_s} \right)^\gamma$$

It then follows

$$Pr^{3\gamma} = \text{constant on } u$$

If attention is restricted to shocks of low enough strength (below 3 or 4 atm overpressure), we may even neglect the entropy changes across the shock front as they affect  $P_s$  and  $\rho_s$ .

Consider the mass particle at the slant distance  $R$  and at time  $t_1$ ; the material velocity will be zero and  $t_1$  marks the end of the positive duration for material velocity, as shown in the lower half of Fig. B.3. But at the same time, conservation of mass and the adiabatic law require the pressure to be at its minimum absolute value at time  $t_1$ , which corresponds closely to the trough of the negative phase in the pressure wave.

These arguments show a fundamental deficiency in the customary procedure of calculating the material velocity directly from the overpressure: the positive duration from material velocity does not correspond to the positive duration for pressure. Although the arguments in the preceding paragraph are only approximate because they assume the logarithmic thickness  $dr/r$  to be constant, they also show that, to a first approximation, the positive duration for the material velocity wave corresponds more nearly to the entire duration of the pressure wave from the shock front to the trough of its negative phase instead of to its positive duration. It also follows from these arguments that, over the wave as a whole and on a normalized basis, the material velocity wave must be substantially above the pressure wave, when both are normalized by dividing by the values of the shock front, and its average decay rate be smaller than the corresponding decay rate for the pressure-time curve.

### B.3 FREE AIR WAVE FORMS FROM MACHINE CALCULATIONS

#### B.3.1 Description

In this section the free air wave forms are based on the machine calculations in IBM Problem M which gave quantitative results. In principle, the calculation is as exact as modern techniques will permit; the divergence for a spherical wave was taken into account, entropy changes have been included, allowances for the departures of air from the ideal equation of state have been made, and, of course, the hydrodynamic equations for the interior of a wave were solved without simplifying approximations. The results used here are taken directly from Report J-17837. Detailed justification for this correlation of the IBM results, including the evaluation of its yield, is contained in Report LA-1664.

Whereas these results apply only to spherical waves, the arguments already presented in Sec. B.2 with regard to divergence lend strong plausibility to the extension of these concepts to the reflected wave over a real surface. The results for detailed wave forms are illustrated for two cases, at peak pressure levels of 7.65 and 4.2 psi, thereby restricting the validity of the conclusions to these fairly low pressures in the region of practical interest.

#### B.3.2 Positive Duration

Fig. B.2 gives the positive duration for the overpressure as well as the dynamic pressure and material velocity for 1 kt in free air over a wide range of pressures. The distance (in feet) at which these durations were computed is shown as a label on the vertical line joining the two curves.

In Fig. B.2 note the following:

1. The positive duration for dynamic pressure is between  $1\frac{1}{2}$  and  $2\frac{1}{2}$  times the positive duration for static overpressure in the range of pressures from 3 to 150 psi.
2. The dynamic pressure positive duration is nearly constant (approximately 0.29 sec) in the region of practical interest. The duration of a reflected wave behaves much like that of a bomb of twice the yield. Hence a useful rule of thumb might be that the dynamic pressure positive duration and material velocity positive duration are each approximately  $0.36 W^{1/3}$  sec.
3. The pressure positive duration decreases with pressure in the region of practical interest. A variety of equations might be used to fit this behavior, but one which could be used for a reflected wave is

$$\begin{aligned} \text{Pressure Positive Duration} &= [0.27 - 0.093 \log_{10} p](2W)^{1/3} \\ &= [0.34 - 0.116 \log_{10} p]W^{1/3} \end{aligned} \quad (\text{B.1})$$

where  $p$  equals the overpressure.

#### B.3.3 Wave Forms

In this section wave forms behind the two specified peak values for pressure, material velocity and dynamic pressure, are presented from the results of the IBM run. They are

UNCLASSIFIED

UNCLASSIFIED

presented not only for the purpose of direct comparison among themselves but also to investigate possible difficulties with conventional fitting procedures.

Because the pressure-time curves are known to concave upward, it is conventional and reasonable to attempt to fit these to an exponential law, basically of the form

$$p = p_{\sigma}(0) e^{-ct} \quad (\text{B.2})$$

But such a curve would asymptotically approach zero pressure as time approaches infinity, and for this reason it is conventional to modify the simple exponential and fit the pressure wave with an equation of the form

$$p = p_{\sigma}(0) e^{-ct/t_0} \left(1 - \frac{t}{t_0}\right) \quad (\text{B.3})$$

where the times are measured from shock arrival. The symbol  $t_0$  refers to the pressure positive duration, and clearly the equation will fit the curve at that point. There are further arguments which support the qualitative correctness of the latter equation because it does permit a negative phase of the usual form, after which the pressure rises asymptotically to zero as time approaches infinity. However, it is felt that the justification for this equation is really no stronger than the arguments just presented, and the great danger in any empirical fit is that it implies some behavior of the wave form which may not be real.

Figures B.3 and B.4 give, on semilogarithmic coordinates, the normalized wave forms from the IBM run for overpressure, square of the material velocity, and the dynamic pressure over periods which represent about two-thirds the pressure positive durations and about one-half the material velocity positive durations. Because each of these wave forms has a positive duration where their respective normalized values go to zero, curves on these coordinates must later turn downward and become vertical at each of the respective positive durations.

In Figs. B.3 and B.4, note that:

1. The exponential fit seems to be a reasonable approximation over the range of interest for all three variables in their normalized form as expressed in Eq. B.2. (In fact, the exponential fit according to Eq. B.2 is better than one should have a right to expect if the form of Eq. B.3 were correct.)

2. The curve for the square of the material velocity decays much like the curve for the pressure itself. This is in direct opposition to the results which are predicted from the usual procedure of calculating the material velocity from the Rankine-Hugoniot equation. By this customary procedure, the velocity itself would decay faster than would the pressure, and the square of the material velocity would be something more than twice as fast as the decay of the pressure. This fit suggests that, if the pressure wave has been fitted by the equation of the form

$$p = p_{\sigma}(0) e^{-ct/t_0} \quad (\text{B.4})$$

then the material velocity could be fit by an equation of the form

$$u = u(0) e^{-ct/2t_0} \quad (\text{B.5})$$

But, because Fig. B.2 shows that the material velocity positive duration is about twice the pressure positive duration, the material velocity might be approximated in a more general form by

$$u = u(0) e^{-ct/t_1} \quad (\text{B.6})$$

where  $t_1$  is the positive duration for the material velocity wave and, happily enough, the decay constant  $c$  is identical with the decay constant for the pressure wave in Eq. B.4.



3. Since the density ratio  $\rho/\rho(0)$ , is also a decreasing function with pressure, it is expected that the decay constant for dynamic pressures is slightly larger than the decay constant for the pressure or the square of the material velocity. But purely from empirical observations the fit of the form

$$\frac{1}{2}\rho v^2 = \left[ \frac{1}{2} \rho(0) u(0)^2 \right] e^{-kt} \quad (\text{B.7})$$

appears to be as well justified as any so far considered.

The attempt was made to fit the pressure-time curve by means of the conventional form of equation.

$$p = p_0(0) e^{-ct/t_0} \left( 1 - \frac{t}{t_0} \right) \quad (\text{B.8})$$

Through the introduction of the linear term in  $t/t_0$  the difficulty in the end of positive duration is circumvented, and Figs. B.5 and B.6 represent the fitted curve from Eq. B.8 over twice the time durations shown in Figs. B.3 and B.4. From the concavity of Figs. B.5 and B.6, one draws one simple conclusion; namely, that the pressure-time curve cannot be fitted by this equation with  $c$  constant even over the first half of the positive duration. This is an especially surprising result, since the simple exponential fits in Figs. B.3 and B.4 appear to be entirely adequate over the first half or even three-quarters of the pressure wave. The deficiency of the conventional equation may be understood by expanding both terms of the equation for small values of  $\tau = t/t_0$ . With the simple exponential fit, this expands as

$$p \cong p_0(0) (1 - c_1\tau) + \text{higher order terms} \quad \tau \ll 1 \quad (\text{B.9})$$

On the other hand the conventional fit similarly expands as

$$p \cong p_0(0) (1 - c_2\tau) (1 - \tau) \cong p_0(0) [1 - (c_2 + 1)\tau] \quad \tau \ll 1 \quad (\text{B.10})$$

Thus, even for small values of  $\tau$ , the introduction of the linear term distorts the decay constant  $c$  in such a way that

$$c_2 = c_1 - 1 \quad (\text{B.11})$$

From Figs. B.3 and B.4 the decay constant  $c_1$  was determined to be approximately 2.5. For each wave the corresponding decay constant is changed materially by the numerical factor of 1 introduced in it by virtue of the linear term in  $t$ . At early times, of course, with  $\tau \ll 1$ , two equations might give similar results, but at later times the low value of  $c_2$  thus computed will seriously affect the shape of the pressure wave.

These results suggest a variety of modifications which might be made to the empirical fit. These modifications would give a reasonable approximation to the IBM wave form over a substantial part of the wave, when the pressures are still fairly high, and at the same time they would permit the description of the wave to give zero pressure at the end of the positive duration. Excellent results were obtained by one such obvious trial in form of

$$p = p_0(0) (1 - \tau^n) \quad (\text{B.12})$$

and the constant  $n$  was determined to be approximately 0.6 for both the pressure-time waves considered here. Additional trials were then made of these comparisons at higher pressures. At a peak of 44 psi, the simple exponential fit again gave excellent results, but there the form in Eq. B.12 was poor, and, for this reason, it is suspected of being only a fortuitous fit in a limited range of pressures.

These discrepancies are of less consequence than first appear. In the long run the primary interest in the pressure-time curve is to give an adequate fit when pressures are high and at the same time permit a ready description in terms of pressure impulse. These comparisons are illustrated in Fig. B.7, in which the true curve is assumed to be of a form shown by the line so labeled in Fig. B.7. Since excellent results were obtained in this special case with the use of Eq. B.12 the curve was fitted in the form

$$n = \frac{\ln 1 - \frac{p}{p_{\sigma}(0)}}{\ln \tau} \quad (\text{B.13})$$

for which the average value of  $n$  was determined to be 0.576. After integrating the impulse in the form of

$$I = p_{\sigma}(0) \int_0^1 (1 - \tau^{0.576}) d\tau \quad (\text{B.14})$$

the impulse becomes

$$I = 0.365 p_{\sigma}(0) t_0$$

The factor 0.365 is the shape factor for the wave in question, the impulse being proportional to both peak pressure and the positive duration. This value for the shape factor is probably as reliable as any for the purposes of the present study. One simple exponential form is used in the form of

$$I = \int_0^1 p_{\sigma}(0) e^{-\frac{1}{2}\tau} d\tau = 0.368 p_{\sigma}(0) t_0 \quad (\text{B.15})$$

which is nearly identical to previous result. We expect this impulse to be high because the curve does not pass through  $p = 0$  at  $\tau = 1$ . The finite value of the pressure at  $\tau = 1$  is indicated by the dashed line in Fig. B.7 and is labeled "simple exponential fit." From Figs. B.5 and B.6, it is clearly impossible to use a fixed decay constant with Eq. B.8 for either curve in question. The decay constant chosen would vary from 2.5 near the shock front to values like 0.7 at the end of the positive duration. With an arbitrary value  $c$  for such a decay constant the impulse becomes

$$\begin{aligned} I &= p_{\sigma}(0) \int_0^1 e^{-c\tau} (1 - \tau) d\tau \\ &= \frac{p_{\sigma}(0) t_0}{c} \left[ 1 - \frac{1}{c} + \frac{e^{-c}}{c} \right] \end{aligned} \quad (\text{B.16})$$

For  $c = 1$

$$I = 0.368 p_{\sigma}(0) t_0$$

For  $c = 2$

$$I = 0.28 p_{\sigma}(0) t_0$$

These values are again in substantial agreement with the impulse derived from the other empirical fit, but the uncertainty in fixing the decay constant amounts to 30 per cent.

These relations are shown qualitatively in Fig. B.7, which gives a comparison between various empirical fits to the pressure-time curve. The full line is the simple power fit and is probably closest to the pressure-time curve, in this case over the entire region. The simple exponential fits best where pressures are high; during the second half of the positive phase it is initially lower than the true curve but obviously is high at the end of the positive duration, where it still has a finite value. The customary form involving both the exponential and the

linear term is high during the first half of the positive phase and low during the second half of the positive phase. There is a striking advantage for the simple exponential fit because it is usually better during the first half of the duration where pressures are high and damage is most important; it fits least best in the second half of the positive phase where the pressures are already low, but even in this region it is somewhat compensating when impulse is calculated.

Granting the fact that the limitation that the simple exponential fit cannot express the behavior of the wave in the last third or half of the positive duration, there are still certain other practical advantages. The positive duration is an exceedingly difficult measurement to make because the pressure-time curves are so flat in this region. In many practical cases, it cannot be determined at all with any degree of reliability from field measurements because of the small shifts in pressure levels as a result of surface and atmospheric perturbation to the blast wave. The simple exponential fit describes the beginning of the wave adequately without requiring measurement of positive duration. Finally, the author has used such fits on many occasions to describe reflected waves and has always found them markedly useful, especially near the shock front where the greatest interest in the time curve occurs. Moreover, although the failure to pass through zero pressure at the end of the duration is annoying from an analytical point of view, there is no graphic difficulty in fairing a pressure-time curve to zero pressure at the end of the positive duration.

#### B.3.4 Dynamic Pressure Impulse

In the region of practical interest for damage to structures, the dynamic pressure is always considerably lower than is the peak static overpressure so that the interest in dynamic pressure is of importance because of its much longer effective duration than that of the static pressure in diffraction.

Figures B.8 and B.9 show the normalized curves on linear coordinates for pressure, square of material velocity, and dynamic pressure plotted from the wave forms in Report J-16837 at slant distances of 960 and 1400 ft from a 1-kt explosion in free air. These again correspond to peak pressure levels of 7.65 and 4.2 psi, respectively, at the standard conditions of 14.5 psi pressure and the sound velocity of 1138 ft/sec. It will be noted in Figs. B.8 and B.9 that the curve for  $[u/u_o(0)]^2$  fits the pressure curve  $p/p_o(0)$  fairly well throughout the positive duration, crossing it twice during that interval. Because of its longer positive phase, the integrated value of  $u^2$  can be expected to exceed that of the pressure. The density curves are not shown, but they present no serious problem. At these low pressures the density can be calculated directly from the adiabatic law, and, although it is slightly more accurate to retrace the earlier history of each mass point and use the peak absolute pressure and peak density at the shock for these conversions, it suffices to use ambient pressure and ambient density. Because the density curve is concave upward the dynamic pressure curve necessarily falls below the  $[u/u_o(0)]^2$  curve. The dynamic pressure curve is nearly congruent to the pressure-time curve during the first quarter of the wave, after which it falls below the pressure curve. Near the end of the positive duration for pressure, the dynamic pressure again exceeds the static overpressure, and, by virtue of long duration (corresponding to that of the material velocity), the dynamic pressure impulse also contributes after the end of the positive duration, since static pressure compensates for the relative lowness of dynamic pressure during the middle portion of the pressure positive duration.

The impulses for both dynamic and static pressures were graphically integrated from Figs. B.8 and B.9 on a normalized basis with the static pressure impulse set equal to 1.0. Results are shown in Figs. B.10 and B.11, in which it will be noted that the normalized dynamic pressure impulse is finally within 10 per cent of the static pressure impulse. This effective proportionality between the dynamic pressure and static pressure impulse greatly simplifies practical consideration. Given any observed free stream pressure measured on the ground, the static pressure impulse may be calculated either graphically or analytically, using whatever method appears appropriate. Because of surface effects, the observed peak pressure will almost always fall below the value expected over an ideal surface. Yet the ideal peak pressure



may always be estimated with a high degree of reliability by a simple exponential fit of the peak static pressure. Based on this ideal value of the peak static overpressure,  $p_{\sigma}(0)$ , the peak dynamic pressure  $\frac{1}{2}(p_{\sigma}(0)u_{\sigma}(0)^2)$  is readily calculable from the Rankine-Hugoniot relations. The dynamic pressure impulse is then determined by

$$\frac{\int_0^{t_1} \left( \frac{1}{2} \rho u^2 \right) dt}{\int_0^{t_1} p dt} = \frac{\frac{1}{2} \rho_{\sigma}(0) u_{\sigma}(0)^2}{p_{\sigma}(0)} \quad (\text{B.17})$$

This remarkably simple law appears to have useful implications in predicting the field variables from atomic weapons. It is at first attractive because it suggests an equipartition of static and dynamic pressure on a normalized basis; namely, the impulse delivered through static or dynamic pressure must always bear the same relation to their peak values, considering their different positive durations. This hypothesis of identical shape factors was tested at high pressures of a 44 psi peak, but, at that level, the dynamic pressure fell far below static pressure, and it is doubtful that this simple law holds over all ranges of pressure. In any case, it is suggested as a working hypothesis both for practical problems and for further research in the field variables.

#### B.4 APPLICABILITY OF DIVERGENCE ARGUMENTS

The verification of the general argument from divergence, as presented in Sec. B.2, by testing with the IBM run in Sec. B.3, lends strong support to the plausibility that similar conclusions may be drawn from reflected waves, especially near the ground surface. Near the ground, the material velocity is always parallel to the ground and hence, a presentation like that of Fig. B.1 which requires only a single space coordinate, may be used to describe the blast wave. Although the geometry would appear to be two-dimensional at first, the mass flow behind the regular reflected wave (in either regular or Mach reflection) is still essentially radial from Ground Zero, and the divergence bears a strong similarity to a spherical wave bisected by the ground plane.

##### B.4.1 Positive Duration

Once the Mach reflection process has set in and at long distances from the bomb, all properties of the wave eventually approach those of a bomb of twice the yield in free air. As a first guess, one might limit the positive duration at normal incidence to that of the incident wave and thereby formulate the rule that, at normal incidence, the positive duration corresponds to the free air wave, and, after Mach reflection, the positive duration gradually approaches that of a bomb of twice the yield. However, Chandrasekhar solved the problem numerically for the reflected wave from a plane shock and found an increase in positive duration of about 10 per cent. For low pressures, the corresponding increase in positive duration with a reflection factor of 2 is roughly 20 per cent. By virtue of this coincidence, it is expected that a reasonable approximation the positive duration for all reflected waves will correspond to that of a bomb of twice the yield.

There is uncertainty whether to apply the reflection factor of 2 to the positive duration at the peak pressure level of the reflected wave or to apply it to the point corresponding to the peak pressure level of the incident wave. It is presently recognized that one cannot hope to derive rigorous rules on the basis of these simple arguments, and that an adequate solution really requires a machine solution with two space coordinates for the blast wave problem over a reflected surface. The most we can presently hope for is to establish reasonably practical and consistent rules and satisfy ourselves as to which is the better choice of a positive duration. From Fig. B.2, we observe that, in the region of practical interest, the positive duration actually decreases with increasing pressure, and it does not seem reasonable to peg the positive duration for the reflected wave at a decreased value because of an increased reflected

pressure. For this reason alone, it appears more reasonable to fix the positive duration on the basis of the incident pressure at the same slant distance.

The basis for the argument for the reflection factor of 2 is fundamentally that of doubling the energy density. Consistent with these arguments, times and distances may scale like  $W^{1/3}$ , but impulse scales like  $W^{2/3}$ . A comparison between the pressure-time curve for a free air wave and a corresponding reflected wave is shown in Fig. B.12. The free air wave is depicted with the peak overpressure  $p_{\sigma}(0)$  and duration 1.0 in the figure. In the acoustic approximation the reflected pressure would increase by a factor  $2^{1/3}$  to  $1.26 p_{\sigma}$ , and, at the same time, the duration would increase to 1.26. The impulse increases by  $2^{2/3}$  if the shape factors remain the same. But, by virtue of the nonlinearity of the reflection process and nonideal property of air, the actual reflected pressure at normal incidence is always considerably greater than that given by a reflection factor of 2, and the reflected pressure actually approaches values like 12 times the incident pressure near normal incidence. Conservation of energy hardly permits this enormous increase to extend over any considerable portion of the wave. For this reason, the state of affairs is probably more like that depicted by the upper curve in Fig. B.12. The abnormally high (above 2) reflection factors are restricted to a relatively sharp peak near the shock front, with a reflection factor of 2 in the positive duration.

At normal incidence, of course, the material velocity is zero behind the reflected wave and the kinetic energy of the incident wave reappears as static pressure in the reflected wave. From this it is an interesting conjecture that the total impulse (dynamic plus static pressure) may be invariant in the reflection process in comparison with the incidence wave.

#### B.4.2 Surface Conditions

Over real surfaces it is well known that peak pressures are markedly reduced by thermal and mechanical effects in the interaction with the ground surface. For the present, it is sufficient to point out that, from the conception of the theory in Report LA-1406, the same remarks do not apply to pressure impulse or the drag winds associated with the blast. In fact, Report LA-1406 contains the argument whereby one expects the ground surface merely to reduce peak pressure either by distributing energy over a larger volume in the thermal effect or by absorbing kinetic internal energy at the shock front through dust loading. In either case there may not be any over-all absorption of energy by the ground surface, and for this reason one may not expect any appreciable decrease in the integrated impulse from either static or dynamic pressure.

#### B.5 CONCLUSIONS

The results may be summarized by the following conclusions.

1. The positive duration for material velocity is from 1.5 to 2.5 times the positive duration of the pressure wave. It corresponds roughly to the absolute minimum in the pressure wave. It is practically constant in the region of practical interest, being approximately  $0.29^{1/3}$  sec for a free air wave at the standard condition of 1 bar and at an ambient sound velocity of 1138 ft/sec (for details see Fig. B.2).
2. The positive duration of a reflected wave is, to a good approximation, the same as that of a free air wave of twice the yield at the same slant distance. This result ensues regardless of height of burst or region of reflection.
3. The customary procedure of calculating the material velocity from the pressure-time curve by using the Rankine-Hugoniot relation is inadequate in regions of practical interest and leads to calculated values of dynamic pressure impulse which are much lower than their actual values.
4. The customary fit of pressure-time curves by expressions of the form

$$p = p_{\sigma}(0) e^{-ct/t_0} \left(1 - \frac{t}{t_0}\right) \quad (B.18)$$

UNCLASSIFIED

~~SECRET - RESTRICTED DATA~~

is probably inadequate because it does not describe the free air wave form. It generally leads to forced fits to the pressure-time curve which, at best, pass through the actual curve during the positive duration.

5. No expression is presently suggested as to the exact fit for the various wave forms, but simple exponential fits of the form

$$p = p_{\sigma}(0) e^{-ct} \quad (\text{B.19})$$

$$u = u_{\sigma}(0) e^{-c_2 t} \quad (\text{B.20})$$

$$p_d = \frac{1}{2} \rho_{\sigma}(0) u_{\sigma}(0)^2 e^{-c_3 t} \quad (\text{B.21})$$

$$\rho = \rho_{\sigma}(0) [p/p_{\sigma}(0)]^{1/\gamma} \quad (\text{B.22})$$

are considered adequate. They describe the first half of the wave well and involve only minor errors in calculated impulse over the true positive durations. With a simple exponential fit, the normalized curve  $[u/u_{\sigma}(0)]^2$  has approximately the same decay constant,  $c$ , as does the pressure-time curve.

6. The dynamic pressure impulse may be calculated with 10 per cent from a measured free-stream overpressure impulse by the relation

$$\begin{aligned} \frac{I(\text{drag})}{I(\text{pressure})} &= \frac{\int_0^{t_2} \frac{1}{2} \rho u^2 dt}{\int_0^t p dt} \\ &= \frac{\frac{1}{2} \rho_{\sigma}(0) u_{\sigma}(0)^2}{p_{\sigma}(0)} \end{aligned} \quad (\text{B.23})$$

7. As a first conjecture, the sum of peak pressure impulse and drag pressure impulse is fairly independent of both height of burst and type of ground surface. As a working approximation, the sum may be taken to be the same as that for a free air wave from a bomb of twice the yield. For points in the region of Mach reflection, it can be taken separately as being equal to that of a bomb of twice the yield.



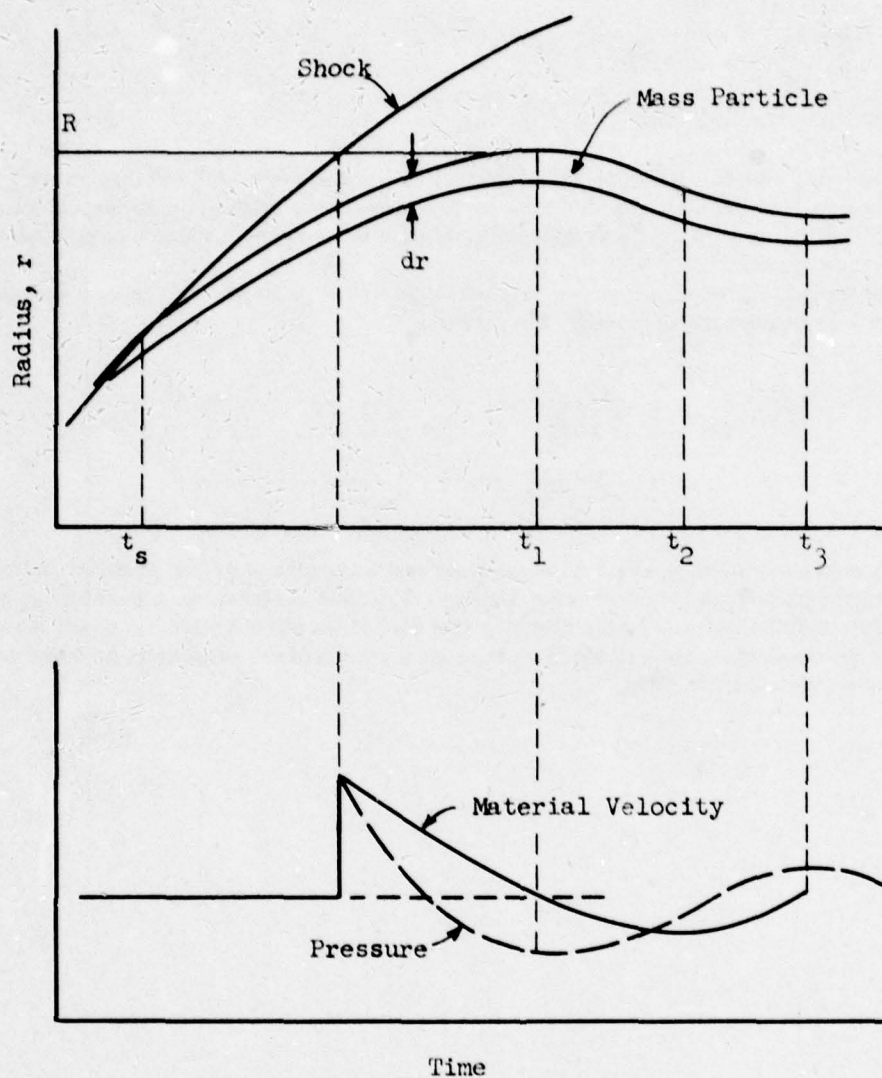


Fig. B.1—Interrelations between radius time, pressure time, and material velocity time in a shock wave.

**UNCLASSIFIED**  
330

~~SECRET RESTRICTED DATA~~

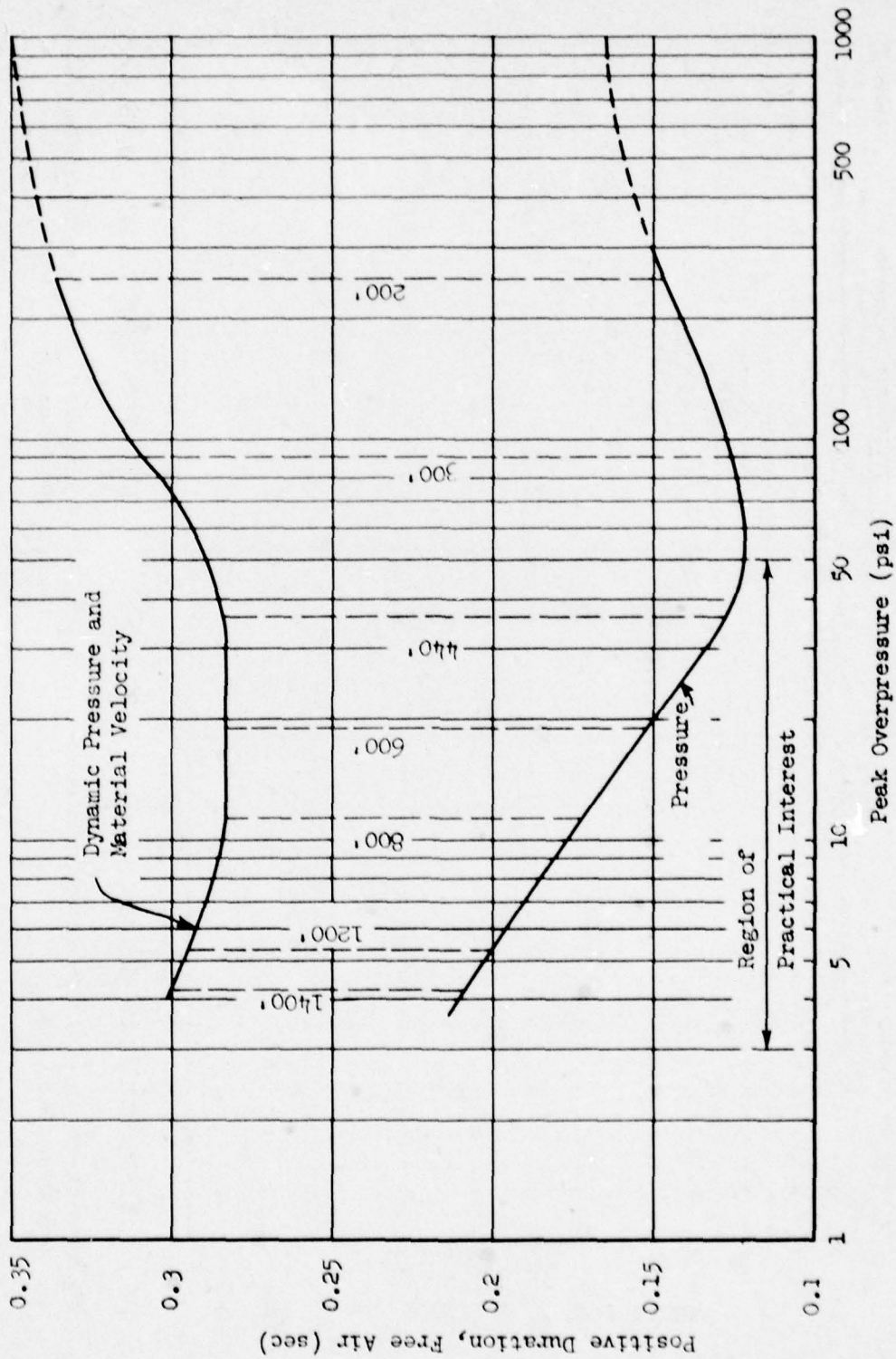


Fig. B.2—Positive durations vs peak overpressure levels, spherical wave, 1 kt, free air.

UNCLASSIFIED

UNCLASSIFIED

~~SECRET - RESTRICTED DATA~~

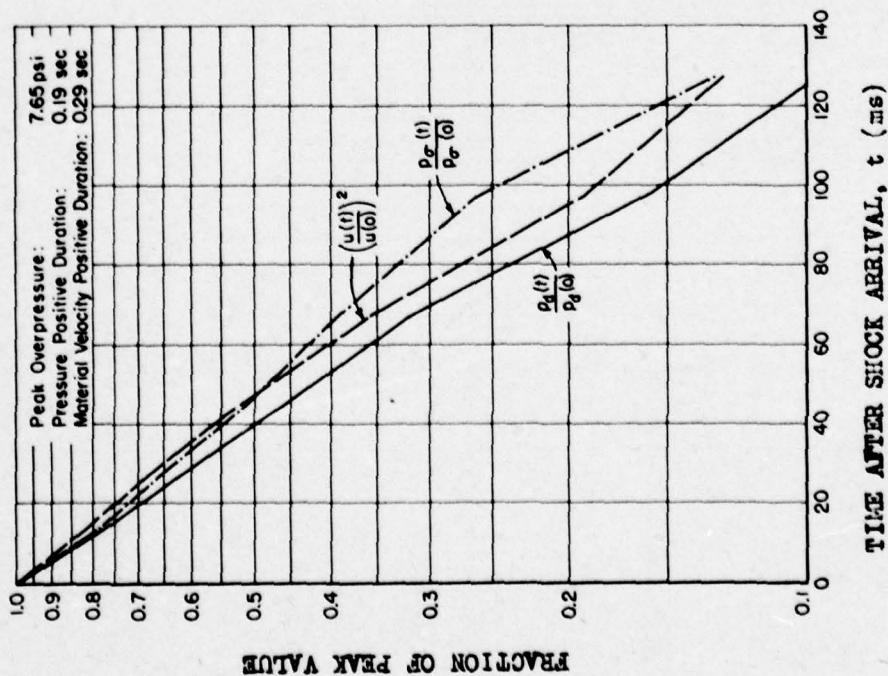


Fig. B.3—Normalized wave forms for a spherical wave in free air, 1-kt yield, 950-ft slant distance.

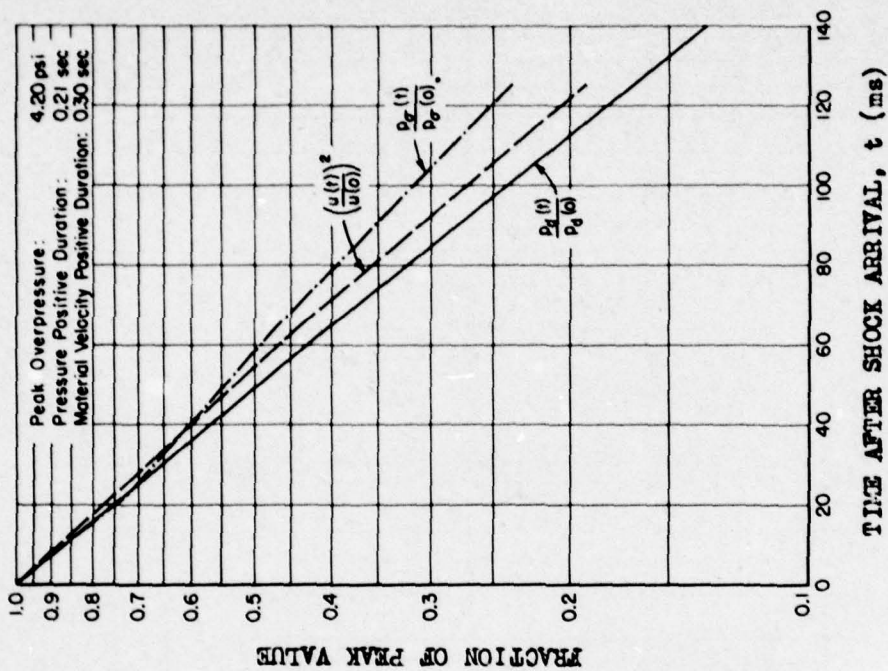


Fig. B.4—Normalized wave forms for a spherical wave in free air, 1-kt yield, 1400-ft slant distance.



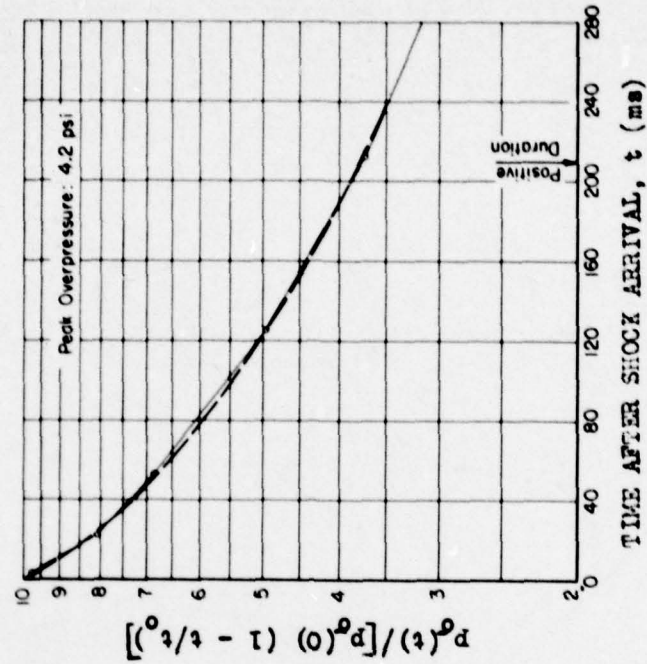


Fig. B.6—Pressure-time fit for a spherical wave in free air, using conventional form at 4.2 psi.

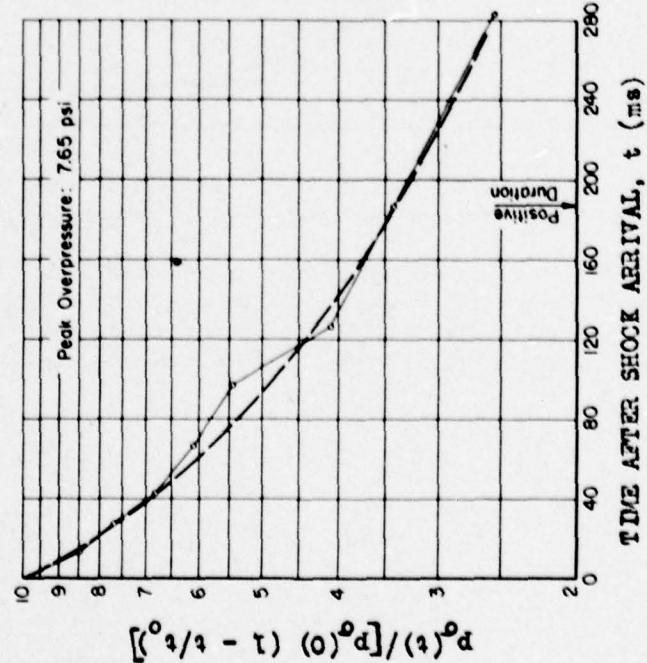


Fig. B.5—Pressure-time fit for a spherical wave in free air, using conventional form at 7.65 psi.

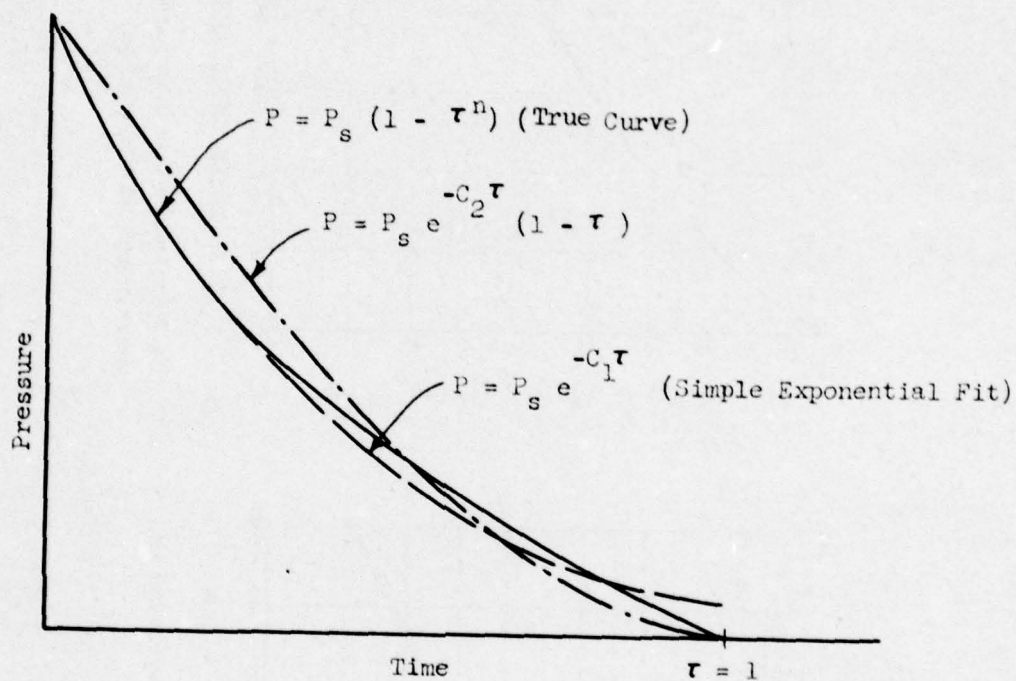


Fig. B.7—Comparisons between various empirical fits to a pressure-time curve.

$P = P_s (1 - \tau^n)$  probably closest in this case, to the actual curve.

$P = P_s e^{-C \tau}$  fits best where pressures are high, becomes low in the latter phases, but correspondingly high at  $\tau = -1$ .

$P = P_s e^{-C_2 \tau} (1 - \tau)$  is high during the first half and low during the second half.

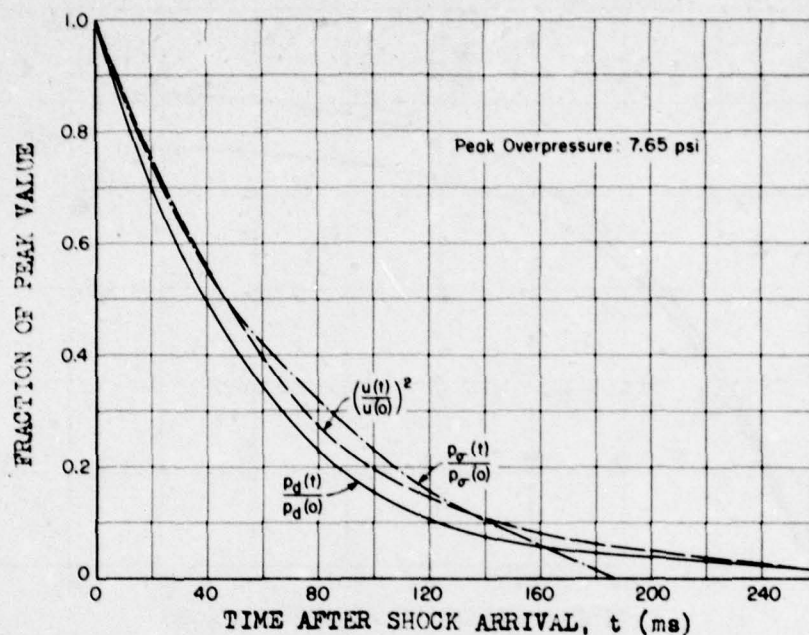


Fig. B.8—Normalized wave forms of pressure, material velocity, and dynamic pressure for a spherical wave in free air, 1-kt yield, 960-ft slant distance.

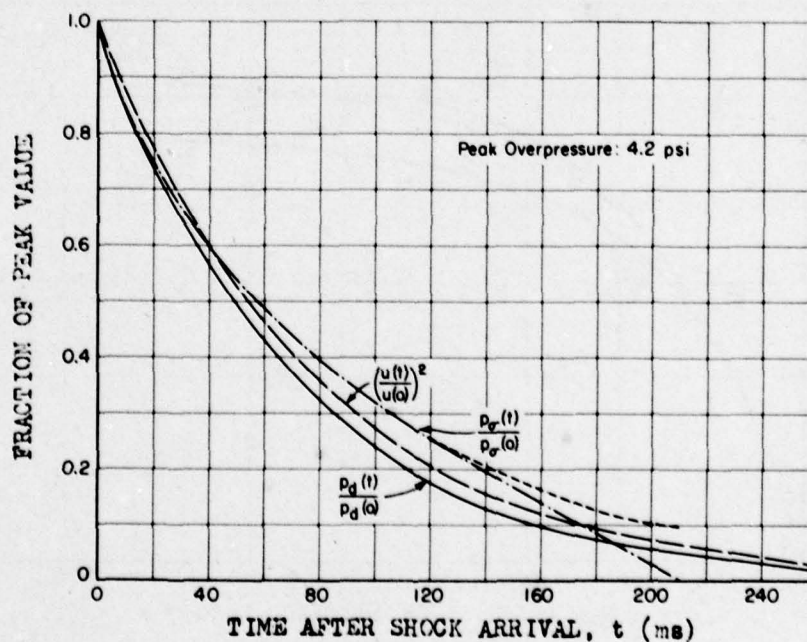


Fig. B.9—Normalized wave forms of pressure, material velocity, and dynamic pressure for a spherical wave in free air, 1-kt yield, 1400-ft slant distance.



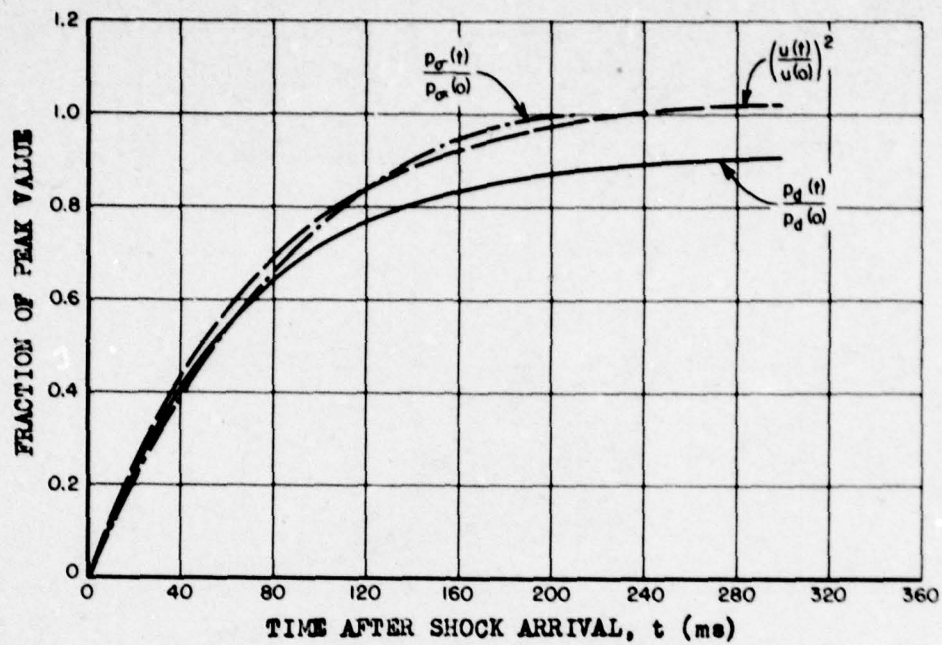


Fig. B.10—Normalized impulses for static pressure, material velocity, and dynamic pressure of Fig. B.8.

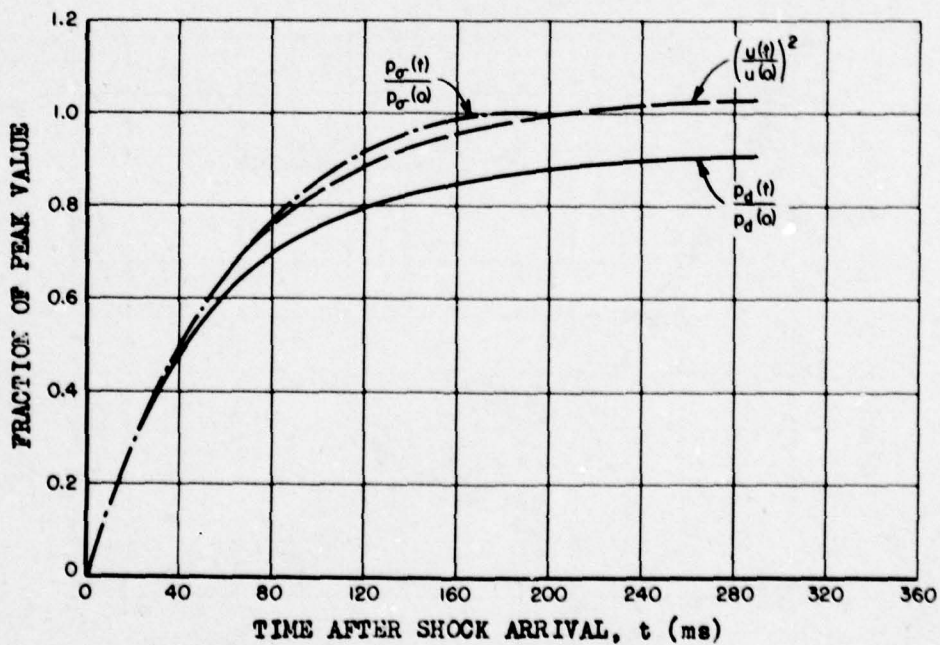


Fig. B.11—Normalized impulses for static pressure, material velocity, and dynamic pressure of Fig. B.9.

UNCLASSIFIED

~~SECRET RESTRICTED DATA~~

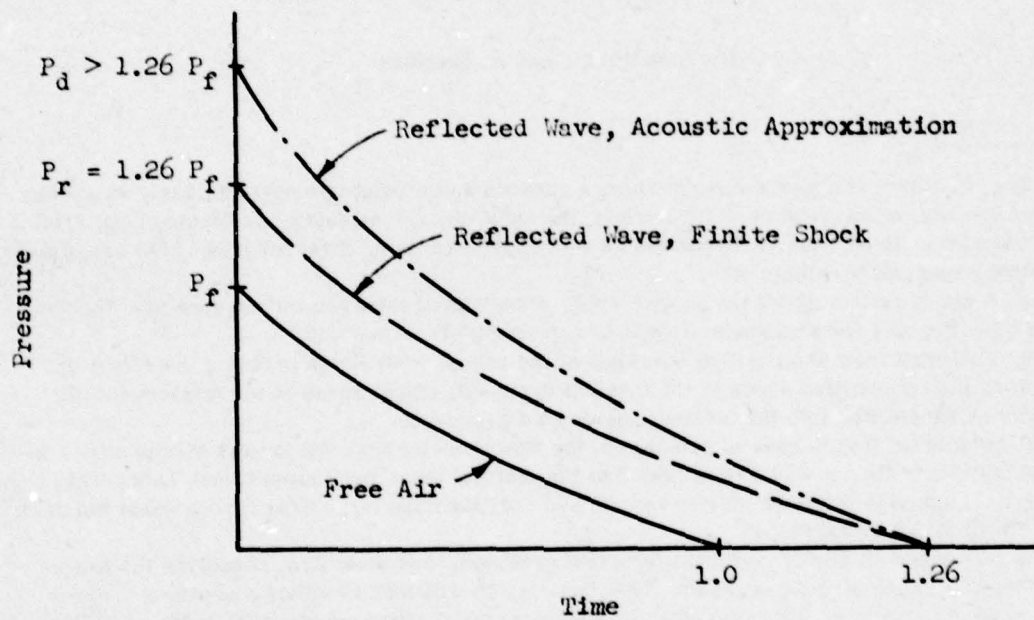


Fig. B.12—Qualitative comparison of a free air wave with its reflected wave.

## APPENDIX C

### REGULAR SHOCK REFRACTION THEORY

By T. Schiffman and A. Sherman

#### C.1 INTRODUCTION

The problems of a shock wave striking a gaseous and a solid interface obliquely have been solved already, although in the former case, the solutions are expressed in terms of material flow velocities which must be solved numerically. By combining these solutions, one can attack the very important problems of:

1. A shock reflecting off the ground which is separated from the atmosphere by a thermal layer (see Fig. C.1 for a cascade of regular refraction problems) and

2. Obtaining from the limiting solutions of the regular refraction problem the conditions for which the transmitted shock in the thermal layer will travel ahead of the triple point and become retransmitted into the incident region as a precursor.

It is believed that in case of problem 1, the flow velocity near the ground will be considerably larger than it would have been had the thermal layer been absent, and, hence, the theoretical analysis might be able to explain and correlate the large drag forces observed in Shot 10, UPSHOT-KNOTHOLE.

Before being able to treat these important problems, one must first reanalyze the basic problem of a shock striking a gaseous interface, which will lead to either a shock or a rarefaction wave being reflected from an interface and a shock being transmitted in the other medium. If the incident shock and angle are given and all the gas data are shown, there remain still five unknown quantities: the transmitted shock strength and angle, the reflected shock or rarefaction strength and angle, and the angle through which the interface turns, due to the shock impact. The first goal is therefore to obtain the necessary equations involving these quantities and solve them by engineering approximations that will eliminate the prohibitive numerical work involved in the known solutions.

Shock wave interactions at a plane boundary separating gases and solids or separating different gases  $c_0$ ,  $\gamma_0$  and  $c_0^*$ ,  $\gamma_1$  have been treated (see references 1 to 6 by Taub, von Neumann, Stoner, and Polachek). They consider a configuration either with three shocks or two shocks and a rarefaction wave as shown in Fig. C.2. An observer traveling with the triple point will see three major regions in which pressures are constant. The incident shock,  $\xi$ , strikes the gas boundary at an angle  $\alpha$ , and, if  $c_0^* \leq c_0$  and  $\gamma_0 = \gamma_1$ , a reflected shock,  $\xi$ , travels back in the incident medium (at least for the case  $\alpha = 0$ ), and a transmitted shock,  $\xi^*$ ,  $\alpha^*$  travels in the lower medium. The original boundary becomes a slipstream displaced by  $\delta$ . For  $c_0^* \geq c_0$  ( $\gamma_0 = \gamma_1$  and  $\alpha = 0$ ), the reflected shock must be replaced by a Prandtl-Meyer rarefaction model. These regimes hold until  $\alpha_t$ , at which angle they interchange. This transition angle is roughly 45 deg for moderate shock strengths. For the case of the shock striking a solid boundary, let the density approach infinity, i.e.,  $c_0^{*2} = \gamma_1(P_0/\rho_0^*) \rightarrow 0$ .



## C.2 BOUNDARY CONDITIONS FOR THE BASIC PROBLEM

The boundary conditions are that (1) the pressures do not change across the slipstream, and that (2) the flow deflected through  $\xi$  and  $\xi'$  must be parallel to that deflected through  $\xi''$ .

## C.3 BASIC EQUATIONS

Polachek and Seeger express the basic equations in terms of normalized material velocities, which lead to a large set of simultaneous transcendental equations which they solve by means of the IBM Selective Sequence Calculator. The goal is to transcribe these equations in terms of the physical measurable quantities  $\xi$ ,  $\xi'$ ,  $\xi''$ ,  $\alpha$ ,  $\alpha'$ ,  $\alpha''$  and  $\delta$ . For  $\alpha$ ,  $\xi$  and all gas characteristics known, one shall obtain five equations for the five remaining unknowns and then by elimination reduce these to two equations in two unknowns, which, similarly to the case of oblique incidence on a solid boundary, can be solved by engineering approximations.

### C.3.1 Shock Regimes

The first two basic equations state that the flow parallel to the original boundary can be calculated from the conditions behind the incidence shock and ahead of the reflected shock and that at the triple point there does not exist a component of flow normal to the original interface. They are expressed in terms of relative flow and shock front velocities which for the case of a rigid boundary,  $\delta = 0$ , reduce to the familiar oblique shock equations. The unknowns  $\delta$ ,  $\xi'$ , and  $\alpha'$  appear on the left hand side of the equations, separated from the known,  $\xi$ ,  $\alpha$  on the right side.

$$\frac{U' \cos \delta}{\sin(\alpha' + \delta)} - u' \sin \alpha' = \frac{U}{\sin \alpha} - u \sin \alpha \quad (C.1)$$

$$\frac{U' \sin \delta}{\sin(\alpha' + \delta)} - u' \cos \alpha' = u \cos \alpha \quad (C.2)$$

where

$$\begin{aligned} u &= \frac{c_0(1 - \lambda_0^2)(\xi - 1)}{\sqrt{(1 + \lambda_0^2)(\xi + \lambda_0^2)}} & u' &= \frac{c_1(1 - \lambda_0^2)(\xi' - 1)}{\sqrt{(1 + \lambda_0^2)(\xi' + \lambda_0^2)}} \\ U &= c_0 \sqrt{\frac{\xi + \lambda_0^2}{1 + \lambda_0^2}} & U' &= \frac{c_1(1 + \lambda_0^2 \xi')}{\sqrt{(1 + \lambda_0^2)(\xi' + \lambda_0^2)}} \\ c_1 &= c_0 \sqrt{\xi \frac{1 + \lambda_0^2 \xi}{\xi + \lambda_0^2}} & \lambda_0^2 &= \frac{\gamma_0 - 1}{\gamma_0 + 1} \end{aligned}$$

Equation C.3 represents the basic boundary condition that the pressure on both sides of the slipstream is the same

$$\xi'' = \xi \xi' \quad \xi' \geq 1 \quad (C.3)$$

The next equation expresses the fact that the shock front components parallel to the original interface above and below that interface must be equal.

$$\begin{aligned} \frac{U}{\sin \alpha} &= \frac{U''}{\sin \alpha''} \\ U'' &= c_0^* \sqrt{\frac{\xi'' + \lambda_1^2}{1 + \lambda_1^2}} & \lambda_1^2 &= \frac{\gamma_1 - 1}{\gamma_1 + 1} \end{aligned} \quad (C.4)$$

In case of  $\xi = \xi' = 1$ , the  $U$  and  $U^*$  of Eq. 4 reduce to  $c_0$  and  $c_0^*$ , respectively, and the ratio of incident to transmitted (reflected angle) is equal to the ratio of sound velocities. This is referred to as Snell's law for sound waves.

Finally by utilizing the fact that the component parallel to the transmitted shock is the same on both sides of the transmitted shock, one can express the normal components of material velocities in terms of the angles between the original and displaced interfaces, and one obtains

$$\frac{\tan(\alpha'' - \delta)}{\tan \alpha''} = \frac{1 + \lambda_1^2 \xi''}{\xi'' + \lambda_1^2} \quad (C.5)$$

which happens to be the ratio of densities across the transmitted shock,  $\xi''$ .

### C.3.2 Shock-rarefaction Regime

This case is similar to the one treated above, except that  $\xi' \leq 1.0$  and hence  $P_1$  and  $P_2$  must be joined by a Prandtl-Meyer rarefaction wave.

There exists an excellent treatment of Prandtl-Meyer expansion in *Introduction to Theoretical Gas Dynamics* by R. Sauer<sup>7</sup> and *Dampf Und Gasturbinen* by A. Stodola,<sup>8</sup> and we repeat here only the results.

Define  $u_1$  as the material speed behind  $\xi$  normalized with respect to the acoustic speed in that region,

$$u_1 = \left[ \frac{(U-u)^2}{c_1^2} + \frac{(U)^2}{c_1^2} \cot^2 \alpha \right]^{1/2}$$

where

$$\frac{U-u}{c_1} = \sqrt{\frac{1+\lambda_0^2}{\xi(1+\lambda_0^2)}} \quad , \quad \frac{U}{c_1} = \frac{\xi + \lambda_0^2}{\sqrt{(1+\lambda_0^2)(1+\lambda_0^2\xi)}} \xi$$

The absolute velocity vector,  $u'$ , after the expansions normalized with respect to  $c_2$  is related to  $u_1$  by

$$\xi \sqrt{2\lambda_0^2/(1+\lambda_0^2)} = \frac{1 - \lambda_0^2(u_1^2 - 1)}{1 + \lambda_0^2(u'^2 - 1)} \quad (C.6)$$

which represents our first basic equation. One other equation is derived by calculating also the change in angle between  $u_1$  and  $u'$ . In terms of this change the angle between the original and displaced interface is

$$\tan \delta = \tan \left[ \alpha + \frac{1}{\lambda_0} \tan^{-1} \left\{ \frac{\lambda_0 [\sqrt{u'^2 - 1} - \sqrt{u_1^2 - 1}]}{1 + \lambda_0^2 \sqrt{(u'^2 - 1)(u_1^2 - 1)}} \right\} - \tan^{-1} \left\{ \frac{\sqrt{u'^2 - 1} - \sqrt{u_1^2 - 1}}{1 + \sqrt{(u'^2 - 1)(u_1^2 - 1)}} \right\} - \tan^{-1} \left\{ \frac{U-u}{U} \tan \alpha \right\} \right] \quad (C.7)$$

The other three basic equations for the two-shock-rarefaction regime coincide with those for the three-shock regime and are also given by Eqs. C.3 to C.5. Care must be exercised in the interpretation of  $\xi'$  in the relation  $\xi'' = \xi \xi'$ . Here  $\xi'$  represents the pressure rise across the Prandtl-Meyer rarefaction wave,  $P_2/P_1$ , and is smaller or equal to 1.

### C.3.3 Transition Between the Two Regimes

The angle where the three-shock regime and the two-shock-rarefaction regime interchange can be computed from the limiting case  $\xi' = 1$ , either from the basic equations of the three-

shock or two-shock-rarefaction configuration. In the former case by dividing Eq. C.1 by Eq. C.2, one obtains  $\tan \delta$  which one sets equal to  $\tan \delta$  derived from Eq. C.5,

$$\tan \delta = \frac{\tan \alpha'' (1 - \eta'')}{1 + \eta'' \tan^2 \alpha''} = \frac{\tan \alpha (1 - \eta)}{1 + \eta \tan^2 \alpha} \quad (\text{C.8})$$

where

$$\eta'' = \frac{1 + \lambda_1^2 \xi''}{\xi'' + \lambda_1^2} \quad \eta = \frac{1 + \lambda_0^2 \xi}{\xi + \lambda_0^2}$$

For  $\xi' = 1$ ,  $\xi'' = \xi$  and by Eq. C.4, one obtains for  $\tan \alpha''$  in terms of  $\sin \alpha = \alpha_t$  and  $\bar{c} = c_0/c_0^*$

$$\tan \alpha'' = \frac{\sin \alpha_t}{\sqrt{\bar{c}^2 - \sin^2 \alpha_t}}$$

and by triangulation

$$\tan \alpha = \frac{\sin \alpha_t}{\sqrt{1 - \sin^2 \alpha_t}}$$

Substituting these expressions for  $\tan \alpha''$  and  $\tan \alpha$  into Eq. C.8, one obtains a quadratic expression for  $\sin^2 \alpha_t$

$$4\gamma_1(\xi^2 - 1) \left[ \frac{\gamma_0 \alpha_1}{\gamma_1 \alpha_0 a} - 1 \right] \sin^4 \alpha_t + \left[ \alpha_0 \alpha_1 \left( a - \frac{1}{a} \right) + 4(\gamma_1 - \gamma_0)(\xi^2 - 1) \right] \sin^2 \alpha_t + \alpha_0(\alpha_0 - \alpha_1 a) = 0 \quad (\text{C.9})$$

where

$$\alpha_0 = (\gamma_0 + 1) \xi + \gamma_0 - 1$$

$$\alpha_1 = (\gamma_1 + 1) \xi + \gamma_1 - 1$$

and

$$a = \bar{c}^2 \frac{\gamma_1}{\gamma_0}$$

For  $\gamma_1 = \gamma_0$

$$\sin^4 \alpha_t - \left[ \frac{\alpha_0^2(a+1)}{4\gamma_0(\xi^2-1)} \cdot \sin^2 \alpha_t \right] + \frac{a \alpha_0^2}{4\gamma_0(\xi^2-1)} = 0 \quad (\text{C.9})$$

This expression is identical with Eq. 14, reference 6 and could have also been obtained by combining Eqs. C.4, C.5, C.6, and C.7 from the two-shock-rarefaction regime by letting  $\xi' = 1$ . For this case one obtains from Eq. C.6

$$u_1 = u'$$

and hence by Eq. C.7 for

$$\tan \delta = \tan \left( \alpha - \tan^{-1} \frac{U-u}{U} \tan \alpha \right)$$



or

$$\tan \delta = \frac{\tan \alpha (1 - \eta)}{1 + \eta \tan^2 \alpha}$$

which is precisely Eq. C.8, and, since Eqs. C.4 and C.5 still apply, it must lead to the same value of  $\sin^2 \alpha_1$  as given by Eq. C.9

We stated previously that if  $\gamma_0 = \gamma_1$  and  $\bar{c} = c_0/c_0^* \geq 1$ , the three-shock configuration must prevail for  $\alpha = 0$ , and  $\bar{c} \leq 1$ , the two-shock-rarefaction regime must exist. We are now in a position from Eq. C.9 to deduce the criterion for the general case  $\gamma_1 \neq \gamma_0$  by considering a transition to occur at  $\alpha_1 = 0$  and thus obtain

$$\alpha_0 = a\alpha_1 \quad (C.10)$$

Since for a solid boundary,  $\bar{c} = \infty$  and hence  $a$  becomes infinite and a reflected shock travels away from the reflected boundary

$$\alpha_0 < a\alpha_1$$

and

$$\alpha_0 > a\alpha_1$$

represent the conditions for a reflected shock and a reflected rarefaction wave respectively to occur at  $\alpha = 0$ .

In order that supersonic flow normal to the reflected wave exist in both configurations, we must also have  $u_1$  (Fig. C.2) at least equal to 1 or

$$u_1^2 = \left[ \frac{(U-u)^2}{c_1^2} + \frac{(U)^2}{c_1^2} \cot^2 \alpha_s \right] = 1$$

or  $\alpha \leq \alpha_s$  with

$$\tan \alpha_s = \frac{U}{\sqrt{c_1^2 - (U-u)^2}} = (\xi + \lambda_0^2) \frac{1}{\sqrt{(1 + \lambda_0^2 \xi)(\xi - 1)}} \quad (C.11)$$

The final limitation on the three-shock solution is of course that the transmitted angle be real. From Eq. C.4

$$\sin^2 \alpha'' = \frac{U'^2}{U^2} \sin^2 \alpha = \frac{1}{c^2} \frac{(\xi'' + \lambda_1^2)}{(\xi + \lambda_0^2)} \frac{(1 + \lambda_0^2)}{(1 + \lambda_1^2)} \sin^2 \alpha_L \leq 1$$

or

$$\sin^2 \alpha_L \leq \bar{c}^2 \frac{(1 + \lambda_1^2)}{(1 + \lambda_0^2)} \frac{(\xi + \lambda_0^2)}{(\xi'' + \lambda_1^2)}$$

Since  $\xi'' > \xi$  for the three-shock configuration, the largest value of  $\sin^2 \alpha_L$  will occur for  $\xi'' = \xi$  and therefore

$$\sin^2 \alpha_L \leq \bar{c}^2 \frac{(1 + \lambda_1^2)(\xi + \lambda_0^2)}{(1 + \lambda_0^2)(\xi + \lambda_1^2)} = a \frac{\alpha_0}{\alpha_1} \quad (C.12)$$

At this angle a precursor will start to form.

### C.3.4 Limiting Solutions for Head-on Reflection

For the limiting case of head-on reflection, we must set  $\alpha = \alpha' = \alpha'' = 0$  in all basic equations. In addition,  $\delta = 0$ , since only a displacement of the original boundary but no rotation takes place. To evaluate the various limits it is best first to eliminate  $\delta$  between Eqs. C.1, C.2, and C.5 for the case of the three-shock configuration. One obtains from Eqs. C.1 and C.2

$$\tan \delta = \frac{\sin \alpha' (u \cos \alpha - u' \cos \alpha')}{U' - u \cos \alpha' \cos \alpha + u' \cos^2 \alpha'} = \frac{\sin \alpha (u \cos \alpha - u' \cos \alpha')}{U - u' \sin \alpha' \sin \alpha - u \sin^2 \alpha} \quad (\text{C.13})$$

whereas, by Eq. C.8

$$\tan \delta = \frac{\tan \alpha'' (1 - \eta'')}{1 + \eta'' \tan^2 \alpha''}$$

Equating Eqs. C.8 and C.13 and dividing by  $\tan \alpha''$ , one obtains in the limit  $\alpha = \alpha' = \alpha'' = 0$

$$\frac{u - u'}{U} = 1 - \eta'' = \frac{u''}{U} \bar{c} \sqrt{\frac{(\xi + \lambda_0^2)(1 + \lambda_1^2)}{(\xi'' + \lambda_1^2)(1 + \lambda_0^2)}} \quad (\text{C.14})$$

But according to Eq. C.4 the quantity multiplying  $u''/U$  equals unity for the limit  $\alpha = \alpha' = 0$  and hence

$$u - u' = u'' \quad (\text{C.15})$$

where

$$u'' = \frac{c_0^* (1 - \lambda_1^2)(\xi'' - 1)}{\sqrt{(1 + \lambda_1^2)(\xi'' + \lambda_1^2)}}$$

represents the normalized particle flow velocity behind the transmitted shock. Therefore according to Eq. C.15, the sum of the incidence, reflected, and transmitted flow velocities is equal to zero.

For a reflected shock wave  $u'$  is given by Eq. C.2 and for a rarefaction wave one obtains  $u'$  by taking the limit of Eq. C.7 for  $\alpha = 0$

$$\tan \delta = \tan \left\{ \alpha + \frac{1 - \lambda_0^2}{\lambda_0^2} \frac{c_1}{U} \left[ 1 - \xi' [\lambda_0^2 / (1 + \lambda_0^2)] \right] \right\} \tan \alpha - \frac{U - u}{U} \tan \alpha$$

or by combining with Eq. C.14

$$\frac{\tan \delta}{\tan \alpha''} = \frac{u''}{U} = \frac{u - c_1 \frac{1 - \lambda_0^2}{\lambda_0^2} \left[ 1 - \xi' [\lambda_0^2 / (1 + \lambda_0^2)] \right]}{U}$$

Expressing the right-hand side formally in terms of  $u'$  analogous to the case of the reflected shock, one obtains

$$u - u' = u''$$

where  $u'$  is the velocity behind the reflected rarefaction wave given by

$$u' = \frac{2c_1}{\gamma_0 - 1} \left[ 1 - \xi' [(\gamma_0 - 1)/2\gamma_0] \right] = \bar{c}_1 \left[ \frac{1 - \lambda_0^2}{\lambda_0^2} \left[ 1 - \xi' [\lambda_0^2 / (1 + \lambda_0^2)] \right] \right] \quad (\text{C.16})$$

The cases of head-on reflection assume great importance because Polachek's results (Eqs. C.4 and C.6) indicate that for other angles there exists little deviation in  $\xi'$  and hence in  $\xi''$  from their head-on values. Hence any possible engineering approximations should be based on the head-on values.

#### C.4 ENGINEERING APPROXIMATIONS

To derive useful engineering approximations, it is convenient to rewrite the five basic equations as follows:

For the three-shock regime

$$\tan \delta = \frac{u \cos \alpha - u' \cos \alpha'}{(U/\sin \alpha) - u \sin \alpha - u' \sin \alpha'} = \frac{u'' \cos \alpha''}{(U/\sin \alpha) - u'' \sin \alpha''} \quad (\text{C.17, 18a})$$

$$U' - U \frac{\sin \alpha'}{\sin \alpha} - u \cos (\alpha + \alpha') + u' \cos 2\alpha' = 0 \quad (\text{C.19a})$$

For the two-shock-rarefaction regime,

$$\tan \delta = \tan \left\{ \epsilon + \frac{1}{\lambda_0} \tan^{-1} \frac{\lambda_0(\phi - \psi)}{1 + \lambda_0^2 \phi \psi} - \tan^{-1} \left( \frac{\phi - \psi}{1 + \phi \psi} \right) \right\} = \frac{u'' \cos \alpha''}{(U/\sin \alpha) - u'' \sin \alpha''}$$

where

$$\begin{aligned} \phi &= \frac{1}{\lambda_0} \left[ (1 + \lambda_0^2 \psi^2) \xi' - 2\lambda_0^2 / (1 + \lambda_0^2) - 1 \right]^{1/2} \\ \psi &= \frac{1}{\lambda_1} \left[ (U - u)^2 + U^2 \cot^2 \alpha - \lambda_1^2 \right]^{1/2} \\ \epsilon &= \alpha - \tan^{-1} \left\{ \frac{U - u}{U} \tan \alpha \right\} \end{aligned} \quad (\text{C.17, 18, 19b})$$

For both regimes

$$\sin \alpha'' = \sqrt{\frac{\alpha_1}{a\alpha_0}} \sin \alpha \sqrt{\frac{\xi'' + \lambda_1^2}{\xi + \lambda_1^2}} \quad (\text{C.20})$$

and

$$\xi'' = \xi \xi' \quad (\text{C.21})$$

##### C.4.1 Three-shock Regimes

###### C.4.1.1 Approximations Near $\alpha = 0$

(a) The Reflected Shock,  $\xi'$ . From Eq. C.17 for  $\alpha = \alpha' = \alpha'' = 0$ , one obtains

$$u - u' = u'' \quad (\text{C.22})$$

or

$$\xi - 1 - \sqrt{\xi(1 + \xi\lambda_0^2)} \frac{\xi' - 1}{\sqrt{\xi' + \lambda_0^2}} = \sqrt{\frac{\alpha_0(\xi + \lambda_1^2)}{a\alpha_1}} \frac{\xi'' - 1}{\sqrt{\xi'' + \lambda_1^2}}$$

UNCLASSIFIED



Two types of approximations are considered, one for which  $\sqrt{(\alpha_0/a\alpha_1)} \sim 1$ , i.e., the gases are not too dissimilar and the other, where  $a$ , and hence the temperature, is so large that the parameter  $\sqrt{(\alpha_0/a\alpha_1)}$  is small enough to approach the case of a rigid boundary. For the former, one assumes that

$$\xi' = 1 + \Delta\xi'_0 \quad (C.23)$$

and obtains by Eq. 7

$$\Delta\xi'_0 = \frac{(\xi - 1) \left(1 - \sqrt{\frac{\alpha_0}{a\alpha_1}}\right)}{\frac{1}{2} \left(1 + \frac{(1 + \lambda_1^2)}{\xi + \lambda_1^2}\right) \xi \sqrt{\frac{\alpha_0}{a\alpha_1}} + \sqrt{\frac{(1 + \xi\lambda_0^2)\xi}{1 + \lambda_0^2}}} \quad (C.24)$$

which reduces for the case  $\gamma_0 = \gamma_1 = 1.4$  to

$$\Delta\xi'_0 = \frac{(\xi - 1)(1 - c_0^*/c_0)}{\xi \frac{c_0^*}{c_0} \frac{(3\xi + 4)}{(1 + 6\xi)} + \sqrt{\frac{\xi(6 + \xi)}{7}}}$$

For the case of the nearly rigid boundary, one assumes

$$\xi' = \xi'_0 - \Delta\xi'_0 \quad (C.25)$$

where  $\xi'_0$  is the solution to Eq. C.6 for a  $\infty$

$$\xi'_0 = \xi - \lambda_0^2 \frac{(\xi - 1)^2}{1 + \xi\lambda_0^2} \quad (C.26)$$

With the substitution of Eq. C.25 into C.22 and dropping the higher order terms, one obtains

$$\Delta\xi'_0 = \frac{2 \sqrt{\frac{\alpha_0}{a\alpha_1}} \sqrt{\frac{\xi + \lambda_1^2}{\xi(1 + \xi\lambda_0^2)}} \frac{\xi\xi'_0 - 1}{\sqrt{\xi\xi'_0 + \lambda_1^2}}}{\frac{1}{\sqrt{\xi'_0 + \lambda_0^2}} \left(1 + \frac{1 + \lambda_0^2}{\xi'_0 + \lambda_0^2}\right) + \sqrt{\frac{\alpha_0}{a\alpha_1}} \times \sqrt{\frac{(\xi + \lambda_1^2)\xi}{(1 + \xi\lambda_0^2)(\xi\xi'_0 + \lambda_1^2)}} \left(1 + \frac{1 + \lambda_1^2}{\xi\xi'_0 + \lambda_1^2}\right)} \quad (C.27)$$

(b) The Reflected Angle,  $\alpha'$ . Since (by Eqs. C.17, 18a) the slope at the origin  $d\xi'/d\alpha = 0$  at  $\alpha = 0$ , it is expected that the approximations (Eq. C.3 and C.12) will hold for a considerable range of finite  $\alpha$ . However,  $\alpha' = 0$  only at  $\alpha = 0$  and hence even the first order correction must involve all basic equations.

Squaring Eqs. C.1 and C.2 and adding gives

$$\frac{U'^2}{\sin^2(\alpha' + \delta)} + u'^2 - 2 U' u = \frac{U^2}{\sin^2 \alpha} + u^2 - 2 U u$$

or

$$U'^2 \cot^2(\alpha' + \delta) + (U' - u')^2 = U^2 \cot^2 \alpha + (U - u)^2 \quad (C.28)$$

Let

$$\alpha' + \delta = \alpha + \Delta\alpha' \quad (C.29)$$

UNCLASSIFIED

~~SECRET RESTRICTED DATA~~ UNCLASSIFIED

an assumption well borne out by Polachek's and Stoner's results (references 4 and 6); substituting Eq. C.19a into Eq. C.17 gives for  $\Delta\alpha'$ , if higher order terms are neglected

$$\Delta\alpha' = (\tan \alpha/2) \left\{ \frac{(U' - u')^2 - (U - u)^2 + \cot^2 \alpha (U'^2 - U^2)}{[U'^2 - (U' - u')^2 + (U - u)^2 + U^2 \cot^2 \alpha]} \right\} \quad (C.30)$$

or in view of the definition of  $u, U, u', U'$  one obtains for  $\Delta\alpha'$

$$\Delta\alpha' = \frac{(\xi\xi' - 1) \tan \alpha}{2} \left\{ \frac{[\lambda_0^4(1 + \xi\xi') + \lambda_0^4\xi' + \xi(2\lambda_0^4 - 1)] + \tan^2 \alpha [(1 + \xi\lambda_0^2)(\xi' + \lambda_0^2)]}{[(\xi + \lambda_0^2)(\xi' + \lambda_0^2)] + \tan^2 \alpha (1 + \lambda_0^2\xi)[\lambda_0^2(1 + \xi\xi') + \xi^2\xi(\lambda_0^4 - 1) + \xi + \xi']} \right\} \quad (C.31)$$

Having obtained  $\Delta\alpha'$ , one can solve for  $\delta$  from Eq. C.18a and obtain for the first approximation for  $\alpha'$  by Eq. C.29

$$\alpha' = \alpha'_0 + \Delta\alpha - \tan^{-1} \{(u'' \cos \alpha'')/(U/\sin \alpha) - u'' \sin \alpha''\} \quad (C.32)$$

In terms of this value for  $\alpha' = \alpha'_0$ , one can obtain by Eq. C.19a a second correction

$$\xi' = \xi'_1 = \xi'_0 + \Delta_1\xi' \quad (C.33)$$

Substituting Eqs. C.32 and C.33 into Eq. C.18a and neglecting higher terms of  $\Delta_1\xi'$  gives

$$\Delta_1\xi' = \frac{2(\xi'_0 + \lambda_0^2)}{[\lambda_0^2\xi'_0 + 2\lambda_0^4 - 1] + [(1 - \lambda_0^2)(\xi'_0 + 2\lambda_0^2 + 1)] \cos 2\alpha'_0} \left\{ \frac{\xi'_0 + \lambda_0^2}{\xi(1 + \lambda_0^2\xi)} \left[ (\xi + \lambda_0^2) \frac{\sin \alpha'_0}{\sin \alpha} \right. \right. \\ \left. \left. + (1 - \lambda_0^2)(\xi - 1) \cos (\alpha + \alpha'_0) \right] - (1 + \lambda_0^2\xi'_0) - (\xi'_0 - 1)(1 - \lambda_0^2) \cos 2\alpha'_0 \right\} \quad (C.34)$$

which for the case of  $\gamma_0 = 1.4$  reduces to

$$\Delta_1\xi' = \frac{6\xi'_0 + 1}{3\xi'_0 - 17 + 5(18\xi'_0 + 19) \cos 2\alpha'_0} \left\{ \sqrt{\frac{6\xi'_0 + 1}{\xi(6 + \xi)}} \left[ (6 + \xi) \frac{\sin \alpha'_0}{\sin \alpha} + 5(\xi - 1) \cos (\alpha'_0 + \alpha) \right] \right. \\ \left. - (6 + \xi'_0) - 5(\xi'_0 - 1) \cos 2\alpha'_0 \right\} \quad (C.35)$$

With this improved value for  $\xi'$ , one can by Eqs. C.18a, C.29, and C.30 find a second approximation for  $\alpha'$  and thus reiterate Eqs. C.17a and C.18a until one obtains a convergence for both  $\xi'$  and  $\alpha'$ . Since Eqs. C.17a and C.18a were obtained by the rigorous elimination of all the other variables, this must represent the exact solution to the three-shock problem. Since for  $\alpha$  up to  $\alpha_t$  the value of  $\xi'$  does not differ appreciably from the head-on value,  $\xi'_0$ , the quantity  $\Delta_1\xi'$  from Eq. C.35 will be quite often negligibly small, and hence the first approximations for  $\xi'$  and  $\alpha'$  suffice.

#### C.4.1.2 Approximations Near $\alpha = \alpha_t$

(a) The Reflected Shock,  $\xi'$ . This approximation is obtained by assuming

$$\xi' = 1 + \Delta\xi'_t \quad (C.36)$$

and

$$\alpha' = \alpha'_t = \Delta\alpha'_t \quad (C.37)$$

Substitution into Eqs. C.18a and C.19a and neglecting second order terms gives

$$\tan \delta = X_3 + \Delta \xi'_t X_t = X_1[(\xi + 1) + \xi \Delta \xi'_t X_2] \quad (C.38)$$

where

$$X_1 = \frac{\frac{c_0^*(1-\lambda_1^2)}{\sqrt{(1+\lambda_1^2)(\xi+\lambda_1^2)}} \sin \alpha \sqrt{1 - \frac{\alpha_1}{a\alpha_0} \sin^2 \alpha}}{c_0 \sqrt{\frac{\xi+\lambda_0^2}{1+\lambda_0^2}} - c_0^* \sqrt{\frac{\alpha_1}{a\alpha_0} \sin^2 \alpha} \frac{(\xi-1)(1-\lambda_1^2)}{\sqrt{(1+\lambda_1^2)(\xi+\lambda_1^2)}}}$$

for  $\gamma_0 = \gamma_1 = 1.4$

$$X_1 = \frac{\frac{5c_0^*}{c_0} \sin \alpha \sqrt{1 - \left(\frac{c_0^*}{c_0}\right)^2 \sin^2 \alpha}}{1 + 6\xi - 5(\xi-1)\left(\frac{c_0^*}{c_0}\right)^2 \sin^2 \alpha}$$

$$X_2 = 1 - \frac{\xi-1}{2(\xi+\lambda_1^2)\left(1 - \frac{\alpha}{a\alpha_0} \sin^2 \alpha\right)} + \frac{\sqrt{\frac{\alpha_1}{a\alpha_0}} (\xi-1) \sin \alpha}{\sqrt{1 - \frac{\alpha_1}{a\alpha_0} \sin^2 \alpha}} X_1$$

for  $\gamma_0 = \gamma_1 = 1.4$

$$X_2 = 1 - \frac{3(\xi-1)}{(1+6\xi)\left[1 - \left(\frac{c_0^*}{c_0}\right)^2 \sin^2 \alpha\right]} + \frac{5\left(\frac{c_0^*}{c_0}\right)^2 (\xi-1) \sin^2 \alpha}{1 + 6\xi - 5(\xi-1)\left(\frac{c_0^*}{c_0}\right)^2 \sin^2 \alpha}$$

$$X_3 = \frac{(1-\lambda_0^2)(\xi-1) \sin 2\alpha}{2[(\xi+\lambda_0^2) - (1-\lambda_0^2)(\xi-1) \sin^2 \alpha]}$$

for  $\gamma_0 = \gamma_1 = 1.4$

$$X_3 = \frac{5(\xi-1) \sin 2\alpha}{2[1 + 6\xi - 5(\xi-1) \sin^2 \alpha]}$$

$$X_4 = \frac{(1-\lambda_0^2) \sin \alpha \sqrt{\xi(1+\xi\lambda_0^2)}}{\sqrt{1+\lambda_0^2} [(\xi+\lambda_0^2) - (1-\lambda_0^2)(\xi-1) \sin^2 \alpha]^2} \left\{ (1-\lambda_0^2)(\xi-1) \frac{\sin 2\alpha}{2} \sin \alpha'_t \right. \\ \left. - [\xi + \lambda_0^2 - (1-\lambda_0^2)(\xi-1) \sin^2 \alpha] \cos \alpha'_t \right\}$$

for  $\gamma_0 = \gamma_1 = 1.4$

$$X_4 = \frac{5 \sin \alpha \sqrt{\xi(6+\xi)} \left\{ 5(\xi-1) \cdot \frac{\sin 2\alpha}{2} \sin \alpha'_t - [1 + 6\xi - 5(\xi-1) \sin^2 \alpha] \cos \alpha'_t \right\}}{\sqrt{7} [1 + 6\xi - 5(\xi-1) \sin^2 \alpha]^2}$$

where  $\alpha'_t$  is the solution to the quadratic equation, C.19a, for  $\xi' = 1$ ,  $\alpha = \alpha_t$ ,  $\alpha' = \alpha'_t$ , i.e., for  $y \Delta \cos \alpha'_t$

$$y^2 - y \left( \frac{2c_t u \cos \alpha_t \sin^2 \alpha_t}{U^2 - 2Uu \sin^2 \alpha_t + u^2 \sin^2 \alpha_t} \right) + \frac{c_t^2 \sin^2 \alpha_t - u^2 \sin^4 \alpha_t + 2Uu \sin^2 \alpha_t - U^2}{U^2 - 2Uu \sin^2 \alpha_t + u^2 \sin^2 \alpha_t} = 0$$



or

$$y^2 - \left[ \frac{2 \sin^2 \alpha_t \cos \alpha_t (1 - \lambda_0^2)(\xi - 1) \sqrt{\xi(1 + \lambda_0^2\xi)(1 + \lambda_0^2)}}{(\xi + \lambda_0^2)^2 - (1 - \lambda_0^2)(\xi^2 - 1) \sin^2 \alpha_t} \right] y + \frac{\sin^2 \alpha_t [\xi^2(2 - \lambda_0^2 + \lambda_0^4) + \xi(-1 + 5\lambda_0^2 - 2\lambda_0^4) + 2\lambda_0^2(\lambda_0^2 - 1)] - (1 - \lambda_0^2)^2 (\xi - 1)^2 \sin^4 \alpha_t - (\xi + \lambda_0^2)^2}{(\xi + \lambda_0^2)^2 - (1 - \lambda_0^2) \sin^2 \alpha_t} = 0 \quad (C.39)$$

which for  $\gamma_0 = 1.4$  becomes

$$y^2 - \frac{10 \sin^2 \alpha_t \cos \alpha_t (\xi - 1) \sqrt{7\xi(6 + \xi)}}{(1 + 6\xi)^2 - 35(\xi^2 - 1) \sin^2 \alpha_t} y + \frac{\sin^2 \alpha_t (67\xi^2 - 8\xi - 10) - 25(\xi - 1)^2 \sin^4 \alpha_t - (1 + 6\xi)^2}{(1 + 6\xi)^2 - 35(\xi^2 - 1) \sin^2 \alpha_t} = 0$$

Hence by Eq. C.38

$$\Delta \xi'_t = \frac{X_1(\xi - 1) - X_3}{X_4 - X_1 X_2 \xi}$$

for  $\Delta \xi'_t = 0$ ,  $X_1(\xi - 1) = X_3$  gives the transition equation, Eq. C.9.

(b) The Reflected Angle,  $\alpha'$ . Having obtained  $\Delta \xi'_t$ , one can solve for  $\Delta \alpha'_t$  by substituting Eqs. C.36 and C.37 into Eq. C.19a with the result

$$\Delta \alpha'_t = \frac{N}{D} \quad (C.40)$$

where

$$N = (\xi + \lambda_0^2) \sin \alpha'_t + (1 - \lambda_0^2)(\xi - 1) \sin \alpha \cos (\alpha + \alpha'_t) - \sqrt{\xi(1 + \lambda_0^2\xi)} \left[ \sqrt{1 + \lambda_0^2} + \frac{2\lambda_0^2 - 1}{2\sqrt{1 + \lambda_0^2}} \Delta \xi'_t + \frac{1 - \lambda_0^2}{\sqrt{1 + \lambda_0^2}} \Delta \xi'_t \cos 2\alpha'_t \right]$$

$$D = (\xi + \lambda_0^2) \cos \alpha'_t + \sin \alpha \sin (\alpha + \alpha'_t)(1 - \lambda_0^2)(\xi - 1)$$

For  $\gamma_0 = \gamma_1 = 1.4$

$$6N = (6\xi + 1) \sin \alpha'_t + 5(\xi - 1) \sin \alpha \cos (\alpha + \alpha'_t) - \sqrt{\frac{\xi(6 + \xi)}{7}} \left[ 7 + \Delta \xi'_t \frac{15 \cos 2\alpha'_t - 1}{3} \right]$$

$$6D = (6\xi + 1) \cos \alpha'_t + 5(\xi - 1) \sin \alpha \sin (\alpha + \alpha'_t)$$

#### C.4.2 Two-shock Rarefaction Regime

Since the reflected angle  $\alpha'$  does not appear in the basic equations, this section is only concerned with approximations for the reflected shock strength,  $\xi'$ .

##### C.4.2.1 Approximations Near $\alpha = 0$

From Eqs. C.18b and C.19b for  $\alpha = \alpha'' = 0$ , one obtains

$$u - u' = u'' \quad (C.41)$$

where

$$u' = \frac{1 - \lambda_0^2}{\lambda_0^2} c_1 \left[ 1 - \xi' [\lambda_0^2 / (1 + \lambda_0^2)] \right] \quad (C.42)$$

and, hence, instead of Eq. C.23, one obtains now

$$\xi - 1 - \frac{\sqrt{\xi(1 + \lambda_0^2\xi)(1 + \lambda_0^2)}}{\lambda_0^2} \left[ 1 - \xi' [\lambda_0^2 / (1 + \lambda_0^2)] \right] = \sqrt{\frac{\alpha_0(\xi + \lambda_1^2)}{a\alpha_1}} \frac{\xi'' - 1}{\sqrt{\xi'' + 2}} \quad (C.43)$$

whereby Eq. C.5

$$\xi'' = \xi\xi' \leq 1$$

One approximation to be considered is again for similar gases, or

$$\sqrt{\frac{\alpha_0}{a\alpha_1}} \sim 1$$

hence, take

$$\xi' = 1 - \Delta\xi'_0 \quad (C.44)$$

which, when substituted into Eq. C.43 gives

$$\Delta\xi'_0 = \frac{\lambda_0^2(\xi - 1) - \sqrt{\xi[(1 - \lambda_0^2)/(1 + \lambda_0^2)](1 + \xi\lambda_0^2)(1 + \lambda_0^2)(\xi[\lambda_0^2/(1 + \lambda_0^2)] - 1)}}{\lambda_0^2\xi \left[ \left( \sqrt{\frac{\alpha_0}{a\alpha_1}} \cdot \frac{\xi + \lambda_1^2}{1 + \lambda_1^2} \right) + \sqrt{\frac{\xi[(1 - \lambda_0^2)/(1 + \lambda_0^2)](1 + \xi\lambda_0^2)}{1 + \lambda_0^2}} \right]} \quad (C.45)$$

For  $\gamma_0 = \gamma_1 = 1.4$ , Eq. C.45 reduces to

$$\Delta\xi'_0 = \frac{(\xi - 1) \left( \frac{c_0^*}{c_0} - 1 \right)}{\xi \frac{c_0^*}{c_0} \frac{(3\xi + 4)}{6\xi + 1} + \sqrt{\frac{\xi(6 + \xi)}{7}}}$$

Note that the correction term for the two-shock-rarefaction scheme coincides except for sign with that of the three-shock system.

Finally for  $\sqrt{\alpha_0/a\alpha_1} \gg 1$ , assume  $\xi' = (1/\xi) + \Delta\xi'$  and obtain from Eq. C.43

$$\Delta\xi'_0 = \frac{\lambda_0^2(\xi - 1) - \sqrt{\xi[(1 - \lambda_0^2)/(1 + \lambda_0^2)](1 + \xi\lambda_0^2)(1 + \lambda_0^2)(\xi[\lambda_0^2/(1 + \lambda_0^2)] - 1)}}{\lambda_0^2\xi \left[ \sqrt{\frac{\alpha_0}{a\alpha_1}} \frac{\xi + \lambda_1^2}{1 + \lambda_1^2} + \sqrt{\frac{\xi[(1 - \lambda_0^2)/(1 + \lambda_0^2)](1 + \xi\lambda_0^2)}{1 + \lambda_0^2}} \right]} \quad (C.46)$$

which for  $\gamma_0 = \gamma_1 = 1.4$  reduces to

$$\Delta\xi'_0 = \frac{\xi - 1 - \sqrt{7\xi^{3/2}(6 + \xi)(\xi^{1/2} - 1)}}{\xi \sqrt{\frac{1 + 6\xi}{7}} \left( \frac{c_0^*}{c_0} + \sqrt{\xi^{3/2}} \right)} \quad (C.47)$$

which in the limit  $(c_0^*/c_0) \rightarrow \infty$  vanishes.

Since, as was the case with the three-shock regime, according to Eqs. C.18b and C.19b, the shape  $(d\xi'/d\alpha) = 0$ , at  $\alpha = 0$ , the approximation, Eq. C.47, is expected to be valid for a considerable range of finite  $\alpha$ . This can be checked by computing  $\xi'$  near the transition angle,  $\alpha = \alpha_t$ .

#### C.4.2.2 Approximations Near $\alpha = \alpha_t$

Assume

$$\xi'(\alpha) = \xi'(\alpha_t) - \Delta\xi'_t = 1 - \Delta\xi'_t \quad (C.48)$$

and obtain by Eqs. C.18b and C.19b

$$\tan \delta = \tan \left( \epsilon + \frac{\psi}{\gamma_0(1+\psi^2)} \Delta\xi'_t \right) \quad (C.49)$$

but  $\tan \delta$  must be given also by Eq. C.38

$$\tan \delta = X_1[(\xi - 1) - \xi \Delta\xi'_t X_2] \quad (C.50)$$

where  $\Delta\xi'_t$  has been replaced by  $-\Delta\xi'_t$ , since in this regime,

$$\xi' \leq 1$$

Equating Eqs. C.49 and C.50 gives

$$\Delta\xi'_t = \frac{X_1(\xi - 1) - \tan \epsilon}{\xi X_1 X_2 + \frac{\psi \sec^2 \epsilon}{\gamma_0(1+\psi^2)}} \quad (C.51)$$

where  $X_1$  and  $X_2$  are given by Eq. C.38 and by Eq. C.18b. For  $\gamma_0 = 1.4$ ,

$$\epsilon = \alpha - \tan^{-1} \left\{ \frac{(6 + \xi)}{1 + 6\xi} \tan \alpha \right\}$$

and

$$\psi = \left[ \frac{-6(\xi - 1)}{7\xi} + \frac{(1 + 6\xi)^2}{7\xi(6 + \xi)} \cot^2 \alpha \right]^{1/2}$$

Again for  $\xi' = 1$ , i.e.,  $\Delta\xi'_t = 0$ , the equation

$$X_1(\xi - 1) = \tan \epsilon$$

is equivalent to the transition equation for  $\alpha = \alpha_t$ , Eq. C.9. Furthermore,  $\tan \epsilon$  must be identical with  $X_3$  for all  $\alpha$  and with  $\tan \delta$  for  $\alpha = \alpha_t$ .

#### C.5 NUMERICAL EXAMPLE: OXYGEN-NITROGEN AND NITROGEN-OXYGEN REGULAR REFRACTION

In order to illustrate the use of the approximation and to check on their accuracy, we reproduce two typical problems from reference 6. Shocks ranging from  $\xi = 1.11$  to 3.33 are traveling from oxygen into nitrogen, which results in a two-shock-rarefaction configuration for  $\alpha = 0$  and in the inverse problem; they travel from nitrogen into oxygen, which results in a three-shock regime for  $\alpha = 0$ . At the pertinent transition angles the regimes interchange.



The appropriate constants are as follows:

TABLE C.1—Basic Parameters of Chosen Refraction Problems

	$\gamma_0$	$\gamma_1$	$(c_0/c_0^*)$
Oxygen-nitrogen	1.4	1.4	0.9354
Nitrogen-oxygen	1.4	1.4	1.069

The numerical results are as follows:

TABLE C.2—Critical Angles

	$\xi$	$\alpha_t$ (deg)	$\alpha'_t$ (deg)	$\alpha_s$ (deg)	$\alpha_L$ (deg)
Oxygen-nitrogen	1.11	44.09	42.20	74.15	69.295
	2.0	49.43	36.81	65.46	69.295
	3.33	53.39	31.75	61.44	69.295
Nitrogen-oxygen	1.11	48.06	46.56	74.15	
	2.0	54.29	47.39	65.46	
	3.33	59.11	48.03	61.44	

TABLE C.3—The Reflected Shock,  $\xi'$ , at Head-on Reflection,  $\alpha = 0$

	$\xi$	$\Delta\xi'_0$	$\xi'_0$
Oxygen-nitrogen	1.11	0.00349	0.9965
	2.00	0.02186	0.9782
	3.33	0.03591	0.9641
Nitrogen-oxygen	1.11	0.003491	1.0035
	2.0	0.02189	1.022
	3.33	0.03600	1.036

TABLE C.4—Reflected Shock,  $\xi'$ , Before Transition,  $\alpha \leq \alpha_t$

Oxygen-nitrogen							
$\xi$	$\alpha$	$\psi$	$\epsilon$	$X_1$	$X_2$	$\Delta\xi'_t$	$\xi'$
1.11	40°	1.1465	2.11	0.3371	0.9530	0.000861	0.9992
2.0	40°	1.3095	12.7	0.2346	0.7847	0.0129	0.9871
3.33	40°	1.5086	19.55	0.1612	0.7242	0.0277	0.9723
Nitrogen-oxygen							
$\xi$	$\alpha$	$X_1$	$X_2$	$X_3$	$X_4$	$\Delta\xi'_t$	$\xi'$
1.11	40°	0.3218	0.9588	0.0368	-0.304	0.00162	1.0016
2.0	40°	0.2146	0.8000	0.2252	-0.239	0.0181	1.0181
3.33	55°	0.175	0.6900	0.415	-0.233	0.0142	1.0142

The relations for  $\xi'$  are shown on Figs. C.3 and C.4. Since it is known from theory that the slope near the origin is zero, it is felt that the few computed points are sufficient to draw the entire curves. Once  $\xi'$  is determined for all values of  $\alpha$ , the other unknown quantities  $\xi''$ ,  $\alpha'$ ,  $\alpha''$ , and  $\delta$  follow immediately from the formulae in Sec. C.4. In order to solve the cascade problem (Fig. C.1), of particular interest are  $\xi''$  and  $\alpha''$ , the transmitted shock, and transmitted angle, respectively,

TABLE C.5—Reflected Shock,  $\xi'$ , After Transition,  $\alpha \geq \alpha_t$

Oxygen-nitrogen							
$\xi$	$\alpha$	$X_1$	$X_2$	$X_3$	$X_4$	$\Delta\xi'_1$	$\xi'$
1.11	64°	0.1861	0.5056	0.0303	-0.4761	0.0165	1.0165
2.0	56°	0.2262	0.3573	0.2424	-0.4270	0.0275	1.0275
3.33	55°	0.1754	0.3127	0.4162	-0.3760	0.0123	1.0123
Nitrogen-oxygen							
$\xi$	$\alpha$	$\psi$	$\epsilon$	$X_1$	$X_2$	$\Delta\xi'_1$	$\xi'$
1.11	70°	0.2119	1.43	0.2896	0.8681	0.017	0.983
2.0	60°	0.2726	13.17	0.2442	0.6662	0.0197	0.9803
3.33	60°	0.2737	22.41	0.1780	0.6042	0.00518	0.9948

$$\xi'' = \xi\xi' \quad (C.52)$$

and

$$\alpha'' = \sin^{-1} \left\{ \frac{c_0^*}{c_0} \sin \alpha \left[ 1 + \frac{\Delta\xi'}{2(\xi + \lambda_1^2)} \right] \right\}$$

where  $\Delta\xi'$  is evaluated either near zero or near the transition angle. In general, the term  $\Delta\xi'/2(\xi + \lambda_1^2)$  is negligible and for practical purposes Snell's law holds during the entire regular refraction range

$$\alpha'' \approx \sin^{-1} \left( \frac{c_0^*}{c_0} \sin \alpha \right) \quad (C.53)$$

which is confirmed in Figs. C.5 and C.6.

## C.6 APPLICATION TO UPSHOT-KNOTHOLE (SHOT 9)

To illustrate a possible application of the above theory, consider the practical problem of a thermal layer in UPSHOT-KNOTHOLE, Shot 9, which extends roughly to about 2800 ft ground range from Ground Zero, as can be seen from the Mach stem trajectory, given in Fig. 2.13, p.33, reference 9. A graph of the time delay between the incident shock and the reflected shock plotted vs altitude, obtained from gages 14B10, 30 and 50 (p. 104 to 106, reference 10) is presented in Fig. C.7. This figure indicates the formation of a pseudo-Mach stem at roughly 3 ft elevation. It is believed that instead of a small Mach stem present, one deals here with a regular refraction regime where the incident shock refracts through a thermal layer before striking the ground as indicated in Fig. C.1.

The gradient in this thermal layer and its vertical extent are not known but some clue may be gained from Fig. 2.29, p. 52, reference 9, which gives for the 837-ft station an average sound velocity at 1480 ft/sec at the 3½ ft elevation, and 1150 ft/sec (i.e., standard sound velocity), at

the 10-ft elevation. Assuming, therefore, a constant thermal layer of  $3\frac{1}{2}$  ft height associated with the sound velocity  $c_0^* = 1480$  ft/sec ( $T = 320^\circ\text{F}$ ), one calculates the regular refraction quantities of Fig. C.1, and one can explain most measurements at the 837-ft station both at ground level and at the 10-ft elevation, namely, delay times, maximum and minimum pressure values, pressure wave shapes, and even the increase in dynamic pressure. Obviously, physically there must exist a variable vertical temperature gradient whose extent is difficult to define, but the following computation, assuming a constant layer, rough as it may be, tends to confirm the regular refraction trends and seems to indicate that the present pseudo-Mach stem, i.e., containing a single triple point, need not necessarily be assumed.

Consider Fig. C.8, where, from gage 14B10, p. 104, reference 10, at the 837-ft station at 10 ft elevation, the incidence pressure in the regular reflection would be 10.1 psi and for an incidence angle of 19 deg, one would obtain a reflected angle of 13 deg and a ground reflected pressure of 25.4 psi, which is 17 per cent higher than the measured value of 21.7 psi (gage 14B, p. 103, reference 10). Thus there is something wrong with this scheme which neglects the thermal layer.

Now, however, consider Fig. C.6. Here measured and computed values on the ground (see also reference 11) and at the 10-ft station are in remarkable agreement. At the ground station reflected pressure both initial and final values (after reflection off the interface) agree within  $\frac{1}{2}$  per cent, and at the 10-ft station the reflected pressure agrees within  $3\frac{1}{2}$  per cent and even the rarefaction wave trend is confirmed. This can better be studied from Figs. C.10 and C.11, which give a comparison of computed and measured wave shapes at the ground and at the 10-ft station. The measured values were obtained by tracing gages 14B and 14B10 (pp. 103 and 104, reference 10), and the theory can easily be modified by accounting for the measured finite frequency response of the gage, and the fact that there is not really a sharp temperature discontinuity in the physical situation. In any event, the peak values are in agreement.

As a final application of the above regular refraction theory, one could also explain the increase in dynamic pressures at 2100 ft as shown on Fig. 2.19, p. 39, reference 9, without assuming a Mach stem to be present at this distance. The ratio of drag pressures calculated by Mach theory to that of regular reflection theory, according to Fig. 2.19, reference 9, at the 2100-ft station, is roughly equal to 2. By applying regular refraction theory rather than regular reflection theory, the ratio of dynamic pressures is roughly 1.8. This increase is mainly due to the steepening of the angle due to the refraction in the thermal layer, since the dynamic pressure is proportional to  $\sin^2 \alpha$  where  $\alpha$  is the incidence angle with the solid ground, which is always larger than the incidence angle with the thermal layer.

#### REFERENCES

1. A. H. Taub, Refraction of Plane Shock Waves, Phys. Rev., 72: 51(1947).
2. J. von Neumann, Oblique Reflection of Shocks, Navy Dept., Bureau of Ordnance, Explosives Research Report No. 12 (1943).
3. R. G. Stoner, C. L. Woodbridge, and E. B. Davies, "Experimental Observation of the Interaction of Shock Waves at Boundaries Between Various Gases," Pennsylvania State College (1952).
4. R. G. Stoner and E. B. Davies, "Experimental Observation of the Interaction of Shock Waves at Boundaries Between Various Gases, II," Pennsylvania State College (1952).
5. H. Polachek and R. J. Seeger, On Shock Wave Phenomena; Refraction of Shock Waves at a Gaseous Interface, Naval Ordnance Laboratory Memorandum 9971 (1943).
6. H. Polachek and R. J. Seeger, On Shock Wave Phenomena; Refraction of Shock Waves at a Gaseous Interface, Phys. Rev., 84: 922(1951).
7. R. Sauer, "Introduction to Theoretical Gas Dynamics," J. W. Edwards Bros., Ann Arbor (1947).
8. A. Stodola, "Dampf Und Gasturbinen," second edition (1924).



9. Operation UPSHOT-KNOTHOLE, Preliminary Report, Summary Report of the Technical Director, Programs 1-9, June 1953, pp. 33, 39, and 52.
10. Operation UPSHOT-KNOTHOLE, Preliminary Report, Project 1.16 (SRI), Air Pressure vs. Time, Shots 3, 4, 9, 10, and 11, June 1953, pp. 103 to 106.
11. Armour Research Foundation, Planning Program for Air Force Structures Tests, Final Report, Part V, Regular Reflection on Cubical Structures, March 4, 1953, for Air Materiel Command, Contract No. AF33(038)-30029.

**UNCLASSIFIED**

~~SECRET RESTRICTED DATA~~

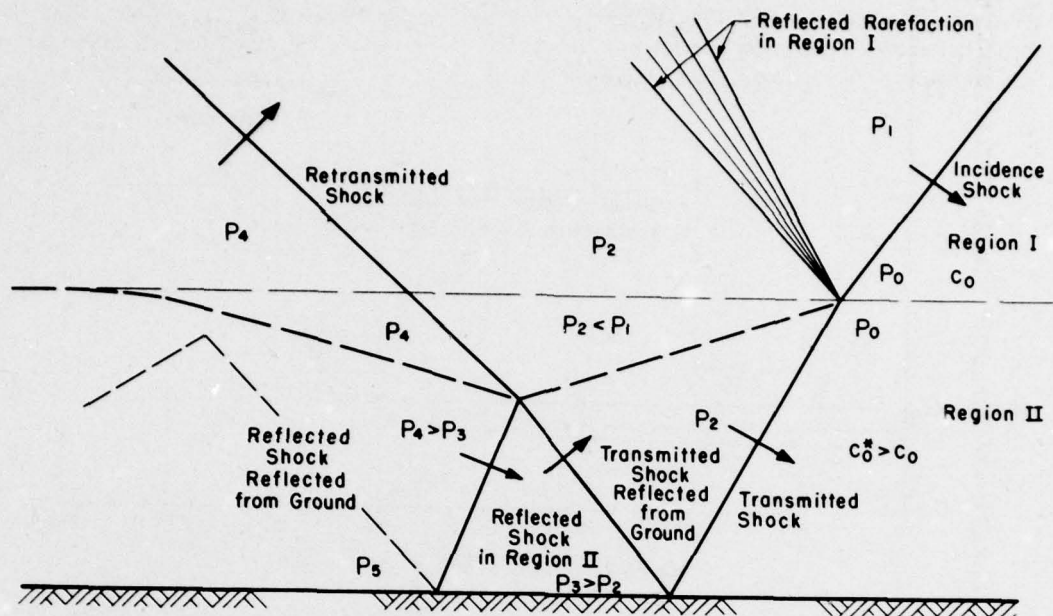


Fig. C.1—Cascade of regular refraction problems.

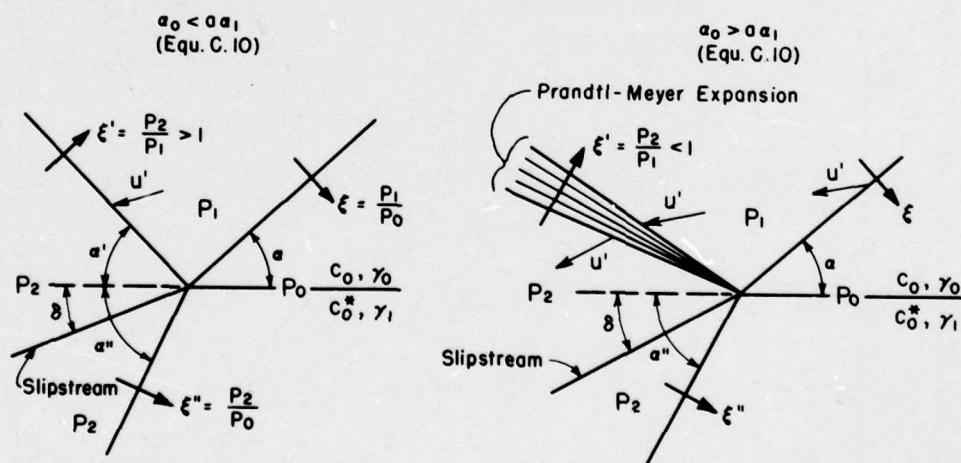


Fig. C.2—Three-shock and two-shock rarefaction regimes.

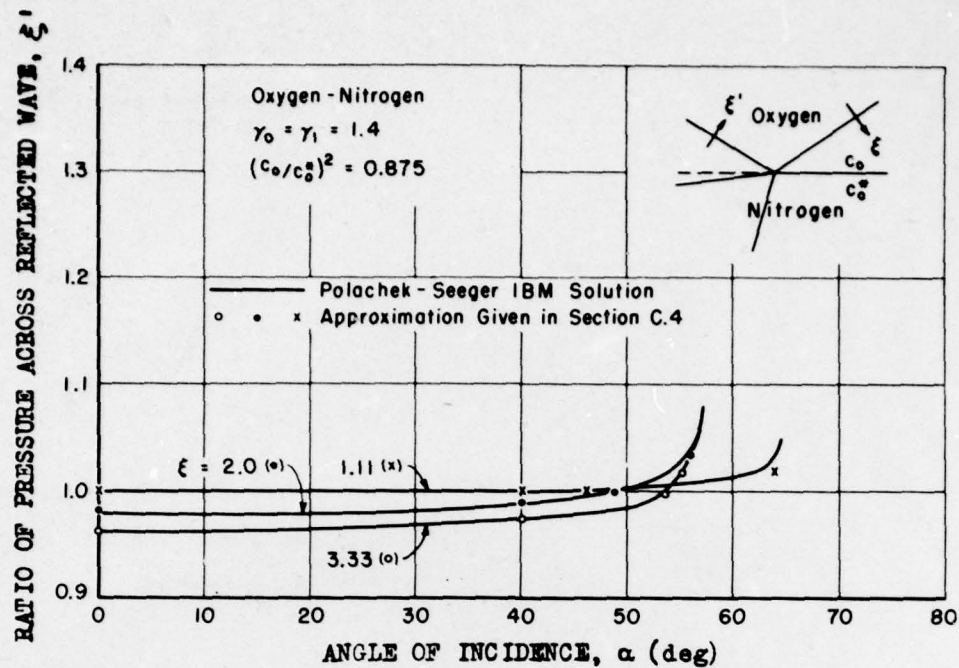


Fig. C.3—The oxygen-nitrogen regular refraction problem [ $\xi'$  vs  $\alpha$  for  $(c_o/c_o')^2 = 0.875$ ].

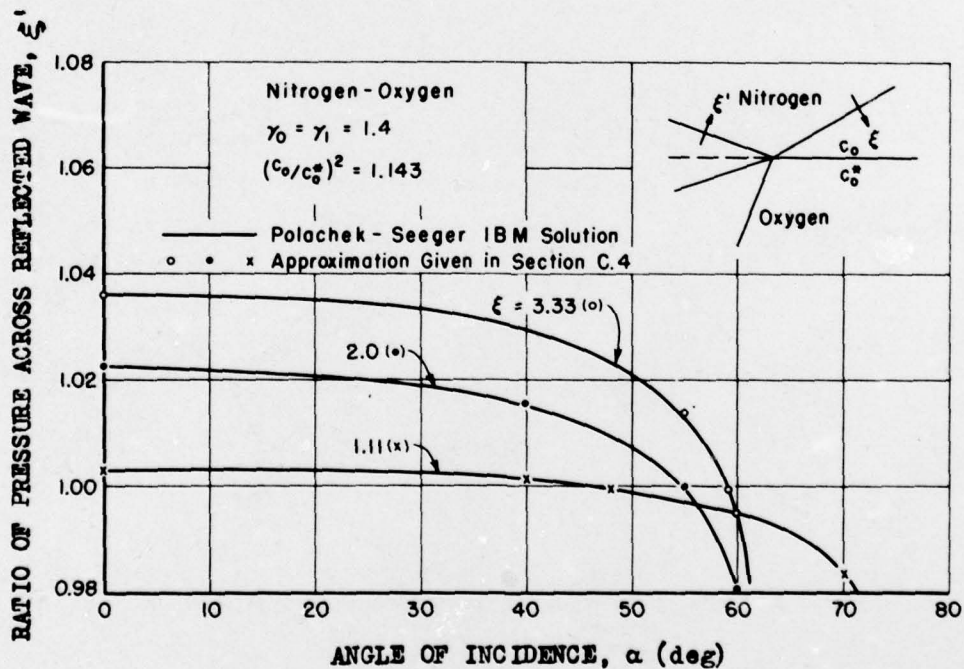


Fig. C.4—The oxygen-nitrogen regular refraction problem [ $\xi'$  vs  $\alpha$  for  $(c_o/c_o')^2 = 1.143$ ].



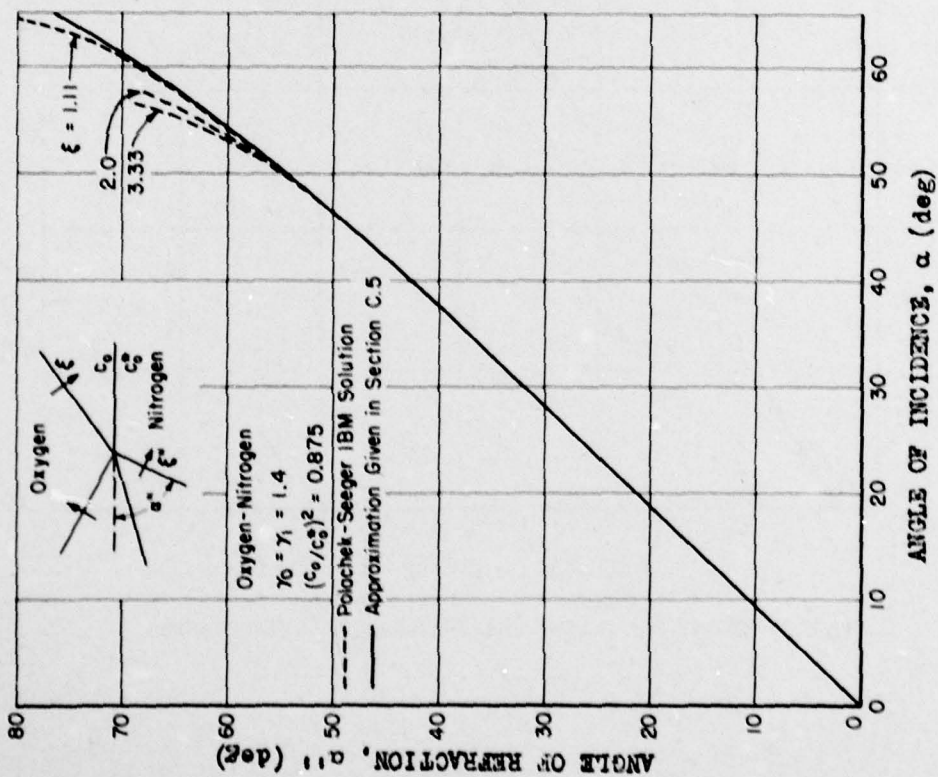


Fig. C.5—The oxygen-nitrogen regular refraction problem  
 $[\alpha'' \text{ vs } \alpha \text{ for } (c_0/c_0^0)^2 = 0.875]$ .

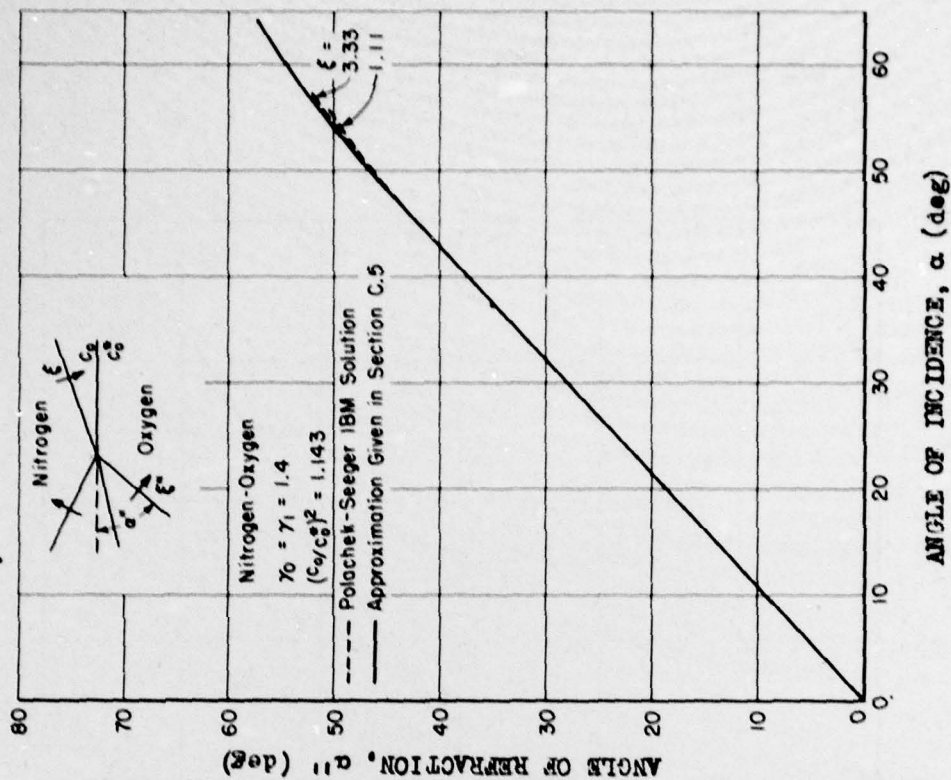


Fig. C.6—The oxygen-nitrogen regular refraction problem  
 $[\alpha'' \text{ vs } \alpha \text{ for } (c_0/c_0^0)^2 = 1.143]$ .

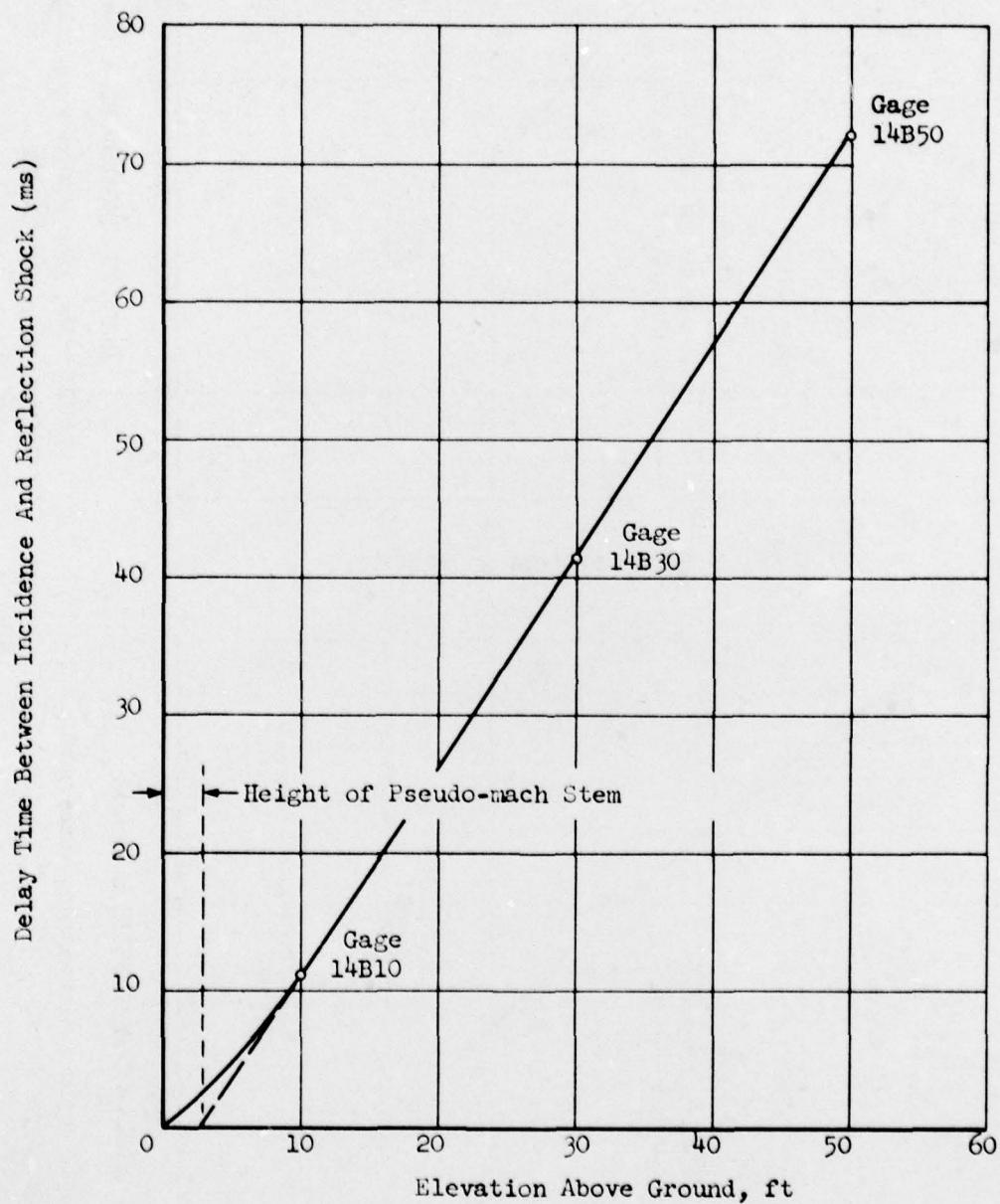


Fig. C.7—Delay Time as a Function of Elevation at 837 Foot Station.

The diagram shows a V-shaped structure with a horizontal base and two inclined sides. The left side is inclined at an angle  $\alpha = 13^\circ$  to the horizontal, and the right side is inclined at an angle  $\alpha = 19^\circ$ . A horizontal line with diagonal hatching is at the bottom. Two arrows point upwards from the base towards the vertex: one on the left side and one on the right side. On the left side, there is a label  $P_r = 25.4 \text{ psi}$  and  $\text{m.v.} = 21.7 \text{ psi}$ . On the right side, there is a label  $P_o = 12.9 \text{ psi}$  and  $\text{m.v.} = 12.9$ . In the upper left area, there is a label  $P = 10.1 \text{ psi}$  and  $\text{m.v.} = 10.1$ . At the top left, there is a label  $\text{m.v. Designates measured values}$ . An arrow points from this label towards the center of the diagram.

The diagram illustrates the reflection of a shock wave off a corner. Key parameters and values are as follows:

- Initial Shock (Left):**
  - Pressure: 23.7 psi
  - Mass Velocity (m.v.): 24.5
  - Angle:  $\alpha = 13.1^\circ$
- First Reflection (Top):**
  - Delay Time: 12 ms
  - Mass Velocity (m.v.): 11
  - Pressure: 8.7 psi
  - Mass Velocity (m.v.): 6
  - Distance: 32.5'
- Second Reflection (Right):**
  - Pressure: 10.1 psi
  - Mass Velocity (m.v.): 10.1
  - Pressure:  $P_o = 12.9$  psi
  - Mass Velocity (m.v.):  $P_o = 12.9$
  - Angle:  $\alpha = 19^\circ$
- Third Reflection (Bottom):**
  - Pressure: 23.5 psi
  - Mass Velocity (m.v.): 23.6
  - Angle:  $\alpha = 13.1^\circ$
  - Distance:  $k = 13'$
  - Angle:  $26^\circ$
  - Angle:  $7^\circ$
  - Angle:  $34^\circ$
  - Angle:  $27.2^\circ$
  - Angle:  $17.7^\circ$
  - Pressure: 8.7 psi
  - Mass Velocity (m.v.): 8.7
  - Angle:  $135.2^\circ$
  - Angle:  $\alpha^* = 20.1^\circ$
  - Angle:  $\alpha^* = 24.7^\circ$
  - Distance: 3.5'
  - Pressure:  $P_o = 12.9$  psi
  - Mass Velocity (m.v.): 12.9
- Other Parameters:**
  - Distance: 6.5'
  - Distance: 32.5'
  - Angle:  $\alpha = 13.1^\circ$
  - Angle:  $\alpha = 19^\circ$
  - Angle:  $26^\circ$
  - Angle:  $7^\circ$
  - Angle:  $34^\circ$
  - Angle:  $27.2^\circ$
  - Angle:  $17.7^\circ$
  - Angle:  $135.2^\circ$
  - Angle:  $\alpha^* = 20.1^\circ$
  - Angle:  $\alpha^* = 24.7^\circ$
  - Distance: 3.5'
  - Pressure:  $P_o = 12.9$  psi
  - Mass Velocity (m.v.): 12.9

**UNCLASSIFIED**



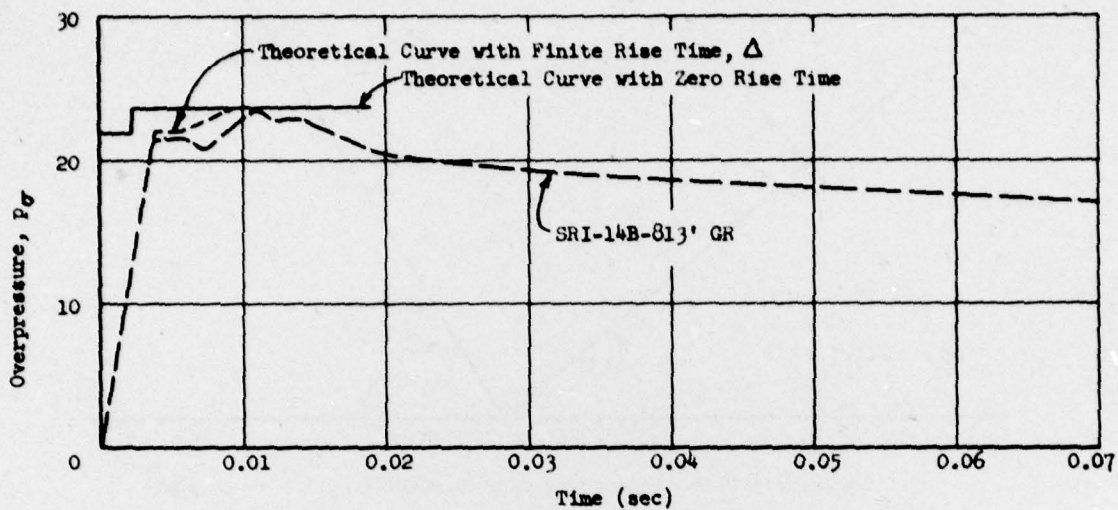


Fig. C.10 — Comparison of Measured and Calculated Wave Shapes at 814 Foot Station, Ground Level.

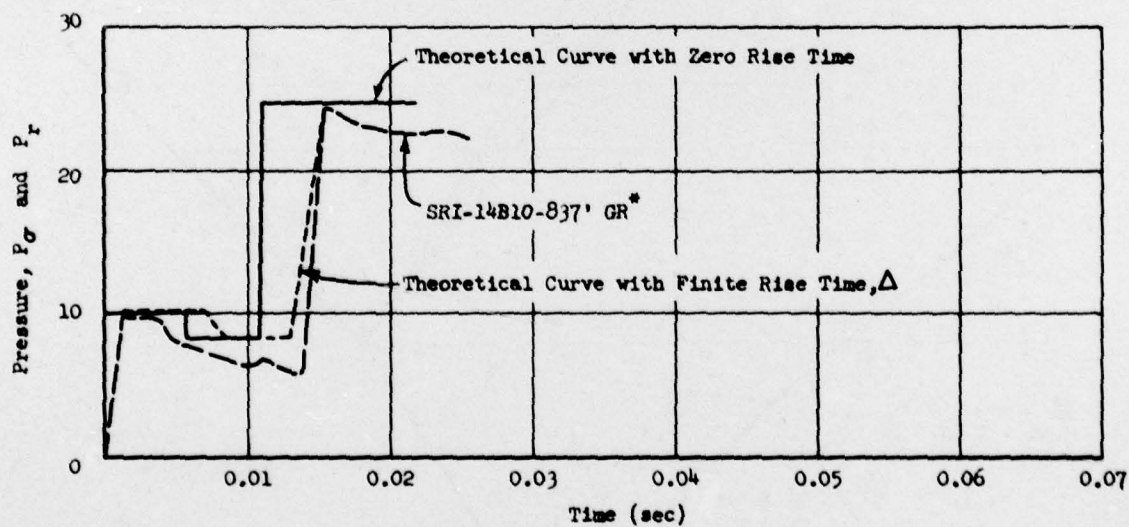


Fig. C.11 — Comparison of Measured and Calculated Wave Shapes at 837 Foot Station, 10 Foot Elevation.

**UNCLASSIFIED**

## APPENDIX D

### SYMBOLS

A list of the symbols used in Chaps. 1 through 6 is given here.

$a_1, a_2, a_3, \dots$ , denotes gages  $p_1, p_2, p_3$ , etc., on Structure 3.1a,  $\dots$ .

3.1aF, 3.1aT, 3.1aR refers to surfaces on structures 3.1a,  $\dots$ , front, top, or rear.

$b_0 = b_0(t)$ , pretest prediction of average pressure on rear surface.

$b_{os} = b_{os}(t)$ , pretest prediction for average pressure on rear surface during pseudo-steady-state phase of loading.

$c$ , exponential coefficient determining wave shape.

$c_1$ , sound velocity behind the reflected shock.

$C_{db}$ , drag coefficient on rear surface.

$C_d$ , net drag pressure coefficient (net pressure divided by drag pressure).

$\bar{C}_d$ , an average drag coefficient in terms of measured and predicted drag impulses. Coefficients are averaged for preserving the measured impulse.

$C_{df}$ , drag coefficient on front surface equal to the difference in surface and side-on pressure divided by drag pressure.

$C_{dr}$ , drag coefficient on roof (top).

$C_{ds}$ , drag coefficient on side surfaces.

$c_0$ , sound velocity in air at standard conditions.

$c_p$ , specific heat of air at constant pressure.

$c_t$ , specific heat of air at constant temperature.

$c_v$ , specific heat of air at constant volume.

$d$ , length or thickness of thin walls.

$f_0 = f_0(t)$ , pretest prediction of average pressure on front surface.

$f_{os} = f_{os}(t)$ , pretest prediction of average pressure on front surface during pseudo-steady-state phase of loading.

$H$ , height.

$I_{DF}$ , diffraction impulse.

$I_{DFC}$ , computed diffraction impulse.

$I_{DFM}$ , measured diffraction impulse.

$I_{p\sigma}$ , impulse of side-on pressure curve.

$I_{p\sigma}/p_{\sigma}(0) \cdot t_0$ , reduced side-on impulse.

$I_{p_0 p_d(0)}/I_{DGP_0(0)}$ , ratio of drag impulse to side on impulse.

$I_{DG}$ , drag impulse.

$I_{DGC}$ , computed drag impulse.

$I_{DG}/p_d(0) \cdot t_0$ , reduced drag impulse.

$I_{TC}$ , computed total impulse.

$I_{TM}$ , measured total impulse.

$L$ , length of structure in direction of flow.

$l_0 = l_0(t)$ , pretest prediction for average pressure on underside.

361  
~~SECRET~~ UNCLASSIFIED

$l_{os} = l_{os}(t)$ , pretest prediction for average pressure on underside during pseudo-steady-state phase of loading.

$n$  = build-up coefficient on rear surface, i.e., coefficient of  $S/U$ .

$P_0$ , atmospheric pressure (standard pressure at sea level is 14.7 psi; standard pressure at test site is 13.2 psi).

$P_1$ , total absolute pressure.

$P_1$ , peak pressure in a channel.

$P_2$ , absolute pressure behind rarefaction wave.

$p_o, p_o(t)$ , side-on pressure.

$p_o(0)$ , value of side-on pressure at time  $t = 0$ .

$p_d, p_d(t)$ , free-stream dynamic head or free stream drag pressure.

$P_m$ , peak underside pressure on elevated structures.

$P_r$ , absolute reflected pressure.

$p_r$ , instantaneous reflected pressure (normal).

$p_{rc}$ , instantaneous reflected pressure (re-entrant corner).

$p_{ro}$ , instantaneous reflected pressure (oblique).

$p_o^*$ , local incident side-on pressure.

$Q$ , oblique reflected pressure on oblique surfaces.

$q$ , measured dynamic pressure.

$r_i = r_i(t)$ , pretest prediction of average pressure on underside of eaves.

$r_{is} = r_{is}(t)$ , pretest prediction of average pressure on underside of eaves during pseudo-steady-state phase of loading.

$r_o = r_o(t)$ , pretest prediction of average pressure on roof (top surfaces).

$r_{os} = r_{os}(t)$ , pretest prediction of average pressure on roof during pseudo-steady-state phase of loading.

$s = s(t)$ , average pressure on side surfaces.

$S$ , clearing or build-up distance on front or rear surfaces.

$S^*$ , clearing or build-up distance on front or rear surfaces of elevated items.

$t$ , time.

$t_a$ , build-up time on front.

$t_0$ , duration of first positive phase.

$t_{rise}$ , finite rise time of a compression wave.

$t^*$ , duration of diffraction phase.

$U$ , velocity of shock front.

$u$ , flow velocity behind shock front.

$u_1$ , particle velocity behind the transmitted shock in the narrow portion of a restricted channel.

$W$ , width.

$W^1, W_1, W_2, W_3$ , dimensions on special Structure 3.1q.

$\alpha$ , angle at which incident shock wave strikes ground.

$\alpha_e$ , limiting angle of incidence for regular reflection.

$\beta$  and  $\gamma$ , quantities used to compute diffraction impulse graphically.

$\Delta H$ , elevation of structure above ground.

$\Delta$ , distance between pairs of thin walls.

$\theta$ , angle of surface orientation, i.e., angle between shock front and structure surface (in a horizontal plane).

$\xi$ , shock strength.

$\xi_1$ , transmitted shock strength in narrow portion of a restricted channel.

$\xi_2$ , reflected shock strength.

$\xi_r$ , shock strength of shock reflected in upstream direction away from narrow portion of a restricted channel.

$\xi^*$ , local incident shock strength.

$\rho$ , density.

$\rho(t)$ , density as a function of time  $t$ .



V, vortex activity.

9BA, BB, FE, etc., denote free stream gage reading, Shot 9.

10BA, BB, BE, etc., denote free stream reading, Shot 10.

F, F(t), measured average pressure on front surface.

B, B(t), measured average on back (rear) surface.

R, R(t), measured average pressure on roof (top) surface.

N, N(t), net horizontal load obtained from measured average pressures on front and back surfaces.

## BIBLIOGRAPHY

Armour Research Foundation, "Ad Hoc Analytical Services," Phase Report No. III, Test VI, Study of Blast Effects in the Regular Reflection Region for Physical Vulnerability Division, Contract No. AF33(600)-25583.

Armour Research Foundation, Blast Loading and Response of Structures, Appendix I to Operation GREENHOUSE, Project 3.3, Vol I for Air Materiel Command, Contract No. AF33(038)-3761, Report WT-87 (1952).

Armour Research Foundation, "Compendium on Air Blast Effects, Compendium Handbook for Director of Intelligence Headquarters, USAF, Contract No. AF33(600)-25734 (1955).

Armour Research Foundation, Planning Program for Air Force Structures Tests, Final Report, Parts I, IV, and V for Air Materiel Command, Contract No. AF33(038)-30029 (1953).

Armour Research Foundation, Study of the Effect of Orientation on Dynamic Loading and Response of Structures. Final Report, Air Materiel Command, Contract No. AF33(616)-166 (1955).

W. Bleakney, The Diffraction of Shock Waves Around Obstacles and the Resulting Transient Loading of Structures, Technical Report II-3, Princeton University Physics Department, Washington, D. C., AFSWP, March 1950.

Bleakney, White, et al, Shock Loading of Rectangular Structures, Technical Report II-11, Princeton University Physics Department, Washington, D. C., AFSWP, January 1952.

Chien, Feng, Wang, Siao, "Wind Tunnel Studies of Pressure Distribution on Elementary Building Forms," Iowa Institute of Hydraulic Research, University of Iowa, ONR N8 onr-500, 1951.

F. W. Geiger and C. W. Mautz, "The Shock Tube as an Instrument for the Investigation of Transonic and Supersonic Flow Patterns," Engineering Research Institute, University of Michigan, June 1949.

J. O. V. Irminger and C. Nøkkentved, "Wind Pressure on Buildings: Experimental Researches" (Second Series), Copenhagen, Ingeniørvidenskabelige Skrifter, 1936.

M. L. Merritt, Some Tests of the Diffraction of Blast Waves, Sandia Corporation, SC-1803(TR), June 1951.

J. von Neumann, Oblique Reflection of Shocks, Navy Dept., Bureau of Ordnance, Explosives Research Report No. 12 (1943).

Operation UPSHOT-KNOTHOLE, Preliminary Report, Project 3.1 Tests on the Loading of Building Shapes, (1953).

Operation UPSHOT-KNOTHOLE, Preliminary Report, Summary Report of the Technical Director, Programs 1-9, Report WT-782 (1953).

Operation UPSHOT-KNOTHOLE, Preliminary Report, Project 1.1.b, SRI, Air Pressure vs Time, Shots 3, 4, 9, 10 and 11 (1953).

Operation UPSHOT-KNOTHOLE, Project 1.1.d, Dynamic Pressure vs Time and Supporting Air Blast Measurements, Sandia Corporation, Report WT-714 (1954).

H. Polachek and R. J. Seeger, On Shock Wave Phenomena; Refraction of Shock Waves at a Gaseous Interface, Naval Ordnance Laboratory Memorandum 9971 (1943).

H. Polachek and R. J. Seeger, On Shock Wave Phenomena; Refraction of Shock Waves at a Gaseous Interface, Phys. Rev. 84:922 (1951).

F. B. Porzel, Height of Burst for Atomic Bombs, Los Alamos Scientific Laboratories, LA-1664, 1665, 1406 (1955).

F. B. Porzel, Theoretical Height of Burst Curves, Los Alamos Scientific Laboratories, J-19704, J-17837, J-19764 (1953).

Sandia Corporation, Prediction of Incident Pressure-time Curves for Nuclear Explosions, Ref. Sym. 5112-(82) (1954).

R. Sauer, "Introduction to Theoretical Gas Dynamics," J. W. Edwards Bros., Ann Arbor (1947).

A. Stodola, "Dampf Und Gasturbien," second edition (1924).

R. G. Stoner and E. B. Davies, "Experimental Observation of the Interaction of Shock Waves at Boundaries between Various Gases II," Pennsylvania State College (1952).

R. G. Stoner, C. L. Woodbridge, and E. B. Davies, "Experimental Observation of the Interaction of Shock Waves at Boundaries between Various Gases," Pennsylvania State College (1952).

A. H. Taub, Refraction of Plane Shock Waves, Phys. Rev., 72, 51 (1947).

**UNCLASSIFIED**

365-366

~~SECRET RESTRICTED DATA~~

**UNCLASSIFIED**



## DISTRIBUTION

*Military Distribution Categories 5-21 and 5-60*

### ARMY ACTIVITIES

Asst. Chief of Staff, G-3, D/A, Washington 25, D.C. ATTN: Dep. CofS, G-3 (RR&SW)	1
Chief of Research and Development, D/A, Washington 25, D.C. ATTN: Special Weapons and Air Defense Division	2
Chief of Ordnance, D/A, Washington 25, D.C. ATTN: ORDTX-AP	3
Chief Signal Officer, D/A, P&O Division, Washington 25, D.C. ATTN: SIGOP	4-6
The Surgeon General, D/A, Washington 25, D.C. ATTN: Chief, R&D Division	7
Chief Chemical Officer, D/A, Washington 25, D.C.	8-9
The Quartermaster General, D/A, Washington 25, D.C. ATTN: Research and Development Div.	10
Chief of Engineers, D/A, Washington 25, D.C. ATTN: ENGNB	11-15
Chief of Transportation, Military Planning and Intelligence Div., Washington 25, D.C.	16
Commanding General, Continental Army Command, Ft. Monroe, Va.	17-19
President, Board #1, Headquarters, Continental Army Command, Ft. Sill, Okla.	20
President, Board #2, Headquarters, Continental Army Command, Ft. Knox, Ky.	21
President, Board #3, Headquarters, Continental Army Command, Ft. Benning, Ga.	22
President, Board #4, Headquarters, Continental Army Command, Ft. Bliss, Tex.	23
Commanding General, U.S. Army Caribbean, Ft. Amador, C.Z. ATTN: Cml. Off.	24
Commander-in-Chief, European Command, APO 128, c/o PM, New York, N.Y.	25
Commander-in-Chief, Far East Command, APO 500, c/o PM, San Francisco, Calif. ATTN: ACofS, J-3	26-27
Commanding General, U.S. Army Europe, APO 403, c/o PM, New York, N.Y. ATTN: OPOT Div., Combat Dev. Br.	28-29
Commandant, Command and General Staff College, Ft. Leavenworth, Kan. ATTN: ALLLS(AS)	30-31
Commandant, The Artillery and Guided Missile School, Ft. Sill, Okla.	32
Secretary, The Antiaircraft Artillery and Guided Missile School, Ft. Bliss, Texas. ATTN: Maj. George L. Alexander, Dept. of Tactics and Combined Arms	33
Commanding General, Army Medical Service School, Brooke Army Medical Center, Ft. Sam Houston, Tex.	34
Director, Special Weapons Development Office, Headquarters, CONARC, Ft. Bliss, Tex. ATTN: Lt. Arthur Jaskierny	35
Commandant, Walter Reed Army Institute of Research, Walter Reed Army Medical Center, Washington 25, D.C.	36
Superintendent, U.S. Military Academy, West Point, N.Y. ATTN: Prof. of Ordnance	37
Commandant, Chemical Corps School, Chemical Corps Training Command, Ft. McClellan, Ala.	38
Commanding General, Research and Engineering Command, Army Chemical Center, Md. ATTN: Deputy for RW and Non-Toxic Material	39
Commanding General, Aberdeen Proving Grounds, Md. (inner envelope) ATTN: RD Control Officer (for Director, Ballistics Research Laboratory)	40-41
Commanding General, The Engineer Center, Ft. Belvoir, Va. ATTN: Asst. Commandant, Engineer School	42-44

Commanding Officer, Engineer Research and Development Laboratory, Ft. Belvoir, Va. ATTN: Chief, Technical Intelligence Branch	45
Commanding Officer, Picatinny Arsenal, Dover, N.J. ATTN: ORDBB-TK	46
Commanding Officer, Army Medical Research Laboratory, Ft. Knox, Ky.	47
Commanding Officer, Chemical Corps Chemical and Radiological Laboratory, Army Chemical Center, Md. ATTN: Tech. Library	48-49
Commanding Officer, Transportation R&D Station, Ft. Eustis, Va.	50
Director, Technical Documents Center, Evans Signal Laboratory, Belmar, N.J.	51
Director, Waterways Experiment Station, PO Box 631, Vicksburg, Miss. ATTN: Library	52
Director, Armed Forces Institute of Pathology, Walter Reed Army Medical Center, 6825 16th Street, N.W., Washington 25, D.C.	53
Director, Operations Research Office, Johns Hopkins University, 7100 Connecticut Ave., Chevy Chase, Md. Washington 15, D.C.	54
Commanding General, Quartermaster Research and Development Command. Quartermaster Research and Development Center, Natick, Mass. ATTN: CBR Liaison Officer	55-56
Technical Information Extension, Oak Ridge, Tenn. (Surplus)	57-63
 NAVY ACTIVITIES	
Chief of Naval Operations, D/N, Washington 25, D.C. ATTN: OP-36	64-65
Chief of Naval Operations, D/N, Washington 25, D.C. ATTN: OP-03EG	66
Director of Naval Intelligence, D/N, Washington 25, D.C. ATTN: OP-922V	67
Chief, Bureau of Medicine and Surgery, D/N, Washington 25, D.C. ATTN: Special Weapons Defense Div.	68
Chief, Bureau of Ordnance, D/N, Washington 25, D.C.	69
Chief, Bureau of Ships, D/N, Washington 25, D.C. ATTN: Code 348	70
Chief, Bureau of Yards and Docks, D/N, Washington 25, D.C. ATTN: D-440	71
Chief, Bureau of Supplies and Accounts, D/N, Washington 25, D.C.	72
Chief, Bureau of Aeronautics, D/N, Washington 25, D.C.	73-74
Chief of Naval Research, Department of the Navy, Washington 25, D.C. ATTN: Code 811	75
Commander-in-Chief, U.S. Pacific Fleet, Fleet Post Office, San Francisco, Calif.	76
Commander-in-Chief, U.S. Atlantic Fleet, U.S. Naval Base, Norfolk 11, Va.	77
Commandant, U.S. Marine Corps, Washington 25, D.C. ATTN: Code A03H	78-81
President, U.S. Naval War College, Newport, R.I.	82
Superintendent, U.S. Naval Postgraduate School, Monterey, Calif.	83
Commanding Officer, U.S. Naval Schools Command, U.S. Naval Station, Treasure Island, San Francisco, Calif.	84
Commanding Officer, U.S. Fleet Training Center, Naval Base, Norfolk 11, Va. ATTN: Special Weapons School	85
Commanding Officer, U.S. Fleet Training Center, Naval Station, San Diego 36, Calif. ATTN: (SPWP School)	86-87
Commanding Officer, Air Development Squadron 5, VX-5, U.S. Naval Air Station, Moffett Field, Calif.	88
Commanding Officer, U.S. Naval Damage Control Training Center, Naval Base, Philadelphia 12, Pa. ATTN: ABC Defense Course	89
Commanding Officer, U.S. Naval Unit, Chemical Corps School, Army Chemical Training Center, Ft. McClellan, Ala.	90
Commander, U.S. Naval Ordnance Laboratory, Silver Spring 19, Md. ATTN: EE	91
Commander, U.S. Naval Ordnance Laboratory, Silver Spring 19, Md. ATTN: EH	92
Commander, U.S. Naval Ordnance Laboratory, Silver Spring 19, Md. ATTN: R	93
Commander, U.S. Naval Ordnance Test Station, Inyokern, China Lake, Calif.	94
Officer-in-Charge, U.S. Naval Civil Engineering Res. and Evaluation Lab., U.S. Naval Construction Battalion Center, Port Hueneme, Calif. ATTN: Code 753	95
Commanding Officer, U.S. Naval Medical Research Inst., National Naval Medical Center, Bethesda 14, Md.	96
Director, Naval Air Experimental Station, Air Material Center, U.S. Naval Base, Philadelphia, Penn.	97



Director, U.S. Naval Research Laboratory, Washington 25, D.C. ATTN: Code 2029	98
Commanding Officer and Director, U.S. Navy Electronics Laboratory, San Diego 52, Calif. ATTN: Code 4223	99
Commanding Officer, U.S. Naval Radiological Defense Laboratory, San Francisco 24, Calif. ATTN: Technical Information Division	100-101
Commanding Officer and Director, David W. Taylor Model Basin, Washington 7, D.C. ATTN: Library	102-103
Commander, U.S. Naval Air Development Center, Johnsville, Pa.	104
Director, Office of Naval Research Branch Office, 1000 Geary St., San Francisco, Calif.	105
Technical Information Extension, Oak Ridge, Tenn. (Surplus)	106-112
 <b>AIR FORCE ACTIVITIES</b>	
Asst. for Atomic Energy, Headquarters, USAF, Washington 25, D.C. ATTN: DCS/O	113
Director of Operations, Headquarters, USAF, Washington 25, D.C. ATTN: Operations Analysis	114
Director of Plans, Headquarters, USAF, Washington 25, D.C. ATTN: War Plans Div.	115
Director of Research and Development, Headquarters, USAF, Washington 25, D.C. ATTN: Combat Components Div.	116
Director of Intelligence, Headquarters, USAF, Washington 25, D.C. ATTN: AFOIN-IB2	117-118
The Surgeon General, Headquarters, USAF, Washington 25, D.C. ATTN: Bio. Def. Br., Pre. Med. Div.	119
Deputy Chief of Staff, Intelligence, Headquarters, U.S. Air Forces Europe, APO 633, c/o PM, New York, N.Y. ATTN: Directorate of Air Targets	120
Commander, 497th Reconnaissance Technical Squadron (Augmented), APO 633, c/o PM, New York, N.Y.	121
Commander, Far East Air Forces, APO 925, c/o PM, San Francisco, Calif.	122
Commander-in-Chief, Strategic Air Command, Offutt Air Force Base, Omaha, Nebraska. ATTN: Special Weapons Branch, Inspector Div., Inspector General	123
Commander, Tactical Air Command, Langley AFB, Va. ATTN: Documents Security Branch	124
Commander, Air Defense Command, Ent AFB, Colo.	125
Commander, Wright Air Development Center, Wright-Patterson AFB, Dayton, O. ATTN: WCRRN, Blast Effects Research	126-127
Commander, Air Training Command, Scott AFB, Belleville, Ill. ATTN: DCS/O GTP	128
Assistant Chief of Staff, Installations, Headquarters, USAF, Washington 25, D.C. ATTN: AFCIE-E	129
Commander, Air Research and Development Command, PO Box 1395, Baltimore, Md. ATTN: RDDN	130
Commander, Air Proving Ground Command, Eglin AFB, Fla. ATTN: Adj./Tech. Report Branch	131
Director, Air University Library, Maxwell AFB, Ala.	132-133
Commander, Flying Training Air Force, Waco, Tex. ATTN: Director of Observer Training	134-141
Commander, Crew Training Air Force, Randolph Field, Tex. ATTN: 2GTS, DCS/O	142
Commander, Headquarters, Technical Training Air Force, Gulfport, Miss. ATTN: TA&D	143
Commandant, Air Force School of Aviation Medicine, Randolph AFB, Tex.	144-145
Commander, Wright Air Development Center, Wright-Patterson AFB, Dayton, O. ATTN: WCOSI	146-151
Commander, Air Force Cambridge Research Center, LG Hanscom Field, Bedford, Mass. ATTN: CRQST-2	152-153
Commander, Air Force Special Weapons Center, Kirtland AFB, N. Mex. ATTN: Library	154-156
Commandant, USAF Institute of Technology, Wright-Patterson AFB, Dayton, O. ATTN: Resident College	157
Commander, Lowry AFB, Denver, Colo. ATTN: Department of Armament Training	158
Commander, 1009th Special Weapons Squadron, Headquarters, USAF, Washington 25, D.C.	159



**UNCLASSIFIED**

**RECEIVED**

The RAND Corporation, 1700 Main Street, Santa Monica, Calif.

ATTN: Nuclear Energy Division

160-161

Commander, Second Air Force, Barksdale AFB, Louisiana. ATTN: Operations Analysis Office

162

Commander, Eighth Air Force, Westover AFB, Mass. ATTN: Operations Analysis Office

163

Commander, Fifteenth Air Force, March AFB, Calif. ATTN: Operations Analysis Office

164

Technical Information Extension, Oak Ridge, Tenn. (Surplus)

165-171

#### OTHER DEPARTMENT OF DEFENSE ACTIVITIES

Asst. Secretary of Defense, Research and Development, D/D, Washington 25, D.C. ATTN: Tech. Library

172

U.S. Documents Officer, Office of the U.S. National Military Representative, SHAPE, APO 55, New York, N.Y.

173

Director, Weapons Systems Evaluation Group, OSD, Rm 2E1006, Pentagon, Washington 25, D.C.

174

Armed Services Explosives Safety Board, D/D, Building T-7, Gravelly Point, Washington 25, D.C.

175

Commandant, Armed Forces Staff College, Norfolk 11, Va. ATTN: Secretary Commanding General, Field Command, Armed Forces Special Weapons Project, PO Box 5100, Albuquerque, N. Mex.

176

Commanding General, Field Command, Armed Forces, Special Weapons Project, PO Box 5100, Albuquerque, N. Mex. ATTN: Technical Training Group

177-182

Chief, Armed Forces Special Weapons Project, Washington 25, D.C. ATTN: Documents Library Branch

183-184

Office of the Technical Director, Directorate of Effects Tests, Field Command, AFSWP, PO Box 577, Menlo Park, Calif. ATTN: Dr. E. B. Doll

185-193

Technical Information Extension, Oak Ridge, Tenn. (Surplus)

194

195-201

#### ATOMIC ENERGY COMMISSION ACTIVITIES

U.S. Atomic Energy Commission, Classified Technical Library, 1901 Constitution Ave., Washington 25, D.C. ATTN: Mrs. J. M. O'Leary (For DMA)

202-204

Los Alamos Scientific Laboratory, Report Library, PO Box 1663, Los Alamos, N. Mex. ATTN: Helen Redman

205-206

Sandia Corporation, Classified Document Division, Sandia Base, Albuquerque, N. Mex. ATTN: Martin Lucero

207-211

University of California Radiation Laboratory, PO Box 808, Livermore, Calif. ATTN: Margaret Edlund

212-214

Weapon Data Section, Technical Information Extension, Oak Ridge, Tenn.

215

Technical Information Extension, Oak Ridge, Tenn. (Surplus)

216-275

**RECEIVED**

**UNCLASSIFIED**